Time Dependent CP Asymmetries and Branching Ratio Measurements in Charmless Three Body B Decays at BABAR

Emanuele Di Marco

SLAC-R-864

Prepared for the Department of Energy
under contract number DE-AC02-76SF00515

Printed in the United States of America. Available from the National Technical Information Service, U.S. Department of Commerce, 5285 Port Royal Road, Springfield, VA 22161.

This document, and the material and data contained therein, was developed under sponsorship of the United States Government. Neither the United States nor the Department of Energy, nor the Leland Stanford Junior University, nor their employees, nor their respective contractors, subcontractors, or their employees, makes an warranty, express or implied, or assumes any liability of responsibility for accuracy, completeness or usefulness of any information, apparatus, product or process disclosed, or represents that its use will not infringe privately owned rights. Mention of any product, its manufacturer, or suppliers shall not, nor is it intended to, imply approval, disapproval, or fitness of any particular use. A royalty-free, nonexclusive right to use and disseminate same of whatsoever, is expressly reserved to the United States and the University.

Università degli Studi di Roma "La Sapienza"

Time dependent *CP* asymmetries and branching ratio measurements in charmless three body *B* decays at *BABAR*

SLAC-REP-864

Thesis submitted by

Emanuele Di Marco

in partial fulfillment of the requirements
for the degree of Doctor Philosophiæ
May/2007

Advisors:
Prof. Fernando Ferroni

Dott. Gianluca Cavoto

Work supported by Department of Energy contract DE-AC02-76SF00515

Stanford Linear Accelerator Center, 2575 Sand Hill Road Menlo Park, CA 94025

II

Contents

A Eugenio Leonori

e ai minatori della Miniera di Cabernardi (AN)

Introduction

The existing theory of fundamental sub-atomic particle interactions (the Standard Model) accounts for a difference in the interactions between matter and anti-matter through a phenomenon known as "CP violation". From this model we can derive how such a difference leads to the dominance of matter in the Universe. From experiments of the past and, with larger accuracy from modern experiments, such as the B-factories, this difference has been found to be smaller, by orders of magnitude, than the observed matter asymmetry in the Universe. This is one of the most evident inconsistencies of the Standard Model in describing the fundamental laws that lead to the actual Universe.

Though most of the experimental measurements of the properties of the sub-atomic particles has precisely agreed with Standard Model predictions, a limitation of this model's construction is that it is not the fundamental theory, but is rather what is known as an "effective" theory describing phenomena to certain distance (or, equivalently, energy) scale. The physics of smaller distance (or higher energy) processes are obscured in parameters which must be measured. What's more, we know that not only the Standard Model is incomplete, but that more importantly, there is physics beyond it which necessarily must explain not understood phenomena.

The main road to go beyond the Standard Model is observing an inconsistency within it. Since the matter/anti-matter difference incorporated in the Standard Model is manifested in merely one parameter, it is an excellent candidate for revealing such an inconsistency. Furthermore our most likely predictions of the physics beyond the Standard Model generally provide more sources of CP violation (for example in Supersymmetric extensions of it). Therefore investigations of the matter/anti-matter asymmetries hold great prospect for providing hints of what lies beyond the Standard Model.

In the previous decade, two particle accelerators were specifically built to study CP violation in the properties of a particle which is an excellent probe of such phenomena: the B meson. These colliders, known as asymmetric "B-factories", provide abundant

samples of this particle in a clean environment to perform detailed measurements of its decays.

One of the primary goals of these experiments is to look for inconsistencies in the Standard Model picture of *CP* violation. Already, they have established that the *CP* violation in B meson decays is non-zero measuring with high precision the angle β of a triangle whose area is related to the amount of *CP* violation: $\sin 2\beta = 0.674 \pm 0.026$ [89, 90].

With the current precision, the Standard Model appears to correctly predict the value of β. In this decade, as the B-factories accumulated hundred of millions of B decays, rare B decays can also be investigated, and their *CP* violation measured. This work focus on a set of rare B decays involving the elementary transition of the b quark to s quark. In the Standard Model they are sensitive to β, but, if this model is only a low energy manifestation of a more general theory where more *CP* violation sources are present, significant deviations from the predicted asymmetry could arise.

The analysis of the most relevant of these decays is presented in this thesis and it is based on data collected at the Stanford Linear Accelerator Center's asymmetric B-factory, which is composed of the PEP-II electron/positron storage ring and the *BABAR* detector.

This thesis attempts to give a comprehensive picture of *BABAR*'s analysis of the B^0 decays to the $K^+K^-K^0$ final state, through the intermediate resonances ϕK^0, $f_0 K^0$, and the non-resonant $K^+K^-K^0$, and of the B^0 decays to $K^0_S K^0_S K^0_S$ final state. Chapter 1 focuses on the theoretical importance of the *CP* violation in these decays, and how relate it to Standard Model parameters. Chapter 2 describes the general experimental approach for a measurement of time-dependent *CP* asymmetry in B decays. Chapter 3 gives the basis of the Dalitz plot technique used to measure the different contributions to the *CP* asymmetry in the $K^+K^-K^0$ final state. Chapters 4 and 5 present an overview of the *BABAR* detector and of the reconstruction of charged and neutral kaons, which plays a fundamental role in the decays described in this thesis. Chapter 6 and 7 present the analyses of $B^0 \to K^+K^-K^0$ and $B^0 \to K^0_S K^0_S K^0_S$ decays, respectively, discussing the details of the experimental technique used. Chapter 8 presents a measurement of branching fraction of $B \to \phi\pi$ (both charged and neutral), which can be used in estimating the Standard Model sub-leading amplitudes of $B^0 \to \phi K^0$ and also to set limits on Supersymmetric models. Finally Chapter 9 evaluates the impact of the measurements presented in this thesis on the knowledge of possible non Standard Model physics.

Chapter 1

CP Violation in B Decays

The actual understanding of the sub-atomic phenomena observed in high energy accelerators and detectors is expressed by the Standard Model (SM) theory of the electromagnetic, weak, and strong interactions. This theory of fundamental interactions provide an explanation of the origins of the CP violation, by means of a unique irreducible complex phase in the CKM matrix of quark flavour mixing.

We will describe how the CP violation can be measured in the neutral B meson system in the framework of the Standard Model. The validity of this model in the flavour sector can be tested by over-constraining its parameters both in CP-violating and in CP-conserving processes, by means of the analysis of the Unitarity Triangle. Through such an analysis of a large number of processes, the Standard Model seems to be the leading rule for the flavour of fundamental particles.

However, problems arise when the Standard Model is extended to the Planck scale. One of the fundamental elements of this theory, the Higgs boson, receives sizable quantum corrections from virtual particles which pull its renormalized mass to the Planck scale, unless a fine tuned cancellation of these corrections is invoked. To avoid this undesirable fine tuning, extensions of the Standard Model has been proposed, one of the most convincing being the Supersymmetry. These theories beyond the Standard Model could provide new sources of CP violation in addition to the CKM one.

These *New Physics* theories should reproduce the flavour structure with the measured amount of CP violation in the processes which to a good approximation are governed by the Standard Model only, and can produce sizable effects in less constrained processes. One of the most promising fields in the B decays to exploit such indirect effects of a physics beyond the Standard Model is the measurement of CP violation in $b \to s$ loop

processes.

We will focus on the specifics of the *CP* violation in B^0 decays to three kaons, and we will interpret the results in the Standard Model framework and possible extensions of it.

1.1 Discrete Symmetries

The discrete space-time operations of parity ($P:\ \mathbf{x} \to -\mathbf{x}$) and time-reversal ($T:\ t \to -t$) have classical interpretations. Testing the parity conservation of a classical theory corresponds to validating the invariance of its laws of motion under a mirror reflection about a coordinate plane followed by π rotation about the axes perpendicular to that plane. Similarly, time-reversal symmetry of a classical theory indicates no time direction preference. These operations were recognized long before the advent of quantum mechanics and quantum field theory as symmetries of classical theories of gravity and electromagnetism. Charge-conjugation (C) operation, however, was first brought to light by relativistic quantum theory prediction of anti-particles. This operation, which corresponds to reversing all quantum numbers of a particle while keeping the mass unchanged, has no classical analogue.

Experiment by Wu *et al.* [1] demonstrated parity violation in β decay of ^{60}Co, and the one by Goldhaber *et al.* [2] discovered C violation observing that neutrinos emitted in electron capture by ^{157}Eu were left-handed.

While C and P are maximally violated in weak interactions, there is no evidence that they are also violated in strong and electromagnetic interactions. In all the interactions, *CP* is conserved to a good approximation, and it was supposed to be an exact symmetry until *CP* violation was firstly observed by Christenson *et al.* [3] in 1964 with the discovery of the decay $K_L^0 \to \pi\pi$. *CP* violation was then suggested as one of the indispensable ingredients of any mechanism leading to matter/anti-matter asymmetry in our universe [4].

In the next few decades, the SM, which encapsulates the Cabibbo-Kobayashi-Maskawa [5] mechanism of CPV through flavor-changing charge currents between three generations of quarks, became established as the fundamental theory of particles and interactions. There was no indication of CPV outside the kaon system until recently (2001), when the B factories met their first major milestone and observed the phenomena in B meson decays to *CP* eigenstates containing charmonium, $B^0 \to [c\bar{c}]K^0$ [6, 7].

1.2 *CP* Violation in Standard Model

The Standard Model of particle physics [8] is based on three fundamental properties:

1. three families of particles, each consisting of two quarks and two leptons, are the building blocks for all matter:

$$\begin{pmatrix} u \\ d \end{pmatrix} \begin{pmatrix} c \\ s \end{pmatrix} \begin{pmatrix} t \\ b \end{pmatrix} \tag{1.1}$$

$$\begin{pmatrix} \nu_e \\ e^- \end{pmatrix} \begin{pmatrix} \nu_\mu \\ \mu^- \end{pmatrix} \begin{pmatrix} \nu_\tau \\ \tau^- \end{pmatrix} \tag{1.2}$$

2. the interactions of these particles are the expression of three local gauge symmetries of nature: $SU(3)_C \otimes SU(2)_L \otimes U(1)_Y$, where $SU(3)_C$ is the symmetry related to the quantum number of strong interaction (Color), $SU(2)_L$ is the weak isospin symmetry and $U(1)$ is hypercharge Y symmetry;

3. interactions with a heavy scalar with a non-zero vacuum expectation value produces mass on all of the particles and breaks the electro-weak gauge symmetry.

1.2.1 The CKM Picture of *CP* Violation

In the Standard Model (SM) [8] of $SU(3)_C \otimes SU(2)_L \otimes U(1)_Y$ gauge symmetry with three fermion generations, *CP* violation arises from a single phase in the mixing matrix for quarks [5]. Each quark generation consists of three multiplets:

$$Q_L^I = \begin{pmatrix} U_L^I \\ D_L^I \end{pmatrix} = (3,2)_{+1/6}, \quad u_R^I = (3,1)_{+2/3}, \quad d_R^I = (3,1)_{-1/3}, \tag{1.3}$$

where $(3,2)_{+1/6}$ denotes a triplet of $SU(3)_C$, doublet of $SU(2)_L$ with hypercharge $Y = Q - T_3 = +1/6$, and similarly for the other representations. The interactions of quarks with the $SU(2)_L$ gauge bosons are given by

$$\mathcal{L}_W = -\frac{1}{2} g \overline{Q_{Li}^I} \gamma^\mu \tau^a \mathbf{1}_{ij} Q_{Lj}^I W_\mu^a, \tag{1.4}$$

where γ^μ operates in Lorentz space, τ^a operates in $SU(2)_L$ space and $\mathbf{1}$ is the unit matrix operating in generation (flavor) space. This unit matrix is written explicitly to make the transformation to mass eigenbasis clearer. The interactions of quarks with the single Higgs scalar doublet $\phi(1,2)_{+1/2}$ of the Standard Model are given by

$$\mathcal{L}_Y = -G_{ij} \overline{Q_{Li}^I} \phi d_{Rj}^I - F_{ij} \overline{Q_{Li}^I} \tilde{\phi} u_{Rj}^I + \text{hermitian conjugate}, \tag{1.5}$$

where G and F are general *complex* 3×3 matrices. Their complex nature is the source of CP violation in the Standard Model. With the spontaneous symmetry breaking, $SU(2)_L \otimes U(1)_Y \to U(1)_{\rm EM}$ due to $\langle \phi \rangle \neq 0$, the two components of the quark doublet become distinguishable, as are the three members of the W^μ triplet. The charged current interaction in (1.4) is given by

$$\mathcal{L}_W = -\sqrt{\frac{1}{2}} g \overline{u^I_{Li}} \gamma^\mu \mathbf{1}_{ij} d^I_{Lj} W^+_\mu + \text{h.c.}. \tag{1.6}$$

The mass terms that arise from the replacement $\Re(\phi^0) \to \sqrt{\frac{1}{2}}(v + H^0)$ in (1.5) are given by

$$\mathcal{L}_M = -\sqrt{\frac{1}{2}} v G_{ij} \overline{d^I_{Li}} d^I_{Rj} - \sqrt{\frac{1}{2}} v F_{ij} \overline{u^I_{Li}} u^I_{Rj} + \text{hermitian conjugate}, \tag{1.7}$$

namely

$$M_d = Gv/\sqrt{2}, \qquad M_u = Fv/\sqrt{2}. \tag{1.8}$$

The phase information is now contained in these mass matrices. To transform to the mass eigenbasis, one defines four unitary matrices such that

$$V_{dL} M_d V^\dagger_{dR} = M_d^{\rm diag}, \qquad V_{uL} M_u V^\dagger_{uR} = M_u^{\rm diag}, \tag{1.9}$$

where $M_q^{\rm diag}$ are diagonal and real, while V_{qL} and V_{qR} are complex. The charged current interactions (1.6) are given in the mass eigenbasis by

$$\mathcal{L}_W = -\sqrt{\frac{1}{2}} g \overline{u_{Li}} \gamma^\mu \bar{V}_{ij} d_{Lj} W^+_\mu + \text{h.c.}. \tag{1.10}$$

(Quark fields with no superscript denote mass eigenbasis.) The matrix $\bar{V} = V_{uL} V^\dagger_{dL}$ is the (unitary) mixing matrix for three quark generations. As such, it generally depends on nine parameters: three can be chosen as real angles (like the Cabibbo angle) and six are phases. However, one may reduce the number of phases in $\bar{V}$ by a transformation

$$\bar{V} \implies V = P_u \bar{V} P^*_d, \tag{1.11}$$

where P_u and P_d are diagonal phase matrices. This is a legitimate transformation because it amounts to redefining the phases of the quark-mass-eigenstate fields, as was discussed earlier:

$$q_{Li} \to (P_q)_{ii} q_{Li}, \quad q_{Ri} \to (P_q)_{ii} q_{Ri}, \tag{1.12}$$

which does not change the real diagonal mass matrix $M_q^{\rm diag}$. The five phase differences among the elements of P_u and P_d can be chosen so that the transformation (1.11) eliminates five of the six independent phases from $\bar{V}$; thus V has one irremovable phase. This phase is called the Kobayashi-Maskawa phase $\delta_{\rm KM}$, and the mixing matrix is called the Cabibbo-Kobayashi-Maskawa (CKM) matrix [5]. It is interesting to note that the same procedure applied to a two-generation Standard Model Lagrangian with a single Higgs field would remove all *CP*-violating phases—that theory could not accommodate *CP* violation without the addition of extra fields. It was this observation that led Kobayashi and Maskawa to suggest a third quark generation long before there was any experimental evidence for it.

The irremovable phase in the CKM matrix allows possible *CP* violation. To see this, we write the *CP* transformation laws on a Dirac spinor:

$$\bar{\psi}_i\psi_j \to \bar{\psi}_j\psi_i, \quad \bar{\psi}_i\gamma^\mu W_\mu(1-\gamma_5)\psi_j \to \bar{\psi}_j\gamma^\mu W_\mu(1-\gamma_5)\psi_i. \tag{1.13}$$

Thus the mass terms and gauge interactions are obviously *CP*-invariant if all the masses and couplings are all real. In particular, consider the coupling of $W^\pm$ to quarks. It has the form

$$gV_{ij}\bar{u}_i\gamma_\mu W^{+\mu}(1-\gamma_5)d_j + gV_{ij}^*\bar{d}_j\gamma_\mu W^{-\mu}(1-\gamma_5)u_i. \tag{1.14}$$

The *CP* operation interchanges the two terms except that V_{ij} and V_{ij}^* are not interchanged. Thus, *CP* is a good symmetry only if there is a mass basis and choice of phase convention where all couplings and masses are real.

CP is not necessarily violated in the three generation Standard Model. If two quarks of the same charge had equal masses, one mixing angle and the phase could be removed from V. This can be written as a condition on quark mass differences: *CP* violation requires

$$(m_t^2-m_c^2)(m_c^2-m_u^2)(m_t^2-m_u^2)(m_b^2-m_s^2)(m_s^2-m_d^2)(m_b^2-m_d^2) \neq 0. \tag{1.15}$$

(The squared masses appear here because the sign of a fermion mass term is not physical.) Likewise, if the value of any of the three mixing angles were 0 or $\pi/2$, then the phase could be removed. Finally, *CP* would not be violated if the value of the single phase were 0 or π. These last eight conditions are elegantly incorporated into one, parameterization independent, condition [9]. To find this condition, note that unitarity of the CKM matrix,

$VV^\dagger = \mathbf{1}$, requires that for any choice of $i, j, k, l = 1, 2, 3$

$$\Im[V_{ij} V_{kl} V_{il}^* V_{kj}^*] = J \sum_{m,n=1}^{3} \epsilon_{ikm} \epsilon_{jln}. \tag{1.16}$$

Then, the conditions on the mixing parameters are summarized by

$$J \neq 0. \tag{1.17}$$

The fourteen conditions incorporated in (1.15) and (1.17) can all be written as a single requirement of the mass matrices in the interaction basis [9]:

$$\Im\{\det[M_d M_d^\dagger, M_u M_u^\dagger]\} \neq 0 \;\Leftrightarrow\; CP \text{ violation}. \tag{1.18}$$

This is a convention independent condition. The quantity J is of much interest in the study of *CP* violation from the CKM matrix. The maximum value that J could in principle assume is $1/(6\sqrt{3}) \approx 0.1$, but it is found to be $\lesssim 4 \times 10^{-5}$, providing a concrete meaning to the notion that *CP* violation in the Standard Model is small.

The fact that the three generation Standard Model with a single Higgs multiplet contains only a single independent *CP*-violating phase makes the possible *CP*-violating effects in this theory all very closely related. It is this that makes the pattern of *CP* violations in B decays strongly constrained in this model. The goal of the B-factory is to test whether this pattern occurs.

1.2.2 Unitarity of the CKM Matrix

The unitarity of the CKM matrix is manifest using an explicit parameterization. There are various useful ways to parameterize it, but the standard choice is the following [10]:

$$V = \begin{pmatrix} c_{12}c_{13} & s_{12}c_{13} & s_{13}e^{-i\delta} \\ -s_{12}c_{23} - c_{12}s_{23}s_{13}e^{i\delta} & c_{12}c_{23} - s_{12}s_{23}s_{13}e^{i\delta} & s_{23}c_{13} \\ s_{12}s_{23} - c_{12}c_{23}s_{13}e^{i\delta} & -c_{12}s_{23} - s_{12}c_{23}s_{13}e^{i\delta} & c_{23}c_{13} \end{pmatrix} \tag{1.19}$$

where $c_{ij} \equiv \cos\theta_{ij}$ and $s_{ij} \equiv \sin\theta_{ij}$. In this parameterization

$$J = c_{12}c_{23}c_{13}^2 s_{12}s_{23}s_{13} \sin\delta. \tag{1.20}$$

This shows explicitly the requirement that all mixing angles are different from $0, \pi/2$ and $\delta \neq 0, \pi$.

The unitarity of the CKM matrix implies various relations among its elements. A full list of these relations can be found in [11]. Three of them are very useful for understanding the Standard Model predictions for *CP* violation:

$$V_{ud}V_{us}^* + V_{cd}V_{cs}^* + V_{td}V_{ts}^* = 0, \tag{1.21}$$

$$V_{us}V_{ub}^* + V_{cs}V_{cb}^* + V_{ts}V_{tb}^* = 0, \tag{1.22}$$

$$V_{ud}V_{ub}^* + V_{cd}V_{cb}^* + V_{td}V_{tb}^* = 0. \tag{1.23}$$

Each of these three relations requires the sum of three complex quantities to vanish and so can be geometrically represented in the complex plane as a triangle. These are "the unitarity triangles"; note that the term "Unitarity Triangle" is reserved for the relation (1.23) only (for reasons soon to be understood).

Equation (1.16) has striking implications for the unitarity triangles:

1. All unitarity triangles are equal in area.

2. The area of each unitarity triangle equals $|J|/2$.

3. The sign of J gives the direction of the complex vectors.

The rescaled Unitarity Triangle (Fig. 1.1) is derived from (1.23) by (a) choosing a phase convention such that $(V_{cd}V_{cb}^*)$ is real, and (b) dividing the lengths of all sides by $|V_{cd}V_{cb}^*|$; (a) aligns one side of the triangle with the real axis, and (b) makes the length of this side 1. The form of the triangle is unchanged. Two vertices of the rescaled Unitarity Triangle are thus fixed at (0,0) and (1,0). The coordinates of the remaining vertex are denoted by (ρ, η). It is customary to express the CKM-matrix in terms of four Wolfenstein parameters (λ, A, ρ, η) with $\lambda = |V_{us}| = 0.22$ playing the role of an expansion parameter and η representing the *CP*-violating phase [12]:

$$V = \begin{pmatrix} 1 - \frac{\lambda^2}{2} & \lambda & A\lambda^3(\rho - i\eta) \\ -\lambda & 1 - \frac{\lambda^2}{2} & A\lambda^2 \\ A\lambda^3(1 - \rho - i\eta) & -A\lambda^2 & 1 \end{pmatrix} + O(\lambda^4). \tag{1.24}$$

λ is small, and for each element in V, the expansion parameter is actually λ^2. Hence it is sufficient to keep only the first few terms in this expansion. The relation between the parameters of (1.19) and (1.24) is given by

$$s_{12} \equiv \lambda, \quad s_{23} \equiv A\lambda^2, \quad s_{13}e^{-i\delta} \equiv A\lambda^3(\rho - i\eta). \tag{1.25}$$

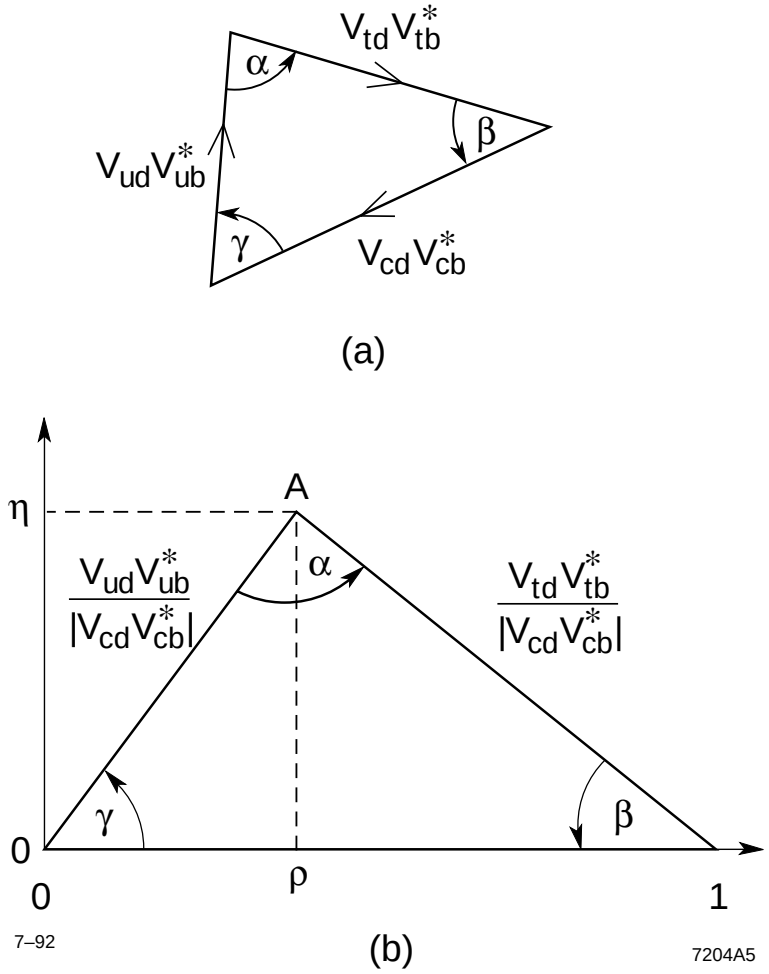

Figure 1.1: The Unitarity Triangle (a) and the rescaled Unitarity Triangle, all sides divided by $V_{cb}^* V_{cd}$ (b)

This specifies the higher order terms in (1.24).

The definition of (λ, A, ρ, η) given in (1.25) is useful because it allows an elegant improvement of the accuracy of the original Wolfenstein parameterization. In particular, defining

$$V_{us} = \lambda, \quad V_{cb} = A\lambda^2, \quad V_{ub} = A\lambda^3(\rho - i\eta), \tag{1.26}$$

one can then write

$$V_{td} = A\lambda^3(1 - \bar{\rho} - i\bar{\eta}), \tag{1.27}$$

$$\Im V_{cd} = -A^2\lambda^5\eta, \quad \Im V_{ts} = -A\lambda^4\eta, \tag{1.28}$$

where

$$\bar{\rho} = \rho(1 - \lambda^2/2), \quad \bar{\eta} = \eta(1 - \lambda^2/2), \tag{1.29}$$

turn out to be excellent approximations to the exact expressions [13]. Depicting the rescaled Unitarity Triangle in the $(\bar{\rho}, \bar{\eta})$ plane, the lengths of the two complex sides are

$$R_b \equiv \sqrt{\bar{\rho}^2 + \bar{\eta}^2} = \frac{1 - \lambda^2/2}{\lambda} \left| \frac{V_{ub}}{V_{cb}} \right|, \quad R_t \equiv \sqrt{(1-\bar{\rho})^2 + \bar{\eta}^2} = \frac{1}{\lambda} \left| \frac{V_{td}}{V_{cb}} \right|. \tag{1.30}$$

The three angles of the Unitarity Triangle are denoted by α, β and γ [14]:

$$\alpha \equiv \arg \left[-\frac{V_{td} V_{tb}^*}{V_{ud} V_{ub}^*} \right], \quad \beta \equiv \arg \left[-\frac{V_{cd} V_{cb}^*}{V_{td} V_{tb}^*} \right], \tag{1.31}$$

The third angle is then

$$\gamma \equiv \arg \left[-\frac{V_{ud} V_{ub}^*}{V_{cd} V_{cb}^*} \right] \equiv \pi - \alpha - \beta. \tag{1.32}$$

These are physical quantities and, as discussed below, can be measured by *CP* asymmetries in various B decays. The consistency of the various measurements provide tests of the Standard model.

The angle β gives, to a good approximation, the Standard Model phase between the neutral B mixing amplitude and its leading decay amplitudes.

1.3 *CP* Violation Phenomenology

We have described how *CP* violation is produced in the Standard Model; in the following we describe how *CP* violation phenomena can be observed in decays of mesons.

1.3.1 Direct *CP* Violation

Consider the transition from the states i and $\bar{i}$ to final states f and $\bar{f}$ with only one amplitude contributing:

$$\begin{aligned} \langle f|T|i\rangle &= A e^{i(\delta+\phi)}, \\ \langle \bar{f}|T|\bar{i}\rangle &= A e^{i(\delta-\phi)}, \end{aligned}$$

where T is the transition operator and A is a positive real number. The *CP*-even phase that is common to both decays, δ, is referred to as a *strong phase*, and the *CP*-odd phase that changes signs, ϕ, is referred to as a *weak phase*. The *CP* operator relates the *CP* conjugate states by inducing arbitrary phases:

$$\begin{aligned} CP|i\rangle = e^{i\eta_i}|\bar{i}\rangle \quad &, \quad CP|\bar{i}\rangle = e^{-i\eta_i}|i\rangle \\ CP|f\rangle = e^{i\eta_f}|\bar{f}\rangle \quad &, \quad CP|\bar{f}\rangle = e^{-i\eta_f}|f\rangle. \end{aligned} \tag{1.33}$$

If CP is conserved by T,

$$\langle f|T|i\rangle = \langle f|(CP)T(CP)^\dagger|i\rangle = e^{i(\eta_i-\eta_f)}\langle \bar{f}|T|\bar{i}\rangle$$

Choosing $\eta_i - \eta_f = 2\phi - \theta$, we see that despite the presence of the CP violating phase ϕ in this transition, the observable amplitudes are incapable of indicating any CP violation in T. CP violation is observable in transitions with two strong and weak phase contributions. Consider

$$\begin{aligned}\langle f|T|i\rangle &= A_1 e^{i(\delta_1+\phi_1)} + A_2 e^{i(\delta_2+\phi_2)},\\ \langle \bar{f}|T|\bar{i}\rangle &= A_1 e^{i(\delta_1-\phi_1+\theta)} + A_2 e^{i(\delta_2-\phi_2+\theta)}.\end{aligned}$$

Here the presence of interference between the two amplitudes allows the construction of the CP violating observable

$$|\langle f|T|i\rangle|^2 - |\langle \bar{f}|T|\bar{i}\rangle|^2 = -4A_1A_2\sin(\delta_1-\delta_2)\sin(\phi_1-\phi_2). \tag{1.34}$$

Note however, that in order to obtain CP violation, at least two differing strong *and* weak phases are necessary. Such expression of CP violation is known as direct CP violation. It is possible to obtain CP violating observables without strong phases when considering decays to two different final states, or when i and $\bar{i}$ decay to the same final state $f = \bar{f}$. We will consider this latter case in the discussions that follow.

1.3.2 Neutral B Mesons

In the absence of the weak interaction, a P^0 meson such as K^0, D^0, or B^0 would be stable and have a common mass with $\bar{P}^0$. Weak transitions, however, permit $P^0 \leftrightarrow \bar{P}^0$ mixing, forming mass/lifetime eigenstates which are a mixture of the flavor eigenstates. Under the Wigner-Weisskopf approximation [15], the Schroedinger equation for the time evolution and decay of the meson system:

$$|\psi(t)\rangle = \psi_1(t)|P^0\rangle + \psi_2(t)|\bar{P}^0\rangle$$

may be written in the $|P^0\rangle/|\bar{P}^0\rangle$ basis as

$$i\frac{d}{dt}\begin{pmatrix}\psi_1\\ \psi_2\end{pmatrix} = \mathcal{H}\begin{pmatrix}\psi_1\\ \psi_2\end{pmatrix} = (\mathbf{M} - \frac{i}{2}\mathbf{\Gamma})\begin{pmatrix}\psi_1\\ \psi_2\end{pmatrix}. \tag{1.35}$$

where $\mathbf{M}$ and $\mathbf{\Gamma}$ are 2×2 Hermitian matrices. CPT invariance guarantees $H_{11} = H_{22}$.

The light P_L and heavy P_H mass eigenstates are given by

$$\begin{aligned} |P_L\rangle &= p|P^0\rangle + q|\bar{P}^0\rangle, \\ |P_H\rangle &= p|P^0\rangle - q|\bar{P}^0\rangle. \end{aligned} \tag{1.36}$$

The complex coefficients p and q obey the normalization condition

$$|q|^2 + |p|^2 = 1. \tag{1.37}$$

Note that $\arg(q/p^*)$ is just an overall common phase for $|P_L\rangle$ and $|P_H\rangle$ and has no physical significance.

The mass difference Δm_P and width difference $\Delta\Gamma_P$ between the neutral P^0 mesons are defined as follows:

$$\Delta m_P \equiv\ M_H - M_L, \quad \Delta\Gamma_P \equiv\ \Gamma_H - \Gamma_L, \tag{1.38}$$

so that Δm_P is positive by definition. Finding the eigenvalues of Eq. 1.35, one gets

$$(\Delta m_P)^2 - \frac{1}{4}(\Delta\Gamma_P)^2 = 4(|M_{12}|^2 - \frac{1}{4}|\Gamma_{12}|^2), \tag{1.39}$$

$$\Delta m_P \Delta\Gamma_P = 4\Re(M_{12}\Gamma_{12}^*). \tag{1.40}$$

The ratio q/p is given by

$$\frac{q}{p} = -\frac{\Delta m_P - \frac{i}{2}\Delta\Gamma_P}{2(M_{12} - \frac{i}{2}\Gamma_{12})} = -\frac{2(M_{12}^* - \frac{i}{2}\Gamma_{12}^*)}{\Delta m_P - \frac{i}{2}\Delta\Gamma_P}, \tag{1.41}$$

Using

$$\begin{aligned} CP|P^0\rangle &= e^{i\eta}|\bar{P}^0\rangle, \\ CP|\bar{P}^0\rangle &= e^{-i\eta}|P^0\rangle, \end{aligned}$$

we find that CP is conserved when

$$\frac{p}{q} = \pm e^{i\eta} \Rightarrow \left|\frac{p}{q}\right| = 1. \tag{1.42}$$

As expected, this condition shows that CP invariance implies that $|P_L\rangle$ and $|P_H\rangle$ are CP eigenstates. Failure of this condition indicates *CP violation in mixing or indirect CP violation.*

1.3.3 *CP* Violating Observables

Consider the decay of the $P^0/\bar{P}^0$ meson to final states $f/\bar{f}$:

$$A_f \equiv \langle f|T|P^0\rangle \quad , \quad \bar{A}_f \equiv \langle f|T|\bar{P}^0\rangle,$$
$$A_{\bar{f}} \equiv \langle \bar{f}|T|P^0\rangle \quad , \quad \bar{A}_{\bar{f}} \equiv \langle \bar{f}|T|\bar{P}^0\rangle,$$

Applying 1.33 and 1.42 to these amplitudes leads to the *CP*-invariance conditions:

$$\bar{A}_{\bar{f}} = e^{i(\eta_f - \eta)} A_f \Rightarrow |A_f| = |\bar{A}_{\bar{f}}|, \tag{1.43}$$
$$A_{\bar{f}} = e^{i(\eta_f + \eta)} \bar{A}_f \Rightarrow |A_{\bar{f}}| = |\bar{A}_f|. \tag{1.44}$$

As expected, the decay probabilities for P^0 to f and $\bar{P}^0$ to $\bar{f}$ must be the same to conserve *CP*. Deviation from these conditions signifies *CP violation in decay*. We may construct a more concise *CP* conservation requirement by combining the individual conditions for mixing and decay. Taking the ratio of the conditions 1.43 and 1.44 we find

$$\frac{A_f A_{\bar{f}}}{\bar{A}_f \bar{A}_{\bar{f}}} = e^{2i\eta} = \frac{q^2}{p^2}. \tag{1.45}$$

Defining

$$\lambda_f \equiv \frac{q}{p}\frac{\bar{A}_f}{A_f}, \ \lambda_{\bar{f}} \equiv \frac{q}{p}\frac{\bar{A}_{\bar{f}}}{A_{\bar{f}}}, \tag{1.46}$$

allows Eq. 1.45 to be written more simply as

$$\lambda = \frac{1}{\lambda_{\bar{f}}} \tag{1.47}$$

This condition encapsulates another possible expression of CP violation. In order to illustrate, let us consider the simplified case when P^0 and $\bar{P}^0$ decay to a *CP* eigenstate (i.e. $CP|f\rangle = \eta_{f_{CP}}|f\rangle, \ \eta_{f_{CP}} = \pm 1$), and there is no *CP* violation in mixing or decay:

$$A_f = Ae^{i(\delta+\phi_D)}, \ \bar{A}_f = \eta_{f_{CP}} Ae^{i(\delta-\phi_D)} \ \Rightarrow \ |A_f| = |\bar{A}_f|, \tag{1.48}$$
$$q/p = e^{2i\phi_M} \ \Rightarrow \ |q/p| = 1. \tag{1.49}$$

we have introduced a strong phase but we have used different mixing and decay weak phases ϕ_M and ϕ_D . In this case, $\lambda_f = \eta_{f_{CP}} e^{2i(\phi_M - \phi_D)}$. However, since $f = \bar{f}$, $\lambda_f = \lambda_{\bar{f}}$, and Eq. 1.47 becomes

$$\lambda_f = \pm 1 = \eta_{f_{CP}} e^{2i(\phi_M - \phi_D)}, \tag{1.50}$$

and a less apparent expression of *CP* violation is revealed: *CP violation in interference between mixing and decay*. In the case of meson decays to *CP* eigenstates, $\lambda \neq \pm 1$ for any of the three types of *CP* violation: *CP* violation in mixing, $|q/p| \neq 1$; *CP* violation in decay, $|\bar{A}_f/A_f| \neq 1$; and *CP* violation in interference between mixing and decay, non-vanishing relative phase between q/p and $\bar{A}_f/A_f$. In the next section we will see how λ_f appears in the time-evolution of neutral mesons, specifically focusing on the B^0. We will also see how λ_f is directly related to CKM parameters for specific B decays.

1.4 Time Evolution of Neutral B_d Mesons

BABAR at PEP-II is a B-factory, i.e. an experiment where a large number of B mesons pairs are produced through the process $e^+e^- \rightarrow \Upsilon(4S) \rightarrow B\overline{B}$. To a very good approximation half of these pairs are the neutral $B^0/\overline{B}^0$ [23]. Studies of the decay of these mesons to *CP* eigenstates provides a mean of measuring angles of the unitarity triangle.

After production, a solitary B^0 (or $\overline{B}^0$) will evolve according to the Schroedinger equation 1.35. Before decaying, the meson may change its flavor several times through the box diagrams in Fig. 1.2. The *time-dependent* mass eigenstates

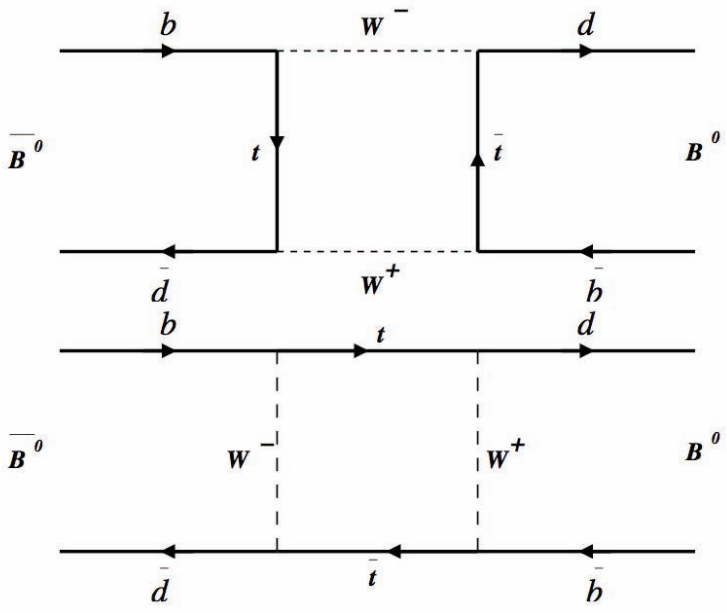

Figure 1.2: The leading diagrams contributing to $B^0 - \overline{B}^0$ mixing.

$$
\begin{aligned}
|B_L(t)\rangle &= e^{-m_L t} e^{-\Gamma_L t/2} |B_L\rangle \\
|B_H(t)\rangle &= e^{-m_H t} e^{-\Gamma_H t/2} |B_H\rangle
\end{aligned}
$$

are related to flavour eigenstates through Eq. 1.36. Therefore

$$
\begin{aligned}
|B^0(t)\rangle = &\left(e^{-(im_H+\Gamma_H/2)t} + e^{-(im_L+\Gamma_L/2)t}\right)|B^0\rangle + \\
&\frac{q}{p}\left(e^{-(im_H+\Gamma_H/2)t} - e^{-(im_L+\Gamma_L/2)t}\right)|\overline{B}^0\rangle, \qquad (1.51)\\
|\overline{B}^0(t)\rangle = &\frac{q}{p}\left(e^{-(im_H+\Gamma_H/2)t} - e^{-(im_L+\Gamma_L/2)t}\right)|B^0\rangle + \\
&\left(e^{-(im_H+\Gamma_H/2)t} + e^{-(im_L+\Gamma_L/2)t}\right)|\overline{B}^0\rangle. \qquad (1.52)
\end{aligned}
$$

$\Upsilon(4S)$ [55] decay, however, produces two neutral B mesons in a coherent anti-symmetric state. This two meson system will consist of one B of each flavor until one particle decays. From that time on, the remaining B will obey Eq. 1.51 until its decay. If one meson decays to a CP eigenstate, there is no means of identifying its flavor. We will refer to this meson as B_{CP} with decay time t_{CP} . However, since at time of the first decay only one meson of each flavor was present, the flavor of B_{CP} may be inferred from the other meson. We will refer to this meson as B_{tag} with decay time t_{tag} . Identifying $\Delta t = t_{CP} - t_{tag} = 0$ as $t = 0$ in Eq. 1.51, the probabilities of the two observable anti-symmetric states (i.e. when B_{tag} is a B^0 or $\overline{B}^0$) are

$$
\begin{aligned}
\Gamma_{B^0}(\Delta t) = &\frac{1}{2}|\langle f|T|B^0(t=t_{CP})\rangle\langle B^0(t=t_{tag})|\overline{B}^0(t=t_{tag})\rangle - \\
&\langle f|T|\overline{B}^0(t=t_{CP})\rangle\langle B^0(t=t_{tag})|B^0(t=t_{tag})\rangle|^2 \\
= &\frac{e^{-\frac{|\Delta t|}{\tau}}}{4\tau}(1 + S_f \sin(\Delta m_d \Delta t) - C_f \cos(\Delta m_d \Delta t)), \qquad (1.53)\\
\Gamma_{\overline{B}^0}(\Delta t) = &\frac{1}{2}|\langle f|T|B^0(t=t_{CP})\rangle\langle B^0(t=t_{tag})|B^0(t=t_{tag})\rangle - \\
&\langle f|T|\overline{B}^0(t=t_{CP})\rangle\langle \overline{B}^0(t=t_{tag})|B^0(t=t_{tag})\rangle|^2 \\
= &\frac{e^{-\frac{|\Delta t|}{\tau}}}{4\tau}(1 - S_f \sin(\Delta m_d \Delta t) + C_f \cos(\Delta m_d \Delta t)), \qquad (1.54)
\end{aligned}
$$

where Δm_d is the mass difference between B_L and B_H and the lifetime difference is assumed to be negligible. Here

$$
\begin{aligned}
S_f &= \frac{2\Im\lambda_f}{1+|\lambda_f|^2}, \qquad (1.55)\\
C_f &= \frac{1-|\lambda_f|^2}{1+|\lambda_f|^2}. \qquad (1.56)
\end{aligned}
$$

where

$$\lambda_f = \eta_{CP}\frac{p}{q}\frac{\bar{A}_f}{A_f} \tag{1.57}$$

and $A = |\langle f|T|B^0\rangle|$, $\bar{A} = |\langle f|T|\overline{B}^0\rangle|$, and η_{CP} is the CP eigenvalue of the final state.

1.4.1 Relating *CP* Violation to CKM Matrix

In general, the SM amplitudes for B decays may carry contributions from multiple Feynman diagrams, each carrying different CKM matrix elements. Therefore the amplitude ratio in λ_f is of the form:

$$\frac{\bar{A}}{A_f} = \frac{A_f^\alpha e^{i\alpha} + A_f^\beta e^{i\beta} + A_f^\gamma e^{i\gamma} + \ldots}{A_f^\alpha e^{-i\alpha} + A_f^\beta e^{-i\beta} + A_f^\gamma e^{-i\gamma} + \ldots}. \tag{1.58}$$

If all of the amplitudes contributing to A and $\bar{A}$ could be calculated for a given decay, λ_f relation to CKM matrix elements and unitary triangle angles would be easy to identify. Unfortunately calculating amplitudes for hadronic B decays is rather complex. Though the short distance processes governed by the weak interaction and hard QCD can be cleanly calculated, long distance processes like hadronization and rescattering are difficult. Decays dominated by one phase require no hadronic calculation. As an example, consider the leading diagrams for the decay $B \to J/\psi K^0$ presented in Fig. 1.3. To highest order

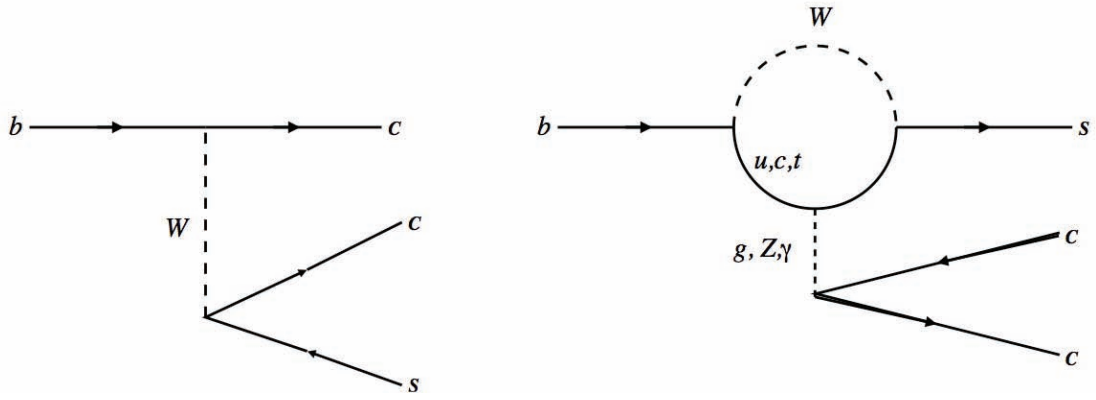

Figure 1.3: The leading diagrams contributing to $B^0 \to J/\psi K^0$ decays. Left: *"tree"* diagram; right: *"penguin"* diagram.

in the Wolfenstein parameter λ, the so-called *"tree"* level diagram containing the factors $V_{cb}V_{cs}^* \approx \lambda^2$ and the leading loop diagram, known as *"penguin"* diagram, containing the

factor $V_{tb}V_{ts}^* \approx \lambda^2 + \mathcal{O}(\lambda^4)e^{-i\gamma}$ carry the same CKM phase [16]. Therefore

$$\lambda_{J/\psi K^0} = -\frac{V_{td}V_{tb}^*}{V_{tb}V_{td}^*}\frac{V_{cb}V_{cs}^*}{V_{cs}V_{cb}^*}\frac{V_{cs}V_{cd}^*}{V_{cd}V_{cs}^*} \Rightarrow \Im\lambda_{J/\psi K^0} = \sin 2\beta, \tag{1.59}$$

where the first term is q/p (from diagrams in Fig. 1.3), the last term comes from $K^0 - \overline{K}^0$ mixing, and the middle term is $\bar{A}/A$. Since $\lambda_{J/\psi K^0}$ is so cleanly related to the angle β, this decay of the B meson is often referred to as "the gold-plated mode".

1.4.2 *CP* Violation in Two-body $B^0 \to \phi K^0$ in Standard Model

Due to the absence of the Flavour Changing Neutral Currents (FCNC) at tree level in the Standard Model, the decay $B^0 \to \phi K^0$ proceeds entirely through $b \to s$ gluonic penguin diagrams (Fig. 1.4). Consequently, they are Cabibbo suppressed with respect to $B^0 \to J/\psi K^0$.

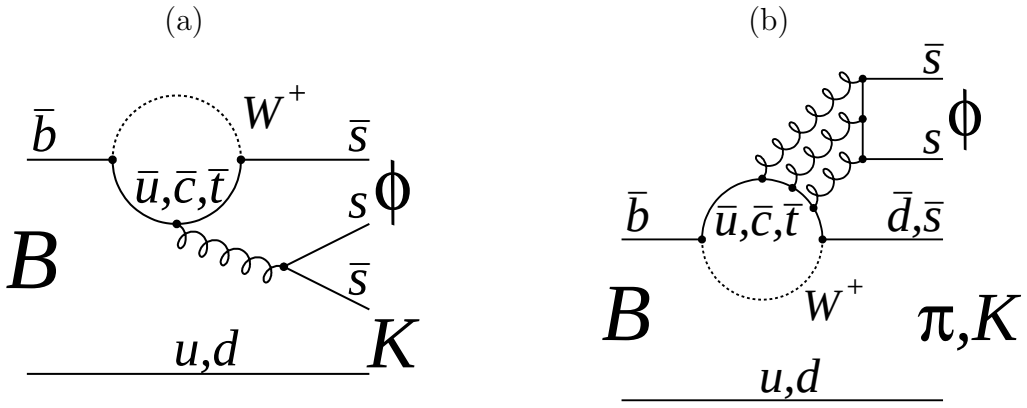

Figure 1.4: Examples of quark level diagrams for $B \to \phi K$ and $B \to \phi\pi$. (a) Internal penguin diagram; (b) flavor singlet penguin diagram.

The interest in these decays stays in the fact that, while in the tree diagrams only real particles can enter, in the *loop* of a penguin amplitude all the virtual particles which can couple to b and s quarks may enter. In the Standard Model, this happens through weak interactions with quark u, c and t. In extensions of such a model other particles can couple with them, these contributions entering the amplitude at the leading order. We will discuss these effects beyond Standard Model in Chapter 9.

In the Standard Model, assuming $\phi = (s\bar{s})$, the decay amplitude is given by:

$$A(B_d^0 \to \phi K^0) = V_{cs}V_{cb}^*(P_c - P_t) + V_{us}V_{ub}^*(P_u - P_t)\ , \tag{1.60}$$

where P_i with $i = u, c, t$ denotes penguin diagram contributions with internal $u,\ c$ and t quarks. With

$$\left|\frac{V_{us}V_{ub}^*}{V_{cs}V_{cb}^*}\right| \leq 0.02, \qquad \frac{P_u - P_t}{P_c - P_t} = \mathcal{O}(1) \tag{1.61}$$

also in this decay a single CKM phase dominates and as the decay phase ϕ_D and the mixing phase ϕ_M are the same as in $B^0 \to J/\psi\, K^0$ we find

$$C_{\phi K_S} = 0, \qquad S_{\phi K_S} = S_{\psi K_S} = \sin 2\beta\ . \tag{1.62}$$

The equality of these two asymmetries need not be perfect as the ϕ meson is not entirely a $s\bar{s}$ state and the approximation of neglecting the second amplitude in (1.60) could be only true within a few percent. However, a detailed analysis shows [17] that these two asymmetries should be very close to each other within the SM: $|S_{\phi K^0} - S_{J/\psi K^0}| \leq 0.04$. Any strong violation of this bound would be a signal for new physics.

In view of this prediction, the first results on this asymmetry from *BABAR* [18] and Belle [19] were truly exciting:

$$(\sin 2\beta)_{\phi K_S} = \begin{cases} -0.19 \pm 0.51\,(\text{stat}) \pm 0.09\,(\text{syst}) & (\text{BaBar}) \\ -0.73 \pm 0.64\,(\text{stat}) \pm 0.18\,(\text{syst}) & (\text{Belle}), \end{cases}$$

implying

$$S_{\phi K_s} = -0.39 \pm 0.41, \qquad C_{\phi K_s} = 0.56 \pm 0.43, \tag{1.63}$$

$$|S_{\phi K_S} - S_{J/\psi K_S}| = 1.12 \pm 0.41 \tag{1.64}$$

and the violation of the bound $|S_{\phi K_S} - S_{J/\psi K_S}| \leq 0.04$ by 2.7σ. These results invited a number of theorists to speculate what kind of new physics could be responsible for this difference. Some references are given in [20]. Enhanced QCD penguins, enhanced Z^0 penguins, rather involved supersymmetric scenarios have been suggested as possible origins of the departure from the SM prediction. Unfortunately the new data presented at the 2004 summer conferences by both collaborations look much closer to the SM predictions

$$(\sin 2\beta)_{\phi K_S} = \begin{cases} 0.50 \pm 0.25\,(\text{stat}) \pm 0.06\,(\text{syst}) & (\text{BaBar}) \\ 0.06 \pm 0.33\,(\text{stat}) \pm 0.09\,(\text{syst}) & (\text{Belle}), \end{cases}$$

implying

$$S_{\phi K_s} = 0.34 \pm 0.20, \qquad C_{\phi K_s} = -0.04 \pm 0.17. \tag{1.65}$$

As can be seen, the fact that this is a rare decay implies that the statistical uncertainty is very large. For these reasons the interest moves to the decays of the B meson in three

body final states, which usually have a larger branching fraction with respect two-body B decays.

In particular, we will concentrate on the decays of the B^0 into three kaons: $B^0 \to K^+K^-K^0$ and $B^0 \to K^0_S K^0_S K^0_S$. The first one includes the mentioned $B^0 \to \phi K^0$, because the ϕ meson decays instantaneously in a pair K^+K^- inside the detector. It will be studied with a completely new approach with respect to the past: a Dalitz plot technique of the whole three kaon phase-space.

The second one has become feasible thanks an experimental technique of the decay vertex reconstruction only recently developed.

1.5 *CP* Eigenvalues for *KKK* Final States

In the case of three-body B decays, the CP eigenstate cannot be always determined. There are two main scenarios in which this is feasible, thus allowing a clean interpretation of measured CP violation parameters:

1. $B \to Q\bar{Q}P$, where $Q = (K^+, \pi^+)$ and $P = (\pi^0, K^0_S, K^0_L)$;

2. $B \to PPX$, where $P, X = (\pi^0, K^0_S, K^0_L)$.

In this work, we will consider $B^0 \to K^+K^-K^0$ for the Type 1 decays and on $B^0 \to K^0_S K^0_S K^0_S$ for the Type 2 decays.

Let us consider as example of Type 1 $B^0 \to K^+K^-K^0$ decays. We can write the final state as

$$|K^+(p_1)K^-(p_2)K^0(p_3)\rangle \tag{1.66}$$

where p_1, p_2 and p_3 are the momenta of the three kaons. In the rest frame of the K^+K^- mesons pair, $p_1 = p = -p_2$. The final state can be characterized by means of the angular momentum between the K^+ and the K^- (l) and the angular momentum of the K^+K^- system and the K^0_S (l'). The conservation of angular momentum in the decay implies

$$J_{B^0} = l \oplus l' \oplus S_{K^+} \oplus S_{K^-} \oplus S_{K^0} \tag{1.67}$$

and, since the B^0,K^+,K^- and K^0 are pseudoscalar mesons ($J^P = 0^-$), the intrinsic angular momentum is zero, then the Eq. 1.67 becomes simply

$$0 = l \oplus l'. \tag{1.68}$$

Therefore, the angular momentum between the K^+K^- system and K^0 (l') must be equal to l. Applying the parity operation P to the final state

$$P|K^+(p)K^-(-p)K^0_S(p') = -1|K^+(p)K^-(-p)K^0_S(p')\rangle \tag{1.69}$$

because the intrinsic parity of a pseudoscalar meson is -1. Applying the charge conjugation C

$$\begin{aligned} C|K^+(p)K^-(-p)K^0_S(p')\rangle = \eta_c(K^0_S)|K^-(p)K^+(-p)K^0_S(p')\rangle = \\ \eta_c(K^0_S)(-1)^l|K^+(p)K^-(-p)K^0_S(p')\rangle = (-1)^{l+1}|K^+(p)K^-(-p)K^0_S(p')\rangle \end{aligned} \tag{1.70}$$

where $\eta_c(K^0_S)$ is the C eigenvalue of the K^0_S.

Finally applying the combination of C and P on the final state

$$\mathcal{CP}|K^+(p)K^-(-p)K^0_S(p')\rangle = (-1)^l|K^+(p)K^-(-p)K^0_S(p')\rangle \tag{1.71}$$

then this is a *CP* eigenstate which has an eigenvalue which depends on the relative angular momentum between the K^+ and K^-. This makes necessary a complete angular analysis to interpret the *CP* violation parameters in terms of CKM parameters (β and direct *CP* violation). We will achieve this purpose through a full Dalitz plot analysis performed simultaneously to the *CP* violation measurement.

A more fortunate case is the one of Type 2 decays. We will consider the case of $B^0 \to K^0_S K^0_S K^0_S$ which we will measure in Chapter 7. In this case in fact the final state we consider is

$$|K^0_S(p)K^0_S(-p)K^0_S(p')\rangle \tag{1.72}$$

where the K^0_S are spin zero mesons, then they follow the *Bose-Einstein* statistics, thus the $K^0_S K^0_S$ wave-function must be symmetric, and hence the angular momentum l between the two K^0_S must be even. This implies that Eq. 1.71 in this case reads:

$$\mathcal{CP}|K^0_S(p)K^0_S(-p)K^0_S(p')\rangle = +|K^0_S(p)K^0_S(-p)K^0_S(p')\rangle. \tag{1.73}$$

Then $K^0_S K^0_S K^0_S$ is a *CP* eigenstate with a definite eigenvalue (*CP* even). In this case, an angular analysis is not needed, and the measurement can be performed like in the case of two body decays (as in $B^0 \to J/\psi K^0_S$). However, measurement of *CP* violation for such decays is challenging for experimental reasons which will be explained in Sec. 2.3.

1.6 Formalism for Charmless Three-body B Decays

A complete understanding of B physics requires the evaluation of the matrix elements of the amplitude. In the case of charmless B decays, the quarks in the final states are light, so the calculation techniques using the *Heavy Quark Expansion Theory* (HQET) [24] cannot be used. In this case a more appropriate approach to estimate decay amplitudes is QCD factorization, even if it is really a good approximation in the limit of $m_b \to \infty$. Said this, the factorization approach results a suitable approximation in the case of charmless three-body B decays, even with the caveat that some non factorizable effect due to the validity of the limit can make possible deviations from its prediction.

In this approach, the matrix element of the $\bar{B} \to \bar{K}\bar{K}K$ decay amplitude is given by

$$\langle \overline{K}\,\overline{K}K|\mathcal{H}_{\rm eff}|\overline{B}\rangle = \frac{G_F}{\sqrt{2}} \sum_{p=u,c} \lambda_p \langle \overline{K}\,\overline{K}K|T_p|\overline{B}\rangle, \tag{1.74}$$

where $\lambda_p \equiv V_{pb}V_{ps}^*$ and [25]

$$\begin{aligned} T_p \;=\; & a_1\delta_{pu}(\bar{u}b)_{V-A}\otimes(\bar{s}u)_{V-A} + a_2\delta_{pu}(\bar{s}b)_{V-A}\otimes(\bar{u}u)_{V-A} + a_3(\bar{s}b)_{V-A}\otimes\sum_q(\bar{q}q)_{V-A} \\ & + a_4^p\sum_q(\bar{q}b)_{V-A}\otimes(\bar{s}q)_{V-A} + a_5(\bar{s}b)_{V-A}\otimes\sum_q(\bar{q}q)_{V+A} \\ & - 2a_6^p\sum_q(\bar{q}b)_{S-P}\otimes(\bar{s}q)_{S+P} + a_7(\bar{s}b)_{V-A}\otimes\sum_q\frac{3}{2}e_q(\bar{q}q)_{V+A} \\ & - 2a_8^p\sum_q(\bar{q}b)_{S-P}\otimes\frac{3}{2}e_q(\bar{s}q)_{S+P} + a_9(\bar{s}b)_{V-A}\otimes\sum_q\frac{3}{2}e_q(\bar{q}q)_{V-A} \\ & + a_{10}^p\sum_q(\bar{q}b)_{V-A}\otimes\frac{3}{2}e_q(\bar{s}q)_{V-A}, \end{aligned} \tag{1.75}$$

with $(\bar{q}q')_{V\pm A} \equiv \bar{q}\gamma_\mu(1\pm\gamma_5)q'$, $(\bar{q}q')_{S\pm P} \equiv \bar{q}(1\pm\gamma_5)q'$ and a summation over $q = u, d, s$ being implied. The factorization approach consists in the fact that the matrix element $\langle \overline{K}\,\overline{K}K|j\otimes j'|\overline{B}\rangle$ corresponds to $\langle \overline{K}K|j|\overline{B}\rangle\langle\overline{K}|j'|0\rangle$ (i.e. the product of the transition of $B\to K\overline{K}$ and the -independent- creation of a $\overline{K}$ by the vacuum), $\langle\overline{K}|j|\overline{B}\rangle\langle\overline{K}K|j'|0\rangle$ (i.e. the product of the transition of $B\to\overline{K}$ and the creation of the $\overline{K}K$ by the vacuum) or $\langle 0|j|\overline{B}\rangle\langle\overline{K}\,\overline{K}K|j'|0\rangle$ (i.e. the creation of $\overline{K\,K\,K}$ by the vacuum), as appropriate, and a_i are the next-to-leading order effective Wilson coefficients. The Wilson coefficients depends on the renormalization scale μ and are calculable perturbatively (while the non-perturbative effects are inside the operators). The normalization scale used is $\mu = m_b/2 = 2.1$ GeV/c^2.

1.6.1 $B^0 \to K^+K^-K^0$ Decay Amplitude

Applying Eqs. (1.74), (1.75) and the equation of motion, one can evaluate the $\overline{B}^0 \to K^+K^-\overline{K}^0$ decay amplitude [26].

In the factorization terms, the $K\overline{K}$ pair can be produced through a transition from the $\overline{B}$ meson or can be created from vacuum through V and S operators. There exist two weak annihilation contributions, where the $\overline{B}$ meson is annihilated and a final state with three kaons is created. The Okubo-Zweig-Iizuka rule suppressed matrix element $\langle K^+K^-|(\bar{d}d)_{V-A}|0\rangle$ is included in the factorization amplitude since it could be enhanced through the long-distance pole contributions via the intermediate vector mesons.

To evaluate the amplitude, one needs to consider the $\overline{B} \to K\overline{K}$, $0 \to K\overline{K}$ and $0 \to \overline{K}\,\overline{K}K$ matrix elements, the so-called two-meson transition, two-meson and three-meson creation matrix elements in addition to the usual one-meson transition and creation ones.

Two-kaon Transition

The two-kaon transition matrix element $\langle\overline{K}^0K^+|(\bar{u}b)_{V-A}|\overline{B}^0\rangle$ has the general expression [27]

$$\begin{aligned}\langle\overline{K}^0(p_1)K^+(p_2)|(\bar{u}b)_{V-A}|\overline{B}^0\rangle &= ir(p_B-p_1-p_2)_\mu + i\omega_+(p_2+p_1)_\mu + i\omega_-(p_2-p_1)_\mu \\ &\quad + h\,\epsilon_{\mu\nu\alpha\beta}p_B^\nu(p_2+p_1)^\alpha(p_2-p_1)^\beta. \end{aligned} \tag{1.76}$$

where r, $\omega_\pm$ and h are form factors which can receive both resonant and non-resonant contributions, which can be evaluated using the *Heavy Meson Chiral Perturbation Theory* (HMChPT) [27]. This leads to

$$\begin{aligned}&\langle K^-(p_3)|(\bar{s}u)_{V-A}|0\rangle\langle\overline{K}^0(p_1)K^+(p_2)|(\bar{u}b)_{V-A}|\overline{B}^0\rangle \\ &\quad = -\frac{f_K}{2}\left[2m_3^2r + (m_B^2 - s_{12} - m_3^2)\omega_+ + (s_{23} - s_{13} - m_2^2 + m_1^2)\omega_-\right], \end{aligned} \tag{1.77}$$

where $s_{ij} \equiv (p_i + p_j)^2$, and f_k is the kaon decay constant.

Three-kaon Creation

The matrix elements involving 3-kaon creation are given by [28]

$$\langle\overline{K}^0(p_1)K^+(p_2)K^-(p_3)|(\bar{s}d)_{V-A}|0\rangle\langle 0|(\bar{d}b)_{V-A}|\overline{B}^0\rangle \approx 0, \tag{1.78}$$

$$\langle\overline{K}^0(p_1)K^+(p_2)K^-(p_3)|\bar{s}\gamma_5 d|0\rangle\langle 0|\bar{d}\gamma_5 b|\overline{B}^0\rangle = v\frac{f_B m_B^2}{f_\pi m_b}\left(1 - \frac{s_{13} - m_1^2 - m_3^2}{m_B^2 - m_K^2}\right)F^{KKK}(m_B^2),$$

where

$$v = \frac{m_{K^+}^2}{m_u + m_s} = \frac{m_K^2 - m_\pi^2}{m_s - m_d}, \tag{1.79}$$

characterizes the quark-order parameter $\langle \bar{q}q \rangle$ which spontaneously breaks the chiral symmetry. Both relations in Eq. (1.78) are originally derived in the chiral limit [28] and hence the quark masses appearing in Eq. (1.79) are referred to the scale ~ 1 GeV . The first relation reflects helicity suppression which is expected to be even more effective for energetic kaons. For the second relation, the form factor F^{KKK} is introduced to extrapolate the chiral result to the physical region.

Two-kaon Creation

We now turn to the 2-kaon creation matrix element which can be expressed in terms of time-like kaon current form factors as

$$\begin{aligned} \langle K^+(p_{K^+})K^-(p_{K^-})|\bar{q}\gamma_\mu q|0\rangle &= (p_{K^+} - p_{K^-})_\mu F_q^{K^+K^-}, \\ \langle K^0(p_{K^0})\overline{K}^0(p_{\bar{K}^0})|\bar{q}\gamma_\mu q|0\rangle &= (p_{K^0} - p_{\bar{K}^0})_\mu F_q^{K^0\bar{K}^0}. \end{aligned} \tag{1.80}$$

The weak vector form factors $F_q^{K^+K^-}$ and $F_q^{K^0\bar{K}^0}$ can be related to the kaon electromagnetic (e.m.) form factors $F_{em}^{K^+K^-}$ and $F_{em}^{K^0\bar{K}^0}$ for the charged and neutral kaons, respectively. Phenomenologically, the e.m. form factors receive resonant and non-resonant contributions and can be expressed by

$$F_{em}^{K^+K^-} = F_\rho + F_\omega + F_\phi + F_{NR}, \qquad F_{em}^{K^0\bar{K}^0} = -F_\rho + F_\omega + F_\phi + F'_{NR}. \tag{1.81}$$

It follows from Eqs. (1.80) and (1.81) that

$$\begin{aligned} F_u^{K^+K^-} &= F_d^{K^0\bar{K}^0} = F_\rho + 3F_\omega + \frac{1}{3}(3F_{NR} - F'_{NR}), \\ F_d^{K^+K^-} &= F_u^{K^0\bar{K}^0} = -F_\rho + 3F_\omega, \\ F_s^{K^+K^-} &= F_s^{K^0\bar{K}^0} = -3F_\phi - \frac{1}{3}(3F_{NR} + 2F'_{NR}), \end{aligned} \tag{1.82}$$

where use of isospin symmetry has been made.

The form factors $F_{\rho,\omega,\phi}$ in Eqs. (1.81) and (1.82) include the contributions from the vector mesons $\rho(770)$, $\rho(1450)$, $\rho(1700)$, $\omega(782)$, $\omega(1420)$, $\omega(1650)$, $\phi(1020)$ and $\phi(1680)$.

Two-kaon Scalar Contribution

We also need to specify the 2-body matrix element $\langle K^+K^-|\bar{s}s|0\rangle$ induced from the scalar density. It receives resonant and non-resonant contributions:

$$\begin{aligned}\langle K^+(p_2)K^-(p_3)|\bar{s}s|0\rangle &\equiv f_s^{K^+K^-}(s_{23}) = \sum_i \frac{m_i \bar{f}_i g^{i\to KK}}{m_i^2 - s_{23} - im_i\Gamma_i} + f_s^{NR},\\ f_s^{NR} &= \frac{v}{3}(3F_{NR} + 2F'_{NR}) + v\frac{\sigma}{s_{23}^2}\left[\ln\left(\frac{s_{23}}{\tilde{\Lambda}^2}\right)\right]^{-1}, \end{aligned} \tag{1.83}$$

where the scalar decay constant $\tilde{f}_i$ is defined in $\langle i|\bar{s}s|0\rangle = m_i\bar{f}_i$, $g^{i\to KK}$ is the $i \to KK$ strong coupling, and the non-resonant terms are related to those in $F_s^{K^+K^-}$ through the equation of motion. The main scalar meson pole contributions are those that have dominant $s\bar{s}$ content and large coupling to $K\overline{K}$. It is found in [29] that among the f_0 mesons, only $f_0(980)$ and $f_0(1530)$ have the largest couplings with the $K\overline{K}$ pair. Note that $f_0(1530)$ is a very broad state with the width of order 1 GeV/c^2 [29].

Amplitude for $B^0 \to K^+K^-K^0$

Collecting all the relevant matrix elements evaluated above, we are ready to compute the amplitude $A(\overline{B}^0 \to K_{S(L)}K^+K^-) = \pm A(\overline{B}^0 \to \overline{K}^0K^+K^-)/\sqrt{2}$. Since under CP-conjugation we have $K_S(\vec{p}_1) \to K_S(-\vec{p}_1)$, $K^+(\vec{p}_2) \to K^-(-\vec{p}_2)$ and $K^-(\vec{p}_3) \to K^+(-\vec{p}_3)$, the $\overline{B}^0 \to K_SK^+K^-$ amplitude can be decomposed into CP-odd and CP-even components

$$\begin{aligned}&A[\overline{B}^0 \to K_S(p_1)K^+(p_2)K^-(p_3)] = A(s_{12}, s_{13}, s_{23}) = A_{CP-} + A_{CP+},\\ &A_{CP\pm} = \frac{1}{2}[A(s_{12}, s_{13}, s_{23}) \pm A(s_{13}, s_{12}, s_{23})].\end{aligned} \tag{1.84}$$

Correspondingly, we have

$$\begin{aligned}\Gamma &= \Gamma_{CP+} + \Gamma_{CP-},\\ \Gamma_{CP\pm} &= \frac{1}{(2\pi)^3}\frac{1}{32m_B^3}\int |A_{CP\pm}|^2 ds_{12}ds_{13} = \frac{1}{(2\pi)^3}\frac{1}{32m_B^3}\int |A_{CP\pm}|^2 ds_{12}ds_{23}.\end{aligned} \tag{1.85}$$

The vanishing cross terms due to the interference between CP-odd and CP-even components can be easily seen from the (anti)symmetric properties of the amplitude and the integration variables under the interchange of $s_{12} \leftrightarrow s_{13}$. Similar relations hold for the conjugated B^0 decay rate $\bar{\Gamma}$. The CP-even fraction f_+ is defined by

$$f_+ \equiv \left.\frac{\Gamma_{CP+} + \overline{\Gamma}_{CP+}}{\Gamma + \overline{\Gamma}}\right|_{\phi K_S \text{ excluded.}} \tag{1.86}$$

Note that results for the $K^+K^-K_L$ mode are identical to the $K^+K^-K_S$ ones with the *CP* eigenstates interchanged. For example, results for $(K^+K^-K_L)_{CP+}$ are the same as those for $(K^+K^-K_S)_{CP-}$ and hence f_+ in $K^+K^-K_S$ corresponds to f_- in $K^+K^-K_L$.

1.6.2 $B^0 \to K^0_s K^0_s K^0_s$ Decay Amplitude

In an analogous way, the decay amplitudes of $\overline{B^0} \to K^0_S K^0_S K^0_S$ decays can be evaluated:

$$\begin{aligned} A[\overline{B}^0 \to K_S(p_1)K_S(p_2)K_{S,L}(p_3)] &= \left(\frac{1}{2}\right)^{3/2}\Big\{ \pm A[\overline{B}^0 \to K^0(p_1)\overline{K}^0(p_2)\overline{K}^0(p_3)] \\ &\quad \pm A[\overline{B}^0 \to K^0(p_2)\overline{K}^0(p_3)\overline{K}^0(p_1)] \\ &\quad + A[\overline{B}^0 \to K^0(p_3)\overline{K}^0(p_1)\overline{K}^0(p_2)]\Big\}, \quad (1.87) \end{aligned}$$

with

$$\begin{aligned} A[\overline{B}^0 \to K^0(p_1)\overline{K}^0(p_2)\overline{K}^0(p_3)] &= \frac{G_F}{\sqrt{2}}\sum_{p=u,c}\lambda_p\Bigg\{\Big[\langle K^0(p_1)\overline{K}^0(p_2)|(\bar{d}b)_{V-A}|\overline{B}^0\rangle\langle\overline{K}^0(p_3)|(\bar{s}d)_{V-A}|0\rangle \\ &\quad + \langle K^0(p_1)\overline{K}^0(p_3)|(\bar{d}b)_{V-A}|\overline{B}^0\rangle\langle\overline{K}^0(p_2)|(\bar{s}d)_{V-A}|0\rangle\Big] \\ &\quad \times\Big(a^p_4 + \frac{1}{2}a^p_{10} - (a^p_6 - \frac{1}{2}a^p_8)r_\chi\Big) \\ &\quad + \Big[\langle\overline{K}^0(p_2)|\bar{s}b|\overline{B}^0\rangle\langle K^0(p_1)\overline{K}^0(p_3)|\bar{s}s|0\rangle \\ &\quad + \langle\overline{K}^0(p_3)|\bar{s}b|\overline{B}^0\rangle\langle K^0(p_1)\overline{K}^0(p_2)|\bar{s}s|0\rangle\Big](-2a^p_6 + a^p_8) \\ &\quad + \langle K^0(p_1)\overline{K}^0(p_2)\overline{K}^0(p_3)|\bar{s}\gamma_5 d|0\rangle\langle 0|\bar{d}\gamma_5 b|\overline{B}^0\rangle(-2a^p_6 + a^p_8) \\ &\quad + \Big[\langle\overline{K}^0(p_2)|(\bar{s}b)_{V-A}|\overline{B}^0\rangle\langle K^0(p_1)\overline{K}^0(p_3)|(\bar{s}s)_{V-A}|0\rangle \\ &\quad + \langle\overline{K}^0(p_3)|(\bar{s}b)_{V-A}|\overline{B}^0\rangle\langle K^0(p_1)\overline{K}^0(p_2)|(\bar{s}s)_{V-A}|0\rangle\Big] \\ &\quad \times\left[a_3 + a^p_4 + a_5 - \frac{1}{2}(a_7 + a_9 + a_{10})\right]\Bigg\}, \quad (1.88) \end{aligned}$$

where the last term will not contribute to the purely *CP*-even decay $\overline{B}^0 \to K_S K_S K_S$. Decay rates for the $K_S K_S K_S$ and $K_S K_S K_L$ modes can be obtained from Eq. (1.85) with an additional factor of 1/3! and 1/2!, respectively, for identical particles in the final state.

1.6.3 *CP* Asymmetries

We now consider the *CP* asymmetries for $\overline{B}^0 \to K^+K^-K_{S(L)}$, $K_SK_SK_{S(L)}$ decays. The direct *CP* asymmetry and the mixing induced *CP* violation are defined by

$$\begin{aligned}
A_{KKK} &= \frac{\Gamma - \overline{\Gamma}}{\Gamma + \overline{\Gamma}} \\
&= \frac{\int |A|^2 ds_{12} ds_{23} - \int |\bar{A}|^2 ds_{12} ds_{23}}{\int |A|^2 ds_{12} ds_{23} + \int |\bar{A}|^2 ds_{12} ds_{23}}, \\
S_{KKK,CP\pm} &= \frac{2\int \mathrm{Im}(e^{-2i\beta} A_{CP\pm} \bar{A}^*_{CP\pm}) ds_{12} ds_{23}}{\int |A_{CP\pm}|^2 ds_{12} ds_{23} + \int |\bar{A}_{CP\pm}|^2 ds_{12} ds_{23}}, \\
S_{KKK} &= \frac{2\int \mathrm{Im}(e^{-2i\beta} A \bar{A}^*) ds_{12} ds_{23}}{\int |A|^2 ds_{12} ds_{23} + \int |\bar{A}|^2 ds_{12} ds_{23}} \\
&= f_+ \, S_{KKK,CP+} + (1 - f_+) \, S_{KKK,CP-}, \qquad (1.89)
\end{aligned}$$

where $\bar{A}$ is the decay amplitude of $B^0 \to K^+K^-K_{S(L)}$ or $K_SK_SK_{S(L)}$. For the $K^+K^-K_S$ mode, it is understood that the contribution from ϕK_S is excluded. It is expected in the SM that $S_{KKK,CP+} \equiv \sin 2\beta_{\rm eff} \approx \sin 2\beta$, $S_{KKK,CP-} \approx -\sin 2\beta$ and hence $S_{KKK} \approx -(2f_+ - 1)\sin 2\beta$.[1]

The numerical expectation values for the *CP* asymmetries are shown in Table 1.1 [26].

Final State	$\sin 2\beta_{\rm eff}$
$(K^+K^-K_S)_{\phi K_S \text{ excluded}}$	$0.749^{+0.080+0.024+0.004}_{-0.013-0.011-0.015}$
$(K^+K^-K_S)_{CP+}$	$0.770^{+0.113+0.040+0.002}_{-0.031-0.023-0.013}$
$(K^+K^-K_L)_{\phi K_L \text{ excluded}}$	$0.749^{+0.080+0.024+0.004}_{-0.013-0.011-0.015}$
$K_SK_SK_S$	$0.748^{+0.000+0.000+0.007}_{-0.000-0.000-0.018}$
$K_SK_SK_L$	$0.748^{+0.001+0.000+0.007}_{-0.001-0.000-0.018}$
	$A_f(\%)$
$(K^+K^-K_S)_{\phi K_S \text{ excluded}}$	$0.16^{+0.95+0.29+0.01}_{-0.11-0.32-0.02}$
$(K^+K^-K_S)_{CP+}$	$-0.09^{+0.73+0.16+0.01}_{-0.00-0.27-0.01}$
$(K^+K^-K_L)_{\phi K_L \text{ excluded}}$	$0.16^{+0.95+0.29+0.01}_{-0.11-0.32-0.02}$
$K_SK_SK_S$	$0.74^{+0.02+0.00+0.05}_{-0.06-0.01-0.06}$
$K_SK_SK_L$	$0.77^{+0.12+0.08+0.06}_{-0.28-0.11-0.07}$

Table 1.1: Mixing-induced and direct *CP* asymmetries $\sin 2\beta_{\rm eff}$ (top) and A_f (in %, bottom), respectively, in $B^0 \to K^+K^-K_S$ and $K_SK_SK_S$ decays. Results for $(K^+K^-K_L)_{CP\pm}$ are identical to those for $(K^+K^-K_S)_{CP\mp}$.

The K^+K^- mass spectra of the $\overline{B}^0 \to K^+K^-K_S$ decay from CP-even and CP-odd contributions are shown in Fig. 1.5. In the spectra, there are peaks at the threshold and a

[1] Writing the *CP*-conjugated decay amplitude as $\bar{A} = \bar{A}_{CP+} + \bar{A}_{CP-}$, we have $\bar{A}_{CP\pm} = \pm A_{CP\pm}$ with $\lambda_p \to \lambda_p^*$. This leads to $S_{KKK,CP-} \approx -S_{KKK,CP+}$.

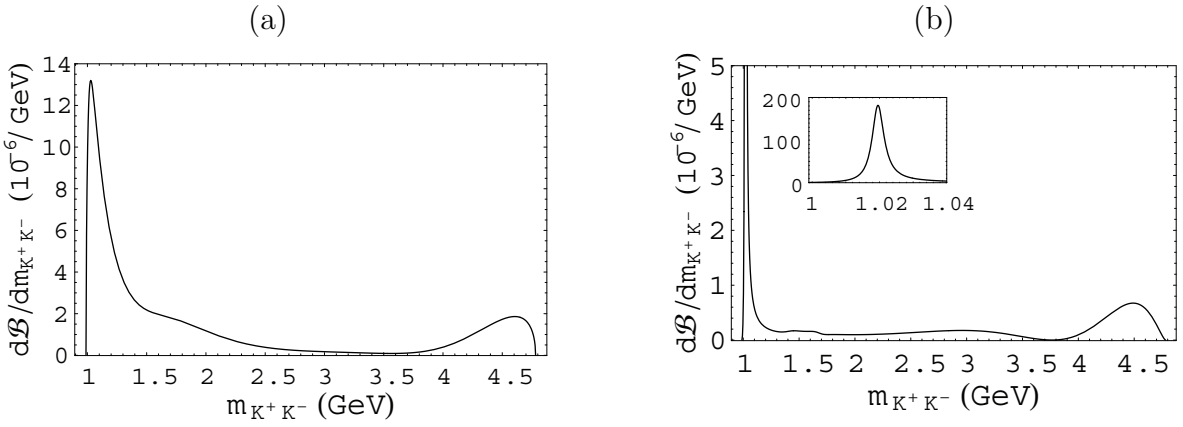

Figure 1.5: The K^+K^- mass spectra for $\overline{B}^0 \to K^+K^-K_S$ decay from (a) CP-even and (b) CP-odd contributions. The insert in (b) is for the ϕ region. Results for $(K^+K^-K_L)_{CP\pm}$ are identical to those for $(K^+K^-K_S)_{CP\mp}$.

milder one in the large $m_{K^+K^-}$ region. For the CP-even part, the threshold enhancement arises from the $f_0(980)K_S$ and the non-resonant contributions, while the peak at large $m_{K^+K^-}$ comes from the non-resonant two-meson transition $\overline{B}^0 \to K^+K_S$ followed by a current produced K^-. For the CP-odd spectrum the bump at the large $m_{K^+K^-}$ end originates from the same two-meson transition term, while the peak on the lower end corresponds to the ϕK_s contribution, which is also shown in the insert. The full $K^+K^-K_S$ spectrum is basically the sum of the CP-even and the CP-odd parts.

The deviation of the mixing-induced CP asymmetry in $B^0 \to K^+K^-K_S$ and $K_SK_SK_S$ from that measured in $B \to J/\psi K_S$ (or the fitted CKM's $\sin 2\beta$ [30]), namely, $\Delta \sin 2\beta_{\rm eff} \equiv \sin 2\beta_{\rm eff} - \sin 2\beta_{J/\psi K_S\,(CKM)}$, is calculated from Table 1.1 to be

$$\Delta \sin 2\beta_{K^+K^-K_S} = 0.06^{+0.08}_{-0.02}\ (0.02^{+0.08}_{-0.02}), \tag{1.90}$$

$$\Delta \sin 2\beta_{K_SK_SK_S} = 0.06^{+0.00}_{-0.00}\ (0.02^{+0.00}_{-0.00}). \tag{1.91}$$

Note that part of the deviation comes from that between the measured $\sin 2\beta_{J/\psi K_S}$ and the fitted CKM's $\sin 2\beta$. The $K^+K^-K_S$ has a potentially sizable $\Delta \sin 2\beta$, as this penguin-dominated mode is subject to a tree pollution due to the presence of color-allowed tree contributions. For the $K_SK_SK_S$ mode, the central value and the error on $\Delta \sin 2\beta$ are small.

It is also useful to exploit the dependence of $\sin 2\beta_{\rm eff}$ on the K^+K^- invariant mass, $m_{K^+K^-} \equiv m_{23} = \sqrt{s_{23}}$. For the phase space integration in Eq. (1.89), for a given s_{23}, the upper and lower bounds of s_{12} are fixed. The invariant mass m_{23} is integrated from

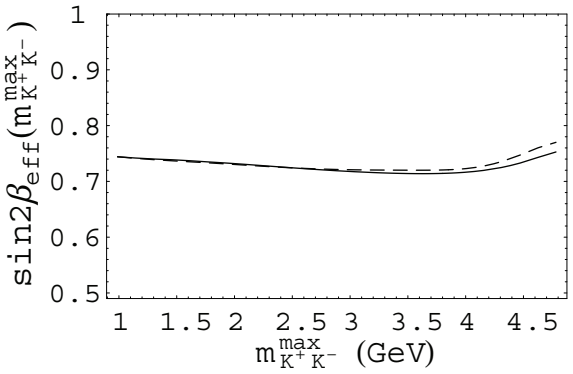

Figure 1.6: Mixing-induced *CP* asymmetry $\sin 2\beta_{\rm eff}(m^{\rm max}_{K^+K^-})$ (see the text for the definition) versus the invariant mass $m^{\rm max}_{K^+K^-}$ for $K^+K^-K_S$ with ϕK_S excluded (solid line) and for *CP*-even $K^+K^-K_S$ (dashed line). When $m^{\rm max}_{K^+K^-}$ approaches the upper limit $m_B - m_{K_S}$, the whole phase space is saturated and $\sin 2\beta_{\rm eff}(m^{\rm max}_{K^+K^-})$ is reduced to the usual $\sin 2\beta_{\rm eff}$. This result also applies to the $K^+K^-K_L$ mode.

$m^-_{23} = m_2 + m_3$ to $m^+_{23} = m_B - m_1$. When the variable s_{23} or m_{23} is integrated from m^-_{23} to a fixed $m^{\rm max}_{23}$ (of course, $m^-_{23} < m^{\rm max}_{23} \leq m^+_{23}$), the effective $\sin 2\beta$ thus obtained is designated as $\sin 2\beta_{\rm eff}(m^{\rm max}_{23})$. Fig. 1.6 shows the plot of $\sin 2\beta_{\rm eff}(m^{\rm max}_{K^+K^-})$ versus $m^{\rm max}_{K^+K^-}$ for $K^+K^-K_S$. Since there are two different methods for the determination of $\sin 2\beta_{\rm eff}$, the results are depicted in two different curves. It is interesting that $\sin 2\beta(m^{\rm max}_{23})$ is slightly below $\sin 2\beta_{CKM}$ at the bulk of the $m_{K^+K^-}$ region and gradually increases and becomes slightly larger than $\sin 2\beta_{CKM}$ when the phase space is getting saturated. The deviation $\Delta \sin 2\beta_{K^+K^-K_S}$ arises mainly from the large $m_{K^+K^-}$ region.

Direct *CP* violation is found to be very small in both $K^+K^-K_S$ and $K_SK_SK_S$ modes. It is interesting to notice that direct *CP* asymmetry in the *CP*-even $K^+K^-K_S$ mode is only of order 10^{-3}, but it becomes 0.2×10^{-2} in $K^+K^-K_S$ with ϕK_S excluded. Since these direct *CP* asymmetries are so small they can be used as approximate null tests of the SM.

Chapter 2

Time Dependent *CP* Asymmetry for Neutral *B* Decays

The *CP* violation in $B\overline{B}$ system can be measured determining the asymmetry in the number of decays of the B^0 and $\overline{B}^0$ mesons in the final state f and its *CP* conjugate $\bar{f}$:

$$\mathcal{A}_{CP} = \frac{\Gamma(\bar{B}^0 \to \bar{f}) - \Gamma(B^0 \to f)}{\Gamma(\bar{B}^0 \to \bar{f}) + \Gamma(B^0 \to f)}. \tag{2.1}$$

Once the B candidate is reconstructed in a certain final state, the measurement of $\mathcal{A}_{CP}$ requires the knowledge of the flavour of the other B (called *tag* B: B_{tag}). The asymmetry defined in Eq. 2.1, also called *direct CP asymmetry*, can be measured simply by counting the number of B and $\bar{B}$ mesons decaying in self tagging final states (as $B^0 \to K^+\pi^-$ and $\overline{B}^0 \to K^-\pi^+$). In the case of time-dependent *CP* asymmetry, it corresponds to the parameter C of the time evolution of the $B^0\overline{B}^0$ quantum system, when one of the B's decays into a *CP* eigenstate:

$$\Gamma^{B^0}_{\overline{B}^0}(\Delta t) = \frac{e^{-\frac{\Delta t}{\tau}}}{4\tau}\left(1 \pm S\sin(\Delta m_d \Delta t) \mp C\cos(\Delta m_d \Delta t)\right) \tag{2.2}$$

where $\Gamma^{B^0}_{\overline{B}^0}$ corresponds to the flavour of the tag B^0 ($\overline{B}^0$). The most powerful strategy for measuring *CP* violation, is to measure the parameter S of Eq. 2.2, which is connected with the weak phase that produces the *CP* violation.

The main two ingredients to measure the time-dependent *CP* asymmetry parameters in Eq. 2.2 are:

1. the knowledge of the flavour of the other B meson (*flavour tagging* procedure);

2. the measurement of time distance between the two B decays Δt. This is the one of the main goals of an asymmetric B-factory, as the BABAR experiment. In such

an experimental framework, Δt information can be accessed measuring the spatial distance Δz between the decay vertex of the signal B and the decay vertex of the B_{tag}, through the relation

$$\Delta z = \beta\gamma\Delta t \tag{2.3}$$

In the following we will discuss the B flavour tagging and the methods to determine the decay vertex of a B meson. For this purpose, we will present two techniques to reconstruct the decay vertex. The standard one is used for the decay $B^0 \to K^+K^-K^0$, for which there are two charged tracks originating directly from the B vertex. A different vertexing technique has to be used for $B^0 \to K^0_S K^0_S K^0_S$ decays, for which there are no charged tracks from the primary vertex. In this case the information on the vertex position is extrapolated using the K^0_S flight direction and the knowledge of the beam spot position. This technique is called *Beam Spot Constrained* vertexing.

Both the tagging and the vertexing techniques avoid the inefficiencies of the exclusive reconstruction of the other meson by inclusively inferring its flavour and decay vertex from its final decay products. In order to estimate their performance, the flavour *mistag* probabilities and vertexing resolution are measured on a sample of fully reconstructed B decays to self-tagging final states, where the physics of the flavour and time structure of the events are known.

2.1 *b*-Flavour Tagging

Neutral B mesons often decay to final states, which are only accessible to either a b or a $\bar{b}$ quark, therefore revealing the meson's flavour. For example, a positively charged lepton from $B^0 \to D^{*-}l^+\nu$ identifies the presence of a $\bar{b}$ quark and allows the meson to be *tagged* as a B^0. Despite the impressively large number of B decays recorded by *BABAR* detector, the reconstruction efficiency of such self-tagging modes, along with the small branching fraction of *CP* final states, produces insufficient yields to exclusively reconstruct also the tagging B. However an inclusive method, which allows b flavour tagging on a probability basis, provides adequate information for *CP* measurements.

The *BABAR* flavour tagging algorithm is designed to exploit correlations between the b flavour and the charges of the final products of six distinct b quark decay modes. It is tuned and tested on Monte Carlo events where the flavour of the B mesons are known. However, since the Monte Carlo does not perfectly reproduces the data, the performances

Decay mode	Branching fraction (%)
$B^0 \to D^{*-}\pi^+$	0.28 ± 0.02
$B^0 \to D^{*-}\rho^+$	0.73 ± 0.15
$B^0 \to D^{*-}a_1^+$	1.30 ± 0.27
$B^0 \to D^-\pi^+$	0.30 ± 0.04
$B^0 \to D^-\rho^+$	0.78 ± 0.14
$B^0 \to D^-a_1^+$	0.60 ± 0.33

Table 2.1: The measured branching fraction of the fully reconstructed self tagging B decays in the `BReco` sample

of the tagging algorithm are tested on samples of fully reconstructed B decays (the so-called `BReco` sample). Table 2.1 lists the seven self-tagging B^0 decays which are fully reconstructed to compose the fully `BReco` sample.

The performances of the tagging algorithm are quantified by the parameter

$$Q = \varepsilon^t(1-2\omega)^2 = \varepsilon^t D^2 \tag{2.4}$$

where ε^t is the tagging efficiency, defined as the fraction of events to which a b flavour tag can be assigned and the mistag fraction ω, defined as the fraction of events for which the tagging algorithm mis-identifies the flavour of the B meson; $D \equiv (1-2\omega)$ is defined as the *dilution* factor associated to the tagging algorithm.

Large values of the quantity Q indicate good tagging performance, since they come from a large fraction of tagged events and/or a large probability to get the right answer from the algorithm. In particular, we will show (Sec.2.1.7) that the error on $S = \sin 2\beta$ in the time-dependent *CP* asymmetry is proportional to $\sqrt{1/Q}$.

In the following we present the different decays which are used by the tagging algorithm.

2.1.1 Leptons from Semi-leptonic Decays

Semi-leptonic $B \to Xl\nu$ decays (Fig. 2.1a), which constitute roughly 20% of the B branching fraction, produce electrons or muons whose charge has same sign as the b quark. Since these leptons are the primary product of the virtual W boson emitted by the b quark, they carry large momenta p_l^* in the center of mass of the B and may therefore be distinguished from softer secondary leptons from $\bar{b} \to \bar{c} \to \bar{s}$ transitions (Fig. 2.1b) which exhibit the opposite lepton/b quark correlation. The primary leptons are also faster than most pi-

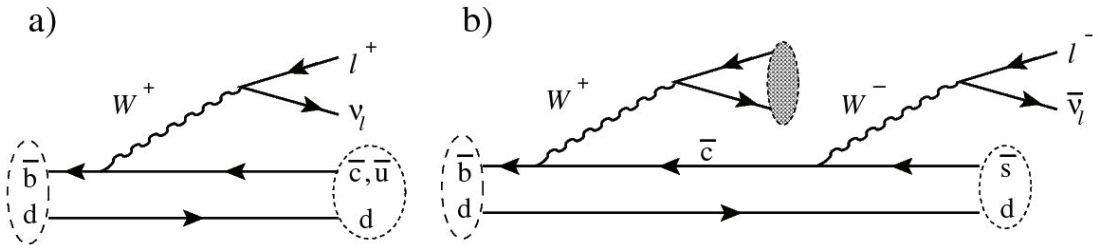

Figure 2.1: Leading lepton producing neutral B meson decays. The b quark and lepton charges are correlated in (a) $B \to Xl\nu$ and anti-correlated in the (b) $\bar{b} \to \bar{c} \to \bar{s}$.

ons and kaons produced by B decays, allowing additional discrimination of misidentified leptons and also permitting purely kinematic selection of the $B \to Xl\nu$ lepton when no particle identification is available.

Three separate neural networks (NN) recognize primary leptons. Two of them examine identified electrons or muons, while the other considers only kinematic informations. In addition to p_l^*, these NN also moderately benefit from two other kinematic variables: the total energy in the hemisphere defined by the W direction, which is generally smaller for $B \to Xl\nu$ than its inclusive backgrounds, and the CM angle between missing momentum (i.e. the ν direction) and the primary lepton, which is also small for real semi-leptonic decays. Ultimately kinematics and strict lepton identification make the semi-leptonic B decays the cleanest and hence most reliable flavour tagging signature. Though tagging using leptons is not very efficient ($\varepsilon^t \approx 9\%$), it is very accurate ($\omega \approx 3\%$), resulting in $Q \approx 0.08$.

2.1.2 Kaons from $b \to c \to s$ Transitions

The correlation of final state kaons and the b quark charge comes from the hierarchy among elements of CKM matrix involved in B and D decays. The average number of positively charged kaons in the B^0 decay products is $0.58 \pm 0.01 \pm 0.08$, while the negatively charged kaon multiplicity is $0.13 \pm 0.01 \pm 0.05$ [32]. Fig. 2.2 shows an example a of $\bar{b} \to \bar{c} \to \bar{s}$ transition which produces each of the three kaon sources which are relevant in this case. The $\bar{s}$ quark in the $\bar{b} \to \bar{c} \to \bar{s}$ transition is the primary source of the positive (or right-sign) correlation between the b quark and kaon charge. However, the decay chain of the $\bar{c}$ quark also generates a W boson, which occasionally produces kaons. In the specific process diagrammed in Fig. 2.2, the W^+ boson produces a Cabbibo suppressed

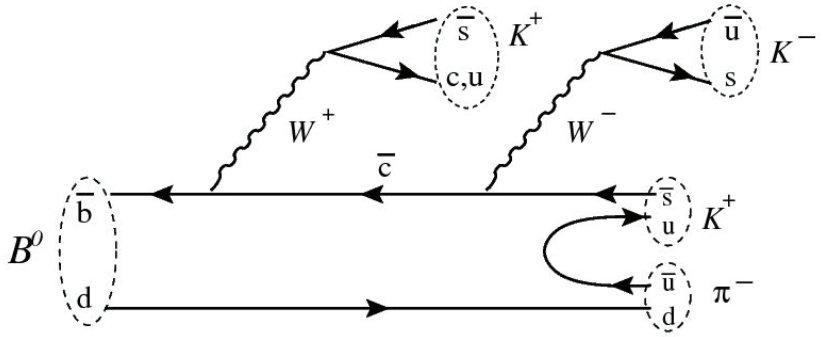

Figure 2.2: An example of a $\bar{b} \to \bar{c} \to \bar{s}$ transition which produces kaons whose charge has both the same and opposite sign as the b quark.

$u\bar{s}$ quark pair, which results in another right-sign kaon. The W^- boson from the $\bar{c}$ decay results in a wrong-sign kaon. Unlike the case of leptonic tagging, no kinematic separation between the right and wrong sign kaons is available, since kaon identification is left as the only signature, resulting in a less clean tagging. The tagger identifies kaons using one NN which examines the three best kaon candidates and determines the b flavour from the sum of the product of each kaon charge and likelihood to be a kaon, which is calculated using the DCH dE/dx and DIRC θ_c measurements. Flavour tags from kaons are generally more efficient than lepton tags, but less accurate. The best kaon tagged events have $\varepsilon^t \approx 17\%$ and $D \approx 0.8$ resulting in $Q \approx 0.11$.

2.1.3 Soft Pions from $D^{*\pm}$ Decays

In the decay $D^{*+} \to D^0\pi^+$, the D^{*+} and D^0 masses are so close (≈ 142 MeV/c^2) that the additional pion carries very little momentum and flies in the same direction as the D^0. This pion is usually described as slow or soft. When the D^* originates from a B meson decay, as in Fig. 2.3, the D^* charge and hence its slow-pion charge are opposite to that of the original b quark. The slow-pion NN is a neural network which examines pions with CM momentum $p^*_{\pi_s}$ less than 250 MeV and identifies a slow-pion from its momentum $p^*_{\pi_s}$, the angle between its flight direction and the thrust axis of the rest of the B meson products, and particle identification information. Another NN attempts to exploit correlations between the kaon and slow-pion from the D^* to produce a more reliable tag. This neural network-based algorithm examines all oppositely charged slow pion and kaon combinations along with the kaon likelihood, the slow-pion NN output,

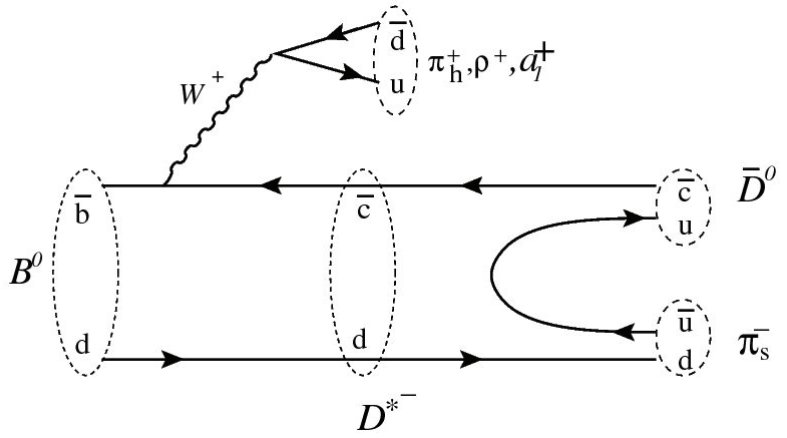

Figure 2.3: Diagram of $B^0 \to D^{*-}\pi^+, \rho^+, a_1^+$ decays, producing a soft pion (π_s^-) whose charge has the opposite sign as the b quark. In contrast the π^+, ρ^+, or a_1^+ emitted from the W^+ carry the same charge as the b quark.

and the angle between the kaon and slow-pion. The resulting performance is $\epsilon^t \approx 14\%$ and $D \approx 0.35$, resulting in a $Q \approx 1.8\%$.

2.1.4 Hard Pions from $B^0 \to D^{*-}\pi^+$, ρ^+, a_1^+ Decays

The charge of the virtual W^+ boson in Fig. 2.3 carries the same sign as the b quark charge. When this boson hadronizes into a pion (or into a ρ^+, or a_1^+), the b quark flavour may be identified from the characteristically fast momentum of this prompt B meson product. A maximum p^* NN attempts to capture the b flavour from these particles by selecting the track with the highest CM momentum which originates from less than 1 mm far from the beams in the $x-y$ plane. This procedure also captures prompt leptons which were missed by the lepton NN and which fortunately have the same charge/b flavour correlation.

2.1.5 Fast-slow Correlations and Λ Baryon Decays

Two additional kinds of information can be used to increase the efficiency of the tagging process. This information is usually based on a weak correlation among a physics process and the b quark charge, resulting in a higher mistag rate probability.

Fast-slow Correlations

The b flavour can be inferred in events where in the B rest frame the soft pion coming from the decay of a $D^{*\pm}$ is found together with a opposite charge track which comes from

	ϵ^t (%)	$\Delta\epsilon^t$ (%)	ω (%)	$\Delta\omega$ (%)	Q (%)	ΔQ (%)
Lepton	8.67 ± 0.08	0.1 ± 0.2	3.0 ± 0.3	-0.2 ± 0.6	7.67 ± 0.13	0.14 ± 0.42
kaon I	10.96 ± 0.09	0.1 ± 0.2	5.3 ± 0.4	-0.6 ± 0.7	8.74 ± 0.16	0.27 ± 0.53
kaon II	17.21 ± 0.10	0.1 ± 0.3	15.5 ± 0.4	-0.4 ± 0.7	8.21 ± 0.19	0.25 ± 0.57
kaon-pion	13.77 ± 0.10	-0.5 ± 0.3	23.5 ± 0.5	-2.4 ± 0.8	3.87 ± 0.14	0.56 ± 0.40
pion	14.38 ± 0.10	-0.8 ± 0.3	33.0 ± 0.5	5.2 ± 0.8	1.67 ± 0.10	-1.12 ± 0.27
other	9.61 ± 0.08	0.5 ± 0.2	41.9 ± 0.6	4.6 ± 0.9	0.25 ± 0.04	-0.27 ± 0.10
Total	74.60 ± 0.12	-0.6 ± 0.7			30.4 ± 0.3	-0.2 ± 1.0

Table 2.2: Summary of tagging performances: tagging efficiency (ϵ^t), mistag probability (ω) and Q factor.

the W boson exchange. The angular correlation allows to determine if the two particles are back-to-back, as expected.

Λ Decays

The presence of a Λ baryon is a good signature of a $\bar{b} \to \bar{c} \to \bar{s}$. A Λ baryon, reconstructed in the final state $p\pi^-$, is a signature of a B^0 decay, while a $\bar{\Lambda}$, reconstructed in the final state $\bar{p}\pi^+$ is a signature of a $\overline{B}^0$ decay.

2.1.6 Combining the Tag Signatures

A given set of particles belonging to a B meson may exhibit the signature of any number of the described six flavour-tagging physics processes, and therefore may be identified by several of the seven NN. In general, each NN i may provide an output r_1^i whose sign and magnitude reflect the B flavour and the confidence in the result. A higher level NN attempts to optimally combine these outputs in order to produce an output r_2 which captures the most reliable tag of the meson flavour considering all available information.

The low-level NN and the high-level NN outputs, r_1^i and r_2 , are fed to a decision algorithm which assigns the tag to one of six hierarchical and mutually exclusive physics-signature categories (in descending order of reliability): lepton, kaon I, kaon II, kaon-(slow)pion, (slow)pion and other (mostly hard pions). Events which do not satisfy the requirements of any of these categories are marked as untagged.

In this way, the overall tagging performance is $Q = 31\%$, as shown in Table 2.2. The remaining 25% of untagged events has $\omega = 0.5$ and $Q = 0$.

2.1.7 Tagging Imperfections

The Monte Carlo event generator incomplete knowledge of B branching fractions and the not perfect simulation of the detector response makes necessary to extract from data the values of these quantities that define the tagger performance. This is made possible since B^0 mixing may be exploited to measure tagging parameters. In fact, applying Eq. 1.51 to B decays to a flavor eigenstate, one obtains the time-dependent probability distributions for four different possible flavour combinations:

$$\begin{aligned}\Gamma_{B^0,\overline{B}^0}(\Delta t) &= \Gamma_{\overline{B}^0,B^0}(\Delta t) = \frac{e^{-\frac{|\Delta t|}{\tau}}}{4\tau}(1+\cos(\Delta m_d \Delta t)),\\ \Gamma_{B^0,B^0}(\Delta t) &= \Gamma_{\overline{B}^0,\overline{B}^0}(\Delta t) = \frac{e^{-\frac{|\Delta t|}{\tau}}}{4\tau}(1-\cos(\Delta m_d \Delta t)),\end{aligned} \tag{2.5}$$

where the $\cos(\Delta m_d \Delta t)$ terms are due to B^0-$\overline{B}^0$ mixing. These two decay distributions are usually referred to as the *unmixed* and *mixed* probabilities, respectively. For the extraction of the tagging performance, one B meson (B_{rec}) is fully reconstructed, so its flavour is known. Then the tagger is supplied to the particles which are not daughter of B_{rec}, in order to determine the flavour of the other B. Several imperfections in this procedure modify Eq. 2.5. In particular for a tagging category i:

1. The tagging algorithm may produce a wrong-tag. We will denote this mis-tag probability as $\bar{\omega}_i$.
2. There may be different mis-tag probabilities, ω_{i+} and ω_{i-} for B^0 and $\overline{B}^0$ tags. So $\bar{\omega}_i = (\omega_{i+} + \omega_{i-})/2$
3. The tagging process costs on efficiency ϵ_i^t, which depends on tag signature
4. There may be different efficiencies, ${\varepsilon^t}_{i+}$ and ${\varepsilon^t}_{i-}$ for tagging a B^0 and $\overline{B}^0$
5. There may be different efficiencies, ${\varepsilon^r}_{i+}$ and ${\varepsilon^r}_{i-}$ for fully reconstructed B^0 and $\overline{B}^0$
6. There is an experimental resolution associated to the measurement of Δt. We will address this issue in Sec. 2.2.4.

Using these definitions and Eq. 2.5, the probability distribution for *observing* an event with a tagged flavour $T = \pm$ ($+ = B^0$, $- = \overline{B}^0$) for one meson and reconstructed flavour $R = \pm$ for the other is:

$$P_i(\Delta t, T, R) = \frac{{\varepsilon^r}_{i(R)}}{{\varepsilon^r}_{i(R)} + {\varepsilon^r}_{i(-R)}} \left[{\varepsilon^t}_{i(T)}(1-\omega_{i(T)})\Gamma_{(R),(T)} + {\varepsilon^t}_{i(T)}\omega_{i(-T)}\Gamma_{(-R),(T)} \right], \tag{2.6}$$

where the first term in the sum is for the correct (T, R) tags and the second term accounts for mis-tags which are actually $(-T, R)$. Rearranging this expression and properly normalizing in each category [1], one obtains

$$\begin{aligned} P(\Delta t, T, T, R; \hat{q}_i) &= \frac{\bar{\varepsilon}_i^t}{8\tau} \frac{1 + R\nu_i}{1 - \mu_i \nu_i \xi} e^{-\frac{|\Delta t|}{\tau}} \times \\ &\quad ([\mu_i T D_i + B_i] - [T D_i + \mu_i B_i] R \cos(\Delta m_d \Delta t)) \end{aligned} \tag{2.7}$$

where $\xi \equiv \frac{1}{1+(\tau \Delta m_d)^2}$, $B_i = \left(1 + T\frac{\Delta D_i}{2}\right)$ and the parameters $\hat{q}_i$ are

- $D_i \equiv 1 - 2\bar{\omega}_i$, which is called *dilution*,
- the dilution difference $\Delta D_i \equiv 2(\omega_{i-} - \omega_{i+})$,
- the reconstruction efficiency asymmetries $\nu_i \equiv \frac{\varepsilon_{i+}^r - \varepsilon_{i-}^r}{\varepsilon_{i+}^r + \varepsilon_{i-}^r}$,
- tagging efficiency asymmetries $\mu_i \equiv \frac{\varepsilon_{i+}^t - \varepsilon_{i-}^t}{\varepsilon_{i+}^t + \varepsilon_{i-}^t}$, and
- the average tagging efficiency $\varepsilon_i^t \equiv \frac{1}{2}(\varepsilon_{i+}^t + \varepsilon_{i-}^t)$.

Then, if the Δt resolution and flavour tagging were perfect, the asymmetry as a function of Δt

$$A_{\text{mixing}}(\Delta t) = \frac{N_{\text{unmix}}(\Delta t) - N_{\text{mix}}(\Delta t)}{N_{\text{unmix}}(\Delta t) + N_{\text{mix}}(\Delta t)} \tag{2.8}$$

would describe a cosine function with unit amplitude (Eq. 2.5). The effect of the tagging imperfections on the Δt distributions for *mixed* and *unmixed* events is shown in Fig. 2.4.

The asymmetry goes through zero near 2.1 B^0 proper lifetimes and the sensitivity to Δm_d, which is proportional to $\Delta t^2 \mathrm{e}^{-\Gamma|\Delta t|} \sin^2 \Delta m_d \Delta t$, reaches a maximum in this region. The mistag fraction, and the resolution parameters can be extracted from this mixing asymmetry simultaneously to Δm_d.

The effect of tagging on time-dependent *CP* measurements, where the flavour of the fully reconstructed B meson is unknown, is similar. Incorporating the tagging flaws into Eq. 2.1 leads to the probability distributions

$$\begin{aligned} P(\Delta t, T; \hat{q}_i) &= \frac{\bar{\varepsilon}_i^t}{4\tau} \frac{1}{1 - \mu_i \xi C} e^{-\frac{|\Delta t|}{\tau}} \times \\ &\quad \left(\left[\mu_i T D_i + (1 + T\frac{\Delta D_i}{2}) \right] + \left[T D_i + \mu_i (1 + T\frac{\Delta D_i}{2}) \right] \right) A(\Delta t) \end{aligned} \tag{2.9}$$

[1] The normalization requires that the probabilities of observing each of the four flavor combinations in each category add to the probability of tagging in that category, i.e. $\sum_{T,R} P_i(\Delta t, T, R) = \varepsilon^t{}_i$.

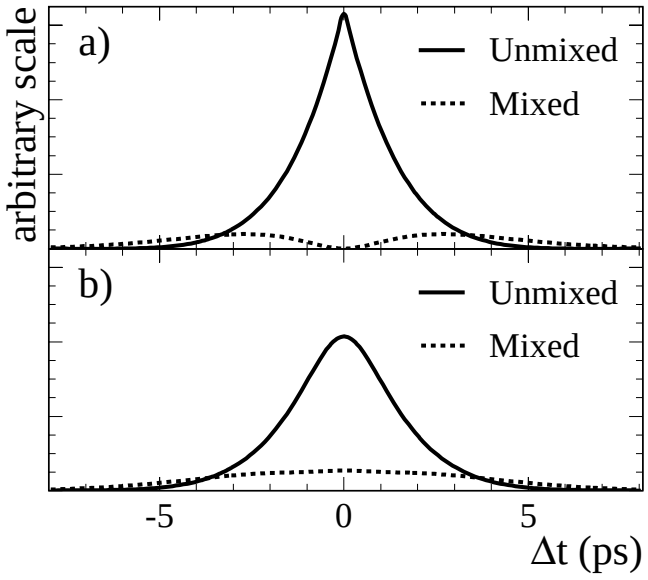

Figure 2.4: Expected Δt distribution for *mixed* and *unmixed* events a) with perfect tagging and Δt resolution, and b) with typical mistag rates and Δt resolution.

where $A(\Delta t) \equiv S\sin(\Delta m_d \Delta t) \mp C\cos(\Delta m_d \Delta t)$. Setting $\nu_i = \mu_i = \Delta D_i = 0$ in this equation illustrates the result of mistakes by the tagging algorithm. In this case

$$P(\Delta t, T) = \frac{\bar{\varepsilon}_i^t}{4\tau} e^{-\frac{|\Delta t|}{\tau}} [1 + T D_i (S\sin(\Delta m_d \Delta t) \mp C\cos(\Delta m_d \Delta t))] \tag{2.10}$$

and the only change in the functional form of Eq. 2.1 is the suppression of the amplitude of the sine and cosine by D_i. This effect, which is the dominant product of the tagging algorithm, dilutes the difference between B^0 and $\overline{B}^0$ tags. To a good approximation, the error on the determination of S and C in category i is inversely proportional to $Q_i \equiv \varepsilon_i^t D_i^2$.

2.2 The B Vertexing and Measurement of Δt

We now describe the procedure to extract the Δt information. We start from the *standard* vertexing algorithm (`GeoKin`), where hadronic B decays are reconstructed using a geometric constraint to the charged tracks of the event. This technique is applied to the measurement of the *CP* asymmetry of $B^0 \to K^+K^-K^0$ decays. We then describe the *Beam Spot Constrained* vertexing algorithm, which is used for $B^0 \to K^0_S K^0_S K^0_S$ decays. In the first case, Δt is calculated in three steps which successively add information: the determination of the B_{rec} vertex, the fit for the Δz, and the conversion to Δt. In the second, a fit of the full $\Upsilon(4S)$ decay tree, with a constraint on sum of the two B lifetimes, is also applied.

2.2.1 Determination of the B_{rec} Vertex

Reconstructing a B candidate begins with the search for possible intermediate decay products such as D mesons or neutral pions and kaons in decays to charged tracks and neutral clusters combinations. The vertices of the composite particles are then simultaneously identified through a geometric fit which alters the momentum vector of the tracks and neutrals with appropriate constraints on the masses and directions of the composite particles. Neutral particles reconstructed in the EMC do not contribute to the vertex determination due to the lack of spatial information near their production. The procedure for finding the best vertex for $B^0 \to K^+K^-K^0$ candidates which will be described in Sec. 6.3 is an application of this technique.

2.2.2 Fit for the B_{tag} Vertex

The B_{tag} vertexing algorithm examines the tracks which were not used in the reconstruction of B_{rec}. Though these particles are generally the final products of the B_{tag} decay, those from intermediate states with long lifetimes do not originate from the B decay vertex and must be eliminated. Therefore, oppositely charged track pair combinations are removed when they are consistent with $K^0_S \to \pi^+\pi^-$ or $\Lambda^+ \to p^+\pi^-$ decays or $\gamma \to e^+e^-$ conversions. Due to the large number of possible final states for D mesons, their decay products are more difficult to eliminate directly. This would introduce a bias in the determination of the decay point of the B_{tag} (*charm bias*). Instead, particles from secondary D meson vertices are removed in an iterative fit for the B_{tag} vertex, where each successive

fit only considers tracks which contributed less than 6 units to the χ^2 of the previous iteration. This process stops when either all tracks satisfy the χ^2 requirement or only two tracks remain. Since the beam energies, beam spot, and the momentum and decay vertex of B_{rec} are well determined, the kinematic and geometric constraints that B_{tag} originates at the beam spot with the momentum vector $p_{B_{tag}} = p_{\Upsilon(4S)} - p_{B_{rec}}$ improves the precision of the vertex fit. Also, in order to correctly account for the correlations between the B_{tag} and B_{rec} vertices induced by these constraints, $\sigma_{\Delta z}$ is directly measured in the fit, so it reflects the errors on each track parameters, the beam energies, and the beam spot. Tests of this algorithm on Monte Carlo events indicate that the difference between the true and measured values of Δz are well described by a triple Gaussian with less than 1% in the widest component (see Sec. 2.2.4). The events which do not lie in this Gaussian ($9.7 \pm 1.0\%$ of the events) have an RMS of 190 μm and the events in the narrowest Gaussian ($89.9 \pm 1.0\%$ of the events) have an RMS of 100 μm.

2.2.3 Conversion to Δt

The naive conversion $\Delta z = \beta\gamma c\Delta t$ provides a good estimate of the time difference between the decays of the two B mesons. However, the relation

$$\Delta z = \beta\gamma\gamma^*_{rec} c\Delta t + \gamma\beta^*_{rec}\gamma^*_{rec}\cos\theta^*_{rec} c\,\langle t_{rec} + t_{tag}\rangle \tag{2.11}$$

which takes into account the B momenta in the $\Upsilon(4S)$ rest frame and the 20 mrad rotation of the beams with respect to the z-axis improves Δt resolution by $\approx 5\%$. Here β^*_{rec}, γ^*_{rec} , and θ^*_{rec} respectively describe the velocity, boost, and polar angle of B_{rec} with respect to the beam axis. $\langle t_{rec} + t_{tag}\rangle$, which is the expected value of the sum of the decay times, is estimated by $\tau_B + |\Delta t|$.

2.2.4 The Δt Resolution Function

Since the Δt resolution is dominated by the B_{tag} vertex, it is generally insensitive to the final state of the fully reconstructed B_{rec}. Nonetheless, if the error on Δt is properly calculated, it must provide a measurement of the resolution of Δt in every event, consequently reflecting any differences between decays. We may then expect to be able to describe the Δt resolution for all B_{rec} final states which have common vertexing technique (as the different sub-modes for $B^0 \to K^+K^-K^0$) with single function of Δt and $\sigma_{\Delta t}$. As illustrated in Fig. 2.5a, studies of simulated events indicate that the measured $\sigma_{\Delta t}$ is directly

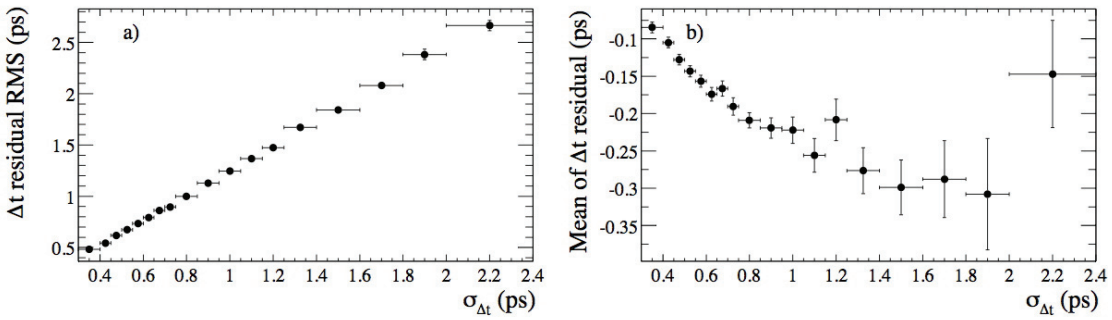

Figure 2.5: (a) The RMS spread and (b) the mean of the residual $\delta_t = \Delta t_{meas} - \Delta t_{true}$ versus the measured $\sigma_{\Delta t}$ in simulated B decays.

proportional to the RMS of Δt in simulated events. Therefore $\sigma_{\Delta t}$ is indeed a measure of the Δt resolution. In fact, the difference $\delta_t = \Delta t_{meas} - \Delta t_{true}$ between the measured and true Δt is well described by the sum of three Gaussians:

$$\mathcal{R}(\delta_t, \sigma_{\Delta t}; \hat{v}_i) = \sum_{k}^{core,tail} \frac{f_k}{S_k \sigma_{\Delta t}\sqrt{2\pi}} \exp\left(-\frac{(\delta_t - b_k^i \sigma_{\Delta t})^2}{2(S_k\sigma_{\Delta t})^2}\right) + \frac{f_{outl}}{\sigma_{outl}\sqrt{2\pi}} \exp\left(-\frac{\delta_t^2}{2\sigma_{outl}^2}\right) \tag{2.12}$$

with descending fractions of events f_{core}, f_{tail}, and $f_{outlier}$, and outlier width $\sigma_{outl} = 8$ ps. The parameters $\hat{v}_i$ are:

1. the fractions f_k;
2. the scale factors S_k;
3. the scaled biases b_k^i.

Note that the widths of the core and tail Gaussians are scaled by the measured $\sigma_{\Delta t}$ for each event, taking advantage of this error estimate of the Δt resolution. Under ideal conditions S_k, which corresponds to the slope in Fig. 2.5a, would be 1. This resolution function also provides a shift in the means of the core and tail Gaussians to account for any bias from secondary vertices of charm decays (i.e. D mesons) due to residual tracks which are not removed by the iterative procedure (*charm bias*). The size of this bias is different depending on the direction of the D meson. A D meson traveling parallel (as opposed to perpendicular) to the beam axis pulls harder on the z coordinate of the B_{tag} vertex. As Fig. 2.5b illustrates, this bias is proportional to the Δt resolution. Therefore

in order to better estimate the bias for each Δt measurement, the resolution function of Eq. 2.12 exploits this correlation and scales the mean of the core and tail Gaussians by $\sigma_{\Delta t}$. Finally, since b flavor tagging separates events based on the signatures of a specific set of B decays, the charm content of the final state depends on the tagging category. Therefore, a different bias is used for each tagging category.

Once this function is convoluted with the resolution function of Eq. 2.12, the time-dependent *CP* asymmetry is given by

$$\mathcal{A}_{CP} = D\,(S\sin(\Delta m_d \Delta t) - C\cos(\Delta m_d \Delta t)) \otimes \mathcal{R}(\delta_t, \sigma_{\Delta t}; \hat{v}_i) \tag{2.13}$$

The combined effect of the mistag and of the resolution effects on Δt distribution are illustrated in Fig. 2.6.

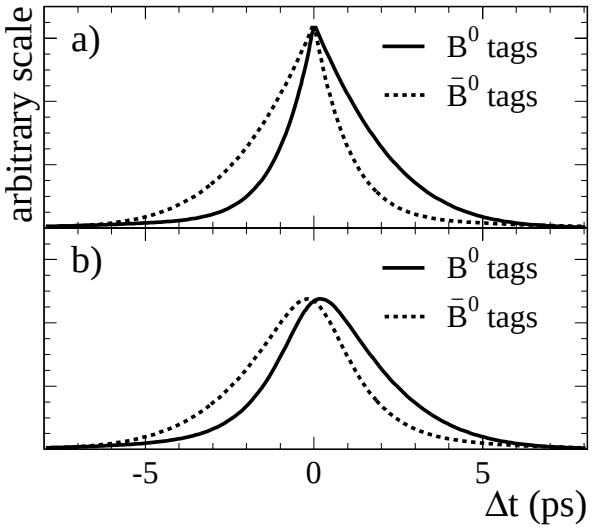

Figure 2.6: Δt distribution for B^0 and $\overline{B}^0$-tagged *CP* events a) with perfect tagging and Δt resolution, and b) with typical mistag rates and Δt resolution.

2.3 The Beam Spot Constrained Vertexing

While for the $B^0 \to K^+K^-K^0$ decays the B vertex can be exploited with the technique described in the previous section, for the $B^0 \to K^0_S K^0_S K^0_S$ decays the tracks from the $K^0_S \to \pi^+\pi^-$ decay cannot be used in this way to determine the vertex of the B_{rec} because of the non-zero lifetime of the K^0_S meson.

A new vertexing technique has been developed by *BABAR* firstly for the measurement of *CP* asymmetry in $B^0 \to K^0_S\pi^0$ decays [31], which uses only the K^0_S flight direction.

The basic point is that at an asymmetric B-factory, because of the Lorentz boost, the momentum of the B is projected in the forward direction ($p_\perp^{B^0} \ll p_\parallel^{B^0}$). Because of that, the B^0 transverse motion (which is ≈ 30 μm) can be neglected, and the B^0 decay vertex position can be inferred by intersecting the $K^0_S \to \pi^+\pi^-$ flight direction with the beam trajectory.

The intersection is realized by constraining the B decay point to the beam spot on the (x, y) plane and inflating the beam spot uncertainty by 30 μm to take into account the neglected flight length of the B meson on the transverse plane. This is justified by the fact that the intrinsic beam spot size is ≈ 4 μm in y direction, ≈ 200 μm in x direction, i.e. about one order of magnitude less than the decay length of the B meson. This introduces a bias in Δt measurement, because of the B meson lifetime is forced to be zero, as illustrated by Fig. 2.7. This problem is then avoided applying the constraint on

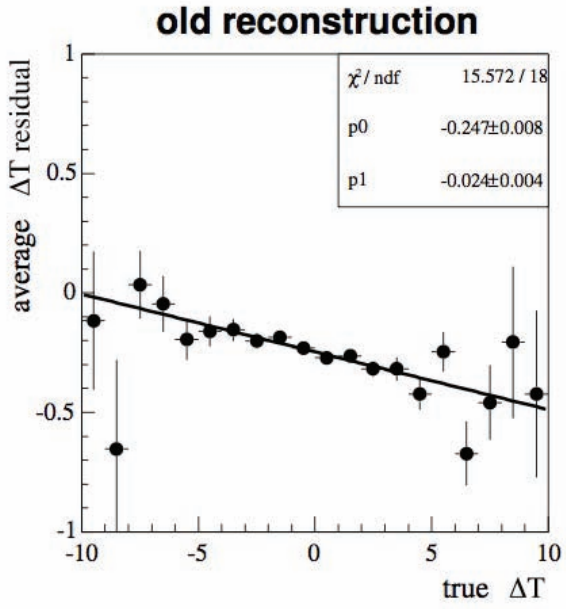

Figure 2.7: Residuals $\Delta t_{meas} - \Delta t_{true}$ as a function of Δt_{meas}, for signal Monte Carlo events of $B^0 \to K^0_S\pi^0$, with old vertexing reconstruction, with the Beam Spot constraint applied on the decay vertex of the B^0.

the production point, rather than to the decay point of the B. For this purpose, a new vertexing algorithm was developed, `TreeFitter`, which is designed to fit an entire decay

tree simultaneously, using the Kalman filter technique [33]. `TreeFitter` can be applied simultaneously on the entire $\Upsilon(4S)$ decay tree, including both reconstructed and tagged side. This feature offers the opportunity to apply the constraint on the production point of the two B mesons, avoiding the bias, but paying in terms of resolution on Δt, which is in part improved by the implicit lifetime constraint. The worsening in the Δt resolution is less evident in $B^0 \to K^0_S K^0_S K^0_S$ than in $B^0 \to K^0_S \pi^0$, because of the presence of multiple K^0_S's adds vertexing information. This can be seen in part in the sub-mode with only two $K^0_S \to \pi^+\pi^-$. However, the bias can be removed (Fig. 2.8a) and the original resolution, $\approx$ 1.4 ps, retained (Fig. 2.8b) by applying a constraint on the sum of the lifetimes of the two B mesons on the $\Upsilon(4S)$ decay tree. From Fig. 2.8a, it is evident that after this

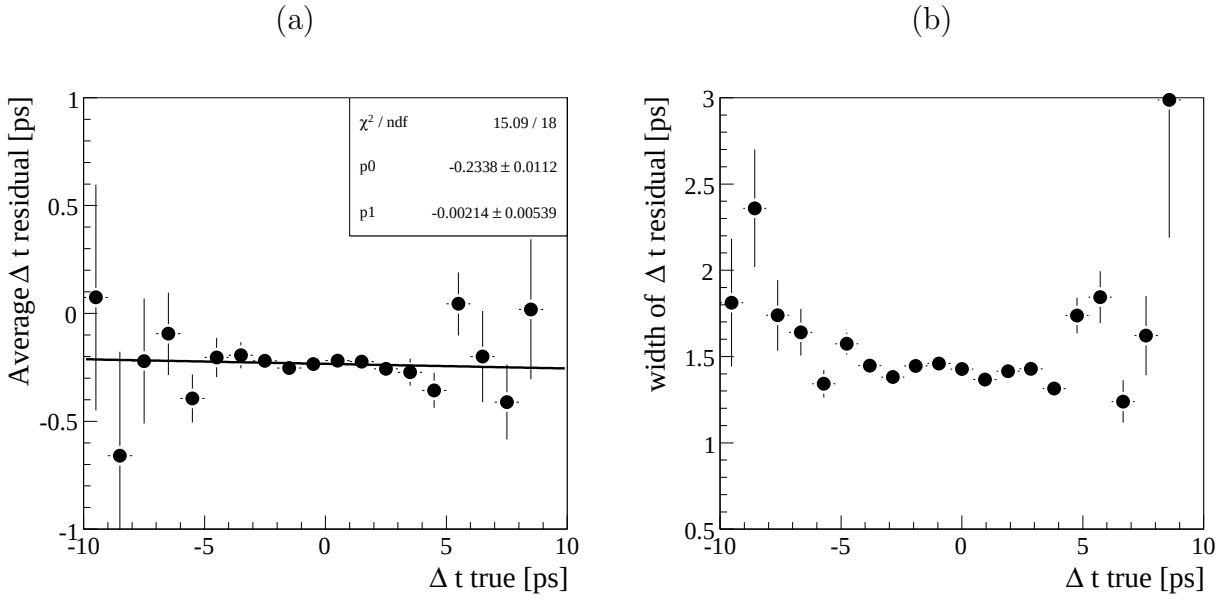

Figure 2.8: (a) Mean and (b) width of the residuals $\Delta t_{meas} - \Delta t_{true}$ as a function of Δt_{meas}, for signal Monte Carlo events of $B^0 \to K^0_S K^0_S K^0_S$, in the sub-mode with one $K^0_S \to \pi^0\pi^0$. The resolution in Δt is also better for the sub-mode with all three K^0_S decaying into $\pi^+\pi^-$. This distributions are obtained after the Beam Spot Constraint vertexing on the production vertex of the B and the B_{rec} and B_{tag} lifetime sum constraint.

constraint is applied, only the constant offset of $\approx$ -0.2 ps on the Δt residuals is left, coming from the *charm bias*. This bias is present also in the nominal vertexing, and is already taken into account by the scaled bias parameters of the resolution function (Eq. 2.12).

Since the described vertexing algorithm does not include the b flavour tagging, the full

procedure is made by three steps:

1. the B^0 candidate is fitted with `TreeFitter` with a 3D Beam Spot constraint on the B production vertex;

2. the fitted candidate is passed to the default *BABAR* tagging and vertexing algorithm;

3. the resulting $\Upsilon(4S) \to B\overline{B}$ candidate is refitted with `TreeFitter` applying the B lifetime constraint. A Gaussian uncertainty of $\sqrt{2}\sigma(\tau_B)$ is associated to the sum of the two B lifetimes.

The standard tagging and vertexing algorithm of step (2) applies a beam spot constraint to the B candidate, which is incorrect since that constraint is already applied before the tag vertexing is called. However, the final $\Upsilon(4S)$ fit takes care that all constraints are applied only once.

Since `TreeFitter` uses a Kalman filter with a high number of degrees of freedom, in the case of $B^0 \to K^0_S K^0_S K^0_S$ with one K^0_S decaying into $\pi^0\pi^0$ sub-mode we do not include the poor vertexing informations which come from $K^0_S \to \pi^0\pi^0$ decays. This reduces the number of failed fits to the B vertex to a negligible level.

2.3.1 SVT Classes Definition

The B vertex determined with beam Spot constraint relies on the determination of the K^0_S flight direction, then the resolution in the vertex strongly depends upon the point in the inner tracking system (SVT) in which the K^0_S is decayed. This is shown in Fig. 2.9, where the average resolution is shown as a function of K^0_S decay length, superimposed to the events distribution for $B^0 \to K^0_S K^0_S K^0_S$. It is clear that the K^0_S mesons decaying in the outer part of the SVT (the step near 12 cm in the $(x-y)$ plane correspond to the fourth layer of the SVT) are useless for a determination of B vertex.

We define four different and mutually exclusive classes of K^0_S which describe the vertexing quality:

- Class I – decays, having both pions with at least 1 ϕ and 1 z hit in any of the first three inner SVT layers.

- Class II – decays, having both pions with at least 1 ϕ and 1 z hit in the SVT (not belonging to class I). These events mostly correspond to K^0_S decays beyond the inner 3 SVT layers.

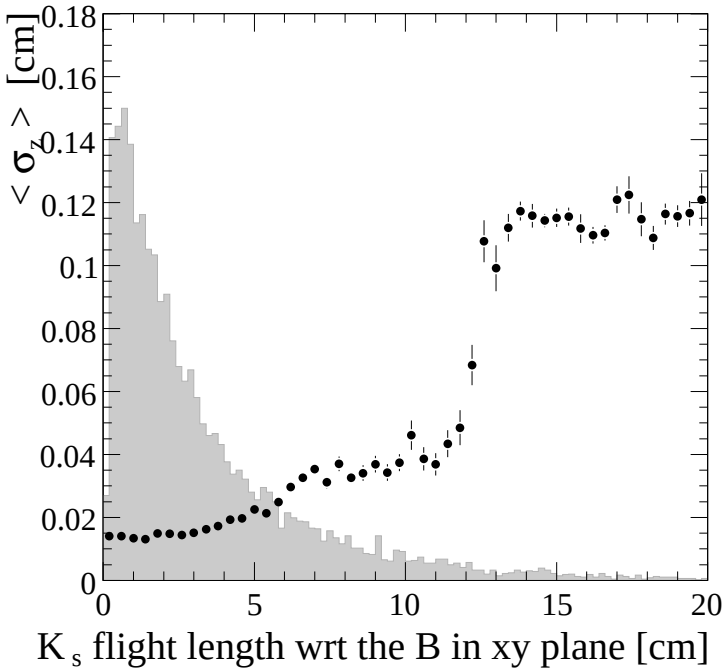

Figure 2.9: Average estimated uncertainty in z_{B^0} (dots) as a function of the K_S^0 decay length. The steps in the distribution indicate the position of the SVT layers. The superimposed histogram shows the decay length distribution (with arbitrary scale) for $B^0 \to K_S^0 K_S^0 K_S^0$ signal Monte Carlo events.

- Class III – decays where either of the two pions has at least one SVT hit, but that do not satisfy the requirements of class I or II.

- Class IV – decays where neither pion has any SVT hits.

Since only one $K^0_S \to \pi^+\pi^-$ is necessary in determining the B^0 vertex, when more than one $K^0_S \to \pi^+\pi^-$ is present in the final state, we define the B^0 class as the best class associated to the K^0_S's. For this reason the presence of the three or two K^0_S useful for the vertexing procedure makes the fraction of best B classes high (See 7.5). We show in Fig. 2.10 we show the $\sigma_{\Delta t}$ distribution for the four classes. The most of event belongs to

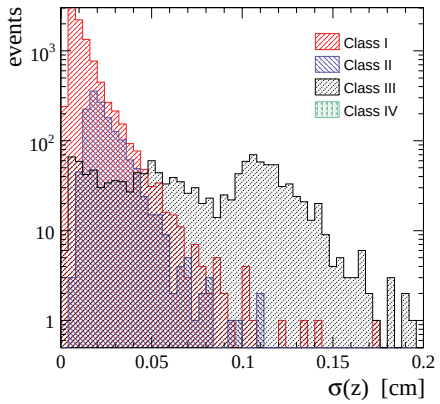

Figure 2.10: Distribution for the estimated uncertainty in Δt for signal Monte Carlo events of $B^0 \to K^0_S K^0_S K^0_S(\pi^0\pi^0)$.

the first two classes. The Class IV events are rejected since the resolution in Δt is worse than 2.5 ps (events which we reject also in the standard vertexing). We do not use also Class III events because of poor vertexing informations. We define as *Good* candidates for the time-dependent fit those events belonging to Class I or Class II and satisfying the requirements $|\Delta t| < 20$ ps and $\sigma_{\Delta t} < 2.5$ ps. The fraction of *Good* events is about 98% for submode with all three K^0_S's decaying into $\pi^+\pi^-$ (we will denote it with $K^0_S K^0_S K^0_S(\pi^+\pi^-)$) and 93% for $K^0_S K^0_S K^0_S(\pi^0\pi^0)$ submode (we will denote it with $K^0_S K^0_S K^0_S(\pi^0\pi^0)$). The not *Good* events (*Bad* events) are not rejected in the analysis, since they are useful for the signal yield extraction and for the determination of direct *CP* asymmetry C for which only the tag information is needed.

The largest contributions are the uncertainty on the K^0_S trajectory and on the position

of the beam spot. The beam spot contributions can be expressed as:

$$\begin{aligned} \sigma^2_{z,beam} &= \left[\left(\frac{p_y}{\sigma_y p_z}\right)^2 + \left(\frac{p_z}{\sigma_x p_z}\right)^2\right]^{-1} = \\ &= \frac{1}{\tan^2\theta}\left[\frac{\sin^2\phi}{\sigma_y^2} + \frac{\cos^2\phi}{\sigma_z^2}\right]^{-1}. \end{aligned} \tag{2.14}$$

Fig. 2.11a shows the estimated σ_z uncertainty as a function of the polar angle of the K^0_S flight direction (for *Good* events). The best vertex determination is achieved when the K^0_S flights in the orthogonal direction to the beam axis. Fig. 2.11b shows σ_z distribution as a function of the azimuthal angle of the K^0_S. The expected not flat contribution of the beam spot as a function of the azimuthal angle comes from the asymmetry introduced by the beam spot constraint, since the beam spot position is known with different precision on the x and y directions. The real distribution becomes again flat thanks to the third step of the B vertexing, which, applying a further constraint on the $\Upsilon(4S)$, decreases the dependency from the beam spot introduced by the first step.

2.3.2 Validation of Vertexing Procedure

The vertexing procedure has been validated for the $B^0 \to K^0_S\pi^0$ decays, which uses the same vertexing technique. The validation makes use of the more abundant and more clean decay $B^0 \to J/\psi\, K^0_S$, ignoring the informations coming from the charged tracks which are the decay products of the J/ψ, and applying the same beam spot constrained vertexing procedure (determination of "mangled" Δt).

Assuming as the true value the Δt value obtained with the standard technique, one can evaluate the agreement of the two results. In these tests, the mangled $B^0 \to J/\psi\, K^0_S$ candidates and the $B^0 \to K^0_S\pi^0$ show the same properties in both the Δt resolution function and the determination of the B^0 decay position. This feature is related to the fact that the total resolution, in both cases, is dominated by the tag side. As a consequence of this, even if the two vertexing techniques are different, we do not expect differences in the description of the Δt resolution function, thanks to the smearing effect of the B_{tag} vertex reconstruction.

In order to prove that the validation done for $B^0 \to K^0_S\pi^0$ is valid also for $B^0 \to K^0_S K^0_S K^0_S$ we compare the properties of the Δt residuals and of the Δz resolution, using signal Monte Carlo samples of the two decay modes. We observe an optimal agreement

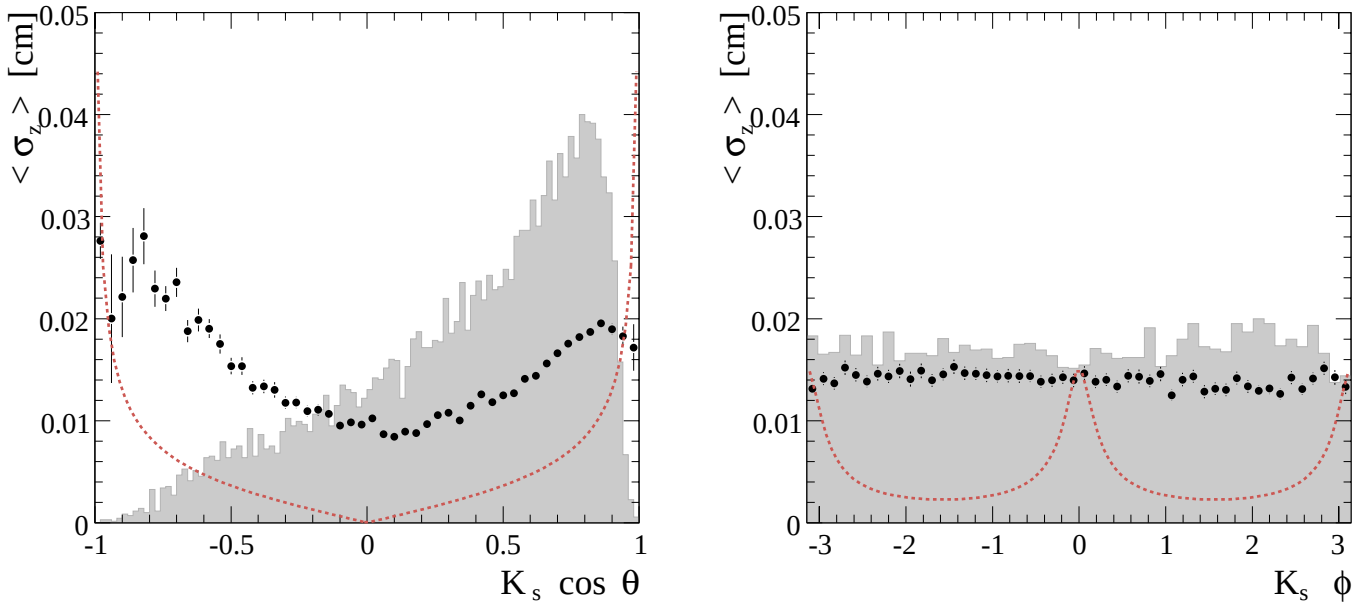

Figure 2.11: Distribution for the estimated uncertainty in z (dots) for $B^0 \to K^0_S K^0_S K^0_S$ signal Monte Carlo events as a function of the K^0_S polar angle (left) and azimuthal angle (right). The red dashed line represents contribution from the beam spot only after the first step of the B vertexing (Eq. 2.14). The superimposed histogram shows the angular distributions of the K^0_S with the best class, with arbitrary scale.

between the two samples, so that any conclusion of the $B^0 \to K^0_S\pi^0$ validation study can be used even in this case.

We use the Δt resolution function defined by the Eq. 2.12, and we will use the data-Monte Carlo (dis)agreement in mangled $B^0 \to J/\psi K^0_S$ events to evaluate a systematic uncertainty associated to the vertexing technique (Sec. 7.5).

Chapter 3

Measurement of *CP* Violation for Three-body B Decays with Dalitz Plot Analysis

In general, the decay of the neutral B meson into three kaons is not a CP eigenstate, due to the presence of CP-even and CP-odd contributions. This mixture of two opposite CP contributions can dilute the measurement of the time-dependent CP asymmetry. The best way to take into account this feature of the three body B decays is to measure CP violation simultaneously to the CP contributions, with a time-dependent analysis of the B Dalitz plot [34].

This approach will be used for the decays of the neutral B meson into $K^+K^-K^0$.

Moreover, a Dalitz plot analysis of neutral B decays that includes time-evolution of the $B^0\overline{B}^0$ pair was proposed as a way to remove ambiguities in the measurement of angle α in $B^0 \to \pi^+\pi^-\pi^0$ decays [35]. A similar method was proposed for ambiguity-free measurement of β in $B \to DPP$ decays, where P is a pseudoscalar meson [36].

In our case, the interference between CP-odd and CP-even amplitudes can be used to measure the CKM angle β in a penguin dominated decay mode of the B meson. The comparison of the angle β measured in this decay with the value measured in tree-level dominated modes like $B^0 \to [c\bar{c}]K^0$ [37, 38] constitute the most powerful way to search for physics beyond the Standard Model in $b \to s$ transitions [100, 101, 102]

3.1 Time-dependent Decay Rate of $B^0 \to K^+K^-K^0$

The decay rate for the $B^0 \to K^+K^-K^0$ decay can be written as a function of the flavour of the initial state q, the time difference between B^0 and $\overline{B}^0$ decay time Δt and the position

in the three body phase space as:

$$\begin{aligned}\frac{d\Gamma(\Delta t, q, m_{12}, m_{13})}{d\Delta t dm_{13}^2 dm_{23}^2} &= \frac{1}{(2\pi)^3}\frac{1}{32M_{B^0}^3}\frac{e^{-|\Delta t|/\tau}}{4\tau}\times \\ &[|\mathcal{A}|^2 + \left|\bar{\mathcal{A}}\right|^2 \\ &+\eta_{CP} q\ 2Im\left(\bar{\mathcal{A}}\mathcal{A}^* e^{-2i\beta}\right)\sin\Delta m_d \Delta t \\ &-q\ \left(|\mathcal{A}|^2 - \left|\bar{\mathcal{A}}\right|^2\right)\cos\Delta m_d \Delta t]\end{aligned} \tag{3.1}$$

where we have assumed $q/p = e^{-2i\beta}$ in the $B^0 - \overline{B}^0$ mixing. The invariant masses of the B daughter pairs $m_{ij} = (p_i + p_j)^2$, where p_1, p_2 and p_3 are the four-momenta of the K^+, K^-, K^0, respectively, are called Dalitz plot coordinates. They represent a way of describing the position in the $K^+K^-K^0$ phase space (decay kinematics). The sign $q = +1$ (-1) is for decays of B^0 into $K^+K^-K_S^0$ $(K^+K^-K_L^0)$, when the other B meson is identified as a B^0 $(\overline{B}^0)$ using the tagging technique. The $\mathcal{A}$ $(\bar{\mathcal{A}})$ is the complex amplitude for the decay $B^0 \to K^+K^-K^0$ $(\overline{B}^0 \to K^+K^-\overline{K}^0)$. It contains the three-body decay dynamics (See Sec. 1.6.1). We will discuss in the following sections the phenomenological model used to describe this amplitude.

Using the four-momentum conservation in a three-body decay one can write the relation

$$M_{B^0}^2 + m_1^2 + m_2^2 + m_3^2 = m_{12}^2 + m_{13}^2 + m_{23}^2 \tag{3.2}$$

which allows a choice of only two independent invariant masses of daughter pairs to describe the decay dynamics of a spin 0 particle. In the following, we will use this convention for the indices: $m_{12} = m_{K^+K^-}$, $m_{13} = m_{K^+K^0}$, $m_{23} = m_{K^-K^0}$.

3.2 Dalitz Plot Model and *K*-matrix Formalism

The K-matrix formalism provides an elegant way of dealing with strongly overlapping resonances and multi-channel dynamics (resonances). It allows to generalize two-body channel amplitudes to resonance production with final-state interaction. It was originally introduced by Wigner and Eisbud [39, 40] for the study of resonances in nuclear reactions. The first use in particle physics goes back to an analysis of resonance production in $K\pi$ scattering by Dalitz and Tuan [41]. Figure 3.1 displays a typical two-body scattering process for which unitarity is a strong requirement. Such a reaction can be parameterized in terms of the K-matrix and it can be extended to describe the decay process of a B meson into three daughters, as presented in Fig. 3.2.

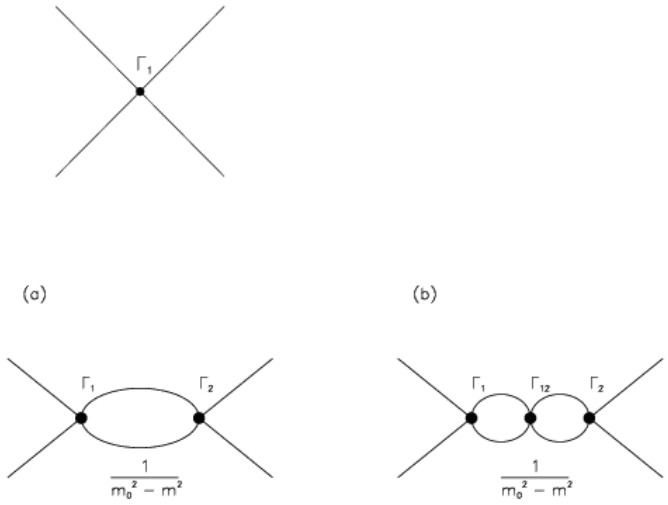

Figure 3.1: *Top: Local interaction. (a) Single channel resonance of mass m_0 with couplings Γ_1 and Γ_2 to the initial and final state, respectively. (b) Two channel rescattering during the lifetime of the resonance.*

3.2.1 Two-body Scattering

S-matrix formalism was developed by Heisenberg in 1942 [42]. In general, the amplitude for an initial state $|i>$ to be found in the final state $|f>$ is written as:

$$S_{fi} =< f|S|i> \ , \tag{3.3}$$

where S is called the scattering operator. One may remove the probability that the initial and final states do not interact at all, by defining the transition operator T through:

$$S = I + 2i\sqrt{\rho}T\sqrt{\rho} \ , \tag{3.4}$$

where I is the identity operator. The factors 2 and i are introduced for convenience. ρ represents the phase-space matrix and it is diagonal by definition.

From conservation of probability, the scattering operator S is unitary:

$$SS^{\dagger} = S^{\dagger}S = I \ . \tag{3.5}$$

From the unitarity of S follows that:

$$(T^{-1} + i\rho)^{\dagger} = (T^{-1} + i\rho) \tag{3.6}$$

which leads to the definition of the K-matrix:

$$K^{-1} = (T^{-1} + i\rho) \ . \tag{3.7}$$

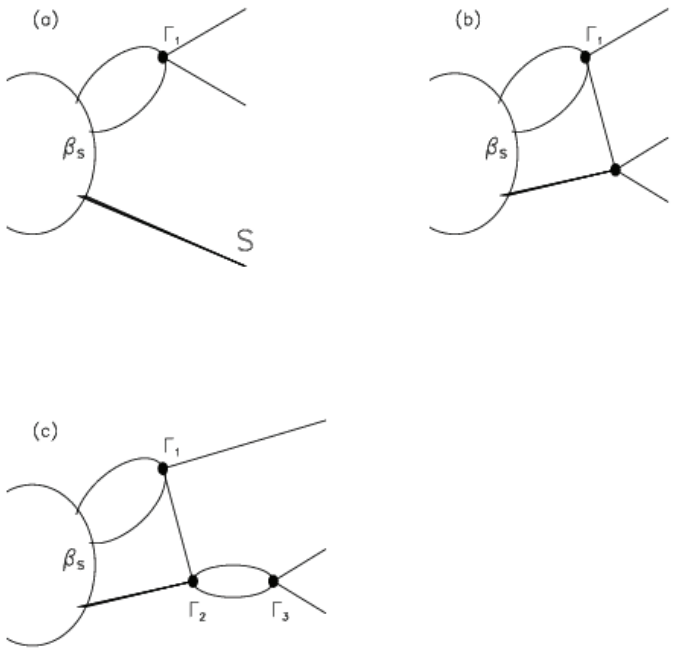

Figure 3.2: *(a): Single resonance production. (b): Single resonance and non-resonant. (c): Single resonance and rescattering.*

From Eq. 3.6 one finds that the K operator is Hermitian:

$$K = K^{\dagger} \ . \tag{3.8}$$

From time reversal invariance of S and T it follows that the K operator must be symmetric, i.e. the corresponding K-matrix is real and symmetric.

It is possible to eliminate the inverse operators in Eq. 3.7 by multiplying by K and T from left and right and vice versa, to obtain:

$$T = K + iK\rho T = K + iT\rho K \ , \tag{3.9}$$

obtaining for T:

$$T = K(I - i\rho K)^{-1} = (I + iK\rho)^{-1}K \ . \tag{3.10}$$

Then, the T matrix is complex only through the i which appears in this formula, *i.e.* T^{-1} has been explicitly broken up into real and imaginary parts.

3.2.2 Resonances in the *K*-matrix formalism

There are two possibilities for parameterizing resonances in the K-matrix formalism:

1. Resonances can arise from constant K-matrix elements with the energy variation supplied by phase space

2. from strongly varying pole terms corresponding to a phase motion [43].

They differ in their dynamical character. In case (1) they are assumed to arise from exchange forces in the corresponding hadronic channels (molecular resonances), so that dominant effects are expected near corresponding thresholds. The latter (2) (normal resonances) correspond to dynamical sources at the constituent level, coupling to the observed hadrons through decay [43]. The dynamical origin of resonances has to be determined experimentally. In the approximation that the transition amplitude is dominated by resonance production (scattering) one form for the K-matrix is the following:

$$K_{ij} = \sum_{\alpha} \frac{g_{\alpha i}(m) g_{\alpha j}(m)}{(m_{\alpha}^2 - m^2)\sqrt{\rho_i \rho_j}} + c_{ij} \ , \tag{3.11}$$

where i and j are referred to the initial and final states, the sum on α runs over the number of poles with masses m_α and the coupling (or residual functions, expressed in units of energy; $s = m^2$) are given by:

$$g_{\alpha i}^2(m) = m_\alpha \Gamma_{\alpha i} \ , \tag{3.12}$$

where $g_{\alpha i}(m)$ is real (but could be negative) above the threshold channel i. The constant K-matrix elements have to be real and unit-less to preserve unitarity. The corresponding width $\Gamma_\alpha(m)$ is

$$\Gamma_\alpha(m) = \sum_i \Gamma_{\alpha i}(m) \tag{3.13}$$

for each pole α. In the simplest case of an isolated resonance and one single channel open it reproduces the Lorentz-invariant Breit-Wigner resonance formula.

Let us consider a single, well isolated resonance α coupling to n open two-body channels, where the mass m_α far above the thresholds of all two-body channels. The partial widths may be given by the expression:

$$\Gamma_{\alpha i}(m) = \frac{g_{\alpha i}^2(m)}{m_\alpha} = \gamma_{\alpha i}^2 \Gamma_\alpha^0 B_{l;\alpha i}^2(q_i, q_{\alpha i}) \rho_i \tag{3.14}$$

and the residual function by:

$$g_{\alpha i}(m) = \gamma_{\alpha i} \sqrt{m_\alpha \Gamma_\alpha^0} B_{l;\alpha i}(q_i, q_{\alpha i}) \sqrt{\rho_i} \ . \tag{3.15}$$

where $q_{\alpha i} = q_i(m_\alpha)$ is the breakup momentum [44] in channel i at the K-matrix pole $m = m_\alpha$.

The $B_{l;\alpha i}(m)$ are ratios of centrifugal barrier factors in terms of the momentum in channel i and the resonance breakup momentum for the orbital angular momentum l. Some of the parameterizations where some will be discussed in Sec. 3.2.3.

The γ's are real constants (but they can be negative) and fulfill the normalization:

$$\sum_i \gamma_{\alpha i}^2 = 1 \tag{3.16}$$

which is motivated by unitarity. In practice, not all possible open channels are available so that this normalization condition is difficult to implement. As fit variable is preferred:

$$g_{\alpha i}^0 = \gamma_{\alpha i}\sqrt{m_\alpha \Gamma_\alpha^0} \tag{3.17}$$

The residual function is then given by:

$$g_{\alpha i}(m) = g_{\alpha i}^0 B_{l;\alpha i}(q_i, q_{\alpha i})\sqrt{\rho_i} \ . \tag{3.18}$$

The K-matrix total width $\tilde{\Gamma}_\alpha$ and the K-matrix partial widths $\tilde{\Gamma}_{\alpha i}$ are defined by:

$$\tilde{\Gamma}_\alpha = \sum \tilde{\Gamma}_{\alpha i} = \Gamma_\alpha^0 \sum_i \gamma_{\alpha i}^2 \rho_i(m_\alpha) \ . \tag{3.19}$$

From these relations it follows that:

$$\begin{aligned} g_{\alpha i}^0 &= \sqrt{\frac{m_\alpha \tilde{\Gamma}_{\alpha i}}{\rho_i(m_\alpha)}} \ , \\ \Gamma_\alpha^0 &= \sum \tilde{\Gamma}_{\alpha i}\rho_i(m_\alpha) \ , \\ \gamma_{\alpha i}^2 &= \frac{\tilde{\Gamma}_{\alpha i}}{\Gamma_\alpha^0 \rho_i(m_\alpha)} \ . \end{aligned} \tag{3.20}$$

It is important to notice, that the K-matrix total width $\tilde{\Gamma}_\alpha$ does not need to be identical to the width which is observed in an experimental mass distribution nor with the width of the T-matrix pole in the complex energy plane.

We will discuss the simple case of a Breit-Wigner resonance far above the threshold for one possible open channel, in which the different definitions of widths coincide. If the masses of the decay particles can be neglected compared to m_α, it is possible to write $\Gamma(m_\alpha) \simeq \Gamma_\alpha^0$. In terms of $g_{\alpha i}^0$, the invariant K-matrix assumes the simple form:

$$K_{ij} = \sum_\alpha \frac{g_{\alpha i}^0 g_{\alpha j}^0 B_{l;\alpha i}(q_i, q_{\alpha i}) B_{l;\alpha j}(q_j, q_{\alpha j})}{m_\alpha^2 - m^2} + c_{ij} \ . \tag{3.21}$$

In particular the possibility that the g^0's can be negative is allowed.

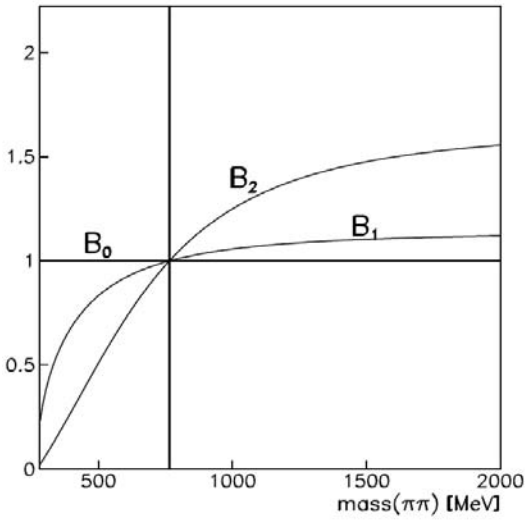

Figure 3.3: *Ratios $B_l(m, m_\alpha) = F_l(m)/F_l(m_\alpha)$ of Blatt-Weisskopf factors using a resonance mass $m_\alpha = 765\ MeV/c^2$ (marked by the line) for $l = 0, 1, 2$.*

3.2.3 Penetration factors

The threshold behavior of low energy scattering of hadrons may be studied in terms of a non-relativistic potential V of range R, where $V(r > R) = 0$ in the typical behavior of strong interaction. Assuming purely elastic scattering of spin zero particles the potential in its radial form is given as:

$$V = V(r) + \frac{l(l+1)}{r^2} \tag{3.22}$$

the second term being the centrifugal potential. Assuming $qR \ll l$ near threshold, the solutions of the Schrodinger equation approximately can be written in terms of the phase shift δ_l of the partial wave l

$$\tan(\delta_l)(qR \ll l) = 2q \cdot a_l \cdot (q)^{2l} \ . \tag{3.23}$$

The factor $(q)^{2l}$ arises here due to the presence of the centrifugal potential and is accordingly called "penetration factor". The factor a_l is constant and is the "scattering length".

The pion creation of nuclear resonances is inadequately described by only q^{2l}. Hence, Blatt and Weisskopf [45] proposed the more general form of the penetration factor which is obtained by solving the radial equation for all qR. With these factors, the fits to the (low-energy) cross sections become more realistic. Widely used are Blatt-Weisskopf barrier factors according to Ref. [47]. They are given in terms of the ratio $z = (q/q_R)^2$,

where q_R corresponds to the range of the interaction. The factors $F_l(z)$, normalized to $F_l(1) = 1$, up to angular momenta $l = 2$ are:

$$\begin{aligned} F_0(z) &= 1 \,, \\ F_1(z) &= \sqrt{\frac{2z}{z+1}} \,, \\ F_2(z) &= \sqrt{\frac{13z^2}{(z-3)^2+9z}} \,. \end{aligned} \tag{3.24}$$

In general, the penetration factors are part of a more complex form factor. The form factors parameterize the underlying interaction (vertexes)[1]. Hence, they introduce a model dependence in the analysis. In many formulations, phenomenological corrections are added to the penetration factors, which in practice are indistinguishable on data due to their small in influence on the lineshape of resonances .

Fig. 3.3 shows the ratios $B_l(m, m_\alpha) = \frac{F_l(m)}{F_l(m_\alpha)}$ of Blatt-Weisskopf factors using a resonance mass $m_\alpha = 765$ MeV/c^2 for $l = 0, 1, 2$.

3.3 Resonance Lineshapes

The decay dynamics of the $B^0 \to K^+K^-K^0$ involve both single channel resonances, like the $\phi(1020) \to K^+K^-$, and double channel resonances. This situation occurs in the $\pi\pi$ S-wave, where the $\mathsf{f_0(980)}$ is just at the $K\bar{K}$ threshold. There are further complications due to strongly overlapping resonances for the $\pi\pi$ S-wave. They will be discussed in Sec. 3.3.2.

3.3.1 One Channel Resonances

In the case of a single resonance with one single channel opened, the K-matrix assumes the form:

$$K = \frac{m_0\Gamma(m)}{(m_0^2 - m^2)\rho} \tag{3.25}$$

where m_0 if the mass of the resonance. The mass dependent width is given by:

$$\Gamma(m) = \Gamma_0 \left(\frac{\rho(m)}{\rho_0}\right) B(q(m), q(m_0))^2 \,, \tag{3.26}$$

where Γ_0 is the K-matrix width and $q(m_0)$ is the breakup momentum for the mass $m(m_0)$. Neglecting the angular momentum dependence of the amplitude, the invariant scattering

[1] as before, here a strong potential is assumed

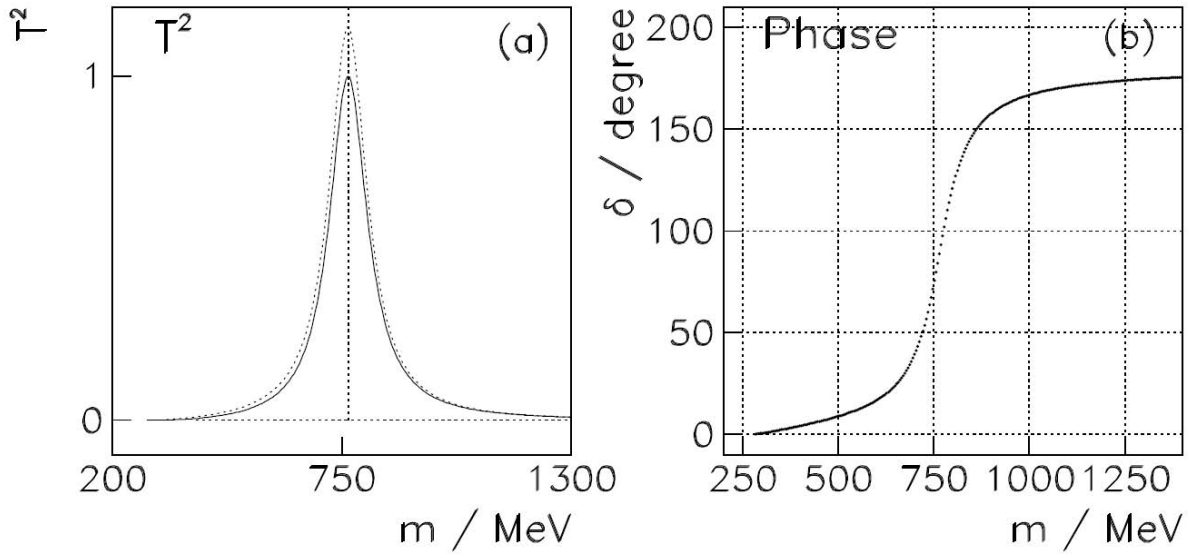

Figure 3.4: **(a):** *Breit-Wigner amplitude squared ($|\rho T|^2$) as function of invariant $\pi\pi$ mass. The invariant amplitude $|T|^2$ is superimposed as dotted line.* **(b):** *$\pi\pi$ phase shift δ which reaches 90° at the resonance mass.*

amplitude is:

$$T = \frac{m_0\Gamma_0}{m_0^2 - m^2 - im_0\Gamma(m)} B(q(m), q_0)^2 \frac{1}{\rho_0} \ . \tag{3.27}$$

Eq. 3.27 contains the usual Breit-Wigner form. In this simple case observed width and K-matrix width are identical. The Breit-Wigner lineshape and the phase shift for the $\rho(770)$ ($\pi\pi$ elastic scattering) ($m_0 = 765$ MeV/c^2, $\Gamma_0 = 110$ MeV/c^2) are shown in Fig. 3.4 (a) and (b), respectively. The phase in degree is calculated from the complex amplitude T, using the following relation:

$$\delta = \frac{180}{\pi} \cdot tan^{-1}\left(\frac{Im(T)}{Re(T)}\right) . \tag{3.28}$$

In the elastic case unitarity implies that the amplitude ρT can be identified with a unitarity circle in the complex plane $(Re(\rho T); Im(\rho T))$ centered at $(0; 0.5)$, which reaches the maximum i at the resonance position. This is the so called Argand diagram displayed in Fig. 3.5. One can define the inelasticity as the deviation from the unitary circle inwards, corresponding to intensity vanishing in the other channels the amplitude couples to. It can be calculated from T as:

$$\eta = 2 \cdot \sqrt{(Re(\rho T))^2 + (Im(\rho T) - 0.5)^2} \ . \tag{3.29}$$

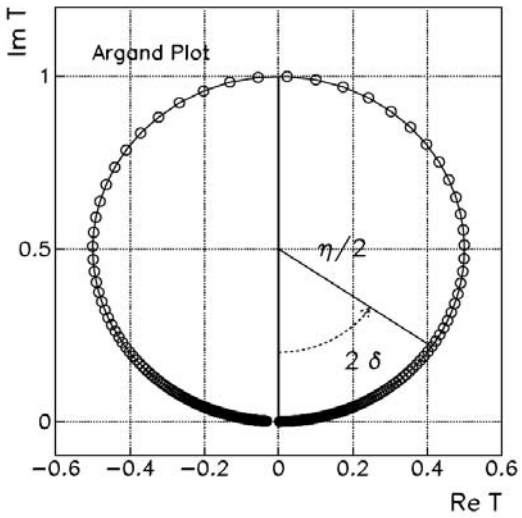

Figure 3.5: *Argand diagram of the Breit-Wigner amplitude ρT: $(Re(\rho T); Im(\rho T))$. Since the process is completely elastic unitarity demands that the amplitude follows the unity circle. The dots are plotted at equidistant $\pi\pi$ masses. The circle starts at (0,0). The phase shift δ and the inelasticity are marked.*

3.3.2 Overlapping Resonances

In the case of two resonances of masses m_A and m_B in $\pi\pi$ scattering at mass m [2] the formulation of the K-matrix is:

$$K = \frac{m_A \Gamma_A(m)}{m_A^2 - m^2} + \frac{m_B \Gamma_B(m)}{m_B^2 - m^2} \ . \tag{3.30}$$

The mass dependent widths are given by:

$$\Gamma_\alpha(m) = \Gamma_{\alpha 0} \left(\frac{m_\alpha}{m}\right) \left(\frac{q}{q_\alpha}\right) B(q, q_\alpha)^2 \ . \tag{3.31}$$

In the case $|m_B - m_A| \gg |\Gamma_B + \Gamma_A|$ the K-matrix is dominated by either the first or the second resonance, depending whether m is near m_A or m_B. The transition amplitude T is then reducible to the naïve approximation:

$$T \approx T_A + T_B = \left[\frac{m_A \Gamma_A(m)}{m_A^2 - m^2 - i m_A \Gamma_A(m)}\right] + \left[\frac{m_B \Gamma_B(m)}{m_B^2 - m^2 - i m_B \Gamma_B(m)}\right] \tag{3.32}$$

that is the sum of two Breit-Wigner form factors. This approximation is not always valid: in the case of $m_0 = m_A = m_B$ one can write:

$$T = \frac{m_0(\Gamma_A(m) + \Gamma_B(m))}{m_0^2 - m^2 - i m_0(\Gamma_A(m) + \Gamma_B(m))} \tag{3.33}$$

[2] This can occur in reality for the resonances $A = f_2(1270)$ and $B = f_2(1560)$ which are both broad and close enough to each other to overlap in their tails: $\Gamma_A = 180$ MeV/c^2 and $\Gamma_B = 160$ MeV/c^2.

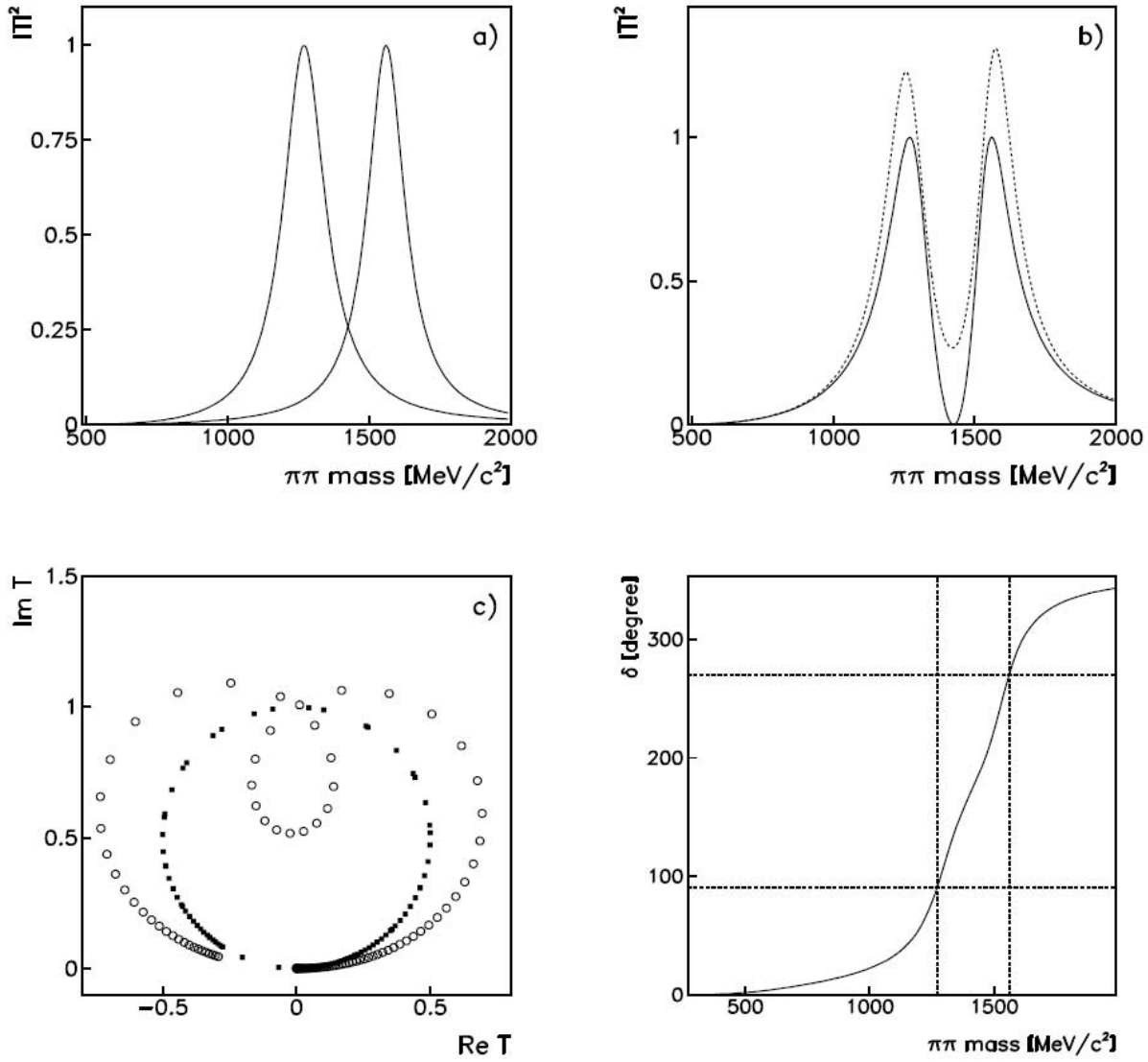

Figure 3.6: *Two overlapping resonances with the parameters:* $m_A = 1270\ MeV/c^2$, $\Gamma_A = 180\ MeV/c^2$, $m_B = 1560\ MeV/c^2$, $\Gamma_B = 160\ MeV/c^2$. *The plot (a) shows the amplitude squared,* $|T|^2$, *for the two individual Breit-Wigner resonances. Plot (b) shows the result of adding the resonance poles in the K-matrix (solid line). The dashed line corresponds to the naive sum of the two Breit-Wigner amplitudes* $|T_A + T_B|^2$, *which exceeds 1 close to the resonance positions. Also the intensity does not drop to zero between the resonance peaks. Plot (c) shows the corresponding Argand diagrams for the naive summation (open circles) and the K-matrix parameterization (black squares). While the latter follows the unitarity circle the Breit-Wigner summation clearly is outside the unity circle in contradiction to the unitarity requirement. Plot (d) shows the phase motion for the K-matrix parameterization, where dashed lines mark the 900 and 2700 steps which cross the phase shift at the masses* m_A *and* m_B.

that is a single Breit-Wigner form, with the total width being the sum of the individuals widths.

Fig. 3.6 shows that the unitarity is violated when two Breit-Wigner amplitudes are added ($T_A + T_B$ instead of T from $K_A + K_B$).

3.3.3 Two-channel Resonances

Here we discuss the case of the $\mathsf{f_0(980)}$ which is coupled both to $\pi\pi$ and $K\bar{K}$ channel, the latter being just over the threshold.

We consider a single resonance. The elements of the invariant K-matrix for the coupling to two channels can be written:

$$K_{11} = \frac{\gamma_1^2 m_0 \Gamma_0}{m_0^2 - m^2} \tag{3.34}$$

$$K_{12} = \hat{K}_{21} = \frac{\gamma_1 \gamma_2 m_0 \Gamma_0}{m_0^2 - m^2} \tag{3.35}$$

$$K_{22} = \frac{\gamma_2^2 m_0 \Gamma_0}{m_0^2 - m^2} \tag{3.36}$$

The normalized couplings fulfill the condition: $\gamma_1^2 + \gamma_2^2 = 1$. Then the T-matrix is given as:

$$T = \frac{m_0 \Gamma_0}{m_0^2 - m^2 - i m_0 \Gamma_0 (\rho_1 \gamma_1^2 + \rho_2 \gamma_2^2)} \begin{pmatrix} \gamma_1^2 & \gamma_1 \gamma_2 \\ \gamma_1 \gamma_2 & \gamma_2^2 \end{pmatrix} \tag{3.37}$$

We redefine the couplings according to Eqn. 3.20, so that:

$$g_i = \gamma_i \sqrt{m_0 \Gamma_0} \tag{3.38}$$

$$g_1^2 + g_2^2 = m_0 \Gamma_0 \tag{3.39}$$

and obtain:

$$T = \frac{\begin{pmatrix} \gamma_1^2 & \gamma_1 \gamma_2 \\ \gamma_1 \gamma_2 & \gamma_2^2 \end{pmatrix}}{m_0^2 - m^2 - i(\rho_1 g_1^2 + \rho_2 g_2^2)} \tag{3.40}$$

This formula was firstly proposed by Flatté in 1976 [48].

The $\mathsf{f_0(980)}$ appears as a regular resonance in the $\pi\pi$ system. The comparable Breit-Wigner denominator for m near m_r is:

$$m_r^2 - m^2 - i m_r \Gamma_r \tag{3.41}$$

in the resonance approximation. We can identify:

$$\begin{aligned} m_0^2 &= m_r^2 + \left(\frac{\gamma_2}{\gamma_1}\right)^2 \left[\frac{|\rho_2(m_r)|}{|\rho_1(m_r)|}\right] m_r\Gamma_r \\ \Gamma_0 &= \frac{m_r\Gamma_r}{m_0\rho_1(m_r)\gamma_1^2} \end{aligned} \tag{3.42}$$

in terms of the mass m_r and width Γ_r. The ρ_i is evaluated at $m = m_r$, where T is expected to reach its maximum value. But the formulas Eqn. 3.42 actually are not very helpful to find starting points for fits to data. In practice the parameters m_0 and Γ_0 need to be varied. The ratio $r = (\gamma_2/\gamma_1)^2$ is a priori correlated with the width. Only if the lineshape is strongly distorted due to strong couplings to the second channel this can be resolved.

3.4 The Production or Decay Amplitude

So far "formation" of resonances, observed in two-body scattering $ab \to cd$ has been considered. The K-matrix formalism can be generalized to describe the case of "production" of resonances in more complex reactions. The key assumption is that the two-body system in the final state does not simultaneously interact with the rest of the final state. This model is called "isobar model" (See Fig. 3.2).

To preserve the two-body unitarity an approach was proposed by Aitchison [49]. The Lorentz invariant amplitude, F, is given as:

$$F = (I - iK\rho)^{-1}P = TK^{-1}P \ . \tag{3.43}$$

This introduces the production vector P parameterizing the resonance production in the open channels. For n contributing channels P and F are n-dimensional column vectors.

If the K-matrix is given as a sum of poles (Eq. 3.11), then the corresponding P-vector is:

$$P_i = \sum_\alpha \frac{\beta_\alpha B_{L;\alpha i}(p_i, p_{\alpha i}) g^0_{\alpha i} B_{l;\alpha i}(q_i, q_{\alpha i})}{m_\alpha^2 - m^2} \ , \tag{3.44}$$

where β_α (expressed in units of energy) carries the coupling of the resonance α to the initial state. The centrifugal barrier factor, $B_{L;\alpha i}(p_i, p_{\alpha i})$, is introduced *ad hoc* and depends on the angular momentum in production, L. It is a function of the recoil momentum p_i of the resonance against the spectator. The constant β_α is in general complex ($\beta_\alpha = b_\alpha e^{i\phi}$,

ϕ is a phase due to the initial production process). For convenience β_α is formulated in terms of the dimensionless β^0_α

$$\beta_\alpha = \beta^0_\alpha \sqrt{\sum_i (g^0_{\alpha i})^2} \ . \tag{3.45}$$

In the case of an isolated resonance in a single channel, the P-vector is parameterized as:

$$P = \beta_0 \cdot B_L(p, p_0) \cdot \frac{g_0^2 B_l(q, q_0)}{m_0^2 - m^2} \tag{3.46}$$

and Eq. 3.11 is written as:

$$K = \frac{g_0^2 B_l^2(q, q_0)}{m_0^2 - m^2} \ . \tag{3.47}$$

The Lorentz invariant amplitude, F, is given as:

$$F(m) = \beta_0 \cdot B_L(p, p_0) \cdot \frac{m_0 \Gamma_0}{m_0^2 - m^2 - i m_0 \Gamma(m)} \frac{B_l(q, q_0)}{\rho_0} \ . \tag{3.48}$$

This is the relativistic Breit-Wigner form multiplied by an arbitrary complex constant (production strength) β_0 and the centrifugal factor $B_L(p, p_0)$. This form, obtained with the K-matrix model, is equivalent to the one obtained with the Breit-Wigner model.

3.5 Non-resonant Amplitudes

Beside decays that proceed through intermediate resonances, there are also the so called non-resonant decays that are not associated with any known resonant structure, but lead to the same final state. It was found experimentally that B decays to three-body final states could contain a large fraction of such decays. The origin of these decays is not fully understood: they can come from kinematic tails of higher-B mass states, contact terms or decays of wide scalar resonances.

None of the proposed theoretical parameterizations of the non-resonant decays reproduces well the features in data [26, 28, 50, 51]. For this reason, and because the large fraction of non-resonant events in three-body B decays, a phenomenological parameterization is needed. This will be discussed in Sec. 6.6.1.

3.6 *CP* Violation in the Isobar Model

In Sec. 3.4 we described in general the production of resonances in the approximation that the two-body system is the final state does not simultaneously interact with the rest

of the final state. In practice, in this so-called "isobar model", we describe the complex transition amplitude $\mathcal{A}$ of a B meson decaying into three kaons as a sum of individual amplitudes, associated to the various resonances:

$$\mathcal{A} \equiv \mathcal{A}(B^0 \to K^+K^-K^0_S; m_{12}, m_{13}) \;=\; \sum_r c_r \cdot f_r \tag{3.49}$$

where c_r are complex coefficients describing the strength and phase of each resonance relative to other resonances (isobar coefficients). The Dalitz-plot distribution of each resonance is described with a complex amplitude f_r, and the index r runs over all resonant states.

When the initial state is $\overline{B}^0$ meson, we have similar description

$$\bar{\mathcal{A}} \equiv \mathcal{A}(\overline{B}^0 \to K^+K^-K^0_S; m_{12}, m_{13}) \;=\; \sum_r \bar{c_r} \cdot \bar{f}_r \tag{3.50}$$

where complex coefficients $\bar{c_r}$ and c_r are in general different.

3.6.1 Transition Amplitudes

In Equations (3.49) and (3.50), isobar coefficients c_r give strengths and relative phases of each resonance. Each resonant state can be reached through tree and penguin topology with different weak and strong phases. Applying unitarity of the CKM matrix, we can write

$$c_r = V_{cb}V^*_{cs}a^c_r + V_{ub}V^*_{us}a^u_r \tag{3.51}$$

where the a^u_r is often called *Standard Model pollution*. Defining a weak phase difference γ and a strong phase difference δ, we can re-write this for B^0 decays as

$$c_r = P_r e^{i\phi_r}\left(1 + \xi_r e^{i\gamma} e^{i\delta_r}\right) \tag{3.52}$$

where P_r is strength of Cabibbo allowed "penguin" part and ξ is fraction of Cabibbo suppressed ("SM pollution") amplitudes. Similarly for $\overline{B}^0$ decays, we can write

$$\bar{c_r} = P_r e^{i\phi_r}\left(1 + \xi_r e^{-i\gamma} e^{i\delta_r}\right) \tag{3.53}$$

where we made assumptions of equal strong phases, strengths for identical decay topology and a resonant state r. Parameters P_r, ϕ_r, ξ_r, δ_r need to be determined from a fit.

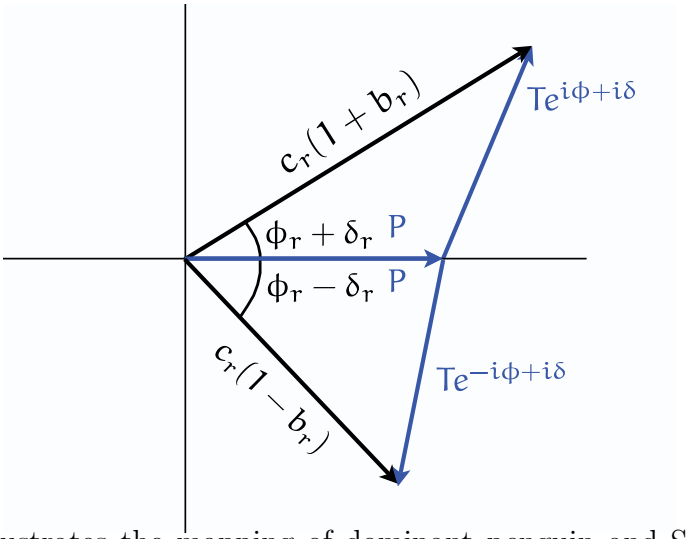

Figure 3.7: Illustrates the mapping of dominant penguin and SM pollution amplitudes and phases (Sec. 3.6.1) to the polar isobar parameters (Eqn. 3.55).

Fit Coefficients: Polar Coordinates

We choose the following parameterization of complex isobar coefficients in Eq.(3.49) in terms of real fit coefficients

$$c_r \rightarrow c_r(1+b_r)\, e^{i(\phi_r+\delta_r)} \cdot e^{+i\beta} \tag{3.54}$$

$$\bar{c_r} \rightarrow c_r(1-b_r)\, e^{i(\phi_r-\delta_r)} \cdot e^{-i\beta} \cdot \eta_r \tag{3.55}$$

where c, ϕ are the average amplitude and phase in B^0 and $\overline{B}^0$ decays, respectively, and b, δ account for the *asymmetry* in the amplitude and phase. These parameters are determined from a fit. The $e^{i\beta}$ factor comes from mixing, and it is absorbed into the definition of isobar amplitude for simplicity. Note that β is correlated with the δ's, or in other words, we can define

$$\beta_{eff}(r) \equiv \beta + \delta_r \tag{3.56}$$

where we choose a constant offset $\beta = \beta_{SM} = 0.379$ so the δ_r's are expected to be the deviation from SM expectations.

The parameters P_r, ϕ_r, ξ_r, and δ_r from 3.6.1 do not map in a simple way to the parameters c_r, ϕ_r, b_r, and δ_r in this section (e.g. The phases in this section are both non-trivial combinations of strong and weak phases). A graphical representation of this mapping is shown in Fig. 3.7. The η's are *CP*-eigenvalues of the final states.

Chapter 4

The *BABAR* Detector

4.1 Introduction

The primary goal of the *BABAR* experiment is the study of CP-violating asymmetries in the decay of the B meson. Secondary goals are precision measurement of decays of bottom and charm mesons and of τ leptons, searches for rare processes accessible because of the high luminosity of PEP-II B-factory.

The PEP-II B-factory is an e^+e^- asymmetric collider running at a center of mass energy of 10.58 GeV corresponding to the mass of the $\Upsilon(4S)$ resonance. The small Q-value of the $\Upsilon(4S) \to B\bar{B}$ decay results in B mesons almost at rest in the center of mass frame. The electron beam in the High Energy Ring (HER) has 9.0 GeV and the positron beam in the Low Energy Ring (LER) has 3.1 GeV. The $\Upsilon(4S)$ is therefore produced with a Lorentz boost of $\beta\gamma = 0.56$. This boost makes it possible to reconstruct the decay vertexes of the two B mesons, to determine their relative decay times Δt, and thus to measure the time dependence of their decay rates, since, without boost, this distance would be too small ($\sim 30\ \mu$) to be measured by any vertex tracker.

The *BABAR* detector [52] has been optimized to reach the primary goal of the CP asymmetry measurement. This measurement needs the complete reconstruction of a B decay in a CP eigenstate, the flavor identification (tagging) of the non-CP B and a measure of the distance of the two decay vertexes. To fulfill these needs, a very good vertex resolution, both transverse and parallel to the beam direction, excellent reconstruction efficiency for charged particles and a very good momentum resolution, efficient electron and muon identification, with low misidentification probabilities for hadrons, are required.

A longitudinal section of the *BABAR* detector is shown in Fig. 4.1. The detector inner

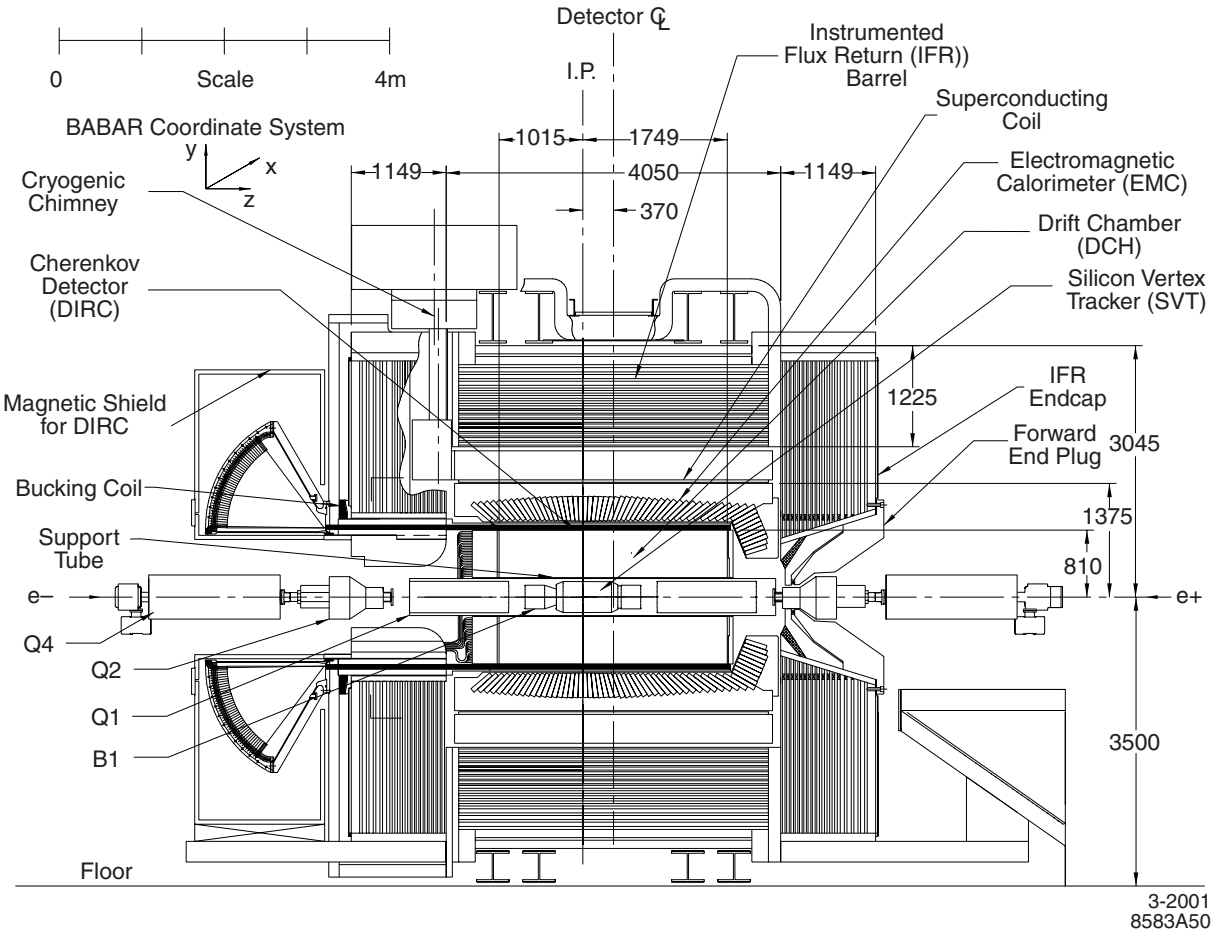

Figure 4.1: *BABAR* detector longitudinal section.

most part is reserved for the silicon vertex tracker (SVT), then there is the drift chamber (DCH), the *Č*erenkov light detector (DIRC) and the CsI electromagnetic calorimeter (EMC). All those detector sub-systems are surrounded by a solenoidal superconductor magnetic field. The iron used for the return flux has been instrumented (IFR) for muons and neutral hadrons, like K_L and neutrons, detection.

The detector geometry is cylindrical in the inner zone and hexagonal in the outermost zone: the central part of the structure is called *barrel* and it's closed forward and backward by *end caps*. The covered polar angle ranges from 350 mrad, in the forward, to 400 mrad in the backward directions (defined with respect to the high energy beam direction). The *BABAR* coordinate system has the z axis along the boost direction (or the beam direction): the y axis is vertical and the x axis is horizontal and goes toward the external part of the ring. In order to maximize the geometrical acceptance for $\Upsilon(4S)$ decays the whole

detector is offset, with respect to the beam-beam interaction point (IP), by 0.37 m in the direction of the lower energy beam.

A trigger system is used to separate collisions producing interesting events from those that constitutes the noise, or the background, for instance, beam interactions with residual gas. The trigger system is divided in two consequent levels: the level one trigger ($L1$) is hardware based and is designed to have a maximum output rate of 2 kHz and a maximum time delay of 12 μs, while the other level ($L3$), software based, has a throughput rate limited to 120Hz in order to permit an easy storage and processing of collected data.

4.2 PEP-II B-factory

PEP-II is a system consisting of two accumulating asymmetric rings designed in order to operate at a center of mass energy of the $\Upsilon(4S)$ resonance mass, 10.58 GeV. Tab. 4.1 shows the various sub-systems parameters: a comparison between typical and design values is presented. As can be easily seen from the table, PEP-II parameters have exceeded the project ones in terms of instant luminosity and daily integrated luminosity achieving recently the peak value of $1 \times 10^{34}\ cm^{-2}\ s^{-1}$ with a daily integrated luminosity of 700 pb^{-1}.

Parameters	Design	Typical
Energy HER/LER (GeV)	9.0/3.1	9.0/3.1
Current HER/LER (A)	0.75/2.15	1.48/2.5
# of bunch	1658	553-829
bunch time separation (ns)	4.2	6.3-10.5
σ_{Lx} (μm)	110	120
σ_{Ly} (μm)	3.3	5.6
σ_{Lz} (μm)	9000	9000
Luminosity ($10^{33}\ cm^{-2}s^{-1}$)	3	9
Daily average integrated luminosity (pb^{-1}/d)	135	700

Table 4.1: PEP-II beam parameters. Design and typical values are quoted.

Data is mostly collected at $\Upsilon(4S)$ peak energy. Tab. 4.2 shows the active processes cross sections breakdown at peak energy. From now on the production of light quark pairs (u, d, s) and *charm* quark pairs will be referred to as "continuum production". In order to study this non-resonant production $\sim 12\%$ of data is collected with a center of mass energy 40 MeV below the $\Upsilon(4S)$ mass value.

PEP-II measures radiative Bhabha scattering to provide a luminosity fast monitor

$e^+e^- \rightarrow$	Cross section (nb)
$b\bar{b}$	1.05
$c\bar{c}$	1.30
$s\bar{s}$	0.35
$u\bar{u}$	1.39
$d\bar{d}$	0.35
$\tau^+\tau^-$	0.94
$\mu^+\mu^-$	1.16
e^+e^-	~ 40

Table 4.2: Various processes cross sections at $\sqrt{s} = M_{\Upsilon(4S)}$. *Bhabha* cross section is an effective cross section, within the experimental acceptance.

useful for operations. *BABAR* derives the absolute luminosity offline from other QED processes, mainly e^+e^- and $\mu^+\mu^-$ pairs: the systematic uncertainty on the absolute value of the luminosity is estimated to be about 1.5%. This error is dominated by uncertainties in the Monte Carlo generator and the simulation of the detector.

The beam energies of the two beams are calculated from the total magnetic bending strength and the average deviations of the accelerating frequencies from their central values. The systematic error on the PEP-II calculation of the absolute beam energies is estimated to be $5 - 10$ MeV, while the relative energy setting for each beam is accurate and stable to about 1 MeV.

The interaction region design, with the two beams crossing in a single interaction point with particles trajectories modified in order to have head on collisions, is realized with a magnetic field, produced by a dipole magnetic system, acting near the interaction point. The collision axis is off-set from the z-axis of the *BABAR* detector by about 20 mrad in the horizontal plane to minimize the perturbation of the beams by the solenoidal field. In this configuration the particles and the beams are kept far apart in the horizontal plane outside the interaction region and parasite collisions are minimized. Magnetic quadrupoles included inside the detector's magnetic field, and hence realized in Samarium-Cobalt, are strongly focusing the beams inside the interaction region.

In order to keep track of PEP-II beams displacement with respect to the *BABAR* detector, the interaction point position is computed on periodic intervals, using two-track events. Interaction region dimensions (beam-spot) computed in that way are $\sim 150\ \mu m$ along x, $\sim 50\ \mu m$ along y and 1 cm along z axis. The y dimension estimate is completely

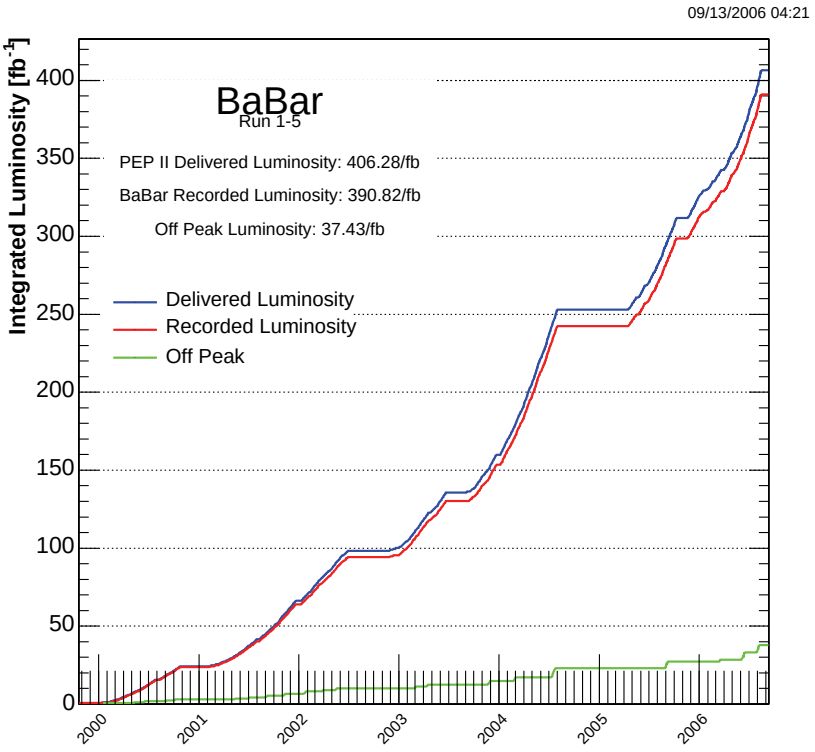

Figure 4.2: Integrated luminosity and obtained by PEP-II and collected by *BABAR* from November 1999 to September 2006.

dominated by tracking resolution and can be improved by looking at luminosity variations as a function of relative beams position. In particular, knowing the beam currents and the x beam-spot dimension, it is possible to get a resolution on y (σ_y) $\sim$ 5 μm, value that remain stable within 10% in a one hour time scale. Those measurements can be also verified offline by measuring the primary vertex of multi-hadron events [1].

Fig. 4.2 shows the integrated luminosity obtained by PEP-II and collected by *BABAR* from the beginning of data taking (November 1999) to the end of August 2006. This work will make use only of data collected in **Run 1-5** data taking periods (before August 2006). This data sample corresponds to an integrated luminosity of 353 fb^{-1} recorded at the $\Upsilon(4S)$ resonance, corresponding to about $374 \cdot 10^6$ $B\bar{B}$ pairs.

[1]By reconstructing all the tracks in one event it is possible to have an estimate of primary vertex position: $\Upsilon(4S)$ decay point in transverse plane. Given that the boost along the z axis produces a relative displacement of the two B mesons this method has a relative poor resolution that get worse in presence of long-lived particles.

4.3 Tracking system

The charged particle tracking system consists of two different components: the silicon vertex tracker (SVT) and the drift chamber (DCH). The main purpose of this tracking system is the efficient detection of charged particles and the measurement of their momentum and angles with high precision. These track measurements are important for the extrapolation to the DIRC, the EMC and the IFR. At lower momenta, the SVT measurements are more important while at higher momenta the DCH dominates.

4.3.1 The Silicon Vertex Tracker: SVT

The vertex detector has a radius of 20 cm from the primary interaction region: it is placed inside the support tube of the beam magnets and consists of five layers of double-sided silicon strip sensors detectors to provide five measurements of the positions of all charged particles with polar angles in the region $20.1^\circ < \theta < 150^\circ$. Because of the presence of a 1.5 T magnetic field, the charged particle tracks with transverse momenta lower than ~ 100 MeV/c cannot reach the drift chamber active volume. So the SVT has to provide stand-alone tracking for particles with transverse momentum less than 120 MeV/c, the minimum that can be measured reliably in the DCH alone. This feature is essential for the identification of slow pions from D^{*-} meson decays. Because of these, the SVT has to provide redundant measurements.

Beyond the stand-alone tracking capability, the SVT provides the best measurement of track angles which is required to achieve design resolution for the Čerenkov angle for high momentum tracks. The SVT is very close to the production vertex in order to provide a very precise measure of points on the charged particles trajectories on both longitudinal (z) and transverse directions. The longitudinal coordinate information is necessary to measure the decay vertex distance, while the transverse information allows a better separation between secondary vertices coming from decay cascades.

More precisely, the design of the SVT was carried out according to some important guidelines:

- The number of impact points of a single charged particle has to be greater than 3 to make a stand-alone tracking possible, and to provide an independent momentum measure.

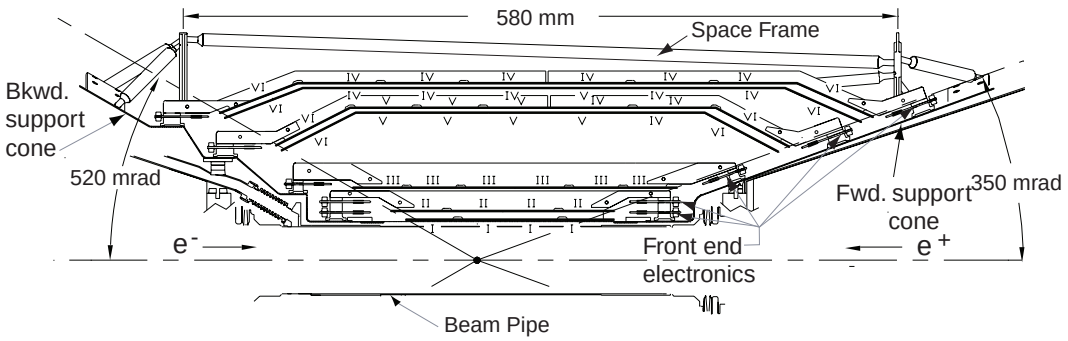

Figure 4.3: SVT schematic view: longitudinal section.

- The first three layers are placed as close as possible to the impact point to achieve the best resolution on the z position of the B meson decay vertices.
- The two outer layers are close to each other, but comparatively far from the inner layers, to allow a good measurement of the track angles.
- The SVT must withstand 2 MRad of ionizing radiation: the expected radiation dose is 1 Rad/day in the horizontal plane immediately outside the beam pipe and 0.1 Rad/day on average.
- Since the vertex detector is inaccessible during normal detector operations, it has to be reliable and robust.

These guidelines have led to the choice of a SVT made of five layers of double-sided silicon strip sensors. The spatial resolution, for perpendicular tracks must be $10 - 15\,\mu m$ in the three inner layers and about $40\,\mu m$ in the two outer layers. The three inner layers perform the impact parameter measurement, while the outer layers are necessary for pattern recognition and low p_t tracking. The silicon detectors are double-sided (contain active strips on both sides) because this technology reduces the thickness of the materials the particles have to cross, thus reducing the energy loss and multiple scattering probability compared to single-sided detectors. The sensors are organized in modules (Fig. 4.3). The SVT five layers contain 340 silicon strip detectors with AC-coupled silicon strips.

Each detector is $300\,\mu m$-thick but sides range from $41\,mm$ to $71\,mm$ and there are 6 different detector types. Each of the three inner layers has a hexagonal transverse

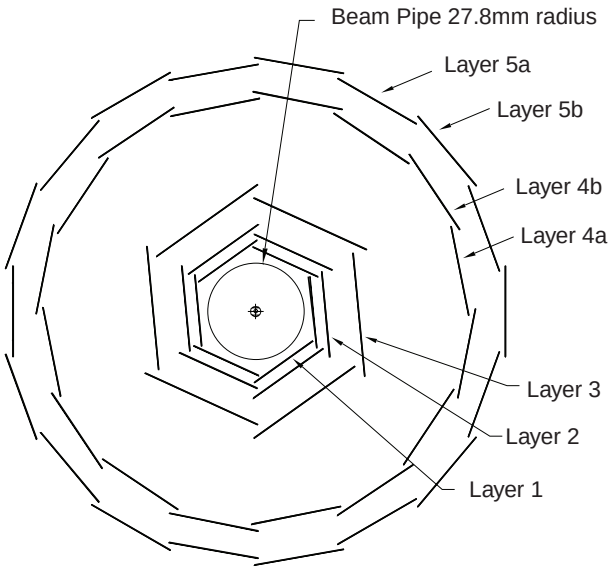

Figure 4.4: Cross-sectional view of the SVT in a plane perpendicular to the beam axis.

cross-section and it is made up of 6 detector modules, arrayed azimuthally around the beam pipe, while the outer two layers consist of 16 and 18 detector modules, respectively. The inner detector modules are barrel-style structures, while the outer detector modules employ the novel arch structure in which the detectors are electrically connected across an angle. This arch design was chosen to minimize the amount of silicon required to cover the solid angle while increasing the solid angle for particles near the edges of acceptance: having incidence angles on the detector closer to 90 degrees at small dip angles insures a better resolution on impact points. One of the main features of the SVT design is the mounting of the readout electronics entirely outside the active detector volume.

The strips on the two sides of the rectangular detectors in the barrel regions are oriented parallel (ϕ strips) or perpendicular (z strips) to the beam line: in other words, the inner sides of the detectors have strips oriented perpendicular to the beam direction to measure the z coordinate (z-size), whereas the outer sides, with longitudinal strips, allow the ϕ-coordinate measurement (ϕ-side). In the forward and backward regions of the two outer layers, the angle between the strips on the two sides of the trapezoidal detectors is approximately 90° and the ϕ strips are tapered.

The inner modules are tilted in ϕ by 5°, allowing an overlap region between adjacent modules: this provide full azimuthal coverage and is convenient for alignment. The outer modules are not tilted, but are divided into sub-layers and placed at slightly different

radii (see Fig. 4.4).

The total silicon area in the SVT is $0.94\,m^2$ and the number of readout channels is about 150 000. The geometrical acceptance of SVT is 90% of the solid angle in the c.m. system and typically 80% are used in charged particle tracking.

The z-side strips are connected to the read-out electronics with flexible *Upilex* fanout circuits glued to the inner faces of half-modules: as a matter of fact, each module is divided into two electrically separated forward and backward half-modules. The fanout circuits consist of conductive traces on a thin flexible insulator (copper traces on Kapton): the traces are wire-bonded to the end of the strips.

In the two outer layers, in each module the number of z strips exceeds the number of read-out channels, so that a fraction of the strips is "ganged", i.e., two strips are connected to the same read-out channel. The "ganging" is performed by the fanout circuits. The length of a z strip is about $50\,\mu m$ (case of no ganging) or $100\,\mu m$ (case of two strip connected): the ganging introduces an ambiguity on the z coordinate measurement, which must be resolved by the pattern recognition algorithms. The ϕ strips are daisy-chained between detectors, resulting in a total strip length of up to $26\,cm$. Also, for the ϕ-side, a short fanout extension is needed to connect the ends of the strips to the read-out electronics.

	1st layer	2nd layer	3rd layer	4th layer	5th layer
radius (mm)	32	40	54	91-127	114-144
modules/layer	6	6	6	16	18
wafers/module	4	4	6	7	8
read-out pitch (μm)					
ϕ	50-100	55-110	55-110	100	100
z	100	100	100	210	210

Table 4.3: Parameters of the SVT layout: these characteristics are shown for each layer.

The signals from the read-out strips are processed using a new technique, bringing in several advantages. After amplification and shaping, the signals are compared to a preset threshold and the time they exceed this threshold (time over threshold, or ToT) is measured. This time interval is related to the charge induced in the strip by the charged particle crossing it. Unlike the traditional peak-amplitude measurement in the shaper

output, the ToT has the advantage of an approximately logarithmic relation of the time interval to the charge signal. This compresses the active dynamic range of the signal, ensuring a good sensitivity in the lower range. When a particle crosses a silicon detector a cluster of adjoining strips producing a signal is formed. The good signal resolution in the lower range ensures a good determination of the tails of the cluster thus improving the resolution on the impact point measurement.

The electronic noise measured is found to vary between 700 and 1500 electrons ENC (equivalent noise charge), depending on the layer and the readout view: this can be compared to the typical energy deposition for a minimum ionizing particle at normal incidence, which is equivalent to ~ 24000 electrons.

During normal running conditions, the average occupancy of the SVT in a time window of $1\,\mu s$ is about 2% for the inner layers, where it is dominated by machine backgrounds, and less than 1% for the outer layers, where noise hits dominate.

The cluster reconstruction is based on a cluster finding algorithm: first the charge pulse height of a single pulse is calculated from the ToT value and clusters are formed grouping adjacent strips with consistent times. The position x of a cluster formed by n strips is evaluated with an algorithm called "head-to-tail" algorithm:

$$x = \frac{(x_1 + x_n)}{2} + \frac{p}{2}\frac{(Q_n - Q_1)}{(Q_n + Q_1)} \tag{4.1}$$

where x_i and Q_i are the position and the collected charge of i-th strip and p is the read-out pitch. This formula always gives a cluster position within $p/2$ of the geometrical center of the cluster. The cluster pulse height is simply the sum of the strip charges, while the cluster time is the average of the signal times.

The SVT efficiency can be calculated for each half-module by comparing the number of associated hits to the number of tracks crossing the active area of the half-module. Excluding defective readout sections (2 over 208), the combined hardware and software efficiency is 97%.

The spatial resolution of SVT hits is calculated by measuring the distance (in the plane of the sensor) between the track trajectory and the hit, using high-momentum tracks in two prong events: the uncertainty due to the track trajectory is subtracted from the width of the residual distribution to obtain the hit resolution. The track hit residuals are defined as the distance between track and hit, projected onto the wafer plane and along either the ϕ or z direction. The width of this residual distribution is then the SVT hit

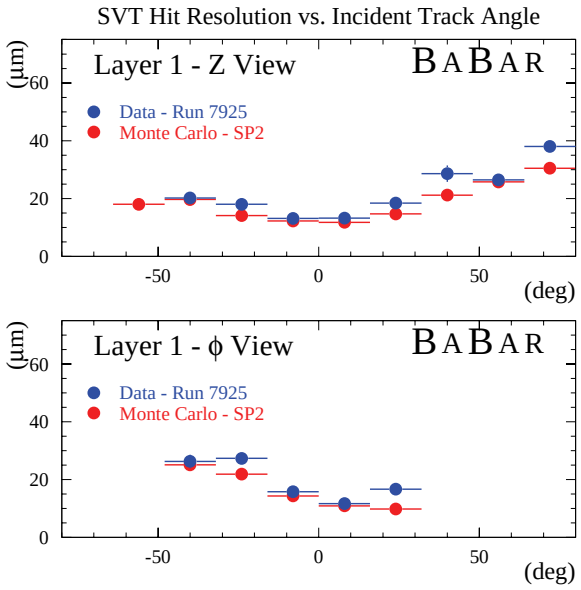

Figure 4.5: SVT hit resolution in the z and ϕ coordinate in microns, plotted as functions of the track incident angle in degrees.

resolution. Fig. 4.5 shows the SVT hit resolution for z and ϕ side hits as a function of the track incident angle: the measured resolutions are in very good agreement with the Monte Carlo expected ones. Over the whole SVT, resolutions are raging from $10-15\,\mu m$ (inner layers) to $30-40\,\mu m$ (outer layers) for normal tracks.

For low-momentum tracks ($p_t < 120$ MeV/c), the SVT provides the only particle identification information. The measure of the ToT value enables to obtain the pulse height and hence the ionization dE/dx: the value of ToT are converted to pulse height using a look-up table computed from the pulse shapes. The double-sided sensors provide up to ten measurements of dE/dx per track: with signals from at least four sensors, a 60% truncated mean dE/dx is calculated. For MIPs, the resolution on the truncated mean dE/dx is approximately 14%: a 2σ separation between kaons and pions can be achieved up to momentum of 500 MeV/c and between kaons and protons beyond 1 GeV/c.

4.3.2 The drift chamber: DCH

The drift chamber is the second part of *BABAR* tracking system. Its principal purpose is the efficient detection of charged particles and the measurement of their momenta and angles with high precision. The DCH complements the measurements of the impact pa-

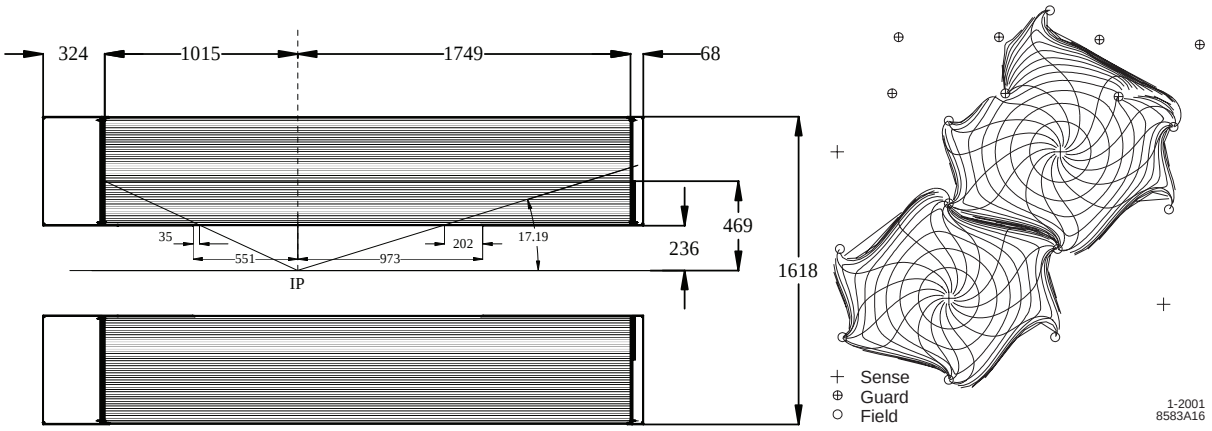

Figure 4.6: Side view of the *BABAR* drift chamber (the dimensions are in mm) and isochrones (i.e. contours of equal drift time of ions) in cells of layer 3 and 4 of an axial super-layer. The isochrones are spaced by $100\,ns$.

rameter and the directions of charged tracks provided by the SVT near the impact point (IP). At lower momenta, the DCH measurements dominate the errors on the extrapolation of charged tracks to the DIRC, EMC and IFR. The reconstruction of decay and interaction vertices outside of the SVT volume, for instance the K^0_S decays, relies only on the DCH. For these reasons, the chamber should provide maximal solid angle coverage, good measurement of the transverse momenta and positions but also of the longitudinal positions of tracks with a resolution of $\sim 1\,mm$, efficient reconstruction of tracks at momenta as low as 100 MeV/c and it has to minimally degrade the performance of the calorimeter and particle identification devices (the most external detectors). The DCH also needs to supply information for the charged particle trigger. For low momentum particles, the DCH is required to provide particle identification by measuring the ionization loss (dE/dx). A resolution of about 7% allows π/K separation up to 700 MeV/c. This particle identification (PID) measurement is complementary to that of the DIRC in the barrel region, while in the extreme backward and forward region, the DCH is the only device providing some discrimination of particles of different mass. The DCH should also be able to operate in presence of large beam-generated backgrounds having expected rates of about $5\,kHz$/cell in the innermost layers.

To meet the above requirements, the DCH is a $280\,cm$-long cylinder (see left plot in Fig. 4.6), with an inner radius of $23.6\,cm$ and an outer radius of $80.9\,cm$. It is bounded by the support tube at its inner radius and the particle identification device at its outer

radius. The flat end-plates are made of aluminum. Since the *BABAR* events will be boosted in the forward direction, the design of the detector is optimized to reduce the material in the forward end. The forward end-plate is made thinner ($12\,mm$) in the acceptance region of the detector compared to the rear end-plate ($24\,mm$), and all the electronics is mounted on the rear end-plate. The device is asymmetrically located with respect to the IP: the forward length of 174.9 cm is chosen so that particles emitted at polar angles of 17.2° traverse at least half of the layers of the chamber before exiting through the front end-plate. In the backward direction, the length of $101.5\,cm$ means that particles with polar angles down to 152.6° traverse at least half of the layers.

The inner cylinder is made of $1\,mm$ beryllium and the outer cylinder consists of two layers of carbon fiber glued on a Nomex core: the inner cylindrical wall is kept thin to facilitate the matching of SVT and DCH tracks, to improve the track resolution for high momentum tracks and to minimize the background from photon conversions and interactions. Material in the outer wall and in the forward direction is also minimized in order not to degrade the performance of the DIRC and the EMC.

The region between the two cylinders is filled up by a gas mixture consisting of Helium-isobutane (80% : 20%): the chosen mixture has a radiation length that is five times larger than commonly used argon-based gases. 40 layers of wires fill the DCH volume and form 7104 hexagonal cells with typical dimensions of $1.2\times1.9\,cm^2$ along the radial and azimuthal directions, respectively (see right plot in Fig. 4.6). The hexagonal cell configuration has been chosen because approximate circular symmetry can be achieved over a large portion of the cell. Each cell consist of one sense wire surrounded by six field wires: the sense wires are $20\,\mu m$ gold-plated tungsten-rhenium, the field wires are $120\,\mu m$ and $80\,\mu m$ gold-plated aluminum. By using the low-mass aluminum field wires and the helium-based gas mixture, the multiple scattering inside the DCH is reduced to a minimum, representing less than $0.2\%X_0$ of material. The total thickness of the DCH at normal incidence is $1.08\%X_0$.

The drift cells are arranged in 10 super-layers of 4 cylindrical layers each: the super-layers contain wires oriented in the same direction: to measure the z coordinate, axial wire super-layers and super-layers with slightly rotated wires (*stereo*) are alternated. In the stereo super-layers a single wire corresponds to different ϕ angles and the z coordinate is determined by comparing the ϕ measurements from axial wires and the measurements from rotated wires. The stereo angles vary between $\pm45mrad$ and $\pm76mrad$.

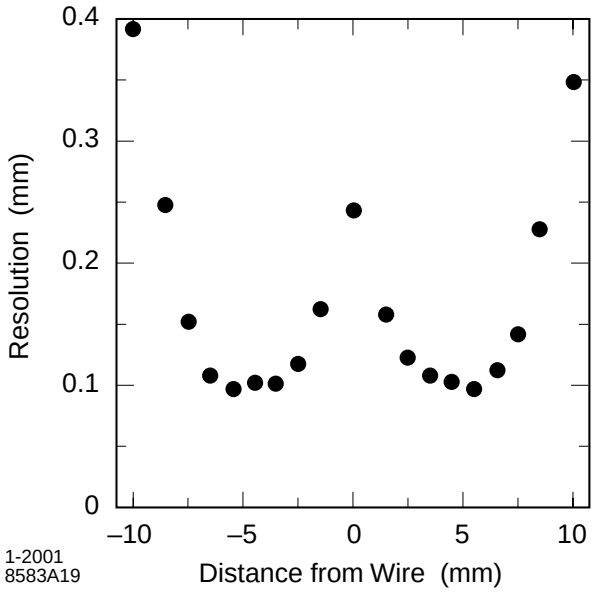

Figure 4.7: DCH position resolution as a function of the drift chamber in layer 18, for tracks on the left and right side of the sense wire. The data are averaged over all cells in the layer.

While the field wires are at ground potential, a positive high voltage is applied to the sense wires: an avalanche gain of approximately 5×10^4 is obtained at a typical operating voltage of $1960\,V$ and a $80:20$ helium:isobutane gas mixture.

In each cell, the track reconstruction is obtained by the electron time of flight: the precise relation between the measured drift time and drift distance is determined from sample of e^+e^- and $\mu^+\mu^-$ events. For each signal, the drift distance is estimated by computing the distance of closest approach between the track and the wire. To avoid bias, the fit does not include the hit of the wire under consideration. The estimated drift distances and the measured drift times are averaged over all wires in a layer.

The DCH expected position resolution is lower than $100\,\mu m$ in the transverse plane, while it is about $1\,mm$ in the z direction. The minimum reconstruction and momentum measure threshold is about 100 MeV/c and it is limited by the DCH inner radius. The design resolution on the single hit is about $140\,\mu m$ while the achieved weighted average resolution is about $125\,\mu m$. Fig. 4.7 shows the position resolution as a function of the drift distance, separately for the left and the right side of the sense wire. The resolution is taken from Gaussian fits to the distributions of residuals obtained from unbiased track fits. The results are based on multi-hadron events for data averaged over all cells in layer

18.

The specific energy loss (dE/dx) for charged particles through the DCH is derived from the measurement of the total charge collected in each drift cell. The specific energy loss per track is computed as a truncated mean from the lowest 80% of the individual dE/dx measurements. Various corrections are applied to remove sources of bias: these corrections include changes in gas pressure and temperature ($\pm 9\%$ in dE/dx), differences in cell geometry and charge collection ($\pm 8\%$), signal saturation due to space charge buildup ($\pm 11\%$), non-linearities in the most probable energy loss at large dip angles ($\pm 2.5\%$) and variation of cell charge collection as a function of the entrance angle ($\pm 2.5\%$).

4.4 Čerenkov Light Detector: DIRC

The particle identification system is crucial for *BABAR* since the CP violation analysis requires the ability to fully reconstruct one of the B meson and to tag the flavor of the other B decay: the momenta of the kaons used for flavor tagging extend up to about 2 GeV/c with most of them below 1 GeV/c. On the other hand, pions and kaons from the rare two-body decays $B^0 \to \pi^+\pi^-$ and $B^0 \to K^+\pi^-$ must be well separated: they have momenta between 1.7 and 4.2 GeV/c with a strong momentum-polar angle correlation of the tracks (higher momenta occur at more forward angles because of the c.m. system boost).

The particle identification of charged kaons is a crucial point of most of the measurements presented in this work.

So the particle identification system should be:

- thin and uniform in term of radiation lengths to minimize degradation of the calorimeter energy resolution
- small in the radial dimension to reduce the volume (cost) of the calorimeter
- with fast signal response
- able to tolerate high background

DIRC stands for Detection of Internally Reflected Čerenkov light and it refers to a new kind of ring-imaging Čerenkov detector which meets the above requirements. The particle identification in the DIRC is based on the Čerenkov radiation produced by charged

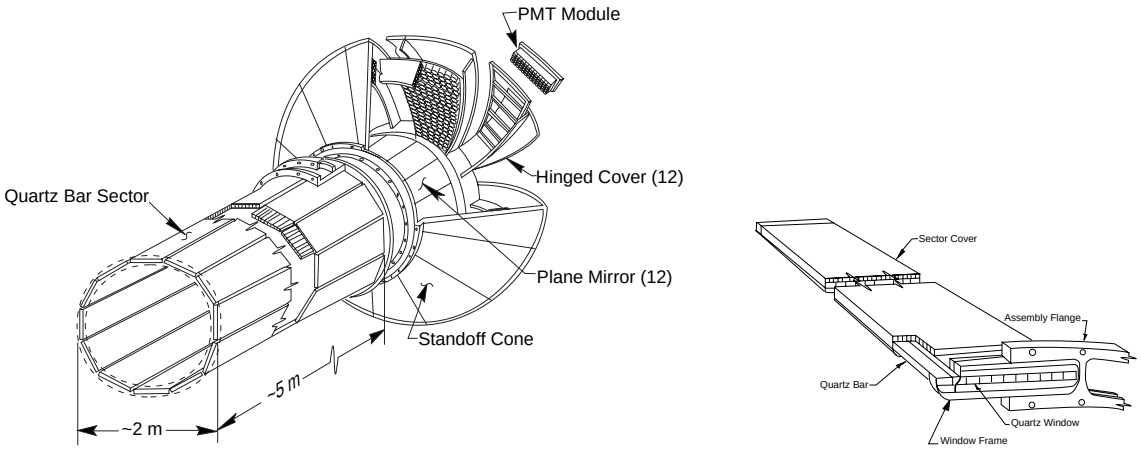

Figure 4.8: Mechanical elements of the DIRC and schematic view of bars assembled into a mechanical and optical sector.

particles crossing a material with a speed higher than light speed in that material. The angular opening of the Čerenkov radiation cone depends on the particle speed:

$$\cos\theta_c = \frac{1}{n\beta} \tag{4.2}$$

where θ_c is the Čerenkov cone opening angle, n is the refractive index of the material and β is the particle velocity over c. The principle of the detection is based on the fact that the magnitudes of angles are maintained upon reflection from a flat surface.

Since particles are produced mainly forward in the detector because of the boost, the DIRC photon detector is placed at the backward end: the principal components of the DIRC are shown in Fig. 4.8. The DIRC is placed in the barrel region and consists of 144 long, straight bars arranged in a 12-sided polygonal barrel. The bars are $1.7\,cm$-thick, $3.5\,cm$-wide and $4.90\,m$-long: they are placed into 12 hermetically sealed containers, called *bar boxes*, made of very thin aluminum-hexcel panels. Within a single bar box, 12 bars are optically isolated by a $\sim 150\,\mu m$ air gap enforced by custom shims made from aluminum foil.

The radiator material used for the bars is synthetic fused silica: the bars serve both as radiators and as light pipes for the portion of the light trapped in the radiator by total internal reflection. Synthetic silica has been chosen because of its resistance to ionizing radiation, its long attenuation length, its large index of refraction, its low chromatic dispersion within its wavelength acceptance.

The Čerenkov radiation is produced within these bars and is brought, through succes-

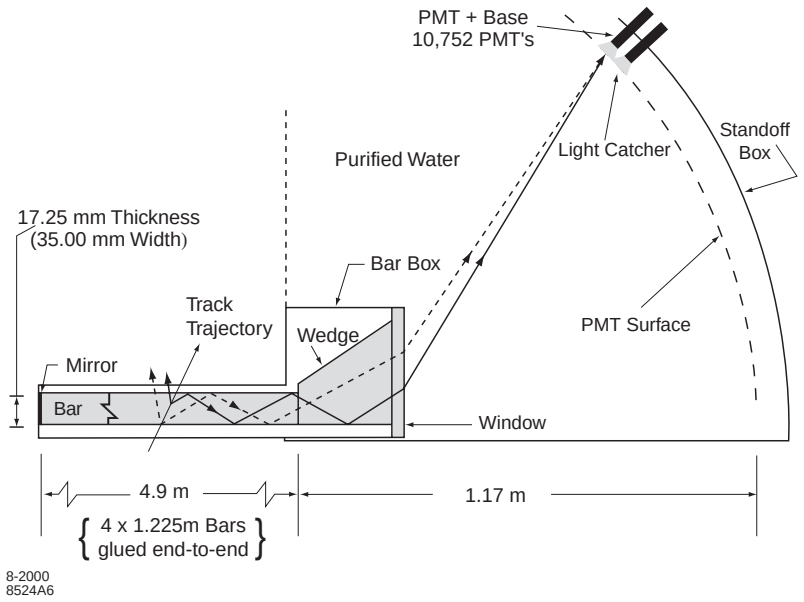

Figure 4.9: Schematics of the DIRC fused silica radiator bar and imaging region. Not shown is a 6 mrad angle on the bottom surface of the wedge.

sive total internal reflections, in the backward direction outside the tracking and magnetic volumes: only the backward end of the bars is instrumented. A mirror placed at the other end on each bar reflects forward-going photons to the instrumented end. The Čerenkov angle at which a photon was produced is preserved in the propagation, modulo some discrete ambiguities (the forward-backward ambiguity can be resolved by the photon arrival-time measurement, for example). The DIRC efficiency grows together with the particle incidence angle because more light is produced and a larger fraction of this light is totally reflected. To maximize the total reflection, the material must have a refractive index (fused silica index is $n = 1.473$) higher than the surrounding environment (the DIRC is surrounded by air with index $n = 1.0002$).

Once photons arrive at the instrumented end, most of them emerge into a water-filled expansion region (see Fig. 4.9), called the *Standoff Box*: the purified water, whose refractive index matches reasonably well that of the bars ($n_{H_2O} = 1.346$), is used to minimize the total internal reflection at the bar-water interface.

The standoff box is made of stainless steel and consists of a cone, cylinder and 12 sectors of PMTs: it contains about 6000 liters of purified water. Each of the 12 PMTs sectors contains 896 PMTs in a close-packed array inside the water volume: the PMTs are linear focused 2.9 cm diameter photo-multiplier tubes, lying on an approximately toroidal

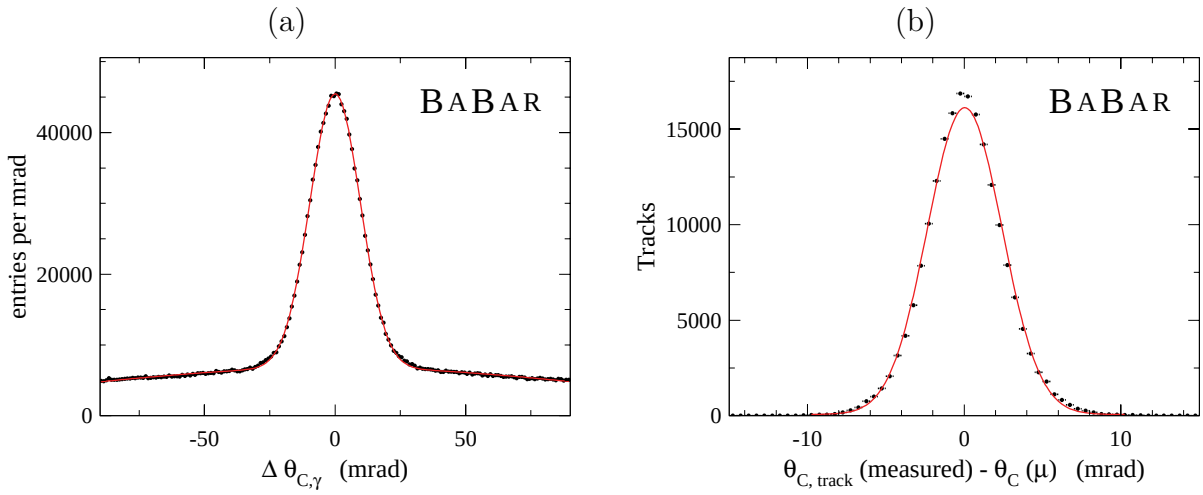

Figure 4.10: From di-muon data events, (a) single photon Čerenkov angle resolution. The distribution is fitted with a double-Gaussian and the width of the narrow Gaussian is 9.6 *mrad*. (b) Reconstructed Čerenkov angle for single muons. The difference between the measured and expected Čerenkov angle is plotted and the curve represents a Gaussian distribution fit to the data with a width of 2.4 *mrad*.

surface.

The DIRC occupies only 8 cm of radial space, which allows for a relatively large radius for the drift chamber while keeping the volume of the CsI Calorimeter reasonably low: it corresponds to about 17% X_0 at normal incidence. The angular coverage is the 94% of the ϕ azimuthal angle and the 83% of $\cos\theta_{CM}$.

Čerenkov photons are detected in the visible and near-UV range by the PMT array. A small piece of fused silica with a trapezoidal profile glued at the back end of each bar allows for significant reduction in the area requiring instrumentation because it folds one half of the image onto the other half. The PMTs are operated directly in water and are equipped with light concentrators: the photo-multiplier tubes are about 1.2 m away from the end of the bars. This distance from the bar end to the PMTs, together with the size of the bars and PMTs, gives a geometric contribution to the single photon Čerenkov angle resolution of about 7 *mrad*. This is a bit larger than the resolution contribution from Čerenkov light production (mostly a 5.4 *mrad* chromatic term) and transmission dispersions. The overall single photon resolution expected is about 9 *mrad*.

The image from the Čerenkov photons on the sensitive part of the detector is a cone cross-section whose opening angle is the Čerenkov angle modulo the refraction effects on

the fused silica-water surface. In the most general case, the image consists of two cone cross-sections out of phase one from the other by a value related to an angle which is twice the particle incidence angle. In order to associate the photon signals with a track traversing a bar, the vector pointing from the center of the bar end to the center of each PMT is taken as a measure of the photon propagation angles α_x, α_y and α_z. Since the track position and angles are known from the tracking system, the three α angles can be used to determine the two Čerenkov angles θ_C and ϕ_C. In addition, the arrival time of the signal provides an independent measurement of the propagation of the photon and can be related to the propagation angles α. This over-constraint on the angles and the signal timing are useful in dealing with ambiguities in the signal association and high background rates.

The expected number of photo-electrons (N_{pe}) is ~ 28 for a $\beta = 1$ particle entering normal to the surface at the center of a bar and increases by over a factor of two in the forward and backward directions.

The time distribution of real Čerenkov photons from a single event is of the order of $50\,ns$ wide and during normal data taking they are accompanied by hundreds of random photons in a flat background distribution within the trigger acceptance window. The Čerenkov angle has to be determined in an ambiguity that can be up to 16-fold: the goal of the reconstruction program is to associate the correct track with the candidate PMT signal with the requirement that the transit time of the photon from its creation in the bar to its detection at the PMT be consistent with the measurement error of about $1.5\,ns$.

4.5 Electromagnetic calorimeter: EMC

The understanding of CP violation in the B meson system requires the reconstruction of final state containing a direct π^0 or that can be reconstructed through a decay chain containing one or more daughter π^0s. The electromagnetic calorimeter is designed to measure electromagnetic showers with excellent efficiency and energy and angular resolution over the energy range from 20 MeV to 9 GeV. This capability should allow the detection of photons from π^0 and η decays as well as from electromagnetic and radiative processes. By identifying electrons, the EMC contributes to the flavor tagging of neutral B mesons via semi-leptonic decays. The upper bound of the energy range is given by the need to measure QED processes like $e^+e^- \to e^+e^-(\gamma)$ and $e^+e^- \to \gamma\gamma$ for calibration

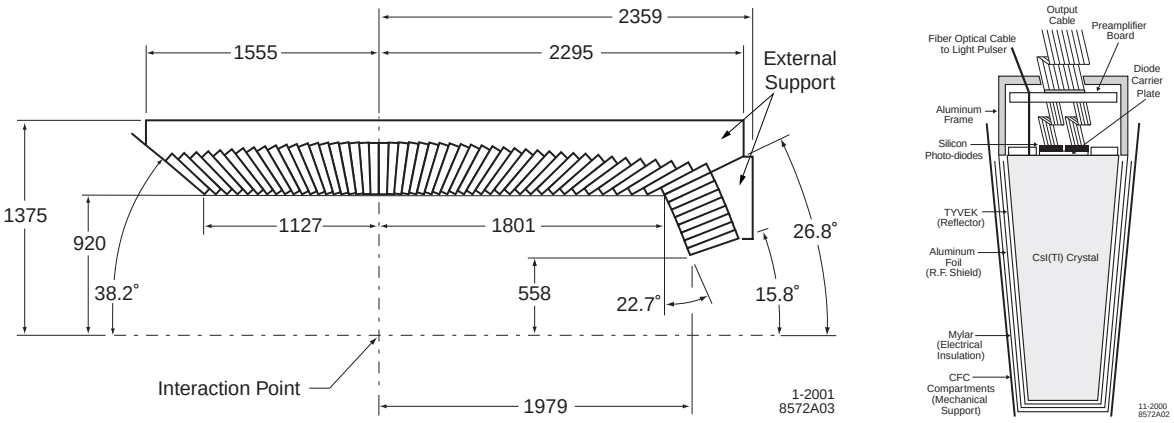

Figure 4.11: The electromagnetic calorimeter layout in a longitudinal cross section and a schematic view of the wrapped CsI(Tl) crystal with the front-end readout package mounted on the rear face (not to scale).

and luminosity determination. The lower bound is set by the need for highly efficient reconstruction of B-meson decays containing multiple π^0s and η^0s. The measurement of very rare decays containing π^0s in the final state (for example, $B^0 \to \pi^0\pi^0$) puts the most stringent requirements on energy resolution, expected to be of the order of $1-2\%$. Below 2 GeV energy, the π^0 mass resolution is dominated by the energy resolution, while at higher energies, the angular resolution becomes dominant and it is required to be of the order of few *mrad*. The EMC is also used for electron identification and for completing the IFR output on μ and K_L^0 identification. It also has to operate in a $1.5\,T$ magnetic field.

The EMC has been chosen to be composed of a finely segmented array of thallium-doped cesium iodide (CsI(Tl)) crystals. The crystals are read out with silicon photo-diodes that are matched to the spectrum of scintillation light. The energy resolution of a homogeneous crystal calorimeter can be described empirically in terms of a sum of two terms added in quadrature:

$$\frac{\sigma_E}{E} = \frac{a}{\sqrt[4]{E(GeV)}} \oplus b \tag{4.3}$$

where E and σ_E refer to the energy of a photon and its rms error, measured in GeV. The energy dependent term $a(\sim 2\%)$ arises basically from the fluctuations in photon statistics, but also from the electronic noise of the photon detector and electronics and from the beam-generated background that leads to large numbers of additional photons. This first term dominates at low energy, while the constant term $b(\sim 1.8\%)$ is dominant at higher energies (> 1 GeV). It derives from non-uniformity in light collection, leakage

or absorption in the material in front of the crystals and uncertainties in the calibration.

The angular resolution is determined by the transverse crystal size and the distance from the interaction point: it can be empirically parameterized as a sum of an energy dependent and a constant term

$$\sigma_\theta = \sigma_\phi = \frac{c}{\sqrt{E(GeV)}} + d \tag{4.4}$$

where E is measured in GeV and with $c \sim 4\ mrad$ and $d \sim 0\ mrad$.

In CsI(Tl), the intrinsic efficiency for the detection of photons is close to 100% down to a few MeV, but the minimum measurable energy in colliding beam data is about 20 MeV for the EMC: this limit is determined by beam and event-related background and the amount of material in front of the calorimeter. Because of the sensitivity of the π^0 efficiency to the minimum detectable photon energy, it is extremely important to keep the amount of material in front of the EMC to the lowest possible level.

Thallium-doped CsI has high light yield and small Molière radius in order to allow for excellent energy and angular resolution. It is also characterized by a short radiation length for shower containment at *BABAR* energies. The transverse size of the crystals is chosen to be comparable to the Molière radius achieving the required angular resolution at low energies while limiting the total number of crystals and readout channels.

The *BABAR* EMC (left plot in Fig. 4.11) consists of a cylindrical barrel and a conical forward end-cap: it has a full angle coverage in azimuth while in polar angle it extends from 15.8° to 141.8° corresponding to a solid angle coverage of 90% in the CM frame. Radially the barrel is located outside the particle ID system and within the magnet cryostat: the barrel has an inner radius of $92\,cm$ and an outer radius of $137.5\,cm$ and it's located asymmetrically about the interaction point, extending $112.7\,cm$ in the backward direction and $180.1\,cm$ in the forward direction. The barrel contains 5760 crystals arranged in 48 rings with 120 identical crystals each: the end-cap holds 820 crystals arranged in eight rings, adding up to a total of 6580 crystals. They are truncated-pyramid CsI(Tl) crystals (right plot in Fig. 4.11): they are tapered along their length with trapezoidal cross-sections with typical transverse dimensions of $4.7 \times 4.7\,cm^2$ at the front face, flaring out toward the back to about $6.1 \cdot 6.1\,cm^2$. All crystals in the backward half of the barrel have a length of $29.6\,cm$: toward the forward end of the barrel, crystal lengths increase up to $32.4\,cm$ in order to limit the effects of shower leakage from increasingly higher energy particles. All end-cap crystals are of $32.4\,cm$ length. The barrel and end-cap have total crystal

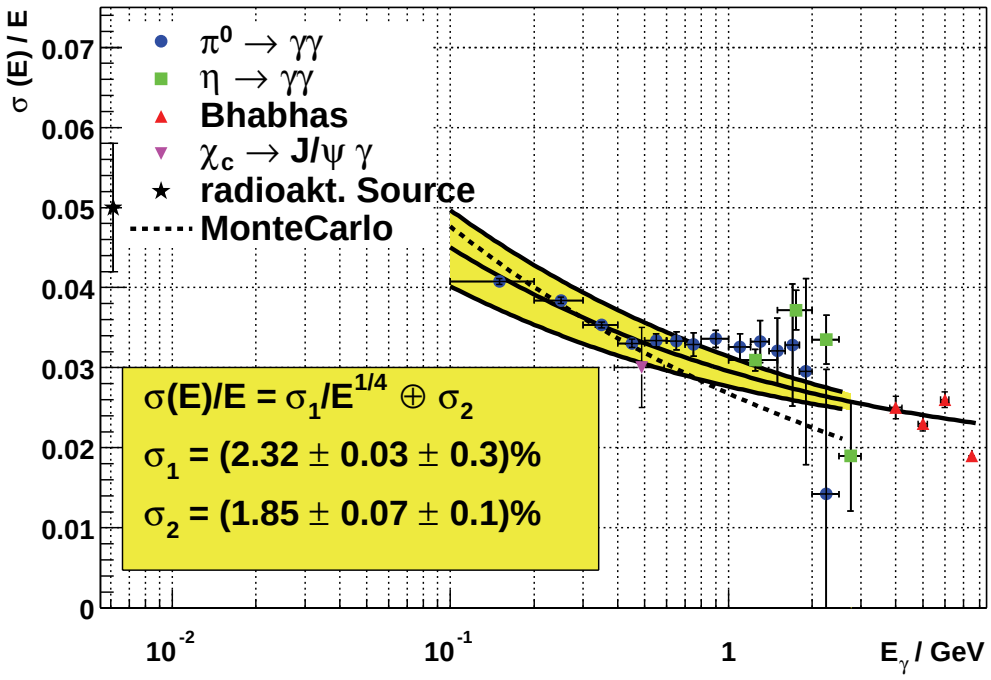

Figure 4.12: EMC resolution as a function of the energy.

volumes of $5.2\,m^3$ and $0.7\,m^3$, respectively. The CsI(Tl) scintillation light spectrum has a peak emission at $560\,nm$: two independent photodiodes collect this scintillation light from each crystal. The readout package consists of two silicon PIN diodes, closely coupled to the crystal and to two low-noise, charge-sensitive preamplifiers, all enclosed in a metallic housing.

A typical electromagnetic shower spreads over many adjacent crystals, forming a *cluster* of energy deposit: pattern recognition algorithms have been developed to identify these clusters and to discriminate single clusters with one energy maximum from merged clusters with more than one local energy maximum, referred to as *bumps*. The algorithms also determine whether a bump is generated by a charged or a neutral particle. Clusters are required to contain at least one seed crystal with an energy above 10 MeV: surrounding crystals are considered as part of the cluster if their energy exceeds a threshold of 1 MeV or if they are contiguous neighbors of a crystal with at least 3 MeV signal. The level of these thresholds depends on the current level of electronic noise and beam-generated background.

A bump is associated with a charged particle by projecting a track to the inner face of the calorimeter: the distance between the track impact point and the bump centroid is calculated and if it is consistent with the angle and momentum of the track, the bump is

associated with this charged particle. Otherwise it is assumed to originate from a neutral particle.

On average, 15.8 clusters are detected per hadronic event: 10.2 are not associated to any charged particle. Currently, the beam-induced background contributes on average with 1.4 neutral clusters with energy above 20 MeV.

At low energy, the energy resolution of the EMC is measured directly with a 6.13 MeV radioactive photon source (a neutron-activated fluorocarbon fluid) yielding $\sigma_E/E = 5.0 \pm 0.8\%$. At high energy, the resolution is derived from Bhabha scattering where the energy of the detected shower can be predicted from the polar angle of the electrons and positrons. The measured resolution is $\sigma_E/E = 1.9 \pm 0.1\%$ at 7.5 GeV. Fig. 4.12 shows the energy resolution on data compared with expectations from Monte Carlo. From a fit to the experimental results to eq. 4.3, $a = 2.32 \pm 0.30\%$ and $b = 1.85 \pm 0.12\%$ are obtained. The constant term comes out to be greater than expected: this is mainly caused by a cross talk effect, still not corrected, in the front-end electronics.

The measurement of the angular resolution is based on Bhabha events and ranges between 12 *mrad* and 3 *mrad* going from low to high energies. A fit to eq. 4.4 results in $c = (3.87 \pm 0.07)$ *mrad* and $d = (0.00 \pm 0.04)$ *mrad*.

4.6 Instrumented Flux Return: IFR

IFR (*Instrumented Flux Return*) detector is dedicated to muon identification and neutral hadrons detection (mainly K_L^0) in a wide range of momentum and angles.

The IFR, as all the other *BABAR* subsystems, has an asymmetric structure with a polar angle coverage that is $17° \leq \theta_{lab} \leq 150°$. The IFR (Fig. 4.13) is made of 19 layers of Resistive Plate Chambers (RPC) in the barrel region and 18 layers in forward and backward regions, that are placed inside the iron layers used for the solenoidal magnetic field return joke. The iron structure is subdivided in three main parts: the barrel one surrounding the solenoid, made of 6 sextants covering the radial distance between 1.820 m and 3.045 m with a length of 3.750 m (along the z axis); the forward end-cap and backward end-cap covering the forward (positive z axis) and backward regions. Moreover, two cylindrical RPC layers have been installed between the calorimeter and the magnet cryostat in order to reveal particles exiting from the EMC. Those layers should cover the ϕ regions not covered by the barrel. Cylindrical layers are subdivided in four sections,

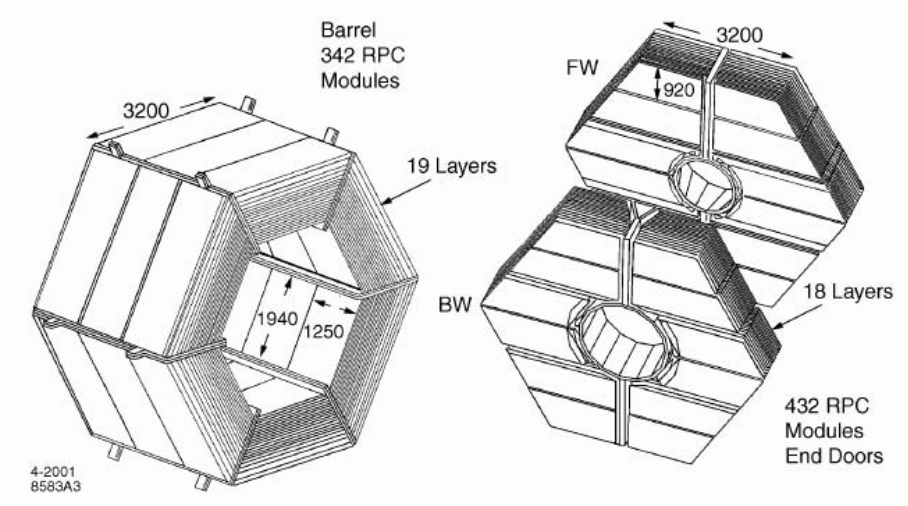

Figure 4.13: IFR view;

section	# di sectors	coor.	readout # layer	# strip layer/sector	strip len. (cm)	strip larg. (mm)	total # channel
barrel	6	ϕ	19	96	350	19.7-32.8	$\approx$ 11k
		z	19	96	190-318	38.5	$\approx$ 11k
end-cap	4	y	18	6x32	124-262	28.3	13,824
		x	18	3x64	10-180	38.0	$\approx$ 15k
cyl.	4	ϕ	1	128	370	16.0	512
		z	1	128	211	29.0	512
		u	1	128	10-422	29.0	512
		v	1	128	10-423	29.0	512

Table 4.4: IFR readout segmentation. Total number of channels is $\sim$ 53k.

each of them covering one fourth of the circumference: each of them has four RPC groups with orthogonal readout strips. $u - v$ helicoidal strips are placed inside along module's diagonals while ϕ and z parallel strips are placed outside. The summary of IFR readout segmentation is given in Tab. 4.4.

Each end-cap has an hexagonal shape and is vertically subdivided in two halves in order to allow internal subsystems access, if necessary. Vacuum tube and PEP-II focusing elements are placed in the middle. Iron plates have a thickness ranging from 2 *cm*, for the inner ones placed nearest to the interaction region, to 10 *cm* for the outer ones; this means a total thickness of steel at normal incidence of $\sim$ 65 *cm* (nearly corresponding to

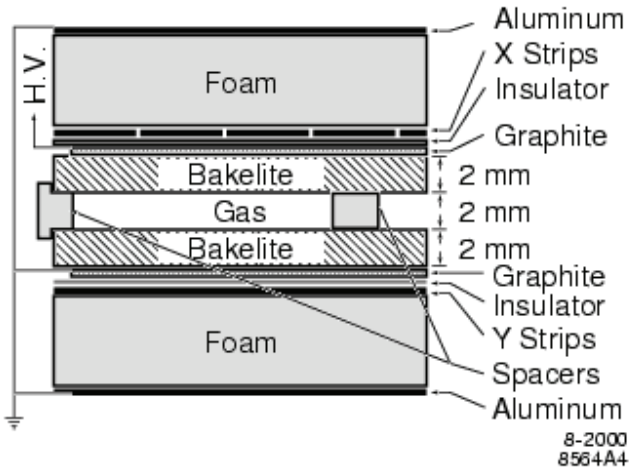

Figure 4.14: Planar RPC section with HV connection scheme.

$\sim$ 4 interaction lengths) in the barrel and $\sim$ 60 *cm* in the end-caps. Nominal distance between iron layers in the inner barrel region is 3.5 *cm* while is 3.2 *cm* everywhere else. The increased granularity of inner layers with respect to the outer ones is due to the fact that the largest part of particles detected inside the IFR are interacting in the very first material layers. Chosen segmentation is also the result of a compromise between the subsystem cost (proportional to the volume) and the need of a good efficiency for low momentum ($>$ 700 MeV/c) muon detection, minimizing, at the same time, fraction of K_L^0's that are not interacting inside the IFR. Result of this optimization is a not uniform segmentation with iron plates that have thickness increasing with distance from beam line. RPC section is shown in Fig. 4.14.

In each barrel sextant layers are kept together by a structure that reduces the coverage of solid angle with active detectors of $\sim$ 7%. Active coverage of IFR detector is $\approx$ 2000 m^2, for a total RPC modules number that is $\sim$ 900. Signals produced by particles crossing the gas gap inside the RPCs are collected on both sides of the chamber by using thin strips (thickness $\sim$ 40 μm) with width of the order of a centimeter. Strips are applied in two orthogonal directions on insulating planes 200 μm thick, in order to have a bi-dimensional view. In each barrel sextant each gap is hosting a chamber. This consist of a set of 3 RPC modules of rectangular shape. Each module is $\sim$ 125 *cm* long along beams direction with variable width in order to completely fill the gap. Each chamber is equipped with 96 $\phi - strip$ placed along z axis that are measuring the ϕ angle inside the barrel and 96

$z-strip$ orthogonal to beams direction that are measuring z coordinate. $z-strips$ are subdivided into 3 panels of 32 strips with largeness, function of chamber radial position, ranging between 1.78 and 3.37 cm. This projective geometry allows a constant number of strips for all the various layers without decreasing detector resolution (each strip covers the same azimuthal angle). The used gas mixture is made of 56.7% Argon, 38.8% Freon-134a and 4.5% Isobutane. Working voltage for RPCs is $\sim 7.5\ kV$. Iron layers keeping apart RPC planes are chilled by a water system that keeps the temperature $\sim 20^oC$.

RPC efficiencies have been measured by using cosmics taken on a weekly base. Mean efficiency during 2000 run has been $\sim$ 78% for the barrel and $\sim$ 87% for the forward end-cap, less than that one measured in June 1999 ($\sim$ 92%). During the Summer 1999 the ambient temperature increased very much reaching about 32° to 38° inside the iron. During such period the IFR had problems to run the full detector because the dark current drawn by the chambers exceeded the total current limit provided by the power supply. All the chambers drawing more than $200\mu A$ were disconnected. In October the chambers were re-connected but they didn't recover the full efficiency. The forward end-cap has been completely reconstructed and installed in the Summer 2002: 5 intermediate RPC layers were replaced by 2.54 cm of brass, 10 cm of steel were added after the last RPC layer, an RPC (layer 19) was added in front of the forward end-cap, an RPC belt was added in the barrel–end-cap overlap region. Barrel efficiencies are still decreasing and are at $\sim$ 40% level while in the new forward end-cap, they are greater than 90%.

Muons are identified by measuring the number of traversed interaction lengths in the entire detector and comparing it with the number of expected interaction lengths for a muon of a given momentum. Moreover, the projected intersections of a track with the RPC planes are computed and, for each readout plane, all strips clusters detected within a predefined distance from the predicted intersection are associated with the track: the average number and the r.m.s. of the distribution of RPC strips per layer gives additional μ/π discriminating power. It is expected in fact the average number of strips per layer to be larger for pions producing an hadronic interaction than for muons. Other variables exploiting clusters distribution shapes are constructed. Selection criteria based on all these variables are applied to select muons. The performance of the muon selection has been tested on samples of kinematically identified muons from $\mu\mu ee$ and $\mu\mu\gamma$ final states and pions from three-prong τ decays and $K_S \to \pi^+\pi^-$ decays.

At the end of the summer 2004 RPC from Top and Bottom Barrel sextant have been

substituted with limited streamer tube (LST). Data recording **Run-5** has been started only in the second half of April 2005. In these days (summer 2006) all the remaining sextants of the barrel are going to be replaced with LST's.

The efficiency of the LST is monitored daily using $\mu\mu$ pairs from colliding beams and monthly from cosmic rays. The calculated efficiency results to be constant around 90%. The geometric efficiency is 92.5%. The fluctuation of the efficiency are mostly related to the fluctuation on the number of silent channels, but no loss of efficiency for each single LST is detected.

Fig. 4.15 shows the efficiency map for the layer 10 of the IFR barrel, comparing the bottom and top sextants with LST and remaining RPC's which are going to be replaced during Summer 2006.

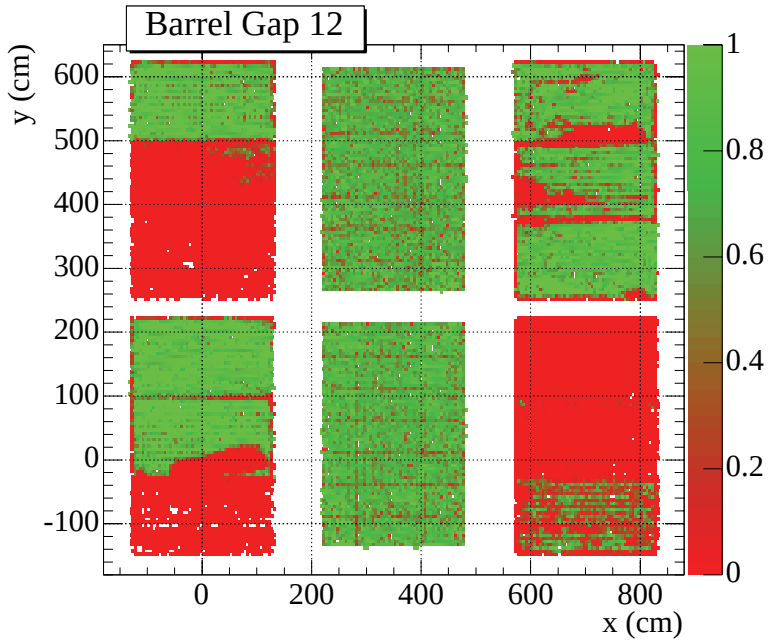

Figure 4.15: Efficiency map for layer 10 of IFR barrel for a run 62018 (middle of Run5). Left and right columns represent RPC-instrumented sextants, central column represent LST-instrumented layers (top and bottom layers). The remaining RPC's in the IFR barrel are going to be replaced with LST's in Summer 2006.

For the π/μ discrimination the LST appear to work better than RPC ever did.

Since the forward RPC's began to show degradation of efficiency in the inner regions closest to the beam axis, where the machine background is higher, half of the central RPC chambers for layer one and three have been switched to avalanche mode. This had as effect an expected higher strip occupancy, but led to the full recovery of efficiency in the

inner radii of the chambers. This effect is shown in Fig. 4.16

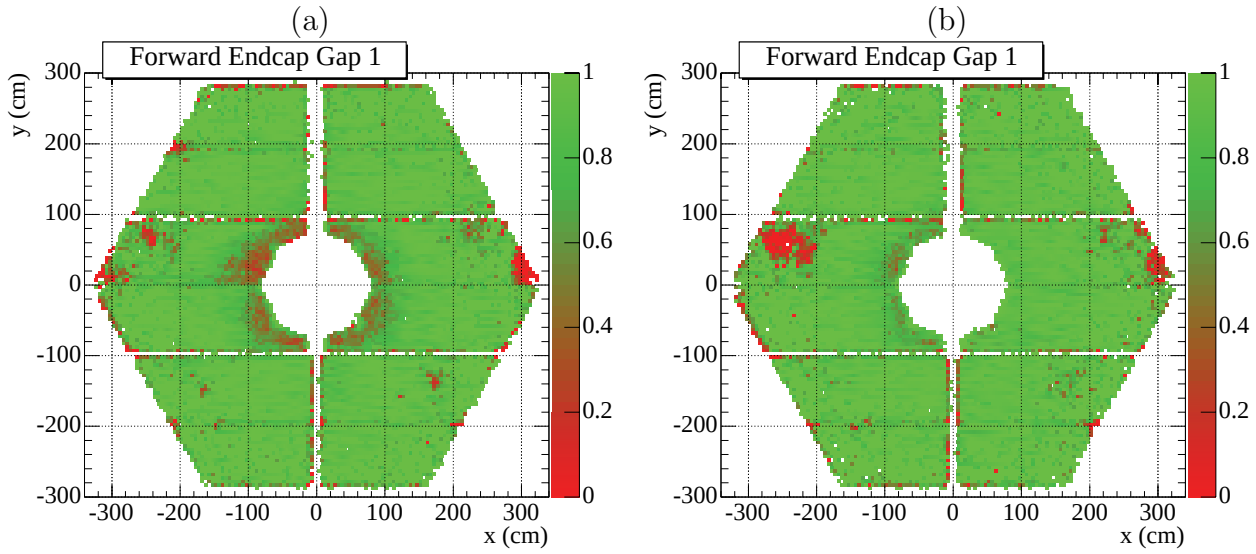

Figure 4.16: Efficiency map for the first layer of forward endcap IFR. (a) Run 58700 (end of Run4) with all RPC in streamer mode; (b) Run 62018 (middle of Run5) with the central RPC chamber ($x > 0$ cm and $|y| < 100$ cm) in avalanche mode. The two runs have been chosen having approximately the same luminosity. (b) shows a full recovery of the efficiency at small radii which was degraded with the chamber in streamer mode.

This is mostly important for the future run periods, where the plan is to raise significantly the luminosity, with a consequent increase in the beam backgrounds. Due to the good results of the test on these two layers, during this summer the central RPC chambers of the forward endcap will be all converted to avalanche regime.

Chapter 5

Charged and Neutral Kaon Reconstruction

All the measurements we will present in this work involve neutral or charged kaons. We will describe the selection of charged tracks and kaon/pion particle identification (PID) through the informations coming from the inner tracking system and, above all, the DIRC θ_c measurements.

We then will describe the quite standard reconstruction of K^0_S decaying in $\pi^+\pi^-$ or $\pi^0\pi^0$, even if some of the details may differ in $B^0 \to K^+K^-K^0_S$ or in $B^0 \to K^0_SK^0_SK^0_S$ decays, because of different signal to background ratios.

Finally, an original work on the K^0_L identification, using the informations on both the EMC and the IFR detectors, which made possible the measurement of the *CP* asymmetry in $B^0 \to K^+K^-K^0_L$ decays, is presented.

5.1 Track Reconstruction

The reconstruction of charged particle is based on the SVT and the DCH detectors. Charged particle tracking has been studied with large samples of cosmic ray muons, e^+e^-, $\mu^+\mu^-$ and $\tau^+\tau^-$ events, as well as multi-hadrons.

Charged tracks are defined by five parameters $(d_0, \phi_0, \omega, z_0, \tan\lambda)$ and their associated error matrix. These parameters are measured at the point of closest approach to the z-axis; d_0 and z_0 are the distances of this point from the origin of the coordinate system in the x–y plane and along the z-axis, respectively. The angle ϕ_0 is the azimuth of the track, λ the dip angle relative to the transverse plane, and ω is the curvature. d_0 and ω are signed variables; their sign depends on the charge of the track.

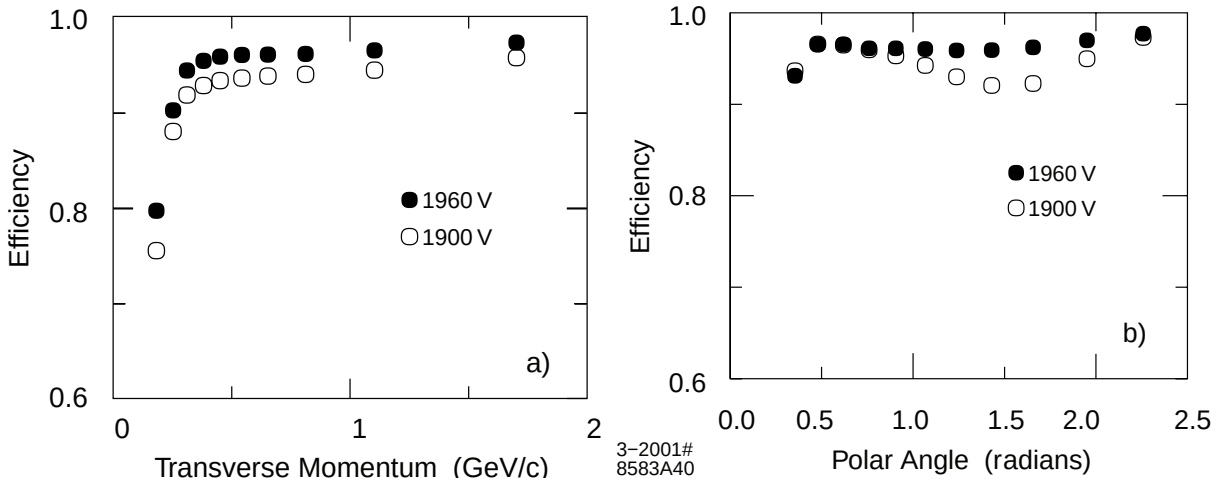

Figure 5.1: *Track reconstruction efficiency in the DCH at operating voltages of* $1960\,V$ *and* $1900\,V$ *as a function of transverse momentum (left plot) and of polar angle (right plot). The efficiency is measured in multi-hadron events.*

The track finding and the fitting procedures make use of Kalman filter algorithm [33] [53] that takes into account the detailed distribution of material in the detector and the full map of the magnetic field. First of all, tracks are reconstructed with DCH hits through a stand-alone DCH algorithm, the resulting tracks are then extrapolated into the SVT and SVT track segments are added and a Kalman fit is performed to the full set of DCH and SVT hits. Any remaining SVT are passed to the SVT stand-alone track finding algorithms. Finally, an attempt is made to use in the Kalman filter tracks that are only found by one of the two tracking systems and thus recover tracks scattered in the material of the support tube.

The efficiency for track reconstruction in the DCH has been measured as a function of transverse momentum, polar and azimuthal angles in multi-track events. These measurement rely on specific final states and exploit the fact that the track reconstruction can be performed independently in the SVT and the DCH. The absolute DCH tracking efficiency is determined as the ratio of the number of reconstructed DCH tracks to the number of tracks detected in the SVT with the requirement that they fall within the acceptance of the DCH. Left plot in Fig. 5.1 shows the efficiency in the DCH as a function of transverse momentum in multi-hadron events.

At design voltage of $1960\,V$, the efficiency averages $98\pm1\%$ per track above $200\ \mathrm{MeV}/c$: the data recorded at $1900\,V$ show a reduction in efficiency by about 5% for tracks almost

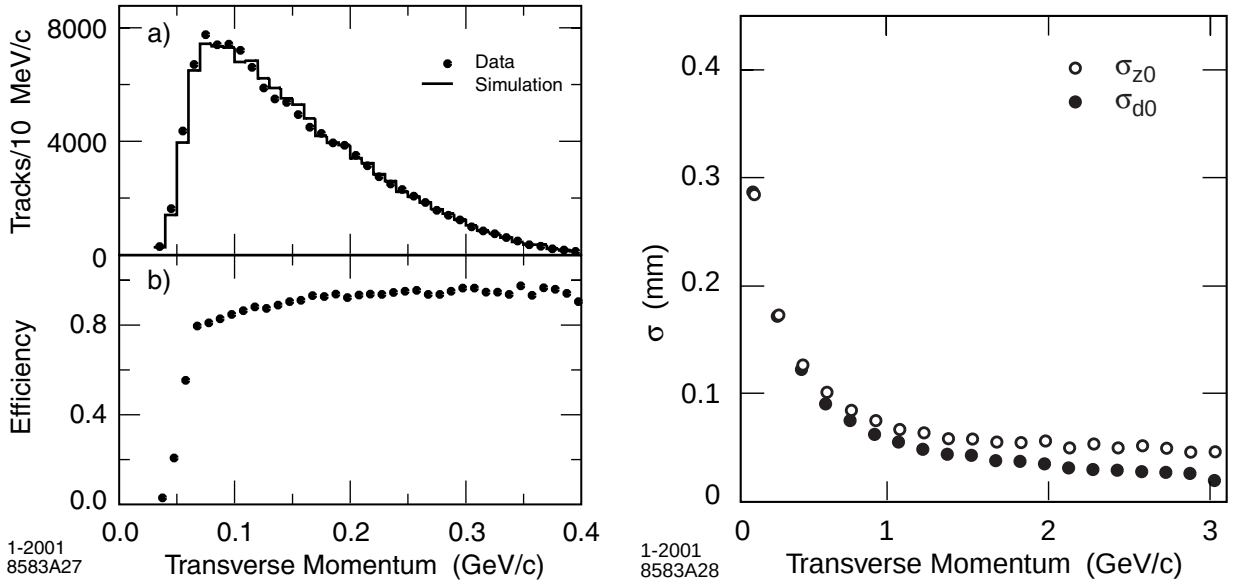

Figure 5.2: Left: Monte Carlo studies of low momentum tracks in the SVT on $D^{*+} \to D^0\pi^+$ events. (a) comparison with data in $B\overline{B}$ events and (b) efficiency for slow pion detection derived from simulated events. Right: resolution in the parameters d_0 and z_0 for tracks in multi-hadron events as a function of the transverse momentum.

at normal incidence, indicating that the cells are not fully efficient at this voltage (see right plot in Fig. 5.1).

The stand-alone SVT tracking algorithms have a high efficiency for tracks with low transverse momentum: to estimate the tracking efficiency for these low momentum tracks, a detailed Monte Carlo study was performed. The pion spectrum was derived from simulation of the inclusive D^* production in $B\bar{B}$ events and Monte Carlo events were selected in the same way as the data: since the agreement with Monte Carlo is very good, the detection efficiency has been derived from Monte Carlo simulation. The SVT extends the capability of the charge particle reconstruction down to transverse momenta of ~ 50 MeV/c (see left plot in Fig. 5.2).

The resolution in the five track parameters is monitored using e^+e^- and $\mu^+\mu^-$ pair events: the resolution is derived from the difference of the measured parameters for the upper and lower halves of the cosmic ray tracks traversing the DCH and the SVT. On this sample with transverse momenta above 3 GeV/c, the resolution for single tracks is $23\,\mu m$ in d_0 and $29\,\mu m$ in z_0. To study the dependence of resolution from transverse momentum, a sample of multi-hadron events is used: the resolution is determined from the width of the distribution of the difference between the measured parameters (d_0 and z_0) and the

coordinates of the vertex reconstructed from the remaining tracks in the event: right plot in Fig. 5.2 shows the dependence of the resolution in d_0 and z_0 as a function of p_t. The measured resolutions are about $25\,\mu m$ in d_0 and $40\,\mu m$ in z_0 for p_t of 3 GeV/c: these values are in good agreement with the Monte Carlo studies and in reasonable agreement also with the results from cosmic rays.

Besides the criteria described above the tracks selected for this analysis are requested to satisfy additional requests:

- A cut on the distance of closest approach to the beam spot in the $x-y$ plane ($|d_{xy}| < 1.5\ cm$) and along the z axis ($|d_z| < 10\ cm$) is applied. This reduces fake tracks and background tracks not originating from the vicinity of the interaction point. This cut is not applied to the tracks coming from the K_S decay since the K_S decay vertex is distant from the interaction point.

- For tracks with $p_\perp > 0.2$ GeV/c at least one DCH hit is required. This cut is not used for low momentum tracks to retain slow pions (for instance the ones produced in the $D^* \to D^0\pi$ decays).

- tracks momentum must satisfy $p_{lab} < 10$ GeV/c (where p_{lab} is the laboratory momentum of the track) is applied. This removes tracks not compatible with the beam energies.

- Tracks are required to be within the polar angle acceptance of the detector: $0.410 < \theta_{lab} < 2.54$ rad. This ensures a well-understood tracking efficiency.

- Tracks with transverse momentum $p_\perp < 0.18$ GeV/c do not reach the EMC and therefore they will spiral inside the drift chamber ("loopers"). The tracking algorithms of *BABAR* will not combine the different fragments of these tracks into a single track. Therefore dedicated cuts have been developed to reject track fragments compatible with originating from a looper based on their distance from the beam spot. In order to identify looper candidates, the minimal difference in $p_\perp$, ϕ and θ to all other tracks in the event is determined. Tracks passing selection criteria (see Tab. 5.1), different for same-sign and opposite-sign track pairs, are flagged as loopers and only the track fragment with $|d_z|$ closest to the beam spot is retained.

  These criteria remove roughly 13% of all low-momentum tracks in the central part

of the detector. On average, they lower the mean charged multiplicity per B meson by less than 1%.

- If two tracks are very closely aligned to each other, one of the two is called "ghost". These cases arise when the tracking algorithms splits the DCH hits in two track fragments. If two tracks are very close in phase space (as defined in Tab. 5.1), only the track with the largest number of DCH hits is retained. This ensures that the fragment with the better momentum measurement is kept in the analysis.

Select tracks with	Selection criteria
distance in $x-y$ plane	$\|d_{xy}\| < 1.5\ cm$
distance in z axis	$\|d_z\| < 10\ cm$
minimum number of DCH hits	$N_{DCH} > 0$ if $p_\perp > 0.2$ GeV/c
maximum momentum	$p_{lab} < 10$ GeV/c
geometrical acceptance	$0.410 < \theta_{lab} < 2.54$ rad
Reject tracks if	$\Delta p_t = 100$ MeV/c to other tracks and
loopers ($p_\perp < 0.18$ GeV/c)	Same sign: $\|\Delta\phi\| < 220$ & $\|\Delta\theta\| < 215$ mrad
	Opposite sign: $\|\Delta\phi\| < 190$ & $\|\Delta\theta\| < 300$ mrad
ghosts ($p_\perp < 0.35$ GeV/c)	$\|\Delta\phi\| < 220$ & $\|\Delta\theta\| < 215$ mrad

Table 5.1: *Summary of track selection criteria.*

5.1.1 Particle Identification

In order to identify the charged particles, informations from SVT, DCH and DIRC informations are used. Below the Čerenkov threshold of the DIRC, the DCH dE/dx measurements dominate *BABAR*'s particle identification of tracks. The DCH algorithms extract the charge collected per single cell. For each track, a 80% truncated mean of ≈ 40 such measurements, corrected for gas pressure and temperature variations, cell geometry, signal saturation, non-linearity's at large dip angles, and cell entrance angle, provides a 7.5% precision on dE/dx. Fig. 5.3 displays the momentum dependence of this measurement in a sample consisting of particles with various masses.

The DIRC measurement of the Čerenkov cone angle θ_c is *BABAR* primary tool for identifying high momentum tracks. The reconstruction algorithm associates PMT signals with tracks, extracting a θ_c measurement when sufficient photons are available for a fit. Starting from the entrance angle of a track into a particular fused silica bar, the emission

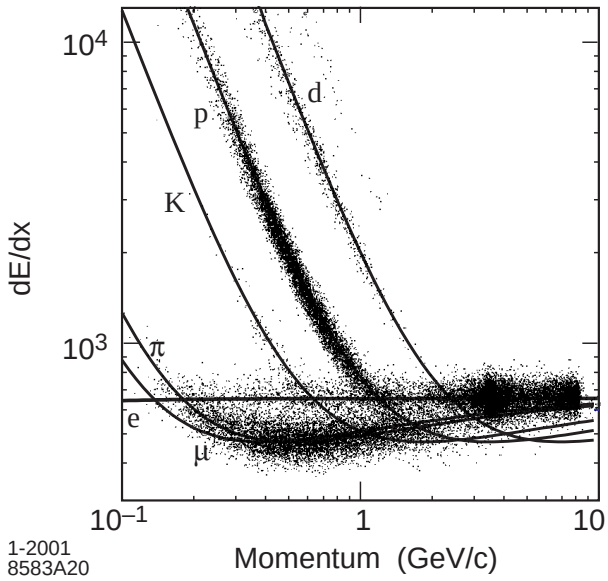

Figure 5.3: Measurement of dE/dx in the DCH as a function of the track momenta. The data include large samples of beam background triggers as evident from the high rate of protons. The curves show the Bethe-Bloch predictions derived from selected control samples of particles of different masses.

angle and arrival time of possible Čerenkov photons is reconstructed from the space-time coordinates of candidate PMT signals, providing a measurement of each photon θ_c and ϕ_c (the azimuth angle of the Čerenkov photon around the track direction) with a 16-fold ambiguity. Timing and geometrical considerations typically reduce the number of ambiguous solutions to 3 and the background by a factor of 40. Finally, a maximum likelihood fit to the photons associated to each track extracts its θ_c and number of signal (N_γ) and background photons. The resulting θ_c resolution scales as $1/\sqrt{N_\gamma}$, where N_γ is around 20 for short track path lengths in the radiator, typically at small polar angles, and 65 for the longer path lengths at the extreme polar angles. Sec. 8.1.2 discusses a technique to estimate the θ_c resolution, applied to $B^+ \to \phi h^+$ decays, where h^+ is π^+ or K^+. The average θ_c resolution is ≈ 3 mrad, which provides pion/kaon separation of $>2.2\sigma$ at 4 GeV/c. Fig. 5.4 plots the θ_c versus momentum profile and the measured standard deviations of separation between pions and kaons over the momentum range covered by tracks of B decays involved in this work.

Eventually, the informations associated to the expected value of the Čerenkov angle, given by the relation $\cos\theta_c = 1/\beta n$, where β is the Lorentz factor, $\beta = p/E$ and n is the refraction index for the material crossed by the particle (n=1.473 for the silica bars), the

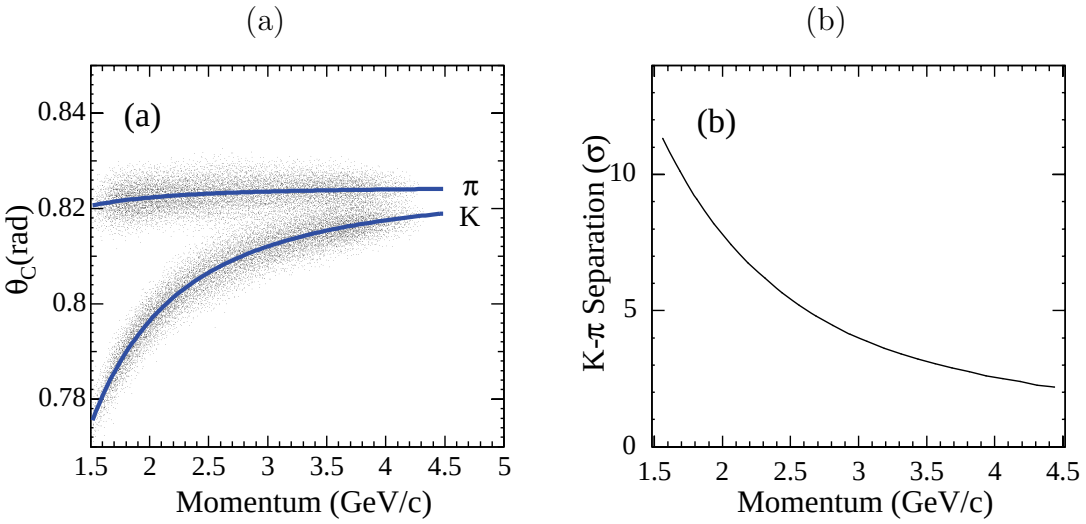

Figure 5.4: (a) The θ_c of kaons and pions versus the track momenta, and (b) the separation in standard deviations between pions and kaons as a function of momentum, from the control sample described in Sec. 8.1.2.

measured $\check{C}$erenkov angle, and the dE/dx informations from SVT and DCH are combined in a global likelihood. The ratio of the two considered hypotheses h_1 and h_2 is compared to a given threshold ($l_{h_1}/l_{h_2} > \tau_{h_2}$) in order to decide if the track is in agreement with the h_1 hypothesis more than h_2 one. One of these selectors, likelihood-based, provides five different selection criteria, based on the different likelihood threshold. The goodness of the selection criteria is fixed by the fraction of tracks identified as kaons, out of a pure sample, and the pion misidentification, i.e. the fraction of tracks identified as kaons, out of a pure pion sample.

The charged kaon efficiency is compared to the charged pion misidentification in Figures 5.5 and 5.6 as a function of momentum and polar angle, respectively. In the reconstruction of the invariant mass of the hadronic system, given the difference in the kaon momentum spectrum, a charged track is identified as kaon if $p_K > 300$ MeV/c.

A requirement based on these selectors is used for all tracks in this work, with the exception of the primary track in $B^+ \to \phi h^+$ decays, where h^+ mass hypothesis is estimated with a likelihood fit which combines the kinematics of the decay and a parameterization of θ_c information.

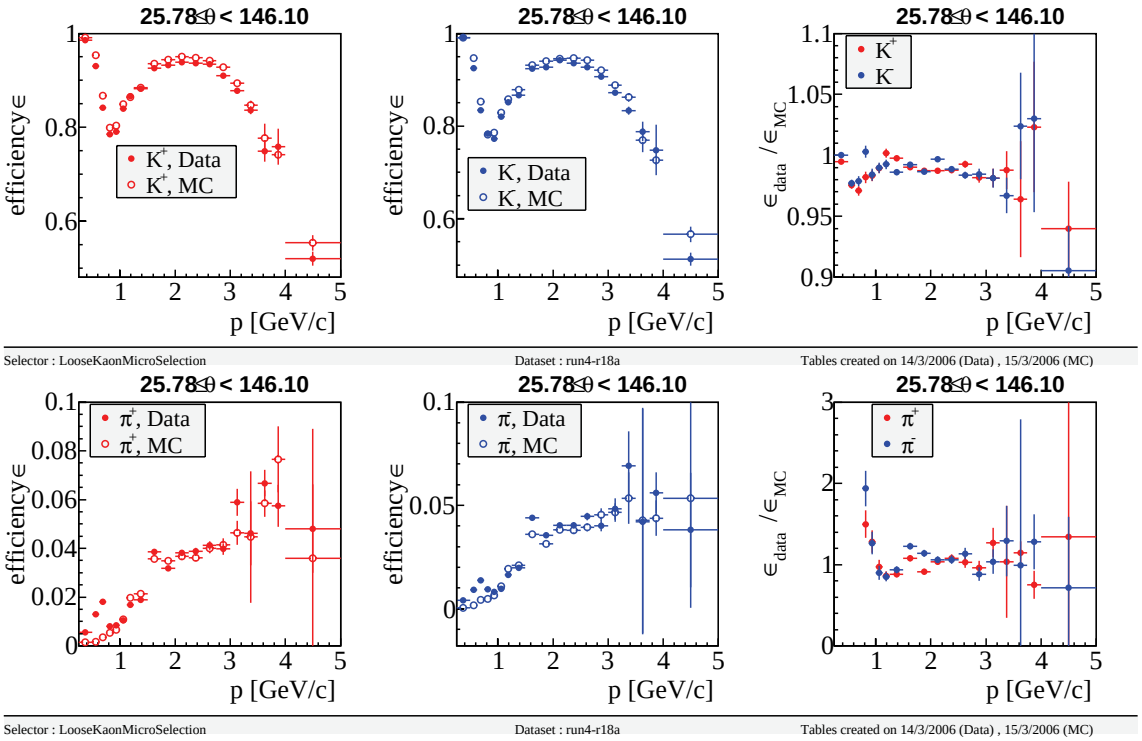

Figure 5.5: Charged kaon identification (top) and charged pion fake rate (bottom) for the loose kaon "likelihood" selector as a function of momentum. Left: efficiency for positive particles; middle: efficiency for negative particles; right: ratio of the efficiency between data and Monte Carlo for positive and negative particles.

5.2 K^0_S Reconstruction

In $B^0 \to K^+K^-K^0_S$ and $B^0 \to K^0_SK^0_SK^0_S$ decay analysis, we reconstruct K^0_S mesons in both $\pi^+\pi^-$ and $\pi^0\pi^0$ decay modes.

5.2.1 $K^0_S \to \pi^+\pi^-$ Reconstruction

In this case K^0_S mesons are reconstructed from a pair of opposite charged tracks, geometrically constrained to come from a common vertex. The vertex is identified using different techniques in the different analyses:

1. for $B^0 \to K^+K^-K^0_S$, we used the standard *BABAR* K^0_S vertexing, which is based on a geometric constraint on the two tracks: starting from the point of closest approach in the 3D space, the vertexing algorithm minimizes the χ^2, expressed in the position-momentum representation;

2. for $B^0 \to K^0_SK^0_SK^0_S$, because of the fact that no charged tracks originates di-

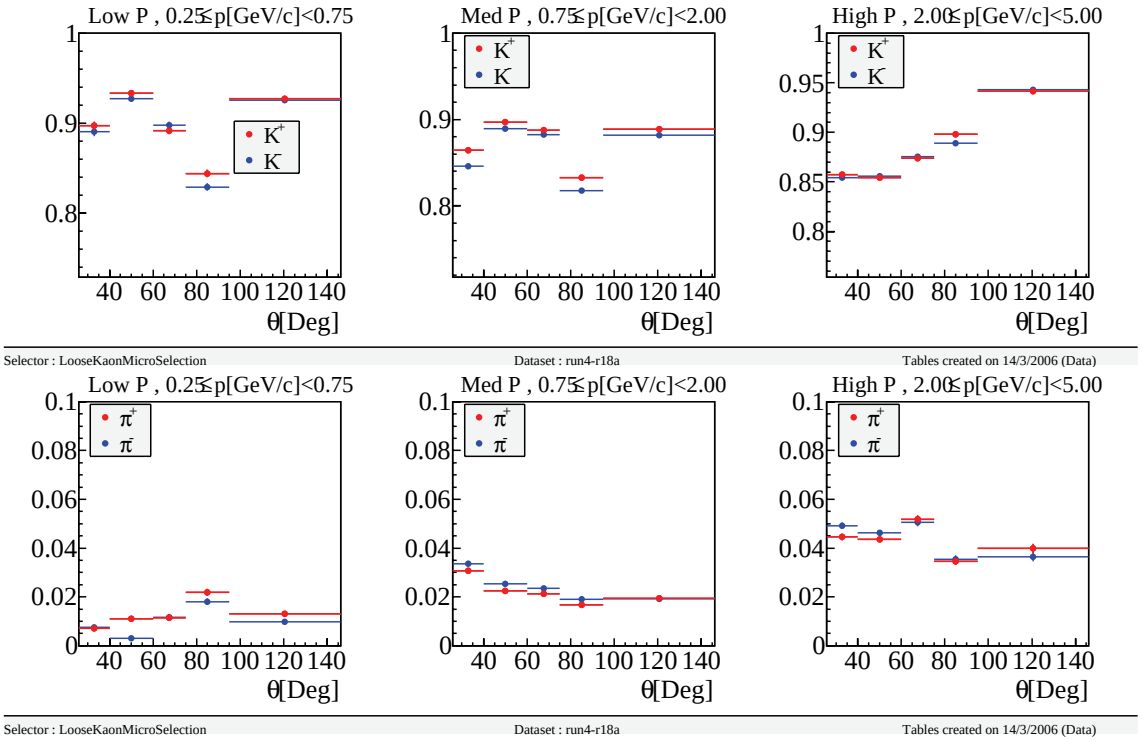

Figure 5.6: Charged kaon identification (top) and charged pion fake rate (bottom) for the loose kaon "likelihood" selector as a function of the polar angle in different bins of momentum. Left: $0.25 \leq p < 0.75$ GeV/c; middle: $0.75 \leq p < 2.00$ GeV/c; right: $2.00 \leq p < 5.00$ GeV/c.

rectly from th B meson, the B vertexing is achieved with the special algorithm `TreeFitter`, which fits simultaneously all the B decay tree (see Sec. 2.3) using a Kalman filter technique [33]. In this way we get the K^0_S vertex together with the primary vertex.

We only reject candidates for which the vertexing algorithm has failed. We start from a common standard selection of these candidates, and then eventually we refine the selection for the different analyses depending on the specific signal-to-background ratio. We require for $B^0 \to K^+K^-K^0_S(\pi^+\pi^-)$ and $B^0 \to K^0_SK^0_SK^0_S(\pi^+\pi^-)$ decays ($B^0 \to K^0_SK^0_SK^0_S(\pi^0\pi^0)$ decays):

1. $|m_{\pi^+\pi^-} - m^{\rm PDG}_{K^0_S}| < 12(11)\,{\rm MeV}/c^2$;

2. 2D decay distance: $0.2(0.15) < r_{\rm dec} < 40(60)\,{\rm cm}$;

3. $K^0_S \to \pi^+\pi^-$ pointing angle $\alpha < 200$ mrad;

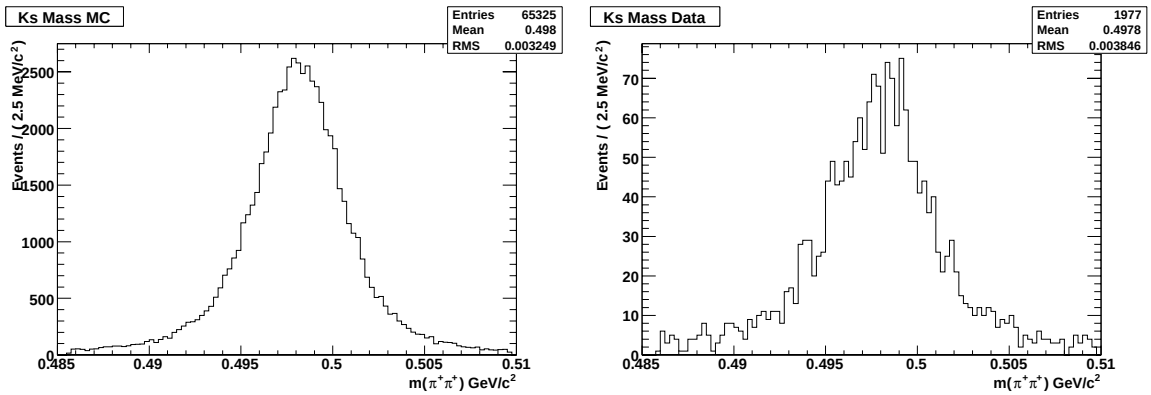

Figure 5.7: The $m_{\pi^+\pi^-}$ distributions of signal $B^0 \to K^0_S K^0_S K^0_S(\pi^+\pi^-)$ Monte Carlo (left), and events in the on-resonance data sample (right).

4. K^0_S vertex probability $P(\chi^2) > 10^{-6}$;

5. (K^0_S decay time significance, $\tau_{K^0_S}/\sigma(\tau_{K^0_S}) > 5$),

where $m_{\pi^+\pi^-}$ is the invariant mass of the two tracks in the pion mass hypothesis after the vertexing, and $m^{\rm PDG}_{K^0_S}$ is the nominal K^0_S mass [21]. $r_{\rm dec}$ is defined as the 2D decay distance from the beam-spot,

$$r_{\rm dec} = \sqrt{(x_{\rm vtx} - x_{\rm bs})^2 + (y_{\rm vtx} - y_{\rm bs})^2}. \tag{5.1}$$

The pointing angle α is the two-dimensional angle between the vector from the beam-spot to the decay vertex of the K^0_S and the momentum vector (in xy plane), $\cos\alpha = \hat{r}_{\rm dec} \cdot \hat{P}_{\rm xy}$ when $\hat{r}_{\rm dec}$ and $\hat{P}_{\rm xy}$ are unit vectors.

Figs. 5.7, 5.8, 5.9, and 5.10 show the K^0_S mass, momentum, decay length, and α distributions respectively for data and Monte Carlo for $B^0 \to K^0_S K^0_S K^0_S(\pi^+\pi^-)$. The plot of the K^0_S mass shows that the level of background is quite low and most K^0_Ss in the plot are likely to be real K^0_S.

Fig. 5.11 shows the decay time significance for $K^0_S \to \pi^+\pi^-$ candidates in signal Monte Carlo and background events for $B^0 \to K^0_S K^0_S K^0_S(\pi^0\pi^0)$ mode.

The selections are chosen with an optimization which maximizes the statistical significance of the signal, defined as:

$$N_\sigma = N_S/\sqrt{N_S + N_B} \tag{5.2}$$

where N_S and N_B are the expected numbers of signal and background events in the final dataset.

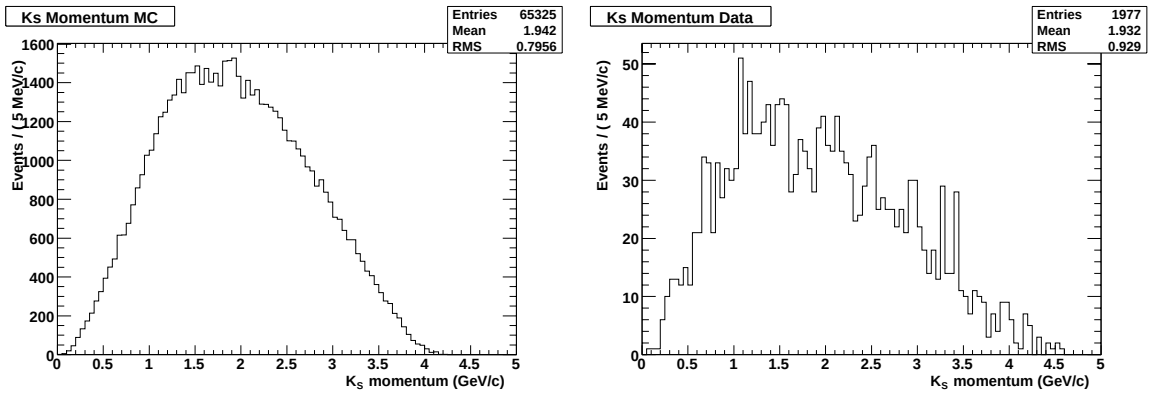

Figure 5.8: The K^0_S momentum distributions of signal $B^0 \to K^0_S K^0_S K^0_S(\pi^+\pi^-)$ Monte Carlo (left), and events in the on-resonance data sample (right).

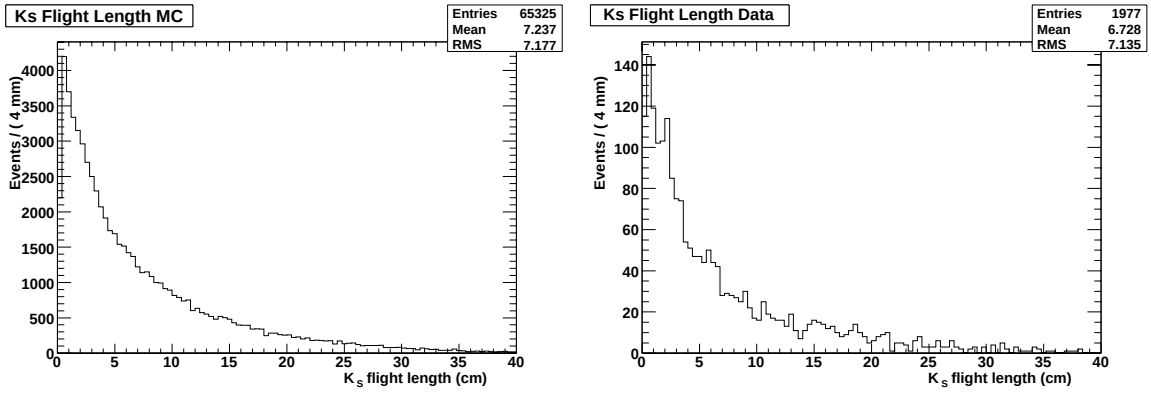

Figure 5.9: The K^0_S flight length distributions of signal $B^0 \to K^0_S K^0_S K^0_S(\pi^+\pi^-)$ Monte Carlo (left), and events in the on-resonance data sample (right). There's a cut at 2 mm.

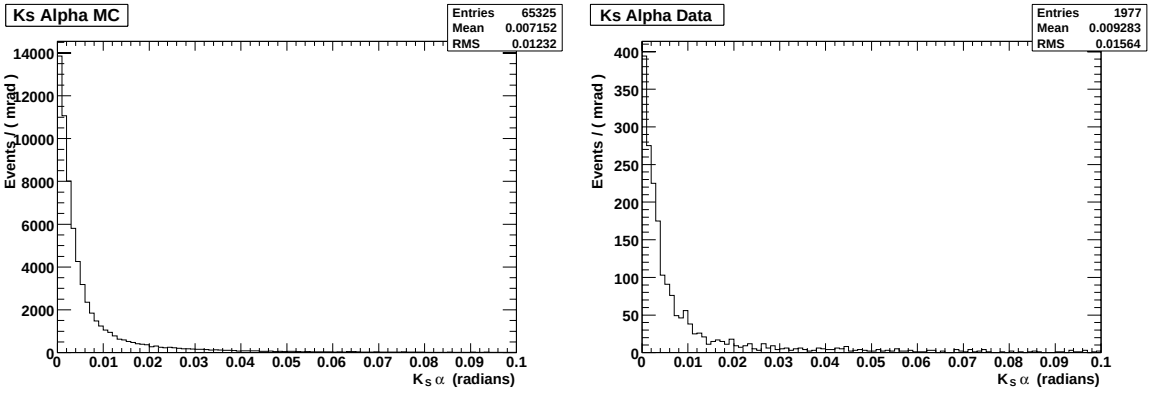

Figure 5.10: The K^0_S α distributions of signal $B^0 \to K^0_S K^0_S K^0_S(\pi^+\pi^-)$ Monte Carlo (left), and events in the on-resonance data sample (right).

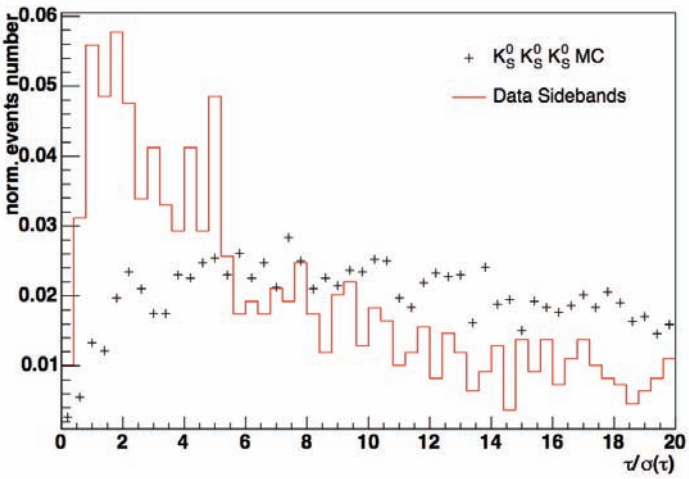

Figure 5.11: The K^0_S $\tau_{K^0_S}/\sigma(\tau_{K^0_S})$ distributions of signal $B^0 \to K^0_S K^0_S K^0_S(\pi^0\pi^0)$ Monte Carlo (crosses), and background events in the on-resonance data sample (solid histogram).

5.2.2 $K^0_s \to \pi^0\pi^0$ Reconstruction

In order to reconstruct $K^0_S \to \pi^0\pi^0$ decays we form $\pi^0 \to \gamma\gamma$ candidates from pairs of photon candidates in the EMC, which are not matched to any track of the event.

The electromagnetic shower produced by a charged or neutral particle in the EMC forms a cluster of energy deposits spread over many adjacent crystals. Meanwhile, photons from high momentum $\pi^0 \to \gamma\gamma$ decays often illuminate adjacent crystals, producing two energy maxima (known as bumps) within one cluster. The EMC reconstruction algorithm searches for seed crystals which register an energy deposit of $E > 10$ MeV, and then builds a cluster by adding crystals with $E > 1$ MeV which are either adjacent to another $E > 3$ MeV crystal in the cluster or the seed. Crystals with energy E satisfying $E'/E < 0.5(N-2.5)$, where E' is the highest energy of the neighboring N crystals with > 2 MeV, are identified as constituting a local maxima. Bumps are built from these crystals with an energy determined by an algorithm which iterates the fraction of energy contributed by each crystal in the cluster until the bump centroid is stable up to a tolerance of 1 mm. Another center-of-gravity algorithm locates the bump position using logarithmic crystal weights. A cluster association with a charged particle is made if the projection from the bump centroid to the inner face of the calorimeter is consistent with a track trajectory. Otherwise, the bump is considered as a neutral particle with a trajectory originating at the interaction point. Good clusters are defined as possessing energy $E > 30$ MeV/c, lab

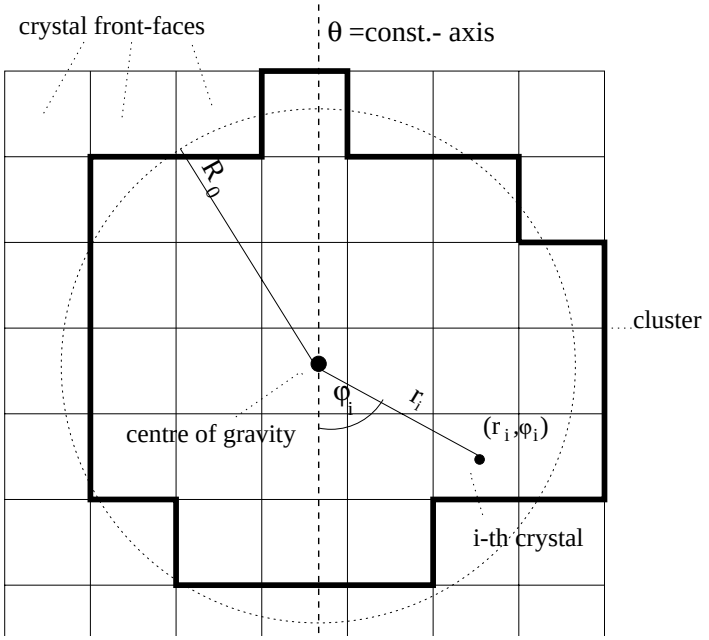

Figure 5.12: $\theta - \phi$ representation of a region of the calorimeter. All the variables entering the definition of EMC-related quantities are shown.

frame polar angle $0.41 < \theta_{LAB} < 2.409$ (i.e. within the fiducial volume of the EMC), and lateral shape parameter $LAT < 1.1$ [54]:

$$\frac{\sum_{i=2,n} E_i \cdot r_i^2}{\left(\sum_{i=2,n} E_i \cdot r_i^2\right) + 25(E_0 + E_1)} \tag{5.3}$$

with the crystals in descending energy (E_i) order, N the number of crystals composing the reconstructed cluster, and r_i and ϕ_i are the polar coordinates of the same crystal on the plane perpendicular to the line going from the B vertex to the center of the shower. r_0 is the typical average distance between two crystals (5 cm in *BABAR* EMC). The variables entering LAT definition are illustrated by Fig. 5.12. This variable is used to distinguish energy clusters coming from electrons and photons from those generated by hadrons. Using the fact that hadronic showers typically have a more irregular shape with respect to those generated by electromagnetic interactions, this variable is defined to maximize the separation between the distributions of these two classes of clusters. Since the two most energetic clusters of an electromagnetic shower bring in average a large fraction of the total energy, LAT values for photons and electrons are typically smaller than for

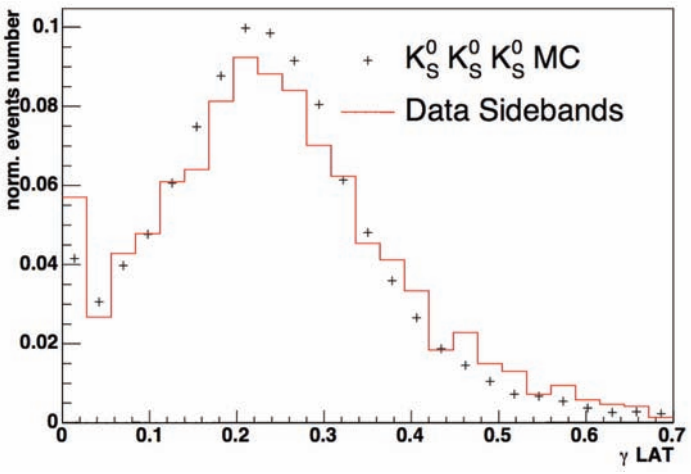

Figure 5.13: Distributions of LAT variable for photons coming from $B^0 \to K^0_S K^0_S K^0_S(\pi^0\pi^0)$ signal Monte Carlo events (crosses) and background events in on-resonance data (solid histogram). The two distributions are normalized to the same area.

hadrons and a loose upper cut removes a large fraction of the hadronic contamination. We found this variable useful also to discriminate true π^0's from random combinations of two photons, since LAT depends on photon energy and γ's coming from signal and background have different spectrum. This is shown in Fig. 5.13.

The photon energy resolution is measured from a radioactive source (at the low end), e^+e^- Bhabha scattering events (at the high end), and decays of χ_{c1}, π^0, η, and other particles (in between). A fit over this data provides the energy dependence of the resolution [55]:

$$\frac{\sigma_E}{E} = \frac{(2.32 \pm 0.30)\%}{\sqrt[4]{E(\,\mathrm{GeV})}} + (1.85 \pm 0.12)\%. \tag{5.4}$$

Similarly, studies of π^0 and η decays to two photons of approximately equal energy provide an empirical parameterization of energy dependence of the angular resolution [55]:

$$\sigma_\theta = \sigma_\phi = \frac{3.87 \pm 0.07}{\sqrt{E(\,\mathrm{GeV})}} + (0.00 \pm 0.04)\mathrm{mrad}. \tag{5.5}$$

Typical π^0 mass resolution in hadronic events is 6.9 MeV/c^2 (Fig. 5.14a). Fig. 5.14b displays the measured over expected energy ratio for radiative Bhabha events.

In order to reject spurious π^0 candidates, we require $(100 < m_{\gamma\gamma} < 141)$ MeV/c^2 for $B^0 \to K^0_S K^0_S K^0_S$ analysis and $(100 < m_{\gamma\gamma} < 0.155)$ MeV/c^2 for $B^0 \to K^+K^-K^0_S(\pi^0\pi^0)$.

Finally we form K^0_S candidates from selected π^0's pairs, requiring they have an invariant mass $(477.6 < m_{\pi^0\pi^0} < 527.6)$ MeV/c^2 for $B^0 \to K^+K^-K^0_S(\pi^0\pi^0)$ decays and an

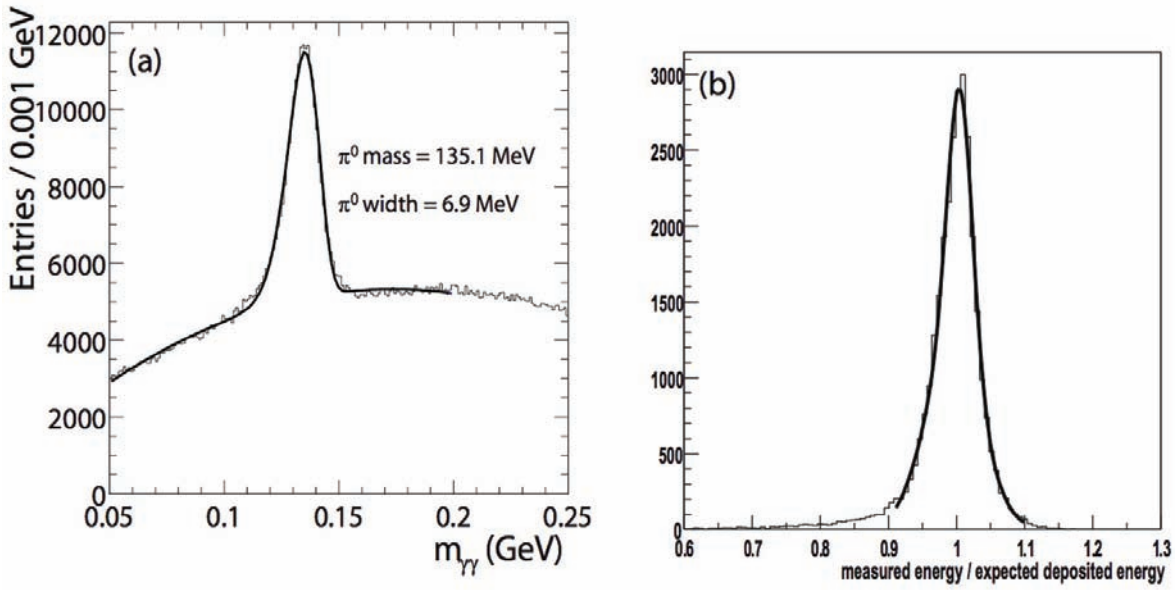

Figure 5.14: (a) The π^0 mass distribution reconstructed from two photon candidates in hadronic events overlaid with a fit to the data. (b) The ratio of measured to expected energy for electrons in radiative Bhabha events overlaid with a Gaussian fit. The expected value is calculated from the production angle. The resolution is 1.9%.

invariant mass $(480 < m_{\pi^0\pi^0} < 520)$ MeV/c^2 for $B^0 \to K_S^0 K_S^0 K_S^0(\pi^0\pi^0)$ decays. We show in Fig. 5.15a the distribution of K_S^0 invariant mass for signal and background events of $B^0 \to K^+K^-K_S^0(\pi^0\pi^0)$, compared with the $K_S^0 \to \pi^+\pi^-$ invariant mass. In Fig. 5.15b the distribution for $\pi^0\pi^0$ invariant mass is shown for signal and background events of $B^0 \to K_S^0 K_S^0 K_S^0(\pi^0\pi^0)$ decays.

5.3 K_L^0 Reconstruction

Due to their long lifetime, K_L^0 mesons decay outside the *BABAR* tracking volume, and they can be reconstructed only via their inelastic nuclear interactions in the crystals of the EMC or in the iron-absorber layers of the IFR [52, 55]. Since *BABAR* has not a hadronic calorimeter, the momentum of the K_L^0 candidate is not measured and only the flight direction can be reconstructed.

In the analyses, a mass constraint of the K_L^0 mother candidate has to be applied to calculate the K_L^0 momentum.

The K_L^0 reconstruction starts by selecting *neutral* clusters, from the available 3D IFR clusters in each event, by checking that no reconstructed track extrapolates (using a

(a) (b)

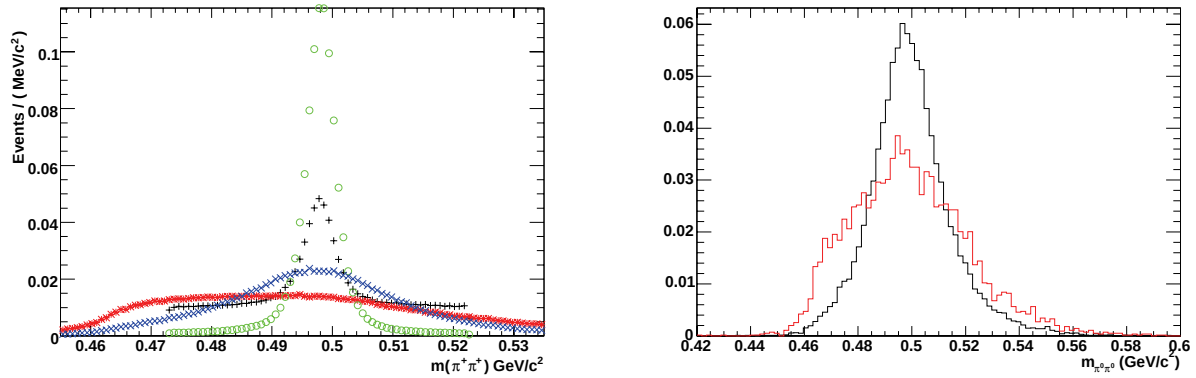

Figure 5.15: (a) Distributions of K^0_S invariant masses in $B^0 \to K^+K^-K^0_S$ events for (green) $K^0_S \to \pi^+\pi^-$ signal Monte Carlo and (black) background candidates; (blue) $K^0_S \to \pi^0\pi^0$ signal Monte Carlo and (red) background candidates. (b) Distributions of $K^0_S \to \pi^0\pi^0$ invariant masses in $B^0 \to K^0_S K^0_S K^0_S(\pi^0\pi^0)$ events for (black) signal Monte Carlo events and (red) background events.

swimmer algorithm) to the IFR cluster position. An algorithm attempts to combine such neutral clusters, as being associated to the same hadronic shower on the basis of a vicinity criterion. The final object output by this process is a neutral cluster aggregate which combines both IFR and Inner RPC response to the particle. Such an object can have components found in different geometric sectors of the IFR and can provide a first estimate of the neutral hadron flight direction.

An association is formed between the above IFR aggregate and calorimeter clusters, assuming that the position of the EMC cluster provides the position of the first interaction, that the shower develops into a cone of tuned opening angle, and taking into account the covariance matrix of the IFR aggregate. Each created association has a significance level based on the χ^2 of the match, which can be used to select different match qualities. The IFR-EMC association is used to create an object representing the neutral hadron. This object provides the implementation of different algorithms for the computation of the flight direction and is available for the physics analysis.

A good resolution for the K^0_L flight direction helps provide a clean reconstruction of the signal channel $B^0 \to K^+K^-K^0_L$. We will discuss in Sec. 5.3.1 the basics of the K^0_L reconstruction in the IFR and in Sec. 5.3.2 the reconstruction in the EMC.

5.3.1 K_L^0 Reconstruction in the IFR

The preliminary selection of K_L^0 candidates in the IFR makes use of the following cuts:

1. At least 2 planar layers;

2. the cluster center-of-gravity must have $-0.75 < \cos\theta < 0.93$. This cut is aimed to reject beam background in the very forward regions;

3. rejection of clusters starting in layer 14 and beyond. Also this cut reduces beam background contributions;

4. The relative position between the cluster centroid and the EMC position of any track with momentum greater than 0.75 GeV/c must satisfy $|\theta_{K_L} - \theta_{trk}| > 350$ mrad, as well as to be out of the interval -750 $< \phi_{K_L} - \phi_{trk} <$ 350 mrad for positively charged tracks, and -300 $< \phi_{K_L} - \phi_{trk} <$ 750 mrad for negatively charged tracks.

5.3.2 K_L^0 Reconstruction in the EMC

The preliminary selection of K_L^0 candidates in the EMC makes use of the following cuts:

1. The centroid of the cluster must have $\cos\theta < 0.935$. This requirement is aimed to reject residual non-matched charged hadrons. In fact, the tracking efficiency is very high, but at some point fails in the very forward region. This is illustrated in Fig. 5.16, where the distribution of *bad* neutral clusters is shown for photons from $\pi^0 \to \gamma\gamma$ decays.

2. The cluster energy range is 200 MeV $< E <$ 2 GeV.

3. Probability of the cluster to match any track $< 1\%$.

4. The K_L candidate can not form a $\gamma\gamma$ invariant mass between 100 to 150 MeV/c^2 with any neutral candidate in the event having at least 30 MeV. This requirement is not applied if Zernike moment $Z_{20} < 0.8$ (see Eq. 5.6).

5. Reject two-bumps clusters with a cluster energy larger than 1 GeV that are consistent with a merged π^0 (m(2 bump) $>$ 110 MeV).

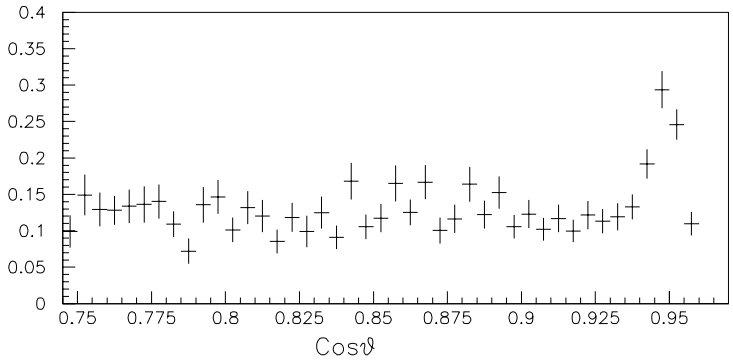

Figure 5.16: Fraction of *bad* clusters as a function of cosθ in the very forward region in a sample of neutral clusters from photons coming from $\pi^0 \to \gamma\gamma$ events. *Bad* clusters are defined as the ones which does not belong to the π^0 peak in Fig. 5.14a.

where the Zernike moments are an expansion of the shape of the shower in terms of Zernike polynomials [56]:

$$Z_{nm} = \sum_{r_i<R_0}^{n} \frac{E_i}{E} \cdot f_{nm}\left(\frac{r_i}{R_0}\right) \cdot e^{-im\phi_i} \tag{5.6}$$

where r_i and E_i have the same meaning of Eq. 5.3, R_0 is the Molière radius (~ 3.8 cm for the *BABAR* EMC crystals) and f_{nm} is the Zernike polynomial of order n, m. The spacial energy distribution of a cluster can be developed as a series of Zernike polynomials (which form a complete basis):

$$E(xE, y) \to \sum_{n,m} Z_{n,m} \cdot \zeta_{n,m}(r, \phi) \tag{5.7}$$

Moments with indices $m > 0$ are ϕ-dependent.

5.3.3 K^0_L Calibration with $e^+e^- \to \phi(K^0_S K^0_L)\gamma$ Decays

The K^0_L detection efficiency can be evaluated using the detailed Monte Carlo simulation; the lack of available experimental data makes the hadron shower simulation not entirely reliable at low momenta, and the results depend somewhat on the hadronic shower generator used. Hence, it is important to find a calibration channel so that identification and detection efficiency can be tested directly with data.

The ideal calibration channel would have a branching ratio much larger than $\sim 1 \times 10^{-5}$, which is the branching ratio of the decay channel $B^0 \to K^+K^-K^0_L$, and should

be as pure as possible, to enable the identification of K_L^0 on an event-by-event basis. Unfortunately there is no single B decay mode with a K_L^0 in the final state, with a branching ratio much larger than the reference channel which can be kinematically selected. The number of K_L^0 from this calibration channel is ≈ 3000 times more than the golden channel $B^0 \to J/\psi\, K_L^0$.

A copious source of K_L^0's, however, is the decay $\phi \to K_S^0 K_L^0$, which is produced abundantly, both in the continuum and in $\Upsilon(4S)$ events with an emission of an hard ISR photon. The inclusive ϕ production rate is very high, $\sim$8% per event, and roughly the same for $\Upsilon(4S)$ events as for continuum events. The continuum cross section is $\sim$3.5 times the peak cross section of $\Upsilon(4S) \to B\overline{B}$, so that the number of K_L^0 from this calibration channel is $\sim$5000 times more than the our signal channel.

The expected distribution of the opening angle between the two kaons in the laboratory frame, has a peak at small angles, due to the average ϕ velocity and to the very small K_L^0 momentum in ϕ centre of mass frame. The inclusive angular distribution between any K_S^0 and any K_L^0 from hadronic e^+e^- interactions (both $\Upsilon(4S)$ and continuum events), is shown in Fig. 5.17a.

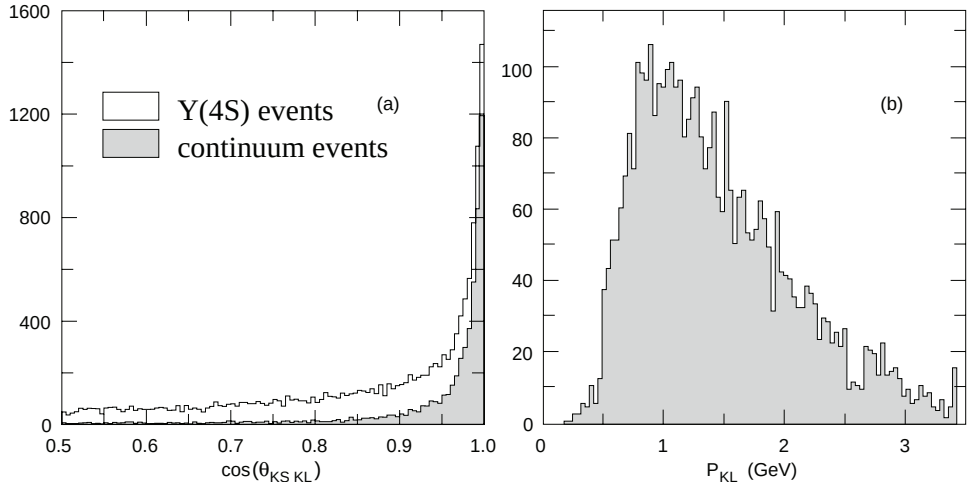

Figure 5.17: (a). Opening angle between K_S^0 and K_L^0 for $\Upsilon(4S)$ events (grey histogram) and continuum events (white histogram); (b). Momentum spectrum of K_L^0 from ϕ decays.

In any such event where a K_S^0 is selected, there is a good probability to find a K_L^0 within a cone of $\sim 10^\circ$, enabling K_L^0 to be selected and their direction to be estimated using observed K_S^0. The corresponding K_L^0 momentum spectrum is shown in Fig. 5.17b. It can be seen that it covers most of the critical range where the detection efficiency needs

to be tested. The K^0_Ls from $B^0 \to K^+K^-K^0_L$ decay typically have momenta of 1–3 GeV/c. In the higher momentum range, the detection efficiency is expected to flatten out anyway.

Further selection criteria can be found to enhance the signal from ϕ decays with respect to the background. From the study of K^0_L from ϕ decay, it is also possible to determine the K^0_L momentum (or the missing momentum of the event) $P_{K^0_L} \equiv p_{miss}$, with reasonable resolution, from the measurement of the momentum $P_{K^0_S}$ of the K^0_S and the opening angle α, with the relationship:

$$M^2_\phi = 2m^2_{K^0} + 2[E_{K^0_L}E_{K^0_S} - P_{K^0_L}P_{K^0_S}\cos\alpha]. \tag{5.8}$$

This equation has two solutions for $P_{K^0_L}$, and thus introduces a two-fold ambiguity. The ambiguous cases can be reduced strongly as follows. First of all, only those events are selected where the solution corresponding to the lower momentum gives a value too small for detection, ($P_L \leq 500$ MeV). Furthermore the correct solution is fairly flat in the ϕ center-of-mass reference frame (the ϕ being mostly unpolarized and the detection efficiency affecting mostly very forward angles). On the contrary the wrong solution is strongly backward-peaked. In cases where only one of the two solutions is in the backward hemisphere, the solution in the forward hemisphere is likely to be correct. This criterion also drastically reduces the combinatorial background, since for these events, both solutions are likely to correspond to backward emission. An additional cut on $P_{K^0_S}$ may halve this background without affecting very much the events from ϕ decay.

We reconstruct a $K^0_S \to \pi^+\pi^-$ with the standard selection described in Sec. 5.2.1. Instead of using the $p_{K^0_L} \equiv p_{miss}$ evaluated in 5.8 we use the missing mass of the event Δm:

$$\Delta m^2 = |p_{K^0_L}|^2 \tag{5.9}$$

In order to further clean the sample we require a very hard ISR photon and apply a loose cut on the reconstructed missing mass. We also apply an "isolation cut" on the missing momentum requiring that in the EMC the signal K^0_L does not overlap with the shower produced by pions coming from the signal K^0_S decay (see Fig. 5.18):

1. $4.0 <$ the energy of highest energy photon < 10.0 GeV (CM frame)
2. $\Delta m > 0.4$ GeV/c^2
3. angle$(p_{miss}, \pi^{+/-}) > 100$ *mrad* in the EMC

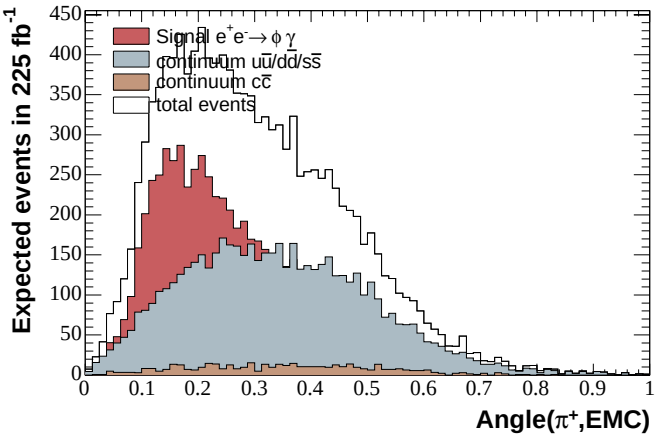

Figure 5.18: Opening angle between missing momentum and π^+ coming from signal K_S^0 decay before the "isolation cut". The distribution for π^- is similar. Signal $e^+e^- \to \phi(K_S^0 K_L^0)\gamma$ events (red), continuum $u\bar{u}/d\bar{d}/s\bar{s}$ (grey), continuum $c\bar{c}$ (brown) and the sum of all these components (white histogram) are normalized to 225 fb^{-1}.

When multiple candidates are present, we look for the minimum χ^2 of the K_S^0 mass to select the best candidate. In Fig. 5.19 the distribution of the missing mass for the different contributions is shown, normalized to 225 fb^{-1}, which is approximately the luminosity of the data used for this analysis (Runs I-IV). This plot shows that the main background comes from light quark continuum production, while the contribution due to $c\bar{c}$ is negligible.

We extract the signal performing a fit to the Δm distribution. We parameterize the signal probability density function (PDF) with a so-called Crystal Ball function [57]:

$$f_{Crystal\ Ball}(x, x_0, \sigma, \alpha, n) = \frac{1}{N} \cdot \begin{cases} e^{-\frac{(x-x_0)^2}{2\sigma^2}}, & x < x_0 + \alpha\sigma \\ \frac{(n/\alpha)^n e^{-\alpha^2/2}}{((x-x_0)/\sigma + n\alpha - \alpha)^n}, & x \geq x_0 + \alpha\sigma \end{cases} \tag{5.10}$$

where x_0 and σ represent the mean and the resolution of the core Gaussian, α is the value of x at which the distribution becomes not Gaussian and n is the exponential of the non-Gaussian tail. The signal Monte Carlo events with the PDF are shown in Fig. 5.20. The continuum background distribution is parameterized with a phase space function, introduced by the ARGUS collaboration [74]:

$$f_{ARGUS}(x) = x\sqrt{1-x^2}\exp\left[-\xi(1-x^2)\right] \tag{5.11}$$

where ξ is a floating parameter describing the slope of the distribution.

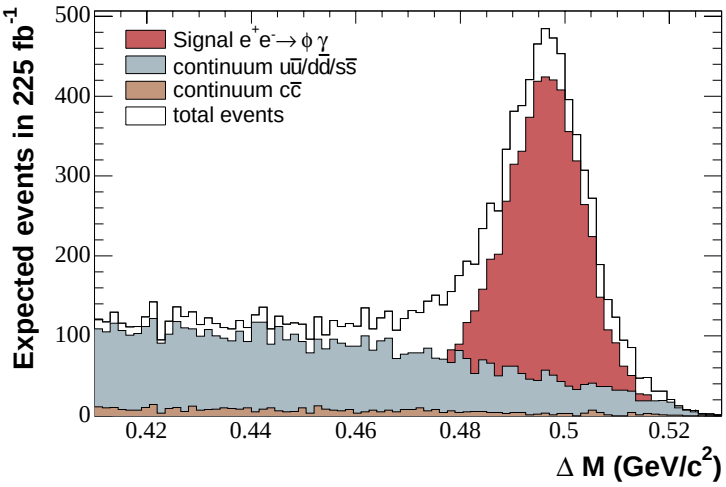

Figure 5.19: Missing mass (Δm) distribution for signal $e^+e^- \to \phi(K_S^0 K_L^0)\gamma$ events (red), continuum $u\bar{u}/d\bar{d}/s\bar{s}$ (grey), continuum $c\bar{c}$ (brown) and the sum of all these components (white histogram) are normalized to 225 fb^{-1}.

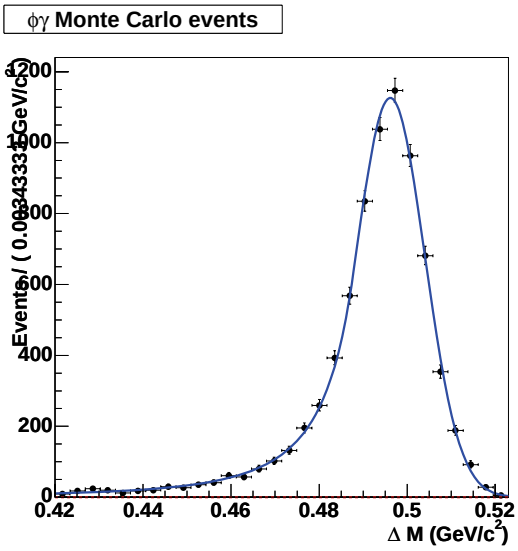

Figure 5.20: Missing mass (Δm) distribution for signal $e^+e^- \to \phi(K_S^0 K_L^0)\gamma$ events, with the signal PDF superimposed. The parameterization is obtained from a maximum likelihood fit to signal Monte Carlo sample with a Crystal Ball function.

We perform the maximum likelihood fit to an on-resonance sample equivalent to 230 fb^{-1}. Since the signal statistics and the signal-to-background ratio are good enough, we fit the mean and the resolution of the signal peak, together with the background slope ξ. The result is shown in Table 5.2. The number of signal events is found to be 11712 $\pm$ 176. The mean of Δm distribution is consistent with the nominal K^0 mass [21]. The

Parameter	value
N_{sig}	11712 $\pm$ 176
N_{bkg}	27840 $\pm$ 226
x_0	(496.7 $\pm$ 0.1) MeV/c^2
σ	(6.9 $\pm$ 0.1) MeV/c^2
ARGUS ξ	-0.10 $\pm$ 0.02

Table 5.2: Fitted yields in a luminosity of 230 fb^{-1} of on-resonance data sample for $e^+e^- \to \phi(K_S^0K_L^0)\gamma$ events, together with the main signal and background parameters.

Δm distribution on the on-resonance dataset, together with the fit result, is shown in Fig. 5.21.

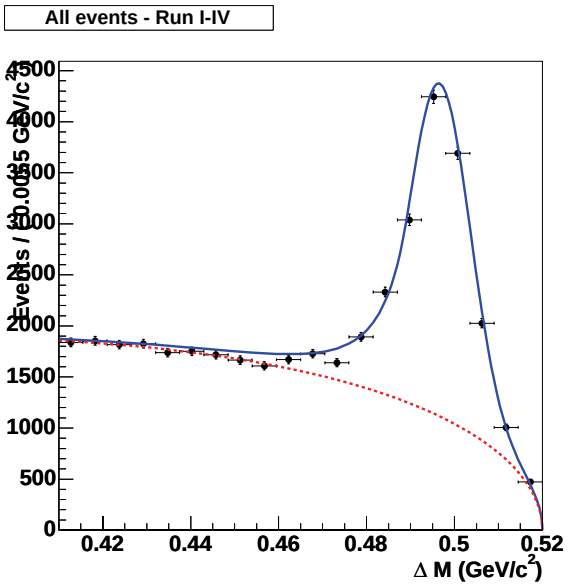

Figure 5.21: Missing mass (Δm) distribution for $e^+e^- \to \phi(K_S^0K_L^0)\gamma$ events in the final RunI-IV dataset, with the fit PDF superimposed. Continuum line: total PDF, dashed line: continuum background only PDF.

The events extracted by this fit represent the normalization sample for our study.

Reconstruction of K_L^0 Clusters

The distribution of this opening angle for EMC (IFR) clusters in the different components is shown in Fig. 5.22 (5.23). We look for EMC and IFR candidates inside a cone of 200 mrad from the missing momentum direction.

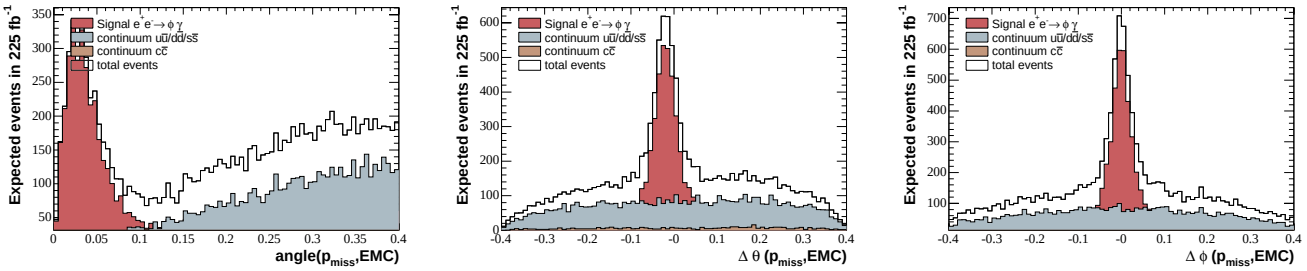

Figure 5.22: Left: distribution of the opening angle between missing momentum direction and EMC cluster one. Middle: difference in the polar angle; right: difference in azimuthal angle. Signal $e^+e^- \to \phi(K_S^0 K_L^0)\gamma$ events (red), continuum $u\bar{u}/d\bar{d}/s\bar{s}$ (grey), continuum $c\bar{c}$ (brown) and the sum of all these components (white histogram) are normalized to 225 fb^{-1}.

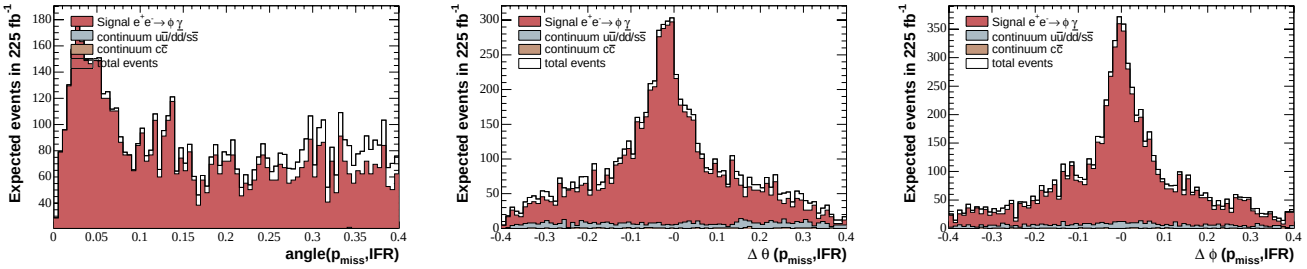

Figure 5.23: Left: distribution of the opening angle between missing momentum direction and IFR cluster one. Middle: difference in the polar angle; right: difference in azimuthal angle. Signal $e^+e^- \to \phi(K_S^0 K_L^0)\gamma$ events (red), continuum $u\bar{u}/d\bar{d}/s\bar{s}$ (grey), continuum $c\bar{c}$ (brown) and the sum of all these components (white histogram) are normalized to 225 fb^{-1}.

Since our main goal is to study K_L^0 signals in the EMC and IFR, we accept only events which have an EMC or IFR cluster inside 200 *mrad* from the missing momentum. In Fig. 5.24 we show the Δm distributions with a reconstructed K_L^0. Since the signal-to-background ratio (and also the nature of the background) is different in the EMC and in the IFR, we divide the sample in one made by events with at least one EMC cluster (and which can have also some IFR interaction) and events without EMC clusters ("IFR-only"

events), consistently with what is done in $B^0 \to K^+K^-K_L^0$ analysis. In Table 5.3 we report the yields for events with reconstructed K_L^0.

Parameter	EMC	IFR-only
N_{sig}	5175 ± 201	1225 ± 76
N_{bkg}	11686 ± 210	1134 ± 76

Table 5.3: Fitted yields in a luminosity of 230 fb^{-1} of on-resonance data sample for $e^+e^- \to \phi(K_S^0K_L^0)\gamma$ events, with a K_L^0 cluster reconstructed in the EMC or IFR in a cone of 200 mrad around the missing momentum.

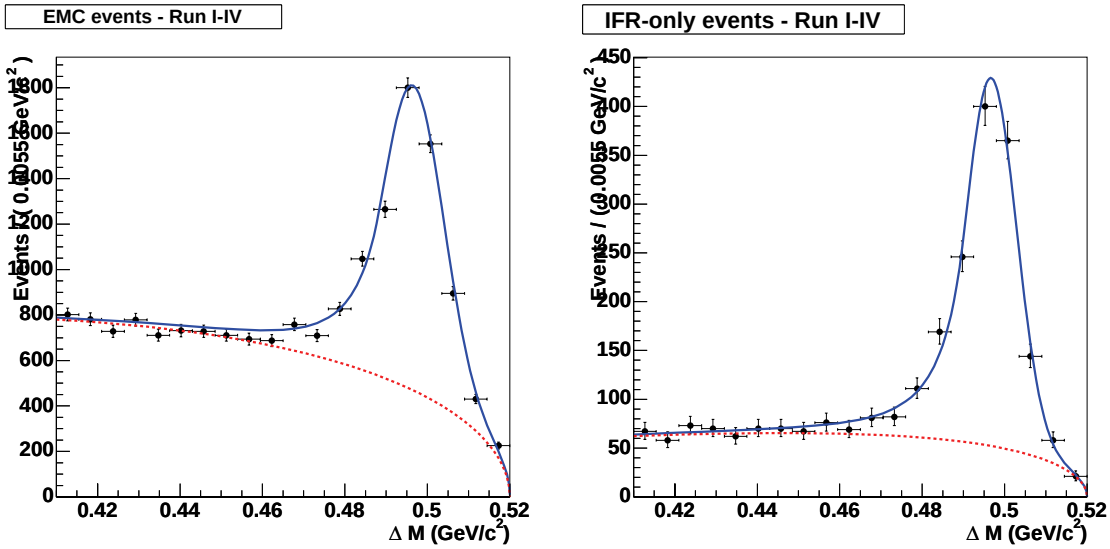

Figure 5.24: Missing mass spectrum for the full RunI-IV $\phi\gamma$ dataset with the fit PDF superimposed. Continuum line: total PDF, dashed line: continuum background only PDF. Left plot: events with at least one reconstructed EMC cluster. Right plot: events with at least one IFR reconstructed cluster without any EMC cluster ("IFR-only" events).

Studies on Monte Carlo samples show that the hadronic cascade development depend somewhat on the hadronic shower simulation used. Unfortunately, existing simulations do not all describe consistently the interactions of K_L^0, above all at low momenta. All the hadronic interaction models accessible through `GEANT` should, however, agree on the general characteristics of the response to penetrating hadrons, namely that:

1. there is a high multiplicity of hadronic shower topologies, distributed over a wide part of the IFR detector;

2. shower longitudinal development depends on momentum and particle direction;

3. shower transverse development depends on the particular pattern of showering physics processes;

4. there is a significant fraction of early hadronic showers in the inner calorimeter.

The dependence on the simulation model of a hadronic shower inside the detector make necessary a reliable study on a K_L^0 control sample. The sample of $e^+e^- \to \phi(K_S^0 K_L^0)\gamma$ events have enough statistics and good purity to test the shower development inside the detector. Since the main background in the analysis of $B^0 \to K^+K^-K_L^0$ decays, which we will present in this work in Chapter 6, comes from badly identified K_L^0's in the EMC, while the IFR-only sample has a better purity, we will study the data-Monte Carlo agreement of the variables which describe the response of the EMC to the passage of neutral hadrons. Finally, we will develop an algorithm for the particle identification of the K_L^0's in the calorimeter and we will validate it on this control sample.

K_L^0 Shower Development in the EMC

In order to study the development of the EMC response at passage of K_L^0's, we exploit a set of topological variables which characterize the shower shape. The most important are the lateral moment (LAT), defined by Eq. 5.3, which describes the spread of the shower in the transverse plane with respect the K_L^0 flight direction. We also use the Zernike moments Z_{nm}, defined in Eq. 5.6. In particular, we will study the two moments Z_{20} and Z_{42}:

- $Z_{20} = 2r^2 - 1$
- $Z_{42} = (4r^4 - 3r^2)\sin 2\phi$

while Z_{20} is correlated with the cluster width, Z_{42} gives additional discrimination power, since it is also sensitive to cluster asymmetries.

The set of other variables we use is defined by:

- **Number of crystals**
- **Second moment:**

$$\frac{\sum E_i \cdot r_i^2}{E_i} \tag{5.12}$$

where E_i is the energy of crystal i and r_i is the distance of crystal i to the cluster center.

- **E1/E9:** The energy of the most energetic crystal (E1) divided by the energy sum of the 3×3 crystal block (E9) with the most energetic crystal in its center.

- **E9/E25:** The energy sum of the 3×3 crystal block (E9) with the most energetic crystal in its center, divided by the energy sum of the 5×5 crystal block (E25) with the most energetic crystal in its center.

To extract the signal shape from data we use the ${}_s\mathcal{P}lots$ weighting technique [80]. The ${}_sWeight$ for each event is calculated using the likelihood function (which is made by the only Δm). The resulting distribution is like a background-subtracted plot, which takes into account the likelihood covariance matrix.

In order to disentangle the dependency of the shape variables from the momentum of the K^0_L we compare the distributions in bins of the EMC calibrated energy E_{cal}. We divide the kinematic phase space in bins of E_{cal} instead of its momentum $p_{K^0_L}$ because this is a measured quantity for K^0_L, while the momentum is evaluated from a kinematic constraint. In the same plots we compare signal $e^+e^- \to \phi(K^0_S K^0_L)\gamma$ Monte Carlo, signal $e^+e^- \to \phi(K^0_S K^0_L)\gamma$ ${}_s\mathcal{P}lots$ and a sample of almost pure $K^\pm$ data. From Fig. 5.25 to Fig. 5.31 we show the comparison for the shape variables.

From this study it is evident that the shape of the hadronic shower in the calorimeter depends highly by the K^0_L kinematics (above all by its momentum, less by its direction). Also, it is evident that we cannot use the $K^\pm$ as a K^0_L control sample because of different energy loss mechanism in the calorimeter: above all the presence of energy loss by ionization at low energies contributes for a higher e.m. component than for neutral kaons (this can be seen in all the shape variables for the first two energy bins).

In figures from 5.32 to 5.38 the same variables divided in the same energy bins are shown for signal and background ${}_s\mathcal{P}lots$ in $e^+e^- \to \phi(K^0_S K^0_L)\gamma$ data.

This study shows that the separation power grows with the energy. In the first two bins there is no separation at all. In fact, the candidates with $E_{cal} < 0.2$ GeV are not included in the $B^0 \to K^+K^-K^0_L$ at all.

The overall conclusion of this study is that the Monte Carlo simulation with its most recent implementation of the hadronic shower (*Bertini cascade* [58]) captures the global

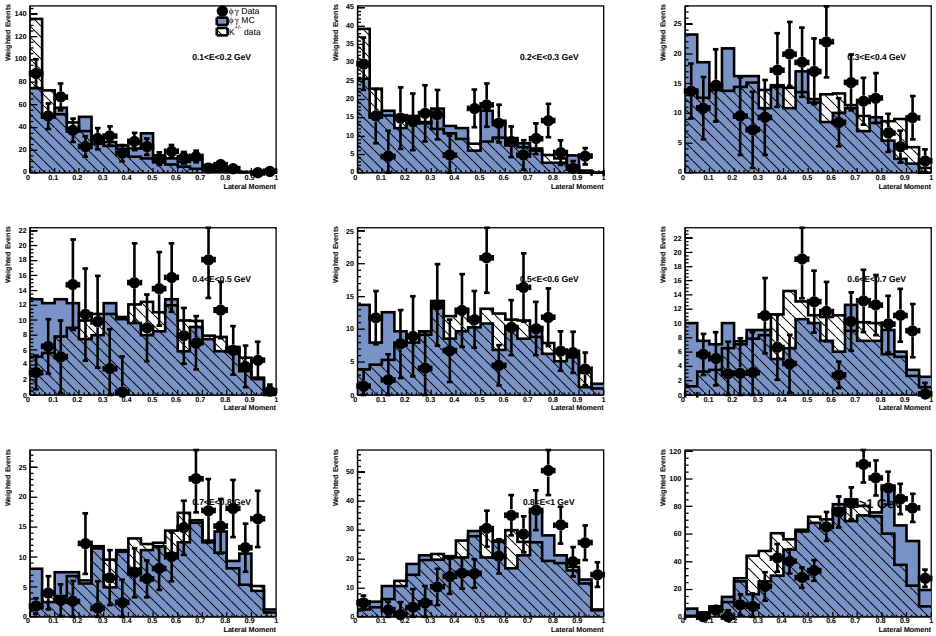

Figure 5.25: Shape of **Lateral Moment** in bins of calorimetric energy. Blue histograms: $e^+e^- \to \phi(K_S^0K_L^0)\gamma$ Monte Carlo. Hatched histogram: $K^\pm$ data. Dots: $e^+e^- \to \phi(K_S^0K_L^0)\gamma$ $_s\mathcal{P}lots$.

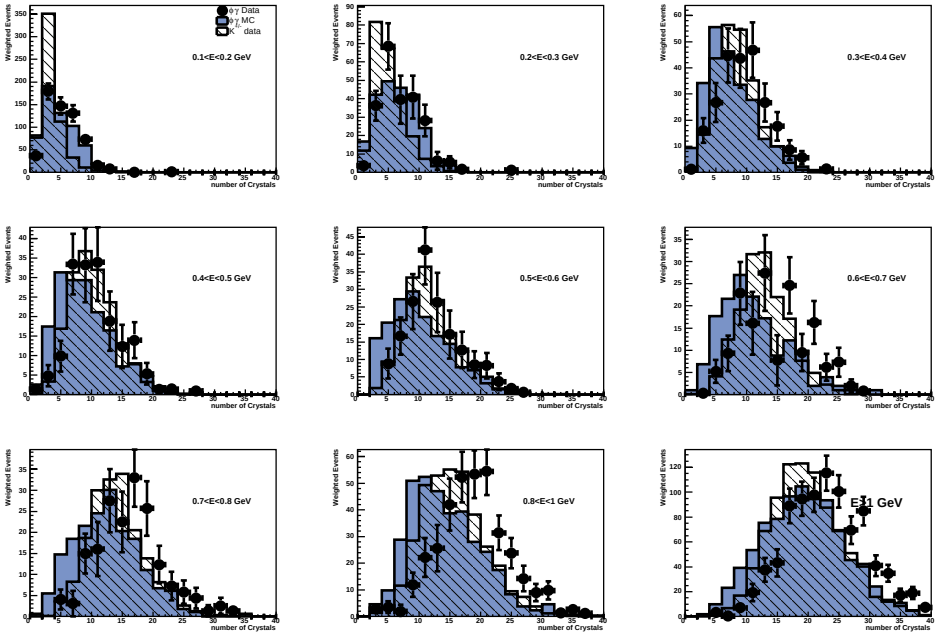

Figure 5.26: Shape of **Number of Crystals** in bins of calorimetric energy. Blue histograms: $e^+e^- \to \phi(K_S^0K_L^0)\gamma$ Monte Carlo. Hatched histogram: $K^\pm$ data. Dots: $e^+e^- \to \phi(K_S^0K_L^0)\gamma$ $_s\mathcal{P}lots$.

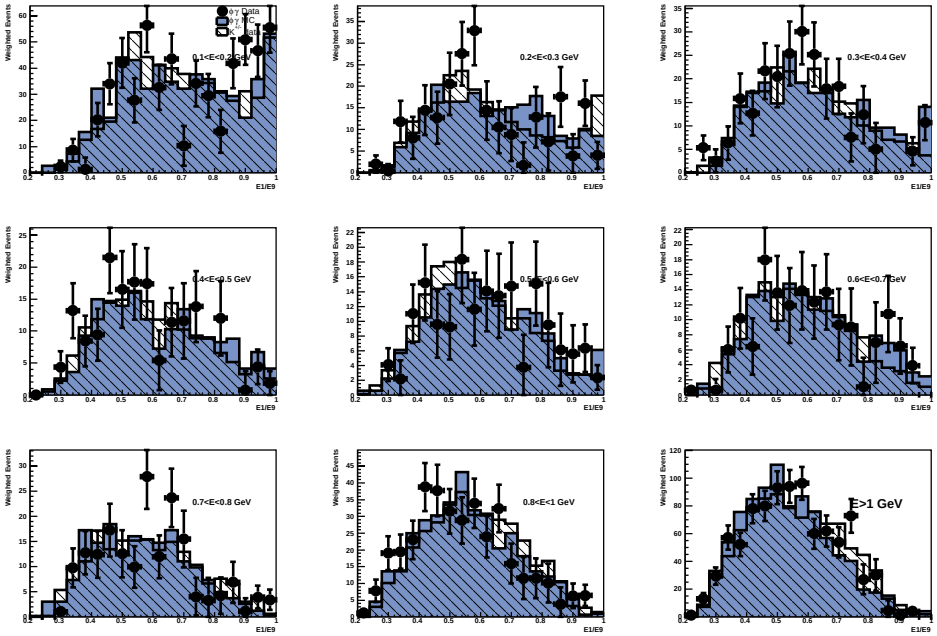

Figure 5.27: Shape of **Energy ratio E1/E9** in bins of calorimetric energy. Blue histograms: $e^+e^- \to \phi(K_S^0K_L^0)\gamma$ Monte Carlo. Hatched histogram: $K^\pm$ data. Dots: $e^+e^- \to \phi(K_S^0K_L^0)\gamma$ $_s\mathcal{P}lots$.

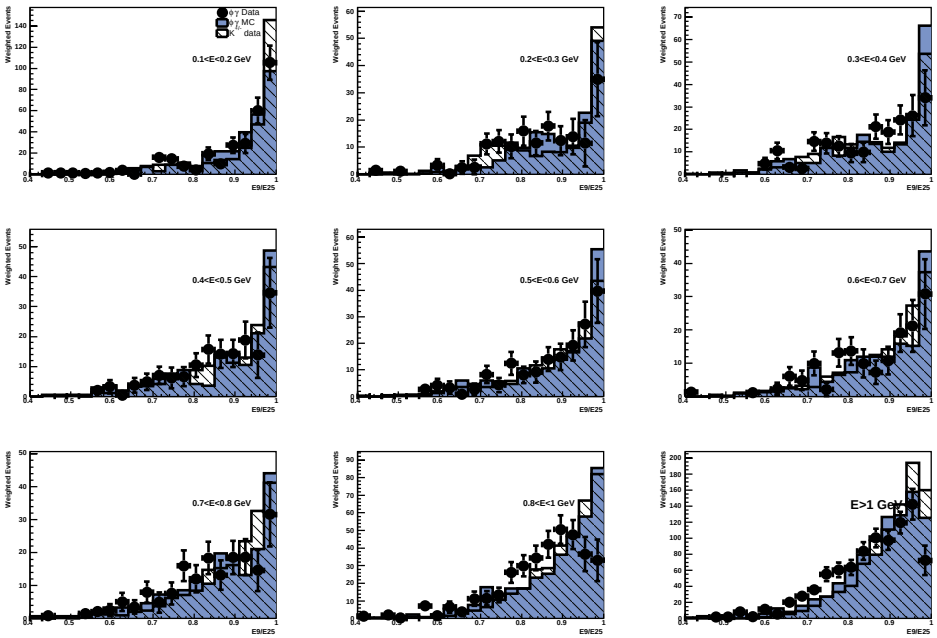

Figure 5.28: Shape of **Energy ratio E9/E25** in bins of calorimetric energy. Blue histograms: $e^+e^- \to \phi(K_S^0K_L^0)\gamma$ Monte Carlo. Hatched histogram: $K^\pm$ data. Dots: $e^+e^- \to \phi(K_S^0K_L^0)\gamma$ $_s\mathcal{P}lots$.

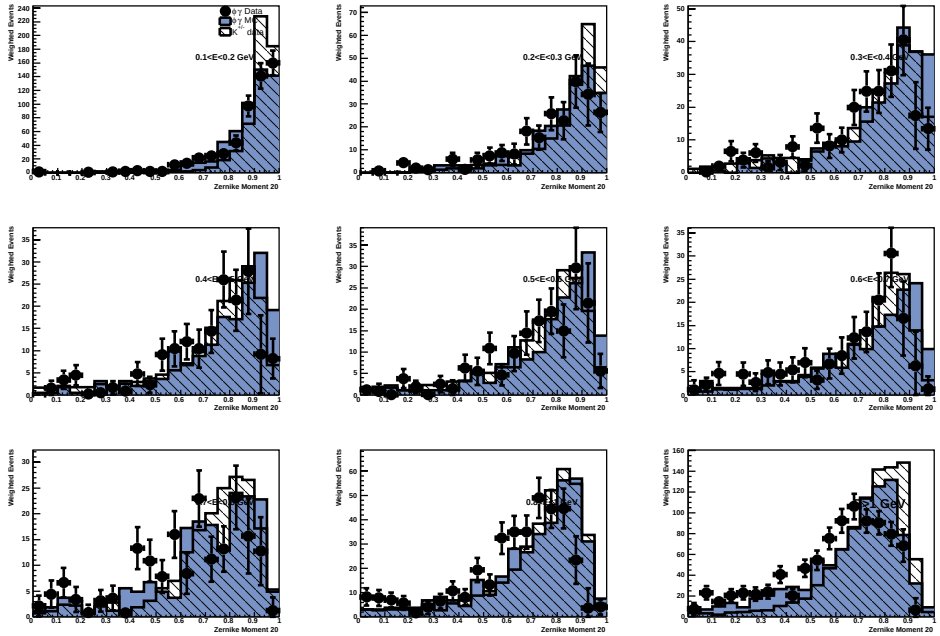

Figure 5.29: Shape of **Zernike moment Z_{20}** in bins of calorimetric energy. Blue histograms: $e^+e^- \to \phi(K^0_S K^0_L)\gamma$ Monte Carlo. Hatched histogram: $K^\pm$ data. Dots: $e^+e^- \to \phi(K^0_S K^0_L)\gamma$ ${}_s\mathcal{P}lots$.

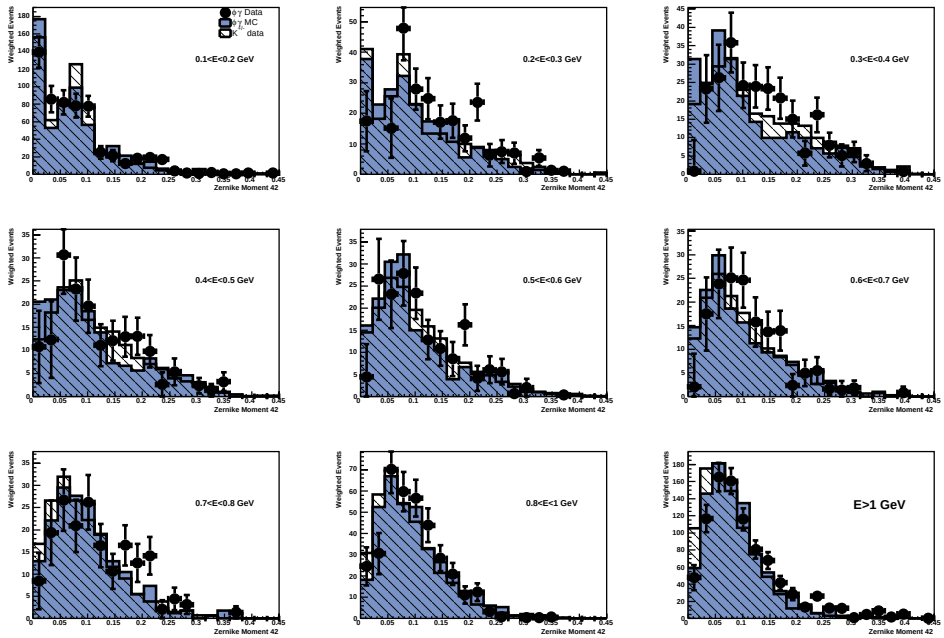

Figure 5.30: Shape of **Zernike moment Z_{42}** in bins of calorimetric energy. Blue histograms: $e^+e^- \to \phi(K^0_S K^0_L)\gamma$ Monte Carlo. Hatched histogram: $K^\pm$ data. Dots: $e^+e^- \to \phi(K^0_S K^0_L)\gamma$ ${}_s\mathcal{P}lots$.

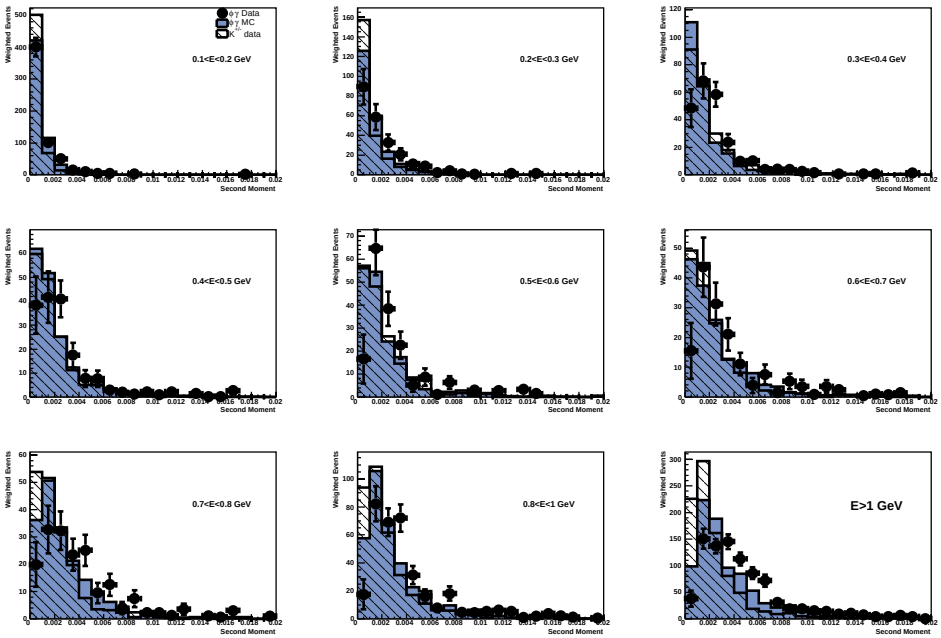

Figure 5.31: Shape of **Second moment** in bins of calorimetric energy. Blue histograms: $e^+e^- \to \phi(K^0_S K^0_L)\gamma$ Monte Carlo. Hatched histogram: $K^\pm$ data. Dots: $e^+e^- \to \phi(K^0_S K^0_L)\gamma$ ${}_s\mathcal{P}lots$.

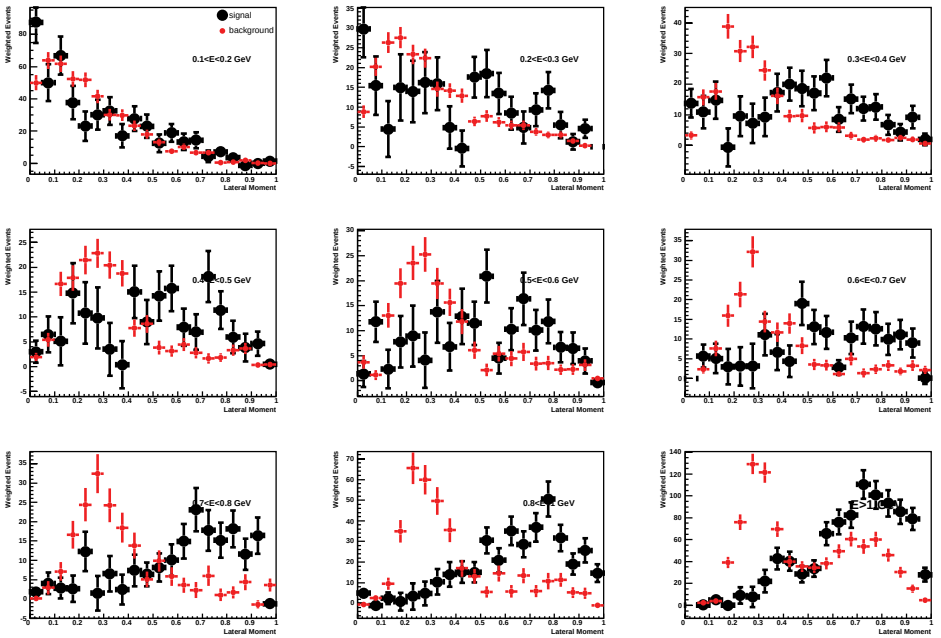

Figure 5.32: Shape of **Lateral Moment** in bins of calorimetric energy. Black dots: signal, red dots: background. Signal and background distributions are obtained with ${}_s\mathcal{P}lots$ weighting technique on $e^+e^- \to \phi(K^0_S K^0_L)\gamma$ data sample.

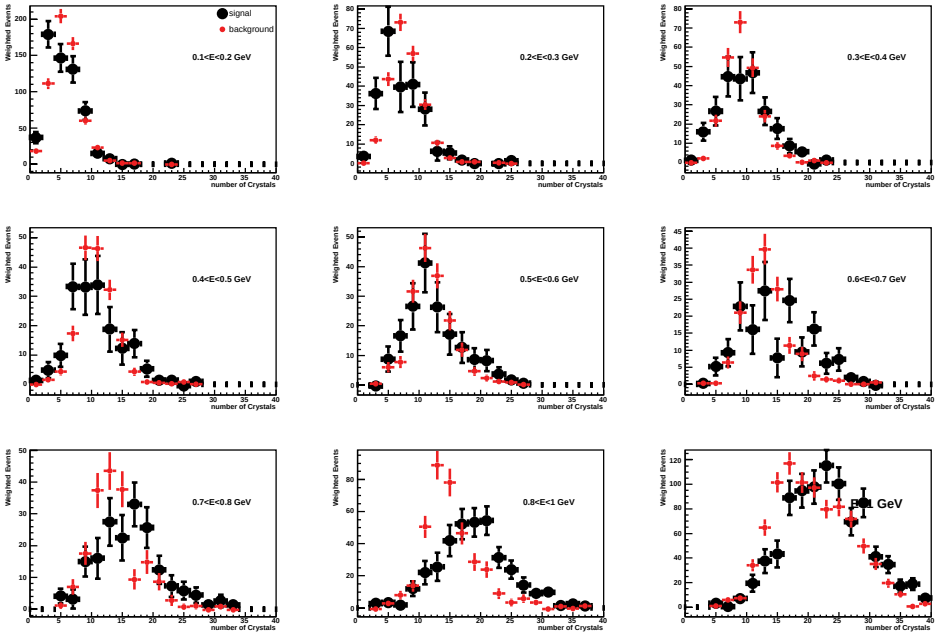

Figure 5.33: Shape of **Number of Crystals** in bins of calorimetric energy. Black dots: signal, red dots: background. Signal and background distributions are obtained with ${}_s\mathcal{P}lots$ weighting technique on $e^+e^- \to \phi(K^0_S K^0_L)\gamma$ data sample.

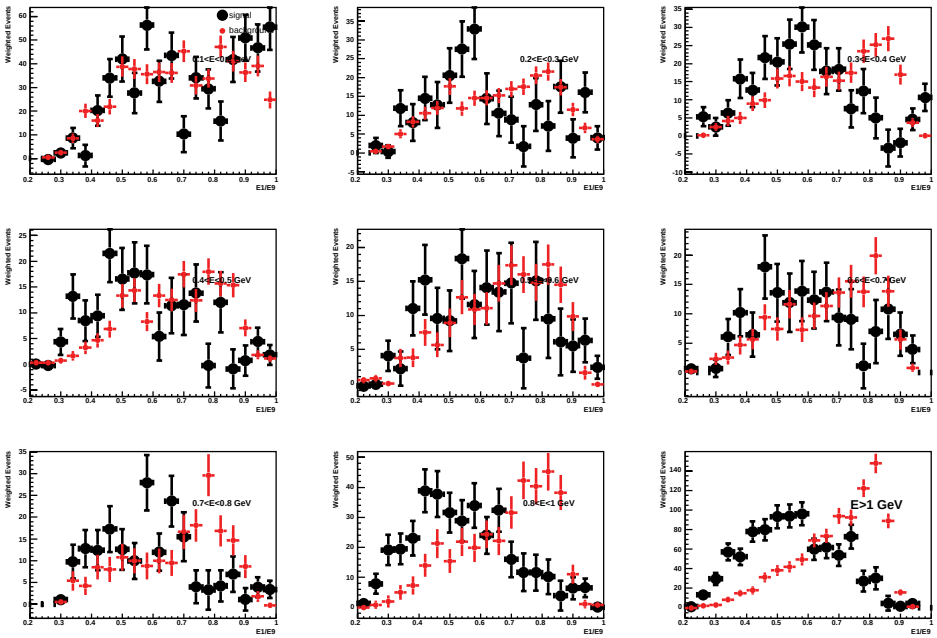

Figure 5.34: Shape of **Energy ratio E1/E9** in bins of calorimetric energy. Black dots: signal, red dots: background. Signal and background distributions are obtained with ${}_s\mathcal{P}lots$ weighting technique on $e^+e^- \to \phi(K^0_S K^0_L)\gamma$ data sample.

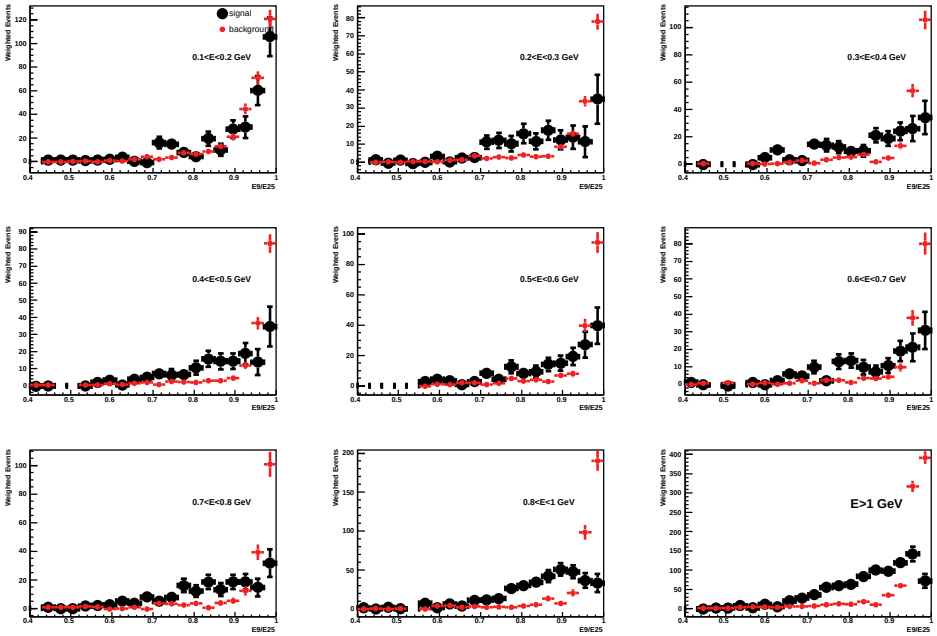

Figure 5.35: Shape of **Energy ratio E9/E25** in bins of calorimetric energy. Black dots: signal, red dots: background. Signal and background distributions are obtained with ${}_s\mathcal{P}lots$ weighting technique on $e^+e^- \to \phi(K_S^0 K_L^0)\gamma$ data sample.

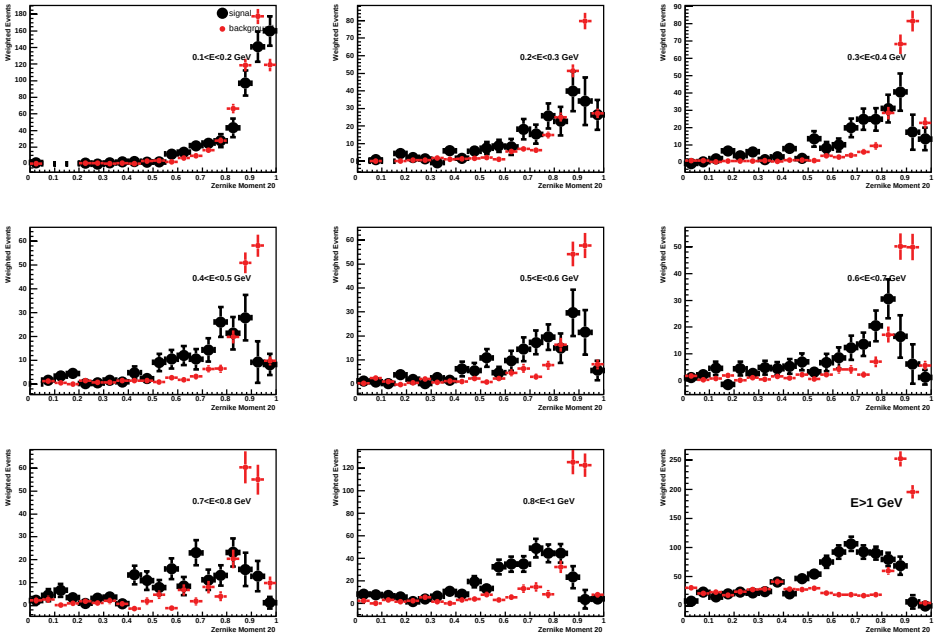

Figure 5.36: Shape of **Zernike moment Z_{20}** in bins of calorimetric energy. Black dots: signal, red dots: background. Signal and background distributions are obtained with ${}_s\mathcal{P}lots$ weighting technique on $e^+e^- \to \phi(K_S^0 K_L^0)\gamma$ data sample.

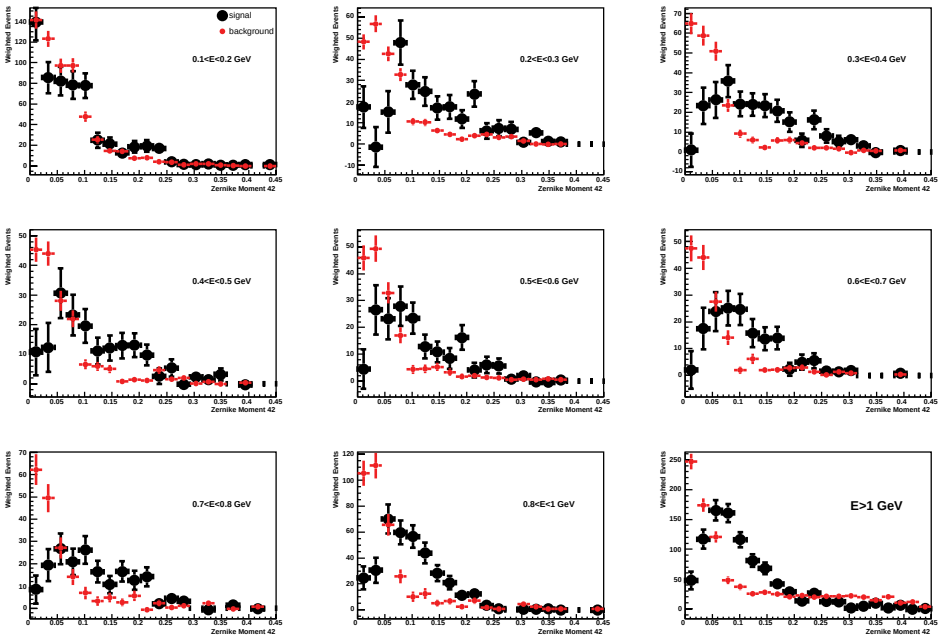

Figure 5.37: Shape of **Zernike moment $\mathbf{Z_{42}}$** in bins of calorimetric energy. Black dots: signal, red dots: background. Signal and background distributions are obtained with ${}_s\mathcal{P}lots$ weighting technique on $e^+e^- \to \phi(K^0_S K^0_L)\gamma$ data sample.

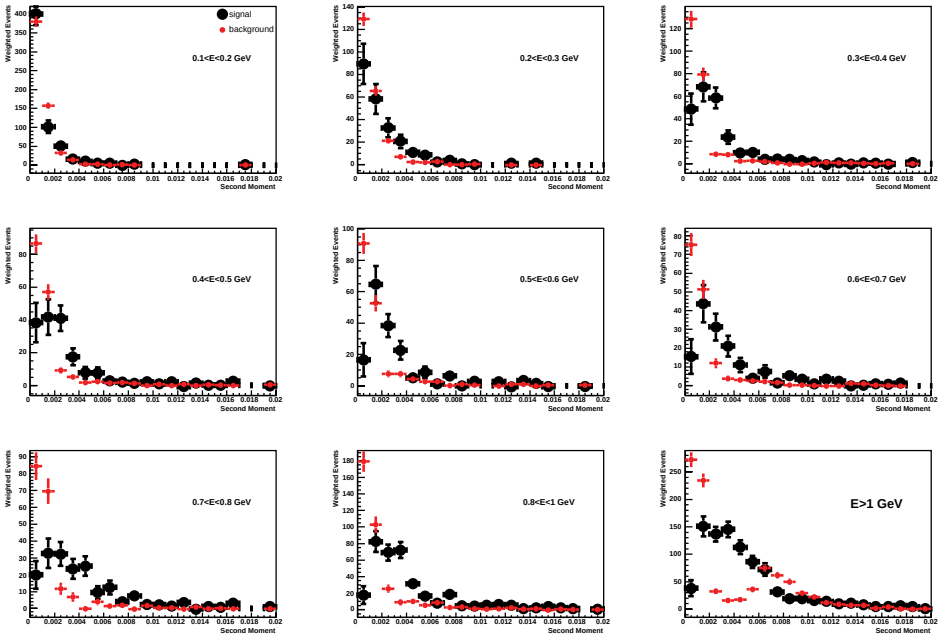

Figure 5.38: Shape of **Second moment** in bins of calorimetric energy. Black dots: signal, red dots: background. Signal and background distributions are obtained with ${}_s\mathcal{P}lots$ weighting technique on $e^+e^- \to \phi(K^0_S K^0_L)\gamma$ data sample.

behaviour of the shape variables, also if some discrepancies are present. However, the dependency on the kinematics is well reproduced by the simulation.

In order to establish if energy is the only kinematic dependency for the shape variables, we divide the $\phi\gamma$ sample in four bins of the polar angle. In Fig. 5.39 we show the distribution of the lateral moment in these bins. Also the other variables show a similar behavior: the shape for $\cos\theta_{LAB} < 0$ (we will call it **Bwd**) is slightly different for the one in $\cos\theta_{LAB} > 0$ (**Fwd**).

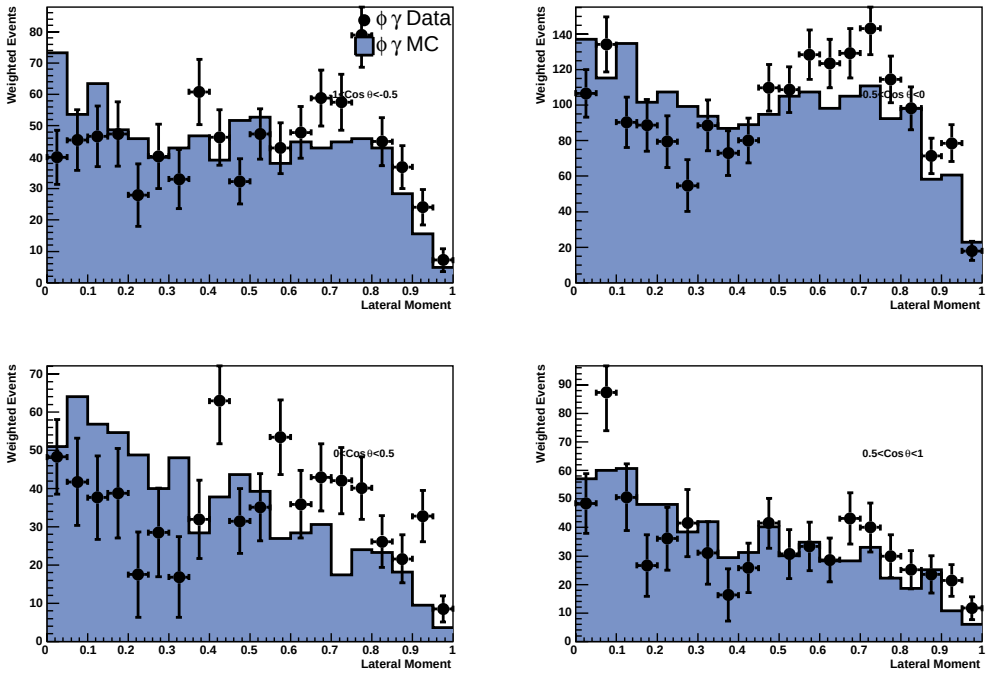

Figure 5.39: Shape of **Lateral moment** in bins of $\cos\theta_{LAB}$. Blue histograms: $\phi\gamma$ MC. Dots: $\phi\gamma$ ${}_s\mathcal{P}lots$.

We propose a kinematic binning in the $E_{cal}-\theta_{LAB}$ space for a K_L^0 particle identification algorithm which should in the same time maintain the main dependency on the kinematics and do a grouping which reduce the finer discrepancies between data and Monte Carlo. We divide the space in two hemispheres, **Fwd** and **Bwd**. Then we divide the momentum space in three regions:

- **Low E**: $E_{cal} < 0.2$ GeV
- **Medium E**: $0.2 < E_{cal} < 0.6$ GeV

- **High E**: $E_{cal} > 0.6$ GeV

These requirements define six K_L^0 kinematic regions. In each of them the PID criteria will be optimized and validated on data control samples.

5.4 K_L^0 Particle Identification

Genetic Algorithms [61] are search algorithms based on the mechanics of Darwinian evolution: survival of the fittest. Each possible solution to a given problem (*e.g.* a set of cuts on some discriminating variables) is considered an *individual*: each cut may be regarded as one *gene*, the set of cuts comprising the individual. The genetic algorithm is designed to find the best solution to the problem from a *population* of possible solutions. The algorithm calculates a *fitness* value for each individual (set of cuts). This is specified by the user with his/her problem in mind, and could be, for example, a measure of the signal to background ratio for each set of cuts (individual). Then the worst candidate solutions (the least fit) are removed from the population. The algorithm then acts on the surviving solutions using three fundamental (genetic) operators: *reproduction*, *crossover* and *mutation*: more individuals are "spawned" from combinations of the surviving ones in order to form a new (descendant) population, which retains the best characteristics of the previous one. The individuals comprising the population improve, on average, after each iteration, i.e. they gain better and better *fitness* values.

In experimental Particle Physics it has been shown [62, 63] that genetic algorithms can help in physics analysis when statistical significance optimization is needed. Applications of genetic algorithms [62] include distinguishing signal from background (in rare decays) and flavour tagging.

In order to tune (i.e. *train*) a particle identification algorithm that is aimed to discriminate K_L^0's from background, we need a sample representing the K_L^0 signal and one representing the background. In our study, we use a simulated sample of $D^0 \to K_L^0\pi^+\pi^-$ decays as signal[1], with K_L^0 candidates matched with true K_L^0 at generation level, and as background non truth matched candidates in the continuum events reconstructed with the same selection algorithm.

Each genetic algorithm needs a validation sample for the training procedure. In prin-

[1]The D^0s are copiously produced in the $e^+e^- \to c\bar{c}$ continuum production. We will describe this other K_L^0 control sample in Sec. 5.5.

ciple, it is sufficient to divide the same sample used for the training in two independent sub-samples. We prefer to use a completely independent sample: K_L^0's coming from $B^0 \rightarrow K^+K^-K_L^0$ decays, which also have a wide momentum spectrum. This allows to test also if the binning is sufficient to represent the characteristics of another decay. Finally, we validate each selector with the data control samples.

We compare the performances of two algorithms: a selector based on a *Neural Network* and another on a *Boosted Decision Trees*.

5.4.1 Neural Network Algorithm

One of the most used genetic algorithms is a non-linear multidimensional method, also called *neural networks* [64].

We train a neural network using 7 input variables: lateral moment, Zernike moments Z_{20} and Z_{42}, energy ratios $E1/E9$ and $E9/E25$, second moment and the number of crystals. We have shown in the previous section that the general behaviour and their dependency on the neutral momentum of these variables are reproduced by the Monte Carlo simulation.

The training procedure is repeated in all the defined 6 kinematic bins. In each bin, different configurations of *learning parameter*, number of *hidden layers* and number of *nodes* in each hidden layer has been tried, in order to obtain the best separation between signal and background.

As discussed previously, we rejected all the reconstructed clusters with $E_{cal} < 0.2$ GeV. We also cut the clusters with ≤ 2 crystals, because of in this case the lateral moment is zero by definition (Eq. 5.3) and this can introduce instabilities in the training procedure. The output of the Neural Network in the previously defined six kinematic regions is shown in Fig. 5.40, while Fig. 5.41 shows the signal efficiencies versus the background rejection (i.e. the figure of merit) for the 6 selectors.

The output of the Neural Network reflects the fact that the discrimination power grows with the energy.

5.4.2 Boosted Decision Trees Algorithm

The algorithm based on *Decision Trees* has been successfully developed and used in the event definition of the MiniBooNE experiment [59, 60]. The basis of this algorithm is

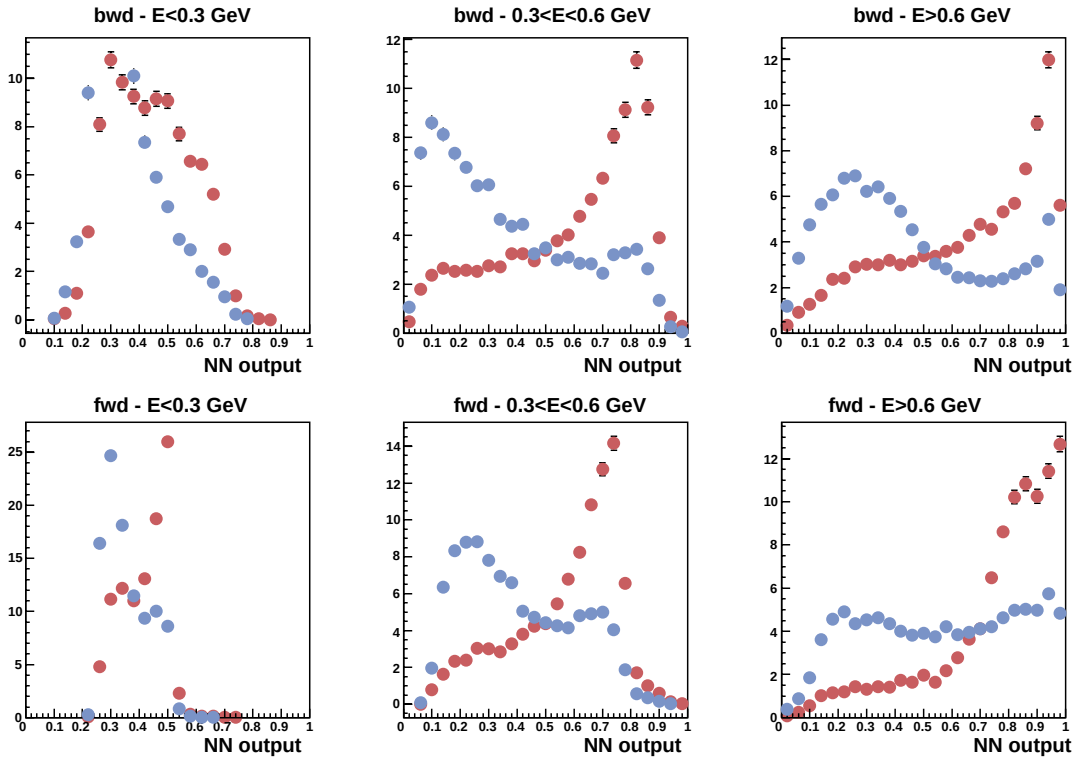

Figure 5.40: Output of the Neural Network algorithm in six kinematic bins. Brown dots: signal. Blue dots: background.

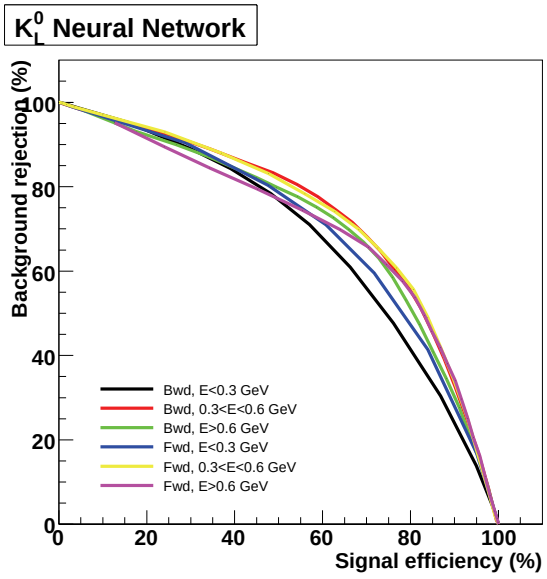

Figure 5.41: Figure of merit of the Neural Network algorithm. The curves represent the different kinematic bins.

shown in Fig. 5.42. For the variable one (let's say LAT) choose the value which has the

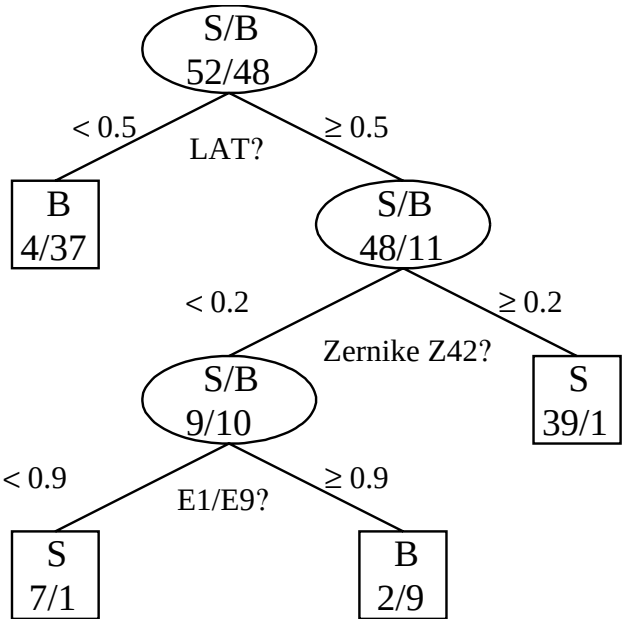

Figure 5.42: Schematic of a decision tree. S for signal, B for background. Terminal nodes (called leaves) are shown in boxes. If signal events are dominant in one leave, then this leave is signal leave; otherwise, background leave.

best separation and split the sample in two, one side having mostly signal (S) and the other having mostly background (B). Then repeat the splitting of these sub-samples according the other variables. The splitting is done until a given number of final branches, called leaves, are obtained, or until each leaf is pure signal or pure background, or has too few events to continue. This process produces the "decision tree". An iterative optimization of the binary splittings is then performed, called "boosting".

MiniBooNE collaboration has shown that this algorithm has better performances than Neural Network algorithm, especially when the input variables are highly correlated (as in our case).

MiniBooNE collaboration have also shown that the output is also more stable than the one of the Neural Networks. We use as a training sample the one used for the Neural Network, with the same input variables.

For each bin we optimize the *minimal leaf size* minimizing the *Gini index*:

$$Gini = \frac{S_1 B_1}{S_1 + B_1} + \frac{S_2 B_2}{S_2 + B_2} \tag{5.13}$$

where if the initial sample is composed by S signal events and B background events, S_i and B_i are the number of signal and background events of each of the two splitted samples (called leaves). The output of the boosting technique has a probabilistic interpretation: if x is a given point in the space (which has N dimension if N is the number of variables used) and $f(x)$ is the output, this can be written as

$$\frac{P(y=+1|x)}{P(y=-1|x)} = e^{2f(x)} \tag{5.14}$$

that is, the ratio of probability of signal over the probability of background for that point is a simple function of the output $f(x)$. In Fig. 5.43 we show the output of this algorithm in the six previously defined kinematic bins, while in Fig. 5.44 the relative figure of merit is displayed.

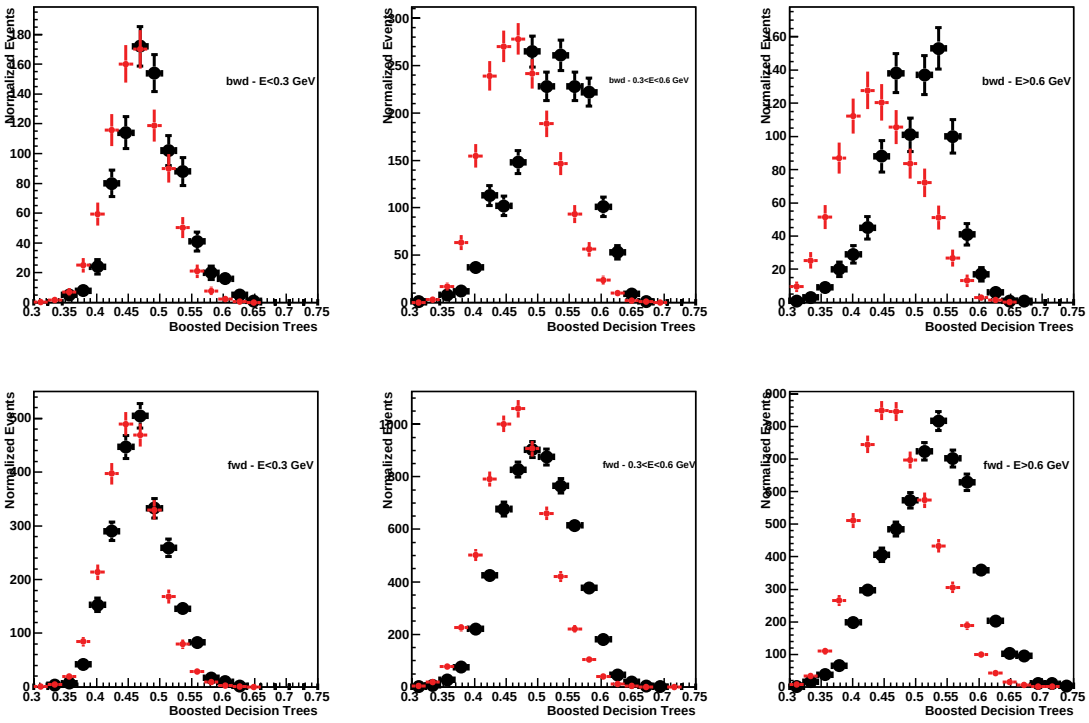

Figure 5.43: Output of the Boosted Decision Trees algorithm. Black dots: signal. Red dots: background.

Also in this case, the best separation is achieved in the high energy region, while for $E_{cal} < 0.3$ GeV the distribution of signal and background are almost the same.

We also note that both for Neural Network and Boosted Decision Trees, in the same energy bin, there is a better separation in the $\cos\theta < 0$ region than in $\cos\theta > 0$. This

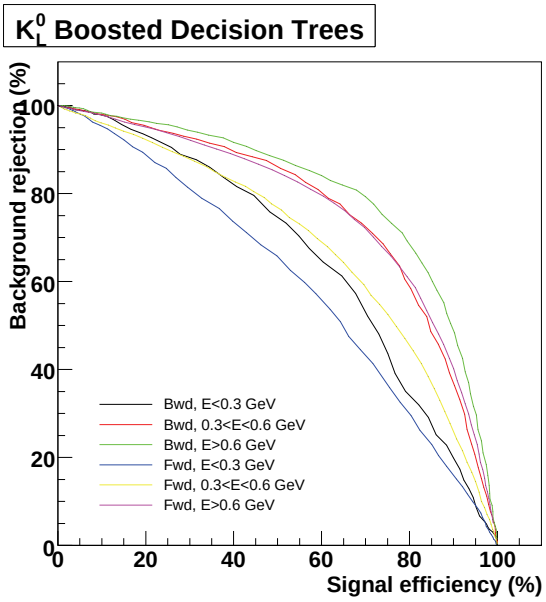

Figure 5.44: Figure of merit of the Boosted Decision Trees algorithm. The curves represent the different kinematic bins.

reflects the more photon-like shape of the variables in the **Bwd** bin (see for example lateral moment in Fig. 5.39). In Fig. 5.45 we compare the two selectors in the two spatial hemispheres.

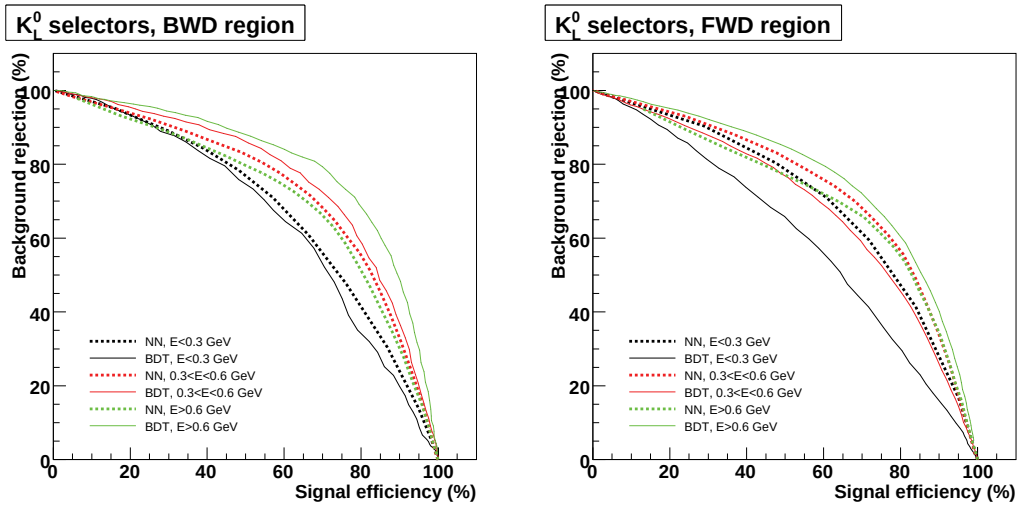

Figure 5.45: Comparison of the figures of merit of the Neural Network and Boosted Decision Trees algorithms in the two hemispheres **Bwd** (left plot) and **Fwd** (right plot).

From the comparison we conclude that there is not a large difference in the perfor-

mances between the two algorithms, but Boosted Decision Trees seems to be better in the regions of most interest for the analyses ($E_{cal} > 0.3$ GeV). Also, Boosted Decision Trees seems to be more stable in the sense that if the input shapes have a small change, the output shows only small changes, while Neural Network can change a lot. Also, the Boosted Decision Trees have a shape which is more easily parameterizable than the irregular output of the Neural Network.

We will denote the group of the 6 selectors obtained with Boosted Decision Trees as *Totti selector* [2].

5.4.3 Validation of K_L^0 Selector on Data

We validate the output of the *Totti selector* using $e^+e^- \to \phi(K_S^0 K_L^0)\gamma$ data control sample. We evaluate the algorithm output for each event using the trained configuration. At each event the ${}_sWeight$ is assigned using the likelihood function. The output in the 6 bins for signal and background events is shown in Fig. 5.46. Comparing the shapes of the selector with the one obtained on Monte Carlo and sideband data in Fig. 5.43, it is evident that the selector has a similar discrimination power in the two cases. The test is also significant because the kinematics of the K_L^0 in $e^+e^- \to \phi(K_S^0 K_L^0)\gamma$ is very different to the one of the training sample ($D^0 \to K_L^0\pi^+\pi^-$). In fact, since the ϕ recoils against the hard ISR photon, the K_L^0 direction accumulates in the **Bwd** region. Concluding, this is a successfully test of the generality of the selector. In order to give a more quantitative estimation of the data-Monte Carlo agreement, we superimpose the distributions for $e^+e^- \to \phi(K_S^0 K_L^0)\gamma$ signal Monte Carlo and ${}_s\mathcal{P}lot$ weighted data, and evaluated a χ^2 for each kinematic bin. The comparison is given in Fig. 5.47.

Even if the uncertainties on data events are high, due to the low statistics (above all in the low energy bins), the behaviors are very well reproduced in 5/6 bins. In $[Fwd, HighE_{cal}]$ there is a shift and the presence of a tail for lower values (even if the discrimination power with respect to background is similar to the one obtained with Monte Carlo). The final shape can be taken from Monte Carlo in the 5/6 bins where the agreement is very good, and from $\phi\gamma$ signal ${}_s\mathcal{P}lot$s for the bin where there is disagreement, since in that bin there is enough statistics on data.

[2] After the name of the famous Italian football player and world champion, *Francesco Totti*

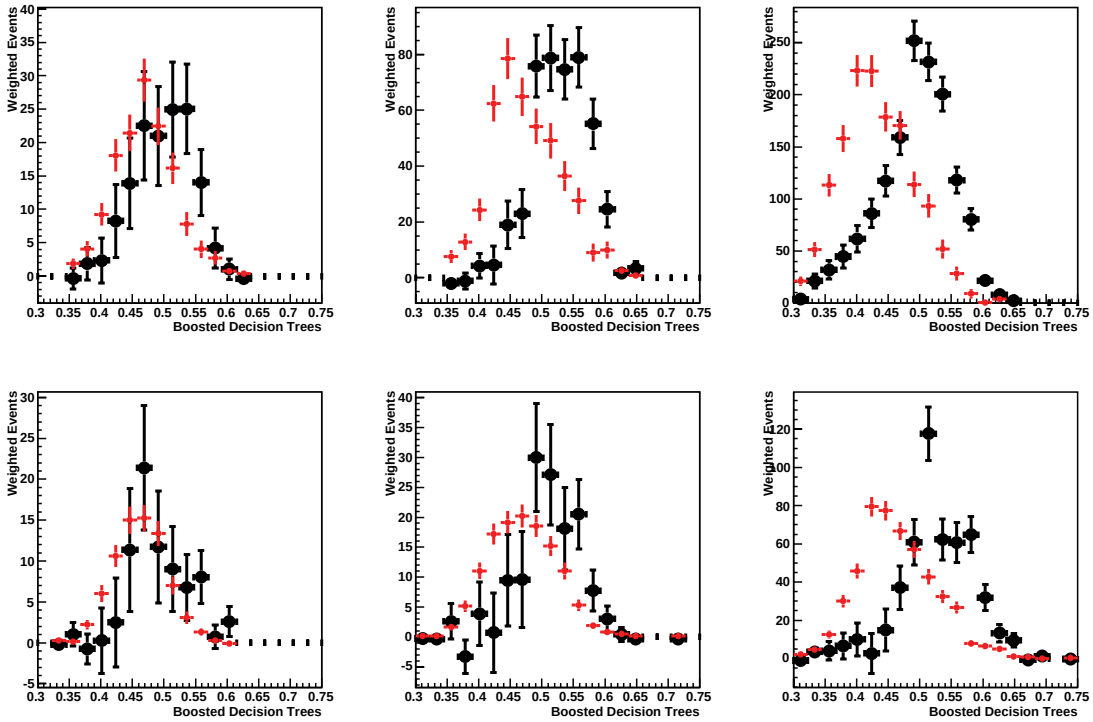

Figure 5.46: Output of Totti selector on $e^+e^- \to \phi(K_S^0 K_L^0)\gamma$ control sample. The signal (black dots) and background (red dots) distributions are obtained with the ${}_s\mathcal{P}lots$ weighting technique.

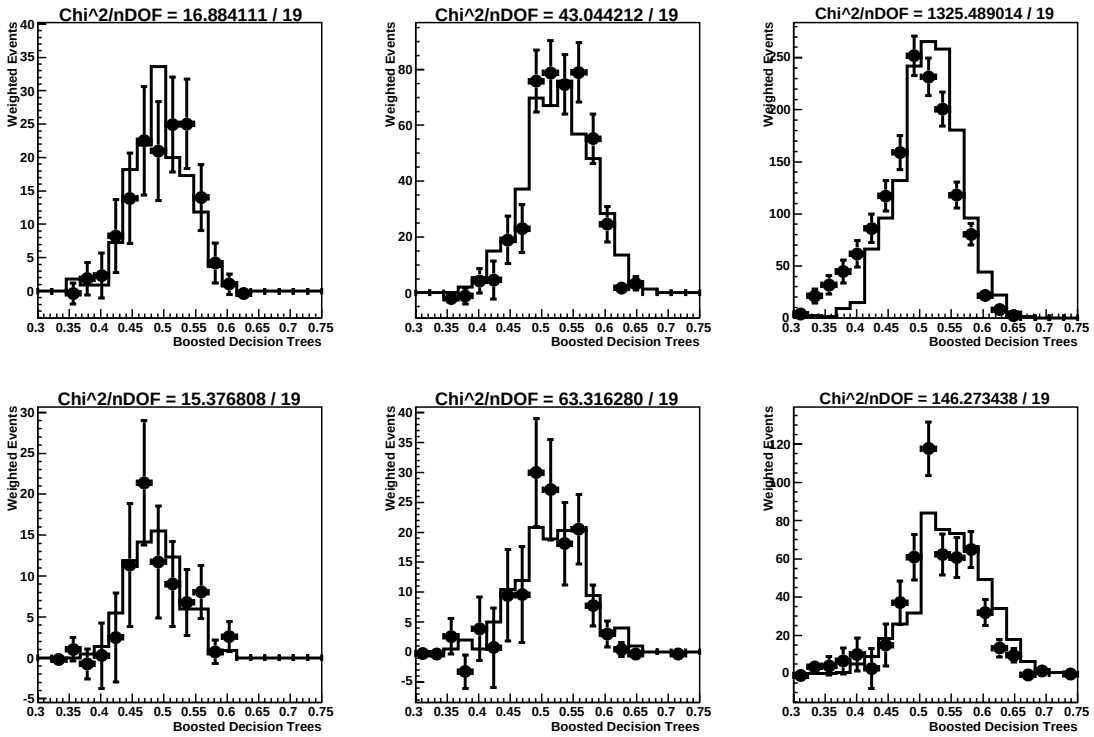

Figure 5.47: Data - Monte Carlo comparison of the output of the Totti selector on the $e^+e^- \to \phi(K^0_S K^0_L)\gamma$ sample. Histogram is signal Monte Carlo, while dots are data, weighted with the ${}_s\mathcal{P}lots$ technique.

5.5 K^0_L Efficiency Calibration with $D^0 \to K^0_L\pi^+\pi^-$ Decays

One of the measurements presented in this work is the *CP* asymmetry in the $B^0 \to K^+K^-K^0$ decays with Dalitz plot technique (Chapter 6). We both consider $K^0 \to K^0_S$ and $K^0 \to K^0_L$ sub-modes. In order to modulate correctly the Dalitz plot model for $B^0 \to K^+K^-K^0_L$ decays, we need a correct efficiency map in the Dalitz plot, which means that we need the K^0_L efficiency as a function of the neutral hadron momentum. With this purpose, we need to calibrate it with a data control sample. The $e^+e^- \to \phi(K^0_SK^0_L)\gamma$ sample has not a sufficient number of events to be divided into enough bins in the position-momentum space. Because of that, we decided to use the more copious source of K^0_L's from $D^0 \to K^0_L\pi^+\pi^-$ decays, where the D^0 are produced by $D^{*+} \to D^0\pi^+$ decays, and the D^{*+} come from inclusive production $e^+e^- \to D^{*+}X$. We use both on-resonance and off-resonance events. The high statistics of this samples is determined by the high cross section of the process: $\sigma(e^+e^- \to D^*X) = 580 \pm 70$ pb [65] and from the branching fractions of $D^* \to D^0\pi$ and $D^0 \to K^0_L\pi^+\pi^-$, which are 0.68 and 0.7×10^{-3} [21].

Since the K^0_L momentum is not reconstructed, it is evaluated assuming that it comes from a D^0 decay, using the relation

$$m^2_{D^0} = (E_{K^0_L} + E_{\pi^+\pi^-})^2 - (\mathbf{p_{K^0_L}} + \mathbf{p}_{\pi^+\pi^-})^2 \tag{5.15}$$

where m_{D^0} is the nominal D^0 mass [21], and $(E_{K^0_L}, \mathbf{p_{K^0_L}})$ and $(E_{\pi^+\pi^-}, \mathbf{p}_{\pi^+\pi^-})$ are the four momenta of the K^0_L and the $\pi^+\pi^-$ pair, respectively. To reconstruct the D^* candidate, we look for a *slow* pion among the pions of the event which are not associated to the D^0 decay. The event is then kinematically characterized by the variable Δm, which is the mass difference between the D^* and the D^0. The signal is expected to peak at the mass of the π^+, while the background, made of random combination of particles, shows a more phase-space distribution.

In order to extract the signal we perform a maximum likelihood fit to the data. The signal is parameterized on signal Monte Carlo sample with a double Gaussian, while the background is parameterized with a threshold function:

$$f(x)_{bkg} = (x - x_0)^a \cdot e^{-b(x-x_0)^2 - c(x-x_0)} \tag{5.16}$$

where x_0 is the lower physical limit of the distribution and a, b and c are slope parameters. The result of the fit on data is shown in Fig. 5.48, where the contribution of the background

and of the wide Gaussian component of the signal are also shown. The fit results are shown in Tab. 5.5. The purity of the signal in the interval around one standard deviation (considered as the resolution of the wider Gaussian) from the mean, is $\approx 40\%$. The

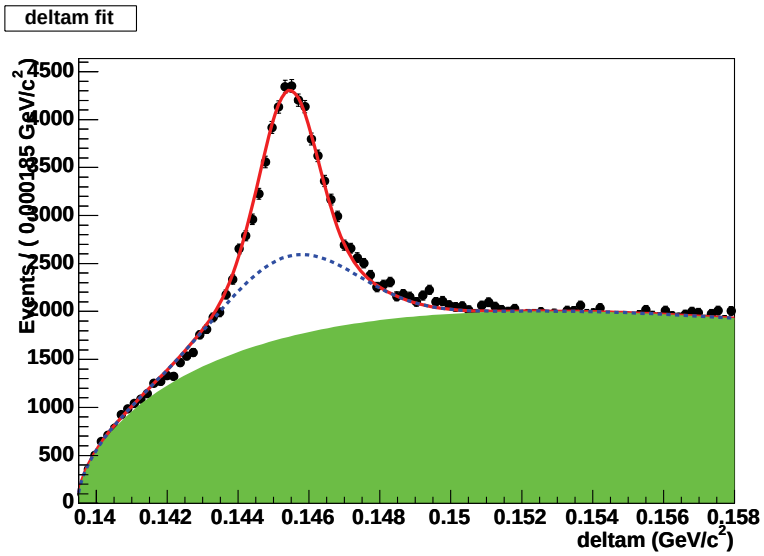

Figure 5.48: Δm distribution on 230 fb^{-1} of data. Green is background, dashed curve corresponds to background plus wide Gaussian component for the signal.

Parameter	Final Value
Δm mean value (signal)	145.48 ± 0.01 MeV/c^2
$\sigma_{\Delta m}$(narrow Gaussian)	0.72 ± 0.03 MeV/c^2
$\sigma_{\Delta m}$(wide Gaussian)	1.71 ± 0.10 MeV/c^2
N_{sig}	55220 ± 3438
N_{bkg}	226980 ± 21398
a	0.59 ± 0.01
b	99 ± 79
c	43.7 ± 2.1

Table 5.4: Results of the Δm fit: a, b and c refer to shape variables in Eq. 5.16.

signal is one order of magnitude higher than the one for $e^+e^- \to \phi(K^0_S K^0_L)\gamma$ sample, even if with lower purity.

Once the K^0_L is identified, we want to use it to obtain a correction of the reconstruction efficiency to apply to the Monte Carlo simulation in the EMC. In order to obtain an

estimation of the correction, let's consider the ratio

$$\left(\frac{\varepsilon_{K^0_{L\ DATA}}}{\varepsilon_{K^0_{L\ MC}}}\right)_{EMC} = \frac{N(K^0_{L\ DATA})}{f_{\mathcal{L}} \times N(K^0_{L\ MC})} \tag{5.17}$$

where $N(K^0_{L\ DATA})$ and $N(K^0_{L\ MC})$ are the signal K^0_L yields respectively obtained from the data and MC $D^0 \to K^0_L\pi^+\pi^-$ samples, and $f_{\mathcal{L}}$ is the scale factor which scales the expected yields to the actual luminosity. This ratio would give us something that depends primarily on the K^0_L EMC interactions if $N(K^0_{L\ MC})$ was properly scaled to the data luminosity $\mathcal{L}$. However, there are inescapable and relatively large uncertainties on the Monte Carlo $f_{\mathcal{L}}$ that do not depend on the K^0_L EMC interactions, but on the D^* production rate, D^0 branching fraction, $D^0 \to K^0_L\pi^+\pi^-$ kinematic in the Dalitz plane and other generator-level quantities.

To isolate data-Monte Carlo discrepancies of K^0_L interactions in the EMC potentially (affecting analyses of other decays involving a K^0_L) from other potential data-Monte Carlo discrepancies (that are specific to the $D^0 \to K^0_L\pi^+\pi^-$ sample), it is better to use the double-ratio of Eq. 5.18:

$$\left(\frac{\varepsilon_{K^0_{L\ DATA}}}{\varepsilon_{K^0_{L\ MC}}}\right)_{EMC} = \frac{\left(\frac{N(K^0_L)}{N(K^0_S)}\right)_{DATA}}{\left(\frac{N(K^0_L)}{N(K^0_S)}\right)_{MC}} = \frac{\left(\frac{N(K^0_{L\ DATA})}{N(K^0_{L\ MC})}\right)}{\left(\frac{N(K^0_{S\ DATA})}{N(K^0_{S\ MC})}\right)} \tag{5.18}$$

where $N(K^0_L)$ and $N(K^0_S)$ are the K^0_L and K^0_S yields (data or Monte Carlo) respectively obtained from the $D^0 \to K^0_L\pi^+\pi^-$ and $D^0 \to K^0_S\pi^+\pi^-$ samples. The latter is obtained reconstructing the decay treating the K^0_S as a K^0_L, which means that the information of the K^0_S daughters is not used to know the K^0_S momentum, which is computed with the D^0 mass constraint as in Eq. 5.15.

The signal is extracted with a similar maximum likelihood fit to data (like for the $D^0 \to K^0_L\pi^+\pi^-$). The result of the fit on Δm variable is shown in Fig. 5.49. The signal yield is 37516 ± 258 events in this case.

In Eq. 5.18, there is no more the luminosity scale factor $f_{\mathcal{L}}$ because that factor is the same for the $D^0 \to K^0_L\pi^+\pi^-$ and $D^0 \to K^0_S\pi^+\pi^-$ samples and hence cancels out. All generator-level effects (i.e. production rates) being cancelled out in the double-ratio of Eq. 5.18, this quantity thus remains sensitive to reconstruction effects only. Since we can safely assume that the K^0_S reconstruction is much better simulated than the K^0_L one, we conclude that deviations of the double-ratio from 1.0 is a good estimator of data/MC

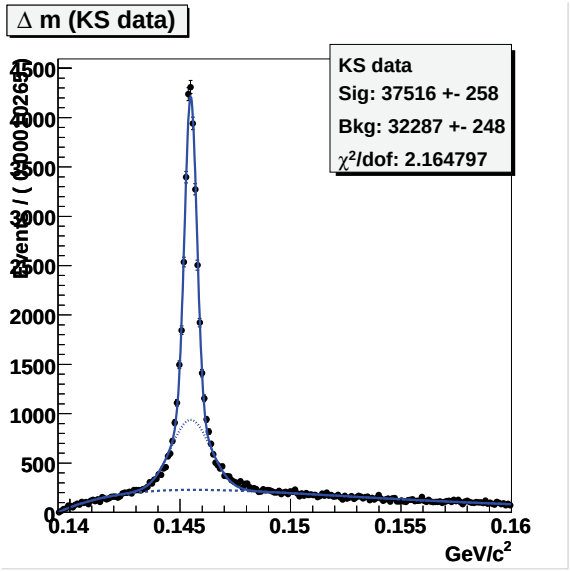

Figure 5.49: Δm distribution fit for the $D^0 \to K^0_S\pi^+\pi^-$ sample in data (230 fb^{-1}).

discrepancies in the reconstruction of K^0_L's in the EMC. To be valid, Eq. 5.18 needs the $D^0 \to K^0_L\pi^+\pi^-$ and $D^0 \to K^0_S\pi^+\pi^-$ samples integrated luminosities to be equal, which is guaranteed by our reconstruction strategy (we reconstruct $D^0 \to K^0_L\pi^+\pi^-$ and $D^0 \to K^0_S\pi^+\pi^-$ samples simultaneously).

We extract the efficiency corrections of Eq. 5.18 from fits in bins of momentum and θ_{LAB}. We use the computed momentum of the K^0_L and not the value of E_{cal}, because the latter variable is not defined for $D^0 \to K^0_S\pi^+\pi^-$ sample (the K^0_S does not reach the calorimeter). In Fig. 5.50 we show the correlation between the computed K^0_L momentum and E_{cal} for $D^0 \to K^0_L\pi^+\pi^-$ events, after the ${}_s\mathcal{P}lot$ weighting technique has been applied. EMC efficiency corrections vs p_{K^0} are shown on Fig. 5.51. These corrections are independent of the kinematic of our $D^0 \to K^0_L\pi^+\pi^-$ sample and can safely be used in other decays. EMC efficiency corrections vs θ_{K^0} are shown on Fig. 5.52. No sharp dependency is observed, and the θ_{K^0} dependency of efficiency can be also neglected.

We also compute an average correction of the efficiency for K^0_L candidates with $E_{cal} > 50$ MeV in different run periods: we evaluate it to be $0.956 \pm 0.021 \pm 0.007$ for the RunI-IV periods and $0.989 \pm 0.043 \pm 0.007$ for RunV period. The first error is statistic and the the second systematic, where the main source of systematic uncertainty comes from the PDFs parameterizations and from possible bias in the fit and in the $p_{K^0_L}$ evaluation.

We will use these results to correct the Monte Carlo efficiency across the Dalitz plot

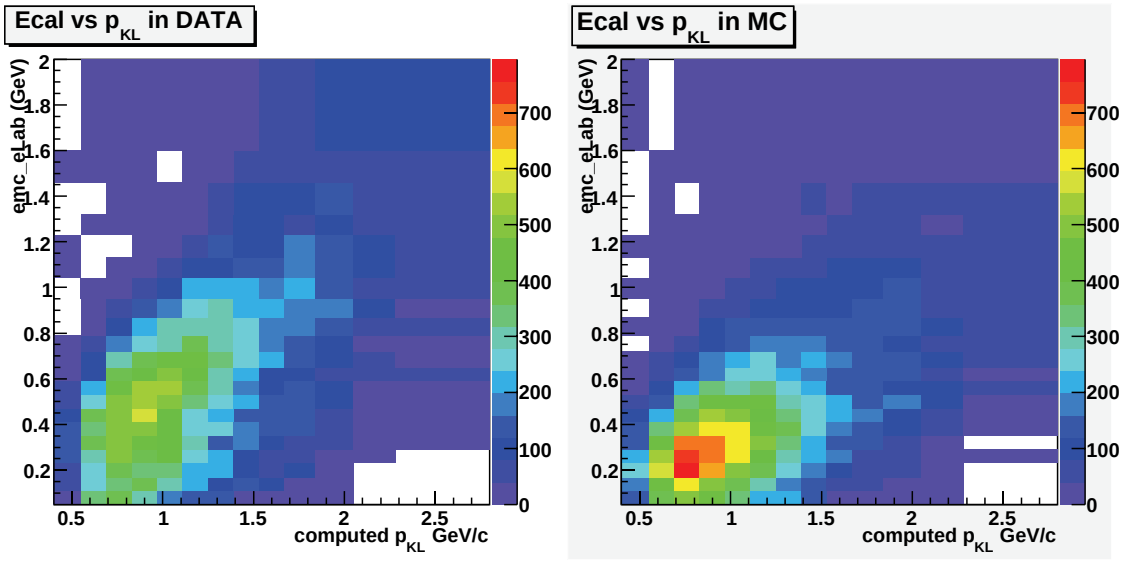

Figure 5.50: 2D ${}_s\mathcal{P}lot$ of $p_{K^0_L}$ vs E_{cal} for data and Monte Carlo.

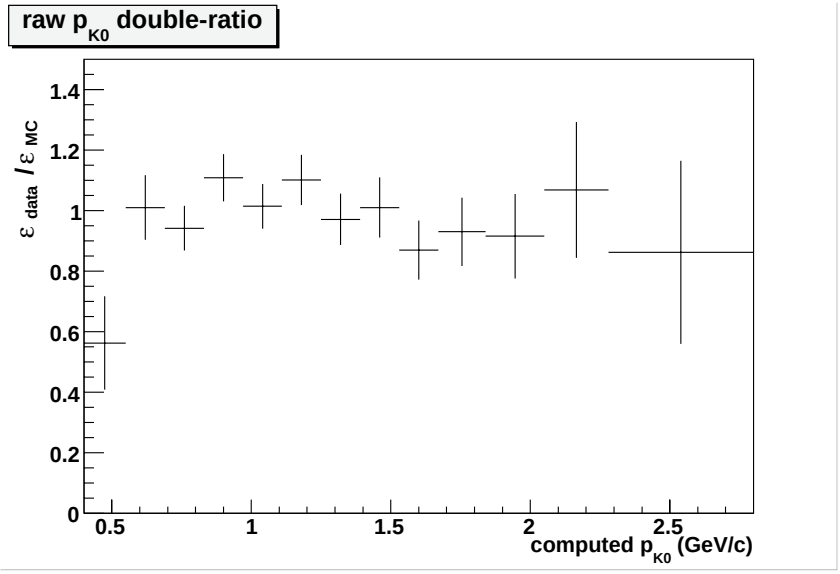

Figure 5.51: Efficiency corrections vs p_{K^0}, independently of $Ecal$, for K^0_L's reconstructed in the EMC.

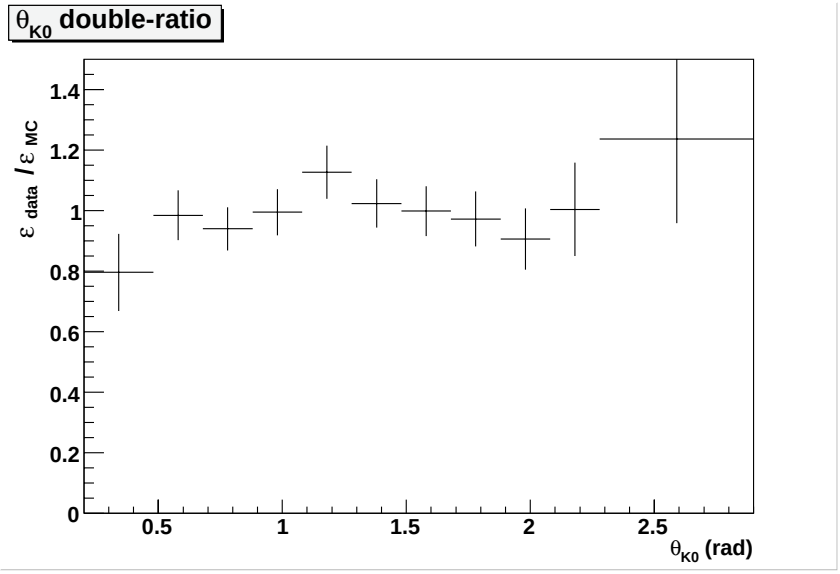

Figure 5.52: Efficiency corrections vs θ_{K^0} for K_L^0's reconstructed in the EMC.

for $B^0 \to K^+K^-K_L^0$ decays (Sec. 6.3.4).

Chapter 6

Measurement of *CP* Asymmetry in $B^0 \to K^+K^-K^0$ Decays

In Chapter 3 we described the dynamics of a decay of a B meson in three kaons. In this Chapter we will focus on the particular decay of the neutral B meson into $K^+K^-K^0$, where the K^0 can be both a K^0_S or a K^0_L.

As discussed in the theoretical introduction of Sec. 1.6, the decay $B^0 \to K^+K^-K^0$ is one of the most promising processes to search for physics beyond the Standard Model.

A full Dalitz plot analysis of these decays is necessary to measure *CP* asymmetry because this final state has not a definite *CP* eigenvalue, but it depends on the relative angular momentum of the K^+K^- system (Sec. 1.5). The Dalitz plot analysis allows to take into account the variation of the *CP*-odd and *CP*-even mixtures across the three-body phase space. Moreover, the contributions from $b \to u\bar{q}q$ tree amplitudes, proportional to the Cabibbo-Kobayashi-Maskawa (CKM) matrix element V_{ub} with a *CP*-violating weak phase γ [21], although small, may depend on the position in the Dalitz plot. In fact, in $B^0 \to \phi(K^+K^-)K^0$ decays the modification of the *CP* asymmetry due to the presence of suppressed tree amplitudes is estimated to be $\mathcal{O}(0.01)$ [66, 67], while at higher K^+K^- masses a larger contribution of the order of $\mathcal{O}(0.1)$ is possible [26].

Furthermore the simultaneous presence of *CP*-odd and *CP*-even amplitudes contributing to the decay rate gives the opportunity to measure the *CP*-violating parameter β, removing with a direct measurement the four-fold ambiguity arising in the case of the time-dependent *CP* asymmetry with only one *CP* contribution, like in $B^0 \to [c\bar{c}]K^0$. In this case, one accesses only the trigonometric function $\sin 2\beta$ of the CKM angle β.

For this measurement we use 347×10^6 $B\bar{B}$ pairs recorded at the $\Upsilon(4S)$ resonance by the *BABAR* detector.

6.1 Removing the Ambiguity in β Using Interference Terms

In this section we show how, using the interference between *CP*-even and *CP*-odd contributions to the decay amplitude in $B^0 \to K^+K^-K^0$ decays one can measure the *CP*-violating parameter β without the four-fold ambiguity.

Let's consider a Dalitz plot with only two resonances. Assuming no *CP* violation, we set the isobar coefficients $b = \delta = 0$ for the asymmetry in the amplitude and in the phase, respectively, as we defined in Sec. 3.6.1. Therefore the average amplitude and the average phase, respectively, are $c = \bar{c}$ and $\phi = \bar{\phi}$, such that for *CP*-even decays $A = \bar{A}$ and for *CP*-odd decays $A = -\bar{A}$.

In the case of the presence of a single partial wave (for example $S + S$-wave in the K^+K^- system), the cosine term disappears

$$|\mathcal{A}|^2 - \left|\bar{\mathcal{A}}\right|^2 = 0$$

and the total rate is

$$|\mathcal{A}|^2 + \left|\bar{\mathcal{A}}\right|^2 \;\; = \;\; 2\left(c_1^2|f_1|^2 + c_2^2|f_2|^2\right) + 4c_1c_2Re\left(e^{i(\phi_1-\phi_2)}f_1f_2^*\right)$$

which contains a "standard" Dalitz plot information on resonance fractions and interference pattern. Additional informations exist in the "sine term". When both resonances are $S(P)$-waves in the K^+K^- mass system, this terms gives:

$$2Im\left(\bar{A}A^*e^{-2i\beta}\right) \;\; = \;\; \mp\sin 2\beta\left[2\left(c_1^2|f_1|^2 + c_2^2|f_2|^2\right) \mp 4c_1c_2Re\left(e^{i(\phi_1-\phi_2)}f_1f_2^*\right)\right].$$

In this approximation (no *CP* violation) the magnitude of the time-dependent asymmetry gives additional information on fractions and phases. In the simplified notation of the "sine" and "cosine" terms of the time-dependent *CP* asymmetry S and C, respectively, which we introduced in Eq. 1.55 for the $B^0 \to [c\bar{c}]K^0$ decays become:

$$S \equiv \frac{2Im(\bar{A}A^*e^{-2i\beta})}{|\mathcal{A}|^2 + |\bar{\mathcal{A}}|^2} = \mp\sin 2\beta$$

and

$$C \equiv \frac{|\mathcal{A}|^2 - |\bar{\mathcal{A}}|^2}{|\mathcal{A}|^2 + |\bar{\mathcal{A}}|^2} = 0.$$

This means that for a single pure partial wave, we measure $\sin 2\beta$ that gives 4-fold ambiguity on β.

When waves with opposite parity are present (for example $S+P$-wave in the K^+K^- system), the "sine term" becomes

$$\begin{aligned} 2Im\left(\bar{A}A^* e^{-2i\beta}\right) &= \sin 2\beta \left[2\left(c_1^2|f_1|^2 - c_2^2|f_2|^2\right)\right] \\ &\quad + \cos 2\beta \left[4c_1c_2 Im\left(e^{i(\phi_1-\phi_2)} f_1 f_2^*\right)\right] \end{aligned}$$

and hence $|S| \neq \sin 2\beta$ and a $\cos 2\beta$ term appears in the equation. This is why interference terms of opposite CP eigenstates allow direct determination of β, instead of just $\sin 2\beta$.

6.2 The Squared Dalitz Plot

The description of the three-body phase space relies onto a set of two independent kinematic variables. The standard Dalitz plot variables are a set of two squared invariant masses of the B daughters. In order to simplify the relation describing the boundary of the Dalitz plot we choose the observables m_{12}, which is the invariant mass of the K^+K^- system, and $\cos\theta_H$, where θ_H is the helicity angle of the K^+K^- system. It is defined as the angle between K^+ and K^0 in the K^+K^- center of mass frame. The Jacobian of the transformation from 'standard' Dalitz-plot variables, Eq.(3.1), to our PDF variables

$$dm_{12}^2\, dm_{13}^2 = |J|(dm_{12})(d\cos\theta_H) \tag{6.1}$$

is given as

$$|J| = (2m_{12}) \times (2pq) \tag{6.2}$$

where p is the momentum of K_S^0 and q is the momentum of K^+, both computed in K^+K^- center of mass frame. The Jacobian of the transformation is shown in Figure 6.1.

In this way the infinitesimal element of the phase space is

$$dPS = dm \cdot d\cos\theta_H \cdot |J| \cdot d\Delta t$$

where Δt is the difference in the decay times of the B^0 and $\overline{B}^0$. The fraction of an individual resonance r is computed as

$$FF(r) = \frac{2c_r^2\,(1+b_r^2)\int dPS \cdot |f_r|^2}{\int dPS \cdot \Gamma} \tag{6.3}$$

and the asymmetry in the B^0-$\overline{B}^0$ rates (*direct CP asymmetry*) is given as

$$\begin{aligned} \mathcal{A}_{CP}(r) &= -\frac{|c_r|^2 - |\bar{c}_r|^2}{|c_r|^2 + |\bar{c}_r|^2} \\ &= -\frac{2b_r}{1+b_r^2} \end{aligned} \tag{6.4}$$

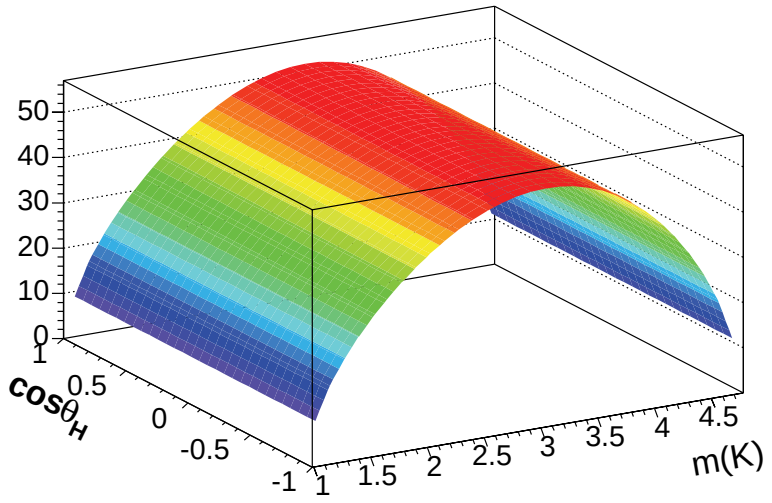

Figure 6.1: Jacobian of transformation $(m_{12}^2, m_{13}^2) \leftrightarrow (m_{12}, \cos\theta_H)$. $m_{K^+K^-}$ is given in GeV/c^2.

6.3 The Event Selection

We reconstruct $B^0 \to K^+K^-K^0$ decays by combining two oppositely charged tracks with a $K_S^0 \to \pi^+\pi^-$, $K_S^0 \to \pi^0\pi^0$ or K_L^0 candidate. The selection of the charged and neutral kaons is described in Chapter 5. In particular for this analysis, we require that the K^+ and K^- tracks have at least 12 measured DCH hits, a minimum transverse momentum of 0.1 GeV/c, and they must originate from the nominal beam spot. The tracks are then identified as kaons using a likelihood ratio that combines dE/dx measured in the SVT and DCH with the Čerenkov angle and number of photons in the DIRC, as described in 5.1.1.

Charmless decays suffer the contamination of two main sources of background:

1. random combination of particles produced in events of the type $e^+e^- \to q\bar{q}$ ($q = u, d, s, c$), when the set of mesons produced by the hadronization of the initial $q\bar{q}$ pair mimics the signal final state

2. other B decays, having a final state similar to the one considered.

In particular, B decays with higher multiplicity can give this kind of background, if one of the particles in the final state is lost in reconstruction. In this case, the energy of the

misreconstructed event is typically lower than for the well reconstructed one, so that the two components can be easily separated using the kinematic informations.

By far, the higher source of background for these decays is the first one. The branching fractions for the charmless decays we are going to consider are within $[10^{-6} \div 10^{-5}]$, and the cross section of light $q\bar{q}$ pairs at the $\Upsilon(4S)$ is comparable to $b\bar{b}$ cross section (about 1 nb). This means that background suppression has to be powerful enough to bring the signal over background ratio from $\mathcal{O}(10^{-6})$ to (at least) $\mathcal{O}(1)$. The most powerful tool to reject this background is to use the angular distribution of the particles in the final state.

6.3.1 Event Shape for Continuum Rejection

One can exploit different variables to suppress continuum production, all of them relying on the common idea that $q\bar{q}$ events show a typical jet-like structure in the $\Upsilon(4S)$ rest frame. This behaviour can be distinguished from the isotropic distribution of $B\bar{B}$ events.

We can build the following variables, using this feature:

1. The normalized second Fox-Wolfram moment [68]: $R_2 = H_2/H_0$, where H_2 (H_0) is the second order (order zero) Fox Wolfram moment, defined as

$$H_l = \sum_{i,j} \frac{|p_i| \cdot |p_j|}{E_{vis}^2} P_l(\cos\theta_{i,j})$$

   where P_l is the Legendre polynomial of order l, p_i is the momentum of the particle i, θ_{ij} the opening angle between the particles i and j and E_{vis} the measured energy of the event. Ignoring the mass of the particles in the final state, $H_0 = 1$ from four-momentum conservation. Moreover, $H_l \sim 1$ for even values of l in the case of jet-like events. Because of that, we reject those events having $R_2 \sim 1$ to suppress $q\bar{q}$ background.

2. $|\cos\theta_S|$, which quantifies the agreement between the event shape distribution and the jet-like structure. We define the sphericity tensor [69]

$$T_{\alpha\beta} = \sum_j \left(\delta_{\alpha\beta} \cdot p_j^2 - p_{j\alpha} p_{j\beta}\right)$$

   where p_j is the momentum of the particles in the event and the indices α and β run over the components of the momentum vector. Since the tensor is symmetric for the exchange of α and β, it can be diagonalized. Calling $\lambda_1, \lambda_2, \lambda_3$ the three

eigenvalues, the eigenvector associated to the smallest eigenvalue is called sphericity axis. The three eigenvectors identify the three axes of the ellipsoid representing the orientation of the two back-to-back jets. The three eigenvalues give the axis sizes. For a jet-like event, the ellipsoid collapse on the straight line given by the sphericity axis. θ_S is the angle between the sphericity axis of the B candidate decay and that one of the rest of the event (*ROE*). In the case of a jet-like event, $\cos\theta_S \sim 1$ is preferred, while $B\bar{B}$ events show a flat distribution.

3. The sphericity axis is often interchanged with the thrust axis $\hat{T}$ [70] which in practice provides nearly equivalent functionality. $\hat{T}$ is defined as the direction which maximizes the sum of their longitudinal momenta. Typical $|\cos\theta_T|$ distributions, very similar to $|\cos\theta_S|$, are shown in Fig. 6.2 for signal and background samples.

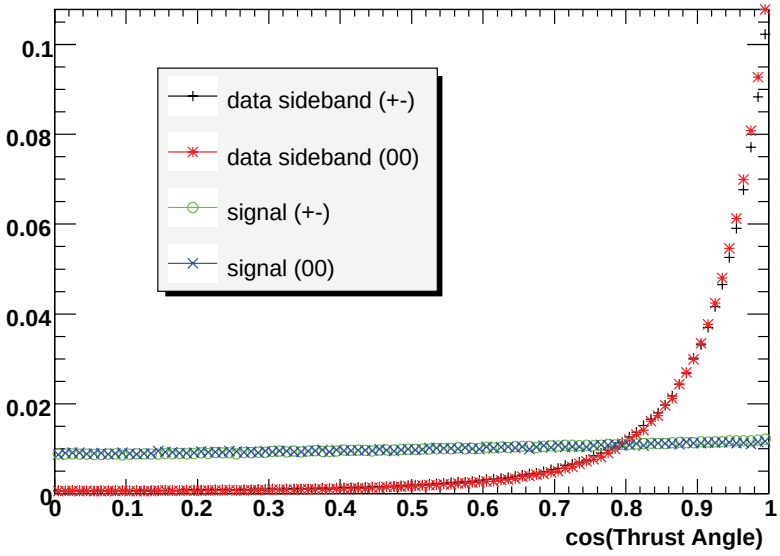

Figure 6.2: $|\cos\theta_T|$ distribution for signal Monte Carlo events and for background data (on-resonance events with $m_{\rm ES} < 5.26$ GeV/c^2). Green and blue circles represent signal Monte Carlo events of $B^0 \to K^+K^-K^0_S(\pi^+\pi^-)$ and $B^0 \to K^+K^-K^0_S(\pi^0\pi^0)$, respectively, while black and red dots represent background events of $B^0 \to K^+K^-K^0_S(\pi^+\pi^-)$ and $B^0 \to K^+K^-K^0_S(\pi^0\pi^0)$, respectively. $|\cos\theta_S|$ shape is very similar to $|\cos\theta_T|$. The distributions are normalized to the same area.

4. Legendre monomials of order zero and two, defined as

$$\begin{aligned} L_0 &= \sum_{i \in ROE} |p_i| \\ L_2 &= \sum_{i \in ROE} |p_i| \cos^2(\theta_i) \end{aligned} \tag{6.5}$$

   where p_i is the momentum of the particles of the *ROE* and θ_i is the angle between the flight direction of the particles and the sphericity axis of the *ROE*.

5. $\cos\theta_B^*$, the polar angle of the reconstructed B meson in the $\Upsilon(4S)$ center of mass system. $\cos\theta_B^*$ follows a $1 - \cos^2\theta_B^*$ distribution, while the continuum background follows a flat distribution. The distributions for $B\bar{B}$ and $q\bar{q}$ events are shown in Fig. 6.3.

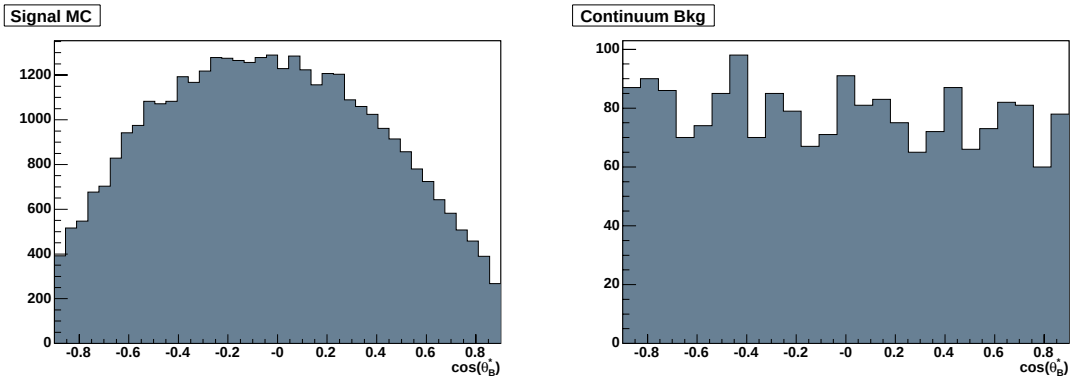

Figure 6.3: $\cos\theta_B^*$ distributions for $B\bar{B}$ Monte Carlo events (left) and $q\bar{q}$ Monte Carlo events (right)

In the analyses we present in this work we use all or a subset of these variables or a combination of them as input of a more complicated algorithm (a *Fisher discriminant* or a Neural Network). The requirements are different for each sub-mode, due to the different purities, and the best ones are chosen with an optimization together with other selection variables, that we will show in the next sections.

6.3.2 Selection of $B^0 \to K^+K^-K_S^0$

For decays $B^0 \to K^+K^-K_S^0$ with $K_S^0 \to \pi^+\pi^-$, K_S^0 candidates are formed from oppositely charged tracks with an invariant mass within 20 MeV/c^2 of the K_S^0 nominal mass [21], which correspond to about 5σ window. The K_S^0 vertexing follows the standard procedure

described in 5.2.1. The lifetime significance of the K^0_S τ/σ_τ is required to be larger than 3. We also require that the angle α between the K^0_S momentum vector and the vector connecting the B^0 and K^0_S vertices must satisfy $\cos\alpha > 0.999$.

For decays $B^0 \to K^+K^-K^0_S$ with $K^0_S \to \pi^0\pi^0$, K^0_S candidates are formed from two $\pi^0 \to \gamma\gamma$ candidates. Each of the four photons must have $E_\gamma > 0.05\,\text{GeV}$ and have a transverse shower shape loosely consistent with an electromagnetic shower[1]. Additionally, we require each π^0 candidate to satisfy $0.100 < m_{\gamma\gamma} < 0.155\,\text{GeV}/c^2$. The resulting $K^0_S \to \pi^0\pi^0$ mass is required to satisfy $0.4776 < m_{\pi^0\pi^0} < 0.5276$ GeV/c^2. A K^0_S mass constraint is then applied for the reconstruction of the B^0 candidate.

In order to reduce the background coming from misidentified charged pions, we apply *PID* requirements on the `Likelihood`-based selector, described in 5.1.1. We require both charged kaons to satisfy a `tight` requirement, except in the region of the Dalitz plot with $m_{K^+K^-} < 1.1$ GeV/c^2, which is the one dominated by the $\phi(1020)$ resonance, where we apply a looser and asymmetric requirement on the kaons: one `loose` and the other `not a pion`. We checked, using Monte Carlo samples of signal and $q\bar{q}$ and $B\bar{B}$ backgrounds, that using this looser *PID* in the $\phi(1020)$ region increases the average signal efficiency by about 13%, with a negligible change in background.

We then finally combine two selected charged kaons with the reconstructed K^0_S candidate forming the B^0 meson candidate. Using the fact that the two B mesons originate from a well defined initial e^+e^- state, the kinematics of the event can be closed. Instead of using the B mass, calculated from the reconstructed energy and momentum, as the definition variable, we use the additional information of the energy of the initial e^+e^- state (known with an uncertainty of the order 2-3 MeV) to define a set of two kinematic variables. They are the *beam energy-substituted mass* (m_{ES}) and the *energy difference* (ΔE).

The *beam energy-substituted mass* is defined as:

$$m_{\text{ES}} = \sqrt{(s/2 + \mathbf{p}_i \cdot \mathbf{p}_B)^2/E_i^2 - \mathbf{p}_B^2} \tag{6.6}$$

where $\sqrt{s}$ is the total e^+e^- CM energy, $(E_i, \mathbf{p}_i)$ is the four-momentum of the initial e^+e^- system and $\mathbf{p}_B$ is the B candidate momentum, both measured in the laboratory frame. The meaning of this variable becomes clearer if we express it in the $\Upsilon(4S)$ rest frame:

$$m_{\text{ES}} = \sqrt{(\sqrt{s}/2)^2 - {p^*_B}^2}$$

[1]The general requirements are described in Sec. 5.2.2

where p^* is the B candidate momentum in the $\Upsilon(4S)$ rest frame. Since the $\Upsilon(4S)$ mass is near the $B\bar{B}$ threshold, the center of mass momenta p^*_B of the B mesons are very small (≈ 340 MeV/c) when compared to the beam energy $\sqrt{s}$ of more than 10.5 GeV. Therefore $|p^*_B| \ll \sqrt{s}/2$, and the beam substituted mass is dominated by the beam energy resulting in a resolution of ≈ 2.6 MeV (which reflects the spread of the beam energy). Typical $m_{\rm ES}$ distribution for signal events is show in Fig. 6.30a.

Making use of energy conservation, we can also define the *energy difference* ΔE as

$$\Delta E = E^*_B - \sqrt{s}/2 \tag{6.7}$$

where E^*_B is the energy of the B candidate in the $\Upsilon(4S)$ rest frame. While $m_{\rm ES}$ variable is related to the measurement of the reconstructed momenta of the final state, ΔE depends on the reconstructed energy, the resolution of the latter depending on the reconstructed B mode. Typical ΔE distribution for signal events is show in Fig. 6.30b. This fact makes these two variables particularly suitable for those analyses having only charged tracks in the final state, as $B^0 \to K^+K^-K^0_S$ with $K^0_S \to \pi^+\pi^-$. In this case, in fact, the two variables show a negligible correlation and can be considered independent. In addition, the resolution of this variable is affected by the detector momentum resolution and by the particle identification in such a a way that a wrong mass assignment implies a shift in ΔE. Because of this, ΔE is also useful to reject $B\bar{B}$ background.

For decays involving photons in the final state, because of energy leakage effects in the calorimeter, the reconstruction of the energy of the photon can be underestimated, producing an asymmetric tail in ΔE distribution. The typical resolution for ΔE is larger than the one of $m_{\rm ES}$, being ≈ 20 MeV, and it is also larger (≈ 40 MeV) in the case of $K^0_S \to \pi^0\pi^0$ with photons in the final state.

In the analyses we will present in this work, the selection on the kinematic variables is loose, and a *sideband* region (defined as the region where the signal is almost absent) is kept in the final dataset. This allows an higher efficiency for the signal and also a background characterization using data.

For $B^0 \to K^+K^-K^0_S$ with $K^0_S \to \pi^+\pi^-$ the requirements on the two kinematic variables are:

- $m_{\rm ES} > 5.26$ GeV/c^2
- $-0.06 < \Delta E < 0.06$ GeV

For $B^0 \to K^+K^-K^0_S$ with $K^0_S \to \pi^0\pi^0$, we apply the same requirement on $m_{\rm ES}$, while we use a looser cut on ΔE because of the wide tail due to energy leakage in the calorimeter:

- $m_{\rm ES} > 5.26$ GeV/c^2
- $-0.12 < \Delta E < 0.06$ GeV

In order to suppress the high $q\overline{q}$ background we apply a preliminary selection requiring the $|\cos\theta_T| < 0.9$, which has an efficiency of about 90% on the signal events. The remaining discrimination power, related to the different topology of a $B\bar{B}$ event and $q\overline{q}$ event, is then collected in an algorithm that uses the given inputs to maximize the separation between signal and background. For $B^0 \to K^+K^-K^0_S$ we use a linear combination of the other event shape variables, called *Fisher discriminant* [71]:

$$\mathcal{F} = \sum_{i=1}^{N} \alpha_i x_i \tag{6.8}$$

The discrimination task consists of determining an axis in the R^N space of the discriminating variables such that the two classes are maximally separated. In order to apply this method, one needs to know just the mean values of each variable over the full sample, ($\bar{\mu}$), the means over signal and background separately, ($\bar{\mu}_b$, $\bar{\mu}_s$), and the total covariance matrix, $U^{b,s}_{ij}$, that characterizes the dispersion of the events relative to the center of gravity of their own sample. The distance between the projected points will naturally be maximum along the direction defined by the line between μ_b and μ_s. Then the segment $(\bar{\mu}_b, \bar{\mu}_s)$ is the projection axis. The coefficients in Eq. 6.8 could be computed from the equation:

$$\alpha_i = \sum_{j=1}^{N} (U^b + U^s)^{-1}_{ij} (\mu^b_j - \mu^s_j) \ . \tag{6.9}$$

We use four variables as input of the Fisher discriminant: $|\cos\theta_S|$ after the preliminary cut, the order zero and order two Legendre monomials L_0 and L_2 and $\cos\theta^*_B$. The distribution of the Fisher variable, for signal Monte Carlo events and for background data (taken from on-resonance events in the region $m_{\rm ES} < 5.26$ GeV/c^2, where the signal contribution is negligible) is displayed in Fig. 6.4. In this figure the shapes for signal and background both for $B^0 \to K^+K^-K^0_S(\pi^+\pi^-)$ and $B^0 \to K^+K^-K^0_S(\pi^0\pi^0)$ are shown. These distributions illustrate that they are very similar for the two decay modes. This is a consequence of the fact that the inputs use the informations of the rest of the event

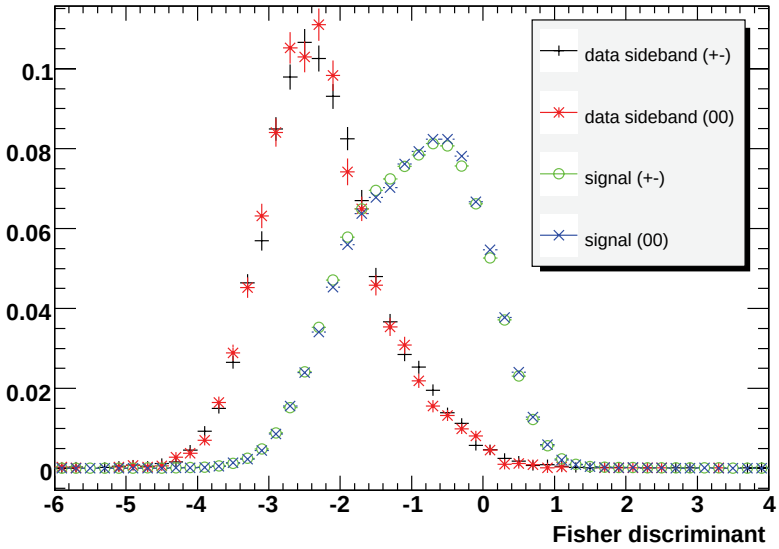

Figure 6.4: Distribution of the Fisher variable, for signal Monte Carlo events and for background data (on-resonance events with $m_{\rm ES} < 5.26$ GeV/c^2). Green and blue dots represent signal Monte Carlo events of $B^0 \to K^+K^-K^0_S(\pi^+\pi^-)$ and $B^0 \to K^+K^-K^0_S(\pi^0\pi^0)$, respectively, while black and red dots represent background events of $B^0 \to K^+K^-K^0_S(\pi^+\pi^-)$ and $B^0 \to K^+K^-K^0_S(\pi^0\pi^0)$, respectively.

(Eqn. 6.5 for example), so that the output of the algorithm does not depend much on the reconstructed decay mode.

We finally reject the events with poor Δt information, requiring $|\Delta t| < 20$ ps and $\sigma_{\Delta t} < 2.5$ ps. The r.m.s. of Δt distribution is 1.1 ps for the events which satisfy these requirements. This selection is quite standard and it is applied in almost all *BABAR* analyses devoted to the measurement of a time-dependent *CP* asymmetry.

Correlation of the Event Shape Variables with the Dalitz Plot

Usually, the information on the event shape is fully used in the maximum likelihood fit, together with the kinematic variables and the time information, as a probability density function (PDF). The necessary condition to include a variable as a factorized PDF in the likelihood function is that it is uncorrelated with the other ones.

While the event shape variables are almost uncorrelated with the kinematic variables, a correlation can arise with the Dalitz plot variables. In signal events, which are all spherical, there is not an evident correlation. As an example, we show in Fig. 6.5 the

distribution of the mean of the ratio $l_2 = L_2/L_0$, where L_0 and L_2 are the zeroth and second order Legendre monomial, for signal Monte Carlo events in different regions of the Dalitz plot. The main correlation usually arises for background events. We investigated

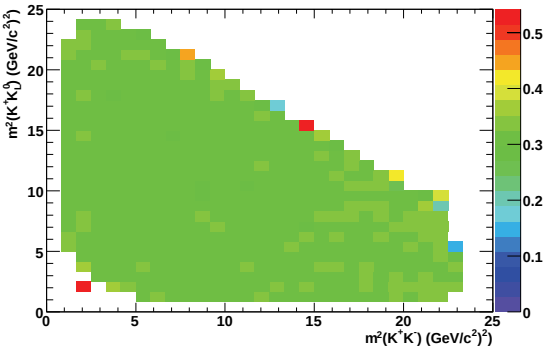

Figure 6.5: l_2 distribution variation in the Dalitz plot for signal Monte Carlo events. The color represent the mean of the l_2 distribution in each bin of the Dalitz plot.

if, after applying a tighter cut on $|\cos\theta_S| < 0.7$ (i.e. removing a large number of jet-like events from the dataset), the correlation with the Dalitz plot position is reduced to acceptable values.

In Fig. 6.6 we show the scatter plot of l_2 vs. the Dalitz plot variables $m(K^+K^-)$ and $\cos\theta_H$. While there is no evidence of a correlation with the K^+ K^- invariant mass, a pattern can be seen with respect to $\cos\theta_H$.

We further check this correlation looking at the variation of l_2 shape across the Dalitz plot. In Fig. 6.7 we show the relative variation of the mean and of the r.m.s. for the l_2 distribution in bins of the Dalitz plot for sideband events. These plots show that the shape for the on-resonance events is more jet like along the contour of the Dalitz plot, while it is more spherical in the central part ($l_2 < \overline{l_2}$). Also the resolution of this variable is not constant in the Dalitz plot. In order to have a more quantitative estimate of the variation of l_2 distribution we define the statistical significance of the compatibility of the mean of the l_2 in a given bin i, m_i, with the average mean in the whole Dalitz plot, $\bar{m}$, with the quantity:

$$N(\sigma) = \frac{m_i - \bar{m}}{r.m.s._i} \cdot \sqrt{N_i}\ , \tag{6.10}$$

where N_i is the number of entries in the bin i. In Fig. 6.8 the distribution of this quantity across the Dalitz plot for background events is shown. As this figure shows, even if the

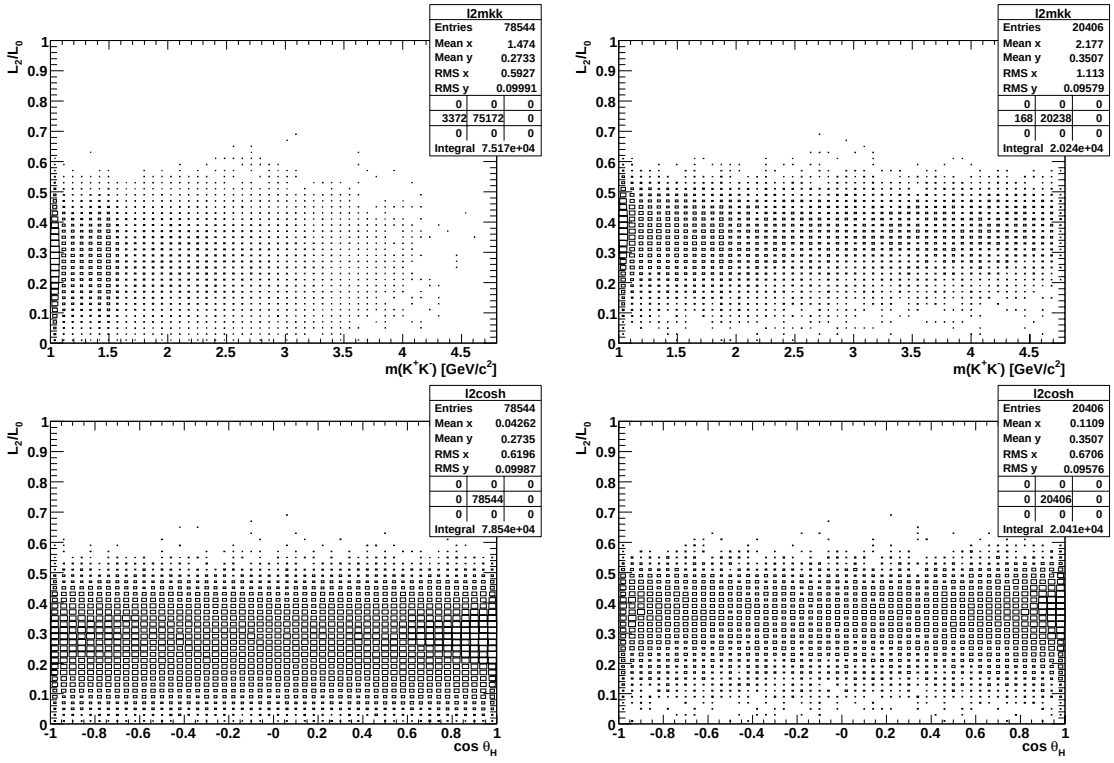

Figure 6.6: Scatter plot of l_2 vs. $m(K^+K^-)$ (top plots) and $\cos\theta_H$ (bottom plots), for signal Monte Carlo events (left) and continuum events from sidebands of on-resonance data.

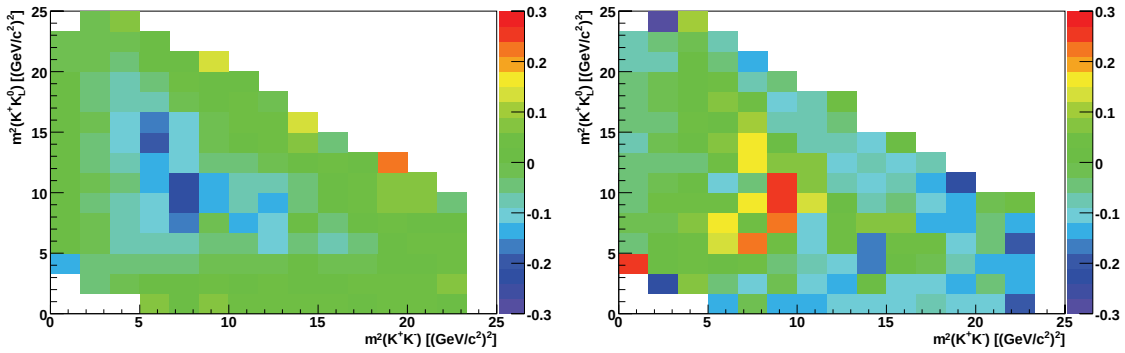

Figure 6.7: Relative variation of l_2 distribution in the Dalitz plot for on resonance events in sideband region. Left: mean relative variation. Right: r.m.s. relative variation.

most of the events on the contour of the Dalitz plot are statistically consistent with the average mean of l_2, the central bins are up to 4 σ away from the mean. This force us not to include this variable in the likelihood, but only apply a cut on it. We require $\mathcal{F} > -2.5$ for both $B^0 \to K^+K^-K^0_S(\pi^+\pi^-)$ and $B^0 \to K^+K^-K^0_S(\pi^0\pi^0)$. This selection has been

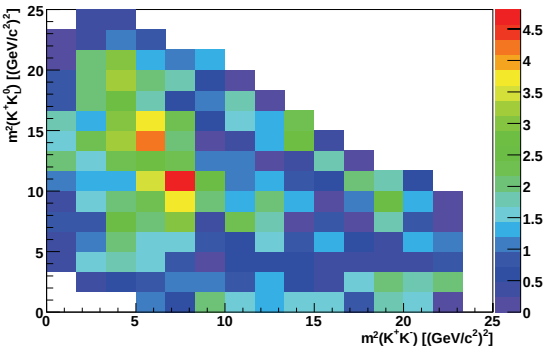

Figure 6.8: "Statistical significance" of the compatibility of the mean of l_2 distribution across the Dalitz plot with the average mean. The color represents the $N(\sigma)$ compatibility, as defined in Eq. 6.10, for on resonance events in the sideband region.

chosen in such a way to maximize the statistical significance of the signal, defined as in Eq. 5.2.

Best Candidate Selection

After applying the full selection to $K^+K^-K^0_S$ sub-modes, we select 3091 events for $B^0 \to K^+K^-K^0_S(\pi^+\pi^-)$ and 1599 events for $B^0 \to K^+K^-K^0_S(\pi^0\pi^0)$.

The event multiplicity for $K^+K^-K^0_S(\pi^+\pi^-)$ mode is 1.004 for signal events, while for $K^+K^-K^0_S(\pi^0\pi^0)$ is 1.10. Where more than one B^0 candidate passes the selection criteria in a given event, the best candidate is taken to be that one with a $\pi\pi$ invariant mass closest to the K^0_S nominal mass [21]. If multiple candidates share the best K^0_S candidate, the B^0 candidate with kaons passing the tightest PID selector is chosen. In case any multiple candidate still remains, the B^0 candidate with the best vertex probability from the B kinematic fit is selected.

Study of Misreconstructed $K^+K^-K^0_S$ Events

In a sample of simulated signal events, we associate reconstructed tracks with their Monte Carlo partners. These candidates can be classified into radiative and signal-cross-feed events:

- events that have all candidates properly matched, but with a not reconstructed photon from QED final state radiation, so the total combination fails the truth matching,

- all daughters with correct PID, but at least one of them coming from the other B meson,
- at least one daughter with incorrect PID taken from the other B meson.

The first group has very signal-like $m_{\rm ES}$ and ΔE distribution and it is evenly distributed across the Dalitz plane. We merge these candidates with the properly matched signal events. The other two groups (defined as Self Cross Feed or SXF) have continuum-like distributions of $m_{\rm ES}$ and ΔE and pile up in the corners of the Dalitz plot. Hence, to remove a possible bias on our measurement we apply the cuts on the kinematic variables introduced in Sec. 6.3.2, which significantly reduce the number of these events (to $\sim 11\%$) while retaining almost all truth-matched signal events ($\sim 97\%$). The final breakdown of the non-truth matched events in the $K^+K^-K^0_S(\pi^+\pi^-)$ sub-mode is given in Table 6.1. Since the fraction of cross feed events in signal decays is smaller than 0.4%, we do not include these events in the nominal fit.

	fraction of non-truth matched events	fraction of all events
all non-truth matched	100%	4.6%
radiative	92%	4.3%
SXF (correct PID)	7%	0.3%
SXF (wrong PID)	1%	0.02%

Table 6.1: Breakdown of the non-truth matched events in the $K^+K^-K^0_S(\pi^+\pi^-)$ mode.

Misreconstructed signal is much more common in the $K^+K^-K^0_S(\pi^0\pi^0)$ mode, due to large number of fake K^0_S candidates coming from a wrong combination of photons. The breakdown of misreconstructed events is given in Table 6.2. At high values of $m_{K^+K^-}$, the K^0_S is soft, leading to a high fraction of misreconstructed events. The SXF fraction in bins on the square Dalitz Plot is shown in Fig. 6.9.

	fraction of non-truth matched events	fraction of all events
all non-truth matched	100%	29%
radiative	11%	3.2%
SXF (correct PID)	89%	26%
SXF (wrong PID)	0.1%	0.03%

Table 6.2: Breakdown of the non-truth matched events in the $K^+K^-K^0_S(\pi^0\pi^0)$ mode.

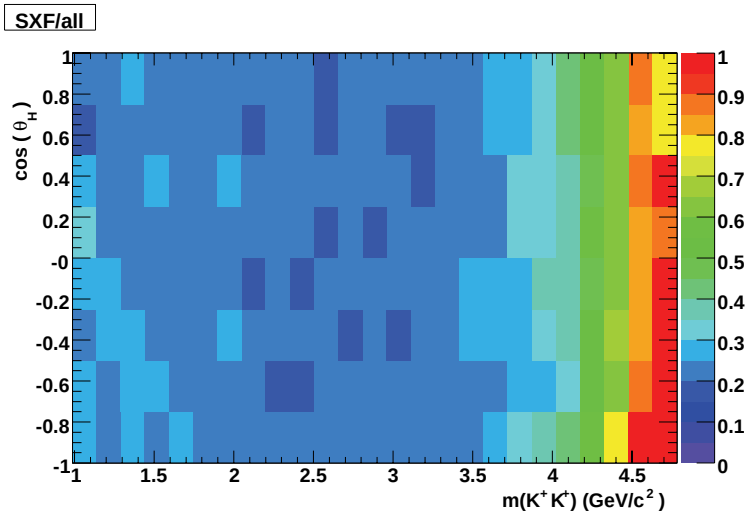

Figure 6.9: Self cross feed fraction in the $K^+K^-K^0_S(\pi^0\pi^0)$ mode: the number of misreconstructed events divided by the total number of reconstructed events in signal MC. The fraction is fairly constant except at high values of $m_{K^+K^-}$, where they are the majority.

6.3.3 Selection of $B^0 \to K^+K^-K^0_L$

In order to reconstruct a $B^0 \to K^+K^-K^0_L$ candidate, we select a pair of charged tracks of the event and apply to them the same PID requirements to suppress the pion contribution. We then combine this pair of tracks to a K^0_L candidate to form the B^0. We identify a K^0_L candidate either as a cluster of energy deposited in EMC or a cluster of hits in two or more layers of the IFR, not associable with any charged track in the event (as described in Sec. 5.3).

Because of the presence of a K^0_L in the final state, the kinematic of the B meson cannot be closed: only K^0_L flight direction is measured in the IFR, while the energy measured in the EMC is not calibrated for a hadron. The procedure in this case is to impose a mass constraint to the B mass, in order to calculate the K^0_L momentum from the momentum of the other B daughters (the K^+K^- pair). This is achieved using the relation

$$M_B^2 = \left(E_{K^+K^-} + \sqrt{p^2_{K^0_L} + m^2_{K^0_L}}\right)^2 - |p_{K^+K^-} + p_{K^0_L}|^2. \tag{6.11}$$

Applying this B mass constraint, we lose one of the two kinematic variables ($m_{\rm ES}$), but we calculate the other one using the computed K^0_L momentum (ΔE). Since the ΔE variable is evaluated after the B mass constraint, its shape is $m_{\rm ES}$-like. In addition, it exhibits a very good resolution (about 3 MeV (4 MeV) for EMC (IFR) candidates). The difference between EMC and IFR is produced by the different angular resolution of the two cases. ΔE is peaked at zero for signal events, while it exhibits a phase space distribution ranging to larger values for events coming from continuum production. ΔE distribution for $K^+K^-K^0_L$ signal events is shown in Fig. 6.32.

The fact that $B^0 \to K^+K^-K^0_L$ decays have only one kinematic variable reduces the discrimination power against $q\overline{q}$ background. For this reason, the selection of the events for $B^0 \to K^+K^-K^0_L$ has been optimized independently from $B^0 \to K^+K^-K^0_S$. We require $\Delta E < 30$ MeV, which is a good compromise between a tight cut (to remove the large background pollution) and the need of a sufficiently wide sideband region (to characterize the background).

As it has been described in Sec. 5.4, the separation between photons and K^0_L candidates in the EMC become worse at low momenta of the neutral cluster. $K^+K^-K^0_L$ candidates with slow K^0_L daughters correspond to events with higher K^+K^- invariant mass. For this reason we choose to optimize the selection separately in the lower and higher invariant $m(K^+K^-)$ regions. For consistency with $B^0 \to K^+K^-K^0_S$ selection we divide the sample

in $m(K^+K^-) < (>)1.1$ GeV/c^2, the lower being dominated by the $\phi(1020)$ resonance.

In order to suppress the $q\overline{q}$ background we use only the $|\cos\theta_S|$ variable in the lower mass region, while we use both $|\cos\theta_S|$ and the ratio $l_2 = L_2/L_0$ of the Legendre monomials elsewhere.

We also require, as it was done for $B^0 \to K^+K^-K^0_S$, $|\Delta t| < 20$ ps and $\sigma_{\Delta t} < 2.5$ ps.

Finally, we maximize the purity of the K^0_L sample optimizing the selection of the K^0_L. This consists of two main issues: the missing momentum requirement (valid for both EMC and IFR candidates) and the PID of the K^0_L based on the cluster shape (only for EMC events), whose implementation has been described in 5.4.2. We will discuss them in the following sections.

Missing Momentum of the Event

In order to clean the sample, one can tune the selection in such a way that the transverse missing momentum of the entire event is consistent with the K^0_L momentum calculated for the candidate. The missing momentum is calculated from all charged tracks and EMC clusters (not including the K^0_L candidate) of the event and projected onto the axis of the K^0_L candidate in the transverse plane. The expected transverse momentum of the K^0_L is then subtracted from the projection. We will refer to this variable as p^T_{miss}. The reason we use only the transverse component of the missing momentum is to minimize the influence of the EMC endcap leakage. The pollution coming from semi-leptonic B decays is reduced by using the projection onto the direction of the K^0_L candidate: since missing momentum originating from semi-leptonic decays is uncorrelated to the direction of the K^0_L candidate, it will not bias the projected missing momentum (it can just decrease its resolution). Fig. 6.10 shows the distribution of this projected missing momentum for signal MC events and on-resonance sideband data for background. The discriminating power of the variable is less for the IFR because there is already significantly less background in this sample than for the EMC. Also, incorrectly identifying an EMC cluster as a K^0_L will alter the calculation of the missing momentum in the event, thus accentuating the effect. Since IFR clusters are not used in the missing momentum calculation, the distribution for signal events peaks at 0 for IFR-only candidates, while it is shifted for EMC candidates.

Another useful variable, correlated to the missing momentum, is the missing energy of the event. We define the variable ΔE_{vis} as the difference between the sum of the measured energy of all charged tracks and all neutrals of the event (not including the

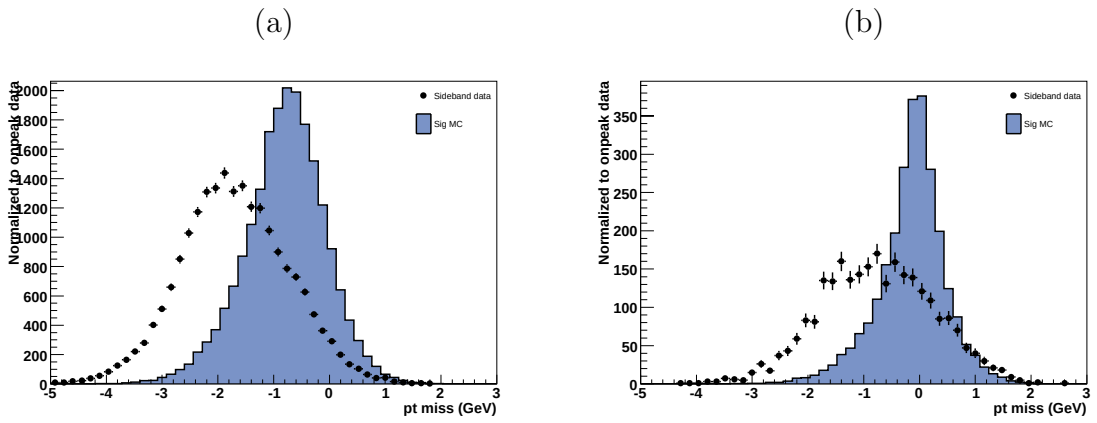

Figure 6.10: The projected missing transverse momentum minus the expected value for a K_L^0 from signal MC events (solid histogram) and sideband data (dots). (a) EMC candidates. (b) IFR candidates.

K_L^0 candidate) (E_{vis}) and the sum of the energies of the two charged kaons which come from the reconstructed B decay. Since for a photon the energy of the cluster is correctly calibrated, while for a K_L^0 it is not, the mean value of the distribution for signal is shifted with respect to the background one. This can be seen in Fig. 6.11a.

Last, we use the opening angle between the missing momentum and the K_L^0 direction in the laboratory frame. This variable is expected to peak at small values for true K_L^0's, while it presents a tail at higher angles for fake K_L^0's (Fig. 6.11b).

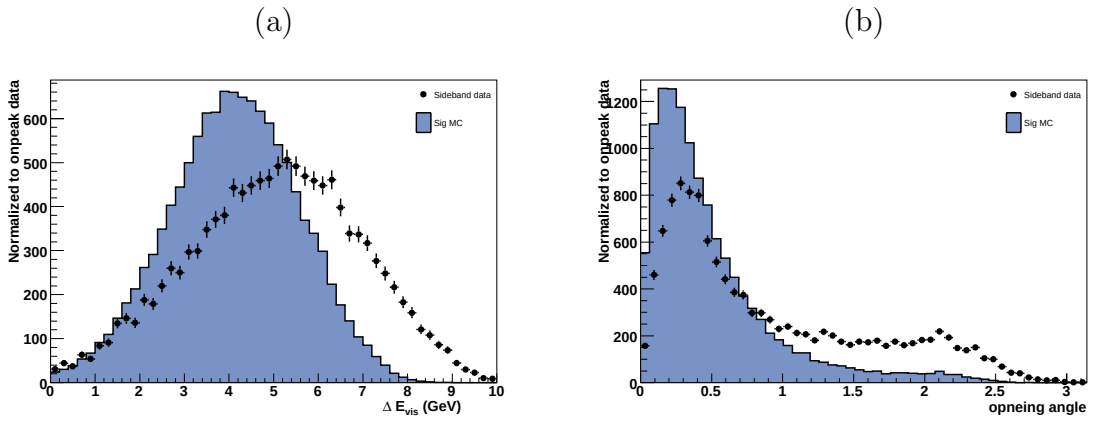

Figure 6.11: (a) Difference between the total measured energy of the event and the sum of the reconstructed kaons from the B decay (referred as ΔE_{vis}). (b) Opening angle between the missing momentum and the K_L^0 direction in the laboratory frame. (Since for this variable the shape of EMC and IFR candidates is quite similar, the plot show the sum of the two categories).

Since these three variables have a large correlation (see Fig. 6.12), we define a Fisher discriminant [71] based on these three variables to account for the correlations. We train two separate Fisher discriminants for EMC and IFR-only candidates. We use signal and continuum Monte Carlo events as training samples for signal and background, respectively. The functional relation defining the Fisher discriminant is given by

$$\mathcal{F} = a_0 + a_1 p^T_{\rm miss} + a_2 \Delta E_{\rm vis} + a_3 angle(p_{\rm miss} - K^0_L) \tag{6.12}$$

where the coefficients for EMC and IFR discriminant are given in Table 6.3.

Coeff	EMC	IFR
a_0	4.2326	3.48184
a_1	1.03421	1.45664
a_2	-0.341054	-0.222554
a_3	-0.712522	0.0797307

Table 6.3: Coefficient of the linear Fisher discriminant of K^0_L missing momentum defined in Eq. 6.12.

We validate the output using an independent sample of signal Monte Carlo events and sideband data as background. In Fig. 6.13 we show the distribution of the output

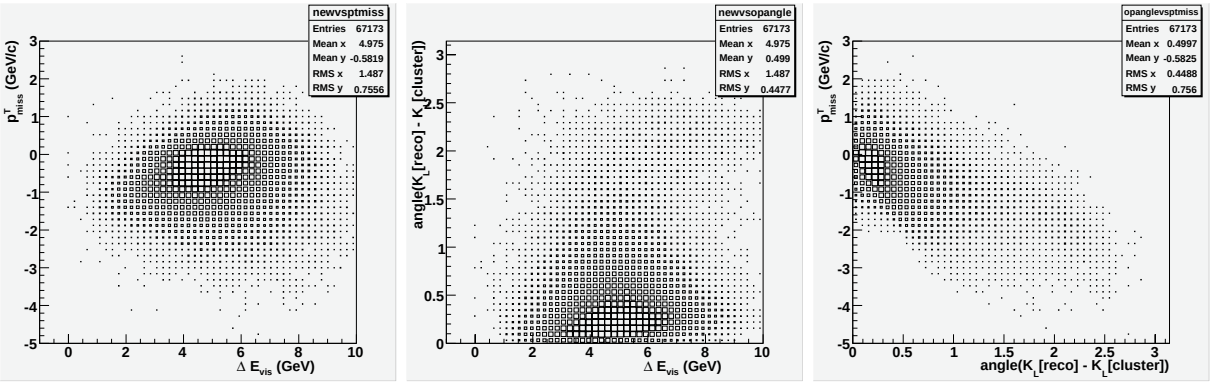

Figure 6.12: Correlation between the missing momentum variables entering the Fisher discriminant. Left: ΔE_{miss} vs. p^T_{miss}. Center: ΔE_{miss} vs. opening angle between missing momentum and K^0_L direction. Right: opening angle between missing momentum and K^0_L direction vs. p^T_{miss}.

of the trained linear Fisher discriminant for EMC and IFR-only events for both signal MC and sideband data events. As a final concern, we observe that a cut on a variable related to the missing momentum of the event could in principle introduce a bias in the

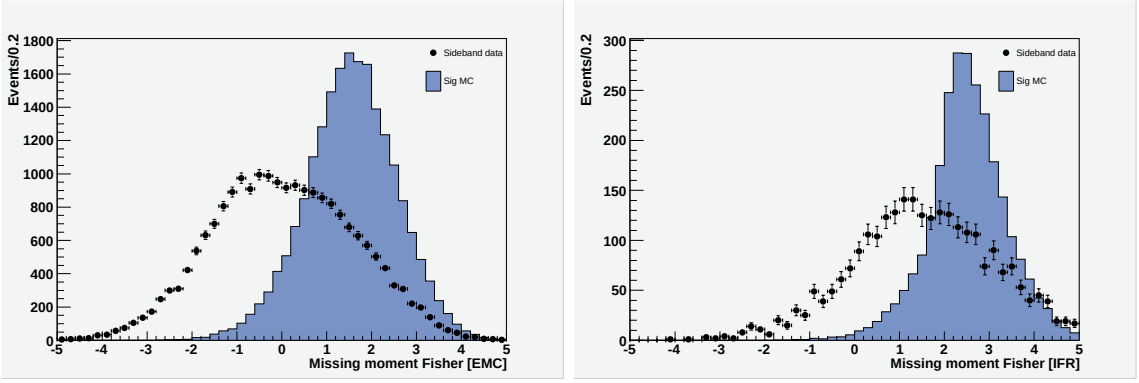

Figure 6.13: Distribution of the output of the Fisher discriminant for EMC candidates (left) and IFR-only candidates (right). Histogram represent signal MC events, while dots represent background (sideband data).

lepton based flavour tagging: if we require a large missing momentum in the event, the probability that this event contains a semi-leptonic decay would increase. Fig. 6.14 shows the leptonic tagging fraction as a function of the cut on these variables: there is a wide range for the variable where the fraction does not change. We will check that the final cut on the Fisher does not bias the leptonic tagging fraction (Section 2.1). We optimize the

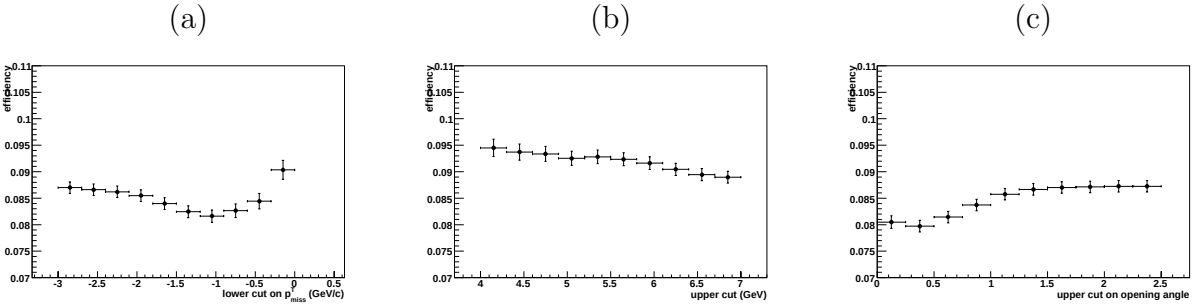

Figure 6.14: Fraction of the leptonic tagging category as a function of (a) the cut on p^T_{miss}, (b) ΔE_{vis}, (c) opening angle between missing momentum of the event and K^0_L direction.

lower cut on the Fisher maximizing the statistical significance, (as defined in Eqn. 5.2). In Fig. 6.15 we show the statistical significance as a function of the lower cut on the Fisher for EMC or IFR candidates. For both EMC and IFR samples we choose a cut of Fisher>1, having an efficiency of about 86% on signal events, while rejects 65% of the continuum.

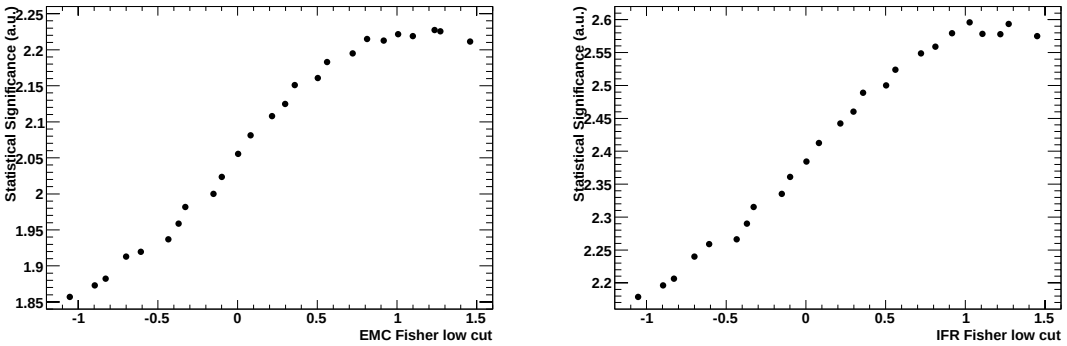

Figure 6.15: Statistical significance as a function of the lower cut on the output of missing momentum Fisher. Left: EMC Fisher. Right: IFR Fisher.

PID Selection for EMC K_L^0

In order to increase the purity of the selected sample, we also apply the developed PID algorithm for the EMC K_L^0 candidates based on the shower cluster shape (`Totti selector`, Sec. 5.4.2). This selector is very useful to reject the main background in the EMC, due to misreconstructed photons (because it has been trained in different kinematic bins), in particular for K_L^0's coming from $B^0 \to K^+K^-K_L^0$ decays, which cover a wide momentum spectrum.

After the rest of the selection for $K^+K^-K_L^0$ candidates has been fixed, the requirement on this variable is chosen maximizing the sensitivity to β, separately in the lower and higher K^+K^- invariant mass, using a toy Monte Carlo technique. With this procedure, we take into account both the statistical uncertainty and the main systematic one, which is the poor knowledge on the *CP* asymmetry of the main $B\bar{B}$ backgrounds (see Sec. 6.4.2). The total uncertainty on β, evaluated adding in quadrature the statistical and systematic contributions, is shown in Fig. 6.16 as a function of the lower cut on the `Totti` selector for $m(K^+K^-) < 1.1$ GeV/c^2.

The optimal cut on the output of `Totti` selector, $\mathcal{T}$, is found to be:

- $m(K^+K^-) < 1.1$ GeV/c^2: $\mathcal{T} > 0.465$
- $m(K^+K^-) > 1.1$ GeV/c^2: $\mathcal{T} > 0.500$

After the whole selection, the average efficiency is about 25% for events in the lower mass region, while it is about 10% in the higher mass region. The main difference in

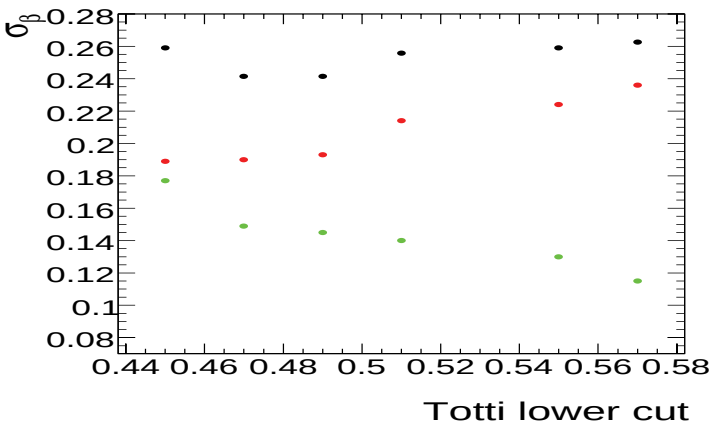

Figure 6.16: Statistical error on β as a function of the lower cut on the output of `Totti` selector $\mathcal{T}$ (red), systematic uncertainty due to the poor knowledge of the *CP* asymmetry of the $B\bar{B}$ background (green). Black is the total uncertainty evaluated by summing up in quadrature the statistical and the systematic uncertainty (black). This optimization is for events with $m(K^+K^-) < 1.1$ GeV/c^2.

the two selections comes from the quite different PID purity for the charged and neutral kaons and the different requirements on the event shape, as can be seen in Table 6.4.

Best Candidate Selection

After the described selection, 22341 $K^+K^-K^0_L$ events survive. The final multiplicity is higher than in the $K^+K^-K^0_S$ modes. In fact we find about 2.3 B^0 candidates reconstructed per event in a sample of signal Monte Carlo decays. This large combinatorial requires an accurate best-candidate selection. First, the best K^0_L is chosen using the criteria based on EMC and IFR quality:

1. if multiple EMC candidates are present, select the one with the highest cluster energy;

2. if multiple IFR candidates are present, select the one with the largest number of layers;

3. if both an EMC and IFR candidate pass the relative filters, the EMC candidate is selected, as the EMC has a better K^0_L direction resolution than the IFR.

A small fraction (4.8%) of the events has multiple candidates after the best K^0_L selection, due to different combinations of K^+K^-. Then, the best B candidate is chosen as the one

Selection	$m_{K^+K^-} < 1.1\,\mathrm{GeV}/c^2$**:** ε (%)	$m_{K^+K^-} > 1.1\,\mathrm{GeV}/c^2$**:** ε (%)
reco	62.4 ± 0.2	66.5 ± 0.2
$E_{\mathrm{cal}} > 200$ MeV	89.2 ± 0.1	88.1 ± 0.1
$\lvert\cos\theta_{\mathrm{SPH}}\rvert < 0.8$	80.1 ± 0.1	-
$\lvert\cos\theta_{\mathrm{SPH}}\rvert < 0.7$	-	69.2 ± 0.1
$l_2 < 0.35$	-	80.0 ± 0.1
PID: Tight × Tight	94.7 ± 0.1	-
PID: NotAPion × Loose	-	63.6 ± 0.1
$\lvert\Delta t\rvert < 20$ ps	96.8 ± 0.1	98.1 ± 0.1
$\sigma(\Delta t) < 2.5$ ps	95.1 ± 0.1	97.9 ± 0.1
$\mathcal{T} > 0.465$	83.0 ± 0.1	-
$\mathcal{T} > 0.50$	-	68.1 ± 0.1
Fisher (EMC,IFR) > 1	85.9 ± 0.1	85.6 ± 0.1
-0.01 $< \Delta E <$ 0.03 GeV	88.0 ± 0.1	87.8 ± 0.1
Total efficiency	24.9 ± 0.1	9.5 ± 0.1

Table 6.4: Average selection efficiency for $B^0 \to K^+K^-K^0_L$ signal Monte Carlo events. Left: efficiency for lower mass region ($m(K^+K^-) < 1.1$ GeV/c^2). Right: efficiency for higher mass region. The efficiency of each cut is evaluated with respect to the previous cut.

with the best vertex probability, associated with the B kinematic fit.

We describe the sources of remaining misreconstructed events in the next section.

Study of misreconstructed $K^+K^-K^0_L$ Events

As we have shown in Sec. 6.3.2, we study the breakdown of misreconstructed events in the Dalitz plot. While for the tracks the Monte Carlo truth association is done in the usual way, this is not possible for K^0_L, because the associator algorithm is based on the kinematics and the reconstructed K^0_L has not a defined momentum before the B mass constraint. So we use a criterion based only on the direction of the reconstructed K^0_L. We define a reconstructed K^0_L truth-matched if its direction lies inside a cone which has its axis along the direction of the Monte Carlo generated K^0_L, with an opening angle of 5σ, where σ is the angular resolution of the EMC. The angular resolution of the EMC is a quantity which varies as a function of the K^0_L momentum (Eq. 5.5). Since this is the nominal angular resolution for a photon at a polar angle of 90°, this criterion could be very inefficient for K^0_L candidates. We check that requiring 5 σ or 7 σ does not change the fraction of "truth-matched" K^0_L significantly. We distinguish four categories of events:

- truth-matched events

- non truth-matched events with one of the charged kaons taken from the decay products of the other B meson. This happens for 0.5% of the events, mostly in the corners of the Dalitz plot (where the kaons have lower momentum).

- non truth-matched events with a wrong K^0_L. This constitutes the most of self cross feed: 4.5% of the events. This happens mostly in the corner of high K^+K^- invariant mass. Even in the case of the neutral K^0_L's, the separation from background get worse when the kaon is slow.

- non truth-matched events excluding the previous cases. This includes the case where one or two charged kaons have the wrong PID. This accounts for a very small fraction of self cross feed (0.5%).

The distribution of these different categories of self cross feed over the Dalitz plot are shown in Fig. 6.17. In Fig. 6.18 the ΔE distributions for truth-matched events and for mis-reconstructed events of the three different categories is shown.

6.3.4 Efficiency Over the Dalitz Plot and Related Systematics

In Sec. 6.3.2 and 6.3.3 we have reported the selection criteria for reconstructing $B^0 \to K^+K^-K^0_S$ and $B^0 \to K^+K^-K^0_L$ candidates, respectively. These criteria are chosen in order to maximize the sensitivity to the *CP* asymmetry parameters, reducing the main backgrounds. The efficiency of the final selection is studied across the squared Dalitz plot ($m_{K^+K^-}$ and $\cos\theta_H$) using a signal Monte Carlo sample with a flat Dalitz distribution, in order to equally populate all the regions of the phase space. The squared Dalitz plot is binned in 20 bins in $m_{K^+K^-}$ and 20 bins in $\cos\theta_H$.

For the systematics evaluation due to tracking and K^0_S and K^0_L reconstruction, the efficiency over the Dalitz plot has to be weighted according to the tracking efficiency and K^0_S and K^0_L reconstruction.

In particular, we have studied possible differences between data and Monte Carlo efficiencies for K^0_L reconstruction using data control samples (see Sec. 5.5). The corrections, computed as a function of the momentum and the direction of the K^0_L, are translated as a function of the position in the Dalitz plot. The result is the distribution of the corrections in Fig. 6.19. We then apply the corrections to the efficiency distribution over squared Dalitz plot obtained from Monte Carlo.

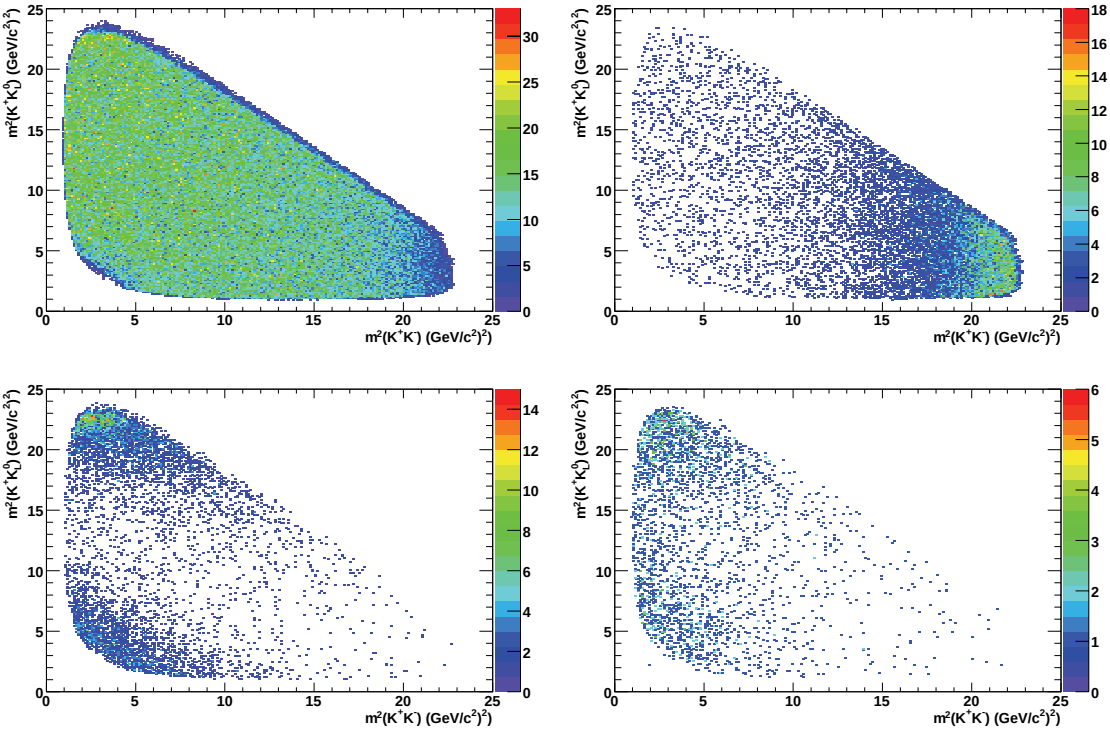

Figure 6.17: Distribution of signal Monte Carlo events for truth-matched events (top left), for self cross feed events with a mis-ID K^0_L (top right), with one misi-ID K^+ (bottom left) and the other cases, including one or both charged kaons with the wrong PID (bottom right).

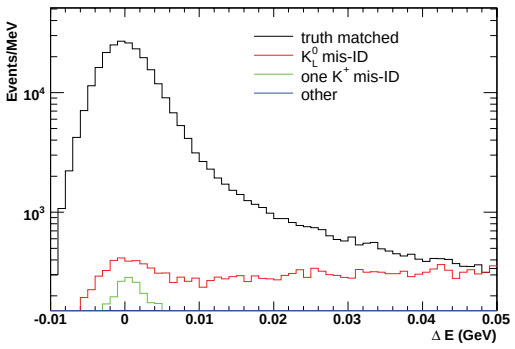

Figure 6.18: ΔE distribution of truth-matched events and self cross feed events. The other component of the self cross feed is too small to be visible in this plot.

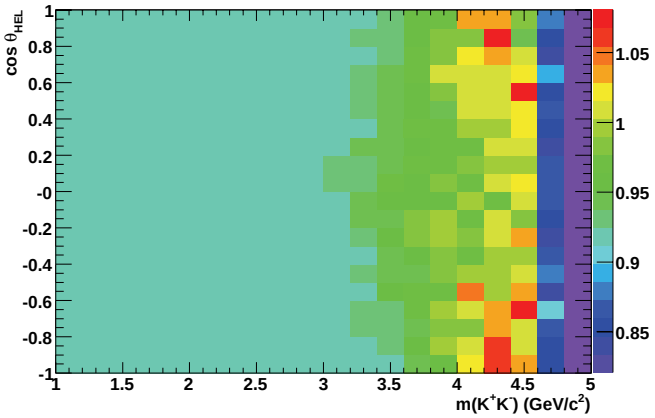

Figure 6.19: Efficiency corrections $\varepsilon^{\rm data}_{K^0_L}/\varepsilon^{\rm MC}_{K^0_L}$ as a function of Dalitz plot position, as evaluated from $D^0 \to K^0_L\pi^+\pi^-$ control sample.

The distributions of corrected efficiencies in bins of the squared Dalitz plot are shown in Fig. 6.20 together with the distribution of errors due to finite Monte Carlo statistics and PID efficiency corrections, for $B^0 \to K^+K^-K^0_S(\pi^+\pi^-)$, $B^0 \to K^+K^-K^0_S(\pi^0\pi^0)$ and $B^0 \to K^+K^-K^0_L$.

6.4 Background in the Dalitz Plot

In order to perform the maximum likelihood fit, which is described in Sec.6.5, we parameterize the shape of the Dalitz plot for the different categories of background events. We model the probability density function of Dalitz plot for continuum and $B\bar{B}$ background as a variable-binning 2D histogram PDF. The non uniform binning is made in order to have higher granularity around the main expected resonances: values of $m_{K^+K^-}$ where the $\phi(1020)$ and the D^0 peak, and the region around $|\cos\theta_H| \approx 1$.

6.4.1 Continuum Background

We fill the 2D histogram with events taken from $m_{\rm ES}$, ΔE sidebands for $B^0 \to K^+K^-K^0_S$ and from ΔE sidebands for $B^0 \to K^+K^-K^0_L$.

The binning of the histogram and the PDF for continuum $B^0 \to K^+K^-K^0_L$, which has the highest background, is shown in Fig. 6.21. In Fig. 6.22 we show the projection of the 2D histogram on $m_{K^+K^-}$ and $\cos\theta_H$.

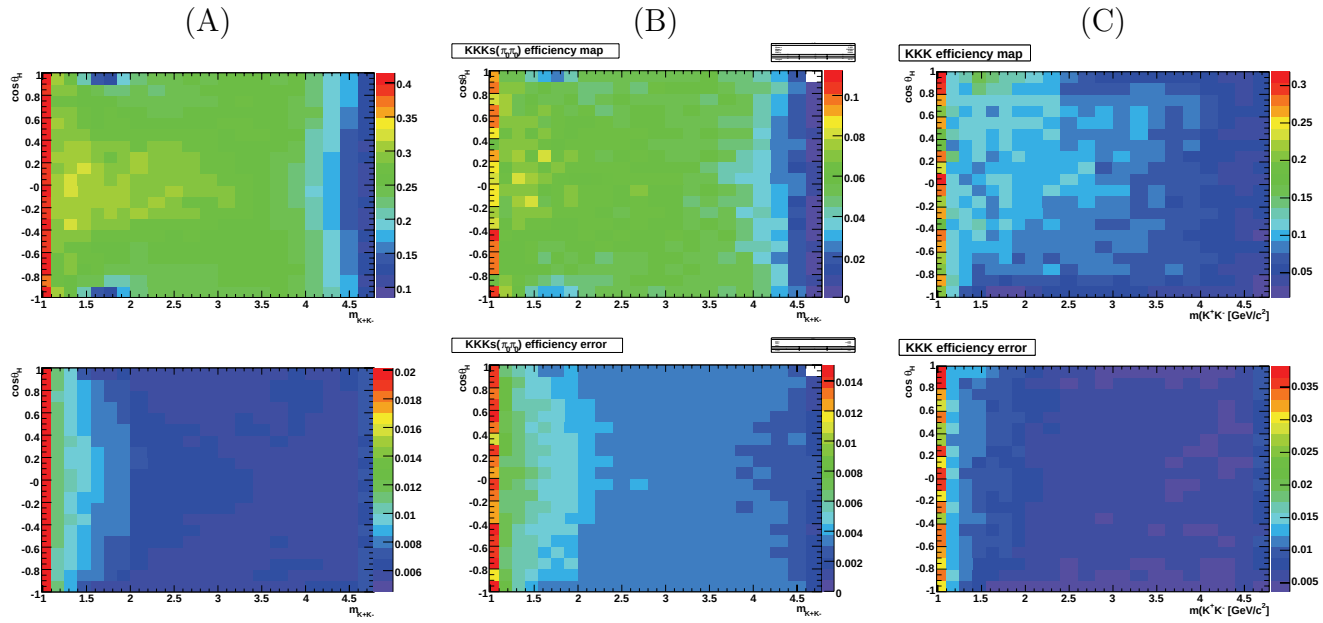

Figure 6.20: Top: efficiency variation across the squared Dalitz plot for: (A) $B^0 \to K^+K^-K^0_S(\pi^+\pi^-)$ events. (B) $B^0 \to K^+K^-K^0_S(\pi^0\pi^0)$ events. (C) $B^0 \to K^+K^-K^0_L$ events. Bottom: for the same set of candidates, the uncertainty on the efficiency due to finite Monte Carlo statistics and PID efficiency corrections.

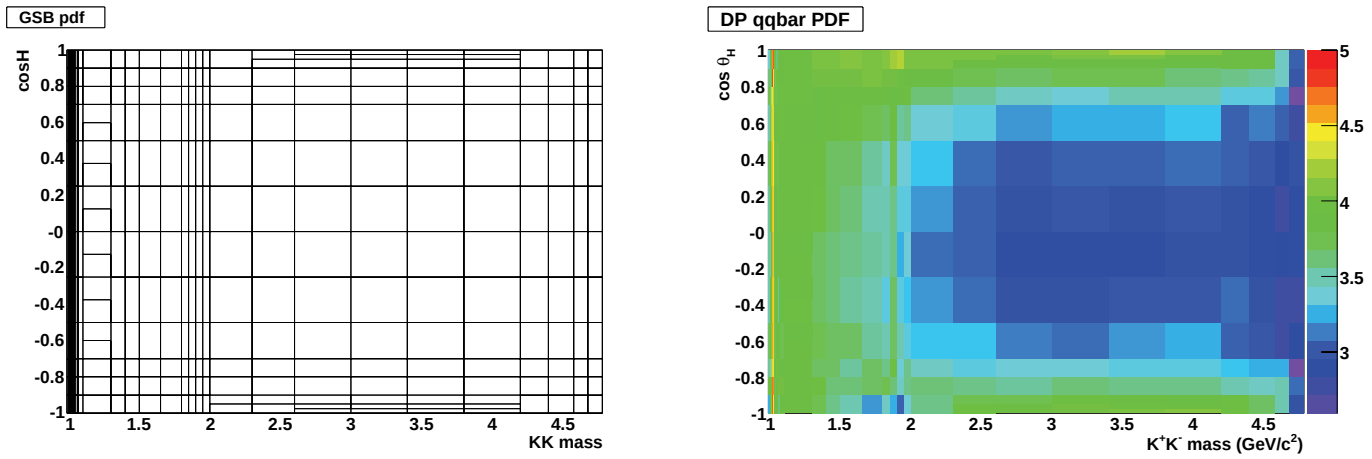

Figure 6.21: Continuum background squared Dalitz plot PDF. The model is a 2D histogram PDF with finer binning around the main structures of the Dalitz plot (left). The weights come from the histogram filling with the on resonance ΔE sideband of $B^0 \to K^+K^-K^0_L$, shown on a $\log_{10}$ scale (right).

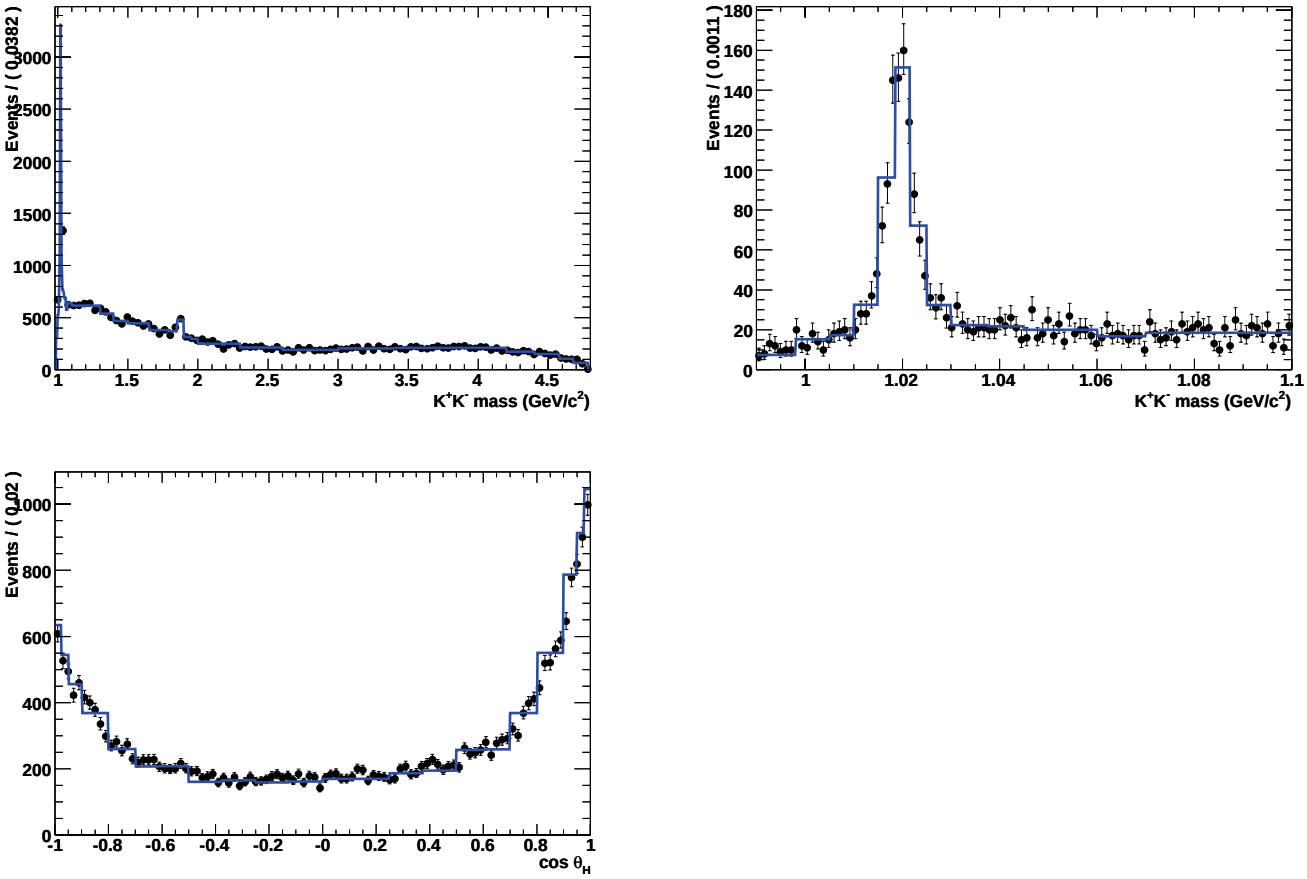

Figure 6.22: Projections of the continuum background 2D histogram PDF shown in Fig. 6.21. The dots are the on resonance sideband data for $B^0 \to K^+K^-K^0_L$, while the line is the PDF projection. Top: K^+K^- invariant mass projection in the whole spectrum (left) and . a zoom in the $mKK < 1.1$ GeV/c^2 region showing the finer binning around the $\phi(1020)$ peak (right). Bottom: $\cos\theta_H$ projection.

6.4.2 $B\bar{B}$ Background

Another source of background comes from other decays of B mesons, which can mimic a $B^0 \to K^+K^-K^0$ decay, if they contain the same three particles of the signal in the final state, and at least another particle, having low momentum, which is lost in reconstruction. In order to identify the complete list of these decays, we apply our reconstruction criteria on a sample of generic $B\bar{B}$ decays, simulated using Monte Carlo technique. With the knowledge or a reasonable assumption of the branching fraction of these decay modes, we can estimate the breakdown of the different decays different from signal one into our final dataset.

Charmless B Decays

Background from other charmless B decays for $B^0 \to K^+K^-K^0$ consist of $B^0 \to K^+K^-K^0h$, where h is a charged or neutral pion omitted from reconstruction (the most frequent is the decay $B^0 \to K^+K^-K^*$, with $K^* \to K^0\pi$). The efficiency for this kind of $B\bar{B}$ background is very sensitive to the allowed window for the ΔE variable. In fact, when a particle is not reconstructed, its energy is lost, and as a consequence ΔE is shifted to lower values.

The main source of problems related to the inclusion of these events comes from the fact that their topological behaviour is identical to the case of the signal events (because they also come from a decay of a B meson), but their CP asymmetry is different (and in most of cases unknown). This means that a $B\bar{B}$ component in the fit introduces a dilution in the determination of the signal CP asymmetry. So this would introduce a large systematic uncertainty.

For $B^0 \to K^+K^-K^0_S$ this background is completely removed with the tight ΔE cut described in Sec. 6.3.2, which, at cost of a small increase in the statistical error, avoids a larger systematic error due to the unknown $B\bar{B}$ CP content.

For $B^0 \to K^+K^-K^0_L$, an analogous cut is not possible, since ΔE is the only kinematic variable defining the B meson. This background cannot be removed from the fit and the unknown CP asymmetry of the $B\bar{B}$ background will constitute one of the principal systematic uncertainties. This uncertainty has been taken into account in the optimization of the selection described in Sec. 6.3.3. In particular, we identify neutral B decays: $B^0 \to K^+K^-K^{*0}(K^0_L\pi^0)$, $B^0 \to K^{*+}(K^+\pi^0)K^-K^0_L$ and charged B decays: $B^+ \to K^+K^-K^{*+}(K^0_L\pi^+)$, $B^+ \to K^{*-}(K^-\pi^0)K^+K^0_L$. BABAR Collaboration has recently

measured the branching fraction: $\mathcal{B}(B^+ \to K^{*+}K^-K^+) = (36.8 \pm 3.4 \pm 3.5) \times 10^{-6}$, while only an upper limit exists on the neutral B decay: $\mathcal{B}(B^0 \to K^{*0}K^+K^-) < 6.1 \times 10^{-4}$ [21]. Since this upper limit does not give a reliable estimation of the real contribution, we assume also for the neutral modes a branching fraction equal to the one measured for charged mode, assuming SU(3) symmetry. In Fig. 6.23 the distribution of these events in the Dalitz plot is shown. These events have been generated assuming a flat distribution in the Dalitz plot. The observed loss of the edge at high K^+K^- invariant mass can be attributed to the effect of the requirement on the minimum of the calibrated energy associated to the K^0_L candidate and the cut on $\mathcal{T}$, which removes the very slow K^0_L's of these four body final states.

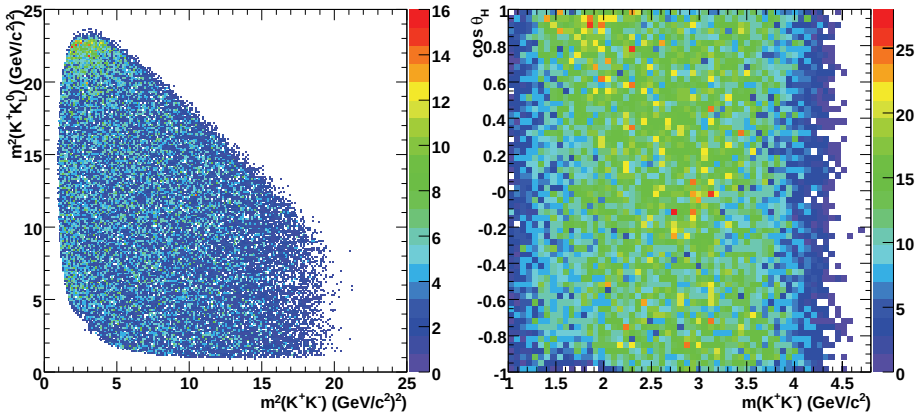

Figure 6.23: Dalitz plot distribution (left) and squared Dalitz plot distribution (right) of peaking $B\bar{B}$ Monte Carlo events.

A purely phase space model for $B \to K^+K^-K^*$ is not a realistic model for this three body decay. A significant contribution is expected to come also from resonant ϕK^*. The $\phi(1020)$ region of the K^+ K^- invariant mass is also the one with the highest K^0_L efficiency (hard K^0_L's). The branching fraction of $B^0 \to \phi K^*(892)$ has been measured in the *quasi-two-body* approximation[2], together with the fraction of longitudinal and transverse polarization. The measured branching fraction [72] is $\mathcal{B}(B^0 \to \phi K^*(892)) = (9.5 \pm 0.9) \times 10^{-6}$ and the polarization fractions are $f_\parallel = 0.52 \pm 0.05$ and $f_\perp = 0.22 \pm 0.05$.

[2]The *quasi-two-body* approximation consists in considering the K^+K^- pair as a quasi-particle (the ϕ), if its invariant mass lies in the region which includes the ϕ spectrum in three standard deviations. The same can be done for the $K\pi$ system forming the K^*. Then the B can be considered as decaying in two particles, the ϕ and the K^*.

Another possible source of B background is $B^0 \to \phi K^*(1430)$. This decay has been observed by *BABAR*, and the branching fraction is [72]: $\mathcal{B}(B^0 \to \phi K^*(1430)) \approx 8.2 \times 10^{-6}$. We mix the ϕK^* Monte Carlo events weighting them by the measured polarization fractions in order to have the correct helicity distribution.

Additional contribution comes from the $B^+ \to \phi K^{*+}$ decays, having [73] $\mathcal{B}(B^+ \to \phi K^{*+}) = (8.30 \pm 0.65) \times 10^{-6}$.

Other sources of resonant $K^+K^-K^*$ modes which contribute to the peaking B background are $f_0(980)K^*$, $f_0(1500)K^*$ and $\chi_{c0}K^*$. Since these single modes have not been measured, we use the branching fraction of $B^+ \to K^+K^-K^{*+}$ and the fit fractions of the single resonances entering the Dalitz plot of $B^+ \to K^+K^-K^+$ [76].

The reconstruction efficiency of these decays is evaluated using high statistics Monte Carlo samples for these specific decay modes. The reconstruction efficiencies, the $\prod_i \mathcal{B}_i$ and the expected number of events in an integrated luminosity of about 350 fb^{-1} are summarized in Table 6.5. We build a Monte Carlo cocktail weighted according to the

Mode	# events	$\prod_i \mathcal{B}_i$ (10^{-6})	ε (%)	N
$B^0 \to \phi(1020)K^{*0}(892)_{\parallel}$	12000	1.23	6.8	28
$B^0 \to \phi(1020)K^{*0}(892)_{\perp}$	12000	0.33	4.2	4.8
$B^0 \to \phi(1020)K^{*0}(1430)$	10000	1.35	5.0	24
$B^0 \to f_0(980)K^{*0}$	12000	0.34	3.4	4.0
$B^0 \to f_0(1500)K^{*0}$	12000	0.31	3.8	4.2
$B^0 \to \chi_{c0}K^{*0}$	12000	0.15	2.5	1.3
$B^0 \to K^+K^-K^{*0}(K^0_L\pi^0)$ NR	57000	5.9	2.3	48
$B^0 \to K^{*+}(K^+\pi^0)K^-K^0_L$ NR	57000	9.0	2.2	69
$B^+ \to \phi(1020)K^{*+}$	12000	2.07	6.0	44
$B^+ \to f_0(980)K^{*+}$	12000	0.51	4.5	8.0
$B^+ \to f_0(1500)K^{*+}$	12000	0.47	4.9	8.1
$B^+ \to \chi_{c0}K^{*+}$	12000	0.23	3.0	2.4
$B^+ \to K^+K^-K^{*+}(K^0_L\pi^+)$ NR	57000	9.0	2.5	79
$B^+ \to K^{*0}(K^-\pi^+)K^0_LK^+$ NR	57000	12.0	2.5	105
Tot				430

Table 6.5: Branching fractions, reconstruction efficiencies and expected number of events from charmless B decays expected in 350 fb^{-1} for $B^0 \to K^+K^-K^0_L$. These events form the peaking component of the B background for $K^+K^-K^0_L$. $\prod_i \mathcal{B}_i$ is the branching fraction of the decay multiplied by the sub-$\mathcal{B}$, which for $\phi K^{*0}(892)$ contains the fraction of $\parallel$ or $\perp$ polarization. The $f_0(980)K^*$, $f_0(1500)K^*$ and $\chi_{c0}K^*$ sub-$\mathcal{B}$ contain the fit fractions measured in the $K^+K^-K^+$ Dalitz plot [76].

yields reported in Table 6.5 to parameterize the charmless peaking component of the B

background for $B^0 \to K^+K^-K^0_L$. This constitute an approximation because this sum of events is made incoherently, thus neglecting the existing interference phases. Anyhow, since this background is smaller than the signal and it has different kinematics, this approximation is acceptable.

As for the continuum background (see Sec. 6.4.1), we describe the Dalitz plot PDF using a 2D histogram. We use the same binning structure as the continuum one, since the main structures (like the $\phi(1020)$) are present also in this case. The 2D PDF is shown in Fig. 6.24, with the projections onto the $m_{K^+K^-}$ and $\cos\theta_H$ shown in Fig. 6.25.

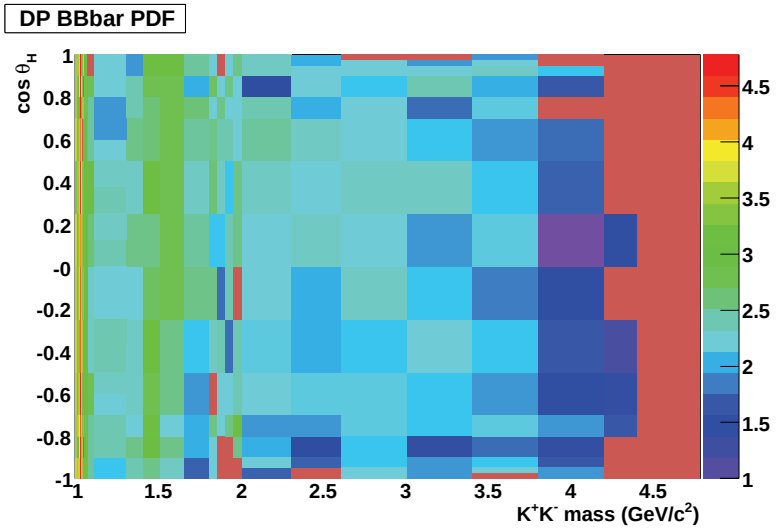

Figure 6.24: Peaking B background square Dalitz plot PDF for $B^0 \to K^+K^-K^0_L$. The model is a 2D histogram PDF with the same binning used for the continuum background. The weights come from the histogram filling with the weighted Monte Carlo cocktail whose components are listed in Table 6.5, shown with a $\log_{10}$ scale.

Charm B Decays

The remaining B background is dominated by the signal-like and combinatorial $b \to c$ decays. A breakdown of dominant decay modes is shown in Table 6.6. The main contributions comes from signal-like D^+, D^+_s and χ_{c0} decays. We include these $b \to c$ decays in our Dalitz plot model as non-interfering Gaussians (D's) and an interfering Breit-Wigner (χ_{c0}). While the kinematic variables are identical to signal events, $B \to DK$ decays can have slightly different Δt distribution from the true signal, due to the displaced D-meson decay vertex. We fit the lifetime of 1.5 thousand exclusive $B^0 \to D^+K^-$ decays assuming the signal Δt model and obtain $\tau_{DK} = 1.61 \pm 0.05$ ps (Figure 6.26) which is

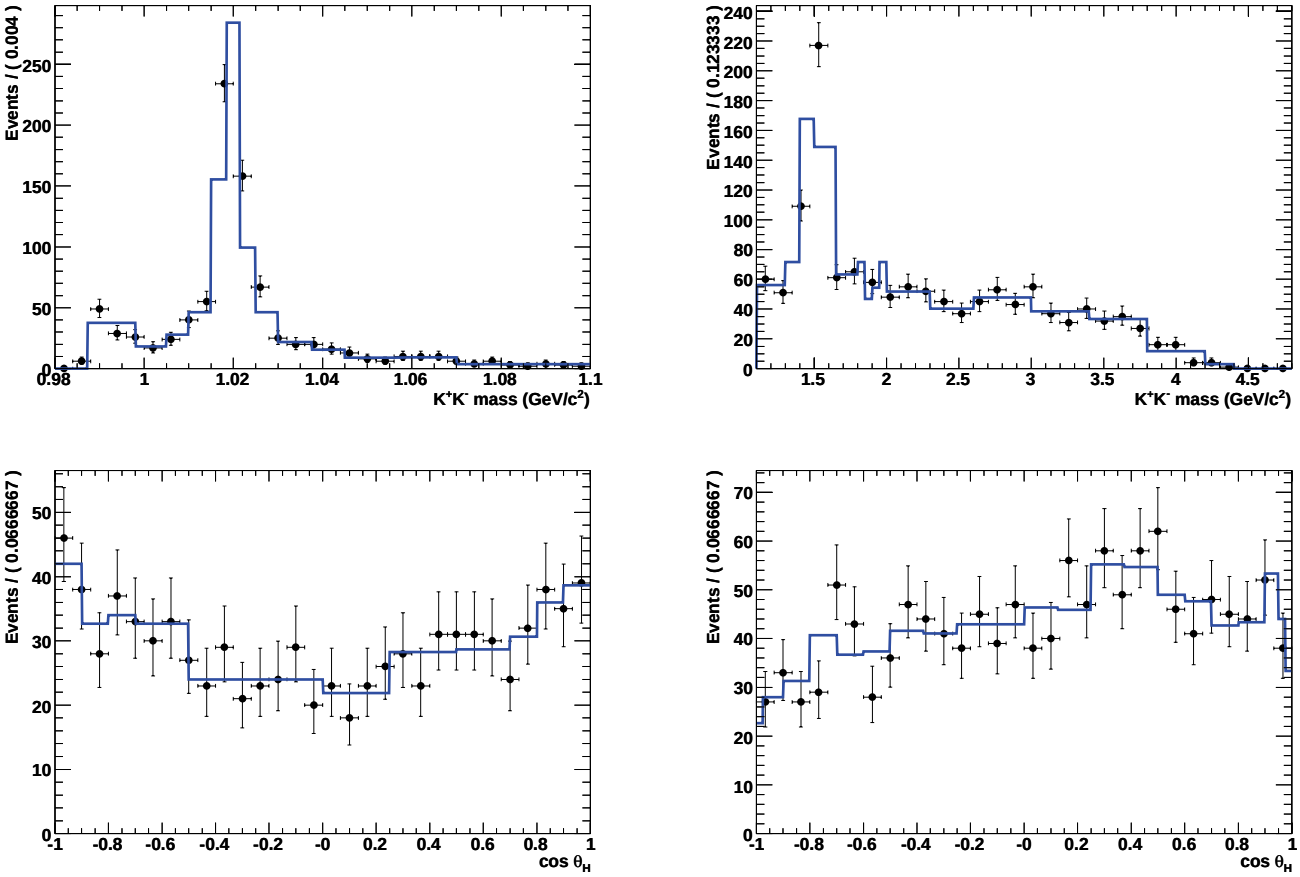

Figure 6.25: Projections of the peaking B background 2D histogram PDF for $B^0 \to K^+K^-K^0_L$ shown in Fig. 6.24. The dots are the Monte Carlo cocktail events, while the line is the PDF projection. Top: K^+K^- invariant mass, bottom: $\cos\theta_H$ projection. Left: events for $m(K^+K^-) < 1.1$ GeV/c^2, right: events for $m(K^+K^-) > 1.1$ GeV/c^2.

consistent with the B^0 lifetime. We expect 10 times less of combined $B^0 \to D^+K^-$ and $B^0 \to D_s^+K^-$ events so any difference in lifetimes between these decays and the charmless signal decays cannot be resolved in data; we use the nominal nominal B^0 lifetime for all decays into $K^+K^-K^0$ final states.

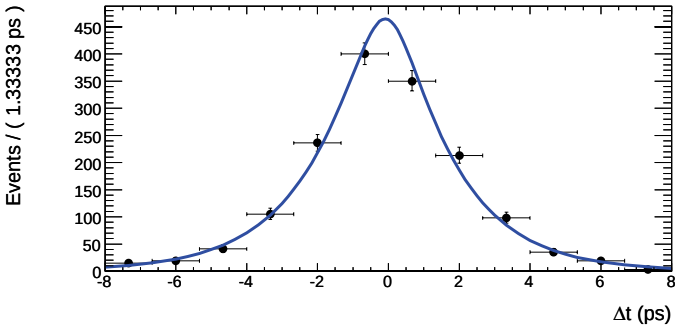

Figure 6.26: $B^0 \to K^+K^-K_S^0(\pi^+\pi^-)$ mode: Δt distribution for $B^0 \to D^+K^-$ decays.

Combinatorial $B\bar{B}$ Background

Distributions of the kinematic variables $m_{\rm ES}$ and ΔE for the remaining, combinatorial $b \to c$ background are very similar to those for continuum events as shown in Fig. 6.27 for $B^0 \to K^+K^-K_S^0(\pi^+\pi^-)$, while the distribution of the Fisher discriminant (not used in this fit) is closer to signal events (since it depends from the rest of the event, not by the reconstructed B). The Δt distribution has only a nonzero-lifetime component with the resolution similar to signal events. Based on generic $B\overline{B}$ Monte Carlo studies, we expect this combinatorial background to make 3-4% of the all background events, both for $B^0 \to K^+K^-K_S^0$ and for $B^0 \to K^+K^-K_L^0$. However, due to similarities in the kinematic PDF's, we are not able to clearly separate the combinatorial $b \to c$ background from the continuum events with events being exchanged between these two combinatorial categories. We perform a fit with 193 combinatorial $B\overline{B}$ events and observe that $11.4 \pm 3.4\%$ of these events leaked into the signal category for $B^0 \to K^+K^-K_S^0(\pi^+\pi^-)$ channel. This means that $\mathcal{O}(1\%)$ of the signal yield in data comes from B background. In order to completely minimize potential cross feed, we include a combinatorial $B\overline{B}$ background component in the likelihood. Due to the low number of expected events ($0.29/\,\mathrm{fb}^{-1}$) and the low statistics of the MC sample, we use the same PDF parameters for all tagging categories.

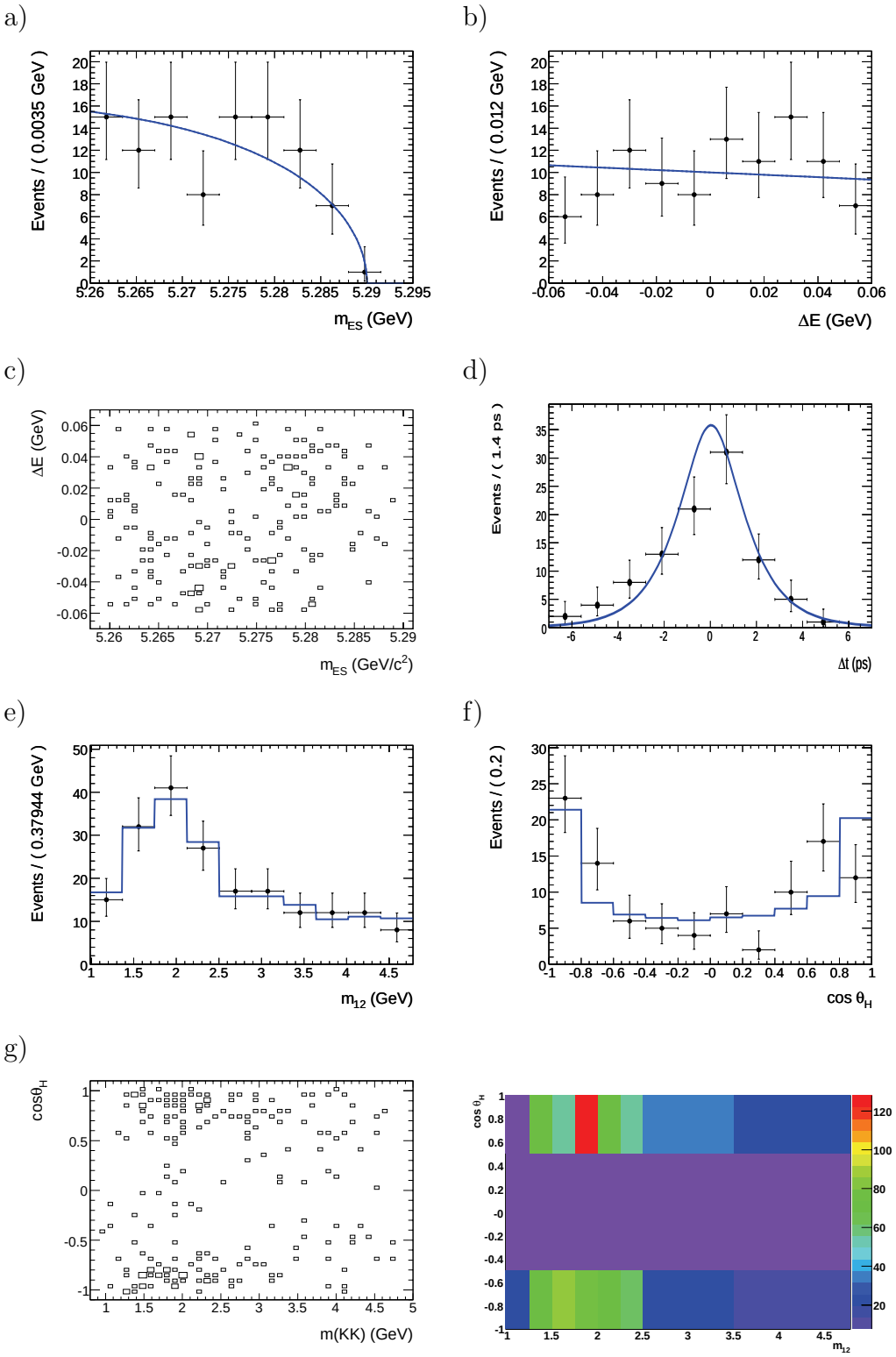

Figure 6.27: $B^0 \to K^+K^-K^0_S(\pi^+\pi^-)$ mode, events in generic $B\overline{B}$ MC which pass all selection cuts, with signal events removed: (a-c) $m_{\rm ES}$ and ΔE, (d) Δt and (e-g) $m(K^+K^-)$ mass and $\cos\theta_H$.

For the $K^+K^-K^0_S(\pi^0\pi^0)$ sub-mode, combinatorial backgrounds from B decays are mostly from events with multiple π^0's which are reconstructed into a fake K^0_S. Despite the cut on ΔE being wider, there is only a negligible possibility of cross feed from $B \to K^+K^-K^0h$ (peaking) modes. In the final dataset, we expect about 50 events of combinatorial B background. So, such a component will be included in the fit. In this case, a correlation arise between the kinematic variables, so we model them with a 2D histogram PDF filled with the selected events in the Monte Carlo of generic B decays. We show this PDF in Fig. 6.28, together with the usual 2D histogram modeling the Dalitz plot for this component.

For the $K^+K^-K^0_L$ sub-mode, combinatorial background arise from misreconstructed K^0_L's, having a distribution of ΔE which is continuum-like. From the study of Monte Carlo for generic B decays, we estimate a number of about 800 events in the final dataset. In Fig. 6.29 we show the projections of the Dalitz plot for these events. This component is included in the fit also for $K^+K^-K^0_L$. Similar considerations to the ones on $K^+K^-K^0_S(\pi^+\pi^-)$ sub-mode can be made about the interchange between continuum and combinatorial $B\bar{B}$ events. Since the amount of background is larger, to simplify the fit we fix the yield for this component to the expected number of events. We checked with toy Monte Carlo technique, described in Sec. 6.7.1, that this does not introduce any bias in the signal parameters.

6.5 Maximum Likelihood Fit

The signal parameters, both the yields for all the $B^0 \to K^+K^-K^0$ sub-modes, and the isobar coefficients which represent the fit fractions of each resonance and the associated *CP* asymmetry, are extracted using a maximum likelihood fit technique. This strategy has the advantage to extract signal parameters simultaneously to the background ones, thanks to the loose selection which keep wide sidebands, in this way avoiding biases in the signal. Furthermore, having a loose selection, this technique allows to keep a higher efficiency with respect a simple cut-and-count analysis, where the signal is extracted in a tight signal window. The price to pay is computational, since, having typically more than one order of magnitude of background events, the fit procedure, above all the one of the Dalitz plot with complicate normalizations involved, it's much slower.

The main ingredients of a maximum likelihood fit are the following:

Decay mode	$\mathcal{B} \cdot 10^{-6}$	Ref.	Relative $\mathcal{B} \cdot \epsilon$ (%)	Comment
$K^+K^-K^0$	8.4	[21]	100	Sig. model
$D^-(K^0_S K^-)K^+$	0.39	[21]	3.8	Sig. model
$D^-(K^0_S \pi^-)K^+$	1.9	[21]	< 0.4	Sidebands/generic B
$D^-(K^0_S K^-)\pi^+$	5.7	[21]	< 1.3	Sidebands/generic B
$D^-(K^0_S \pi^-)\pi^+$	28.0	[21]	< 0.1	Sidebands/generic B
$\bar{D}^0(K^+K^-)K^0_S$	0.067	[21]	0.8	Sidebands/generic B
$\bar{D}^0(K^+\pi^-)K^0_S$	0.66	[21]	< 0.2	Sidebands/generic B
$\bar{D}^0(\pi^+\pi^-)K^0_S$	0.024	[21]	< 0.1	Sidebands/generic B
$D^-_s(K^0_S K^-)K^+$	0.47	[21]	4.5	Sig. model
$D^-_s(K^0_S K^-)\pi^+$	0.35	[21]	< 0.1	Sidebands/generic B
$D^-_s(K^0_S \pi^-)K^+$	< 0.013	[21]	< 0.1	Sidebands/generic B
$D^-_s(K^0_S \pi^-)\pi^+$	< 0.009	[21]	< 0.1	Sidebands/generic B
$J/\psi(K^+K^-)K^0_S$	0.007	[21]	< 0.1	Sidebands/generic B
$\psi(2S)(K^+K^-)K^0_S$	0.051	[21]	0.6	Sidebands/generic B
$\chi_{c0}(K^+K^-)K^0_S$	< 1.0	[21]	< 12	Sig. model

Table 6.6: B meson decays into charm and charmonium final states under consideration in the background study. The $\mathcal{B}$ includes all sub-decay branching fractions.

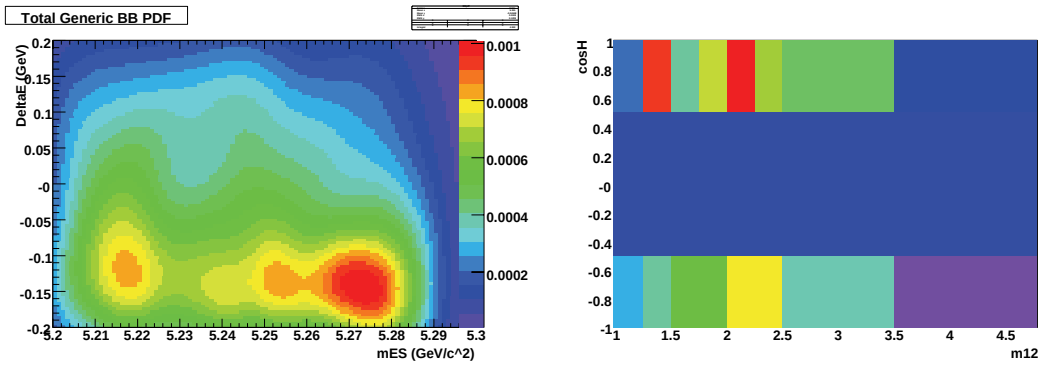

Figure 6.28: $B^0 \to K^+K^-K^0_S(\pi^0\pi^0)$ mode, events in generic $B\overline{B}$ MC which pass all selection cuts, with signal events removed: (left) $m_{\rm ES}$ and ΔE plane, (right) $m(K^+K^-)$ mass and $\cos\theta_H$ plane.

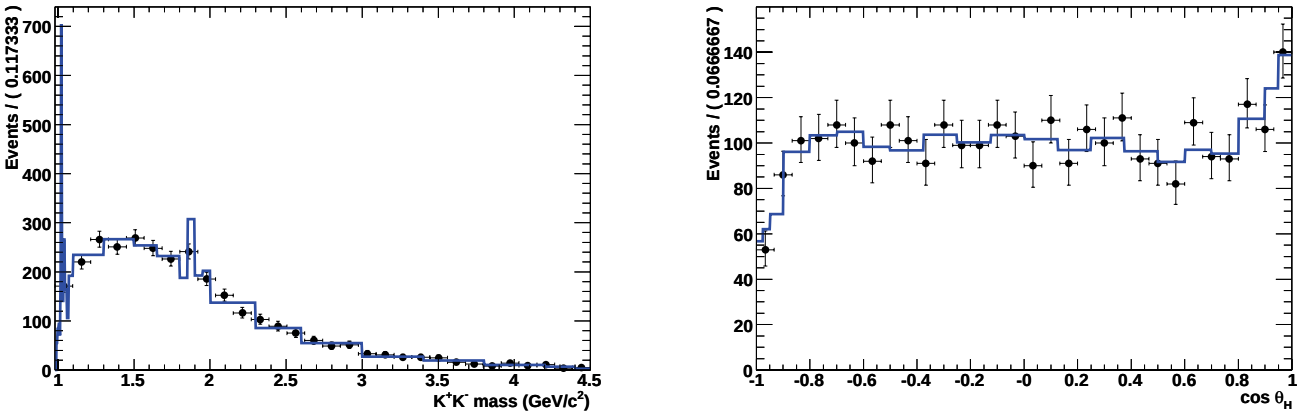

Figure 6.29: $B^0 \to K^+K^-K^0_L$ mode: projections of the Dalitz plot distribution of combinatorial B background. Left: $m_{K^+K^-}$. Right: $\cos\theta_H$. The dots are the Monte Carlo events, while the line is the PDF projection.

1. All the variables entering the likelihood function are assumed to be uncorrelated. Under this hypothesis, the likelihood can be written as a product of the PDF's of the different variables. Otherwise, a more complicated multi-dimensional PDF is needed (as an example the Dalitz plot PDF and the $m_{\rm ES}$-ΔE 2D PDF for $K^+K^-K^0_S(\pi^0\pi^0)$ combinatorial $B\bar{B}$ background);

2. the most of background parameters are extracted from the fit simultaneously to the signal ones. This is possible because of the presence of the wide sidebands, which allow the extrapolation of the background shape in the signal region. This avoid systematic uncertainties on the background shape, typically with a negligible increase of the statistical error;

3. the *CP* asymmetry is extracted as a function of the time distance between the decays of the two B mesons in the event. This information is used in the likelihood using $\Delta t/\sigma(\Delta t)$, namely the pull of the Δt variable;

4. the maximum likelihood is extended. This means that the likelihood function includes a Poisson factor in order to conserve the total number of selected events and to take into account the fact that the number of events produced comes from a Poisson process;

5. the fit is performed unbinned. This allows not to lose any information in binning the

variables entering the likelihood function, in case of small yields (which is typical for charmless B decays).

With these considerations, the general form of the likelihood is

$$\mathcal{L} = e^{-N'}(N')^N \prod_{i=1}^{N} \sum_{j=1}^{N_{spec}} \frac{N_j}{N'} \mathcal{P}_i^j \tag{6.13}$$

where N_i is the number of events for one of the N_{spec} species of events (signal, $q\bar{q}$ background or $B\bar{B}$ backgrounds -peaking and combinatorial-) and $N' = \sum_{j=1}^{N_{spec}} N_j$, N is the total number of selected events and P_i^j is the product of the PDF's of the discriminating variables used in the likelihood for the event i under the hypothesis to belong to the specie j.

In the case of $B^0 \to K^+K^-K^0$ analysis, the PDF is formed from these observables:

$$\mathcal{P} \equiv \mathcal{P}(m_{\rm ES}) \cdot \mathcal{P}(\Delta E) \cdot \mathcal{P}_{DP}(m_{K^+K^-}, \cos\theta_H, \Delta t, q_{tag}) \otimes \mathcal{R}(\Delta t, \sigma_{\Delta t}). \tag{6.14}$$

where q_{tag} is the flavour of the initial state. We will describe our model for the selection variables and the one for the time-dependent Dalitz plot, $\mathcal{P}_{DP}$, in the Sections 6.5.1 and 6.6, respectively. The $\mathcal{P}_{DP}$ PDF is convoluted with $\mathcal{R}$, which is the standard Δt resolution function whose parameters are evaluated in exclusive B^0 decays into final states with a charm meson as in *CP*-asymmetry measurements in $J/\psi K_S^0$ decays [37], (see Sec. 2.2.4). For the $B^0 \to K^+K^-K_L^0$ sub-mode, the $m_{\rm ES}$ variable does not enter the likelihood function defined in Eq. (6.14).

We checked the correlation between the likelihood variables and found all of them to be small for signal component (pure phase-space Monte Carlo sample), the largest one being between $m_{\rm ES}$ and ΔE (13%). We report them in Tables 6.7, 6.8 and 6.9 for $K^+K^-K_S^0(\pi^+\pi^-)$, $K^+K^-K_S^0(\pi^0\pi^0)$ and $K^+K^-K_L^0$, respectively. The correlations in the background events data are even smaller.

6.5.1 Parameterization of Selection Variables

We parameterize signal PDF's using unbinned maximum likelihood fit on the signal Monte Carlo samples of the three sub-modes. The kinematic variables $m_{\rm ES}$ and ΔE for all the sub-modes are parameterized using the same function (labelled as $Cruijff$ function in

Variable	$m_{\rm ES}$	ΔE	$m_{K^+K^-}$	$\cos\theta_H$	Δt
$m_{\rm ES}$	1	-0.13	0.001	-0.002	0.03
ΔE		1	-0.03	0.001	-0.0001
$m_{K^+K^-}$			1	-0.0005	-0.0003
$\cos\theta_H$				1	-0.0005

Table 6.7: $K^+K^-K^0_S(\pi^+\pi^-)$ mode: Correlations between ML fit observables in phase-space signal MC with selection cuts applied

Variable	$m_{\rm ES}$	ΔE	$m_{K^+K^-}$	$\cos\theta_H$	Δt
$m_{\rm ES}$	1	0.03	-0.05	0.0008	0.008
ΔE		1	-0.009	0.001	-0.004
$m_{K^+K^-}$			1	-0.01	-0.001
$\cos\theta_H$				1	-0.002

Table 6.8: $K^+K^-K^0_S(\pi^0\pi^0)$ mode: Correlations between ML fit observables in phase-space signal MC with selection cuts applied

Variable	ΔE	$m_{K^+K^-}$	$\cos\theta_H$	Δt
ΔE	1	-0.016	0.001	-0.006
$m_{K^+K^-}$		1	0.029	0.003
$\cos\theta_H$			1	0.004

Table 6.9: $K^+K^-K^0_L$ mode: Correlations between ML fit observables in phase-space signal MC with selection cuts applied

the following), which is a modified Gaussian including an exponential tail:

$$f_{Cruijff} = \exp\left[-\frac{(x-m)^2}{2\sigma_\pm^2 + \alpha_\pm(x-m)^2}\right] \tag{6.15}$$

where the $+$ $(-)$ sign corresponds to $x > m$ $(x < m)$ region. The $m_{\rm ES}$ and ΔE distributions for $K^+K^-K^0_S(\pi^+\pi^-)$ and $K^+K^-K^0_S(\pi^0\pi^0)$ are shown in Fig. 6.30 and 6.31, respectively.

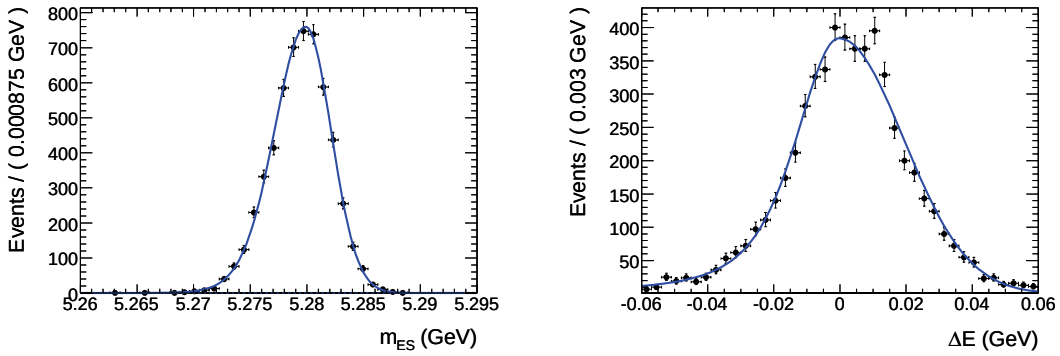

Figure 6.30: $K^+K^-K^0_S(\pi^+\pi^-)$ mode: (left) $m_{\rm ES}$ distribution from signal MC, (right) ΔE distribution from signal MC. All distributions are described with the Cruijff function.

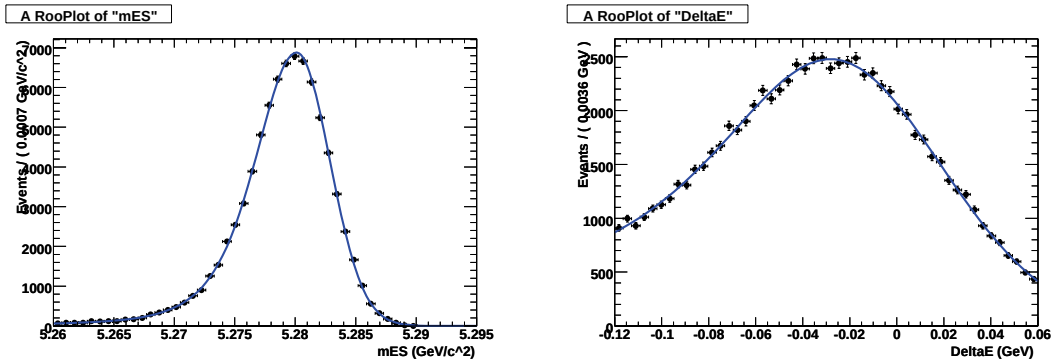

Figure 6.31: $K^+K^-K^0_S(\pi^0\pi^0)$ mode: (left) $m_{\rm ES}$ distribution from signal MC, (right) ΔE distribution from signal MC. All distributions are described with the Cruijff function.

Since, as we have discussed in Sec. 6.3.3, the ΔE distribution for $K^+K^-K^0_L$ candidates has different resolution for IFR or an EMC K^0_L samples, we keep the two components separate, associating them to different PDF's, but forcing the *CP* parameters to be the same. We show the distribution of Monte Carlo events with the PDF in Fig. 6.32.

The decay $B^0 \to J/\psi K^0_L$, which proceeds through $b \to c$ transition, has a considerably higher branching ratio [21] than our charmless decay, then it can be used as a control

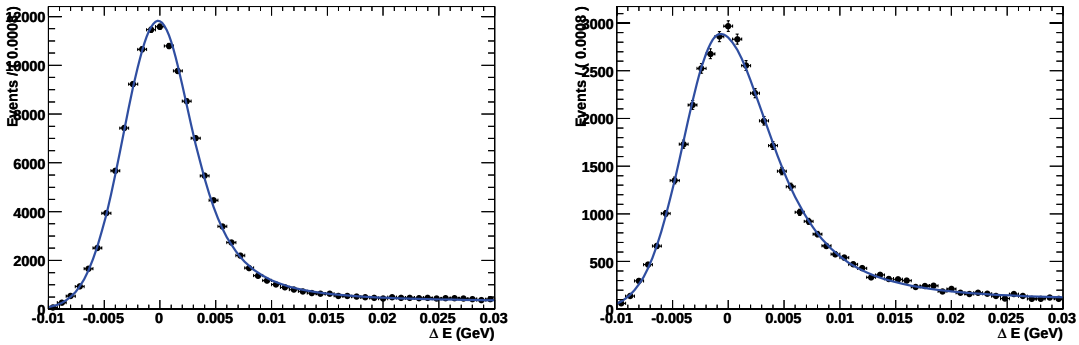

Figure 6.32: Distribution of ΔE for signal Monte Carlo $K^+K^-K^0_L$ events with the Cruijff PDF superimposed. Left: EMC B candidates. Right: IFR B candidates.

sample for the determination of ΔE. In order to check that we can use this decay as a control sample, we checked on signal Monte Carlo samples that $K^+K^-K^0_L$ and $J/\psi K^0_L$ events have consistent ΔE distributions. Even if the number of signal events is considerably high, the purity is not sufficient to determine all the parameters of the signal $Cruijff$ PDF. We take the $\alpha_\pm$ parameters of the Cruijff function of Eq. 6.15 from a fit to signal Monte Carlo events, and fit the mean m and the resolution parameters $\sigma_\pm$ on $B^0 \to J/\psi K^0_L$ events.

We reconstruct J/ψ candidates both from $\mu^+\mu^-$ and e^+e^- pairs, requiring tight PID selectors on the leptons in order to reduce the combinatorial background. We also require the dilepton mass to be within [3.0;3.175] GeV/c^2. The most of background in this way is made by $J/\psi X$ (*inclusive* J/ψ) coming from B-mesons decays, which we parameterize in a similar way than our continuum. We show in Fig. 6.33 the fit to the $B^0 \to J/\psi K^0_L$ EMC and IFR-only events, and we report in Table 6.10 the parameters of the Cruijff function extracted by this fit and which we use for $B^0 \to K^+K^-K^0_L$ signal PDF.

Parameter	EMC	IFR-only
m	-1.0449 ± 6.46 MeV	0.40 ± 1.17 MeV
σ_-	3.53 ± 3.11 MeV	3.73 ± 0.70 MeV
σ_+	2.93 ± 0.95 MeV	3.96 ± 1.38 MeV
α_-	fixed	fixed
α_+	fixed	fixed

Table 6.10: Parameters of the Cruijff function of Eq. 6.15 used to parameterize signal ΔE extracted to a fit to $B^0 \to J/\psi K^0_L$ events reconstructed on-resonance dataset.

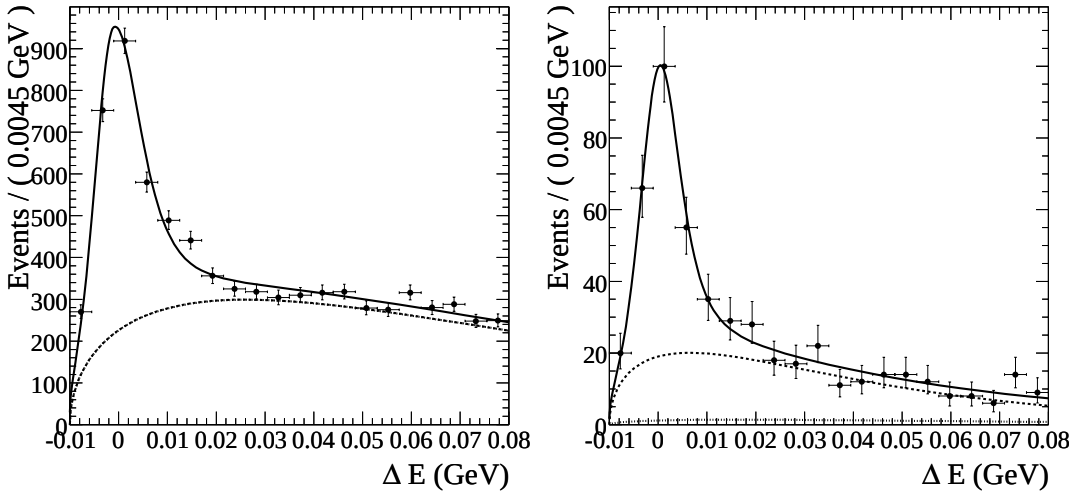

Figure 6.33: ΔE distribution for $B^0 \to J/\psi K^0_L$ in on-resonance events with the result of the fit superimposed. Left: EMC events. Right: IFR-only events. Continuous curve represent the total fitted PDF, the dashed line the total background and the dotted line the non-J/ψ background.

All the parameters of the background PDF's are fitted on data together with the signal ones we want to extract. We parameterize $m_{\rm ES}$ for $K^+K^-K^0_S$ and ΔE for $K^+K^-K^0_L$ with a phase space ARGUS function (Eqn. 5.11).

The ARGUS function for $K^+K^-K^0_L$ has the phase space reflected with respect to the $K^+K^-K^0_S$ one (as for $B^0 \to J/\psi K^0_L$ events). Since the purity of the sample depends on the tagging category (being larger for leptonic category and worse for untagged events) we allow the slope parameter ξ of the phase space function to be different for the different tagging categories. We parameterize the continuum ΔE for $K^+K^-K^0_S$ with a linear shape.

The combinatorial B background for $K^+K^-K^0_S(\pi^+\pi^-)$ mode is parameterized with an ARGUS function for $m_{\rm ES}$ and with a linear shape for ΔE with the parameters taken from selected generic $B\overline{B}$ Monte Carlo and with Their distributions look very similar to those of the continuum (see top plots in Fig. 6.27).

Because of the correlation between $m_{\rm ES}$ and ΔE in combinatorial B background events for $K^+K^-K^0_S(\pi^0\pi^0)$ mode, we use a 2D histogram PDF in this case (see left plot of Fig. 6.28).

For $K^+K^-K^0_L$ mode, we use an ARGUS function to describe both combinatorial and charmless B background ΔE. Since we found that the shape for the latter is different in

EMC and IFR events, we separate the two PDF in the fit, while we use a common ARGUS shape for the combinatorial background. The distributions are shown in Fig. 6.34.

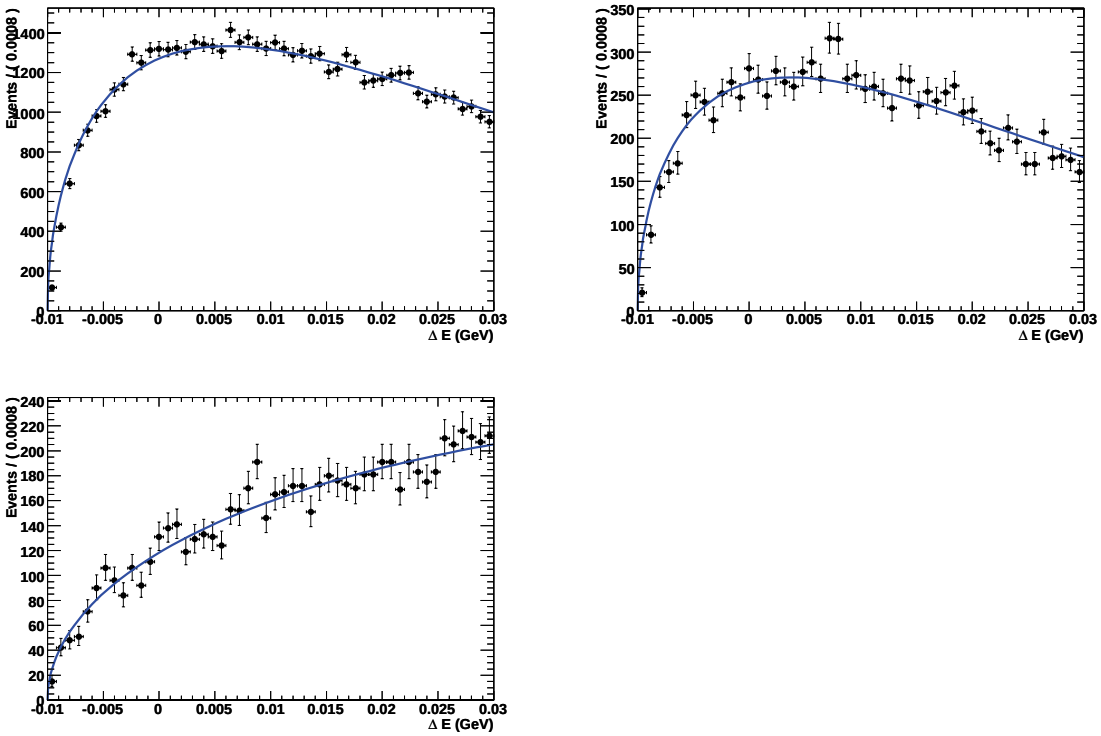

Figure 6.34: Top: ΔE distribution of charmless B background for $K^+K^-K^0_L$ mode. EMC candidates (left) and IFR candidates (right). Bottom: ΔE distribution for combinatorial B background (common for EMC and IFR events). All distributions are parameterized with an ARGUS function.

6.5.2 Parameterization of Background Δt

The parameterization of signal Δt has been already described in Sec. 2.2.4.

We use an effective parameterization of Δt for the continuum background. We allow the presence of a zero-lifetime (prompt) term with fraction of $f_{\tau=0}$, and a term with a finite lifetime, τ_{BG}. The total PDF is given by

$$f_{BG}^{flav} = f_{\tau=0}\,\delta(\Delta t)\,\frac{1}{2}\,[1+m(1-2w_{\tau=0})] + (1-f_{\tau=0})\,\frac{e^{-|\Delta t|/\tau_{BG}}}{4\tau}\,[1+m(1-2w_{\tau>0})] \quad (6.16)$$

where $f_{\tau=0}$ is the prompt fraction, $w_{\tau=0}$ and $w_{\tau>0}$ are "effective mistag rates" for prompt and lifetime fraction, respectively; m is ±1 for unmixed/mixed events. In the nominal

fit, we float the prompt fraction, mistag rates in each of the tagging categories, and the lifetime for all events. The resolution function for the continuum background is composed of three Gaussians, but we fix the mean and width of outlier Gaussian to 0 and 8 ps, respectively.

The B-background component (both peaking and non peaking) has in principle CP asymmetry for the fraction of events which come from neutral B decays and which have a defined tag. We parameterize the *lifetime part* of Δt resolution of the B background as for the signal events, but we also include a *prompt part* as for continuum background. The prompt part should account for tracks associated to reconstructed B coming from both the B-meson decays. The time evolution is explicitly given with

$$\begin{aligned} f^{CP}_{peak} &= f_{\tau=0} + (1 - f_{\tau=0}) \frac{e^{-|\Delta t|/\tau_{B^0}}}{4\tau_{B^0}} \\ &\times (1 + qS_{peak} \sin(\Delta m_d \Delta t) + C_{peak} \cos(\Delta m_d \Delta t)) . \end{aligned} \tag{6.17}$$

The prompt fraction depends on the tagging category, being smaller for leptonic one and increasing for less pure categories. The lifetime and mixing frequency of the peaking background is fixed to B^0 nominal values. Tagging dilution and Δt resolution function are taken from signal `BReco` events. The CP content of the peaking and non peaking background is unknown, because they are a mixture of both charged and neutral modes. The charged modes can show only direct CP asymmetry, while the neutral ones can also produce CP violation in the interference between mixing and in the decay. Because of that, in the nominal fit we fix S and C parameters of the B background to be both 0, and we vary them uniformly from -1 to +1 and take the largest difference in signal β as the systematic error.

6.5.3 Summary of the Maximum Likelihood Function

In Table 6.11 we report the complete list of the parameterizations of the PDF's which define the likelihood function. We also summarize the splitting rules and the samples used to determine each parameter.

6.6 $B^0 \to K^+K^-K^0$ Dalitz Plot Model

We describe signal $B^0 \to K^+K^-K^0$ decays in the time-dependent Dalitz plot using the isobar model, described in Sec. 3.6. Amplitudes are parameterized using polar coordinates,

Component	p.d.f.	splitting rule	parameter	source
$K^+K^-K^0_S$ $m_{\rm ES}$ and ΔE signal	Cruijff	-	all	MC
$K^+K^-K^0_S$ $m_{\rm ES}$ continuum	ARGUS	-	endpoint	continuum MC
$K^+K^-K^0_S$ $m_{\rm ES}$ continuum		Tag cat.	ξ	on-resonance
$K^+K^-K^0_S$ ΔE continuum	linear	-	all	on-resonance
$K^+K^-K^0_S(\pi^+\pi^-)$ $m_{\rm ES}$ $B\overline{B}_{np}$	ARGUS	-	all	generic MC
$K^+K^-K^0_S(\pi^+\pi^-)$ ΔE $B\overline{B}_{np}$	ARGUS	-	all	generic MC
$K^+K^-K^0_S(\pi^0\pi^0)$ $m_{\rm ES}$-ΔE $B\overline{B}_{np}$	2D histogram	-	-	generic MC
$K^+K^-K^0_L$ ΔE signal	Cruijff	K^0_L cat.	mean	$J/\psi K^0_L$ data
			$\sigma_\pm$, $\alpha_\pm$	signal MC
$K^+K^-K^0_L$ ΔE continuum	ARGUS	Tag cat.	ξ	on-resonance, floating
		-	endpoint	continuum MC
$K^+K^-K^0_L$ ΔE $B\bar{B}_p$	ARGUS	K^0_L cat.	all	cocktail MC
$K^+K^-K^0_L$ ΔE $B\bar{B}_{np}$	ARGUS	-	all	generic MC
Dalitz plot signal(Δt)	model (Sec. 6.6)	-	all	on-resonance
		-	β	on-resonance, floating
Dalitz plot continuum	2D histogram	-	all	ΔE sideband
Dalitz plot $B\bar{B}_p$	2D histogram	-	all	cocktail MC
Dalitz plot $B\bar{B}_{np}$	2D histogram	-	all	generic MC
Δt signal $\mathcal{R}$	3 Gaussians	Tag. cat	tag ε	BReco data
		Tag. cat	core Gaussian *bias*	BReco data
		Tag. cat	core Gaussian σ	BReco data
		-	all other	BReco data
Δt continuum	2 Gaussians	-	outlier G. *bias*, σ	fixed
		-	all other	floating
Δt $B\bar{B}_p$	B Decay $\otimes\mathcal{R}$	-	S,C	cocktail MC
		-	all other	BReco data
Δt $B\bar{B}_{np}$	B Decay $\otimes\mathcal{R}$	-	S,C	generic MC
		-	all other	BReco data

Table 6.11: Summary of the parameterization of the likelihood function. The parameters are fixed in the fit, where it is not specified. $\mathcal{R}$ represents the Δt resolution function, and B Decay is the time evolution of a B decay, with CP violation in the decay and in the mixing.

as defined in Eq. 3.55. With these ingredients, the amplitude $\mathcal{A}$ ($\bar{\mathcal{A}}$) for the decay $B^0 \to K^+K^-K^0$ ($\overline{B}^0 \to K^-K^+\overline{K}^0$) can be written as a sum of decays through intermediate resonances:

$$\mathcal{A} = \sum_r c_r(1+b_r)e^{i(\phi_r+\delta_r+\beta)} \cdot f_r, \qquad \text{and} \tag{6.18}$$

$$\bar{\mathcal{A}} = \sum_r c_r(1-b_r)e^{i(\phi_r-\delta_r-\beta)} \cdot \bar{f}_r. \tag{6.19}$$

The parameters c_r and ϕ_r are the magnitude and phase of the amplitude of component r. We allow for different isobar coefficients for B^0 and $\overline{B}^0$ decays through the asymmetry parameters b_r and δ_r. The parameter β is the CKM angle β, coming from B^0-$\overline{B}^0$ mixing. The function $f_r = F_r \times T_r \times Z_r$ describes the dynamic properties of a resonance r, where F_r is the form-factor for the resonance decay vertex, T_r is the resonant mass-lineshape (Sec. 3.3), and Z_r describes the angular distribution in the decay (Sec. 3.2.3 and [45, 46]).

Our model includes the $\phi(1020)$. For the scalar decays included in our model ($f_0(980)$, $X_0(1550)$, and χ_{c0}), we use a constant form-factor. In this case we use the Blatt-Weisskopf centrifugal barrier factor $F_r = 1/\sqrt{1+(Rq)^2}$ [45], where q is the daughter momentum in the resonance frame, and R is the effective meson radius, taken to be $R = 1.5$ GeV (0.3 fm). We omit a similar centrifugal factor for the B^0 decay vertex into the ϕK^0 intermediate state since its effect is negligible due to the small width of the $\phi(1020)$ resonance.

The angular distribution is constant for scalar decays, whereas for vector decays $Z = -4\vec{q}\cdot\vec{p}$, where $\vec{q}$ is the momentum of the resonant daughter, and $\vec{p}$ is the momentum of the third particle in the resonance frame. We describe the line-shape for the $\phi(1020)$, $X_0(1550)$, and χ_{c0} using the relativistic Breit-Wigner function (Eq. 3.27). The mass-dependent width is given as $\Gamma(m_{K^+K^-}) = \Gamma_r \left(q/q_r\right)^{2L+1} \left(m_r/m_{K^+K^-}\right) \left(F_r(q)/F_r(q_r)\right)^2$, where L is the resonance spin and $q = q_r$ when $m_{K^+K^-} = m_r$. For the $\phi(1020)$ and χ_{c0} parameters, we use average measurements [21].

The $f_0(980)$ resonance is described with the coupled-channel (Flatté) function (Eq. 3.40), where the coupling strengths for the KK and $\pi\pi$ channels are taken as $g_\pi = 0.165 \pm 0.018$ GeV/c^2, $g_K/g_\pi = 4.21 \pm 0.33$, and $m_r = 0.965 \pm 0.010$ GeV/c^2 (from a BES experiment measurement [79]).

The $X_0(1550)$ is less well-established. Previous Dalitz plot analyses of $B^+ \to K^+K^+K^-$ [75, 76] report observations of a scalar resonance at around 1.5 GeV/c^2. The scalar nature has

been confirmed by partial-wave analyses [77, 76]. However, previous measurements report inconsistent resonant widths: 0.145 ± 0.029 GeV/c^2 [75] and 0.257 ± 0.033 GeV/c^2 [76]. Branching fractions also disagree, so the nature of this component is still unclear [78]. In our reference fit, we take the resonance parameters from Ref. [76], which is based on a larger sample of $B\overline{B}$ decays than Ref. [75], and consider the narrower width given in the latter in the systematic error studies.

The summary of used components is given in Table 6.12.

Resonance	Amplitude	Parameters	Reference
$\phi(1020)$	RBW	$m = 1.019456$ GeV/c^2	PDG
		$\Gamma = 0.00426$ GeV/c^2	[21]
		$R_{BlattWeiss} = 1.5\,\text{GeV}^{-1}$	
$f_0(980)$	Flatté	$m = 0.965$ GeV/c^2	BES
		$g_\pi = 0.165$ GeV/c^2	[79]
		$g_K = 0.695$ GeV/c^2	
$X_0(1550)$	RBW	$m = 1.539$ GeV/c^2	$B^+ \to K^+K^+K^-$
		$\Gamma = 0.257$ GeV/c^2	[76]
$(K^+K^-K^0_S)_{NR}$	EXP	$\alpha = 0.14$	floated
χ_{c0}	RBW	$m = 3.41519$ GeV/c^2	PDG
		$\Gamma = 0.0101\,\text{GeV}/c^2$	[21]
$D^\pm$	NIG	$m = 1.8694$ GeV/c^2	MC
		$\sigma = 0.0067$ GeV/c^2	
$D_s^\pm$	NIG	$m = 1.9683$ GeV/c^2	MC
		$\sigma = 0.0067$ GeV/c^2	

Table 6.12: List of Dalitz plot components: relativistic Breit-Wigner (RBW), non-interfering Gaussian (NIG), single-pole coupled-channel (Flatté) and exponential (EXP).

6.6.1 Non-resonant Amplitude

As we briefly discussed in general in Sec. 3.5, in addition to resonant decays, we include non-resonant amplitudes. Since the existing theoretical models do not reproduce well the experimental features on data, we rely on a phenomenological parameterization [75] and describe the non-resonant terms as

$$\mathcal{A}_{NR} = \left(c_{12}e^{i\phi_{12}}e^{-\alpha m^2_{12}} + c_{13}e^{i\phi_{13}}e^{-\alpha m^2_{13}} + c_{23}e^{i\phi_{23}}e^{-\alpha m^2_{23}}\right) \cdot (1 + b_{NR}) \cdot e^{i(\beta+\delta_{NR})} \quad (6.20)$$

and similarly for $\bar{\mathcal{A}}_{NR}$. The slope of the exponential function is consistent among existing measurements in charged B decays into three kaons [75, 76], and we use $\alpha = 0.14 \pm 0.02$ GeV$^{-2} \cdot c^4$.

For the systematic studies associated to the non-resonant modeling, we adopt the theoretical model suggested in [26]:

$$f_{nr} \propto \left[\frac{x_1}{s_{12}} + \frac{x_2}{s_{12}^2}\right] \cdot \left[s_{12} \log\left(\frac{s_{12}}{\Lambda^2}\right)\right]^{-1} \tag{6.21}$$

where $\Lambda \approx 0.3$ GeV.

6.7 Full Dalitz Plot Fit

The fit strategy is based on three steps:

1. determine the parameters of the Dalitz plot model fitting the $B^0 \to K^+K^-K^0_S(\pi^+\pi^-)$ dataset, which has the highest statistics and the best purity;

2. add the other two modes, $B^0 \to K^+K^-K^0_S(\pi^0\pi^0)$ and $B^0 \to K^+K^-K^0_L$, to determine the *CP* asymmetry. In this step, we assume that all amplitudes have the same *CP* asymmetry parameters;

3. measure *CP* asymmetry parameters for components with low K^+K^- invariant mass with a reduced model-dependence from the rest of the Dalitz plot (in fact, this region is dominated by only two resonances, $\phi(1020)$ and $f_0(980)$, while the contribution of $X_0(1500)$ and non resonant can be considered negligible). In this case, we fit for separate *CP* asymmetry associated to the most significant resonances. This fit will be described in Sec. 6.8.

6.7.1 Validation Studies

In order to validate fit performances and to check for the absence of any bias in the fit, we perform a toy Monte Carlo validation, which consists in generating and fitting events according to the likelihood function we want to use in the nominal fit. For the values of *CP* asymmetry parameters, we assumed Standard Model values (which means no direct *CP* asymmetry A_{CP} and $\beta_{eff} = \beta_{SM}$). This is equivalent to set to zero the asymmetry in amplitude (b) and in phase (δ) (see Eq. 3.55).

Signal and background yields are generated experiment by experiment using Poisson distributions with yields and background parameters centered at the values we expect to find in data.

We define the pull for the parameter P_i as the quantity

$$pull(P_i) = \frac{P_i^{fit} - P_i^{gen}}{\sigma_i} \tag{6.22}$$

where P_i^{fit} is the fitted value, σ_i is the associated error, and P_i^{gen} is the value used in generation. In case of unbiased fit and with sufficient statistics, the pull variable should follow a Gaussian distribution with mean consistent with zero and a standard deviation consistent with one.

Name	Fitted Value
nSigTot_CPKKKs	878.9 ± 35.7
nBkg_{KaonII}	302.9 ± 19.2
nBkg_{KaonI}	137.3 ± 12.8
nBkg_{KaonPion}	265.9 ± 17.7
nBkg_{Lepton}	7.09 ± 4.63
nBkg_{Notag}	837.3 ± 31.1
nBkg_{Other}	257.4 ± 17.2
nBkg_{Pion}	334.6 ± 19.9
nBBkgTot_np	69.7 ± 23.3

Table 6.13: $K^+K^-K^0_S$ mode: Results for the signal and background yields. $nBkg$ stands for number of continuum background events, while $nBBkgTot$ stands for the number of combinatorial (non-peaking) $B\overline{B}$ background events.

In Fig. 6.35 we show the pulls on the signal and background yields (the latter split by tagging category), while in Fig. 6.36 we show the pulls on isobar amplitudes and phases.

All these toy Monte Carlo tests show that the likelihood fit is able to extract the signal parameters from data without any significant biases.

6.7.2 Fit Results for Isobar Amplitudes and Phases

We perform multiple maximum-likelihood fits to data sample. In each fit we randomize initial parameters in order to look for local minima of likelihood in the entire parameter space.

The complete list of the fitted yields is shown in Table 6.13. We find a signal yield of 879 ± 36 events for $B^0 \to K^+K^-K^0_S$. These results have only a small dependence on the choice of Dalitz plot model and the set of initial parameters. We treat differences as a systematic error.

In Fig. 6.37 we show the fit results on the selection variables $m_{\rm ES}$ and ΔE on the on-resonance dataset. For each component of the likelihood (signal, continuum and $B\overline{B}$ background) we apply the ${}_s\mathcal{P}lot$ event-weighting technique [80].

The fraction for each resonance r is computed by the isobar amplitudes:

$$\mathcal{F}_r \;=\; \frac{\int d\cos\theta_H \; dm_{K^+K^-} \cdot |J| \cdot (|\mathcal{A}_r|^2 + |\bar{\mathcal{A}}_r|^2)}{\int d\cos\theta_H \; dm_{K^+K^-} \cdot |J| \cdot (|\mathcal{A}|^2 + |\bar{\mathcal{A}}|^2)}. \tag{6.23}$$

The sum of the fractions can differ from unity due to interference between the resonances. The isobar amplitudes, phases, and fractions for each resonance are listed in Table 6.14.

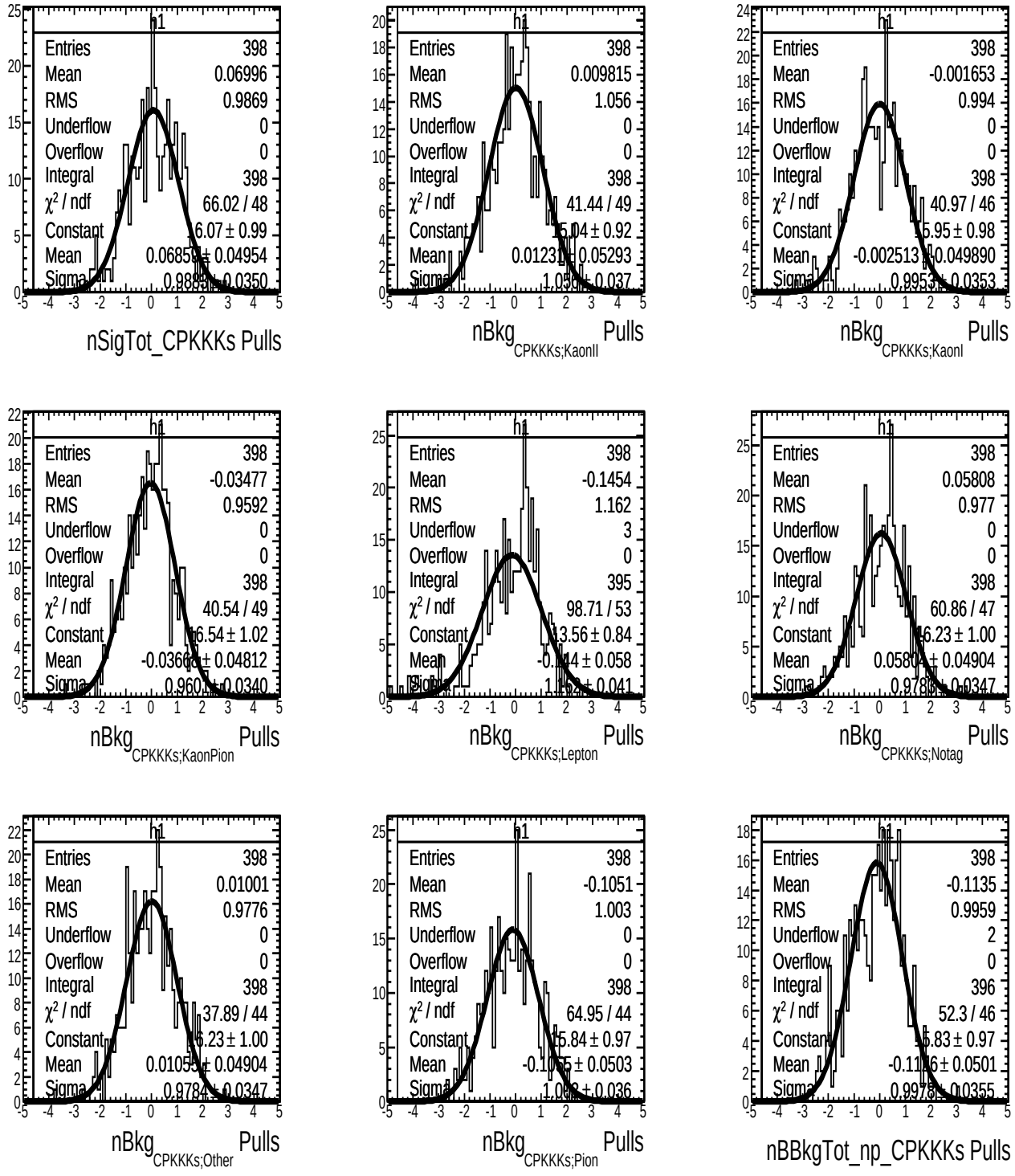

Figure 6.35: Pull distributions of $B^0 \to K^+K^-K^0_S(\pi^+\pi^-)$ yields.

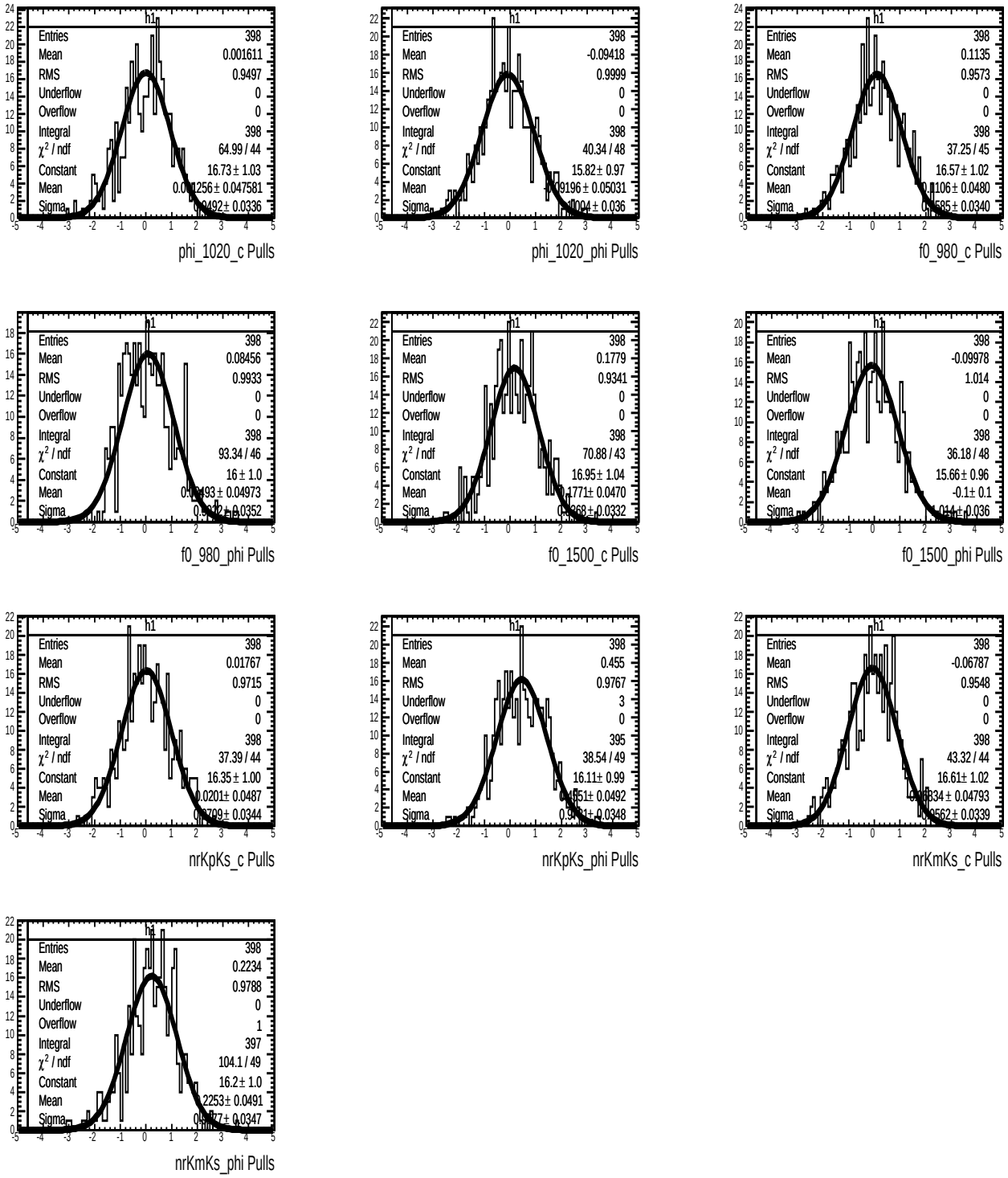

Figure 6.36: Pull distributions of $B^0 \to K^+K^-K^0_S(\pi^+\pi^-)$ isobar amplitudes and phases.

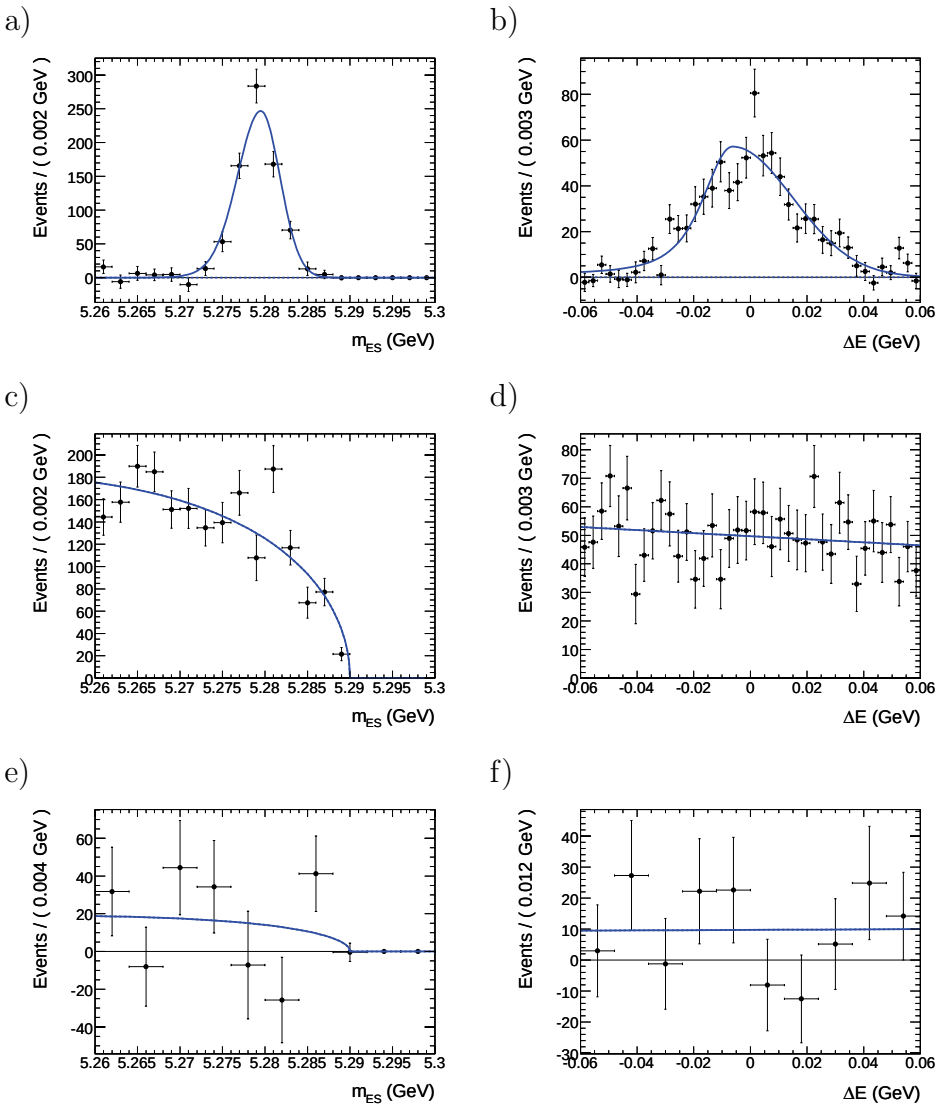

Figure 6.37: $K^+K^-K^0_S(\pi^+\pi^-)$ mode: ${}_s\mathcal{P}lot$'s of selection variables overlaid with PDF for (a-b) signal, (c-d) continuum, and (e-f) combinatorial B background.

Decay	Amplitude c_r	Phase ϕ_r	Fraction $\mathcal{F}_r$ (%)
$\phi(1020)K^0$	0.0098 ± 0.0016	-0.11 ± 0.31	12.9 ± 1.3
$f_0(980)K^0$	0.528 ± 0.063	-0.33 ± 0.26	22.3 ± 8.9
$X_0(1550)K^0$	0.130 ± 0.025	-0.54 ± 0.24	4.1 ± 1.8
$NR \quad (K^+K^-)$	1 (fixed)	0 (fixed)	
(K^+K^0)	0.38 ± 0.11	2.01 ± 0.28	91 ± 19
(K^-K^0)	0.38 ± 0.16	-1.19 ± 0.37	
$\chi_{c0}K^0$	0.0343 ± 0.0067	1.29 ± 0.41	2.84 ± 0.77
D^+K^-	1.18 ± 0.24	–	3.18 ± 0.89
$D_s^+K^-$	0.85 ± 0.20	–	1.72 ± 0.65

Table 6.14: Isobar amplitudes, phases, and fractions from the fit to the $B^0 \to K^+K^-K^0_S(\pi^+\pi^-)$ sample. Three rows for non-resonant contribution correspond to coefficients of exponential functions in Eq. (6.20), while the fraction is given for the combined amplitude. Errors are statistical only.

In Fig. 6.38 we show the ${}_s\mathcal{P}lot$-weighted distributions of the Dalitz plot variables for $B^0 \to K^+K^-K^0_S(\pi^+\pi^-)$.

We compare our fractions with other Dalitz plot analyses using flavor symmetry [81]. We find consistent fractions for decays through the $\phi(1020)$ resonances with the $B^+ \to K^+K^+K^-$ decay [75, 76]. The fraction of $f_0(980)K^0$ decays is consistent with the study of $B^+ \to K^+K^+K^-$ decays by *BABAR* Collaboration, and all $B^+ \to K^+\pi^+\pi^-$ Dalitz plot analyses [75, 76, 82]. The fraction of non-resonant decays, which is predicted to be half of the contribution in $B^+ \to K^+K^+K^-$ [81], is harder to compare since existing measurements in the charged mode are inconsistent. Our result agrees well with *BABAR*'s result [76], and is within two standard deviations of Belle's result [75]. Determination of the wide scalar resonance at 1.5 GeV/c^2, labeled as $X_0(1550)$, is even more uncertain. Using the same resonant parameters as in the analysis of the charged mode, we find a much smaller fraction than in *BABAR*'s analysis [76], but our solution is more consistent with Belle's $B^+ \to K^+K^+K^-$ analysis [75].

6.7.3 Fit to the *CP* Asymmetry in $B^0 \to K^+K^-K^0$

While the other two sub-modes have not sufficient purity to extract the isobar parameters from data, they can be added in the fit for the time-dependent *CP* asymmetry. In-fact, above all $B^0 \to K^+K^-K^0_L$ provide a significant contribution in terms of signal statistics, even if with low purity.

We then fix the isobar amplitudes and phases to the ones fitted in the $K^+K^-K^0_S$

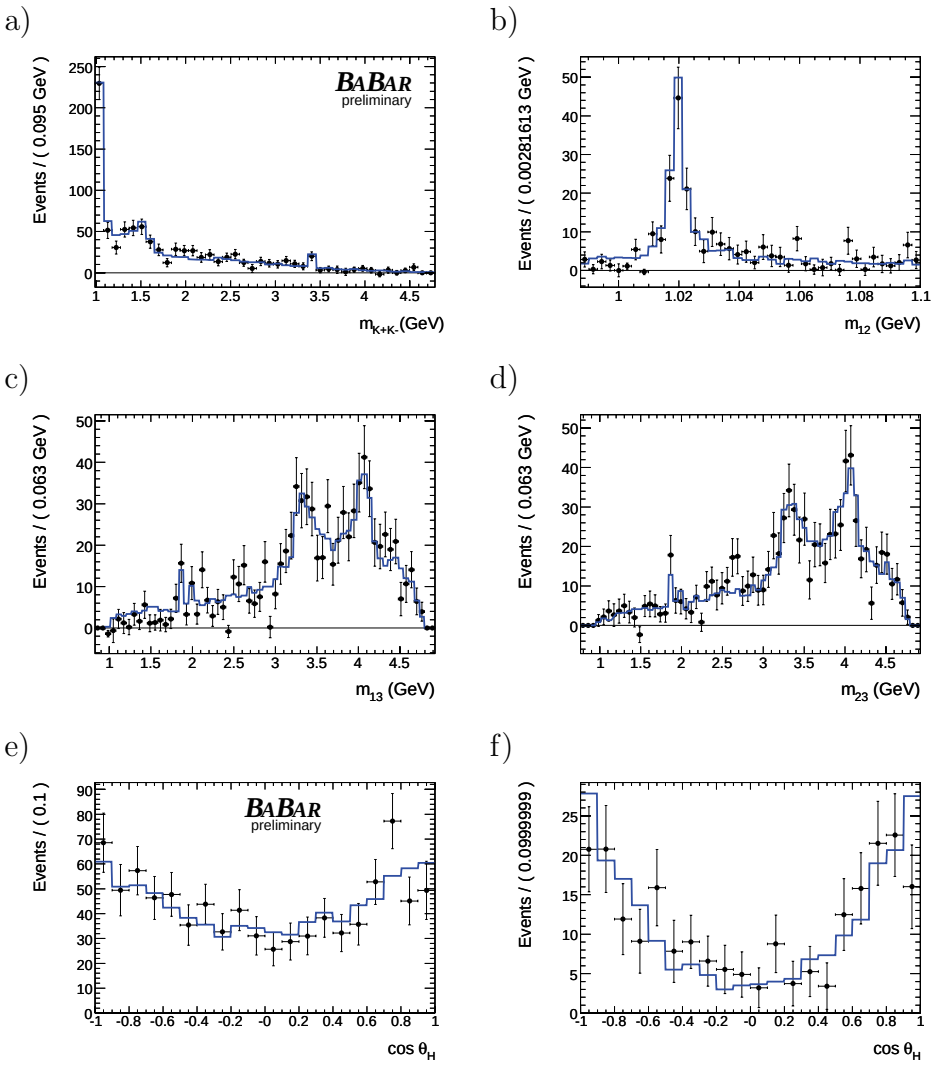

Figure 6.38: $K^+K^-K^0_S(\pi^+\pi^-)$ mode: ${}_s\mathcal{P}lot$'s of Dalitz plot variables overlaid with PDF for signal events. (a) K^+K^- invariant mass in the whole region; (b) K^+K^- invariant mass for the low mass region ($m_{K^+K^-} < 1.1$ GeV/c^2); (c) $K^+K^0_S$ invariant mass; (d) $K^-K^0_S$ invariant mass; The higher peaks in $K^+K^0_S$ and $K^-K^0_S$ are reflections of the $\phi(1020)$, while the bump near 1.8 GeV/c^2 is the D^+ contribution. (e) $\cos\theta_H$ for the whole Dalitz plot (f) $\cos\theta_H$ for the low mass region $m_{K^+K^-} < 1.1$ GeV/c^2.

sample and reported in Table 6.14 and fit the asymmetries in amplitude (b in the polar coordinates) and in the phase (δ in the polar coordinates) simultaneously on the combined $K^+K^-K^0$ data sample. In order to take into account the opposite *CP* eigenvalue of $K^+K^-K^0_L$ decay with respect to $K^+K^-K^0_S$, we have to produce a sign flip in the "sine term" of Eqn. 3.1:

$$+q2Im\left(\bar{\mathcal{A}}\mathcal{A}^* e^{-2i\beta}\right).$$

This is achieved in the fit with the substitution $\beta \to \beta + \pi/2$ in the $K^+K^-K^0_L$ time-dependent Dalitz PDF.

The isobar parameters b and δ can be translated in terms of direct *CP* asymmetry and mixing-induced *CP* asymmetry, respectively:

$$A_{CP} = -\frac{|c|^2 - |\bar{c}|^2}{|c|^2 + |\bar{c}|^2} = -\frac{2b}{1+b^2} \tag{6.24}$$

$$\beta_{eff} = \beta_{SM} + \delta \tag{6.25}$$

where $\beta_{SM} = 0.379$ is a constant offset set to the Standard Model value of the CKM angle β.

Validation of the *CP* Fit

We validate the combined fit with a set of toy Monte Carlo experiments. We fit simultaneously the signal and background yields for the three sub-modes, together with the *CP* asymmetry parameters. In the same time, most of background parameters are left varying in the fit.

In Fig. 6.39 we show the pulls for the signal and background yields for all the modes, while in Fig. 6.40 are the fitted values. In Fig. 6.41 we show the pulls for the background tagging fractions, which are kept varying in the fit.

In Fig. 6.42 we show the pulls, the fitted central values and the distribution of errors on the *CP* parameters b and δ.

From these toy experiments it is evident that the likelihood is able to fit all the signal yields, together with the *CP* asymmetry parameters, without significant bias. Then we perform this fit on the combined $B^0 \to K^+K^-K^0$ dataset.

Results on the *CP* Asymmetry for the Full $B^0 \to K^+K^-K^0$ Dalitz Plot

The results on the $K^+K^-K^0_S(\pi^+\pi^-)$ yields are consistent with the ones obtained with the single mode fit and reported in Table 6.13.

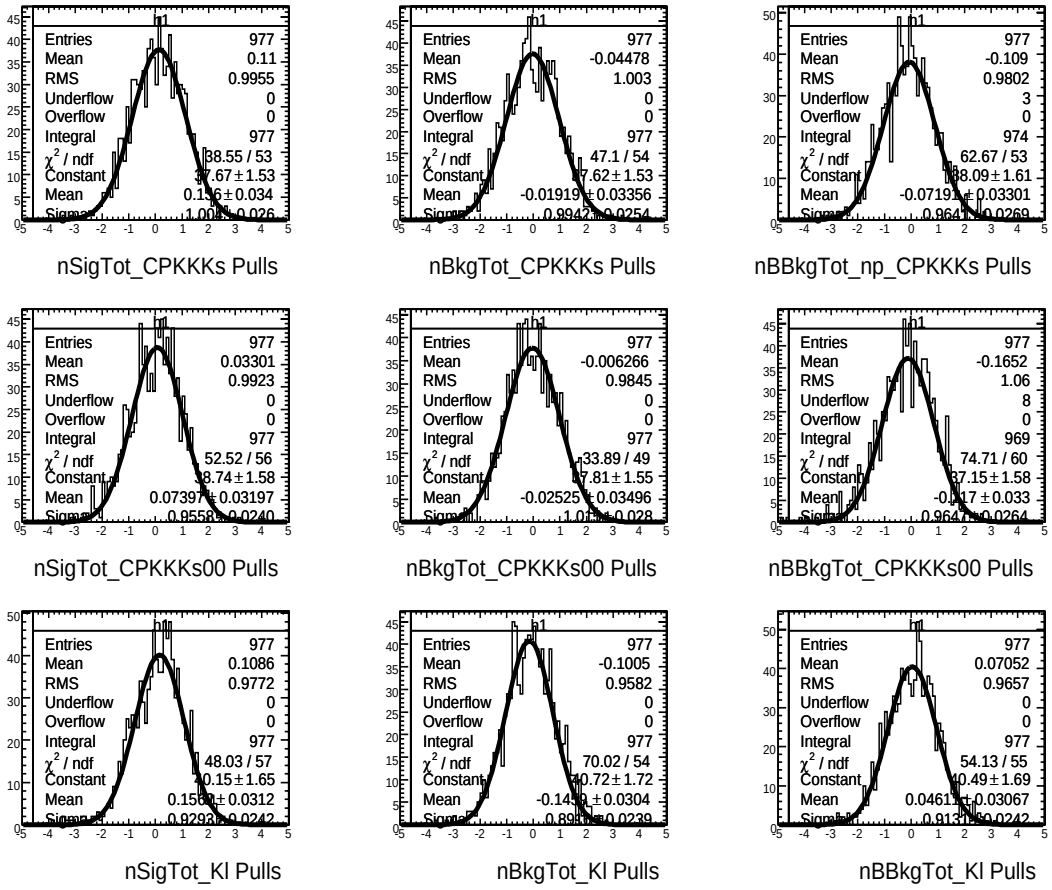

Figure 6.39: Toy results for the combined fit to the whole Dalitz plot for all three submodes: $K^+K^-K^0_S(\pi^+\pi^-)$ (top), $K^+K^-K^0_S(\pi^0\pi^0)$ (middle), and $K^+K^-K^0_L$ (bottom): distributions of pulls for the event yields.

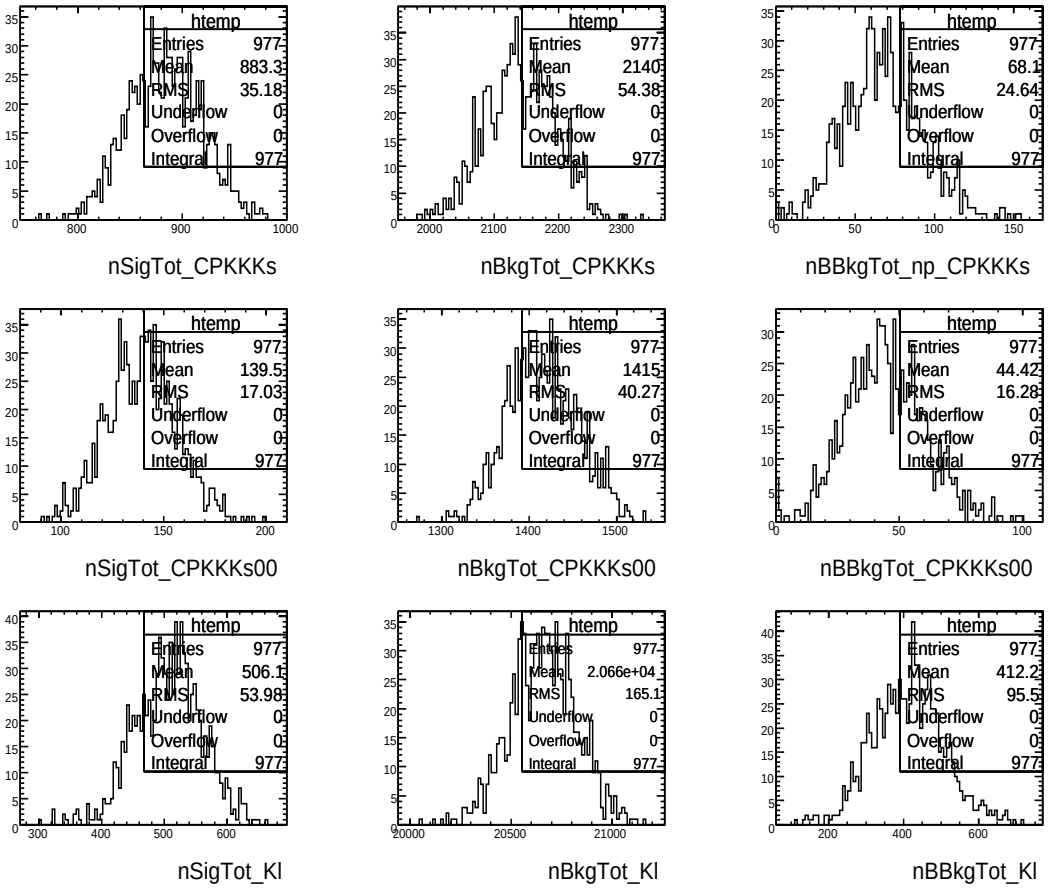

Figure 6.40: Toy results for the combined fit to the whole Dalitz plot for all three submodes: $K^+K^-K^0_S(\pi^+\pi^-)$ (top), $K^+K^-K^0_S(\pi^0\pi^0)$ (middle), and $K^+K^-K^0_L$ (bottom): distributions of central values for the event yields.

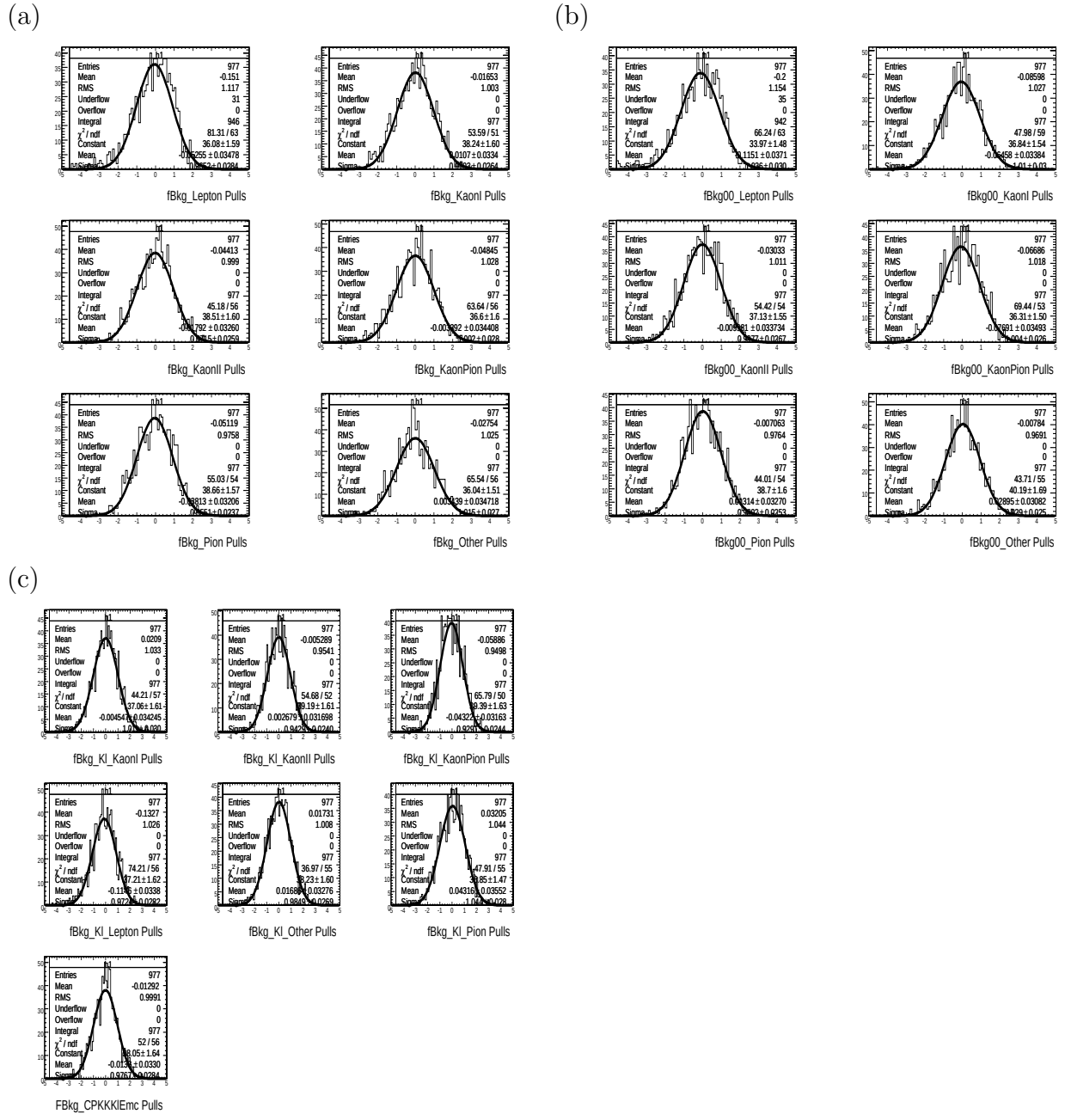

Figure 6.41: Toy results for the combined fit to the whole Dalitz plot. Pulls distributions for the background yield fractions for: (a) $K^+K^-K^0_S(\pi^+\pi^-)$, (b) $K^+K^-K^0_S(\pi^0\pi^0)$, and (c) $K^+K^-K^0_L$.

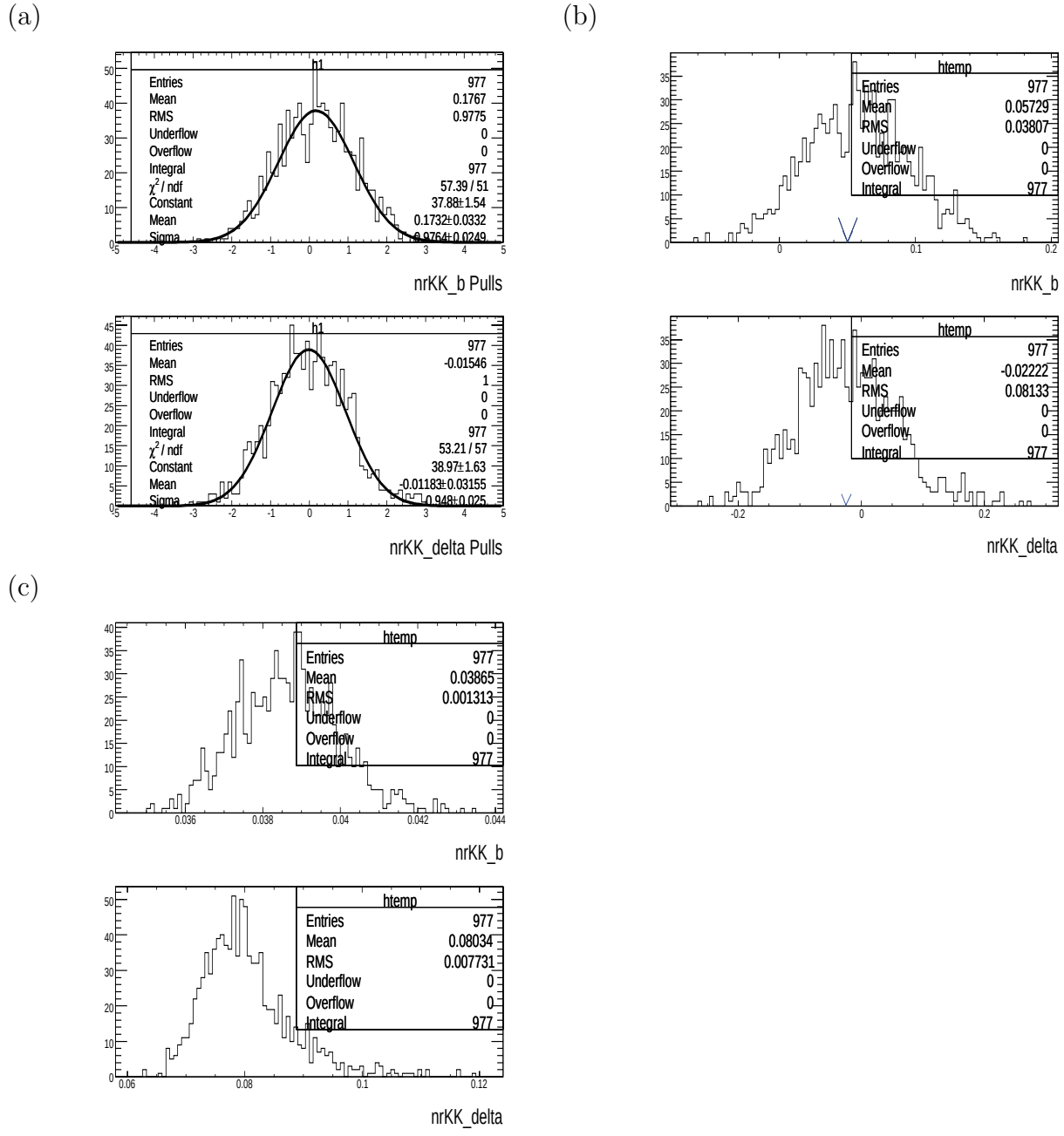

Figure 6.42: Toy results for the combined fit to the whole Dalitz plot for all three sub-modes: $K^+K^-K^0_S(\pi^+\pi^-)$, $K^+K^-K^0_S(\pi^0\pi^0)$, and $K^+K^-K^0_L$: Distributions of (a) pulls, (b) values, and (c) errors for the DP-averaged *CP* parameters. Blue arrowheads in (b) indicate the generated value for the toys.

Name	Fitted Value
nSigTot	138.3 ± 16.9
nBkgTot	1415.1 ± 40.6
nBBkgTot_np	45.6 ± 16.6
fBkg00_KaonI	0.058 ± 0.006
fBkg00_KaonII	0.107 ± 0.009
fBkg00_KaonPion	0.105 ± 0.008
fBkg00_Lepton	0.0036 ± 0.0019
fBkg00_Other	0.137 ± 0.009
fBkg00_Pion	0.160 ± 0.010

Table 6.15: $K^+K^-K^0_S(\pi^0\pi^0)$ mode: Results for the signal and background yields. $nBkg$ stands for number of continuum background events, while $nBBkgTot$ stands for the number of combinatorial (non-peaking) $B\overline{B}$ background events.

Name	Fitted Value
nSigTot	583.1 ± 59.7
nBkgTot	20578 ± 172
nBBkgTot_np	422.2 ± 98.3
fBkgKL_KaonI	0.059 ± 0.001
fBkgKL_KaonII	0.140 ± 0.003
fBkgKL_KaonPion	0.140 ± 0.003
fBkgKL_Lepton	0.0011 ± 0.0009
fBkgKL_Other	0.123 ± 0.002
fBkgKL_Pion	0.167 ± 0.003

Table 6.16: $K^+K^-K^0_S(\pi^0\pi^0)$ mode: Results for the signal and background yields. $nBkg$ stands for number of continuum background events, while $nBBkgTot$ stands for the number of combinatorial (non-peaking) $B\overline{B}$ background events.

The signal and background yields for the $K^+K^-K^0_S(\pi^0\pi^0)$ sub-mode are consistent with what expected (see Table 6.15). We show the signal and background ${}_s\mathcal{P}lot$-weighted distributions for the selection variables $m_{\rm ES}$ and ΔE in Fig. 6.43, while we show in Fig. 6.44 the signal ${}_s\mathcal{P}lot$ distributions for the Dalitz variables.

The results for the yields of $B^0 \to K^+K^-K^0_L$ are reported in Table 6.16.

We show the ΔE distribution in Fig. 6.45, where we apply harder cuts on event shape variables (with 30% efficiency on signal) to enhance the signal in the plot. We show in Fig. 6.46 the signal ${}_s\mathcal{P}lot$ distributions for the Dalitz variables for $K^+K^-K^0_L$ sub-mode.

Note that for all the three sub-modes we use the same Dalitz plot model (which is the one fitted in $K^+K^-K^0_S$ by alone), but the model in the projection plots of Figs. 6.38,

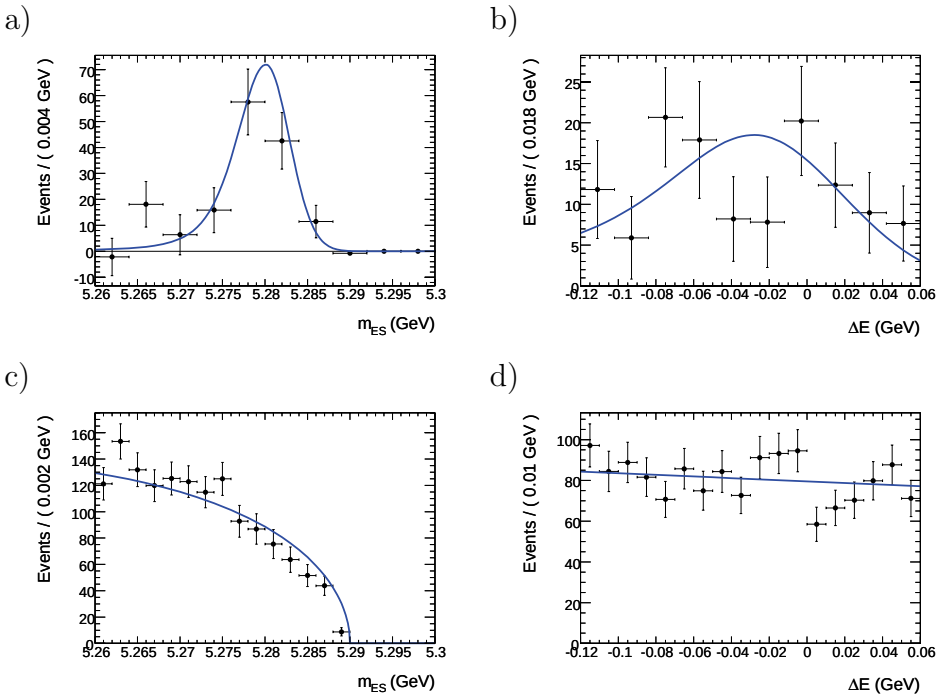

Figure 6.43: $K^+K^-K^0_S(\pi^0\pi^0)$ mode: ${}_s\mathcal{P}lot$-weighted distributions of selection variables overlaid with PDF.

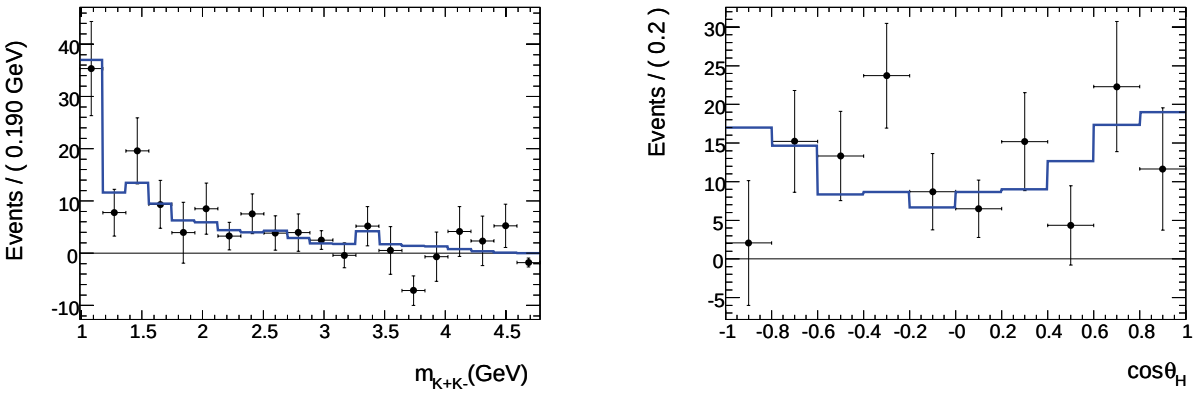

Figure 6.44: Distributions of the Dalitz plot variables (left) $m_{K^+K^-}$ and (right) $\cos\theta_H$ for signal events (points) compared with the fit PDF in the $K^+K^-K^0_S(\pi^0\pi^0)$ sub-sample.

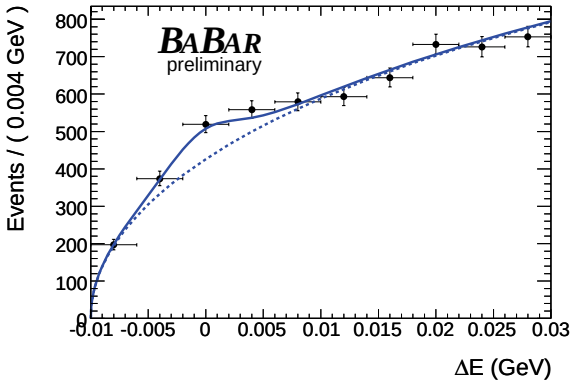

Figure 6.45: Distribution of the kinematic variable ΔE for the $K^+K^-K^0_L$ sub-sample. The solid line represents the total likelihood, while the dashed line represents the sum of continuum and $B\overline{B}$ background. A tight requirement on the event shape variables is applied to enhance the signal, with an efficiency of about 30% for signal.

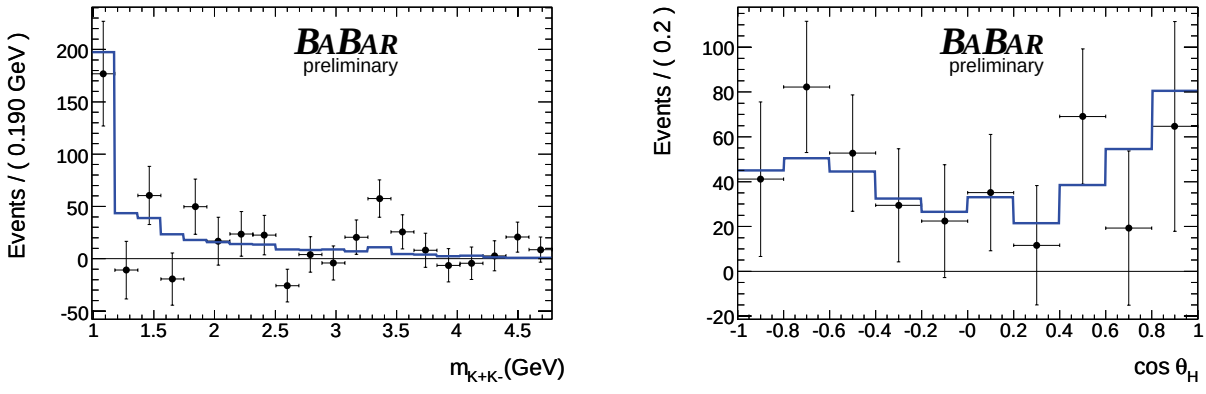

Figure 6.46: Distributions of the Dalitz plot variables (left) $m_{K^+K^-}$ and (right) $\cos\theta_H$ for signal events (points) compared with the fit PDF in the $K^+K^-K^0_L$ sub-sample.

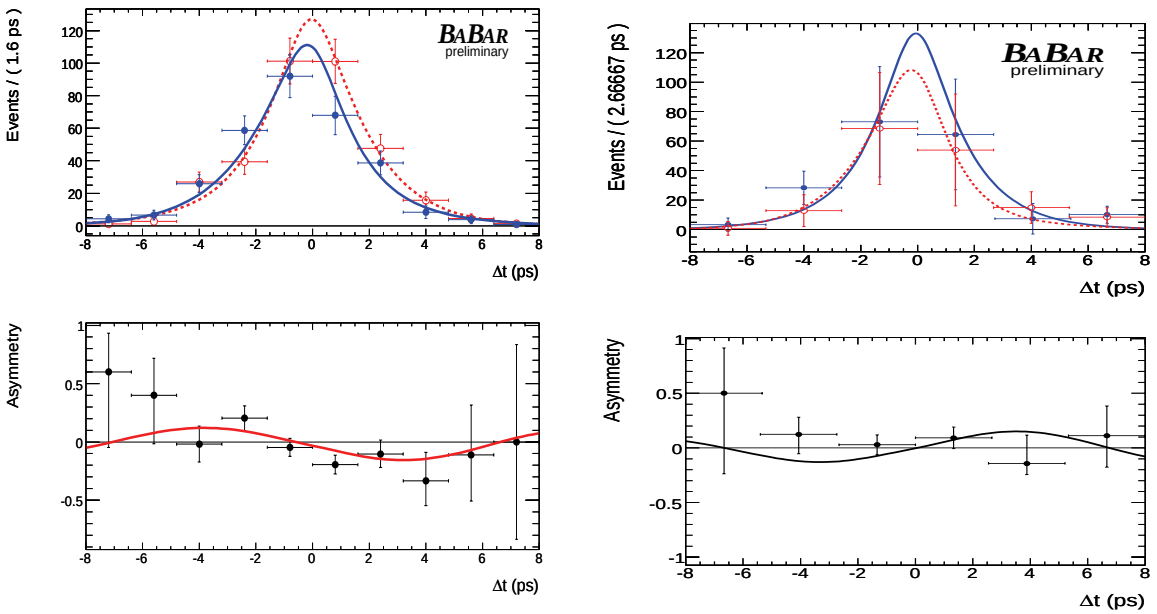

Figure 6.47: (top) Δt distributions and (bottom) asymmetries in the (left) $K^+K^-K^0_S(\pi^+\pi^-)$ and (right) $K^+K^-K^0_L$. For the Δt distributions, B^0- ($\overline{B}^0$-) tagged signal-weighted events are shown as filled (open) circles, with the PDF projection in solid blue (dashed red). We do not show the single $K^+K^-K^0_S(\pi^0\pi^0)$ sub-mode because of the poor statistics.

6.44, 6.46 can be different because the efficiency across the Dalitz plot is different.

In Table 6.17 we report the results on the *CP* asymmetry parameters, expressed in terms of direct *CP* asymmetry A_{CP} and weak phase β_{eff}. The expected values in the Standard Model are A_{CP} =0 and β_{eff} =0.379 [30].

Parameter	$K^+K^-K^0_S(\pi^+\pi^-)$	$K^+K^-K^0_S(\pi^0\pi^0)$	$K^+K^-K^0_L$	Combined
A_{CP}	-0.10 ± 0.09	-0.10 ± 0.28	0.28 ± 0.20	-0.034 ± 0.079 ± 0.025
β_{eff}	0.37 ± 0.08	0.24 ± 0.22	0.29 ± 0.21	0.361 ± 0.079 ± 0.037

Table 6.17: Results for direct *CP* asymmetry A_{CP} and mixing induced *CP* asymmetry parameter β_{eff} in the three different sub-modes studied for the decay $B^0 \to K^+K^-K^0$.

The fitted value for β_{eff} which has the minimum $\log(L)$ is consistent with one standard deviation with the preferred solution by the Unitarity Triangle fit.

We show in Fig. 6.47 the ${}_s\mathcal{P}lot$-weighted time difference distribution Δt for B^0 and $\overline{B}^0$ tags for $B^0 \to K^+K^-K^0_S$ and $B^0 \to K^+K^-K^0_L$, showing a large *CP* asymmetry effect with opposite eigenvalue between K^0_S and K^0_L.

We also remove an ambiguity in the solution for the mixing angle $\beta_{eff} \to \pi/2 -$

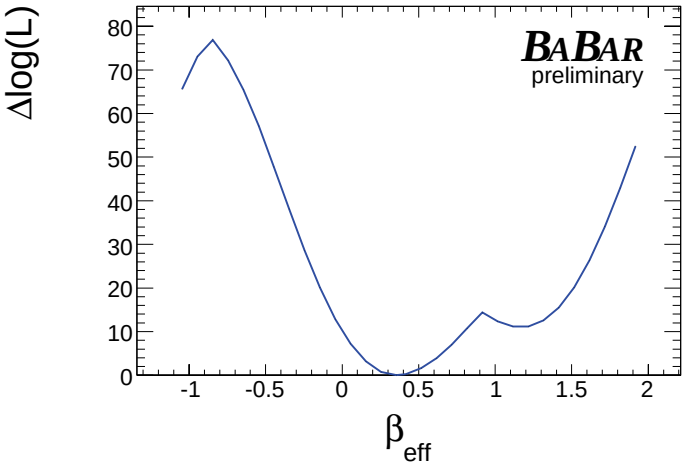

Figure 6.48: Change in the $\Delta \log(\mathcal{L})$ value as a function of β_{eff}. SM expectation value is β_{eff} =0.379.

β_{eff} (present in previous measurements of $\sin(2\beta_{eff})$ in penguin decays). We estimate the significance of the nominal result for β_{eff} compared to the trigonometric reflection where $\beta_{eff} \rightarrow \pi/2 - \beta_{eff}$. In a collection of fits with both isobar coefficients and *CP*-asymmetry parameters allowed to vary, we randomize the initial parameter values and evaluate the likelihood separation between these two solutions. We find $\Delta \log(\mathcal{L}) = 10.4$, which excludes the reflection at a significance of 4.6 standard deviations. Note that the ambiguity $\beta_{eff} \rightarrow \beta_{eff} + \pi$ still remains since we measure the total phase difference between B^0 and $\overline{B}^0$ decays ($2\beta_{eff}$). A scan of the change in likelihood as a function of β_{eff} is shown in Figure 6.48.

Fig. 6.49 shows the allowed 4-fold ambiguity on β by the $\sin 2\beta$ measurement in $B^0 \rightarrow [c\bar{c}]K^0$ decays. Our measurement rejects the band at higher β at 4.6 σs, which is already disfavoured by other measurements of the Unitarity Triangle [30].

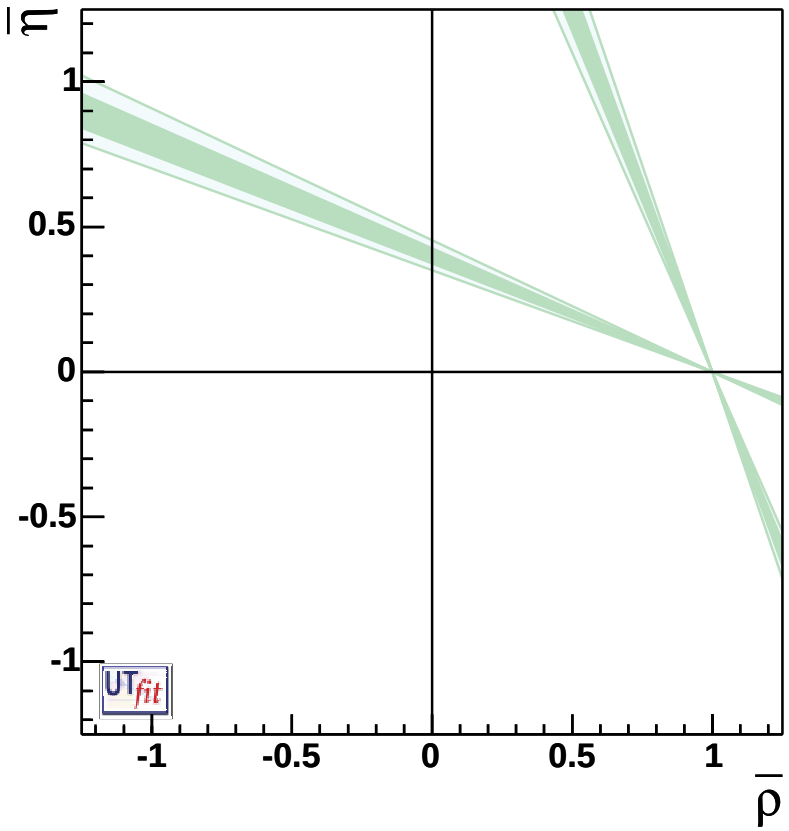

Figure 6.49: Allowed 4-fold bands for β angle of the Unitarity Triangle from measurement of $\sin 2\beta$ in $B^0 \to [c\bar{c}]K^0$ decays. Our measurement removes the higher β band.

6.8 *CP* Asymmetry in the Low K^+K^- Mass Region

The region of low K^+K^- invariant mass is the one where the interference between *CP*-even and *CP*-odd decays is the largest, due to the presence of the strong P-wave contribution of the $\phi(1020)$. The $B^0 \to \phi K^0$ is also the one with the lowest theoretical uncertainties on β_{eff}.

We select events in the low K^+K^- mass region using a cut of $m_{K^+K^-} < 1.1$ GeV/c^2. After this selection, we retain 836 $K^+K^-K^0_S(\pi^+\pi^-)$ candidates, 202 $K^+K^-K^0_S(\pi^0\pi^0)$ candidates, and 4923 $K^+K^-K^0_L$ candidates. The most significant contribution in this region comes from $\phi(1020)K^0$ and $f_0(980)K^0$ decays, with a smaller contribution from a low-K^+K^- tail of non-resonant decays. We vary the isobar parameters for the $\phi(1020)$ and fix all other components to the results of the full Dalitz plot fit. We also vary the *CP* amplitude and phase asymmetries for the $\phi(1020)$ and $f_0(980)$. The asymmetry for the other components is fixed to the SM expectation. This is one of the main difference with respect to the full Dalitz plot fit, i.e. allowing for different resonances to have different *CP* asymmetries, which in practice means allowing $B^0 \to \phi K^0$ to receive different New Physics contributions with respect to $B^0 \to f_0 K^0$ decays.

6.8.1 Validation Studies

We validate also the fitting procedure for the low mass region because of the higher number of floating parameters with respect to the full Dalitz plot fit (different *CP* asymmetry for f_0K^0 and isobar amplitude c_r and phase ϕ_r for ϕK^0). We perform toy Monte Carlo experiments using the Standard Model values as generation values for the *CP* asymmetries for $B^0 \to \phi K^0$ and $B^0 \to f_0 K^0$. In Fig. 6.50 we show the pull distributions for the isobar parameters and the *CP* asymmetries; in Fig. 6.51 and 6.52 the fitted central values and errors on them, respectively.

These fitter test show that the likelihood is able to fit the isobar parameters and the *CP* asymmetries in the low mass region separately for $\phi(1020)$ and $f_0(980)$ resonances.

6.8.2 Fit Results

We perform a fit to all sub-modes, then perform an additional fit to the entire $K^+K^-K^0$ sample. We find signal yields of 252 ± 19, 35 ± 9, and 195 ± 33 events for $K^+K^-K^0_S(\pi^+\pi^-)$, $K^+K^-K^0_S(\pi^0\pi^0)$, and $K^+K^-K^0_L$ respectively. Fig. 6.53 shows projections of the Dalitz

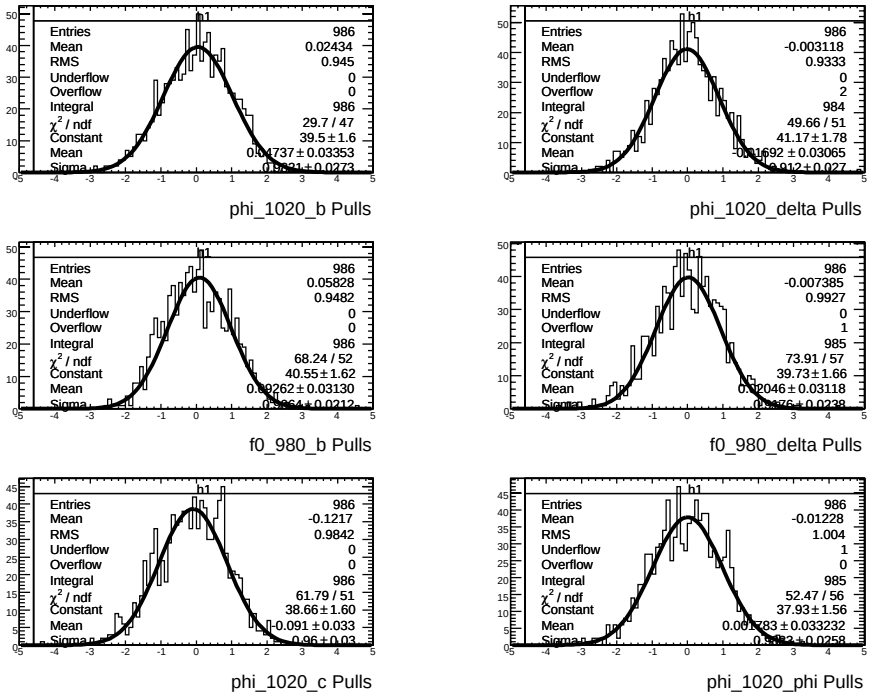

Figure 6.50: Toy results for low-mass fit to all $K^+K^-K^0$ events: pull distributions for the isobar parameters and *CP* asymmetries.

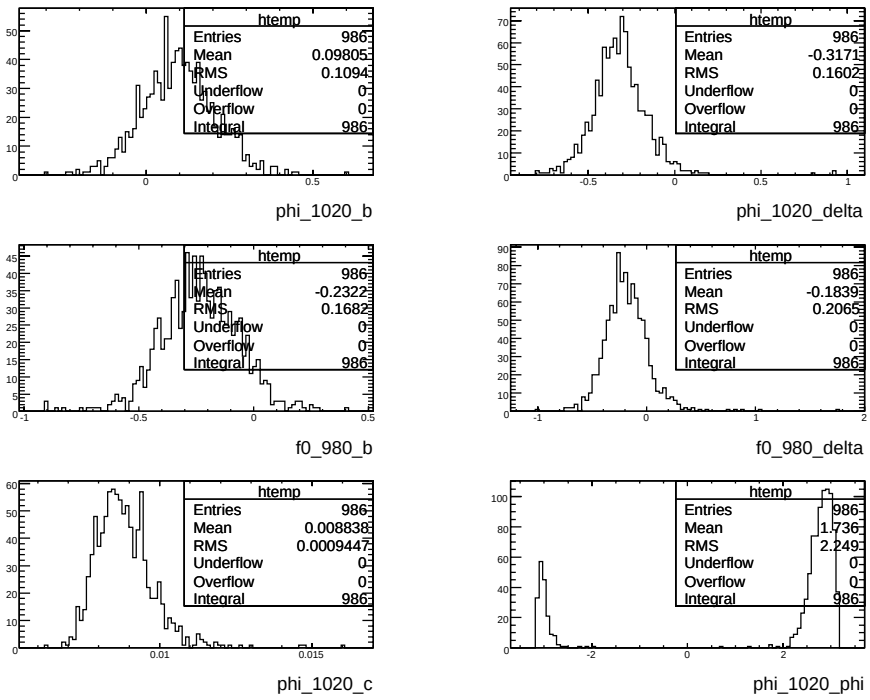

Figure 6.51: Toy results for low-mass fit to all $K^+K^-K^0$ events: distributions of fit values for the isobar parameters and *CP* asymmetries

plot distributions of events in this region. The *CP*-asymmetry results are listed in Table 6.18. The plots in Fig. 6.54 show distributions of Δt for B^0-tagged and $\overline{B}^0$-tagged events, and the asymmetry, obtained with the ${}_s\mathcal{P}lot$ event-weighting technique, for the $K^+K^-K^0_S(\pi^+\pi^-)$ and $K^+K^-K^0_L$ sub-samples.

The decay $B^0 \to \phi K^0$, with highly suppressed tree amplitudes, is, in terms of theoretical uncertainty, the cleanest channel to interpret possible deviations of the *CP*-violation parameters from the SM expectations (A_{CP} =0 and β_{eff} =0.379). Values of β_{eff} are consistent with the value found in $B^0 \to [c\bar{c}]K^0$ decays [37, 38].

Parameter	$K^+K^-K^0_S(\pi^+\pi^-)$	$K^+K^-K^0_S(\pi^0\pi^0)$	$K^+K^-K^0_L$	Combined
$A_{CP}(\phi K^0)$	-0.10 ± 0.23	-0.83 ± 0.43	0.56 ± 0.26	-0.18 ± 0.20 ± 0.10
β_{eff}	0.02 ± 0.16	0.32 ± 0.69	0.90 ± 0.30	0.06 ± 0.16 ± 0.05
$A_{CP}(f_0(980)K^0)$	0.36 ± 0.33	0.37 ± 1.25	0.0 (fixed)	0.45 ± 0.28 ± 0.10
$\beta_{eff}(f_0(980)K^0)$	0.04 ± 0.18	0.50 ± 1.26	0.379 (fixed)	0.18 ± 0.19 ± 0.04

Table 6.18: Results for direct *CP* asymmetry A_{CP} and mixing induced *CP* asymmetry parameter β_{eff} in the three different sub-modes studied for the decay $B^0 \to K^+K^-K^0$. The fits in the $B^0 \to K^+K^-K^0_S$ sub-modes, differently from $B^0 \to K^+K^-K^0_L$ allow the two *CP* asymmetries for $f_0(980)$ to vary, together with the two isobar parameters for the $\phi(1020)$. In $B^0 \to K^+K^-K^0_L$ only fit only the *CP* asymmetries, together with the yields are fitted.

6.8.3 Fit Fractions in Low K^+K^- Mass Region

From the low $m_{K^+K^-}$ fit to the $K^+K^-K^0_S(\pi^+\pi^-)$ mode only we also measure the isobar amplitudes and phases. We report the results on Table 6.19. When isobar parameters are

Name	Fitted Value
$\phi(1020)$ $\mathsf{c_r}$	0.009120 ± 0.000944
$\phi(1020)$ ϕ_r	-0.0304 ± 0.252

Table 6.19: Fitted isobar amplitude (c_r) and phase (ϕ_r) of the $\phi(1020)$ in the region $m_{K^+K^-} < 1.1$ GeV/c^2.

converted to fractions (Eq. 6.23) we get values listed in the second column of Table 6.20. We convert resonant fractions into branching fractions for the $K^+K^-K^0$ final state (full Dalitz plot):

$$\mathcal{B}_i = \frac{F_i \cdot N_{sig}}{N_{B\overline{B}} \cdot \varepsilon_i} \tag{6.26}$$

and list them in the Table 6.20. We also list branching fractions measured in $B^+ \to K^+K^+K^-$ decays [76]. Both charged and neutral channels have the same decay *rates* within flavor-symmetry assumption [81]. Both our branching fractions are within one sigma from previous measurements, although with large errors.

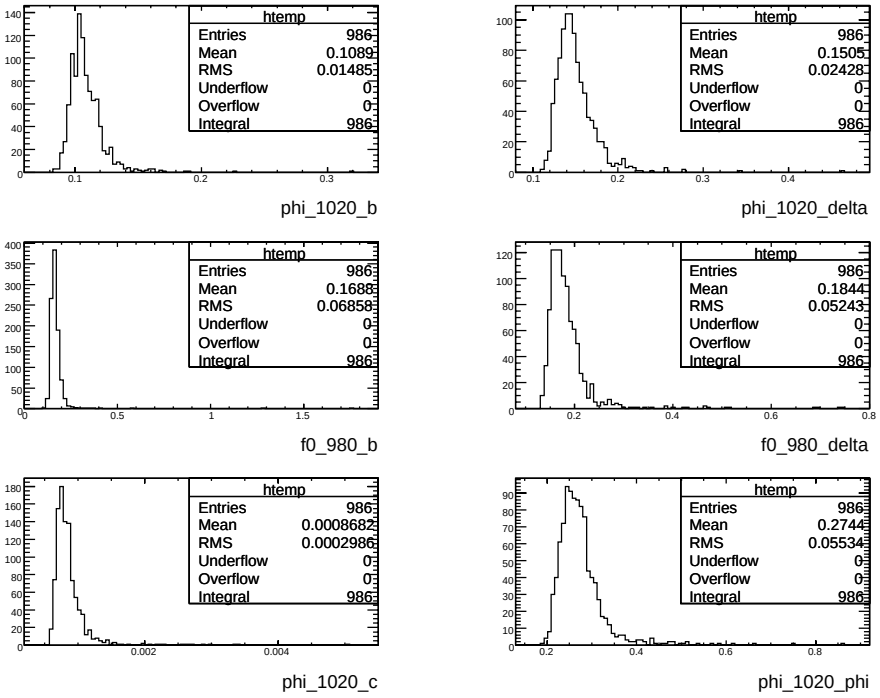

Figure 6.52: Toy results for low-mass fit to all $K^+K^-K^0$ events: distributions of fit errors for the isobar parameters and *CP* asymmetries

Name	F_i [%]	$\mathcal{B}(B^0 \to K^+K^-K^0)$	$\mathcal{B}(B^+ \to K^+K^+K^-) \times \frac{\tau_{B^0}}{\tau_{B^+}}$
ϕK^0_S	56.5 ± 4.6	3.3 ± 0.3(stat)	3.8 ± 0.4
$f_0 K^0_S$	23.4 ± 2.5	4.8 ± 0.5(stat)	6.0 ± 2.7
$(K^+K^-K^0_S)_{NR}$	10.7 ± 1.1	-	-

Table 6.20: $K^+K^-K^0_S(\pi^+\pi^-)$ mode: Fit to low K^+K^- mass data sample using time-dependent Dalitz plot fit. All branching fractions are in units 10^{-6}.

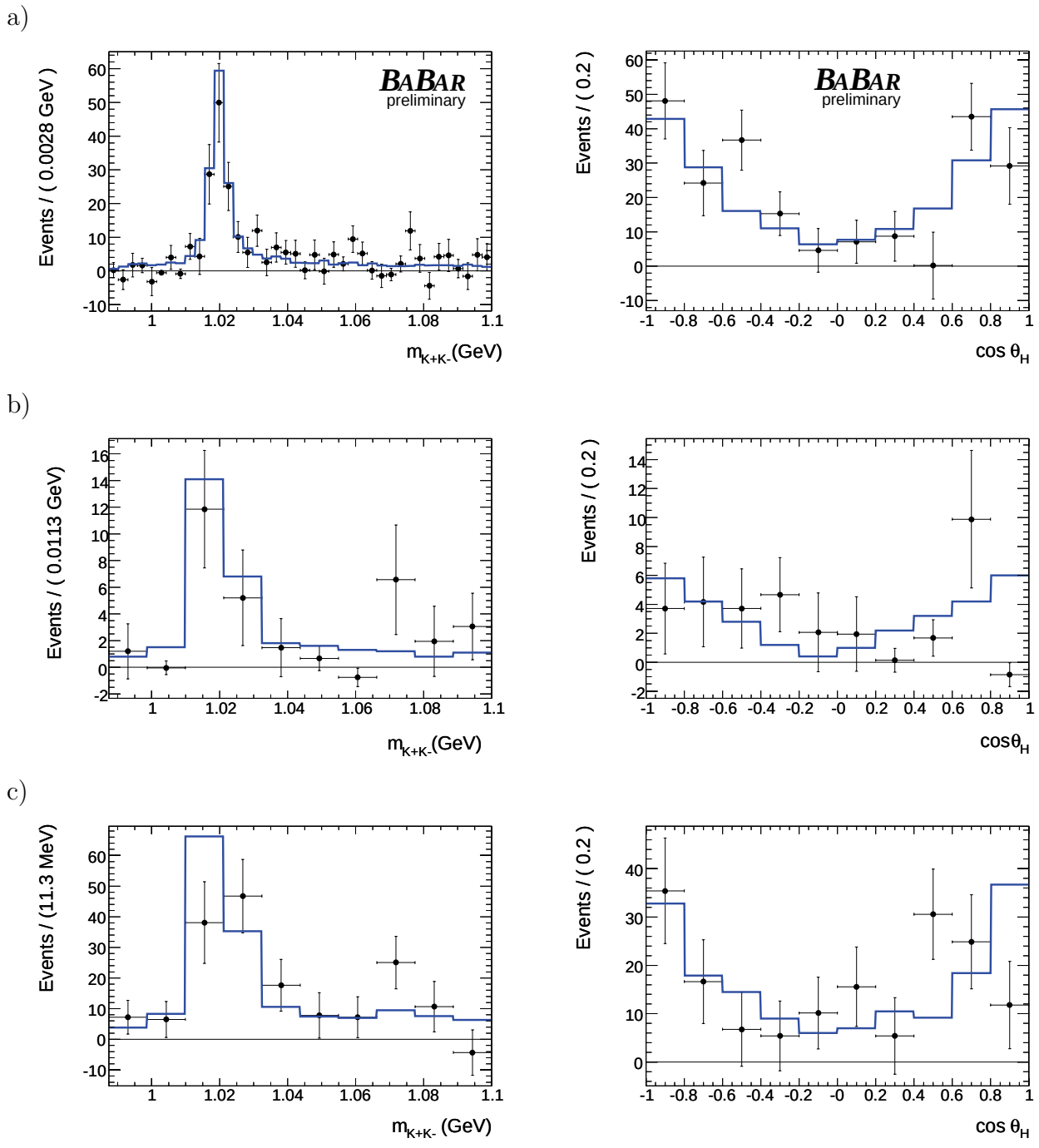

Figure 6.53: For the low-K^+K^- mass Dalitz plot fit, distributions of the Dalitz plot variables (left) $m_{K^+K^-}$ and (right) $\cos\theta_H$ for signal events (points) compared with the fit PDF in the following sub-samples: a) $K^+K^-K^0_S(\pi^+\pi^-)$, b) $K^+K^-K^0_S(\pi^0\pi^0)$, c) $K^+K^-K^0_L$.

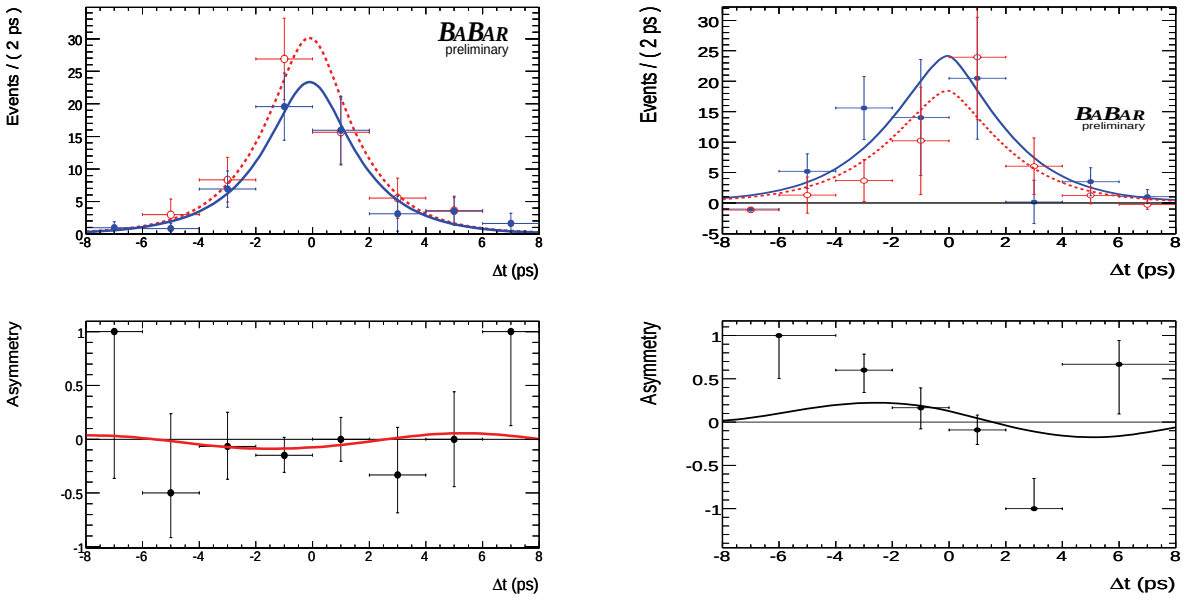

Figure 6.54: (top) Δt distributions and (bottom) asymmetries in the (left) $K^+K^-K^0_S(\pi^+\pi^-)$ and (right) $K^+K^-K^0_L$ in the low mass region $m_{K^+K^-} < 1.1$ GeV/c^2. For the Δt distributions, B^0- ($\overline{B}^0$-) tagged signal-weighted events are shown as filled (open) circles, with the PDF projection in solid blue (dashed red). We do not show the single $K^+K^-K^0_S(\pi^0\pi^0)$ sub-mode because of the poor statistics.

6.9 Systematic Uncertainties

We evaluate systematic uncertainties separately for the full Dalitz plot fit and the low mass fit. In the following we describe the sources of systematic uncertainties, and in Table 6.21 we show the summary of them for both the full Dalitz plot fit and the low mass fit.

Event Selection

We assign systematic uncertainties on the *CP* asymmetries due to parameters which are fixed in the fit. In a large set of toy samples, we perform two fits: first we make the nominal fit, then we vary the parameters by one standard deviation assuming that they follow a Gaussian distribution ("smearing procedure") and we repeat the fit. We take the average observed change from the nominal fit as the systematic error.

Fit Bias

We account for a potential fit bias using values observed in studies with toy MC events and full MC sample generated with a Dalitz plot model. We take the largest values of the bias observed in toy studies as the systematic error.

Vertexing Method and Tagging

We account for fixed Δt resolution parameters, B^0 lifetime, and mixing in the same way we evaluated the fixed parameters of the selection variables.

We also account for possible misalignment in the vertexing detector. We fit a Monte Carlo sample with five possible misalignment scenarios. We then take the largest difference with the nominal fit to the same Monte Carlo sample as the associated systematic.

Beam Spot Position and Calibration

To assign a systematic uncertainty on the beam spot position, we shift the beam spot position in the simulation by $\pm 20 \mu m$ in the y direction. The sensitivity due to eventual calibration problems or time-dependent effects is evaluated by smearing the beam spot position by an additional $\pm 20 \mu m$ in the y direction.

The effect on the position and smearing of the beam spot Δt is very small. We take the largest change in the *CP* asymmetry parameters from the two shifts and add this in

quadrature with the effect of smearing to obtain the total systematic uncertainty.

Tag Side Interference From Doubly CKM Suppressed Decays

The tagging parameters used for asymmetries measurement come from the fit to the fully reconstructed B decays sample, where the charge of decay products are used to determine the flavour of the two B mesons. These decays are dominated by $b \to c\bar{u}d$ transition. However, in a fraction of events, $\bar{b} \to \bar{u}c\bar{d}$ amplitudes can contribute to the final states used for tagging. The interference effects between CKM-favored and doubly-CKM-suppressed decays (DCSD) are not absorbed into the mistag rates, and so a bias in Δt distribution can be induced by neglecting them [83].

The uncertainty on the *CP* parameters due to this effect is evaluated with the procedure described in [83], with the most recent values of CKM parameters.

***CP* Content of the $B\overline{B}$ Background**

The $K^+K^-K^0_S$ sub-modes have not charmless $B\overline{B}$ background, but only combinatorial $B\overline{B}$ background. For this background, is reasonable to assume no *CP* asymmetry as for the continuum. The $K^+K^-K^0_L$ has a remaining contribution from the charmless ("peaking") $B\overline{B}$ background, which is a mixture of channels whose *CP* content is unknown. In the nominal fit we assumed no *CP* asymmetry. We account for this uncertainty varying the direct and mixing-induced *CP* asymmetry in the whole allowed region, repeating the fit, and taking the largest difference with the nominal fit as the systematic uncertainty.

Dalitz Plot Resolution

The nominal Dalitz model assumes perfect mass resolution since it is small compared to the resonant width for all Dalitz plot components. The mass resolution function of signal events in the Dalitz plot is studied by comparing true and reconstructed values of Dalitz plot observables in a sample of Monte Carlo events.

We study only the resolution effects in $m_{K^+K^-}$, since the main resonances decay into K^+K^-. The mass resolution and bias in $m_{K^+K^-}$ for mass constrained B candidates is shown in Fig. 6.55, which show how it is negligible with respect to the resonances width.

We convolve the Dalitz plot PDF with the resolution function shown in Fig. 6.55 and repeating the nominal fit. The difference in *CP* asymmetry parameters between this fit and the nominal one is taken as the systematic error.

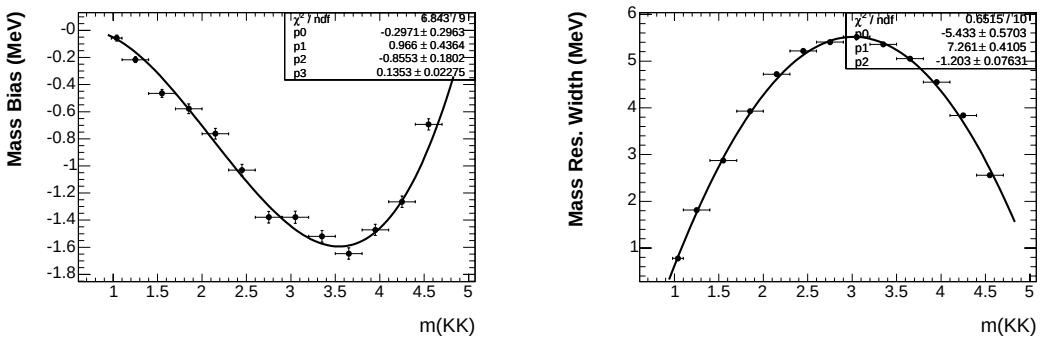

Figure 6.55: Mass resolution for K^+K^- pairs in the $K^+K^-K^0_S(\pi^+\pi^-)$ sub-mode.

Dalitz Plot Model

The systematic uncertainty related to the phenomenological parameterization of the B^0 decay amplitude represents the main systematic error of the analysis. We use a set of toy Monte Carlo experiments to estimate it: we generate toy samples using central values for the Dalitz parameters smeared by their error, and fit with the nominal ones. Then we take the difference as systematic error.

For the low mass fit, where isobar coefficients are fixed for all components except for the $\phi(1020)$, we use errors from full Dalitz plot fit to estimate impact on *CP* parameters for $\phi(1020)$ and $f_0(980)$.

We also assign an error due to uncertainty in the resonant and non-resonant line-shape parameters. For resonant components this includes uncertainty in the mass and width of $X_0(1550)$. To evaluate the effect on the nominal fit we replace the nominal parameters with those found in $B^+ \to K^+K^-K^+$ measurement [75]: $m = 1.491$ GeV/c^2, $\Gamma = 0.145$. We also test a hypothesis that X_0 is the $f_0(1500)$ (i.e. we use $m = 1.507$ GeV/c^2, $\Gamma = 0.109$ GeV [21]). We take the largest observed difference from the nominal fit as the systematic error.

Non-resonant distributions are not motivated by theory so we try three alternative non-resonant models that depend on $K^+K^0_S$ and $K^-K^0_S$ masses: $e^{\alpha_{12}s_{12}}$, $e^{\alpha_{12}s_{12}} + c_{23}e^{i\delta_{23}}\ e^{\alpha_{23}s_{23}}$ and $e^{\alpha_{12}s_{12}} + c_{13}e^{i\delta_{13}}\ e^{\alpha_{13}s_{13}}$. The dominant error comes from non resonant events when $K^+K^0_S$ and $K^-K^0_S$ dependence is switched off since they account for P-wave contribution. We find a negligible change in b, and a large change in δ (0.11). However, inclusion of these non resonant components (which assuming SU(2) symmetry are symmetric in momentum to K^+K^- component) was suggested by theorists [81] so we believe it would

be over-conservative to include this change as a model error. We determine effect of the uncertainty of the shape parameter α to *CP* parameters and include it into error.

For the low-mass fit we evaluate the systematic uncertainties using the same strategy. The gain in this fit is a highly reduced contribution from the Dalitz plot model because the mass region $m_{K^+K^-} < 1.1$ GeV/c^2 receives negligible contributions by the $X_0(1500)$ and the non-resonant. The list of the systematic uncertainties on the *CP* parameters in the full Dalitz plot fit and in the low-mass fit is reported in Table 6.21.

Parameter	ϕK^0		$f_0 K^0$		$K^+K^-K^0$	
	A_{CP}	β_{eff}	A_{CP}	β_{eff}	A_{CP}	β_{eff}
Event selection	0.00	0.01	0.00	0.00	0.003	0.002
Fit Bias	0.04	0.01	0.04	0.02	0.004	0.010
Δt, vertexing, DCSD	0.02	0.03	0.01	0.01	0.010	0.010
Tagging	0.01	0.00	0.01	0.00	0.021	0.002
$B\overline{B}$ *CP*	0.01	0.01	0.01	0.02	0.006	0.007
Dalitz model	0.09	0.03	0.09	0.03	0.011	0.035
Total	0.10	0.05	0.10	0.04	0.025	0.037

Table 6.21: Summary of systematic errors on *CP*-asymmetry parameters. Errors for ϕK^0 and $f_0 K^0$ *CP*-parameters are based on the low-K^+K^--mass sample. The $K^+K^-K^0$ column refers to errors on average *CP* parameters across the Dalitz plot.

6.10 Summary of Results

In the fit to $B^0 \to K^+K^-K^0_S(\pi^+\pi^-)$ decays, we have analyzed the Dalitz plot distribution and measured the fractions of the intermediate states. They are given in Table 6.14. Subsequently, we have extracted the *CP* asymmetry parameters from simultaneous fits to a combined sample of $B^0 \to K^+K^-K^0$ decays with three possible final states of the neutral kaon: $K^0_S \to \pi^+\pi^-$, $K^0_S \to \pi^0\pi^0$ and K^0_L. The average *CP* asymmetry in the Dalitz plot is reported in Table 6.17, and it is found to be $\beta_{eff} = 0.361 \pm 0.079 \pm 0.037$, where the first error is statistic and the second is systematic. This result is fully compatible with the Standard Model expectation ($\beta = 0.379$). We also measured the direct *CP* asymmetry to be consistent with zero.

From a fit to events at low K^+K^- invariant masses, we measured the *CP* asymmetry of the decay $B^0 \to \phi K^0$ which is, in the number of the decays mediated by $b \to s$ transitions, the one with the smallest theoretically uncertainties. For this decay we measured $\beta_{eff} = 0.06 \pm 0.16 \pm 0.05$, which is not significantly different from the Standard Model expectation.

From this fit we measured also the *CP* asymmetry of the decay $B^0 \to f_0 K^0$, and found $\beta_{eff} = 0.18 \pm 0.19 \pm 0.04$. These results are reported in Table 6.18. We also measured the direct *CP* asymmetry for $B^0 \to \phi K^0$ and $B^0 \to f_0 K^0$, and found them consistent with zero, which is the Standard Model expectation.

Chapter 7

Measurement of *CP* Asymmetry in $B^0 \to K^0_S K^0_S K^0_S$ Decays

As discussed in Sec. 1.5, the $B^0 \to K^0_S K^0_S K^0_S$ decay, although it is a three-body decay, has a well defined *CP* eigenvalue (*CP*-even). For this reason a Dalitz plot analysis as in $B^0 \to K^+K^-K^0$ is not necessary for a time-dependent measurement of S and C parameters [84]. For this reason a standard time-dependent measurement of the *CP* asymmetry, like in $B^0 \to [c\bar{c}]K^0$ decays, is feasible.

In order to maximize the statistical significance of the measured *CP* asymmetry, we reconstruct two sub-modes: one with candidates formed by three $K^0_S \to \pi^+\pi^-$, the other with candidates formed by two $K^0_S \to \pi^+\pi^-$ and a third $K^0_S \to \pi^0\pi^0$. In fact, since $\mathcal{B}(K^0_S \to \pi^+\pi^-) \approx 2\mathcal{B}(K^0_S \to \pi^0\pi^0)$, we expect

$$N_{true} = \left(B^0 \to 2K^0_{S\pi^+\pi^-}K^0_{S\pi^0\pi^0}\right) \approx \frac{3}{2} N_{true}\left(B^0 \to 3K^0_{S\pi^+\pi^-}\right), \tag{7.1}$$

where N_{true} indicates the number of B mesons decaying in the specified manner, i.e. without considering the efficiency reconstruction, which is lower for $K^0_S \to \pi^0\pi^0$ with respect $K^0_S \to \pi^+\pi^-$.

For this measurement we use 374×10^6 $B\bar{B}$ pairs recorded at the $\Upsilon(4S)$ resonance by the *BABAR* detector.

7.1 The Event Selection

In this section we describe the selection of events for $B^0 \to K^0_S K^0_S K^0_S$ decays. Because of the different purities of the two sub-modes, we apply different selection criteria on them.

7.1.1 Selection of $B^0 \to K^0_S K^0_S K^0_S(\pi^+\pi^-)$

For this sub-sample we reconstruct $K^0_S \to \pi^+\pi^-$ candidates from pairs of oppositely charged tracks originating from a common vertex, with the procedure described in Sec. 5.2.1. We then combine the three selected K^0_S in the event to form the B^0 candidate. We use the kinematic variables described in Sec. 6.3.2 to define the B meson candidate: $m_{\rm ES}$ and ΔE. Since in this decay there are only charged tracks in the final state (six charged pions), the resolutions for these two variables are similar to ones reported in Sec. 6.3.2 for the $K^+K^-K^0_S$ final state: 2.5 MeV/c^2 and 14 MeV/c^2, respectively. We select B^0 candidates satisfying the following requirements:

- $5.22 < m_{\rm ES} < 5.30$ GeV/c^2
- $-120 < \Delta E < 120$ MeV

These requirements are quite loose in order to keep enough sideband events to characterize backgrounds.

The main background comes from the $e^+e^- \to q\overline{q}$ fragmentation. We apply a requirement on $|\cos\theta_T| < 0.9$ and the shape of a Fisher discriminant $\mathcal{F}$, calculated from the order zero and order two Legendre monomials L_0 and L_2. Contrary to the case of $B^0 \to K^+K^-K^0$ analysis, the Fisher discriminant is uncorrelated from the other variables, so that we can use all the discriminating power including it in the likelihood. This allows to gain in efficiency on signal and in separation power with respect continuum background. We define the wide Fisher allowed region in $-3 < \mathcal{F} < 4$.

We also apply requirements on the $K^0_S K^0_S$ invariant mass in order to veto decays through intermediate charm resonances χ_{c0} and χ_{c2}, which we will discuss in Sec. 7.2. The event selection efficiency is about 6%, and the details on the efficiency of the single requirement are reported in Table 7.1.

7.1.2 Selection of $B^0 \to K^0_S K^0_S K^0_S(\pi^0\pi^0)$

In order to reconstruct the sub-mode $B^0 \to K^0_S K^0_S K^0_S(\pi^0\pi^0)$, we select two $K^0_S \to \pi^+\pi^-$ with the same procedure described for the $K^0_S K^0_S K^0_S(\pi^+\pi^-)$ sub-mode. Then we form a $K^0_S \to \pi^0\pi^0$ using the criteria described in Sec. 5.2.2. We combine the two $K^0_S \to \pi^+\pi^-$ and the $K^0_S \to \pi^0\pi^0$ candidates to form a B meson.

We also impose these very loose requirements:

Cut	Signal MC	
Total Events Before cuts	48956	
$5.22 < mES < 5.3\,\text{GeV}$	84.6	84.6
$\lvert\Delta E\rvert < 120\,\text{MeV}$	90.6	76.7
K^0_S flight length $0.2 < r_{DEC} < 40$ cm	86.5	66.3
K^0_S mass 12 Mev	86.6	57.4
K^0_S angle cut $\alpha < 200$ mrad	94.6	54.3
$\lvert\cos\theta_T\rvert < 0.9$	88.3	47.9
K^0_S vertex prob $P(\chi^2) > 1.25^{-3}$	92.8	44.5
Vetoes on χ_{c0} and χ_{c2}	82.1	36.5
Luminosity/#Generated Signal MC	315 K	
# of Events (ϵ) after cuts	21775 (6.91%)	
# of Events (ϵ) after vetoes	17876 (5.67%)	

Table 7.1: Selection efficiencies for analysis cuts with $B^0 \to K^0_S K^0_S K^0_S(\pi^+\pi^-)$ signal Monte Carlo. We report in the first (second) column the relative (cumulative) efficiency.

1. the total energy of the event has to be less than 20 GeV;

2. at least one track has to be present in the rest of the event.

These requirements, within the presence of the three selected K^0_S, are referred as "pre-selection" in the following.

In order to define the B meson, we use a set of two kinematic variables. While for the sub-mode $K^0_S K^0_S K^0_S(\pi^+\pi^-)$ the usual variables $m_{\rm ES}$ and ΔE are almost uncorrelated (because the final state includes only charged tracks in the final state), this is no longer true when one or more photons are present in the final state. In this case, because of leakage effects in the EMC, the reconstructed energy of the photons can be underestimated, affecting both the reconstructed momentum and energy. This produces a non Gaussian left tail in both $m_{\rm ES}$ and ΔE variables, which increases the correlation between the two variables. A study has been done for the first time for decays $B^0 \to K^0_S\pi^0$ by the *BABAR* Collaboration [31] introducing a set of two new kinematic variables, m_B and m_{miss}, which have less correlation than $m_{\rm ES}$ and ΔE. They are defined as:

$$\begin{aligned} m_B &\equiv |q_{rec}| \\ m_{miss} &\equiv |q_{e^+e^-} - q_{rec}(m_B \equiv 0)| \end{aligned} \tag{7.2}$$

where $q_{e^+e^-}$ is the four-momentum of the e^+e^- system and $q_{rec}(m_B \equiv 0)$ is the four-momentum of the fully reconstructed B meson after a mass constraint is applied. There-

fore, they represent the mass of the fully reconstructed B (m_B), and the mass of the tagging ("missing") B meson with mass constraint on the other one.

To a good approximation, ($m_{\rm ES}$,ΔE) and (m_{miss},m_B) are related by

$$\begin{aligned} m_{\rm ES} &\approx (m_{miss} + m_B^{PDG})/2, \\ \Delta E &\approx m_B - (m_{miss} + m_B^{PDG})/2 \approx m_B - m_B^{PDG} \end{aligned} \tag{7.3}$$

where m_B^{PDG} is the nominal B mass [21]. Therefore, the shape of m_{miss} is $m_{\rm ES}$-like, while m_B is ΔE-like.

By construction, the linear correlation coefficient between m_{miss} and m_B vanishes. This is valid in the limit of perfect reconstruction, but a small correlation can still arise due to energy loss in photon reconstruction, but it is significantly smaller than $m_{\rm ES}$ and ΔE. From a signal Monte Carlo sample, we estimate it to be about 3% for the former pair with respect about 15% of the latter. We then decided to use this set of kinematic variables. We apply the following requirements on these two variables:

- $5.11 < m_{miss} < 5.31$ GeV/c^2
- $-150 < m_B - m_B^{PDG} < 150$ MeV/c^2

which keep a wide sideband region for background characterization.

It comes from their definition that the two Legendre monomials $\mathcal{L}_0$ and L_2 are correlated to the missing energy in the event, as shown in Fig. 7.1. This correlation is reduced in the Fisher discriminant, which linearly combines the two Legendre monomials, but it is almost canceled in the ratio $l_2 = L_2/L_0$. Since the discrimination power of l_2 is similar to the one of the Fisher discriminant, we choose to use this simple variable for the sub-mode $K^0_S K^0_S K^0_S(\pi^0\pi^0)$. A preliminary selection on $|\cos\theta_T| < 0.95$ is applied for computational issues (it is included in "pre-selection") then we use the whole l_2 distribution in the likelihood, without making a selection on it.

In the case of one or more badly reconstructed $K^0_S \to \pi^+\pi^-$ in the $B^0 \to K^0_S K^0_S K^0_S$ decay, the χ^2 of the B vertex fit presents a tail corresponding to non converged fits, as shown in Fig. 7.2. Since the number of wrongly reconstructed K^0_S is lower in signal decays than in background, the vertexing χ^2 has background rejection power. In particular, a requirement $\chi^2 < 20$, equivalent to $P(\chi^2) > 1.25 \cdot 10^{-3}$, we are able to reject (33.6 $\pm$ 0.6)% of $q\overline{q}$ events and (48.9 $\pm$ 1.9)% of $B\overline{B}$ background events, whose composition is described in 7.2. This requirement has a signal efficiency of (92.0 $\pm$ 0.2)%.

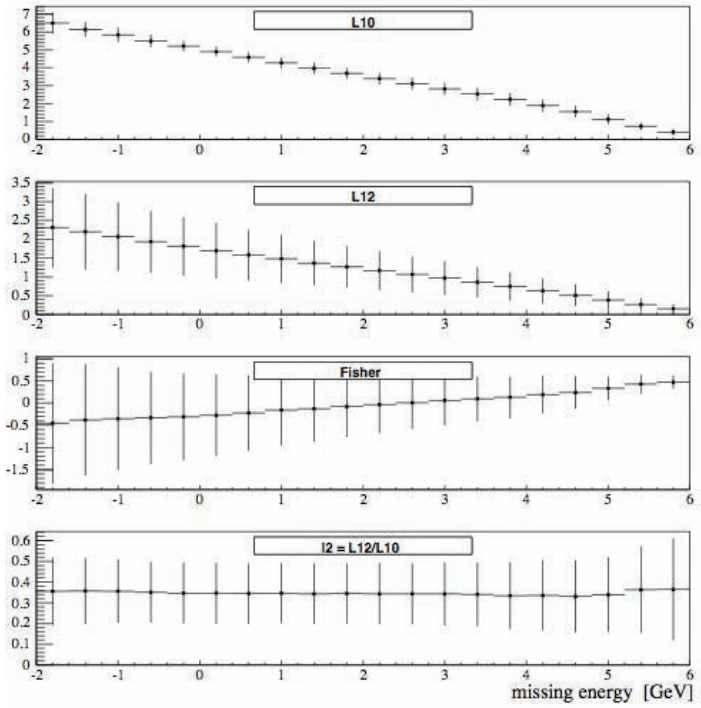

Figure 7.1: Average values for the two Legendre monomials L_0 (top), L_2 (middle top), Fisher discriminant (middle bottom) and $l_2 = L_2/L_0$ (bottom) as a function of the measured missing energy in the event for signal Monte Carlo events. The error bars correspond to the r.m.s. of the distribution.

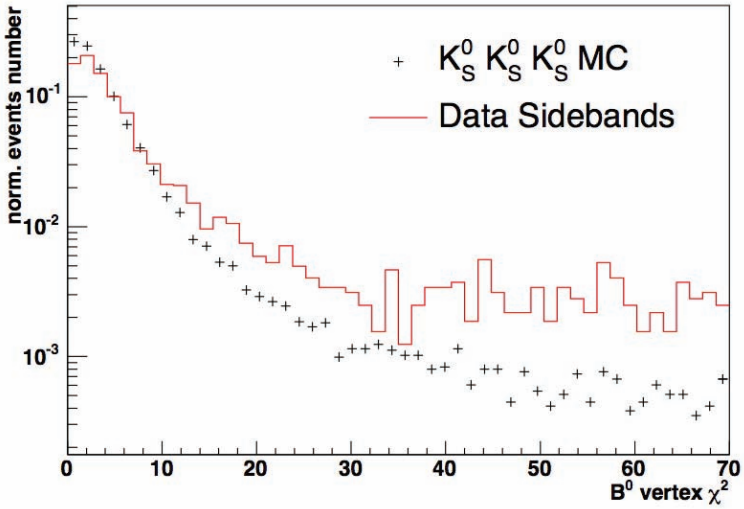

Figure 7.2: Distribution of vertex χ^2 in $B^0 \to K^0_S K^0_S K^0_S(\pi^0\pi^0)$ decays for signal Monte Carlo events (dots) and data sidebands (solid histogram). In the B vertex fit the informations coming from $K^0_S \to \pi^0\pi^0$ are neglected. The distributions are normalized to the same area.

We also apply the veto on charm intermediate resonances χ_{c0} and χ_{c2}, which will be described in Sec. 7.2.

The summary of the selection efficiencies is reported in Table 7.2. The total reconstruction efficiency of this sub-mode is about 3% (This includes the $\mathcal{B}$ of the decay $K^0 \to K^0_S \to \pi^0\pi^0$).

Selection	ε (%)
pre-selection	9.3 ± 0.2
$\lvert m_B - m^{PDG}_{B^0}\rvert < 150$ MeV/c^2	86.3 ± 0.2
$(5.11 < m_{MISS} < 5.31)$ GeV/c^2	99.7 ± 0.2
$LAT < 0.55$	92.0 ± 0.2
$(480 < m_{K^0_{S00}} < 520)$ MeV/c^2	83.7 ± 0.2
$mass_{\pi_0} < 141$ MeV/c^2	91.1 ± 0.2
$E_\gamma > 50$ MeV	87.2 ± 0.2
$\lvert m_{K^0_{S+-}} - m_{K^0_{SPDG}}\rvert < 11$ MeV/c^2	88.6 ± 0.2
K^0_S life time significance > 5	90.7 ± 0.2
$(0.15 < K^0_S$ transverse decay length $< 60)$ cm	99.2 ± 0.2
$\chi^2(B^0) < 20$	92.0 ± 0.2
veto on χ_{c0} and χ_{c2}	83.3 ± 0.2
Total efficiency	3.0 ± 0.2

Table 7.2: $B^0 \to K^0_S K^0_S K^0_S(\pi^0\pi^0)$ mode: reconstruction efficiency, as estimated from signal Monte Carlo events. The efficiency of the single cut is evaluated with respect the previous one.

7.1.3 Best Candidate Selection

The largest part of the selected $B^0 \to K^0_S K^0_S K^0_S(\pi^+\pi^-)$ events has only one reconstructed candidate. For the 1.4% of the events having more than one B^0 candidate, we evaluate a χ^2 based on the three K^0_S invariant masses:

$$\chi^2 = \sum_i \left(\frac{m_{K^0_S,i} - m^{PDG}_{K^0_S}}{\sigma_{m_{K^0_S}}} \right)^2 , \tag{7.4}$$

where $m_{K^0_S}$ is the mass of the reconstructed meson, $\sigma_{m_{K^0_S}}$ is the measured error, and $m^{PDG}_{K^0_S}$ is the nominal K^0_S mass [21]. The candidate with the smallest value of χ^2 is chosen.

The $K^0_S K^0_S K^0_S(\pi^0\pi^0)$ sub-mode has a higher B^0 multiplicity: about 1.7 candidates per events are reconstructed, because of multiple $K^0_S \to \pi^0\pi^0$ combinations. We use the same variable of Eq. 7.4 to choose the best B^0 candidate. Based on a study on Monte Carlo,

we estimate that this criterion matches the right candidate the 81.5% of the times. This value has been evaluated normalizing the number of correctly chosen best candidates to the number of events for which one of the candidates is fully matched by the Monte Carlo truth (i.e. the generated particles). [1]

[1] When no reconstructed candidates matches the true decay, the best candidate selection algorithm necessarily fails. Because of that, we ignore these events in order to evaluate the performance of the chosen criteria.

7.2 $B\overline{B}$ Background

We study the contribution to the background due to other B decays using a high statistics Monte Carlo sample of generic B decays. For this analysis we use 559 M $B^0\overline{B}^0$ decays and 530 M B^+B^- decays, which are approximately equivalent to two times the actual *BABAR* data sample. In this section we describe the contributions to both the sub-modes.

The most relevant background is made by decays which proceed through intermediate charm resonances, which then decay into $K^0_S K^0_S$. This constitute in principle a signal component, because they produce the same final state of the signal decays. They have to be vetoed because they proceed through a $b \to c\bar{c}s$ transition having a pure Standard Model value for the time-dependent *CP* asymmetry ($S \simeq \sin 2\beta$), then they would dilute the sensibility to New Physics effects in signal $b \to s$ events.

Decays of the charmonium resonances $\chi_{c1} \to K^0_S K^0_S$ and $\eta_c \to K^0_S K^0_S$ are forbidden by angular momentum conservation. In fact, the two pseudoscalar K^0_S have even angular momentum (because of Bose-Einstein statistics), and so they cannot be produced by a vector resonance, like the χ_{c1}. Since the K^0_S K^0_S pairs are in S-wave, parity conservation in decays mediated by strong interactions forbids them to come from an η_c, which is a scalar with $\mathcal{P} = -1$. Decays of $J/\psi \to K^0_S K^0_S$ or $\psi(2S) \to K^0_S K^0_S$ are strongly suppressed by the *twist leading accuracy* (which is an exact cancellation in the limit $m_b \to \infty$, where m_b is the mass of the b quark [85]). Then, the only remaining allowed decays through charm resonances are $\chi_{c0} \to K^0_S K^0_S$ and $\chi_{c2} \to K^0_S K^0_S$. To avoid the contamination from these decays, we apply vetoes on the K^0_S K^0_S invariant mass.

We tune the mass veto on a Monte Carlo sample of exclusive $B^0 \to \chi_{c0} K^0_S$ decays, with $\chi_{c0} \to K^0_S K^0_S$. Since resolution in energy and momentum is worse for the $K^0_S \to \pi^0\pi^0$, the resulting mass resolution for $K^0_S(\pi^+\pi^-)K^0_S(\pi^+\pi^-)$ is different than the one for $K^0_S(\pi^+\pi^-)K^0_S(\pi^0\pi^0)$ (Fig. 7.3), and we apply different selections to them. We estimate the mass resolutions using a Gaussian fit.

For $B^0 \to K^0_S K^0_S K^0_S(\pi^+\pi^-)$ sub-mode we apply three standard deviations vetoes to both χ_{c0} and χ_{c2}:

1. $m_{K^0_S K^0_S} \notin (3.3715, 3.4708)\,\mathrm{GeV}/c^2$, and $m_{K^0_S K^0_S} \notin (3.5224, 3.6016)\,\mathrm{GeV}/c^2$.

For $B^0 \to K^0_S K^0_S K^0_S(\pi^0\pi^0)$ sub-mode, the contribution from χ_{c2} resonance is negligible also without applying any veto. We estimate it to be less than 1% of the signal. We then

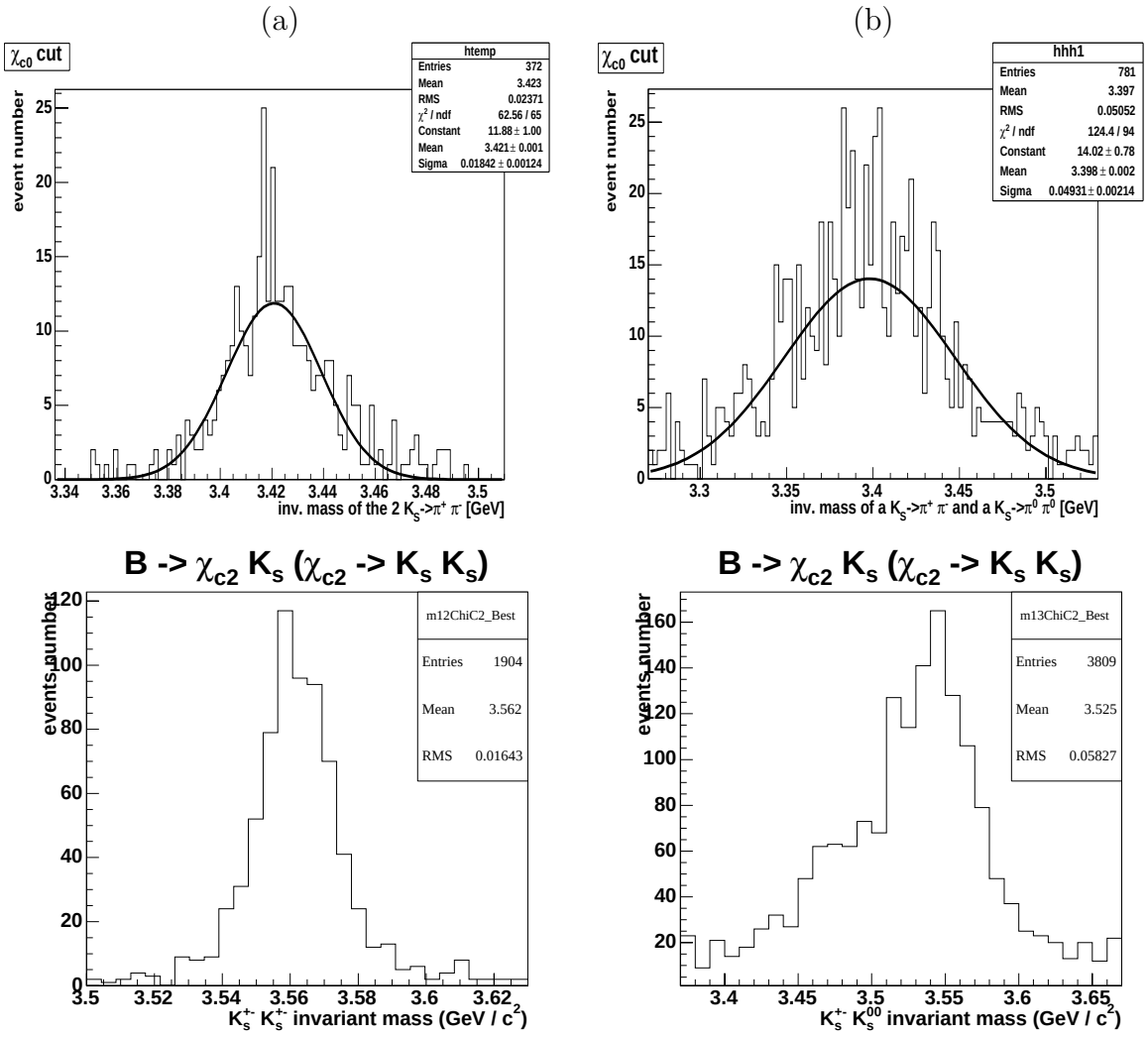

Figure 7.3: $K_S^0 K_S^0$ invariant mass for Monte Carlo events of exclusive $B^0 \to \chi_{c0} K_S^0$ decays (top) and $B^0 \to \chi_{c2} K_S^0$ decays (bottom). (a) $K_S^0(\pi^+\pi^-)K_S^0(\pi^+\pi^-)$ combinations and (b) $K_S^0(\pi^+\pi^-)K_S^0(\pi^0\pi^0)$ combinations. Superimposed is a Gaussian fit to estimate the mass resolution.

Decay mode	# Events	$\mathcal{B}$	Exclusive MC	Eff.	N expected
$B^0 \to K^0_S K^0_S K^0_L$	5	$(2.4 \pm 2.6) \times 10^{-6}$	143K	0.1%	0.4
$B^+ \to K^+ K^0_S K^0_S$	7	$(11.5 \pm 1.3) \times 10^{-6}$	5756K	0.1%	1.9

Table 7.3: Number of background events passing the selection in generic B Monte Carlo samples (559M $B^0\overline{B}^0$, 530M B^+B^-). The assumed branching fraction, the number of generated events of exclusive Monte Carlo, the reconstruction efficiency and the expected number of events in the on-resonance dataset are given.

apply a veto only to χ_{c0} resonance. We define this selection to reject χ_{c0} at two standard deviations:

1. $m(K^0_S(\pi^+\pi^-)K^0_S(\pi^0\pi^0)) \notin (3.300, 3.496)$ GeV/c^2
2. $m(K^0_S(\pi^+\pi^-)K^0_S(\pi^+\pi^-)) \notin (3.385, 3.457)$ GeV/c^2.

This reduces this background to a negligible level.

After vetoing the charm resonances, the contribution to background due to other B decays is found to be negligible for the $K^0_S K^0_S K^0_S(\pi^+\pi^-)$ sub-mode. We show the distributions of $m_{\rm ES}$ and ΔE for events passing the selection in the Monte Carlo of generic B decays in Fig. 7.4. We studied the two principal sources of B background for this mode, $B^0 \to K^0_S K^0_S K^0_L$ and $B^+ \to K^+ K^0_S K^0_S$, using exclusive Monte Carlo samples for these decays. In Table 7.3 we show the reconstruction efficiency and the number of expected events in the final dataset for these decays. In Fig. 7.5 we show the $m_{\rm ES}$, ΔE and $\mathcal{F}$ distributions for them. In the case of $B^0 \to K^0_S K^0_S K^0_L$, the missing K^0_S has to be taken from the rest of event, and the uncorrelation of its momentum with the other two (coming from the reconstructed B candidates) produces a phase-space distribution in $m_{\rm ES}$ similar to continuum one. In the case of $B^0 \to K^+ K^0_S K^0_S$ only charged track has to be taken from the other B, together with a mis-identification of the K^+. This brings to a partially peaking shape in $m_{\rm ES}$ (due to the mass constraint used in the variable definition), while the ΔE variable is completely phase-space like. We tested with a sample of toy Monte Carlo experiments that the effect due to this background on signal yield and *CP* asymmetry parameters is negligible. The toy Monte Carlo are performed adding such a component in generation and fitting without it, and verifying the absence of any bias in the signal parameters. Hence, this component is not included in the maximum likelihood fit.

For the $B^0 \to K^0_S K^0_S K^0_S(\pi^0\pi^0)$ sub-mode the background from generic B decays is

Decay mode	$\mathcal{BF}$	Events in fit region	Events in signal region
$K^0_S K^0_S K^0_S$	$(6.9^{+0.9}_{-0.8} \pm 0.6) \times 10^{-6}$	166.7 +/- 21.7	159.8 +/- 1.1
$\chi_{c2} K^0_S$	unknown	0 ± 1	0 ± 1
$\chi_{c0} K^0_S$	$< 2.5 \times 10^{-4}$	2 ± 1	0 ± 1
$a_0(1450) K^0_S$	unknown	1 ± 1	1 ± 1
$D^+ \rho^-$	$(7.7 \pm 1.3) \times 10^{-3}$	24 ± 4.7	1 ± 1
$D^+ K^{*-}$	$(3.8 \pm 1.5) \times 10^{-5}$	7 ± 1.4	0 ± 1
$D^0 K^{*0}$	$< 1.8 \times 10^{-5}$	1 ± 3	0 ± 1.4
$D^* \rho$	$(6.8 \pm 0.9) \times 10^{-5}$	7 ± 4.7	2 ± 1.4
$f_0(980) K^0_S K^0_S$	unknown	1 ± 1	0 ± 1
$K^{*+} K^0_S K^0_S$	unknown	1 ± 1.4	1 ± 1
$K^{*0} K^0_S K^0_S$	unknown	17 ± 3.7	4 ± 1
$D^0 \rho^+$	$(1.34 \pm 0.18)\%$	17 ± 4.2	1 ± 1.7
$J/\psi K^*$	$(1.31 \pm 0.07) \times 10^{-3}$	0 ± 1.4	0 ± 1
Other		127 ± 11	17 ± 3.1

Table 7.4: $B^0 \to K^0_S K^0_S K^0_S(\pi^0\pi^0)$ sub-mode: events selected in the whole $B^0\bar{B}^0$ and B^+B^- Monte Carlo samples, for an equivalent luminosity of $\sim 906 fb^{-1}$. Charm veto on χ_{c0} is applied. For the modes with unknown branching fraction it has been assumed $\mathcal{B} = 10^{-6}$. The number of expected signal events are evaluated using the most recent measurement of $B \to K^0_S K^0_S K^0_S$ branching fraction.

larger, even if it is still by far negligible with respect to the $q\overline{q}$ one. From the study of the same Monte Carlo samples used for the $K^0_S K^0_S K^0_S(\pi^+\pi^-)$ sub-mode, we identify the main sources of $B\bar{B}$ background. The most dangerous background events are those which accumulate in the *signal box*, i.e. the region in the 2D kinematic plane where the signal events peak. We define this smaller signal box as $5.26 < m_{miss} < 5.30\ GeV/c^2$ and $5.20 < m_{rec} < 5.35\ GeV/c^2$.

The results are reported in Table 7.4. From this study on generic Monte Carlo we find in summary that 205 events pass the final selection on the sample of neutral and charged B decays of about three times the luminosity of the final dataset. Of these events, only 27 events lie in the signal box, as defined before. Assuming an integrated luminosity of 350 fb^{-1}, this corresponds to 79 events in the whole fit region and about 10 events in the signal box. This number is in agreement with the fraction of combinatorial background, under the peak of the signal distribution (i.e. no peaking structures are observed). For comparison, we expect ~ 60 signal events, almost entirely included in the signal box. In Fig. 7.6 and 7.7 we show the distribution of m_{miss} and m_B for the selected events in $B^0\overline{B}^0$ and B^+B^- generic Monte Carlo sample, respectively.

Even if there is not a significant peaking component in the kinematic variables m_{miss} and m_B for these events, they cannot be included in the continuum component because the event shape variable l_2 has a signal like distribution (since these are B decays and the Legendre monomials are sensible to the rest of the event). In part, the same happens to the time evolution, since the fraction of these events which are well reconstructed B has non-zero lifetime, while the rest are prompt (like $q\overline{q}$ events). For these reasons we will include a $B\overline{B}$ component in the fit for $K^0_S K^0_S K^0_S(\pi^0\pi^0)$ sub-mode.

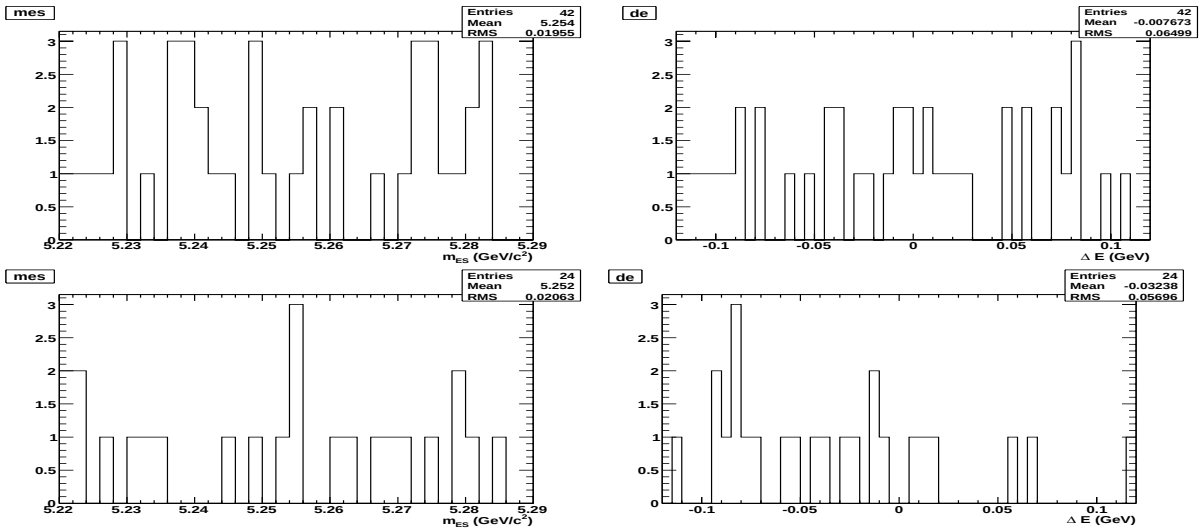

Figure 7.4: B background distributions of $m_{\rm ES}$ (left) and ΔE (right) for $B^0 \to K^0_S K^0_S K^0_S(\pi^+\pi^-)$ mode with events passing pre-selections cuts in samples of 559M $B^0\overline{B}^0$ (top) and 530M B^+B^- (bottom) Monte Carlo.

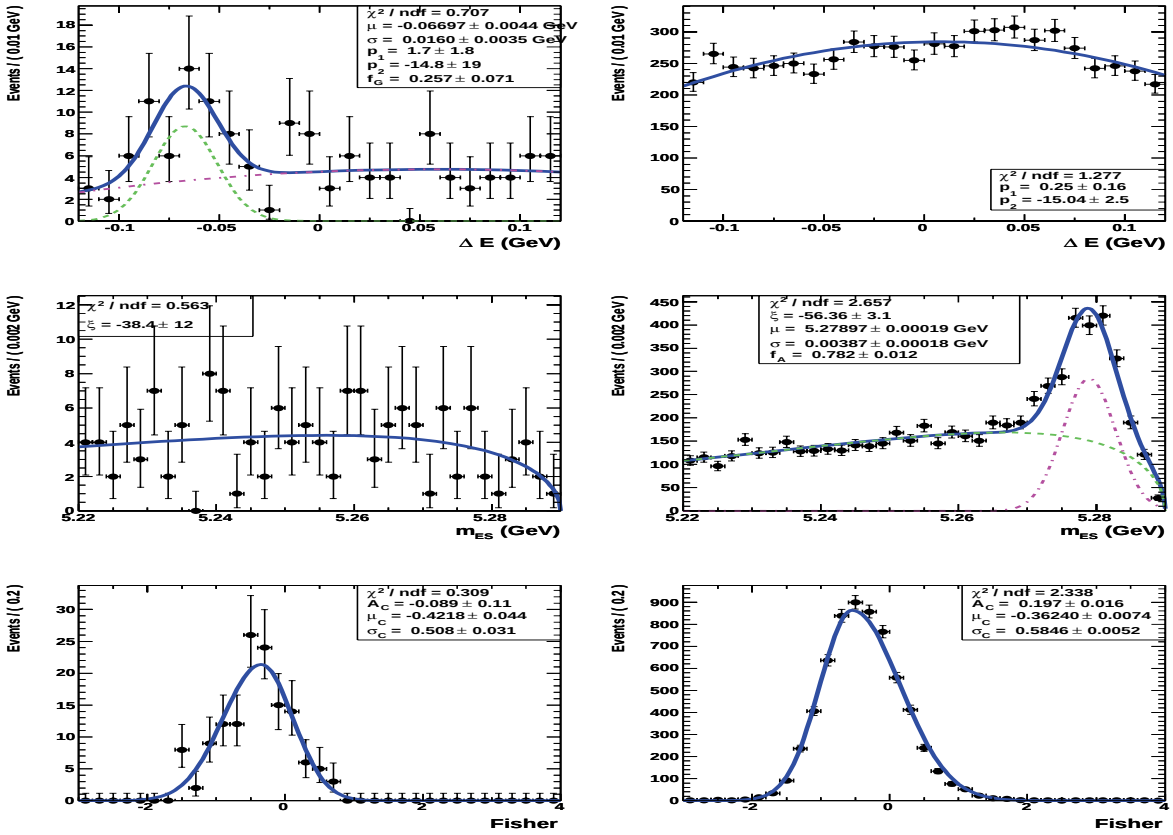

Figure 7.5: B background distributions of ΔE (top), $m_{\rm ES}$ (middle) and $\mathcal{F}$ (bottom) for $B^0 \to K^0_S K^0_S K^0_S(\pi^+\pi^-)$, with the PDF's superimposed. Plots on the left are from $B^0 \to K^0_S K^0_S K^0_L$ Monte Carlo, and those on the right are from $B^+ \to K^+ K^0_S K^0_S$ Monte Carlo. Green curve for $K^0_S K^0_S K^0_L$ ΔE and pink curve for $K^+ K^0_S K^0_L$ represent the "peaking" component of this background, while the rest is phase-space like.

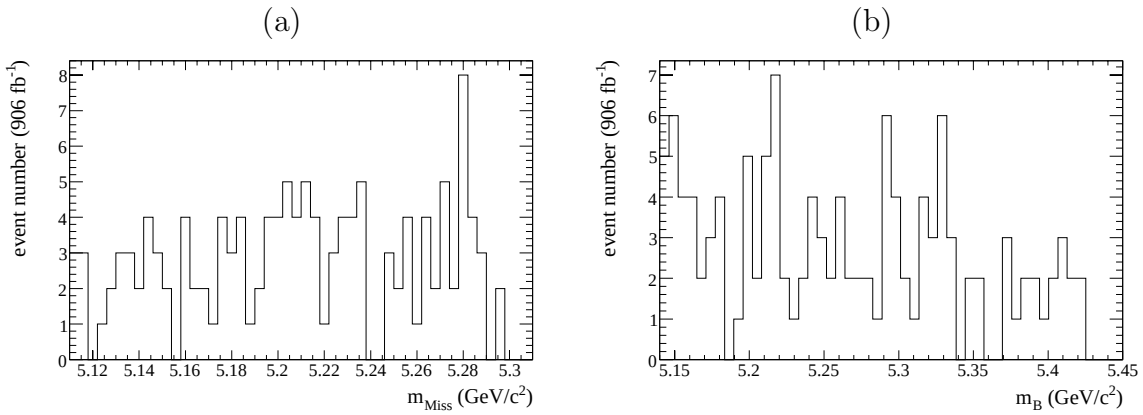

Figure 7.6: Distribution of (a) m_{miss} and (b) m_B for selected events in the Monte Carlo sample of generic B^0 $\overline{B}^0$ decays equivalent to about 906 fb^{-1}.

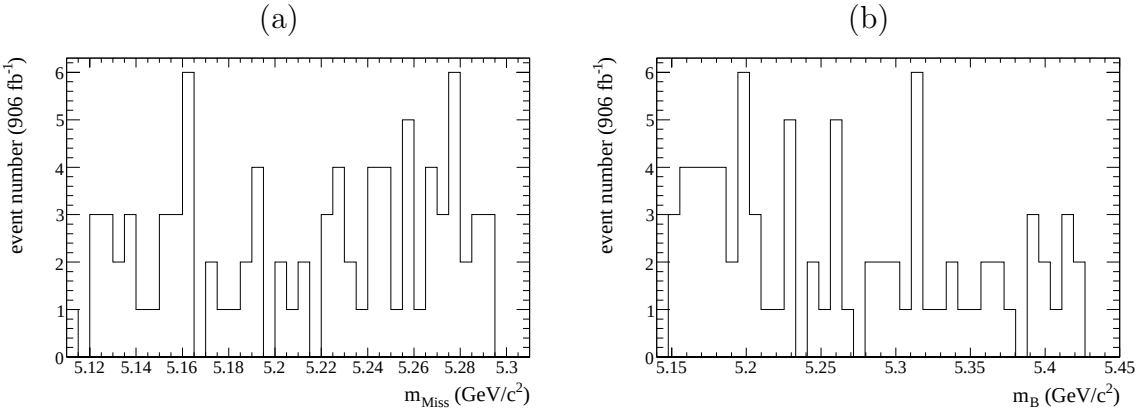

Figure 7.7: Distribution of (a) m_{miss} and (b) m_B for selected events in the Monte Carlo sample of generic B^+ B^- decays equivalent to about 906 fb^{-1}.

7.3 Fit to *CP* Asymmetry

As we have described in Sec. 2.3, even if the vertex of the B^0 for these decays is reconstructed using the $K^0_S \to \pi^+\pi^-$ decay vertex, the unusual Δt resolution function can be used, but only if at least one of the $K^0_S \to \pi^+\pi^-$ decays within the innermost layers of the vertex tracker.

The classification of the goodness of the B vertexing for the *CP* fit has been done in terms of the SVT classes described in Sec. 2.3.1. Since one $K^0_S \to \pi^+\pi^-$ is sufficient to reconstruct the B vertex, we assign the B to the class of the best K^0_S. Clearly, the probability to have a B with all the K^0_S unusable for the *CP* fit is very small (it is about 3.5% for $K^0_S K^0_S K^0_S(\pi^0\pi^0)$, and negligible for $K^0_S K^0_S K^0_S(\pi^+\pi^-)$). This leads to a better signal yield. In Table 7.5 we report the fraction of events for the two $K^0_S K^0_S K^0_S$ sub-modes belonging to the different SVT classes. Then we consider as *good* candidates for the

K^0_S Class	$K^0_S K^0_S K^0_S(\pi^+\pi^-)$ (%)	$K^0_S K^0_S K^0_S(\pi^0\pi^0)$ (%)
Class I	89.5	79.0
Class II	9.1	14.5
Class III	1.0	3.0
Class IV	0.4	3.5

Table 7.5: Fractions of events which belong to the different SVT classes for signal Monte Carlo events of $B^0 \to K^0_S K^0_S K^0_S$.

measurement of S those B^0 which:

1. satisfy $|\Delta t| < 20$ ps
2. satisfy $\sigma(\Delta t) < 2.5$ ps
3. belong to Class I or Class II.

The rest of the sample, called *bad*, is used for the determination of the signal yield and the direct *CP* parameter C. This can be measured from tagging when no Δt information is available by determining the flavour of the B_{tag}. In this case the measured asymmetry is

$$A_{meas} = C/(1 + x_d^2) \tag{7.5}$$

where the dilution factor $1/(1 + x_d^2)$, with $x_d \equiv \Delta m_{B^0}/\Gamma_{B^0} = 0.776 \pm 0.08$ [21], is due to the effect of B^0-$\overline{B}^0$ mixing.

Despite the different vertexing technique, the same resolution function of `BReco` decays can be used, as displayed in Fig. 7.8. This figure shows the good agreement between Δt distribution for signal Monte Carlo events and the PDF obtained on `BReco` data.

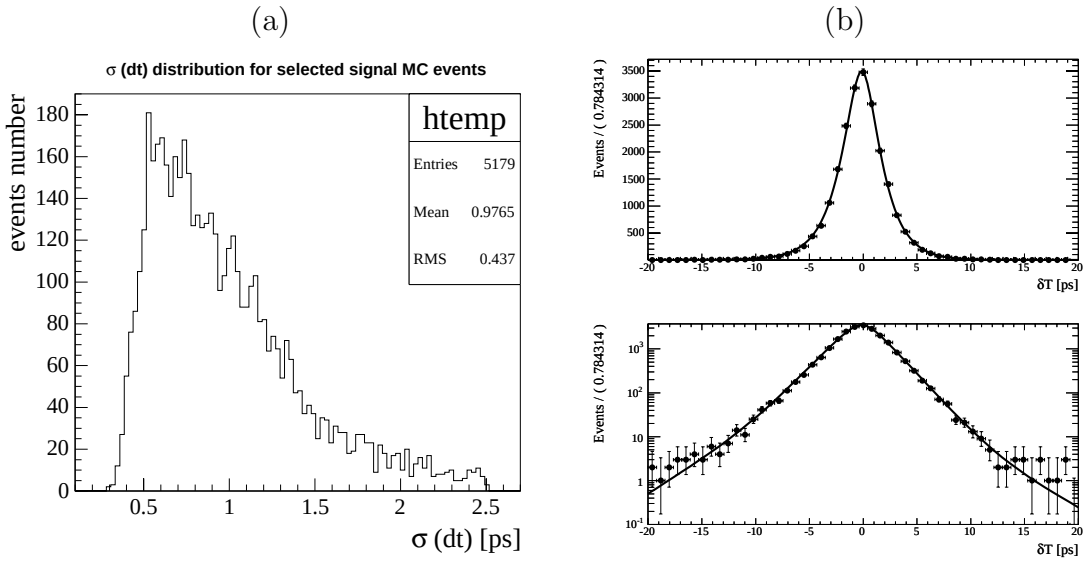

Figure 7.8: Distribution of (a) $\sigma(\Delta t)$ and (b) Δt for *good* candidates in signal Monte Carlo events, with `BReco` PDF superimposed (top: linear scale, bottom: $\log_{10}$ scale).

7.3.1 Likelihood Structure

The signal and background yields, together with the *CP* parameters, are extracted using an unbinned extended maximum likelihood fit, as for the analysis of $B^0 \to K^+K^-K^0$.

The likelihood function for $B^0 \to K^0_S K^0_S K^0_S$ is a bit complicated by the split in *good* and *bad* events for the measurement of S and C. We checked that the correlation between the variables is small (Sec. 7.6), so that the likelihood of the $K^0_S K^0_S K^0_S(\pi^+\pi^-)$ sub-mode

Variable	$M_{\rm Miss}$	M_B	Δt	$\sigma_{\Delta t}$	l_2	$m_{K\to\pi^0\pi^0}$
$M_{\rm Miss}$	1	-0.03	-0.005	-0.02	-0.03	0.01
M_B		1	-0.02	0.01	0.004	0.06
Δt			1	-0.03	-0.004	-0.001
$\sigma_{\Delta t}$				1	-0.03	0.0004
l_2					1	0.002
$m_{K\to\pi^0\pi^0}$						1

Table 7.6: $K^0_S K^0_S K^0_S(\pi^0\pi^0)$ mode: linear correlation for the likelihood variables entering the likelihood function, evaluated in signal Monte Carlo events. The correlations for the background events are smaller.

can be written as a product of independent PDF's as follows:

$$
\begin{aligned}
L = \frac{e^{-(N_S+N_B+N_{BB})/N}}{\sqrt[N]{(N_S+N_B+N_{BB})!}} & \qquad (7.6)\\
\prod_{i\in\text{good}}^{N_{\rm good}} \{ N_S f^S_{\rm good}\epsilon^S_{c_i} \;\cdot\; & P_S(m_{ES,i})P_S(\Delta E_i)P_S(\mathcal{F}_i)P^c_S(\Delta t_i, T|\sigma_{\Delta t_i}) + \\
N_B f^B_{\rm good}\epsilon^B_{c_i} \;\cdot\; & P_B(m_{ES,i})P_B(\Delta E_i)P_B(\mathcal{F}_i)P^c_B(\Delta t_i, T|\sigma_{\Delta t_i}) \\
N_{BB} f^{BB}_{\rm good}\epsilon^{BB}_{c_i} \;\cdot\; & P_{BB}(m_{ES,i})P_{BB}(\Delta E_i)P_{BB}(\mathcal{F}_i)P^c_{BB}(\Delta t_i, T|\sigma_{\Delta t_i})\} + \\
\prod_{i\in\text{bad}}^{N_{\rm bad}} \{ N_S(1-f^S_{\rm good})\epsilon^S_{c_i} \;\cdot\; & P_S(m_{ES,i})P_S(\Delta E_i)P_S(\mathcal{F}_i)P^c_S(T) + \\
N_B(1-f^B_{\rm good})\epsilon^B_{c_i} \;\cdot\; & P_B(m_{ES,i})P_B(\Delta E_i)P_B(\mathcal{F}_i)P^c_B(T) + \\
N_{BB}(1-f^{BB}_{\rm good})\epsilon^{BB}_{c_i} \;\cdot\; & P_{BB}(m_{ES,i})P_{BB}(\Delta E_i)P_{BB}(\mathcal{F}_i)P^c_{BB}(T)\}.
\end{aligned}
$$

where N_S, N_B and N_{BB} are the signal, continuum and $B\bar{B}$ background yields, $f_{\rm good}$ is the fraction of *good* events, ϵ_{c_i} is the tagging efficiency in the category c_i and T is the flavour tag. The same function is used for the $K^0_S K^0_S K^0_S(\pi^0\pi^0)$ mode, substituting $m_{\rm ES} \to m_{miss}$, $\Delta E \to m_B$ and $\mathcal{F} \to l_2$.

We parameterize the signal and background PDF's with unbinned maximum likelihood fits to signal Monte Carlo samples and to data sidebands. As usual, the parameters of the PDF's for the continuum background are extracted simultaneously to the signal event yields and *CP* parameters, since our selection retains sufficient sidebands to allow their determination.

$B^0 \to K^0_S K^0_S K^0_S(\pi^+\pi^-)$ Parameterization

We model ΔE distributions of signal events with a double Gaussian shape. For continuum background we use the on-resonance data selected in the low $m_{\rm ES}$ sideband ($m_{\rm ES} < 5.27$ GeV/c^2) and we parameterize the slope using a second degree polynomial.

We fit the $m_{\rm ES}$ distributions of signal events using double Gaussian functions. For continuum background we use the on-resonance data in ΔE sidebands ($|\Delta E| > 40\,{\rm MeV}$) to obtain the parameters of an ARGUS function, defined by Eq. 5.11.

We use signal Monte Carlo and sideband of on-resonance data ($m_{\rm ES} < 5.27$ GeV/c^2) events to determine the shapes of $\mathcal{F}$ for signal and continuum background, respectively. For signal, we fit with an asymmetric Gaussian plus a Gaussian, and a double Gaussian for continuum background.

We show the distributions for the event selection variables, together with their PDF's, in Fig. 7.9.

We have discussed on Δt parameterization for signal events, while for continuum background we use an effective parameterization which follows the same functional form of the one used for $B^0 \to K^+K^-K^0$ decays, and described in Sec. 6.5.2.

In the final fit, we float as many background parameters as we can so that uncertainties in the values of these parameters contribute to the statistical error on S and C and these parameters can be determined by taking advantage of the larger statistics in the full on-resonance sample.

Since the statistics and purity of the $B^0 \to K^0_S K^0_S K^0_S(\pi^+\pi^-)$ sample are very good, we want to float some of the core parameters of signal component so that the uncertainties of signal PDF parameterization can be transferred into yield uncertainties. From toy Monte Carlo studies we find we can leave varying the mean and sigma of the core Gaussian of ΔE and $m_{\rm ES}$ for signal without introducing any bias in the fit and with a negligible increase of the statistical error on the *CP* asymmetry parameters.

$B^0 \to K^0_S K^0_S K^0_S(\pi^0\pi^0)$ Parameterization

We use a Cruijff function (see Eq. 6.15) to parameterize m_B and m_{miss}, and the sum of two Gaussians for l_2. From a comparison of the distributions of likelihood variables for different tagging categories, we observe a non-negligible effect on the shape variable l_2 (above all, the lepton category with respect the other ones), while m_B and m_{miss} shape does not

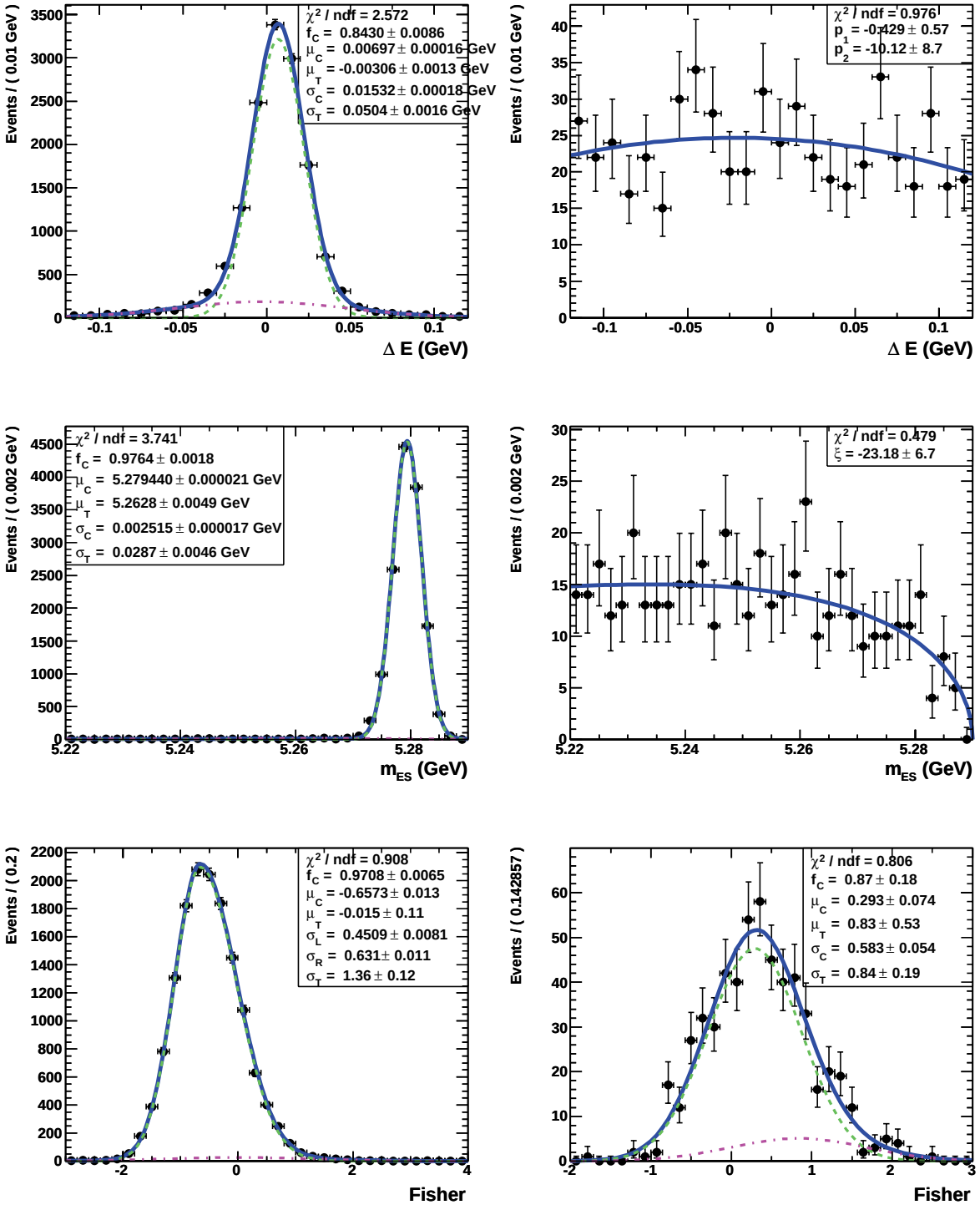

Figure 7.9: ΔE (top), $m_{\rm ES}$ (middle) and $\mathcal{F}$ (bottom) PDF's for $B^0 \to K^0_S K^0_S K^0_S(\pi^+\pi^-)$. Plots on the left are from signal Monte Carlo events. Those on the right are from on-resonance sidebands for continuum background. The $\mathcal{F}$ background plot is drawn on a narrower range to remove zero content bins so that χ^2/ndf is more realistic, but the fit is done on the full range with unbinned maximum likelihood fit. Dashed lines represent the single components when the PDF used is composite.

look correlated to the output of the tagging algorithm (see Fig. 7.10). Because of this, we decided to use the same m_B and m_{miss} parameterizations for different tagging categories, while we split the parameters of l_2 PDF. We parametrize the continuum background on

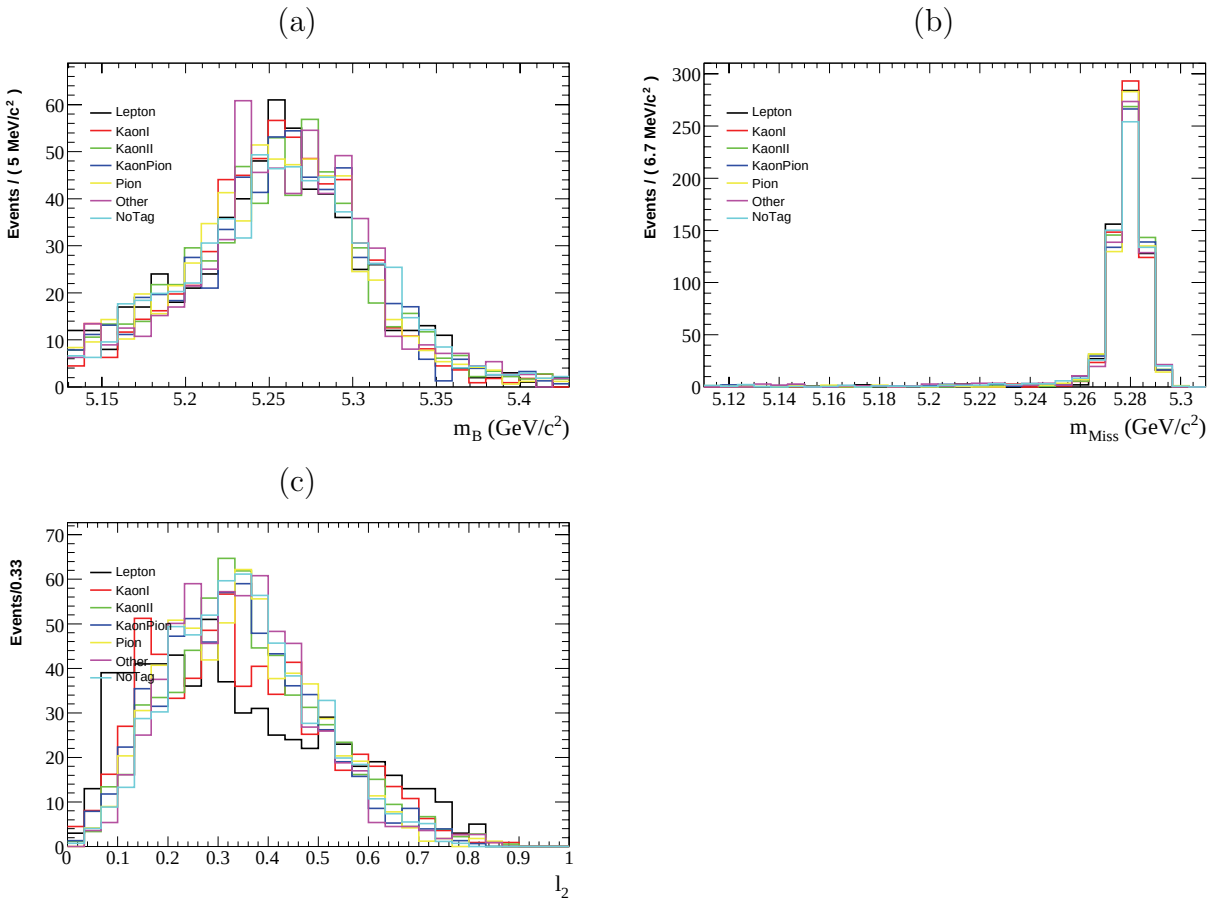

Figure 7.10: $B^0 \to K^0_S K^0_S K^0_S(\pi^0\pi^0)$ sub-mode: distribution of (a) m_B, (b) m_{miss}, and (c) l_2 for different tagging categories, from a sample of signal Monte Carlo events.

$q\bar{q}$ Monte Carlo sample. The fitted parameters are not used in the final fit (since all the parameters except the ARGUS end-point are floated in the nominal fit), but are used in toy Monte Carlo studies and as starting point for the nominal fit. We use an ARGUS function (Eq. 5.11) for m_{miss}, a second order polynomial for m_B and a double Gaussian for l_2.

We parameterize the B-background using the selected events on full generic $B^0\overline{B}^0$ and B^+B^- Monte Carlo sample after removing the signal events. We use an ARGUS function for m_{miss}, a second order polynomial for m_B and a double Gaussian for l_2. Since we have few events surviving the selection on this Monte Carlo sample, and the l_2 shape

is determined by the rest of the event, which is the same for signal and B-background events, we use the same PDF adopted for the signal, of which we have a large statistic sample. We will use an alternative parameterization for l_2 to evaluate the systematic effects. The fraction of B-background events made by neutral B decays have the same time-evolution structure as signal, while the charged decays have not a time-evolution at all, and mis-reconstructed neutral B decays can have an intermediate structure. We assume the same PDF of the signal for Δt, and we will account for possible differences in the systematic uncertainties. The distribution is shown in Fig. 7.11.

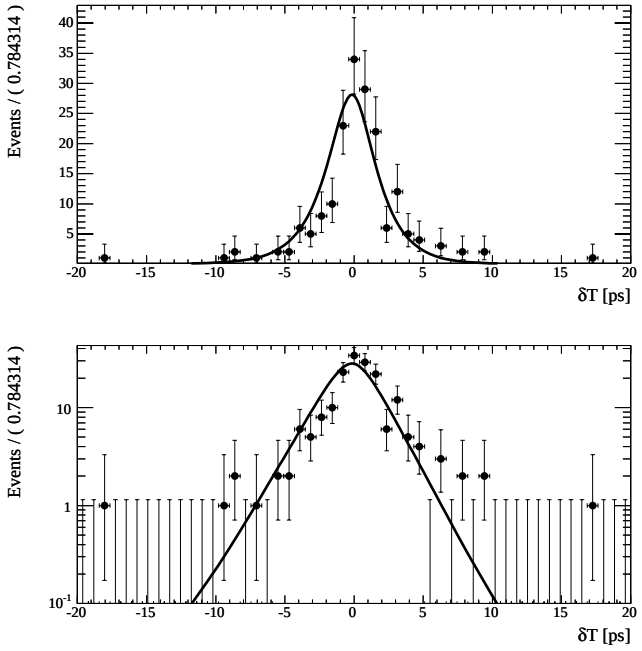

Figure 7.11: $B^0 \to K^0_S K^0_S K^0_S(\pi^0\pi^0)$ sub-mode: distribution of Δt pull for B $\bar{B}$ Monte Carlo events, with `BReco` parameterization superimposed. Top: linear scale, bottom: $\log_{10}$ scale.

All the other parameterizations are shown in Fig. 7.12.

7.3.2 Validation Studies

We first validate independently the fits to the single sub-modes, then the simultaneous fit to the combined $K^0_S K^0_S K^0_S$ sample. For briefness, and since the physics result of this work is the *CP* asymmetry of all $K^0_S K^0_S K^0_S$ events, we present here only the validation studies of the combined fit.

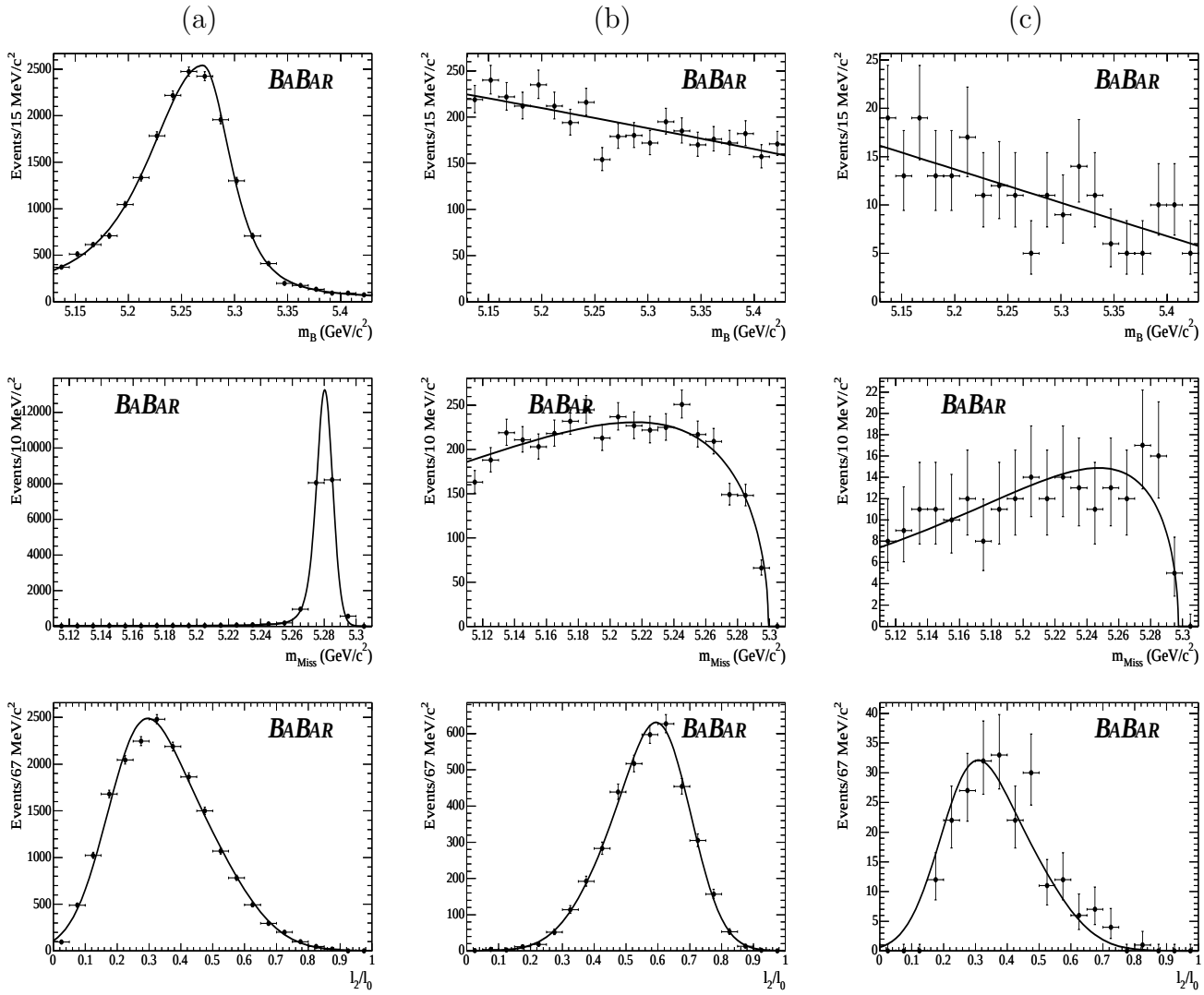

Figure 7.12: m_B (top), m_{miss} (middle), l_2 (bottom) PDF's for $B^0 \to K^0_S K^0_S K^0_S(\pi^0\pi^0)$. (a) Signal Monte Carlo events; (b) continuum Monte Carlo; (c) generic $B\overline{B}$ Monte Carlo with signal events removed.

As we have described for $B^0 \to K^+K^-K^0$ analysis in Sec. 6.7.1, we perform a number of toy Monte Carlo experiments to verify that the fit determines the signal parameters without biases and to compare the expected uncertainties with the results. We generate signal and background yields according to Poisson distributions around the expected values for 350 fb^{-1}: $N^{+-}_{sig} = 150$, $N^{00}_{sig} = 65$, $N^{+-}_{bkg} = 734$, $N^{00}_{bkg} = 4796$, and $N^{00}_{bb} = 49$ with $S = -0.7$ and $C = 0.0$, as expected in the Standard Model. The results are shown in Table 7.7. We expect an error on S (C) of $\sigma(S) = 0.28$ ($\sigma(C) = 0.18$) and we find $\sigma(N^{+-}_{sig}) = 13$ and $\sigma(N^{00}_{sig}) = 12$.

	μ_{Pull}	σ_{Pull}	Average error
N^{+-}_{sig}	0.003 ± 0.041	1.05 ± 0.03	13.3
$N^{+-}_{q\bar{q}}$	0.007 ± 0.037	0.96 ± 0.03	27.5
N^{00}_{sig}	0.040 ± 0.038	1.00 ± 0.03	11.7
$N^{00}_{q\bar{q}}$	0.023 ± 0.038	0.97 ± 0.03	69.9
$N^{00}_{B\bar{B}}$	-0.05 ± 0.04	1.05 ± 0.03	15.4
C	-0.032 ± 0.016	1.04 ± 0.01	0.19
S	-0.06 ± 0.04	1.00 ± 0.03	0.29

Table 7.7: Results on the yield and S and C of the toy Monte Carlo experiments for the combined fit (when we generate S=-0.7 and C=0.0)

These toy Monte Carlo experiments show the fact that the likelihood is able to extract the signal informations (both yields and *CP* asymmetries) from data without significant biases. On the other side, they cannot find problems associated to wrong parameterization of the PDF's or effects due neglected correlation between variables, since the events generated in toy Monte Carlo experiments according the PDF's are, by definition, uncorrelated. For this purpose, only fits to control samples can give a reliable answer on the performances of the fit. We achieve this validation with *embedded* toy Monte Carlo experiments, where we mix signal Monte Carlo events to background events generated according PDF's. The signal Monte Carlo events we embed in the toy datasets is produced with *CP* asymmetry parameters $S = C = 0$. We show the results in Table 7.8. The plots for pulls and average errors are shown in Fig. 7.13 and 7.14 for the yields and in Fig. 7.15 for the *CP* violating parameters S and C.

These tests show that possible correlations in the event variables are not a problem for this fit. A possible problem which can arise in cases when the *CP* parameters are near the physical boundary ($C^2 + S^2 \approx 1$), where the fit show non linear effects. This

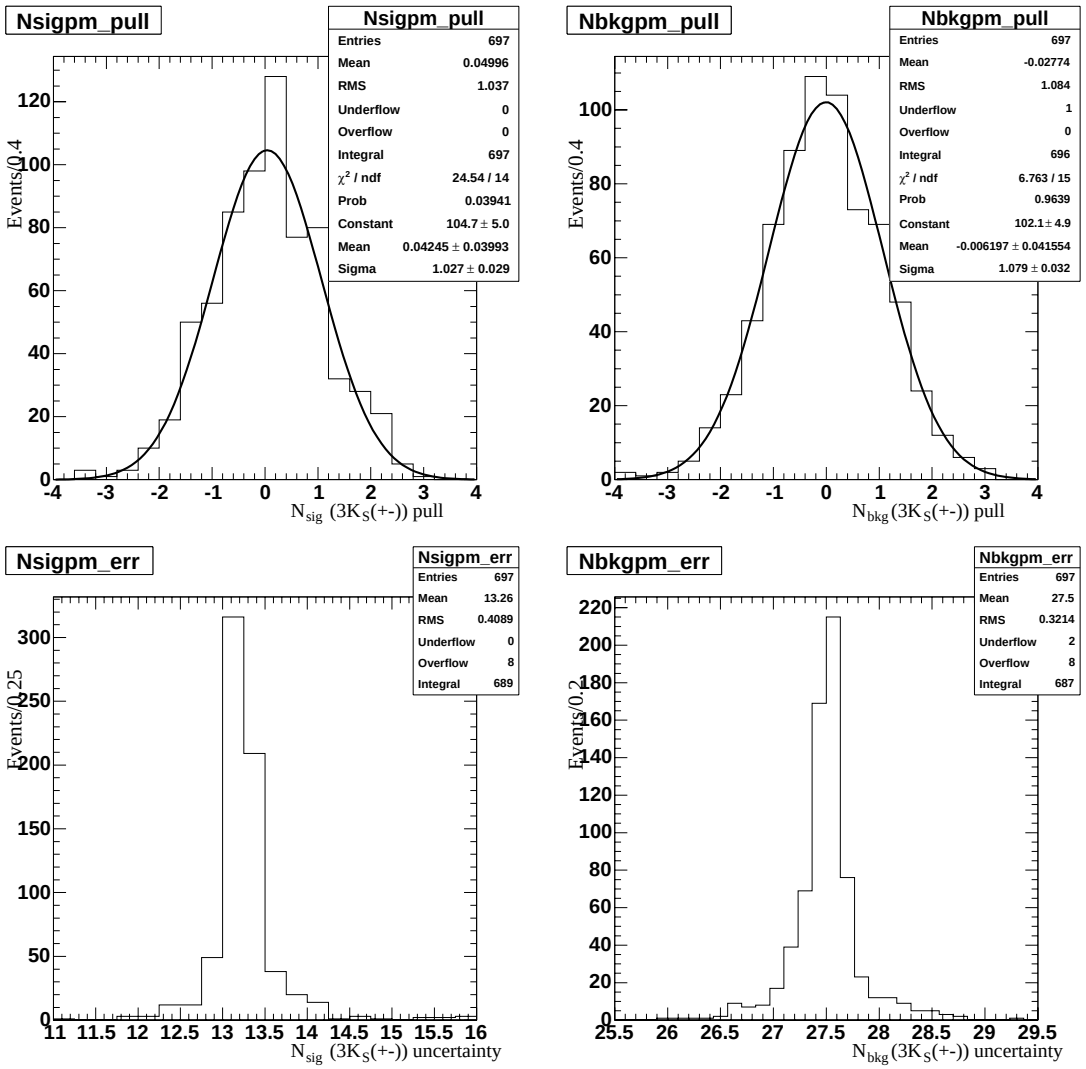

Figure 7.13: Results of toy Monte Carlo experiments with signal Monte Carlo events embedded for the combined fit on the yields of the $K^0_S K^0_S K^0_S(\pi^+\pi^-)$ sub-mode. Pulls (top) and errors (bottom) for Signal (left) and continuum background (right).

	μ_{Pull}	σ_{Pull}	Average error
N^{+-}_{sig}	0.042 ± 0.040	1.03 ± 0.03	13.3
$N^{+-}_{q\bar{q}}$	-0.006 ± 0.041	1.08 ± 0.03	27.5
N^{00}_{sig}	0.109 ± 0.037	0.96 ± 0.03	11.7
$N^{00}_{q\bar{q}}$	-0.016 ± 0.040	1.02 ± 0.03	69.8
$N^{00}_{B\bar{B}}$	-0.17 ± 0.04	1.04 ± 0.03	15.1
C	-0.012 ± 0.041	1.06 ± 0.03	0.18
S	-0.05 ± 0.04	1.10 ± 0.03	0.28

Table 7.8: Results on the yield and S and C of the toy Monte Carlo experiments with signal Monte Carlo events embedded for the combined fit.

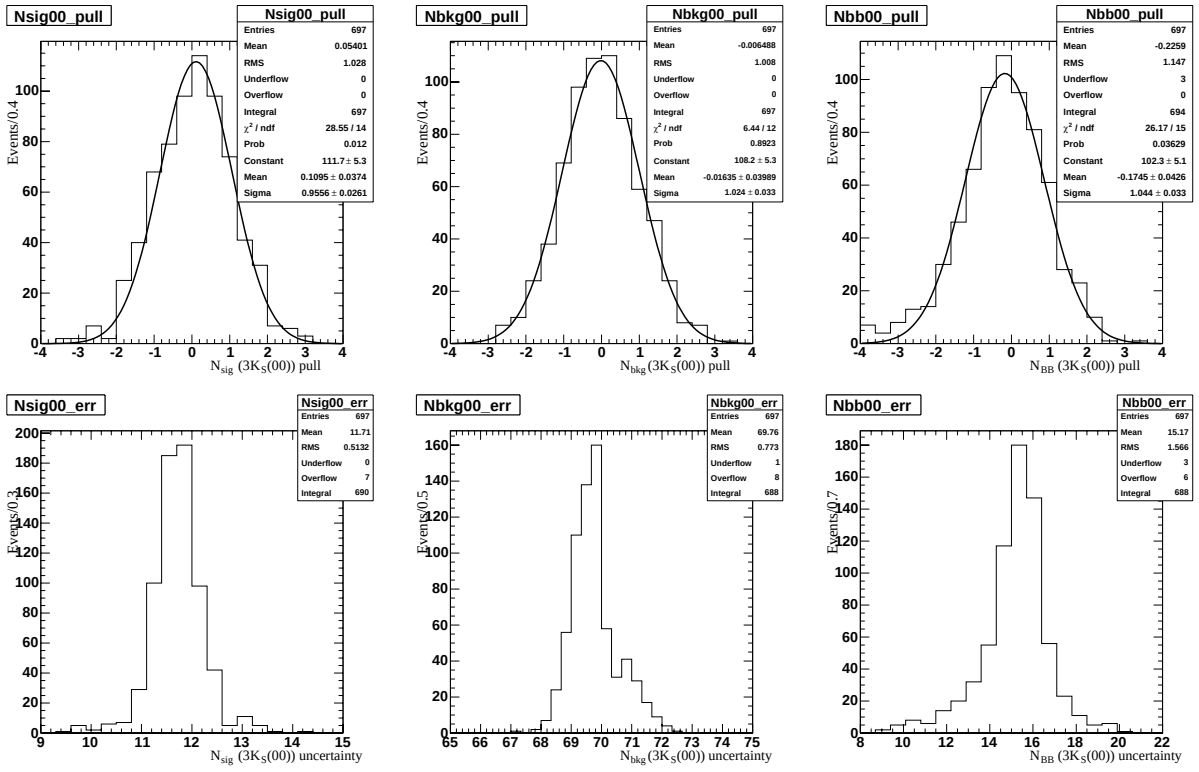

Figure 7.14: Results of toy Monte Carlo experiments with signal Monte Carlo events for the combined fit on the yields of the $K^0_S K^0_S K^0_S(\pi^0\pi^0)$ sub-mode. Pulls (top) and errors (bottom) for Signal (left), and continuum background (middle) and $B\overline{B}$ background (right).

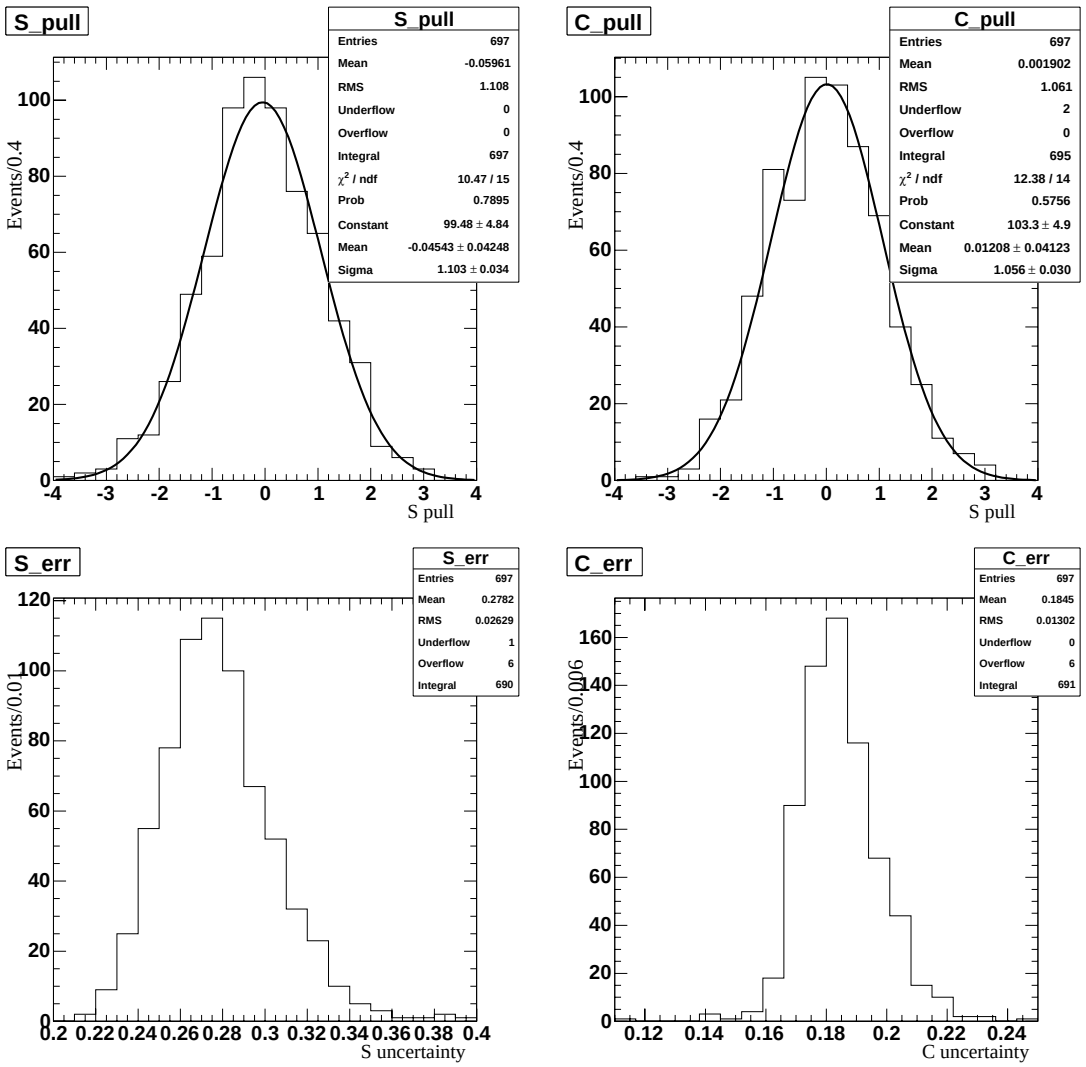

Figure 7.15: Results of toy Monte Carlo experiments with signal Monte Carlo events embedded for the combined fit on the *CP* asymmetry parameters.

effect is mostly evident in the fits to the single mode $B^0 \to K^0_S K^0_S K^0_S(\pi^0\pi^0)$, where the uncertainties on the *CP* parameters are so high that the fitted values can easily hit the physical boundary.

This is reduced to a negligible effect when the two samples are combined, with a consequent sizable decrease in the statistical uncertainty. We study this behaviour with a *linearity test*. This test consists in knowing by toy experiments the relation between the true and the fitted value of S and C, and eventually correct the results of the unblinded fit as a function of the value we get. In order to do this, one has to scan the entire parameter space of S and C and obtain the averaged value (with an associated error) on S_{fit} and C_{fit} for different values of S_{true} and C_{true}. Since S and C can be considered as uncorrelated, one can get the corrections separately. In particular (see below), a linear fit on the two X_{fit} vs X_{true} planes ($X = S, C$) gives a good representation of such relation. The largest the non liner effect of the fit is, the largest will be the deviation of the two parameters p_0 and p_1 of the fit from the expectation values (0 and 1 respectively).

In order to quantify the slope, we performed a set of toy Monte Carlo experiments with different generated values for S and C, scanning the allowed parameter space. In top Fig. 7.16 the fitted vs. generated values of S and C vs. generated values are shown for $B^0 \to K^0_S K^0_S K^0_S(\pi^0\pi^0)$ sub-mode only. The deviation from the expected slope ($X_{fit} = X_{true}$) is clear for those points near the physical boundary. When we repeat the test for the combined sample of $K^0_S K^0_S K^0_S$, this effect disappears. However, we can use the relation $X_{true} = \{(X_{fit})$ as a calibration curve to correct for the (negligible) fit bias once we know the central value from the fit to on-resonance sample. We will account in this way for the "fit bias" systematic uncertainty.

7.4 Fit Results for Yields and *CP* Asymmetries

The selected sample on the on-resonance dataset is made by 786 $K^0_S K^0_S K^0_S(\pi^+\pi^-)$ candidates and 4550 $K^0_S K^0_S K^0_S(\pi^0\pi^0)$ candidates. First we perform the maximum likelihood fit on the separate datasets to extract the event yields and the *CP* asymmetries. Then we perform the fit on the combined sample.

The results of these fits are reported in Table 7.9.

The event yields are consistent with the expected ones with the previous measurements of the $B^0 \to K^0_S K^0_S K^0_S$ branching fractions [21].

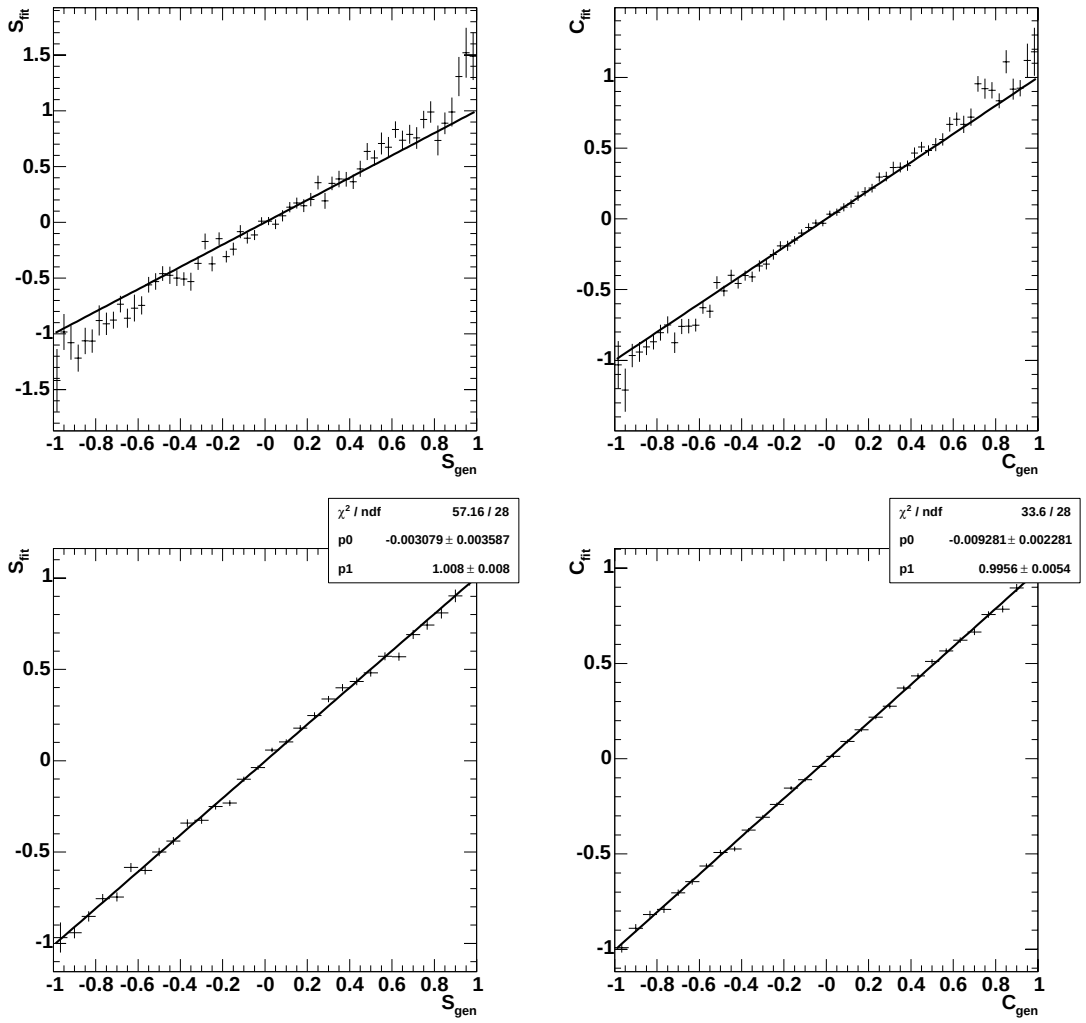

Figure 7.16: Profile plots of fitted vs. generated values for S (left) and C (right), when toy experiments are generated with S and C in the physical boundary ($S^2 + C^2 \leq 1$). Top is the scan for the $B^0 \to K^0_S K^0_S K^0_S(\pi^0\pi^0)$ sub-mode only; bottom is the the scan for the combined $B^0 \to K^0_S K^0_S K^0_S$ sample. The solid line represents the relation $X_{fit} = X_{gen}$, where $X = S, C$.

	$K^0_S K^0_S K^0_S(\pi^+\pi^-)$	$K^0_S K^0_S K^0_S(\pi^0\pi^0)$	Combined
N_S	125 ± 13	64 ± 12	–
$N_{q\overline{q}}$	732 ± 28	4942 ± 77	–
$N_{B\bar{B}}$	–	-14 ± 32	–
S	$-1.06\ ^{+0.25}_{-0.16}$	0.36 ± 0.54	-0.71 ± 0.24
C	$-0.08\ ^{+0.23}_{-0.22}$	0.23 ± 0.38	-0.02 ± 0.21

Table 7.9: Events yields and *CP* asymmetry parameters obtained in the fit to 374×10^6 $B\bar{B}$ pairs. Statistical errors only are shown.

In Fig. 7.17 we show the distribution of the selection variables $m_{\rm ES}$, ΔE and $\mathcal{F}$ after applying the ${}_s\mathcal{P}lot$-weighting technique[80], for the signal and continuum background components. In Fig. 7.18 we show the distribution of the selection variables m_{miss}, ΔE, l_2 after applying the ${}_s\mathcal{P}lot$-weighting technique for the signal, continuum and $B\overline{B}$ background components.

We evaluate the statistical significance of *CP* violation to be 2.6σ by calculating the $2\Delta \log \mathcal{L}$ variation when fitting data with S and C fixed to zero. We also estimate the consistency of the two sub-samples. In order to do this, we generate a number of toy Monte Carlo experiments in which we assume that the measured values for the *CP* parameters on the combined data sample are the true values (generation values). We find that the two sub-samples agree within 1.6 σ.

We show in Fig. 7.19 distributions of Δt for B^0-tagged and $\overline{B}^0$-tagged events, and the time-dependent *CP* asymmetry, after signal ${}_s\mathcal{P}lot$ weighting technique, for the combined data sample.

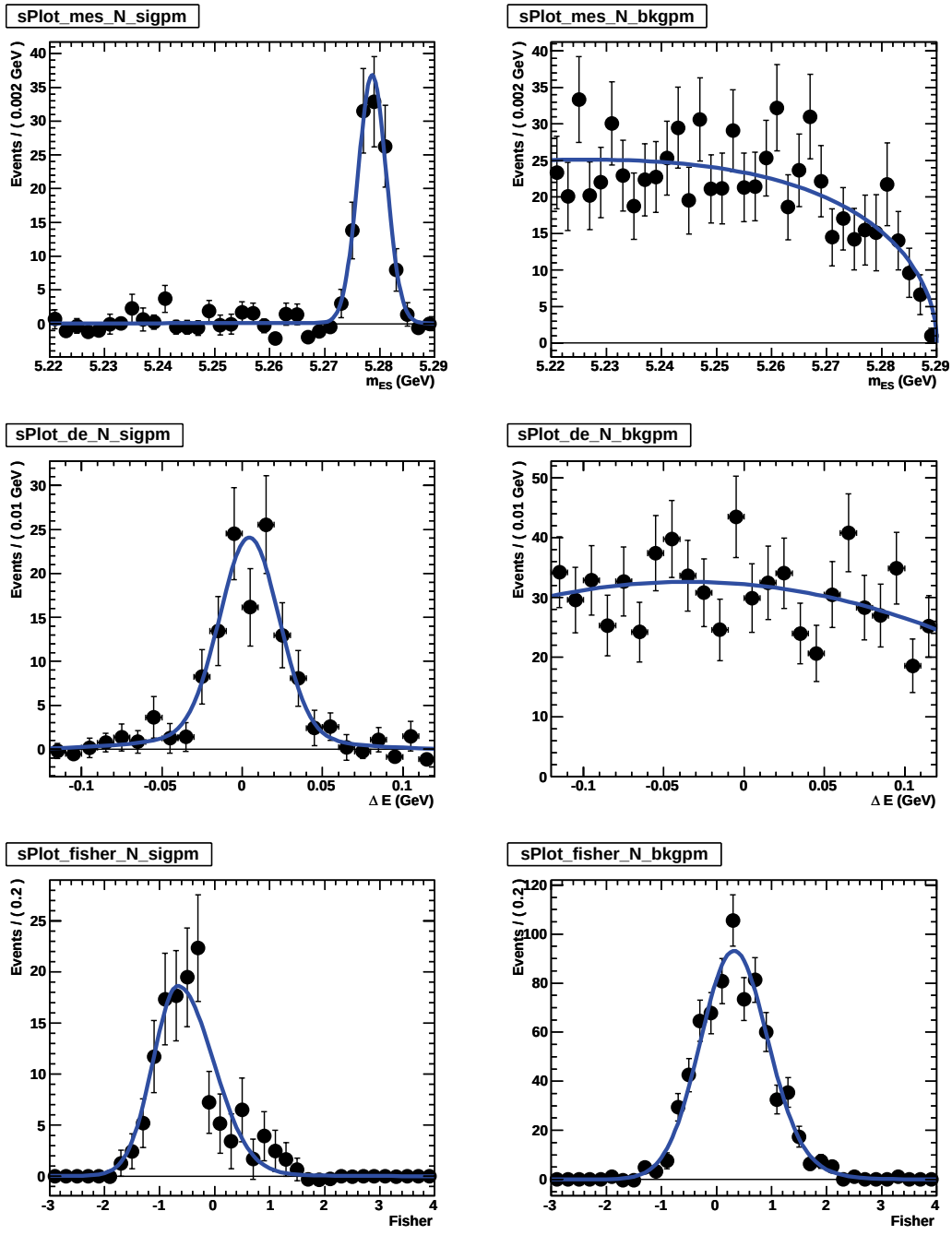

Figure 7.17: $m_{\rm ES}$ (top), ΔE (middle), and $\mathcal{F}$ (bottom) ${}_s\mathcal{P}lot$s for $B^0 \to K^0_S K^0_S K^0_S(\pi^+\pi^-)$ with on-resonance datasets. The left column is signal and the right column is continuum background.

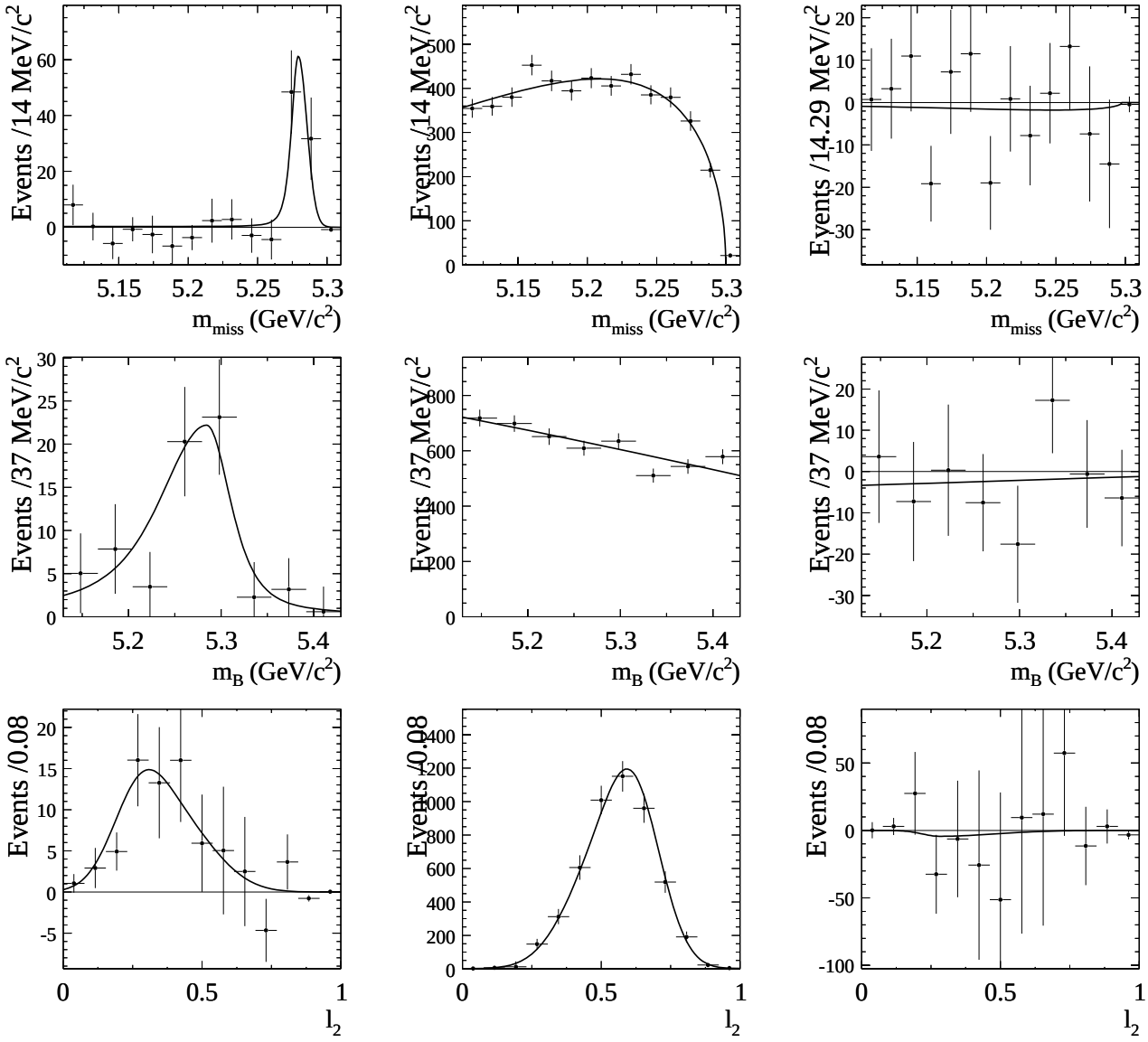

Figure 7.18: m_{miss} (top), m_B (middle), and l_2 (bottom) ${}_s\mathcal{P}lot$s for $B^0 \to K^0_S K^0_S K^0_S(\pi^0\pi^0)$ with on-resonance datasets. The left column is signal, the middle column is continuum background and the right column is $B\overline{B}$ background.

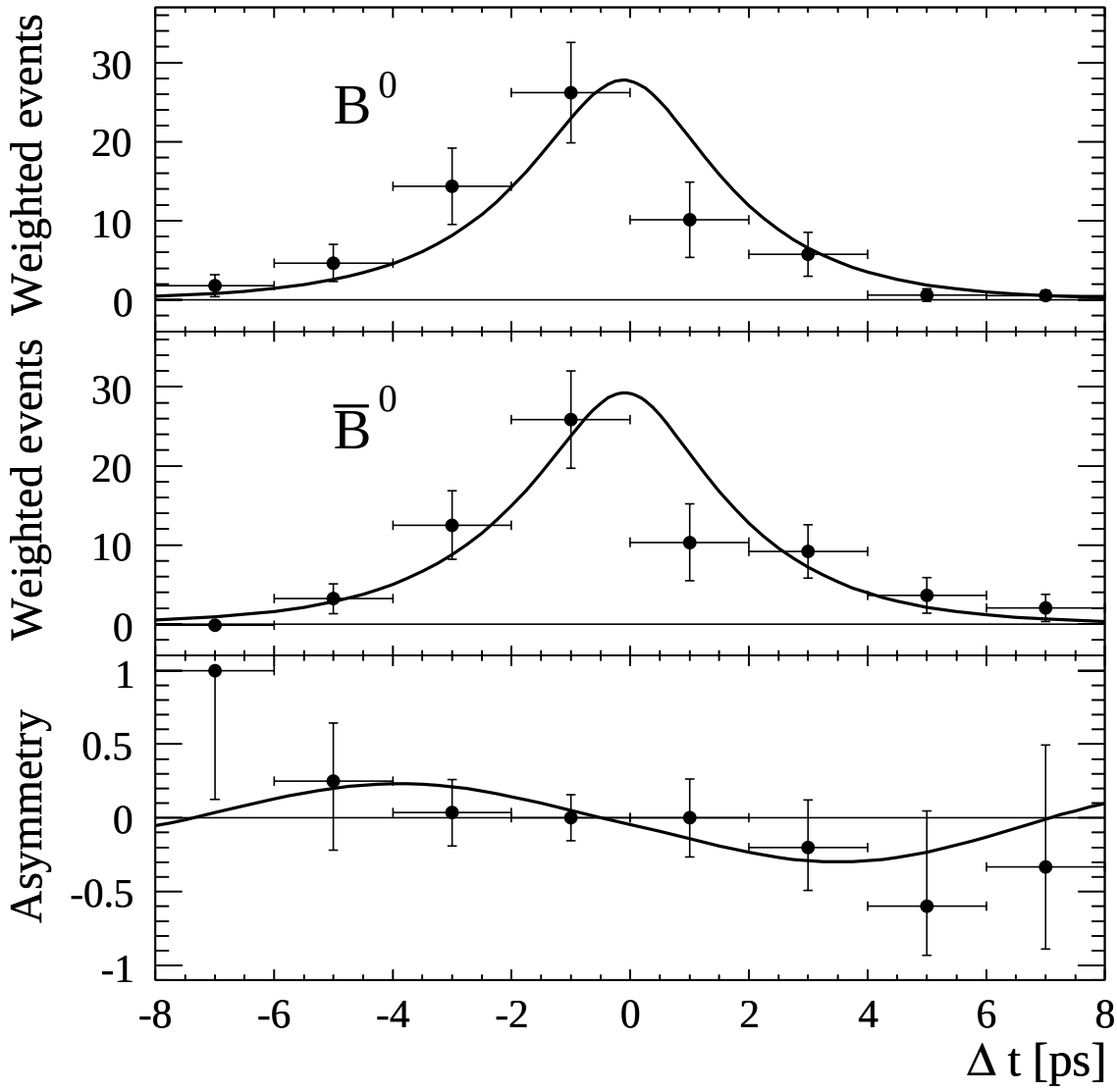

Figure 7.19: Distributions of Δt for events weighted with the ${}_s\mathcal{P}lot$ technique for $B_{\rm tag}$ tagged as B^0 (top) or $\overline{B}^0$ (center), and the asymmetry $\mathcal{A}(\Delta t)$ (bottom). The points are weighted data and the curves are the corresponding PDF projections.

7.5 Systematic Uncertainties

We evaluate systematic uncertainty on the *CP* asymmetry parameters S and C only on the combined fit. In the following we describe the main sources of systematic uncertainties, and in Table 7.12 we report the summary of them.

Event Selection and Data-Monte Carlo Agreement

We evaluate the uncertainty associated to the knowledge of fixed parameters entering the likelihood, related to the size of the available control samples with which we determine the PDF parameters. We evaluate this systematic uncertainty smearing the PDF's by one standard deviation and repeating the fit.

We account for possible disagreement between data and Monte Carlo in the description of the distribution of the variables defining the signal component of the likelihood fit. For the $K^0_S K^0_S K^0_S(\pi^+\pi^-)$ sub-mode the purity allows to fit the the means of $m_{\rm ES}$ and ΔE for the core Gaussians directly on data, so they do not contribute to the systematic uncertainties.

For the $K^0_S K^0_S K^0_S(\pi^0\pi^0)$ sub-mode we use, as data control sample, $B^0 \to J/\psi\, K^0_S$ decays, reconstructing $K^0_S \to \pi^0\pi^0$ in order to have the same topology of the signal in the kinematic variables. We check that the two decays have consistent distributions of m_{miss} and m_B comparing the shapes for the two signal Monte Carlo samples In Table 7.10 we show the comparison between signal parameters extracted by signal $B^0 \to K^0_S K^0_S K^0_S$ Monte Carlo and data $B^0 \to J/\psi K^0_S(\pi^0\pi^0)$. They are in quite good agreement and in the nominal fit we use the values from the control sample, and we use the shape from the signal Monte Carlo as an alternative parameterization to evaluate the systematic uncertainty associated to m_{miss} PDF. In Fig. 7.20 we show the m_{miss} distributions for signal $B^0 \to K^0_S K^0_S K^0_S(\pi^0\pi^0)$ Monte Carlo events and $B^0 \to J/\psi\, K^0_S(\pi^0\pi^0)$ on-resonance data.

In the case of m_B, there is a sizable difference between the shape on signal Monte Carlo and data. In particular, as expected, the simulation fails in reproducing the central value of the distribution. Concerning the other parameters, a simple fit with the four of them (2σ and 2α of the Cruijff function) simultaneously floating might overestimate the disagreement, because of the correlations between them. Because of that, we perform the fit on data fixing the two α's to the output of the fit on Monte Carlo and we use the variation on the σ's as an estimation of the (dis)agreement.

$m_{\rm Miss}$	$K^0_S K^0_S K^0_S$ Monte Carlo	$J/\psi K^0_s$ data
m (GeV/c^2)	5.2803 ± 0.0001	5.2793 +/- 0.0008
σ_- (GeV/c^2)	0.0049 ± 0.0001	0.0045 +/- 0.0007
σ_+ (GeV/c^2)	0.0050 ± 0.0007	0.0062 +/- 0.0006
α_-	0.2683 ± 0.0217	0.1816 +/- 0.0324
α_+	0.2281 ± 0.0069	0.2111 +/- 0.0113

Table 7.10: Comparison of m_{miss} parameterizations from signal Monte Carlo and $B^0 \to J/\psi K^0_S(\pi^0\pi^0)$ data control sample. Parameters are for the Cruijff function (Eqn. 6.15) we use as the m_{miss} PDF.

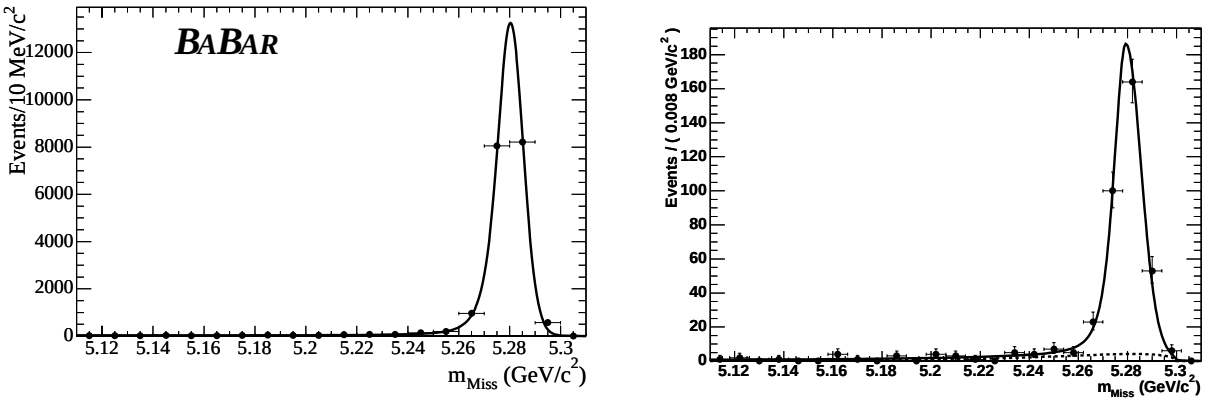

Figure 7.20: Comparison between m_{miss} distributions for signal Monte Carlo events for $B^0 \to K^0_S K^0_S K^0_S(\pi^0\pi^0)$ decays and $B^0 \to J/\psi K^0_S(\pi^0\pi^0)$ data control sample.

m_B	$B^0 \to K^0_S K^0_S K^0_S(\pi^0\pi^0)$ Monte Carlo	$B^0 \to J/\psi K^0_S(\pi^0\pi^0)$ data
m (GeV/c^2)	5.2700 $\pm$ 0.0002	5.2843 $\pm$ 0.0053
σ_- (GeV/c^2)	0.0474 $\pm$ 0.0018	0.0777 $\pm$ 0.0099
σ_+ (GeV/c^2)	0.0244 $\pm$ 0.0007	0.0243 $\pm$ 0.0053
α_-	0.2683 $\pm$ 0.0217	0.2683 (fixed)
α_+	0.2279 $\pm$ 0.0069	0.2279 (fixed)

Table 7.11: Comparison of m_B parameterizations from signal Monte Carlo and $B^0 \to J/\psi K^0_S(\pi^0\pi^0)$ data control sample.

In Table 7.11 we show the parameters found on signal Monte Carlo and $B^0 \to J/\psi K^0_S$ on resonance data, and in Fig. 7.21 we show the m_B distributions for the two samples and the fitted PDF's. We model the background for $B^0 \to J/\psi K^0_S(\pi^0\pi^0)$ data with a second order polynomial, as done for our nominal fit model. Considering the fact that

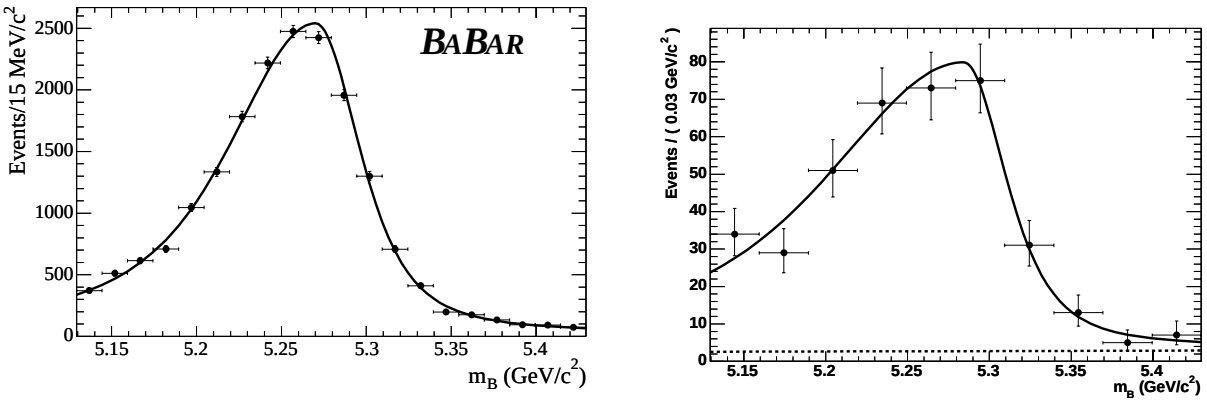

Figure 7.21: Comparison between m_B distributions for signal Monte Carlo events for $B^0 \to K^0_S K^0_S K^0_S(\pi^0\pi^0)$ decays and $B^0 \to J/\psi K^0_S(\pi^0\pi^0)$ data control sample.

the mean value in the case of Monte Carlo is not reliable, we think that it can be taken as it comes from $J/\psi K^0_S$ data even when performing $K^0_S K^0_S K^0_S$ nominal fit. From Monte Carlo study we see that $J/\psi K^0_S(\pi^0\pi^0)$ Monte Carlo does not reproduce well the signal $K^0_S K^0_S K^0_S(\pi^0\pi^0)$ Monte Carlo, so we cannot use the central values of the σs from the data control sample. Because of that, considering that the difference between data and $J/\psi K^0_S$ Monte Carlo for σ_- and σ_+ is not statistically different than zero and that the error on that is dominated by the fit on data, we conclude that we can use for the nominal fit the values on α and σ parameters as they come from $K^0_S K^0_S K^0_S(\pi^0\pi^0)$ Monte Carlo. For the systematics, we associate as an error to each parameter the maximum between the errors

of the two fits in Tab. 7.11.

CP Asymmetry of the $B\overline{B}$ background

Only the $K^0_S K^0_S K^0_S(\pi^0\pi^0)$ sub-mode has a non-zero $B\overline{B}$ background contribution. In the nominal fit we assume that the *CP* parameters of the $B\overline{B}$ background events are both zero, since we have a poor knowledge on *CP* content of the modes which constitute this component. The fraction of events which comes from charged B decays can only show direct *CP* asymmetry, while the part of the neutral B decays which is well reconstructed has a non-null lifetime and can then show both direct *CP* asymmetry and mixing-induced *CP* asymmetry. We estimate from $B\overline{B}$ studies that about half of the contribution comes from neutral B decays, and we assume that half of them have a prompt decay (we achieve this in the fit dividing by half the B^0 lifetime for the $B\overline{B}$ component). We assume complete ignorance on the *CP* parameters and vary $S_{B\overline{B}}$ and $C_{B\overline{B}}$ uniformly from -1 to 1, and take the largest deviation on signal S and C as systematic uncertainty. We find that signal S depends only from $B\bar{B}$ S and it is almost uncorrelated with the value of $B\bar{B}$ C (and vice versa for signal C).

Vertexing Method

We have shown in Sec. 2.3 and in Fig. 7.8 that the standard Δt resolution function taken from the `BReco` sample describes quite well also our signal events for which the vertex has been defined with the *Beam Spot Constraint* (BC) technique. To quantify the agreement between Δt evaluated with the standard vertexing technique and the one with BC vertexing, we make use of the *mangled* $B^0 \to J/\psi K^0_S$ sample. We define the quantity:

$$\chi^2(\Delta t) = \frac{\Delta t_{BC} - \Delta t_{nom}}{\sqrt{\sigma^2_{\Delta t_{BC}} - \sigma^2_{\Delta t_{nom}}}}. \tag{7.7}$$

Assuming the nominal reconstruction (Δt_{nom}) as an estimation of the true value, $\chi^2(\Delta t)$ is a variable which follows a Gaussian distribution with mean value zero and unitary width (pull of Δt). Fig. 7.22 show the distribution of $\chi^2(\Delta t)$ in Monte Carlo and data events for Class I and Class II for $B^0 \to J/\psi K^0_S$ decays. The distributions on data are about 10% wider than in Monte Carlo. From this distributions we can extract the scale factors necessary for the Δt error of the mangled events to make the pull width agree with Monte Carlo. They are 1.0375 for Class I events and 1.129 for Class II events. Taking the relative

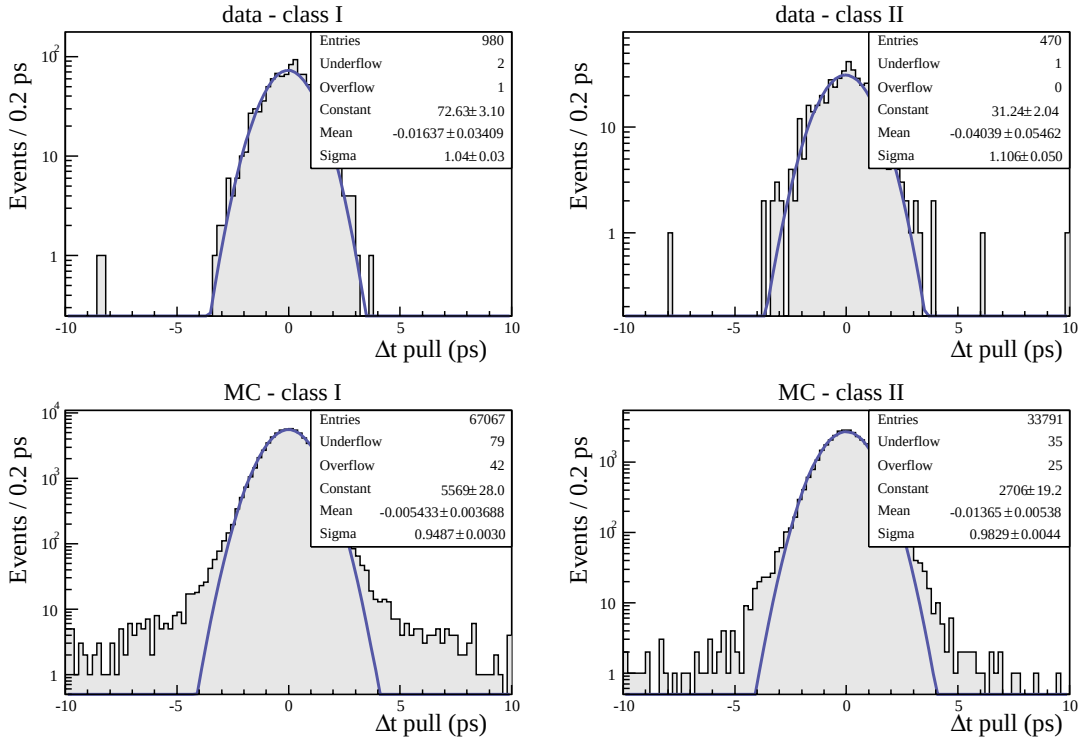

Figure 7.22: Distribution of Δt pulls (BC-minus-nominal) for $B^0 \to J/\psi K^0_S$ events in data (top) and Monte Carlo (bottom) events for Class I (left) and Class II (right).

fraction of Class I and II events in the combined $B^0 \to K^0_S K^0_S K^0_S$ sample into account we can obtain an overall scale factor. The final signal sample, as fitted in on-resonance dataset, is made by 65.3% of $K^0_S K^0_S K^0_S(\pi^+\pi^-)$ events and 34.7% of $K^0_S K^0_S K^0_S(\pi^0\pi^0)$ events. The $K^0_S K^0_S K^0_S(\pi^+\pi^-)$ mode has 89.5% of Class I events and 9.1% of Class II events, while $K^0_S K^0_S K^0_S(\pi^0\pi^0)$ mode has 79.0% of Class I events and 14.5% of Class II events. This brings to a fraction of 85.9% of the $K^0_S K^0_S K^0_S$ signal events in Class I and 14.1% in Class II. Then we can apply an average scale factor of 1.050 to our signal Δt PDF. We repeat the fit on the on-resonance dataset with the scaled Δt PDF and take the difference in *CP* parameters as the systematic error.

Resolution Function and Flavour Tagging

In addition to possible disagreement between the `BReco` resolution function and the true one for signal decays, we also account for the finite statistics with which the parameters of that PDF is evaluated. As has been done for the other PDF's, we smear its parameters by one standard deviation and take the deviation on the *CP* parameters as the systematic

errors.

With the same procedure we account for systematic uncertainties associated to flavour tagging parameters.

We account for the uncertainties on B^0 lifetime and mixing frequency Δm_d varying them by one σ, where σ is the uncertainty on the world average on their measurements [21].

SVT Alignment and Beam Spot Position

We evaluate the systematic uncertainties associated to possible misalignment's in the layers of the vertex tracker and on the knowledge of the beam spot position following the same procedure described for $B^0 \to K^+K^-K^0$ in Sec. 6.9.

Fit Bias

We account for possible neglected correlations in the fit and eventual bias with toy Monte Carlo experiments in which signal full Monte Carlo events are embedded in the fit, together with $B\overline{B}$ background events for the $K^0_SK^0_SK^0_S(\pi^0\pi^0)$ sub-mode. We correct the central value obtained from the fit with the curve $S(C)^{\rm fit}$ vs. $S(C)^{\rm true}$ shown in Fig. 7.16, using the central value extracted from the fit to data.

Tag Side Interference From Doubly CKM Suppressed Decays

Since the size of systematic effect due to possible interference in the tag side does not depends on the details of the fit, but just from the expectation values of the *CP* asymmetries, which are the same than for $B^0 \to K^+K^-K^0$ decays, we take the uncertainty from that analysis.

7.6 Summary of Results

In the fit of $B^0 \to K^0_SK^0_SK^0_S$ decays, reconstructed in the two sub-modes $K^0_SK^0_SK^0_S(\pi^+\pi^-)$ with all the three K^0_S decaying into $\pi^+\pi^-$ and $K^0_SK^0_SK^0_S(\pi^0\pi^0)$ with one K^0_S decaying into $\pi^0\pi^0$, we have measured the time dependent *CP* asymmetries.

We found the mixing-induced *CP* asymmetry parameter $S = -0.71 \pm 0.24 \pm 0.04$ and direct *CP* asymmetry parameter $C = -0.02 \pm 0.21 \pm 0.05$, where the first error is statistical and the second one is systematic. Both are in agreement with the Standard Model expectations, which predicts, for this pure $b \to s$ transition, $S = -\sin 2\beta =$

	$\sigma(S)$	$\sigma(C)$
Vertex reconstruction	0.016	0.003
Resolution function	0.005	0.007
flavour tagging	0.009	0.015
SVT alignment	0.016	0.008
IP position	0.004	0.001
Fit correlation	0.004	0.025
$B\bar{B}$ *CP*	0.007	0.005
Δm_d and τ_{B^0}	0.004	0.007
Tag-side interference	0.001	0.011
$B_{CP(+-)}$ PDF's	0.009	0.019
$B_{CP(00)}$ PDF's	0.024	0.024
Total	0.037	0.046

Table 7.12: Summary of systematic uncertainties on S and C.

-0.685 ± 0.032 and $C = 0$, where β is the CKM parameter measured with high precision in $B^0 \to [c\bar{c}]K^0$ decays [22].

Chapter 8

Measurement of Decay Rate of $B^{0/+} \to \phi\pi^{0/+}$ Decays

$B \to \phi\pi$ transitions take place through $b \to d$ penguin dominated amplitudes, which can be written in the Standard Model as [86]:

$$A(\phi\pi^+) = -V_{ud}V_{ub}^* \left(P_2^{GIM} - EA_1\right) - V_{td}V_{tb}^* P_2 \tag{8.1}$$

$$A(\phi\pi^0) = -V_{ud}V_{ub}^* \left(P_2^{GIM} - EA_2\right) - V_{td}V_{tb}^* P_2 \tag{8.2}$$

where $P_2^{(GIM)}$ labels the Renormalization Group Invariant (RGI) quantity corresponding to charming (GIM) penguin emission topologies and $EA_{1(2)}$ to (OZI suppressed) emission-annihilation topologies. In Fig. 8.1 we show the main Feynman diagram for this process. All these contributions are expected to be smaller than the usual penguin and annihilation

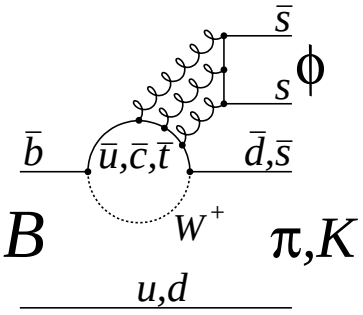

Figure 8.1: Main Feynmam quark level diagram responsible for $B \to \phi\pi$ and $B \to \phi K$: the flavor-singlet penguin.

contributions that enter, for instance, into $B \to \phi K$ decays, because of the additional factor λ (the sine of the Cabibbo angle) with respect to the leading term of $b \to s$ channels.

This strong suppression in the Standard Model and the fact that the main contribution proceed through a penguin amplitude, make $B \to \phi\pi$ decays particularly sensitive to new physics contributions. In particular, a measurement of $\mathcal{B}(B \to \phi\pi) \gtrsim 10^{-7}$ would be evidence for non Standard Model contributions to the amplitude, for example supersymmetric ones [87]. Upper limit can also be useful to set new bounds on *R-parity* violating models in Supersymmetry (see Sec. 9.3). The actual *BABAR* integrated luminosity makes such a branching ratio possible to be measured.

The study of the processes $B^+ \to \phi\pi^+$ and $B^0 \to \phi\pi^0$ is also important to understand the theoretical uncertainties associated with measurements of *CP* asymmetries in $B^0 \to \phi K^0$ decays. The $B \to \phi\pi$ decay amplitudes are related to the sub-leading terms of the $B^0 \to \phi K^0$ decay amplitude and can therefore provide stringent bounds on possible contributions to the time-dependent *CP* asymmetry in $B^0 \to \phi K^0$ [88], which we have described in Chapter 6. In particular, the measurement of the decay rate of these modes can limit the contribution of the electroweak penguins in the $B^0 \to \phi K^0$ decay amplitude [86].

Since the expected yield of this decay is very small, and we are studying only a narrow region in the K^+K^- invariant mass around the $\phi(1020)$ resonance, we do not perform a Dalitz plot analysis of this decay. Instead we adopt a so-called *quasi-two-body* approach, which means we treat the $\phi(1020)$ as a standard particle, neglecting the interference effects within the three-body $K^+K^-\pi$ final state. This is to some extent justified by the very narrow width of the $\phi(1020)$ resonance. We will treat the neglected interference effects as a systematic uncertainty.

For this analysis we use the data collected by *BABAR* detector during RunI-IV periods, corresponding to 232 $\times 10^6$ $B\bar{B}$ pairs.

8.1 The Event Selection

In this section we describe the selection of the neutral and charged B decays. Since the $B^0 \to \phi\pi^0$ decays involves a π^0 in the final state, we decided to use m_{miss} and m_B kinematic variables, which we have shown to be better than $m_{\rm ES}$ and ΔE (see Sec. 7.1.2) in presence of photons in final state. Since this set is not worse than $m_{\rm ES}$-ΔE in the case of all-charged final state, as in the case of $B \to \phi\pi$ decays, for consistency with the neutral mode we also use m_{miss} and m_B.

The reconstruction of both neutral and charged mode starts from the selection of a pair of oppositely-charged kaon candidates in the event. In the *quasi-two-body* approach they are considered as a $\phi(1020)$ candidate if the invariant mass $m_{K^+K^-}$ is within 15 MeV/c^2 of the nominal $\phi(1020)$ mass value [21]. This requirement corresponds to about three times the observed width in the K^+K^- invariant mass spectrum (see Table 6.12). In order to have a better purity, we apply the same particle identification criteria on the kaon candidates we have optimized for $B^0 \to K^+K^-K^0$ analysis in the narrow region of the $m_{K^+K^-}$ dominated by the $\phi(1020)$ (see Sec. 6.3.2). These PID requirements are quite loose due to the good signal-to-background ratio in this region. We have shown in the $B^0 \to K^+K^-K^0$ analysis that this $m_{K^+K^-}$ region has two main contributions: the $\phi(1020)$ and the $f_0(980)$ (see Table 6.20). The $\phi(1020)$ is a vector resonance (P-wave), which has a typical distribution of the helicity angle proportional to $\cos^2\theta_H$. $f_0(980)$, which is a scalar resonance (S-wave), has a flat distribution, as the continuum background, which is made by random combination of particles. The distributions of $\cos\theta_H$ for signal and continuum events are displayed in Fig. 8.2. We do not apply selection on $\cos\theta_H$, but we use this information in the fit.

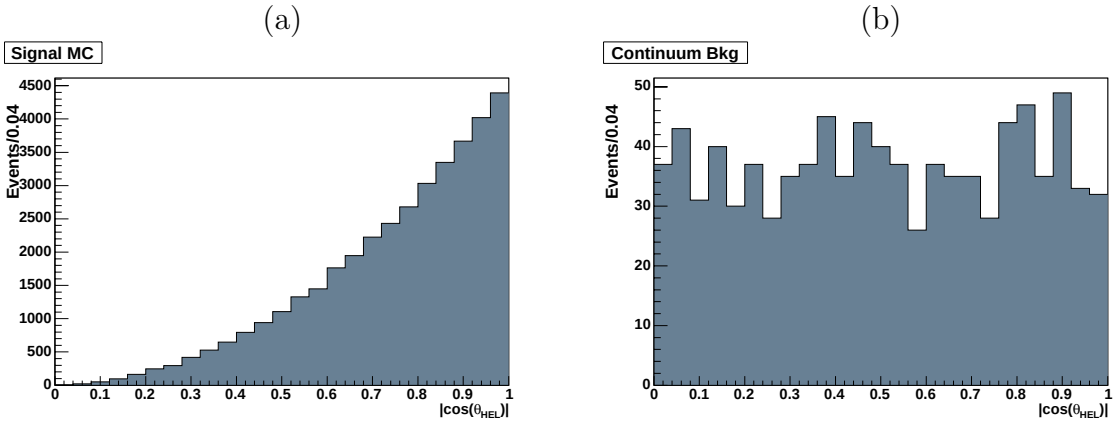

Figure 8.2: Distribution of $|\cos\theta_H|$ for (a) signal Monte Carlo $B^0 \to \phi\pi^0$ and (b) continuum background events.

Then we form a B^0 (B^+) candidate combining the formed $\phi(1020)$ candidate with a π^0 candidate (charged track). We describe these selections in the Sec. 8.1.1 (Sec. 8.1.2).

8.1.1 Selection of $B^0 \to \phi\pi^0$

We reconstruct a π^0 candidate from a pair of energy deposits in the EMC identified as described in Sec. 5.2.2. We then require the invariant mass of the photon pair to be within 110 MeV/c^2 and 160 MeV/c^2, which means about three times the observed width in the $\gamma\gamma$ invariant mass spectrum [21].

We combine the π^0 candidate with the ϕ candidate to form a B^0 if the composite satisfies loose requirements on the consistency with the B^0 mass:

- $|m_B - m_{B^0}^{PDG}| < 150$ MeV/c^2;
- $5.11 < m_{miss} < 5.31$ GeV/c^2;

as usual, these requirements retains, together with the most of the signal events, also wide sideband regions for the background characterization.

Also these decays suffer mostly from background coming from $q\overline{q}$ fragmentation, then we use the event shape variables to reject it. We use the ratio of Legendre monomials $l_2 = L_2/L_0$, described in Sec. 7.1.2. In this case we do not apply a selection on $|\cos\theta_S|$, but we make a cut directly on $l_2 < 0.55$ which is approximately 90% efficient on signal decays. We use the shape of the surviving events in the maximum likelihood fit. Due to the presence of a π^0 in the final state, which can produce energy leakage at the borders of the geometrical acceptance, the kinematic variable m_B shows a small difference when the B^0 decays in that region. Also $\sigma_{\Delta t}$ shows a small dependency on the polar angle, while l_2 is uncorrelated. This correlation can be removed with a very loose cut on the the polar angle of the B^0 meson: $|\cos\theta_B^*| < 0.9$ (typical distributions for B and $q\overline{q}$ events are shown in Fig. 6.3). This is illustrated in Fig. 8.3.

We also apply the two typical requirements which are applied in a time-dependent analysis: $|\Delta t|$ <20 ps and $\sigma_{\Delta t}$ <2.5 ps. These requirements have some rejection power against the continuum events because they typically have a badly formed B vertex.

π^0 Efficiency Corrections

Since in this analysis the target is to measure the rate of the decay, we pay also attention to possible disagreement between data and Monte Carlo reconstruction efficiency. Small contributions come from the tracking efficiency, which will be treated as systematic uncertainties, while a large contribution comes from the π^0 reconstruction efficiency. We apply

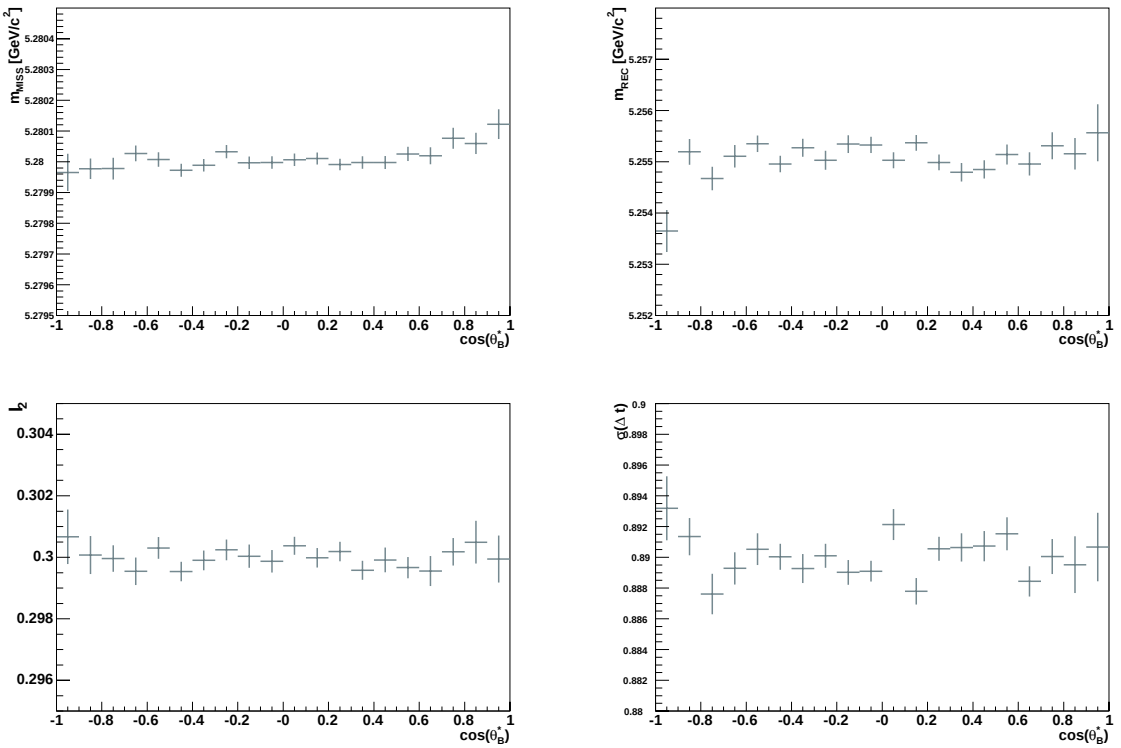

Figure 8.3: Average values for m_{miss}, m_B, l_2, $\sigma_{(\Delta t)}$ for selected $B^0 \to \phi\pi^0$ signal Monte Carlo events.

a correction to it, which has been studied by other analyses in *BABAR*. The correction, η, depends on the π^0 momentum:

$$\eta = 0.9735 + 0.006236 \cdot p_{\pi^0} \pm 0.03(syst) \tag{8.3}$$

where η is the ratio ε(data)/ε(MC). Fig. 8.4 shows the π^0 momentum in the laboratory frame in the signal MC. The average momentum for π^0 coming from $B^0 \to \phi\pi^0$ is 2.84 GeV/c, leading to an efficiency correction of $\eta = 0.991 \pm 0.03$ (syst).

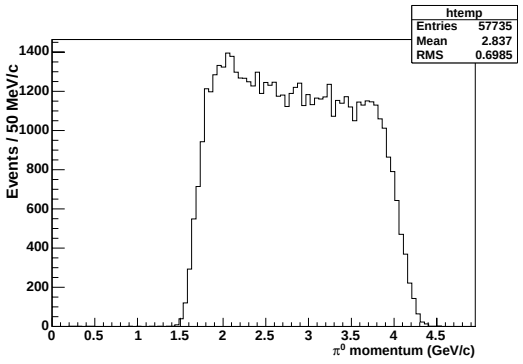

Figure 8.4: Distribution of π^0 momentum for signal Monte Carlo events

Resolution and Scale Corrections

The resolution of m_B variable, which is the variable mostly sensitive to energy leakage in the EMC by neutral particles, varied sensibly during the *BABAR*'s Run periods. In particular, there is a considerably large difference between the early Run I and the rest of Run periods, as it is illustrated in Fig. 8.5. We take into account these differences using a Monte Carlo sample which is weighted with the different Run periods luminosity.

These resolution effects have been studied using large data control samples. These studies provide corrections to apply to simulated events in order to have a better agreement with data. These corrections produce a significant effect only in m_B (Fig. 8.6a), while do not change m_{miss}, whose resolution is forced to be similar to the the beam one because of the B^0 mass constraint (Fig. 8.6b).

Summary of Reconstruction Efficiency and Best B Selection

In Table 8.1 we show the summary of the reconstruction efficiencies for the different requirements and the final one, after having applied the π^0 corrections. The final efficiency is approximately 30%.

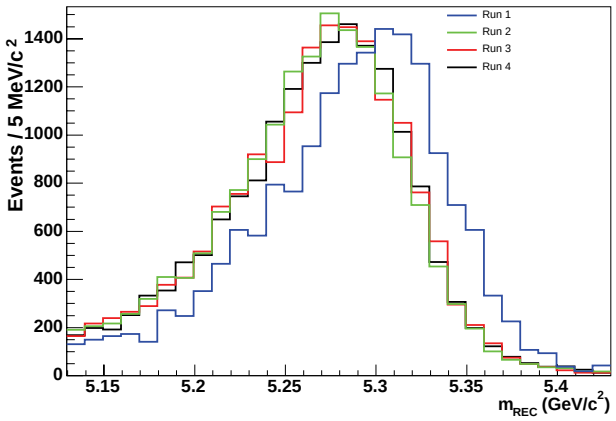

Figure 8.5: Distribution for m_B for $B \to \phi\pi$ signal Monte Carlo events in the different Run periods.

(a) (b)

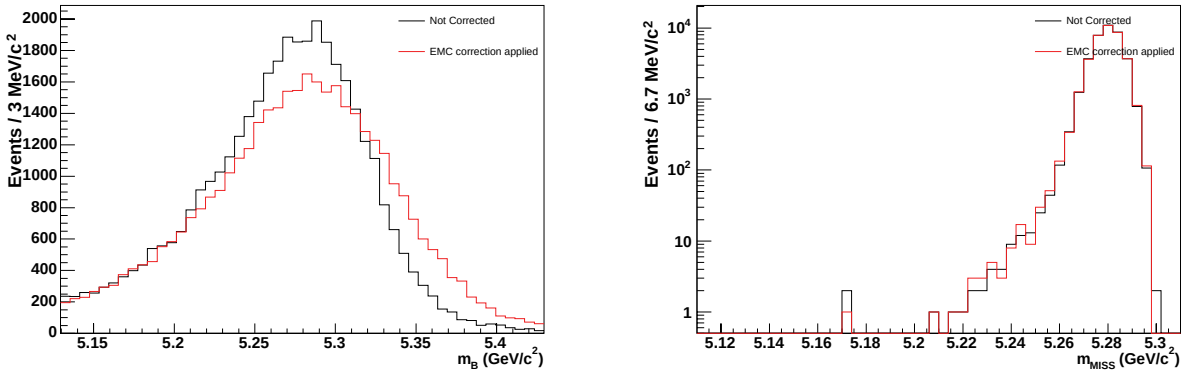

Figure 8.6: Distribution of (a) m_B and (b) m_{miss} for $B^0 \to \phi\pi^0$ signal Monte Carlo events before and after the neutral corrections.

Most of the selected events have only one candidate. The average multiplicity, both on Monte Carlo and data, is 1.003. In events where more than one B^0 is present, we choose the one which has the best χ^2 on the $\gamma\gamma$ invariant mass with respect to the π^0 nominal mass [21].

8.1.2 Selection of $B^+ \to \phi\pi^+$

In order to form $B^+ \to \phi\pi^+$ candidates we combine the formed $\phi(1020)$ composites with a charged track. In this way, the main background arise from another charmless

Selection	$\varepsilon(B^0 \to \phi\pi^0)$
pre-selection	0.451 ± 0.001
Kaon PID	0.976 ± 0.001
$\lvert m_{K^+K^-} - m_\phi^{PDG}\rvert < 15$ MeV/c^2	0.909 ± 0.001
$\lvert\cos\theta_B^*\rvert < 0.9$	0.980 ± 0.001
$l_2 < 0.55$	0.886 ± 0.001
$\lvert\Delta t\rvert < 20$ ps	0.973 ± 0.001
$\sigma_{\Delta t} < 2.5$ ps	0.941 ± 0.001
$\lvert m_B - m_{B^0}^{PDG}\rvert < 150$ MeV/c^2	0.937 ± 0.001
$5.11 < m_{miss} < 5.31\,\mathrm{GeV}/c^2$	0.999 ± 0.001
Total efficiency	0.298 ± 0.001
π^0 correction	0.991 ± 0.03
Total efficiency (corrected)	0.295 ± 0.008

Table 8.1: Reconstruction efficiency, as estimated from $B^0 \to \phi\pi^0$ signal Monte Carlo events. Efficiency correction related to π^0 reconstruction is applied.

decay, which, although being a rare process itself, has a branching fraction which is one order of magnitude larger than the one of the signal we want to explore: $B^+ \to \phi K^+$. This branching ratio has been measured in the full Dalitz plot analysis of $B^+ \to K^+K^-K^+$ [75, 76] to be (world average) $\mathcal{B}(B^+ \to \phi K^+) = (9.3 \pm 1.0) \times 10^{-6}$.

The kinematic difference between the $\phi\pi$ and ϕK combinations provide a handle to separate the particle content of the candidate B decay. We reconstruct the $B^+ \to \phi h^+$, where $h = \pi, K$, assigning to the h^+ track the pion mass. Then the m_B distribution peaks at the correct B^+ mass for $B^+ \to \phi\pi^+$ events, while it is shifted by ≈ 42 MeV/c^2 for $B^+ \to \phi K^+$ events. This is shown in Fig. 8.7. Also, the incorrect mass hypothesis causes this shift in m_B to exhibit a momentum dependence, which produces a smearing of the distribution for the incorrect mass hypothesis which have to be evaluated event by event. If we call m_B^{reco} the reconstructed m_B value with the pion mass hypothesis, with h^+ the true mass hypothesis on the track, the true m_B value would be:

$$m_B^{true} = m_B^{reco} + m_B^{h^+} - m_B^{\pi^+} \tag{8.4}$$

The dependency of the m_B shift from the momentum of the h^+ tracks can be expressed analytically by:

$$m_B^{h^+} - m_B^{\pi^+} = \sqrt{E_\phi^2 + m_{h^+}^2 + 2E_\phi E_{h^+} - |\vec{p_\phi}|^2 - 2\vec{p_\phi} \cdot \vec{p_{h^+}}} \tag{8.5}$$

which will be used for event by event shift of the m_B PDF mean in the maximum likelihood

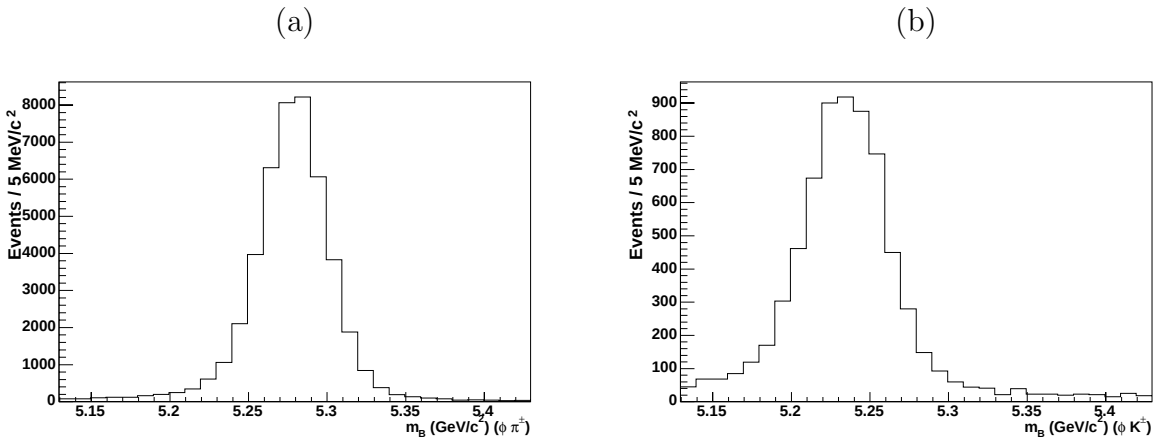

Figure 8.7: Distributions of m_B variable for (a) $B \to \phi\pi$ decays and (b) $B^+ \to \phi K^+$ decays, reconstructed assuming that the track from B decay is a pion.

fit.

In order to separate $\phi\pi$ and ϕK final states we cannot rely only on the difference in m_B, but we have also to exploit the particle identification of the charged tracks (see Sec. 5.1.1). The high momenta of the tracks in these decays limit the viability of the SVT and DCH dE/dx measurements as pion/kaon discriminators for these signal decays. Therefore DIRC θ_c measurement will serve as our particle identification tool, dominating the separation of the two decay modes. In order to have the best sensitivity to the tiny $B^+ \to \phi\pi^+$ signal, we do not apply a requirement on the kaon PID selectors, as we do for the ϕ daughters, but we parameterize the DIRC information in the likelihood and we will fit simultaneously $\phi\pi^+$ and ϕK^+ signals.

Parameterizations of measured θ_c, obtained from highly pure data control samples of charged pions and kaons, are used to calculate π and K likelihoods of each track. These control samples are made by reconstructed decay chain $D^{*+} \to D^0\pi^+ \to (K^-\pi^+)\pi^+$ using only kinematic information and no particle identification. The $D^{*\pm}$ candidates are built through four-momentum addition of tracks with appropriate mass assignment defined by the charge of the slow pion from the D^* decay. A two standard deviation cut on the mass difference of the D^* and D^0 ($\sigma_{\Delta M} = 0.9$ MeV/c^2, see Fig. 8.8), which is measured well due to the small momentum of the slow pion, removes most of mis-reconstructed D^0's. Requiring that the D^0 momentum in the CM frame is > 2.5 GeV/c isolates the continuum D^* candidates and eliminates $B\overline{B}$ events which typically have higher combinatorial backgrounds. Removing events where the kaon track is in line with the D^0 flight direction

in the D^0 rest frame provides further suppression of the combinatorial background. The cosine of this angle $\cos\theta^*_K$ is required to be < 0.8. These selections produce a D^0 sample which has a purity of $\approx 96\%$ (see Fig. 8.8b). The most recent study of this control sample

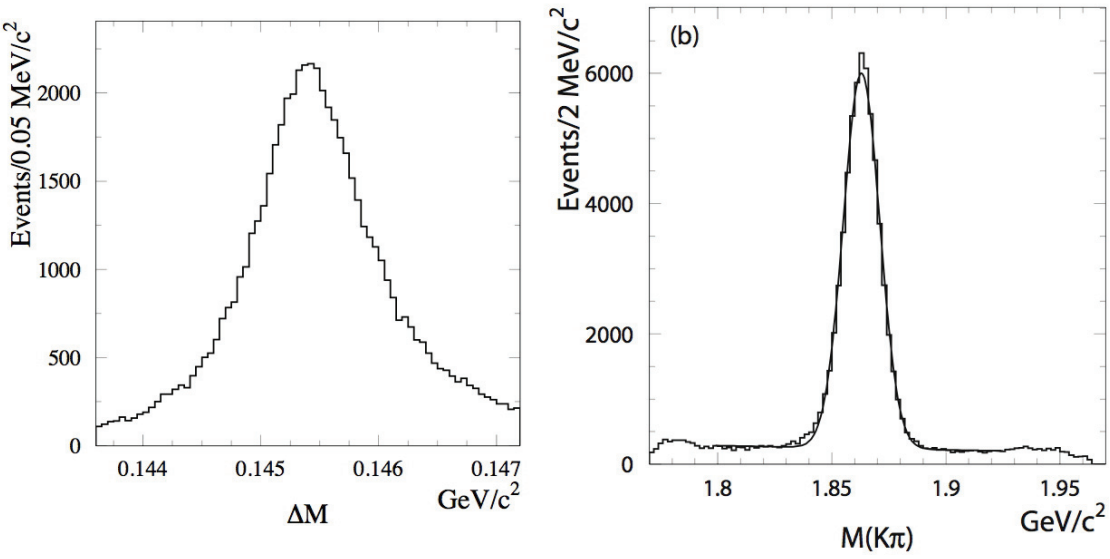

Figure 8.8: The (a) $\Delta M = M(D^*) - M(D^0)$ mass difference and (b) D^0 mass in the control sample used for studying DIRC θ_c measurements.

calibrates the DIRC response by separately parameterizing the θ_c resolution, systematic bias, and charge dependence of the measured θ_c of kaons and pions. We only consider tracks which have sufficient signal Cherenkov photons ($N_\gamma > 5$) and $\theta_c > 0.1$ rad for a good θ_c measurement. The π^+,π^-,K^+ and K^- distributions of the θ_c *pulls*, defined as $\left(\theta_c - \theta_c^{Exp} - \mu^{\pm}_{\pi,K}(\cos\theta)\right)/\sigma^{\pm}_{\pi,K}$, where θ_c and θ_c^{Exp} are the measured and expected θ_c, respectively, are studied separately in bins of track polar angle $\cos\theta$. $\mu^{\pm}_{\pi,K}$ and $\sigma^{\pm}_{\pi,K}$ represent the mean and the measured bias and resolution of the θ_c pulls, whose only observed dependence is on $\cos\theta$, while they are not correlated with momentum. They are measured by a fit with double Gaussian functions.

Pull distributions for the whole sample, which provide likelihoods for discriminating pions and kaons, are shown in Fig. 8.9.

We retain only events which are within 4 standard deviations ($\sigma^{\pm}_{\pi,K}$) of these pulls.

In order to reject the continuum background, we apply the requirements on $l_2 < 0.55$ and $|\cos\theta^*_B| < 0.9$, like in the case of $B^0 \to \phi\pi^0$. The final efficiency for reconstructing $B^+ \to \phi\pi^+$ and $B^+ \to \phi K^+$ events are approximately 37% and 36%, respectively. The

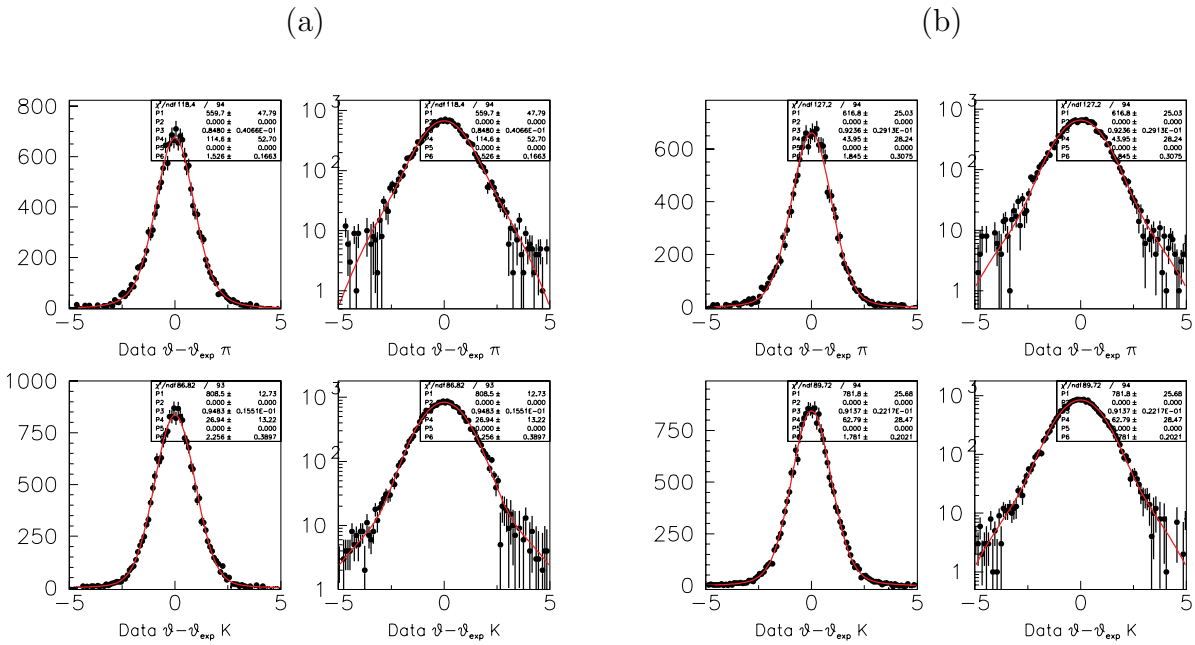

Figure 8.9: The corrected θ_c pull distributions for (a) positively and (b) negatively charged pions (top) and kaons (bottom). The fits are to double Gaussian functions.

breakdown of the efficiencies is reported in Table 8.2.

The slight difference in the efficiency between $B^+ \to \phi\pi^+$ and $B^+ \to \phi K^+$ is due to different combinatorial. The main difference is in the PID - $m_{K^+K^-}$ requirements efficiencies, whose efficiencies are different if compared separately, but their product is about the same. After the pre-selection the candidate multiplicity is similar: 1.36 for $B^+ \to \phi\pi^+$ and 1.40 for $B^+ \to \phi K^+$. Also, the K^+K^- invariant mass resolution in the $\phi(1020)$ region is the same in the two cases. The difference comes from the fake combinations at high values of invariant mass (we accept only events within 15 MeV/c^2 from nominal $\phi(1020)$ mass), which are more for $B^+ \to \phi\pi^+$ than for $B^+ \to \phi K^+$. In Fig. 8.10 the distribution of K^+K^- invariant mass in the whole region after the pre-selection and after the PID requirement is shown for the two Monte Carlo samples. The PID removes a fraction of the fake combinations at high invariant mass of $B^+ \to \phi\pi^+$, while it has no effect on $B^+ \to \phi K^+$.

The event multiplicity after this selection is applied is 1.004 B^+ candidate/event. When more than one candidate is present in an event, we choose the one with the smallest χ^2 of the $\phi(1020) \to K^+K^-$ mass. Since we want to use the lineshape of the $\phi(1020)$ resonance in the maximum likelihood fit, we have checked that this selection of the best

Selection	$\varepsilon(B^+ \to \phi K^+)$	$\varepsilon(B^+ \to \phi K^+)$
pre-selection	0.748 ± 0.001	0.721 ± 0.001
Kaon PID on $\phi(1020)$ tracks	0.932 ± 0.001	0.847 ± 0.001
$\lvert m_{K^+K^-} - m_\phi^{PDG}\rvert < 15$ MeV/c^2	0.774 ± 0.001	0.887 ± 0.001
$\lvert\cos\theta_B\rvert < 0.9$	0.983 ± 0.001	0.983 ± 0.001
$l_2 < 0.55$	0.876 ± 0.001	0.876 ± 0.001
$\lvert m_B - m_{B^0}^{PDG}\rvert < 150$ MeV/c^2	0.973 ± 0.001	0.980 ± 0.001
$5.11 < m_{miss} < 5.31$ GeV/c^2	0.999 ± 0.001	0.999 ± 0.001
$\theta_c > 0.1$ rad	0.853 ± 0.001	0.857 ± 0.001
$N_\gamma > 5$	0.966 ± 0.001	0.976 ± 0.001
θ_c outlier	0.986 ± 0.001	0.987 ± 0.001
Total efficiency	0.362 ± 0.001	0.371 ± 0.001

Table 8.2: Reconstruction efficiency, as estimated from $B^+ \to \phi K^+$ and $B^+ \to \phi\pi^+$ Monte Carlo events.

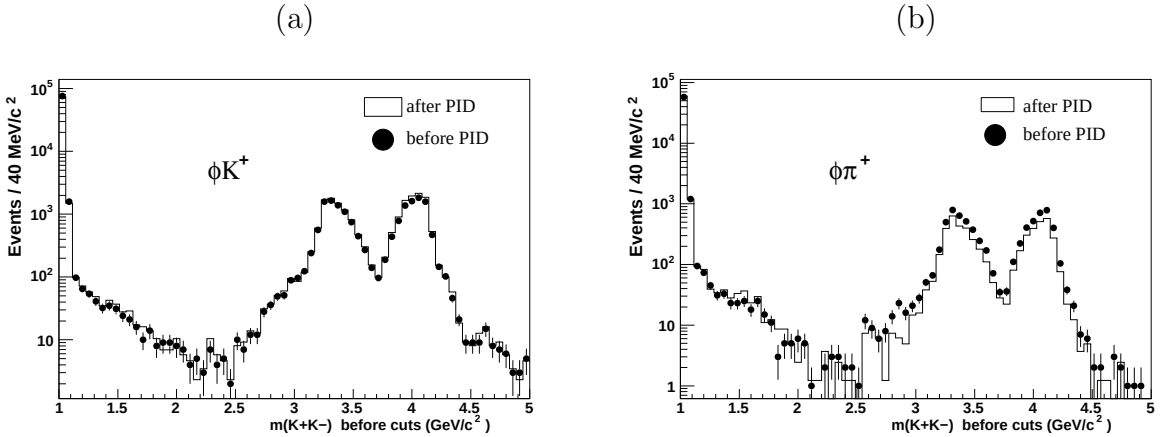

Figure 8.10: K^+K^- invariant mass in the whole kinematically allowed region for (a) $B^+ \to \phi K^+$ and (b) $B^+ \to \phi\pi^+$ Monte Carlo events. Dots: the distribution after the pre-selection. Histogram: distribution after the PID requirements.

candidate, which choose systematically the one with the $m_{K^+K^-}$ nearest to the nominal $\phi(1020)$ mass, does not introduce a narrowing of the lineshape. Because of the very low multiplicity this does not constitute a problem. We verify this assumption with a fit to the K^+K^- mass for signal Monte Carlo events with and without the best B^+ selection which return a consistent width.

8.2 $B\overline{B}$ Background

We study the contributions to the background due to mis-identified other B decays from a sample of generic $B^0\overline{B}^0$ and B^+B^- decays equivalent approximately to five times the used data sample. We study separately the contributions to the charged and neutral mode.

8.2.1 $B\overline{B}$ Background for $B^+ \to \phi h^+$

We study the background contributions removing from the sample the signal events. According to the adopted strategy, we consider as signal both $B^+ \to \phi\pi^+$ and $B^+ \to \phi K^+$ decays.

Since the efficiency for the B background modes is very sensitive to the definition of the signal region, we take particularly care of those modes which present a concentration of events near the B invariant mass in the m_{miss} and m_B variables. According to this criterion, starting from the whole *fit region* (FR)

- $5.11 < m_{miss} < 5.31$ GeV/c^2
- $|m_B - m_{B^0}^{PDG}| < 150$ MeV/c^2

we define a reduced *signal region* (SR)

- $5.26 < m_{miss} < 5.30$ GeV/c^2
- $5.20 < m_B < 5.35$ GeV/c^2

where the *peaking* background events clusters. The events which are selected outside the signal region come usually from random combination of particles from the two different B mesons, so they have a distribution in m_B which is like a $q\bar{q}$ event. We define as *combinatorial* all these events.

The composition of the selected sample is shown in Table 8.3, where the contributions have been rescaled at the luminosity of the used data set (212 fb^{-1}). Since the generic Monte Carlo sample gives too few events to study in detail the reconstruction efficiencies of these modes and the shape of their discriminating variables, we generate a large number of Monte Carlo events for the "peaking" modes $B^+ \to f_0\pi^+$, $B^+ \to a_0\pi^+$, $B^+ \to \phi K^+$, $B^+ \to f_0 K^+$ and apply the selection on them. The $f_0 h^+$ samples are generated assuming the f_0 mass and width values taken from BES experiment data (Table 6.12 and [79]).

Decay mode	Fit Region	Signal Region	BF used (10^{-6})
$\phi\pi^+$	40.1	38.9	1 [MC]
ϕK^+	349.6	346.3	9.3 ± 1.0 [PDG]
$f_0(980)\pi^+$	2.9	2.5 (3.9)	1 [MC] ([MC with BES shape])
$a_0(980)\pi^+$	2.7	2.5	1 [MC]
$f_0(980)K^+$	25.7	24.9 (45.8)	10 [MC]
$D^0\pi^+$	10.7	0.6	5300 [MC]
$D^{*0}\pi^+$	9.3	0.6	4600 [MC]
$D^0\rho^+$	4.7	0.4	13400 [MC]
$D^{*+}\rho^0$	0.4	0	13400 [MC]
`combinatoric`	2.7	0	15500 [MC]
Total	**59.1**	**31.5**	

Table 8.3: Events selected by $B^+ \to \phi h^+$ selection in the whole $B^+\bar{B}^-$ generic Monte Carlo samples, scaled to an equivalent luminosity of $\sim 210 fb^{-1}$. In the total number of B^+B^- background events is not included the number of $B^+ \to \phi K^+$ events, because in this case they are considered as *signal*. The numbers in parenthesis for $B^+ \to f_0(980)h^+$ are evaluated using the $f_0(K^+K^-)/\phi(K^+K^-)$ ratio reported in [76] and the efficiency correction due to the difference in the f_0 lineshape between Monte Carlo and BES experiment data [79], which will be used as nominal shape. The rest of the numbers comes from branching fractions used in the generic Monte Carlo, denoted as [MC] (usually values from [21] or reasonable assumptions from theoretical estimations).

Decay mode	generated	ε
$\phi\pi^+$	121000	0.371 ± 0.001
ϕK^+	163000	0.362 ± 0.001
$f_0\pi^+$	17000	0.118 ± 0.002 (0.024 ± 0.002)
$a_0\pi^+$	23000	0.117 ± 0.002
f_0K^+	148000	0.117 ± 0.001 (0.024 ± 0.001)

Table 8.4: Exclusive B^+ decay modes contributing to $B\overline{B}$ background, generated events and reconstruction efficiencies. The values in parenthesis are the final efficiencies using the BES lineshape for the $f_0 \to K^+K^-$.

We report the efficiencies for these modes in Table 8.4. The scalar modes $f_0\pi^+$ and $a_0\pi^+$ are generated forcing the decay of $f(a)_0 \to K^+K^-$. In order to estimate the contribution of scalars mesons in the signal region we have to know the branching fractions of $f(a)_0 \to K^+K^-$. Measurements exist that give the relative amount of $\frac{\mathcal{BF}(f_0 \to K^+K^-)}{\mathcal{BF}(f_0 \to \pi^+\pi^-)}$, but some of them are not consistent with other ones. For example, regarding the f_0 branching fractions, PDG gives a result for these ratios which come from a combined K-matrix

analysis of Crystal Barrel, GAMS and BNL [29]

$$\Gamma(\pi\pi)/\left[\Gamma(\pi\pi)+\Gamma(K\bar{K})\right] = 0.84 \pm 0.02 \tag{8.6}$$

Considering that the K belongs to an isospin doublet, we estimate that $\mathcal{B}(f_0 \to K^+K^-) \sim 0.08$. This result is similar to the assumption used in the *BABAR* generic Monte Carlo ($\mathcal{B}_{MC}(f_0 \to K^+K^-) = 0.11$). The f_0 contribution which can be estimated from Monte Carlo is so reported in Table 8.3 and is negligible with respect to the signal. With the same assumption the estimated number of f_0K^+ in the final data sample is 25.7 events.

From our Dalitz plot analysis of $B^0 \to K^+K^-K^0$, we get an higher fraction of $\mathsf{f_0(980)}$ in the $\phi(\mathsf{1020})$ mass region: the branching fractions are reported in Table 6.20. They agree with the measurements of the $B^+ \to K^+K^-K^+$ Dalitz plot [76]. With these branching fractions the expected yields of $f_0\pi^+$ and f_0K^+ change drastically. They are also reported in Table 8.3. We will use this estimation for the validation studies.

Similar considerations can be made for the a_0 contribution, where from [21] we have that:

$$\Gamma(K\bar{K})/\Gamma(\eta\pi) = 0.183 \pm 0.024 \tag{8.7}$$

This leads to a $\mathcal{BF} \sim 0.075$ and so the real contribution from $a_0\pi^+$ seems to be negligible.

Because of these uncertainties on K^+K^- S-wave contamination in the ϕ region, we include a generic S-wave component in the fit and we fit its yield. We will verify with toy Monte Carlo experiments the capability of the fit of doing this and to estimate possible biases on their determination. Figure 8.11 (Figure 8.12) shows the m_{miss} and m_B (K^+K^- mass and $\cos\theta_H$) distributions for signal Monte Carlo events and the three different "peaking" B background components. The pollution coming from $B^0\overline{B}^0$ decays is negligible. In the whole generic Monte Carlo sample we find only 1 event, ($B^0 \to \phi K^0_S(\pi^+\pi^-)$). So we do not further consider this component.

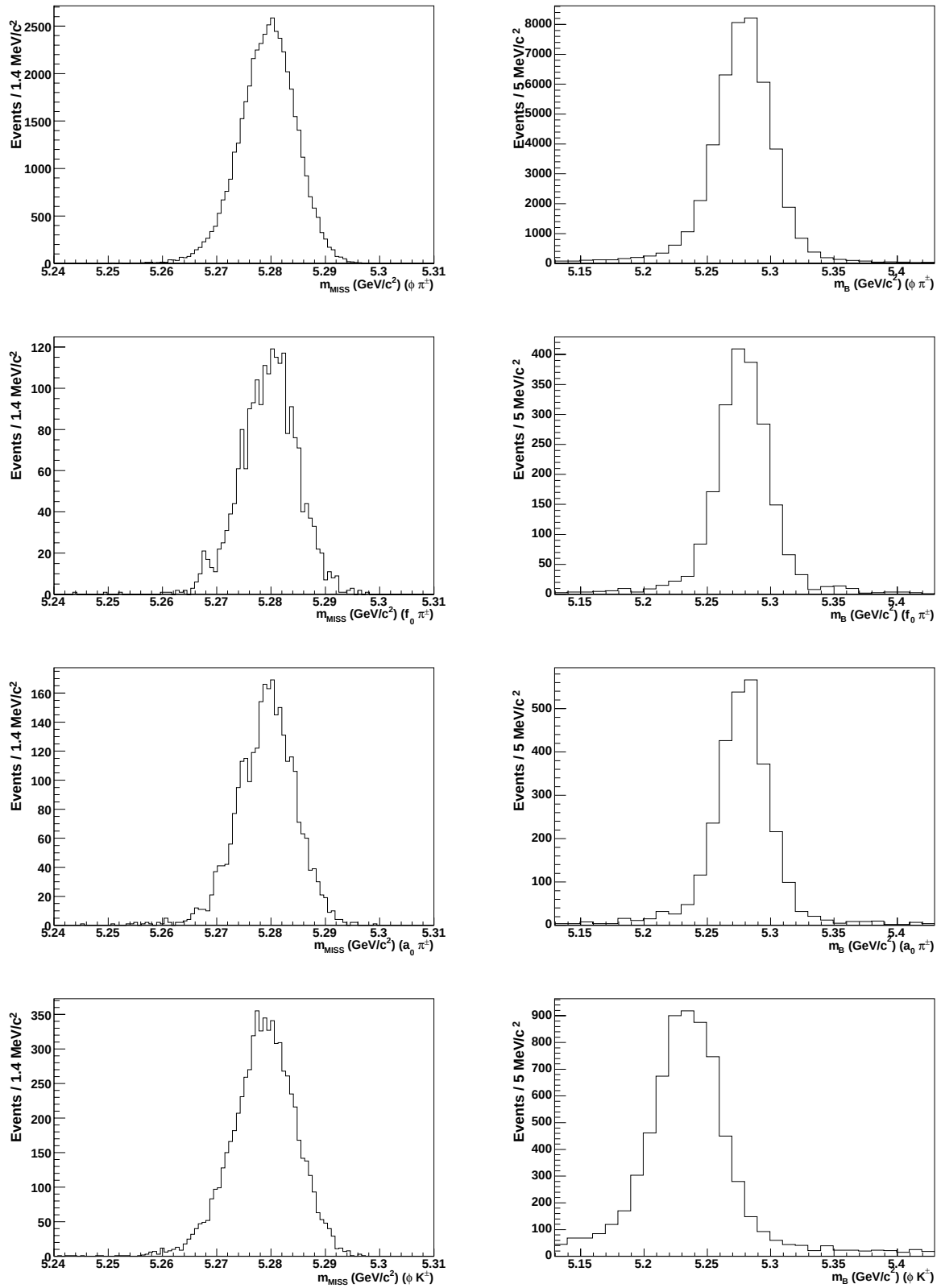

Figure 8.11: m_{miss} (left) and m_B (right) for $B^+ \to \phi\pi^+$ signal Monte Carlo and the main $B\bar{B}$ background modes. m_B is calculated with pion mass hypothesis. 1st row: signal $B^+ \to \phi\pi^+$. 2nd row: $B^+ \to f_0(980)\pi^+$. 3rd row: $B^+ \to a_0(980)\pi^+$. 4th row: $B^+ \to \phi K^+$.

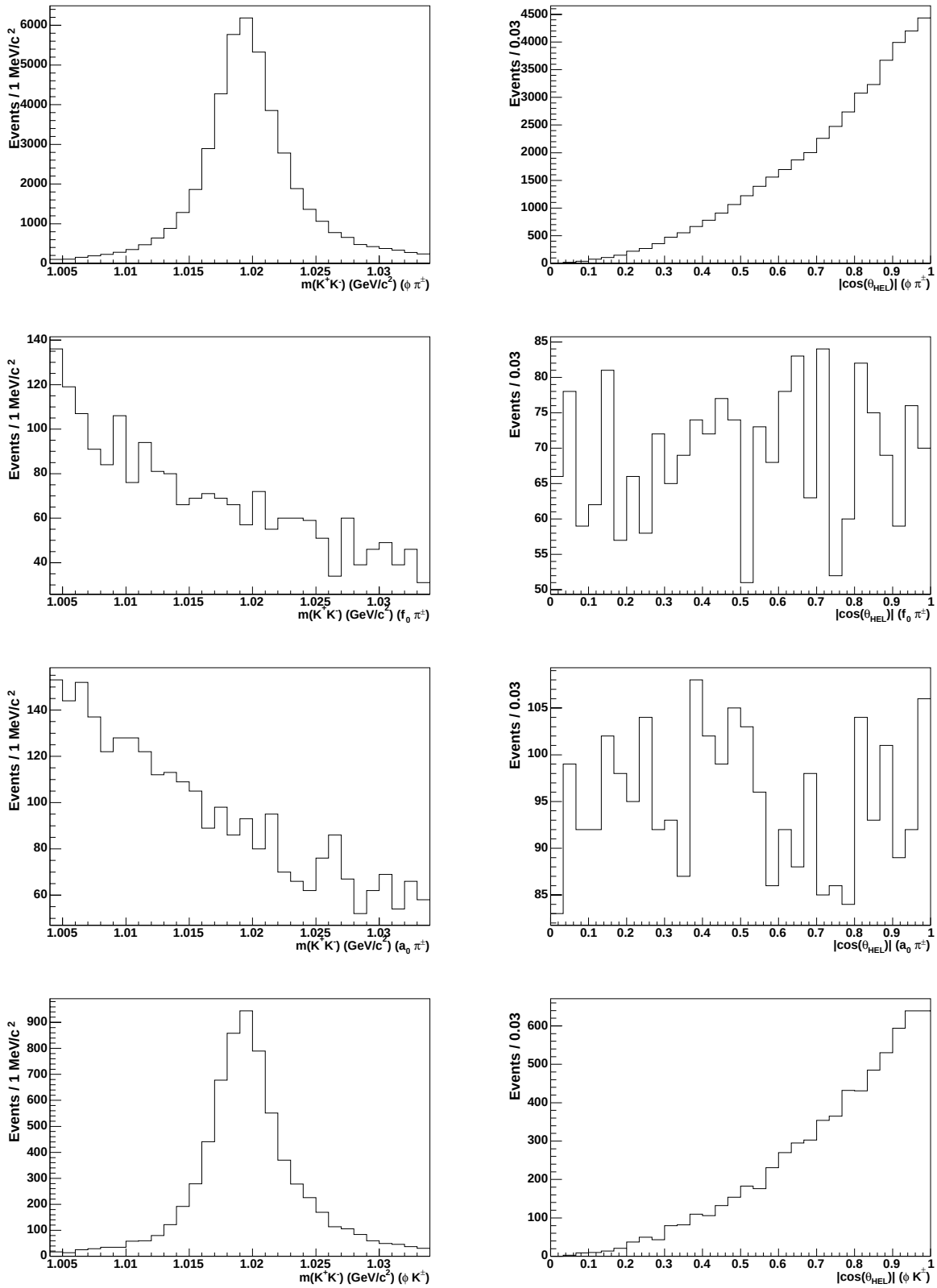

Figure 8.12: K^+K^- invariant mass (left) and $\cos\theta_H$ (right) for $B^+ \to \phi\pi^+$ signal Monte Carlo and the main $B\bar{B}$ background modes. 1st row: signal $B^+ \to \phi\pi^+$. 2nd row: $B^+ \to f_0(980)\pi^+$. 3rd row: $B^+ \to a_0(980)\pi^+$. 4th row: $B^+ \to \phi K^+$.

Decay mode	Fit Region	Signal Region	BF used (10^{-6}) [source]
$\phi\pi^0$	52	50	1 [MC]
$f_0\pi^0$	2.0	2.	1 [MC]
$a_0\pi^0$	2.0	1.6	1 [MC]
$K^*(K^+\pi^-)\pi^0$	1.2	0.8	15 [MC]
$\phi K^0_S(\pi^0\pi^0)$	1.0	1.4	$8.6^{+1.3}_{-1.1} \times 1/3$ [PDG]
$D^{*+}_s K^-$	0.2	0	20 [MC]
$D^{*+}\rho^-$	0.2	0	46 [MC]
$D^{*0}\rho^0$	0.2	0	250 [MC]
$\rho^0\pi^0$	0.2	0	22 [MC]
`combinatorial`	1.2	0	
Total	**8.2**	**5.2**	

Table 8.5: Expected events per 210 fb^{-1} of $B^0\overline{B}^0$ generic decays. The ϕK^0_S and $K^*\pi^0$ yields have been normalized using the measured $\mathcal{B}$s. Branching fractions denoted with [MC] are taken from the simulation, which usually is [21] or reasonable assumption from theoretical estimations.

8.2.2 $B\overline{B}$ Background for $B^0 \to \phi\pi^0$

We repeated the study of the B background composition for the neutral mode. The FR and SR are defined in the same way of the charged mode.

In Table 8.5 we show all the events which satisfy the selection on the whole generic $B^0\overline{B}^0$ and B^+B^- samples, scaled to the luminosity of 212 fb^{-1}. Fig. 8.13 shows the distribution of m_{miss} and m_B for these events. Of these modes, $B^0 \to \phi K^0_S$ and $B^0 \to K^*\pi^0$ has a well established branching fraction: ($\mathcal{B}$ $(B^0 \to \phi K^0) = 8.6^{+1.3}_{-1.1} \times 10^{-6}$ and $\mathcal{B}$ $(K^*\pi^0) = 1.7 \pm 0.8 \times 10^{-6}$ [21]), so for these modes the estimated contribution in Table 8.5 has been evaluated using the measured decay rates. The branching fractions for the scalar mesons decaying in two kaons are not well known, as described in the previous section. Like for the charged mode, we include an S-wave component in the fit and fit its yield.

All the other `peaking` modes in the Monte Carlo are produced with the $\mathcal{B} \equiv 1 \times 10^{-6}$, and we have no measured upper limits, so we can only give a rough estimation of the signal to background yield ratio. With this warning, we estimate that in the "narrower" signal region the B background pollution to the signal is less than 10%.

The pollution from charged B decays is even smaller. We apply the selection on the whole B^+B^- Monte Carlo sample. The selected events are shown in table 8.6. When we re-scale these events to actual data sample we have ~ 3.7 events in the FR, but they are all purely combinatorial-like: in the whole B^+ B^- Monte Carlo dataset we find no events

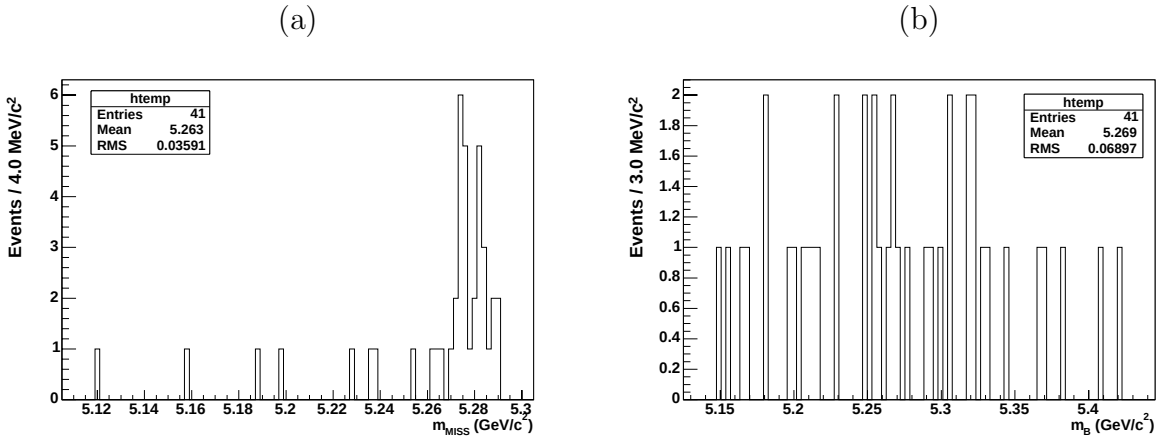

Figure 8.13: Distribution of (a) m_{miss} and (b) m_B for selected events in generic $B^0\overline{B}^0$ Monte Carlo sample.

Decay mode	fit region	signal region
$D^0\rho^+$	5	0
$f_0\pi^0\pi^+$	1	0
$\rho^0\pi^0\pi^+K^+K^-$	1	0
$a^0\rho^+$	1	0
$f_0\rho^+$	1	0
$D^+K_S^0$	1	0
$D^{*0}\rho^+$	1	0
`combinatorial`	7	0
Total	**18**	**0**

Table 8.6: Events selected in the whole B^+B^- generic Monte Carlo sample, for an equivalent luminosity of $\sim 1020 fb^{-1}$ (approximately five times the used data sample).

in the SR. So we will not include this component in the ML fit.

In Table 8.7 the reconstruction efficiencies of the most dangerous decay modes, evaluated with a large number of simulated events of these exclusive B^0 decays, are listed. We find that the efficiency for $K^*\pi^0$ is very small, the invariant mass cut rejecting 98% of the events and the particle identification about 11% of the events. On the contrary, ϕK_S^0 events are reconstructed missing a π^0 coming from K_S^0 decay, and this produces systematically small values of m_B: in the fit region only 18% of the events are selected.

Fig. 8.14 shows the distributions of m_{miss} and m_B for signal Monte Carlo and the different exclusive modes, while in Fig. 8.15 are the distribution of K^+K^- invariant mass and $\cos\theta_H$. Since the expected number of B background events, excluding the discussed

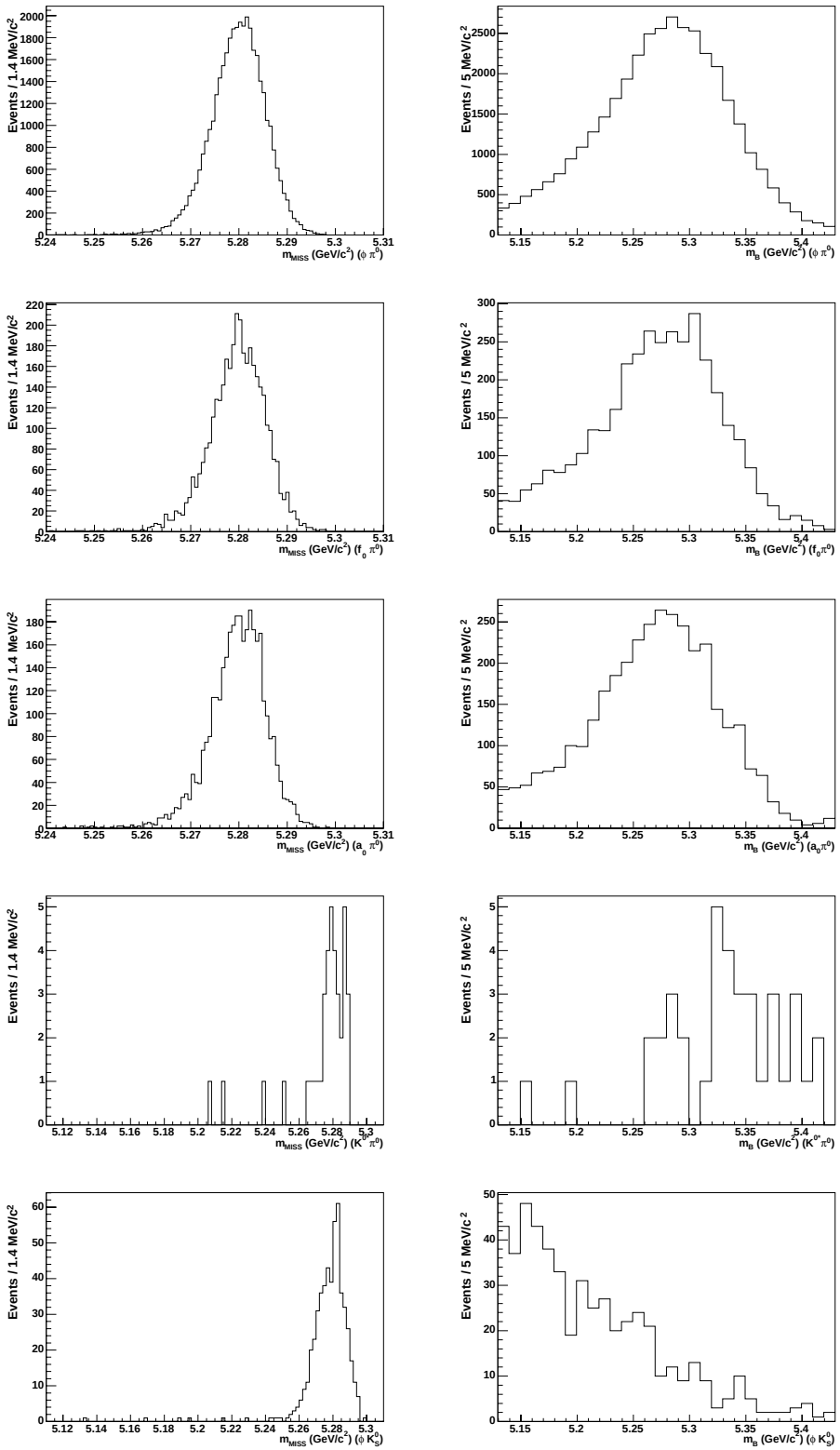

Figure 8.14: m_{miss} (left) and m_B (right) for $B^0 \to \phi\pi^0$ signal Monte Carlo and the main $B\bar{B}$ background modes. 1st row: signal $B^0 \to \phi\pi^0$. 2nd row: $B^0 \to f_0(980)\pi^0$. 3rd row: $B^0 \to a_0(980)\pi^0$. 4th row: $B^0 \to K^*(K^+\pi^-)\pi^0$. 5th row: $B^0 \to \phi K^0_S$.

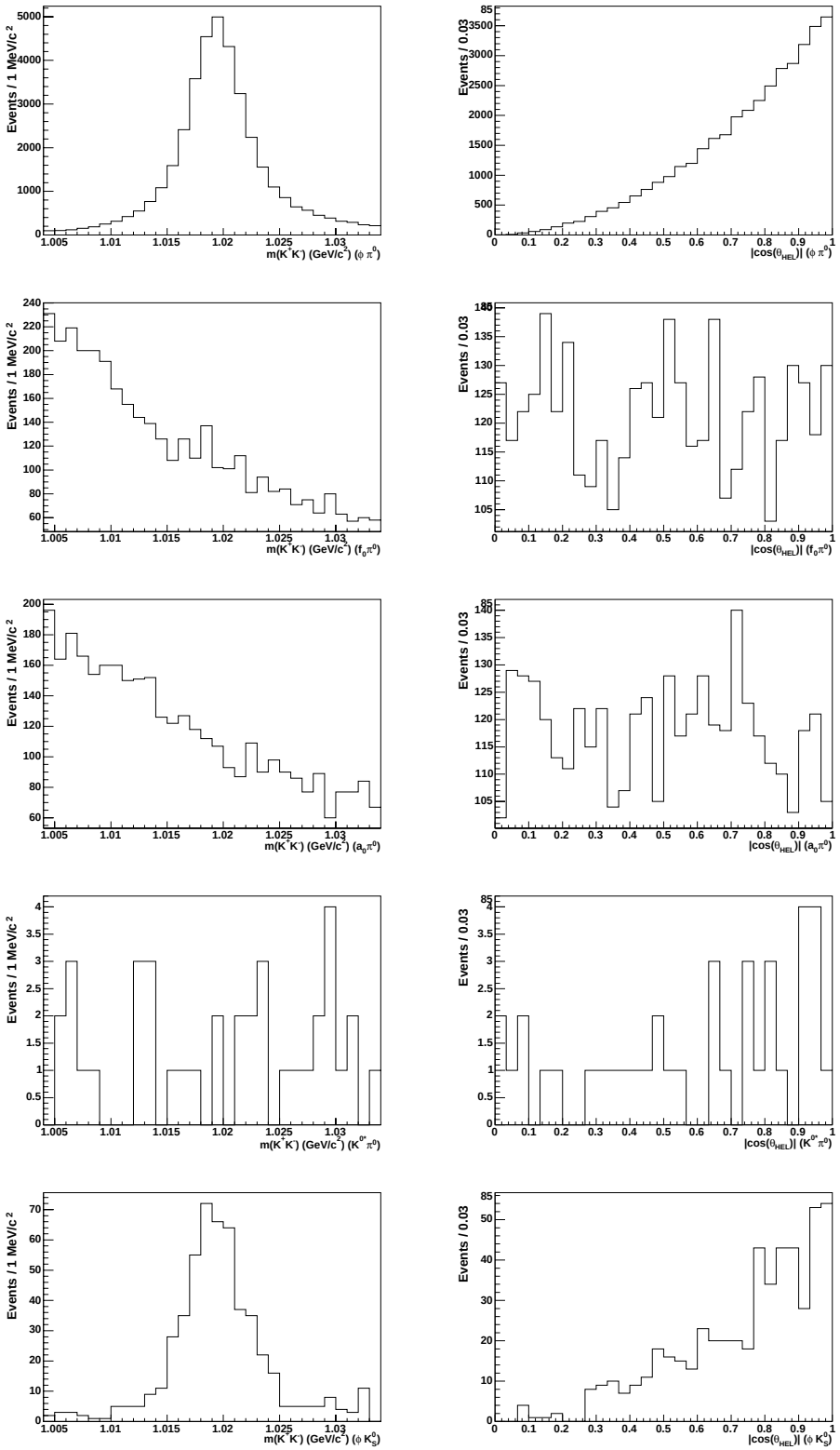

Figure 8.15: K^+K^- invariant mass (left) and $|\cos\theta_H|$ (right) for $B^0 \to \phi\pi^0$ signal Monte Carlo and the main $B\overline{B}$ background modes. 1st row: signal $B^0 \to \phi\pi^0$. 2nd row: $B^0 \to f_0(980)\pi^0$. 3rd row: $B^0 \to a_0(980)\pi^0$. 4th row: $B^0 \to K^*(K^+\pi^-)\pi^0$. 5th row: $B^0 \to \phi K^0_S$.

Decay mode	generated	efficiency
$f_0\pi^0$	49000	0.074 ± 0.001 (0.015 ± 0.001)
$a_0\pi^0$	46000	0.076 ± 0.001
$K^*(K^+\pi^-)\pi^0$	58000	0.0007 ± 0.0001
$\phi K^0_S(\pi^0\pi^0)$	165000	0.0032 ± 0.0001

Table 8.7: Exclusive B^0 decay modes contributing to B background for $B^0 \to \phi\pi^0$ mode, generated events and reconstruction efficiencies. The value in parenthesis is the efficiency when the BES lineshape is adopted for the $f_0 \to K^+K^-$ [79].

	m_{miss}	m_B	l_2	$\lvert\cos\theta_H\rvert$	$m_{K^+K^-}$
m_{miss}	1	0.61(-0.62)%	-0.64(3.96)%	-0.39(-1.78)%	0.25(-1.71)%
m_B	-	1	0.29(-0.78)%	-0.43(1.92)%	1.61(1.27)%
l_2	-	-	1	0.41(-1.17)%	-0.34(3.47)%
$\lvert\cos\theta_H\rvert$	-	-	-	1	1.49(-1.80)%

Table 8.8: Linear correlation coefficients between Likelihood variables as computed on the $B^0 \to \phi\pi^0$ Monte Carlo signal sample (data sideband with $m_{miss} < 5.26$ GeV/c^2).

S-wave component, is small, we neglect this component in the nominal fit.

8.3 The Maximum Likelihood Fit

We extract the signal yields for $B^0 \to \phi\pi^0$ and $B^+ \to \phi h^+$ with an unbinned maximum likelihood fit (Eq. 6.13). For both decay modes, the likelihood function has $N_{spec} = 3$, which are the signal, $q\overline{q}$ background and $B\overline{B}$ background, where for $B\overline{B}$ background we consider the S-wave K^+K^- contribution in the $\phi(1020)$ region (mainly $\mathsf{f_0}(980)$), as discussed in the previous section. We simultaneously extract the event yield of each component, but, in this *quasi-two-body* approach, we neglect interference effects.

8.3.1 Likelihood Function for $B^0 \to \phi\pi^0$

Since correlation between the likelihood variables are negligible both in signal and background events (Table 8.8), we can factorize the PDF in the product of the PDF's for each variable:

$$\mathcal{P} \equiv \mathcal{P}(m_{miss}) \cdot \mathcal{P}(m_B) \cdot \mathcal{P}(l_2) \cdot \mathcal{P}(|\cos\theta_H|) \cdot \mathcal{P}(m_{K^+K^-}) \tag{8.8}$$

We parameterize signal PDF's using unbinned maximum likelihood fit on a signal Monte Carlo sample. We use the Cruijff function (Eq. 6.15) to parameterize m_{miss} and m_B

(Fig. 8.16a,b). We use a second order polynomial for $|\cos\theta_H|$ and a relativistic Breit-Wigner as the $\phi(1020)$ lineshape (Fig. 8.17a,b). Since the distribution of l_2 interrupts at 0.55 because of the selection, we use a step function, i.e. a parametric histogram, to parameterize it. We use a not uniform binning of the step function, with an increased granularity where the most of discrimination between signal and continuum background is needed (Fig. 8.18).

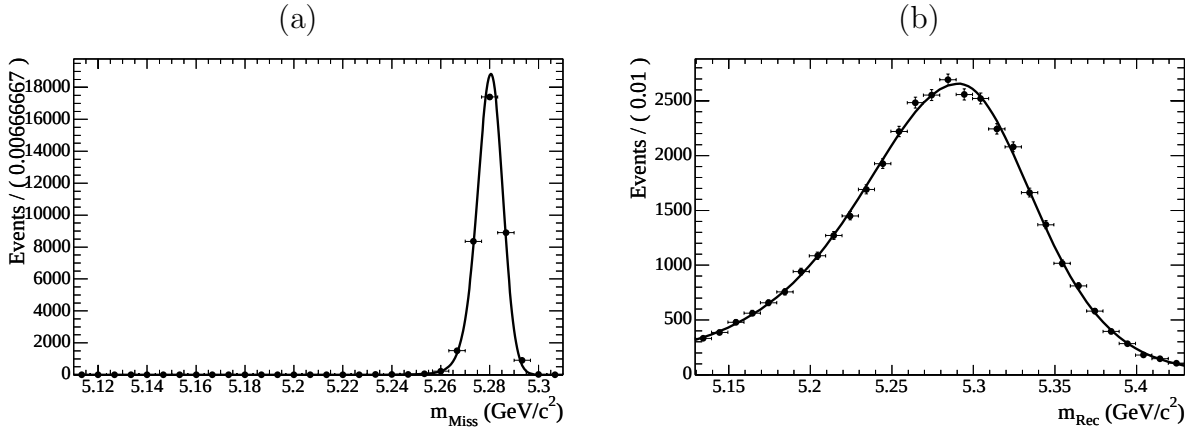

Figure 8.16: Signal PDF's used in the $B^0 \to \phi\pi^0$ likelihood for (a) m_{miss} and (b) m_B. Both parameterizations are obtained from a maximum likelihood fit to signal Monte Carlo sample with a Cruijff function.

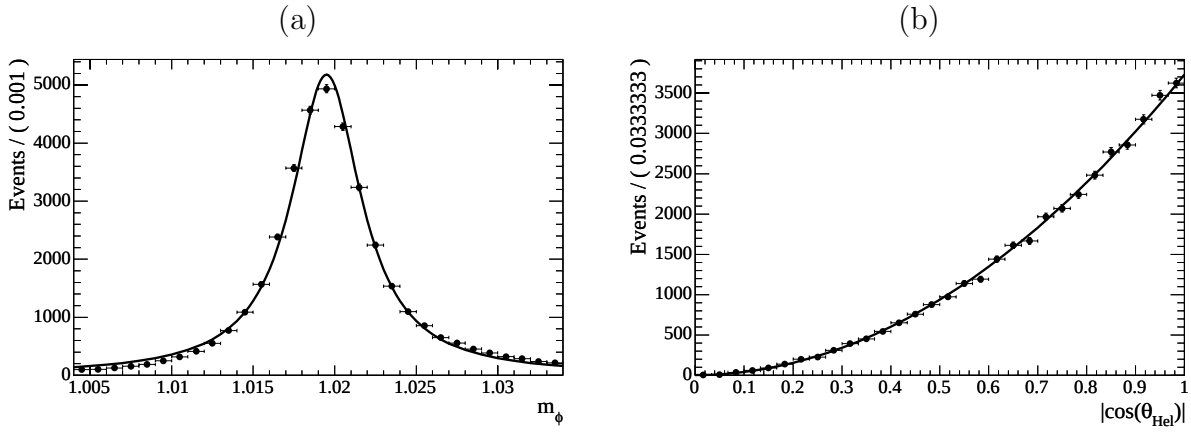

Figure 8.17: Signal PDF's used in the $B^0 \to \phi\pi^0$ likelihood for (a) $m_{K^+K^-}$ and (b) $|\cos\theta_H|$. Parameterizations are obtained from a maximum likelihood fit to signal Monte Carlo sample with a (a) relativistic Breit Wigner and (b) second order polynomial.

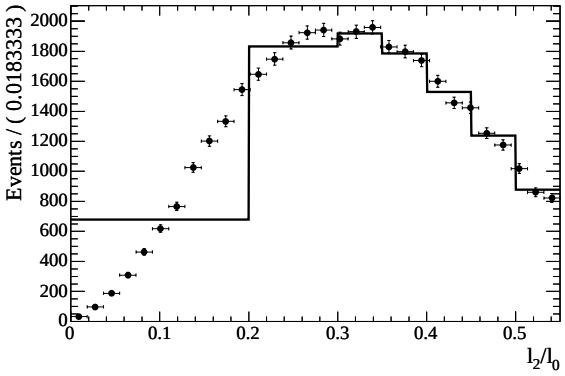

Figure 8.18: Signal PDF used in the $B^0 \to \phi\pi^0$ likelihood for l_2. The parameterization is obtained from a maximum likelihood fit to signal Monte Carlo sample with a parametric step function.

The m_{miss} continuum background is parameterized with an ARGUS function (Eq. 5.11), while a second order polynomial is used for m_B (Fig. 8.19a,b). The ϕ lineshape is parameterized with a relativistic Breit Wigner, because of the presence of true ϕ's in the continuum events, plus an exponential background (Fig. 8.20a), describing the non resonant two-tracks combinations. In the fit we fix the mean value and the width of the Breit Wigner to the values obtained from the fit on the signal Monte Carlo events, while we float the fraction and the parameter of the exponential distribution. The $|\cos\theta_H|$ distribution is parameterized with a second order polynomial (Fig. 8.20b), The l_2 distribution is parameterized with a step function with the same binning of the signal (Fig. 8.21).

As usual, we determine these parameters from a unbinned maximum likelihood fit to the $q\bar{q}$ Monte Carlo sample, to find the best shapes for the PDF's, but since we have sufficient continuum events in the final data sample, we fit their parameters directly on data.

The $B\overline{B}$ contributions (K^+K^- S-wave) can be distinguished from signal only by their Dalitz plot variables $m_{K^+K^-}$ and $\cos\theta_H$. We parameterize variables on the merged sample of exclusive $B^0 \to \mathsf{f_0(980)}\pi^0$ and $B^0 \to a_0(980)\pi^0$ decays. We use the same PDF's as for signal for m_{miss}, m_B and l_2. For $m_{K^+K^-}$ we use a Flatté function (Eq. 3.40) with parameters reported on Table 6.12. The PDF is displayed in Fig. 8.22a, where only the tail of the function over the $K\bar{K}$ threshold is shown. We parameterize the $|\cos\theta_H|$ with a second order polynomial.

We summarize the parameterization of the PDF's for $B^0 \to \phi\pi^0$ in Table 8.9.

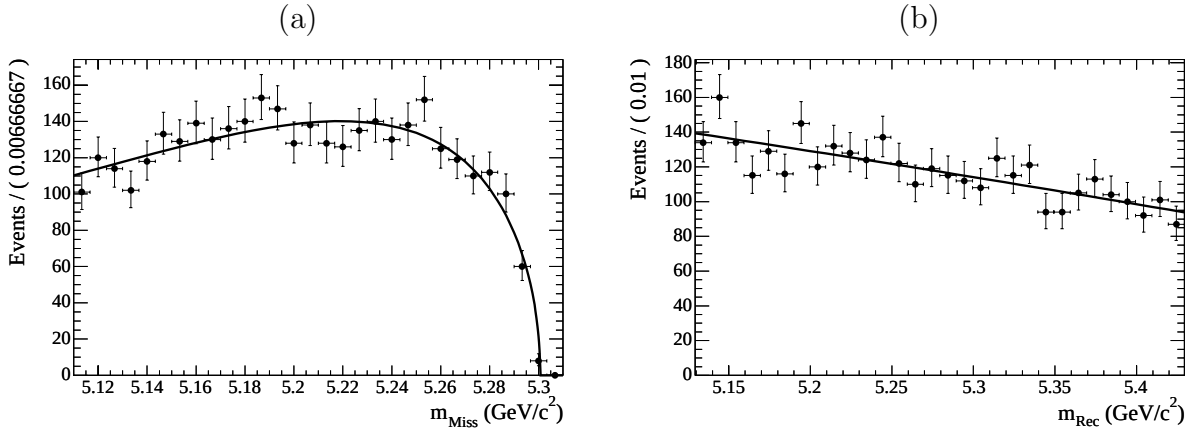

Figure 8.19: $q\overline{q}$ background PDF's used in the $B^0 \to \phi\pi^0$ likelihood for (a) m_{miss} and (b) m_B. Parameterizations are obtained from a maximum likelihood fit to the $q\overline{q}$ Monte Carlo with (a) ARGUS function and (b) 2-nd order polynomial.

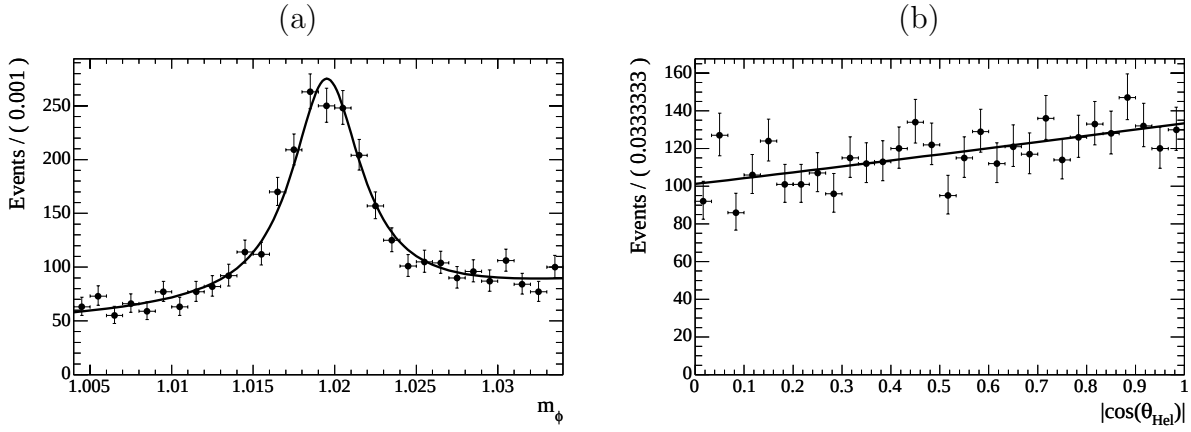

Figure 8.20: $q\overline{q}$ background PDF's used in the $B^0 \to \phi\pi^0$ likelihood for (a) $m_{K^+K^-}$ and (b) $|\cos\theta_H|$. Parameterizations are obtained from a maximum likelihood fit to $q\overline{q}$ Monte Carlo sample with a (a) relativistic Breit Wigner plus exponential and (b) second order polynomial.

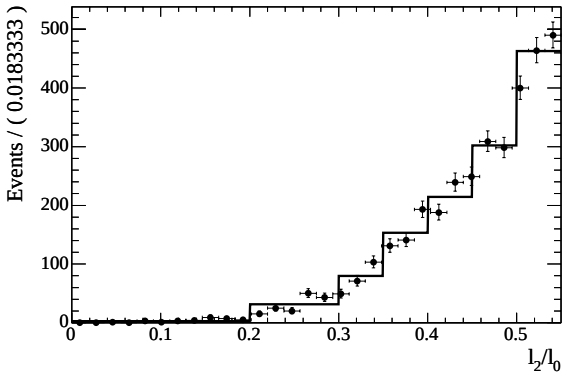

Figure 8.21: $q\overline{q}$ background PDF used in the $B^0 \to \phi\pi^0$ likelihood for l_2. The parameterization is obtained from a maximum likelihood fit to $q\overline{q}$ Monte Carlo sample with a parametric step function.

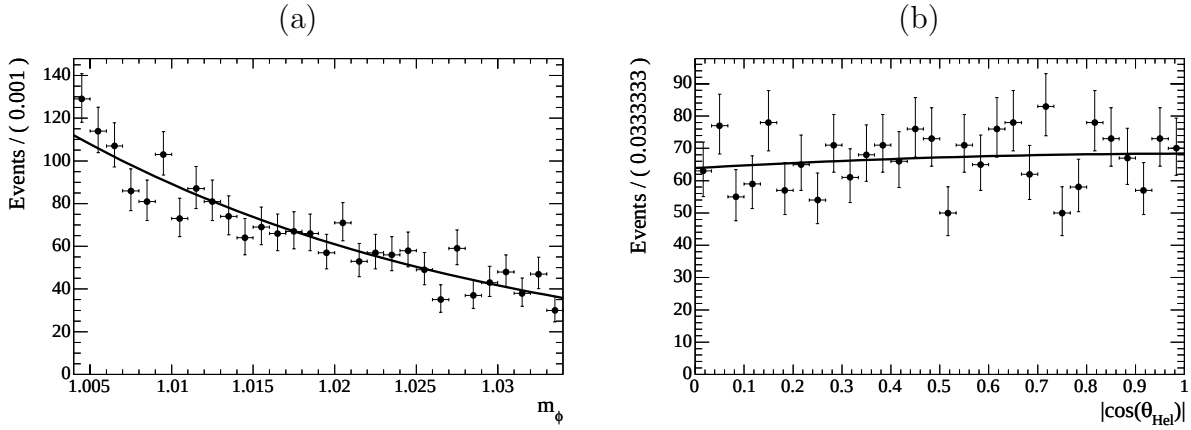

Figure 8.22: $B\overline{B}$ background PDF's used in the $B^0 \to \phi\pi^0$ likelihood for (a) $m_{K^+K^-}$ and (b) $|\cos\theta_H|$. Parameterizations are obtained from a maximum likelihood fit to $q\overline{q}$ Monte Carlo sample with a (a) Flatté function and (b) second order polynomial. For the final fit the parameters of the Flatté function are taken from BES data and not from Monte Carlo, as they are in this figure.

	Signal	$B\overline{B}$ bkg	$q\overline{q}$ bkg
m_{miss}	Cruijff	Cruijff	Argus
m_B	Cruijff	Cruijff	2-nd order polynomial
l_2	Step Function	Step Function	Step Function
$\lvert\cos\theta_H\rvert$	2-nd order polynomial	2-nd order polynomial	2-nd order polynomial
$m_{K^+K^-}$	rel. BW	Flatté	rel. BW + exponential

Table 8.9: Summary of PDF shapes used in the maximum Likelihood parameterization for $B^0 \to \phi\pi^0$. rel. BW stands for relativistic Breit Wigner function.

8.3.2 Likelihood Function for $B^+ \to \phi h^+$

The likelihood function for $B^+ \to \phi h^+$ decays is very similar to the one for $B^0 \to \phi\pi^0$. The main difference is that all the PDF's are duplicated for the two mass hypotheses $h = \pi, K$. Then $N_{spec} = 6$. We also add the PDF's for θ_c to discriminate the track mass hypotheses.

Also for this mode we find negligible correlation between likelihood variables (Table 8.10), so we can factorize the likelihood in the product of the different PDF's:

$$\mathcal{P} \equiv \mathcal{P}(m_{miss}) \cdot \mathcal{P}(m_B) \cdot \mathcal{P}(l_2) \cdot \mathcal{P}(|\cos\theta_H|) \cdot \mathcal{P}(m_{K^+K^-}) \cdot \mathcal{P}(\theta_c\text{pull}) \tag{8.9}$$

	m_{miss}	m_B	l_2	$\lvert\cos\theta_H\rvert$	$m_{K^+K^-}$	θ_c pull
m_{miss}	1	1.42(0.80)%	0.52(1.97)%	0.15(-1.35)%	-0.17(-0.93)%	0.34(-0.12)%
m_B	-	1	0.10(-0.37)%	1.46(0.56)%	3.19(1.56)%	0.45(0.53)%
l_2	-	-	1	0.24(-1.48)%	0.15(0.84)%	1.02(-0.78)%
$\lvert\cos\theta_H\rvert$	-	-	-	1	-0.42(-1.26)%	1.21(-0.98)%
$m_{K^+K^-}$	-	-	-	-	1	-0.12 (-0.56)%

Table 8.10: Correlation coefficients between Likelihood variables as computed on the $B \to \phi\pi$ Monte Carlo signal sample (on-resonance sideband data with $m_{miss} < 5.26$ GeV/c^2).

We parameterize the PDF's with the same functions used in the case of the neutral decay. They are the forced to be the same for $B^+ \to \phi\pi^+$ and $B^+ \to \phi K^+$, except for the θ_c pulls and m_B.

For θ_c pulls we use the double Gaussians PDF's evaluated on data control samples shown in Fig. 8.9. For m_B we use a Cruijff function parameterized on signal Monte Carlo events of $B^+ \to \phi\pi^+$. The equivalent PDF for the K mass hypothesis is evaluated from this one by means of the event-by-event shift of Eq. 8.5, which depends by the momentum

of the track. Resulting parameterizations are shown in Fig. 8.23. The same method is used for $B\overline{B}$ background m_B (between $f_0(980)\pi^+$ and $f_0(980)K^+$).

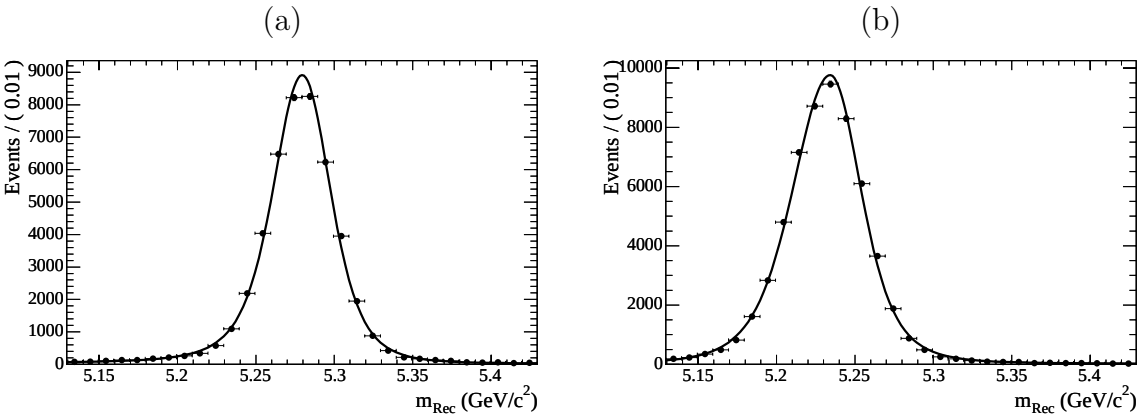

Figure 8.23: Signal PDF's used for m_B parameterization of (a) $B^+ \to \phi\pi^+$ and (b) $B^+ \to \phi K^+$ events. The parameterization is obtained with a Cruijff function for $B^+ \to \phi\pi^+$ and the one for $B^+ \to \phi K^+$ is obtained with a momentum scaling of the one for the π mass hypothesis.

We summarize the parameterization of the PDF's entering the likelihood function in Table 8.11.

	Signal	$B\overline{B}$ bkg	$q\overline{q}$ bkg
m_{miss}	Gaussian	Gaussian	Argus
m_B	Cruijff	Cruijff	2-nd order polynomial
l_2	Step Function	Step Function	Step Function
$\lvert\cos\theta_H\rvert$	2-nd order polynomial	2-nd order polynomial	2-nd order polynomial
$m_{K^+K^-}$	rel. BW	Flatté	rel. BW + exponential
θ_c pulls	mom. dep. Gaussians	mom. dep. Gaussians	mom. dep. Gaussians

Table 8.11: Summary of PDF shapes used in the likelihood parameterization for $B^+ \to \phi h^+$. rel BW stands for relativistic Breit Wigner function.

8.3.3 Data - Monte Carlo Comparison for $B^+ \to \phi h^+$

While for $B^0 \to \phi\pi^0$ accurate studies on neutral particles using data control samples in *BABAR* provide corrections to apply to simulated events to achieve the best data/Monte Carlo agreement, for $B^+ \to \phi h^+$ decays with three tracks in the final state we need a specific control sample. In order to do this we reconstruct $B^+ \to J/\psi K^+$ events both on

m_{miss}	$J/\psi K^+$ data	$J/\psi K^+$ Monte Carlo	$\phi\pi^+$ Monte Carlo	ϕK^+ data
m	5.28030 ± 0.00006	5.27870 ± 0.00005	5.27930 ± 0.00008	5.28010 ± 0.00037
σ	0.00523 ± 0.00008	0.00530 ± 0.00004	0.00529 ± 0.00006	0.00583 ± 0.00029

Table 8.12: Comparison of m_{miss} parameterizations from signal Monte Carlo samples and data. Signal parameterization is obtained with a Gaussian.

Monte Carlo and data. This sample provides a large statistics sample with high purity with can be used to validate the kinematic variables m_{miss} and m_B.

We parameterize the distributions assuming the same functional forms as for $B^+ \to \phi h^+$ signal. We determine the associated parameters through a maximum likelihood fit. In the case of data, we also add a background component to be fitted simultaneously to signal events. In this case, we assume an ARGUS shape for m_{miss} and a second order polynomial for m_B.

The m_{miss} distributions on $B^+ \to J/\psi\, K^+$ signal Monte Carlo and data are shown in Fig. 8.24. The distributions differ for a larger value of the width on Monte Carlo and a small shift in the mean. This is summarized in Table 8.12.

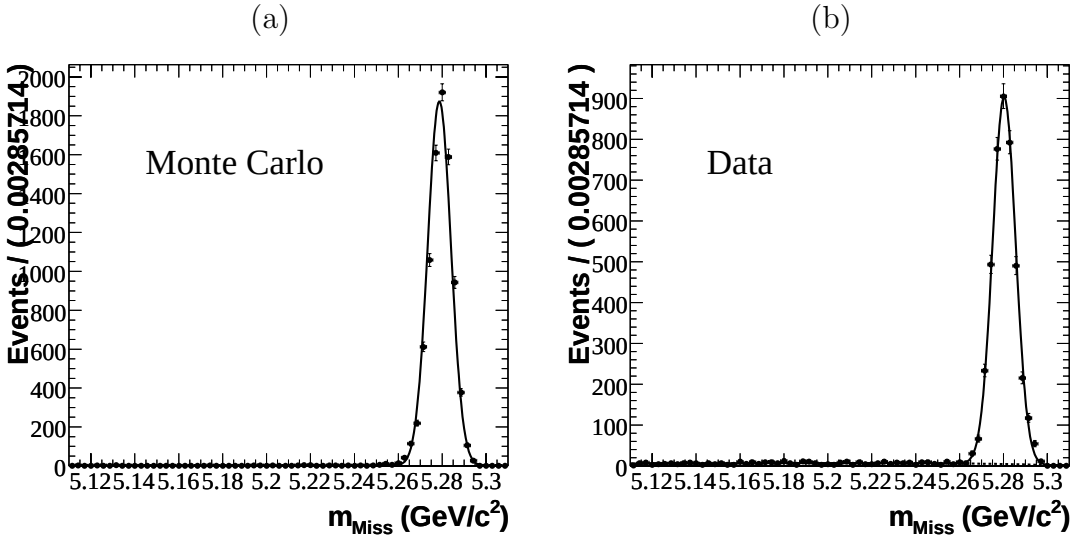

Figure 8.24: Distribution of m_{miss}, as obtained from a sample of (a) signal $B^+ \to J/\psi K^+$ Monte Carlo or (b) on-resonance data. The superimposed curve is obtained fitting the sample with (a) a single Gaussian or (b) a single Gaussian plus ARGUS function which parameterizes the background.

Also for m_B we find a good agreement between data and Monte Carlo (Fig. 8.26).

In order to have a qualitative estimation of the agreement between data and Monte Carlo (in $J/\psi K^+$ events) we compare the Monte Carlo events with data after a background subtraction is applied (Fig. 8.25). From the distribution is evident the very good agreement on m_{miss} and m_B distribution.

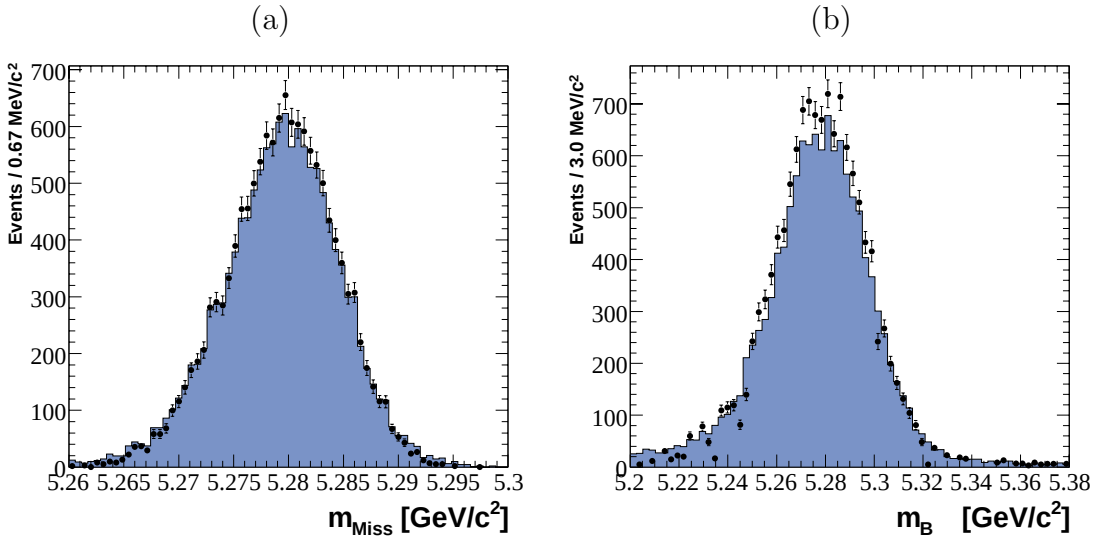

Figure 8.25: Distribution for (a) m_{miss} and (b) m_B for $B^+ \to J/\psi K^+$ Monte Carlo events (histogram) and reconstructed events on RunI-IV data after a background subtraction (dots). The distribution are normalized to the same area.

The conclusion of this study is that the Monte Carlo reproduces quite well the shape of the kinematic variables, even if a small correction is needed to achieve the best agreement with data. In the case of our signal, since we expect more than 300 signal $B^+ \to \phi K^+$ events, we can fit the m_{miss} and m_B signal parameters directly on data (m_{miss} PDF's for K and π hypotheses are the same, and m_B PDF's are correlated between them by the event-by-event shift of Eq. 8.5). This strategy avoids to add a undesirable systematic uncertainty due to m_{miss} and m_B parameterization, and it is also better than taking the shape from $B^+ \to J/\psi(\mu^+\mu^-)K^+$ events. In fact radiative emission by leptons produces a small tail in m_B shape which is not present in $B^+ \to K^+K^-h^+$ events (see Table 8.13).

8.4 Validation Studies

We validate the fit procedure with a number of pure toy Monte Carlo and with embedded toys. We report here only the results of embedded toys, because they give the additional

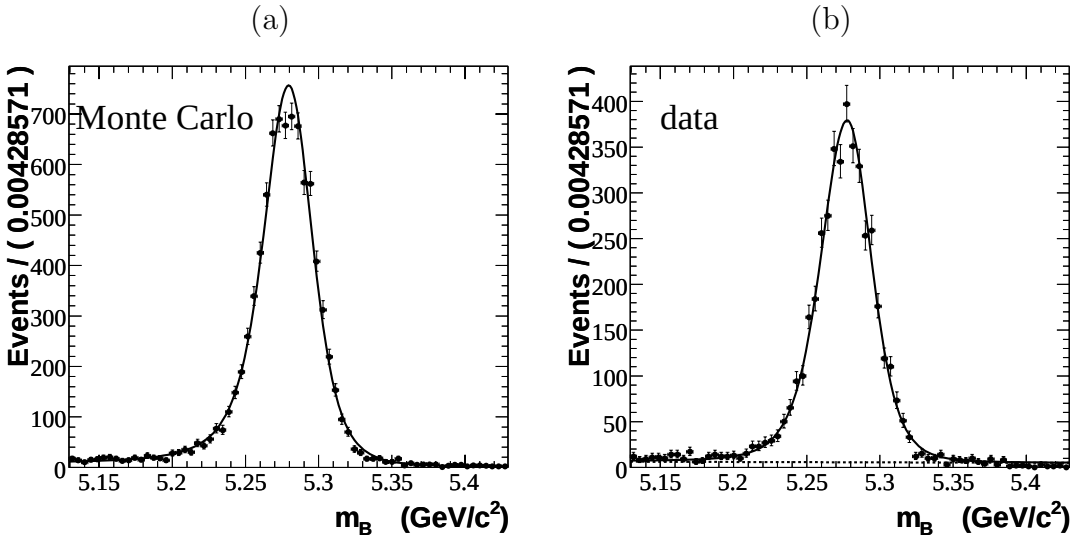

Figure 8.26: Distribution of m_B, as obtained from (a) a sample of signal $B^+ \to J/\psi K^+$ Monte Carlo or (b) data. The superimposed curve is obtained fitting the sample with (a) a single Gaussian or (b) a single Gaussian plus a second order polynomial parameterizing the background.

m_{miss}	$J/\psi K^+$ data	$J/\psi K^+$ Monte Carlo	$\phi\pi^+$ Monte Carlo	ϕK^+ data
m	5.2776 ± 0.0009	5.2795 ± 0.0006	5.2818 ± 0.0008	5.2253 ± 0.0038
σ_L	0.0171 ± 0.0007	0.0163 ± 0.0005	0.0222 ± 0.0006	0.0181 ± 0.0040
σ_R	0.0158 ± 0.0007	0.0146 ± 0.0005	0.0162 ± 0.0006	0.0259 ± 0.0040
α_L	0.1472 ± 0.0086	0.1149 ± 0.0049	0.0999 ± 0.0061	0.1752 ± 0.0813
α_R	0.1202 ± 0.0096	0.1423 ± 0.0051	0.1381 ± 0.0072	0.1182 ± 0.0486

Table 8.13: Comparison of m_B parameterizations from signal Monte Carlo samples and data. Signal parameterization is obtained with a Cruijff function (Eq. 6.15).

information on the effect of the neglected correlations in the fit. Since only upper limits exist on the branching fraction of $B \to \phi\pi$, we use in generation a small number of events for the nominal toys ($N = 5$), and we also perform a scan in the range $N \in [0 \div 10]$. For $B \to \phi K$, whose branching fraction is well established, we use the actual world average [22].

8.4.1 Validation Studies for $B^0 \to \phi\pi^0$

We perform toy Monte Carlo experiments embedding $N_{sig} = 5$ events from selected Monte Carlo events and $N_{B\overline{B}} = 3$, and generating according PDF's $N_{q\overline{q}} = 2700$ continuum events. We show the pulls on the three fitted yields and the expected uncertainties on them in Fig. 8.27.

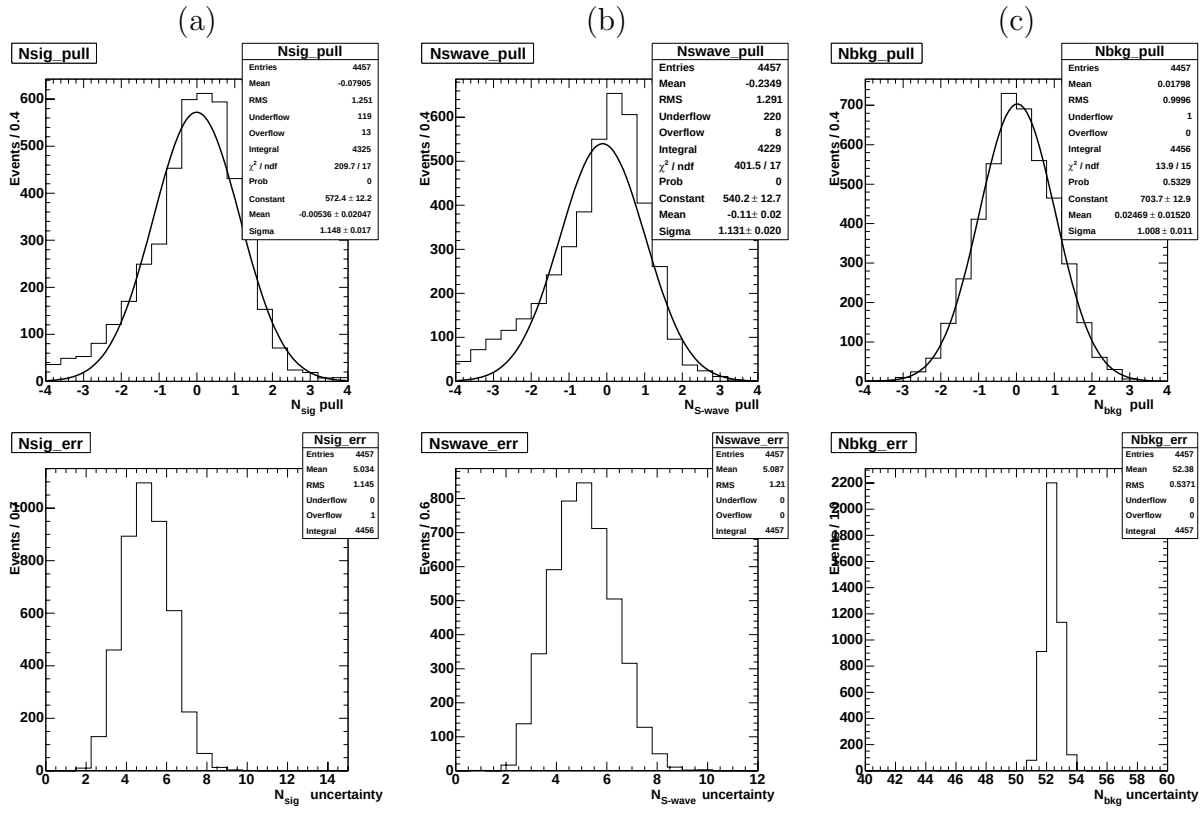

Figure 8.27: Embedded toy Monte Carlo experiments results for $B^0 \to \phi\pi^0$. Pulls (top) and uncertainties on yields (bottom) for (a) signal, (b) $B\overline{B}$ background and (c) $q\overline{q}$ background.

The pulls for signal and $B\overline{B}$ background do not follow Gaussian distributions with mean zero and unitary standard deviation. This behaviour cannot be attributed to an

effective bias in the fit procedure, but to the fact that we are generating 5 and 3 events for signal and $B\overline{B}$ components, respectively. Then these components follow a Poisson distribution, producing the long tail in the pull, with a consequent shift of the mean to lower values. The $q\overline{q}$ background, for which thousand of events are generated, shows a distribution of the pull which is perfectly compatible with a Gaussian regime.

In order to study in detail this effect we perform a toy Monte Carlo scan of the signal and $B\overline{B}$ yields. We then generate experiments varying the number of generated events in the range $N \in [0 \div 10]$. In Fig. 8.28 we show the distribution of the fitted yield vs. the generated value, X^{fit} vs. X^{true}, where $X = N_{sig},\ N_{B\overline{B}}$. For both components, the size of the bias depends on the true value of the yield and tends to be negligible as the number of generated events increase. When the true yield is $\gtrsim 6$, the Gaussian assumption begins to be valid, the maximum of the likelihood becoming a good estimator of the true value.

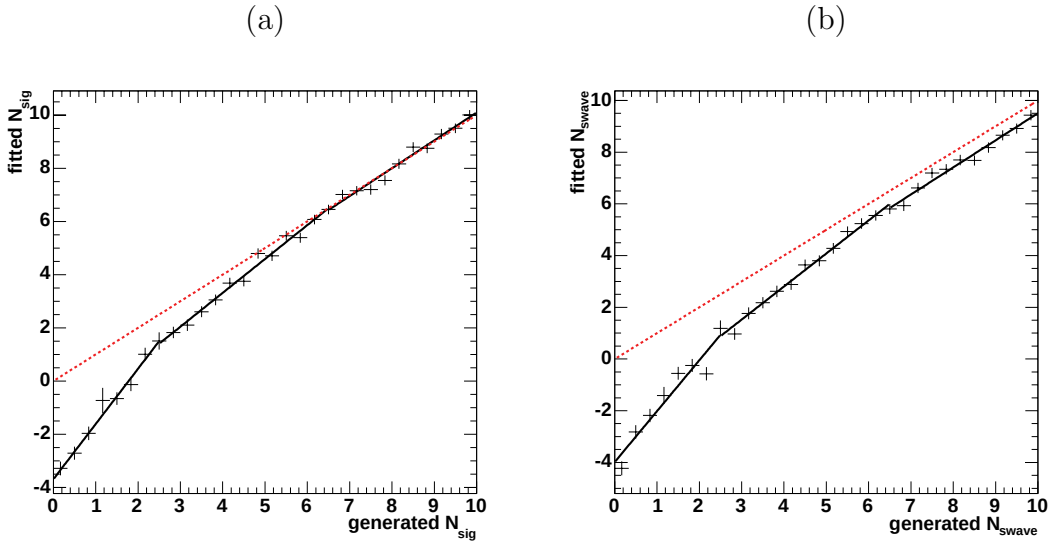

Figure 8.28: Distribution of fitted (maximum of the likelihood) vs. generated values for (a) N_{sig} and (b) $N_{B\overline{B}}$ when $\sim 50\ 10^3$ toy experiments for $B^0 \to \phi\pi^0$ are generated with N_{sig} and $N_{B\overline{B}}$ uniformly distributed in the range $[0 \div 10]$. The red line represents the relation $X^{fit} = X^{true}$, where $X = N_{sig},\ N_{B\overline{B}}$. The black lines represent three linear fits to the distribution in three different sub-ranges.

We then have to define a procedure to interpret the results if a signal yield in the problematic range $[0 \div 6]$ is returned by the fit:

- **setting an Upper Limit:** to set an eventual upper limit we decide to use a Bayesian approach where the likelihood function is integrated defining a 90% prob-

ability interval. In this case, the maximum of the likelihood is not used then the "fit bias" is not a problem;

- **quoting a Central Value:** in this case, the maximum of the likelihood is not an unbiased estimator of the true value of the yield. We find that the median of the likelihood, defined as the value lying at the midpoint of the likelihood function, such that there is an equal probability of falling above or below it, is a less biased estimator of the true yield. This is shown in Fig. 8.29. Even if the median of the

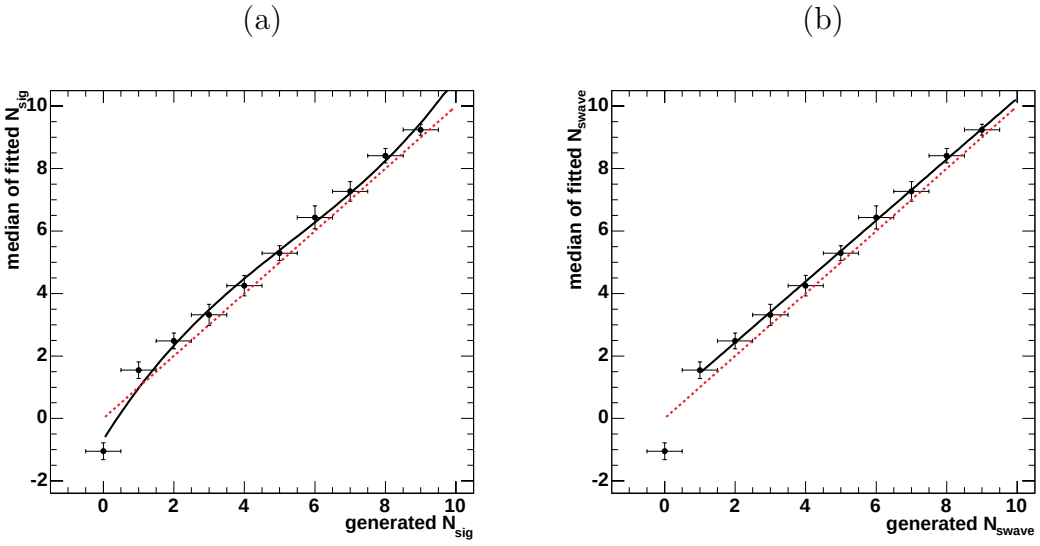

Figure 8.29: Distribution of fitted (median of the likelihood) vs. generated values for (a) N_{sig} and (b) $N_{B\overline{B}}$ when $\sim 10\ 10^3$ toy experiments for $B^0 \to \phi\pi^0$ are generated with N_{sig} and $N_{B\overline{B}}$ uniformly distributed in the range $[0 \div 10]$. The red line represents the relation $X^{fit} = X^{true}$, where $X = N_{sig},\ N_{B\overline{B}}$. The black line represents a fit with a third order polynomial to the distribution.

likelihood is a less biased estimator, still some deviation from the true value can be seen. We parameterize the distribution in Fig. 8.29 with a third order polynomial f_3 which we can use as correction function $X^{true} = f_3(X^{fit})$ once we have the unblinded value X^{fit}.

8.4.2 Validation Studies for $B^+ \to \phi h^+$

We validate the fit to $B^+ \to \phi h^+$ with embedded toy Monte Carlo experiments. We use as generation yields $N_{\phi\pi} = 5$, $N_{\phi K^+} = 350$, $N_{B\overline{B}(\pi^+)} = 3$ and $N_{B\overline{B}(K^+)} = 46$. We generate separately $q\overline{q}$ backgrounds for $\phi\pi^+$ and ϕK^+ species, estimating the relative fractions

from a fit to sideband data. According to these fractions we use $N_{q\overline{q}(\pi^+)} = 6500$ and $N_{q\overline{q}(K^+)} = 4500$.

We generate according to the PDF's the $q\overline{q}$ events, while we embed both signal and $B\overline{B}$ events from full Monte Carlo samples. Together with accounting for correlation among the different likelihood variables, the full Monte Carlo is particularly necessary for this fit involving θ_c because it fully reproduces two important features of the data:

1. the track momentum/polar angle dependence induced by the boost, because it is essential to model the DIRC resolution sensitivity to $\cos\theta$;

2. the correlations between the h^+ track and the recoiling ϕ in the decay, because the separation between kaon and pion depends on the track momentum.

The pulls for the fitted yields of signal and $B\overline{B}$ background are shown in Fig. 8.30, while the pulls for the $q\overline{q}$ background are shown in Fig. 8.31.

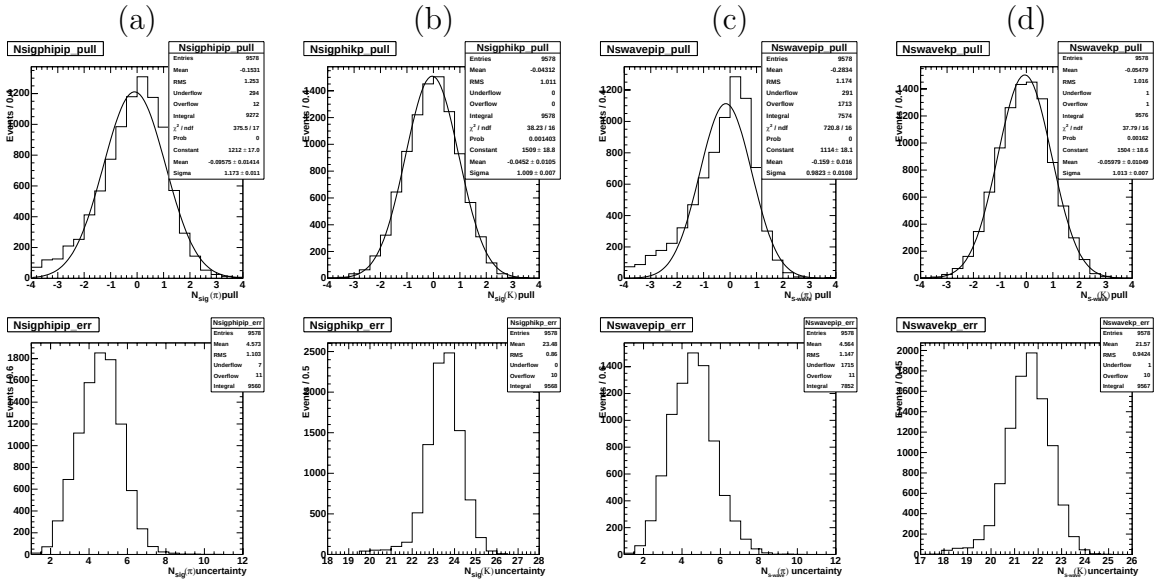

Figure 8.30: Embedded toy Monte Carlo experiments results for $B^+ \to \phi h^+$. Pulls (top) and uncertainties on yields (bottom) for (a) signal $B^+ \to \phi\pi^+$, (b) signal $B^+ \to \phi K^+$, (c) $B^+ \to \phi\pi^+$ $B\overline{B}$ background (d) $B^+ \to \phi K^+$ $B\overline{B}$ background.

The same features due to the limited statistics in generation are visible on the signal and $B\overline{B}$ background for $B^+ \to \phi\pi^+$ component. The yields of signal and $B\overline{B}$ background for $B^+ \to \phi K^+$ show no presence of bias, like for the $q\overline{q}$ background yields.

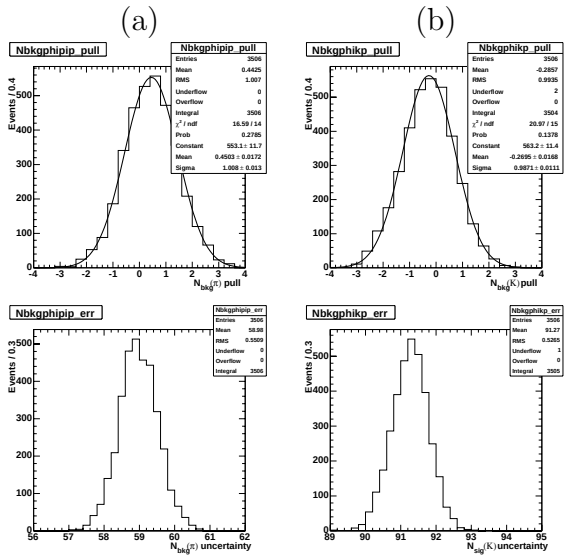

Figure 8.31: Embedded toy Monte Carlo experiments results for $B^+ \to \phi h^+$. Pulls (top) and uncertainties on yields (bottom) for (a) $q\overline{q}$ background for $B^+ \to \phi\pi^+$, (b) $q\overline{q}$ background for $B^+ \to \phi K^+$

We repeat the scan of the yields in the range $[0 \div 10]$ in order to study the "fit bias" as a function of the generated number of events. We obtain the curve of the median of the likelihood versus the generated number of the events which we will use to correct the central value of the branching fraction. The curves are reported in Fig. 8.32.

8.5 Fit Results and Branching Fraction Measurement

The selection retains a sample of 2732 $\phi\pi^0$ candidates and 10990 ϕh^+ candidates. Applying the maximum likelihood fit to these two samples we do not observe evidence of these decays. Table 8.14 reports the results for the $B^0 \to \phi\pi^0$ yields, while in Table 8.15 we report the results for the $B^+ \to \phi h^+$ yields. The reported yields correspond to the maximum of the likelihood.

In Fig. 8.33 we show the distributions of the likelihood variables for $B^0 \to \phi\pi^0$ candidates, with the result of the fit superimposed, after a requirement on the signal-to-background likelihood ratio has been applied to enhance the signal.

In Fig. 8.34 we show similarly likelihood-enhanced plots for the $B^+ \to \phi h^+$ candidates. The requirement on the likelihood ratio considers both $B^+ \to \phi\pi^+$ and $B^+ \to \phi K^+$ as signal: $(L_{\phi\pi^+} + L_{\phi K^+})/(L_{tot})$, where L_{tot} is the sum of the likelihoods for all the

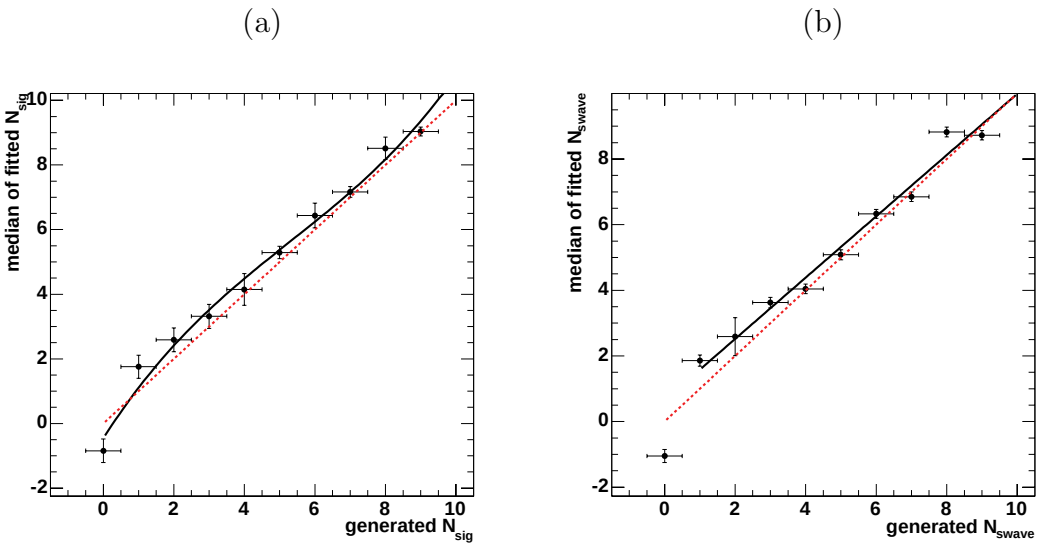

Figure 8.32: Distribution of fitted (median of the likelihood) vs. generated values for (a) N_{sig} and (b) $N_{B\overline{B}}$ when $\sim 10\ 10^3$ toy experiments for $B^+ \to \phi\pi^+$ are generated with N_{sig} and $N_{B\overline{B}}$ uniformly distributed in the range $[0 \div 10]$. The red line represents the relation $X^{fit} = X^{true}$, where $X = N_{sig},\ N_{B\overline{B}}$. The black line represents a fit with a third order polynomial to the distribution.

Yield	Fitted Value	Glb. Correlation
N_S	$3.47^{+3.97}_{-2.56}$	0.21
$N_{B\overline{B}}$	$-1.32^{+4.23}_{-2.96}$	0.52
$N_{q\overline{q}}$	2732^{+53}_{-52}	0.15

Table 8.14: Fitted yields on the on-resonance data sample (232 M of $B\overline{B}$ pairs) for signal (N_S), $B\overline{B}$ background ($N_{B\overline{B}}$) and continuum background ($N_{q\overline{q}}$). These numbers correspond to the maximum of the likelihood.

components. For clearness, we display also the plots where we enhance only the $B^+ \to \phi\pi^+$ component in Fig. 8.35, for the m_{miss} and m_B variables.

The fitted yield for $B^+ \to \phi K^+$ is consistent with the measured branching fraction measured with the Dalitz plot analysis of $B^+ \to K^+K^-K^+$ [76], performed on the same dataset (the number of expected events is 346 using the world average branching ratio). Also, the number of event fitted for the $B\overline{B}$ background, which with good approximation is made only by $\mathsf{f_0(980)K^+}$, is consistent with the *P-wave/S-wave* ratio, in the narrow K^+K^- mass region considered in this analysis, of our measurement in $B^0 \to K^+K^-K^0$ Dalitz plot (see Table 6.20).

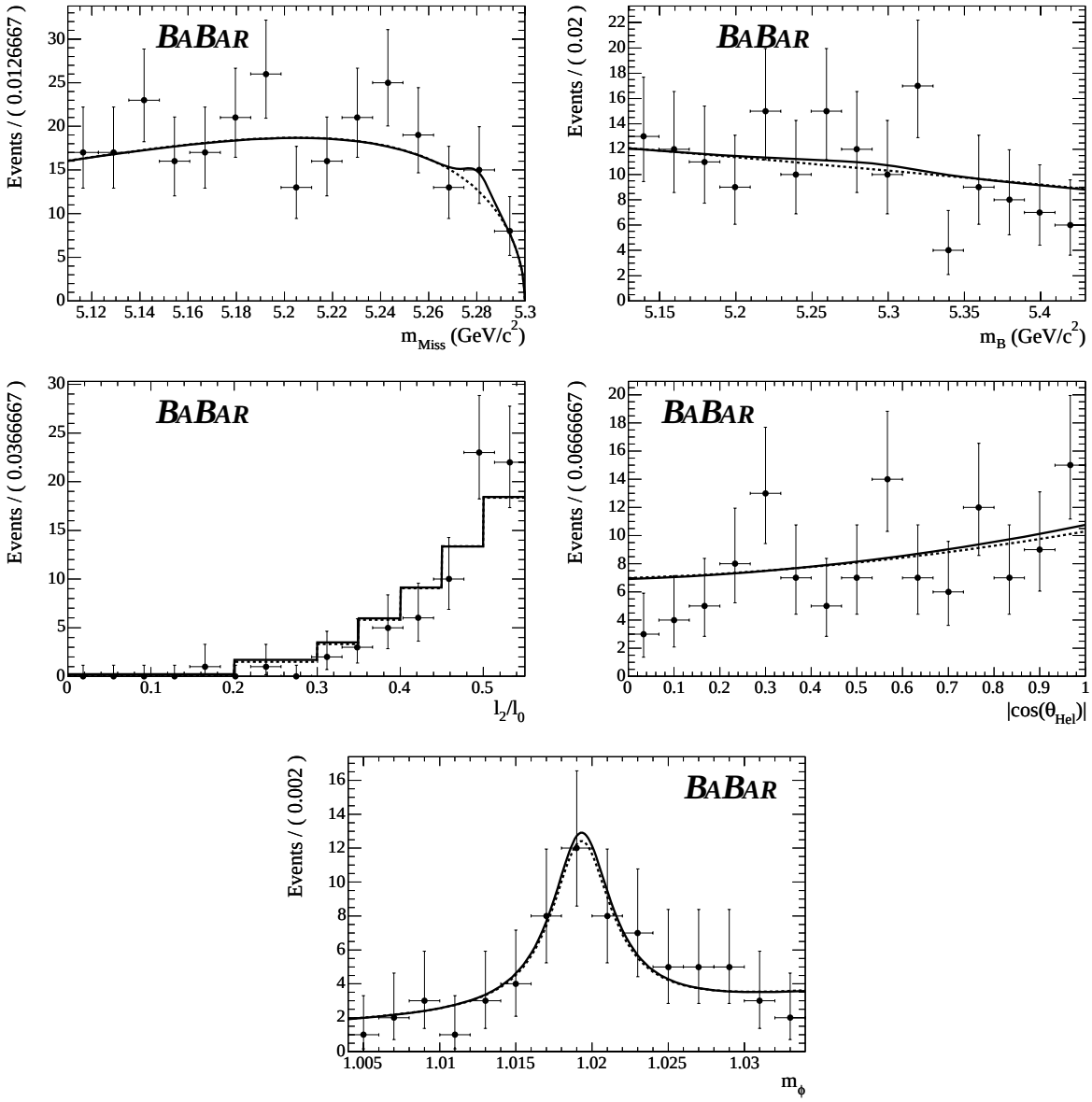

Figure 8.33: Distribution of m_{miss} (top left), m_B (top right) l_2 (middle left), $|\cos\theta_H|$ (middle right), $m_{K^+K^-}$ (bottom) for $B^0 \to \phi\pi^0$ candidates on on-resonance data, together with the result of the maximum likelihood fit after applying a requirement on the ratio of signal likelihood to signal-plus-background likelihood (computed without the displayed variable). The curves are projections from the likelihood fit for total yield (continuum line) and for the continuum background (dashed line). The efficiencies on signal (continuum background) [s-wave background] of the likelihood-ratio cut are: 66% (9%) [17%] for m_{miss}, 91% (6%) [38%] for m_B, 70% (3%) [16%] for l_2, 81% (5%) [36%] for $|\cos\theta_H|$, 76% (3%) [40%] for $m_{K^+K^-}$. We didn't display the $B\overline{B}$ component for clearness of the plot.

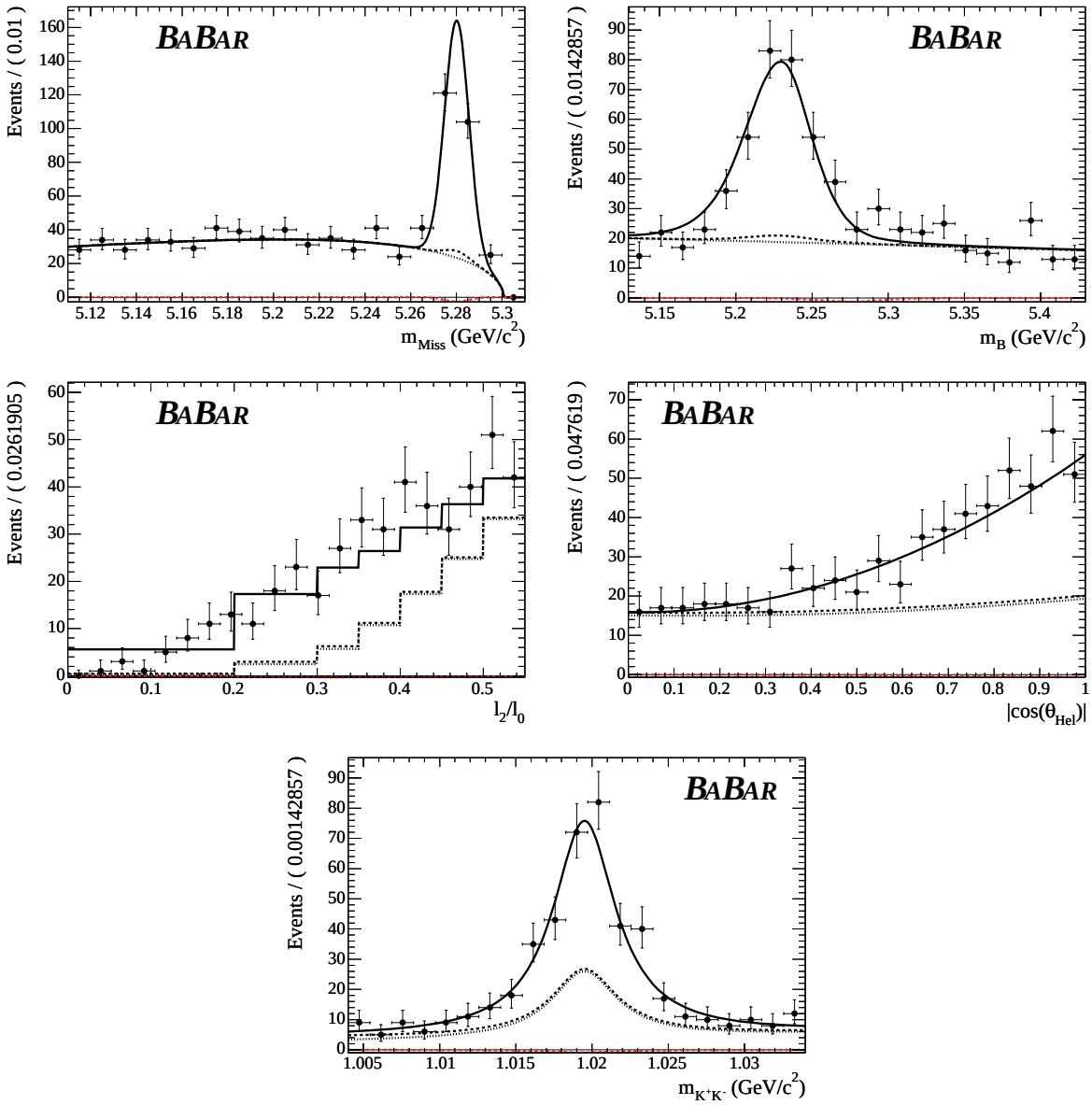

Figure 8.34: Distribution of m_{miss} (top left), m_B (top right) l_2 (middle left), $|\cos\theta_H|$ (middle right), $m_{K^+K^-}$ (bottom) for $B^+ \to \phi h^+$ candidates on on-resonance data, together with the result of the maximum likelihood fit after applying a requirement on the ratio of signal (ϕh^+) likelihood to signal(ϕh^+)-plus-background likelihood (computed without the displayed variable). The curves are projections from the likelihood fit for total yield (continuum line), for the continuum background (fine dashed line) and for continuum plus $B\overline{B}$ component (dashed line). The red dashed line represents the $\phi\pi^+$ component. The efficiencies on signal (continuum background) [s-wave background] of the likelihood-ratio cut are (each one is the sum of $\phi\pi^+$ and ϕK^+): 63% (5%) [13%] for m_{miss}, 79% (4%) [22%] for m_B, 72% (2%) [16%] for l_2, 83% (3%) [36%] for $|\cos\theta_H|$, 78% (2%) [41%] for $m_{K^+K^-}$.

Yield	Fitted Value	Glb. Correlation
$N_S(\phi\pi^+)$	$-2.88^{+6.01}_{-4.56}$	0.37
$N_{B\overline{B}}(\pi^+)$	$2.77^{+7.13}_{-5.65}$	0.36
$N_{q\overline{q}}(\pi^+)$	6254^{+82}_{-81}	0.11
$N_S(\phi K^+)$	$312.2^{+23.0}_{-22.3}$	0.37
$N_{B\overline{B}}(K^+)$	$41.7^{+14.7}_{-13.4}$	0.36
$N_{q\overline{q}}(K^+)$	4386 ± 70	0.11

Table 8.15: Fitted yields on the on-resonance data sample (232 M $B\overline{B}$ pairs) for signal ($N_S(\phi\pi^+, K^+)$), $B\overline{B}$ background ($N_{S-wave}\pi^+, K^+$) and continuum background ($N_{q\overline{q}}\pi^+, K^+$). These numbers correspond to the maximum of the likelihood.

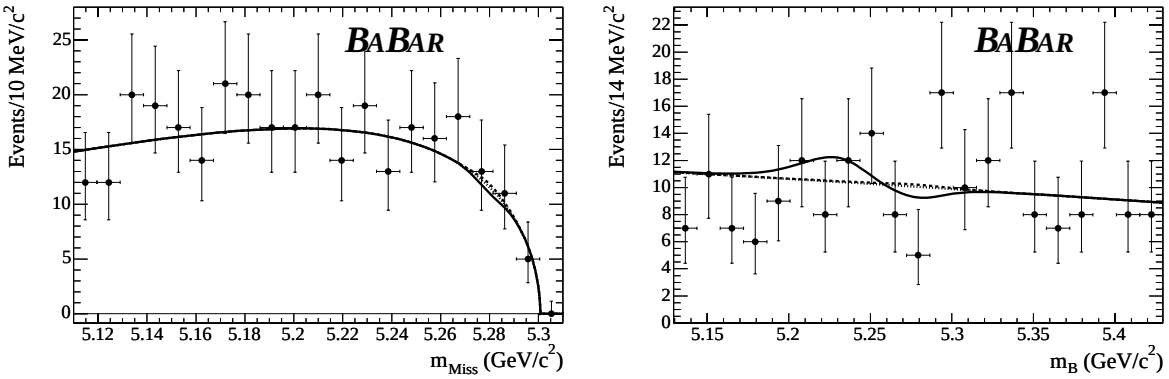

Figure 8.35: Distribution of m_{miss} (left), m_B (right) for $B^+ \to \phi\pi^+$-only candidates on on-resonance data, together with the result of the maximum likelihood fit after applying a requirement on the ratio of signal ($\phi\pi^+$) likelihood to signal($\phi\pi^+$)-plus-background likelihood (computed without the displayed variable). The curves are projections from the likelihood fit for total yield (continuum line), for the continuum background (fine dashed line) and for continuum plus $B\overline{B}$ component (dashed line).

8.5.1 Upper Limits on Branching Fractions

Since we do not observe any signal in both neutral and charged $B \to \phi\pi$ decay, we set upper limits on the branching fractions.

We adopt a Bayesian approach to do it. From the multi-dimensional likelihood defined by Eq. 8.8 or Eq. 8.9 we obtain a modified likelihood function $L(N_S)$:

$$L(N_S) = N_0 \int_0^\infty dN_{\mathrm{S-wave}} \mathcal{L}(N_S, N_{\mathrm{S-wave}}), \tag{8.10}$$

where the normalization N_0 is such that $\int_0^\infty dN_S L(N_S) = 1$. The two dimensional like-

lihood $\mathcal{L}(N_S, N_{\mathrm{S-wave}})$ is given at each point on the N_S-$N_{\mathrm{S-wave}}$ plane by the function defined in Eq. 6.13, maximized with respect to all of the other fit variables. For calculating upper limits, we impose the *a priori* constraints $N_S > 0$ and $N_{\mathrm{S-wave}} > 0$. We show the experimental likelihood on N_S for both neutral and charged mode in Fig. 8.36

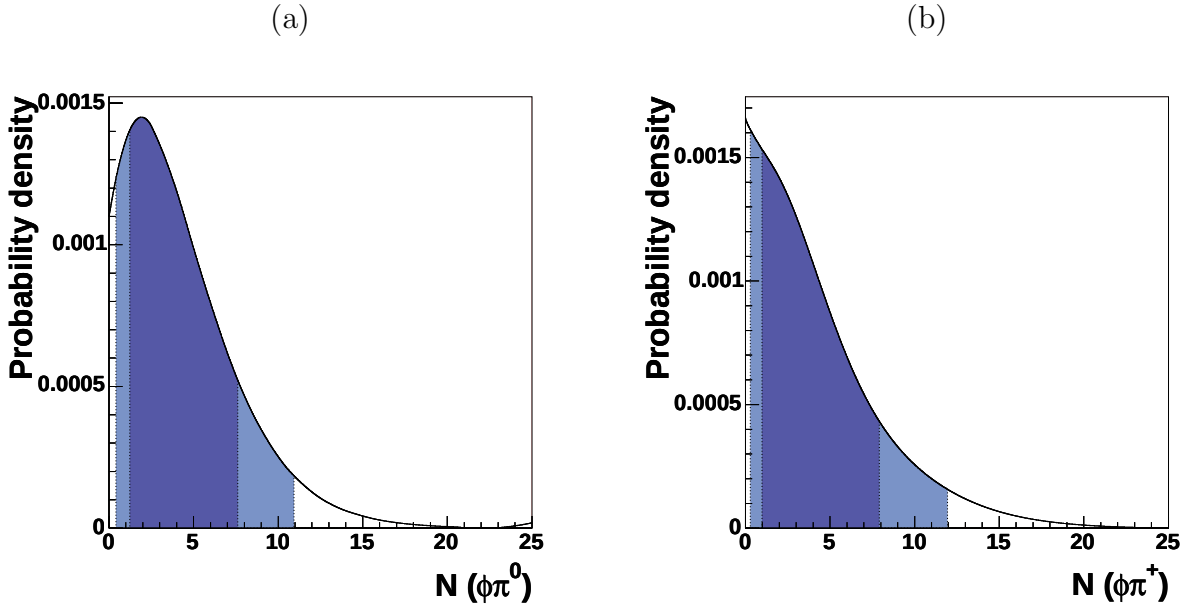

Figure 8.36: Experimental likelihood for the signal yields for (a) $B^0 \to \phi\pi^0$ decays (b) $B^+ \to \phi\pi^+$ decays. The darker region is the 68% probability interval, the other is 90% interval. $N_S > 0$ *a priori* assumption has been assumed.

The branching fraction $\mathcal{B}$ is calculated from the observed number of signal events as

$$\mathcal{B} = \frac{N_S}{\varepsilon \cdot N_{B\bar{B}} \cdot \mathcal{B}(\phi \to K^+K^-)} \tag{8.11}$$

where $N_{B\bar{B}}$ is the number of $B\bar{B}$ pairs produced (232×10^6) and ε is the reconstruction efficiency for the B candidates. In Eq. 8.11 we assume equal branching fractions for $\Upsilon(4S)$ decays to charged and neutral B-meson pairs [23].

Under the assumption that $N_{B\bar{B}}$ and ε are distributed as Gaussians, we obtain a likelihood function, $L_{\mathcal{B}}$, for the branching fraction, $\mathcal{B}$, based on Eq. 8.11, by convolving the likelihood (L in Eq. 8.10) with the distributions of $N_{B\bar{B}}$ and ε. We also include the additional uncertainty coming from the systematic error on the signal yield (which we will discuss in Sec. 8.6). The resulting likelihood is shown in Fig. 8.37 for each of the two decay modes. In the plots, the upper boundary of the dark region represents the 90%

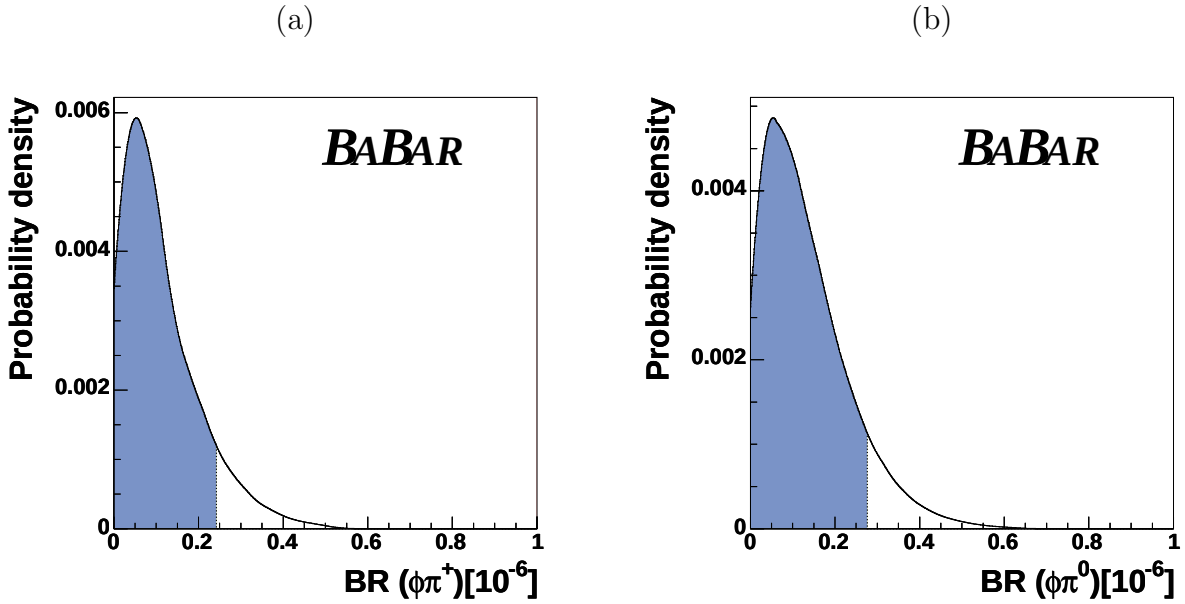

Figure 8.37: Likelihood distribution, $L_{\mathcal{B}}(\mathcal{B})$, for (a) $\mathcal{B}(B^+ \to \phi\pi^+)$ and (b) $\mathcal{B}(B^0 \to \phi\pi^0)$ in arbitrary units. The upper boundary of the dark region represents the 90% probability upper limit.

probability Bayesian upper limit $\mathcal{B}_{\rm UL}$, defined as:

$$\int_0^{\mathcal{B}_{\rm UL}} L_{\mathcal{B}}(\mathcal{B})d\mathcal{B} \;=\; \frac{9}{10}\int_0^{+\infty} L_{\mathcal{B}}(\mathcal{B})d\mathcal{B} \tag{8.12}$$

We determine

$$\begin{aligned} \mathcal{B}(B^+ \to \phi\pi^+) &< 2.4 \times 10^{-7}, \\ \mathcal{B}(B^0 \to \phi\pi^0) &< 2.8 \times 10^{-7}. \end{aligned}$$

These limits are consistent with Standard Model predictions [86].

Central Value of Branching Fraction

Even if the result of this measurement is given by given upper limits on $\mathcal{B}$, or, better, by the experimental likelihoods in Fig. 8.37, we also compute a central value for $\mathcal{B}$ in order to allow world averaging with other experiments which provide only it.

Since the fitted yields lie in the problematic region where the maximum of the likelihood is not a good estimator of the true value (Fig. 8.28), we do not use the yields reported

in Tables 8.14 and 8.15, but instead the median of the likelihood for N_S (Eq. 8.10 and Fig. 8.36). We correct for the residual bias which affects this estimator, using as calibration curve the third order polynomial shown in Fig. 8.29a and Fig. 8.32a for $B^0 \to \phi\pi^0$ and $B^+ \to \phi\pi^+$, respectively. With this method we find the yields reported in Table 8.16. We then evaluate the values for branching fractions with Eq. 8.11 without assuming *a priori* that $N_S > 0$ as for the upper limit evaluation. The results are reported in Table 8.16.

	$B^+ \to \phi\pi^+$	$B^0 \to \phi\pi^0$
Yield	-1.5 ± 5.9	4.0 ± 3.5
$\varepsilon(\%)$	37.1 ± 0.1	29.5 ± 0.8
$\mathcal{B}(10^{-6})$	-0.04 ± 0.17	0.12 ± 0.13
UL$(\mathcal{B})(10^{-7})$	2.4	2.8

Table 8.16: Signal yield (evaluated as the median of the likelihood), detection efficiency ε (the uncertainty includes both statistical and systematic effects), measured branching fraction $\mathcal{B}$ with statistical error, after the correction for the fit bias has been applied, for the two decay modes considered and upper limit at 90% probability.

8.6 Systematic Uncertainties

Sources of systematic uncertainties on the measurement of the branching fraction are the *quasi-two-body* approach which neglects interference effects, the error associated to the counting of produced $B\bar{B}$ couples in our data set, the knowledge of reconstruction efficiency, estimated from signal Monte Carlo and the performances of the particle identification, the knowledge of the shape parameters of the variables used in the fit and the fit biases.

The Quasi-two-body Approximation: Interference Effects

The *quasi-two-body* approximation consists of reducing the kinematically allowed region in the Dalitz plot to a band which is dominated by a single resonance. In the case of the ϕ this assumption is justified by the small width of the resonance, which allow to take a small portion of the Dalitz region where contribution from the scalar meson $f_0(980)$ is highly reduced.

The total $K^+K^+\pi$ amplitude can be written as the coherent sum of the amplitudes of the single resonances, weighted by the form factors F_i which depend from the Dalitz plot

position and the spin of the resonance:

$$A_{K^+K^-\pi} =^0 KF_{f_0\pi}A_{f_0\pi} +^1 KF_{\phi\pi}A_{\phi\pi} +^0 KF_{NR}A_{NR} \tag{8.13}$$

where ${}^JK$ are the kinematic factors:

$$\begin{aligned} {}^0K &= 1, \\ {}^1K &= -4|\vec{p}_{K^+}||\vec{p}_{\pi}|\cos\theta_{K^+\hat{\pi}} = s_{K^+\pi} - s_{K^-\pi} \end{aligned} \tag{8.14}$$

where $\theta_{K^+\hat{\pi}}$ is what we called the helicity angle and s_{ij} is the invariant mass squared of the particles i and j and the three momenta $|\vec{p}_i|$ are given in the rest frame of the resonance. The form factors F_i are represented in the Dalitz plot by Breit Wigner (Eq. 3.27) or Flatté (Eq. **??**) functions.

In the rest of discussion we will assume that the $A_{f_0\pi}$ amplitude is real and that the relative phase between $A_{\phi\pi}$ and $A_{f_0\pi}$ is ϕ. Since we want to evaluate the systematic uncertainty to the yield of $B \to \phi\pi$, we have also to make an assumption on the ratio $|A_{f_0\pi}|/|A_{\phi\pi}|$: we take it equal to the measured ratio $|A_{f_0K^+}|/|A_{\phi K^+}|$. With these assumptions the total rate is given by:

$$|A_{K^+K^-\pi}|^2 = |A_{\phi\pi}|^2 \left[|F_{f_0\pi}|^2 \frac{|A_{f_0K^+}|^2}{|A_{\phi K^+}|^2} +^1 K|F_{\phi\pi}|^2 + 2\frac{|A_{f_0K^+}|}{|A_{\phi K^+}|} F_{f_0\pi}F_{\phi\pi}\ {}^1K\cos\phi \right] \tag{8.15}$$

Allowing the interference between P-wave and S-wave, and using the measured ratio of $|A_{f_0K^+}|^2/|A_{\phi K^+}|^2$ [76], we obtain the mass and helicity angle distributions shown in Fig. 8.38. We used three different relative phases between S- and P-wave: $\phi = \{0, \pi/2, \pi\}$, but the final lineshape doesn't depend very much by this phase. We assume the non resonant (NR) component contribution measured by Belle collaboration in the Dalitz analysis of $B^+ \to K^+K^-K^+$[75]:

$$\mathcal{B} = \left(24.0 \pm 1.5 \pm 1.8^{+1.9}_{-5.7}\right) \times 10^{-6} \tag{8.16}$$

where the first quoted error is statistical, the second is systematic and the third is the model error. We parameterize this component with a flat PDF in $m_{K^+K^-}$ multiplied by the phase space and a flat PDF in the helicity. We also assume the measured phase:

$$NR\ phase(^\circ) = -68 \pm 2. \tag{8.17}$$

We run a lot of toy Monte Carlo experiments generating with the interference on and fitting with the nominal fit, where it is neglected. We define the systematic uncertainty on

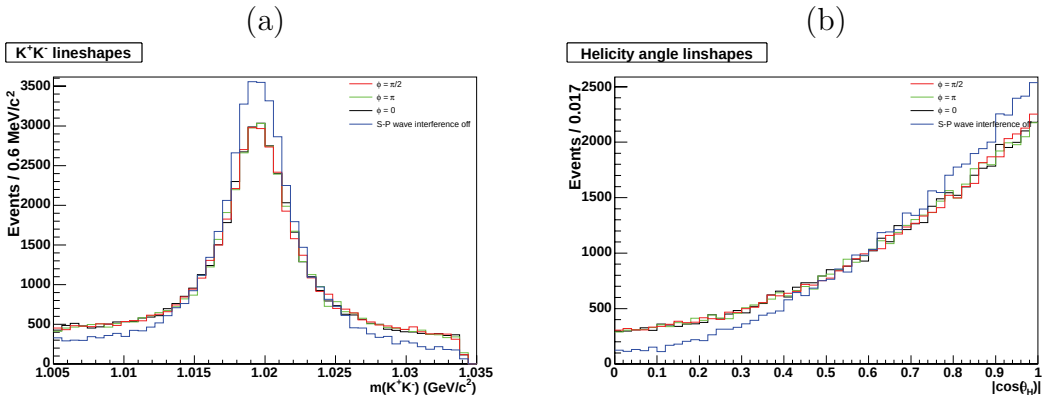

Figure 8.38: Generated distribution of (a) $m_{K^+K^-}$ and (b) $|\cos\theta_H|$ for 31980 $B^+ \to \phi K^+$ events, 4800 $B^+ \to f_0 K^+$ events, once allowing the interference between the two amplitudes with different relative phases ($\phi = \{0, \pi/2, \pi\}$) and once not allowing the interference (blue histogram).

the yield as the difference between the fitted $\phi\pi$ yield and the generated one, divided by the generated yield: $\frac{N_{fit}(nominal) - N_{gen}(interference\ on)}{N_{gen}(interference\ on)}$. We find the effect of neglecting the residual interference to be 4.4% on the $\phi\pi$ yield and 1.1% on ϕK^+ yield. The distributions of the residuals for $\phi\pi^+$ and ϕK^+ are shown in Figure 8.39, the effect on $\phi\pi^0$ is the same of the one for $\phi\pi^+$.

B Counting

The B-counting method described in [23] is used to determine the number of $\Upsilon(4S)$ in the on-resonance data. We assume equal branching fractions for $\Upsilon(4S)$ decays to charged and neutral B-meson pairs. The uncertainty quoted for RunI-IV dataset we use (equivalent to 231.8×10^6 $B\bar{B}$ pairs) is 1.30×10^6.

Reconstruction of π^0

The signal efficiency correction for $B^0 \to \phi\pi^0$ due to discrepancies between Monte Carlo and data is evaluated with neutral particles data control samples. The final correction to the efficiency is *0.991 ± 0.03 (syst)* (see Sec. 8.1.1).

Tracking Efficiency

Using data control samples of charged tracks a flat systematic error of 0.8% per track is assigned.

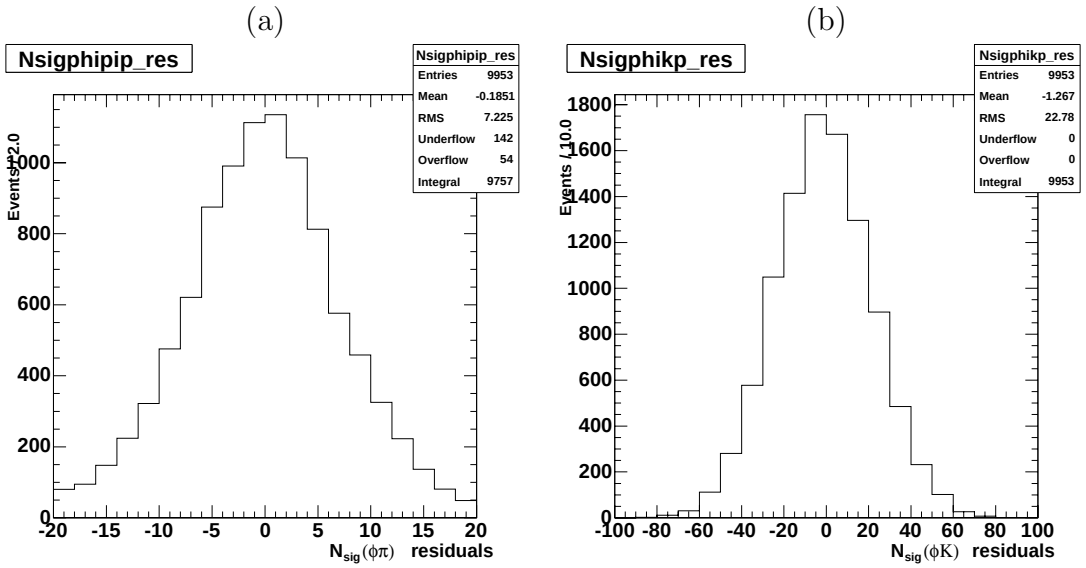

Figure 8.39: Residuals for (a) $\phi\pi^+$ and (b) ϕK^+ (right) yield when in generation the interference between S, P wave and non resonant is allowed.

Particle Identification

Applying the standard PID selectors to Monte Carlo tracks, doesn't fully reproduce the PID efficiencies and purities on data. The efficiencies related to PID cuts in Monte Carlo by using PID selectors are corrected using studies with very pure $\pi^{\pm}$ and $K^{\pm}$ data control samples from $D*^{\pm}$ decays (see Sec. 8.1.2).

PID corrections contain efficiencies and errors on efficiencies, measured for each combination of selector and true particle type in bins of momentum (p, θ and ϕ) in the laboratory frame. PID corrections are generated for both data and Monte Carlo using a number of control samples, so efficiency ratios of data to Monte Carlo using the same momentum binning can be derived from them in a PID ratio table along with the corresponding statistical errors. For each signal track that is required to pass a PID criterion, a correction factor is read off from the ratio table. The true track identity (obtained from Monte Carlo truth-matching) and charge tell us which correction is to be used for that track.

The correction factor for an event is the product of corrections of individual tracks that pass certain PID criteria in that event. The overall error is statistically calculated and assigned as the systematic error on signal efficiency due to PID. We find a correction of 0.5% both for charged and neutral mode, since we apply the same selection on kaons

originating from $\phi(1020)$.

Sub Branching Fractions

The uncertainty on the branching fraction $\mathcal{B}(\phi \to K^+K^-)$ also contribute as systematic error in the determination of the absolute value of the branching fraction of $B \to \phi\pi$ decays. We use the PDG 2004 value: $\mathcal{B}(\phi \to K^+K^-) = 0.491 \pm 0.006$.

PDF's Parameterization of $B^0 \to \phi\pi^0$

We evaluate the uncertainty due to the knowledge of parameters entering the likelihood moving each parameter by $\pm 1\sigma$, where σ is the error associated to each parameter. For m_B, whose shape is sensible to the calorimeter energy scale and resolution, we use as control sample $B^+ \to h^+\pi^0$, taking the shape from the fit on the Run I-IV dataset (the same dataset we are using). Since in this measurement the usual ΔE variable is used instead of m_B, and the parameterization is done with another functional form, a Crystal Ball shape (Eq. 5.10), we cannot simply use those parameters.

Then we generated about 50×10^3 toy Monte Carlo events with ΔE shape fitted on $h^+\pi^0$ data, and then we compare that shape with $\Delta m_B = m_B - m_B^{PDG}$. Figure 8.40 shows that there is not significant difference between our corrected MC and data. We then fit this m_B distribution for $h^+\pi^0$ with a Crujiff function, and use these parameters in the nominal fit. In order to evaluate the systematics, we vary the parameters by $\pm 1\sigma$, where σ is the standard deviation obtained on a fit on a sample rescaled to the actual luminosity, and taking the difference in the yield as the systematic error. For the ϕ mass and $|\cos\theta_H|$ we vary Monte Carlo parameters by 1σ.

The l_2 variable has been used for the first time by $B^0 \to K_S^0\pi^0$ analysis. In that analysis the agreement between data and Monte Carlo has been checked using data control samples. Since we are using the same selection on it ($l_2 < 0.55$) and the same parameterization, and since the shape of this variable does not depend by the reconstructed signal, but only by the rest of the event, we can assign the same systematic uncertainty estimated by their analysis (1.8%).

We consider here only the parameters associated to the signal component, since the background parameters are floated in the nominal fit[1].

[1] with the exception of m_{miss} ARGUS endpoint. The position of the ARGUS endpoint is related to the beam energies, and it is 100% correlated with the m_{miss} mean for the signal, then this systematic

(a) (b)

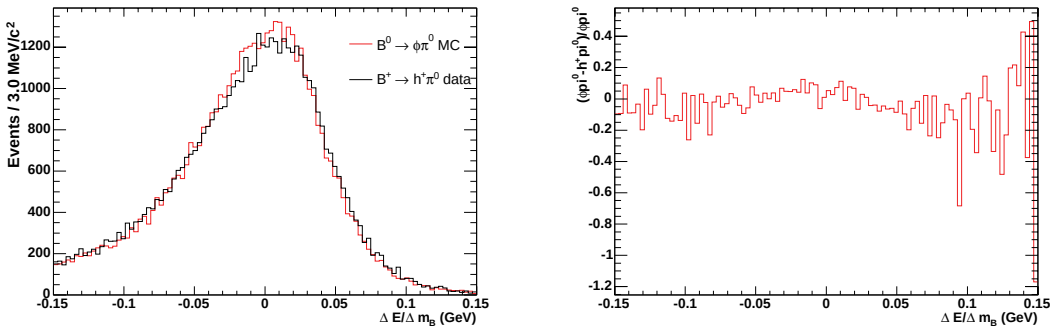

Figure 8.40: (a) Comparison of m_B distribution between $B^0 \to \phi\pi^0$ shape generated according Monte Carlo simulated events and a $B^+ \to h^+\pi^0$ generated with the fitted parameters on on-resonance data. (b) Normalized difference $(m_B^{\phi\pi^0} - m_B^{h^+\pi^0})/m_B^{\phi\pi^0}$ vs. $\Delta m_B^{\phi\pi^0} = m_B - m_B^{PDG}$.

In Table 8.17 we summarize the systematic uncertainties on the yield of $B^0 \to \phi\pi^0$. The total uncertainty is obtained summing up in quadrature all the contributions.

Syst. contribution	$\Delta\ N^+(\phi\pi^0)$	$\Delta\ N^-(\phi\pi^0)$	$\Delta\ N^+(f_0\pi^0)$	$\Delta\ N^-(f_0\pi^0)$
Sig. m_{miss}	0.401	0.382	2.899	3.081
Sig. m_B	0.400	0.377	2.845	3.127
Sig. l_2	0.374	0.475	3.36	3.229
Sig. $\phi(1020)$ lineshape	0.260	0.241	1.880	1.912
Sig. $\lvert\cos\theta_H\rvert$	0.241	0.242	1.888	1.888
$f_0(980)$ modeling	0.675	0.403	2.881	3.803
Tot.	0.891	1.029	6.06	6.69

Table 8.17: Summary of $B^0 \to \phi\pi^0$ systematic uncertainties related to the PDF parameterization.

PDF's Parameterization of $B^+ \to \phi\pi^+$

As for the neutral channel, the main source of contribution to the systematic error comes from the uncertainty on the parameters of the likelihood. In this case the control sample is $B^+ \to \phi K^+$ itself, which has sufficient statistics to allow some PDF's to be determined on data. In the final fit we float the shape parameters of the two kinematic variables, m_{miss} and m_B, and the mass of the ϕ, so they will not contribute to the total systematic

uncertainty is already taken into account.

uncertainty. In this case we evaluate systematic error for the four yields we are floating: $B^+ \to \phi\pi^+$, $B^+ \to \phi K^+$, $B^+ \to f_0\pi^+$, $B^+ \to f_0 K^+$. Also in this case the background parameters, with the exception of ARGUS endpoint are floated in the fit and do not contribute to the systematic error. The total contribution is summarized in Table 8.18

Syst. contribution	$\Delta\ N^+_{\phi\pi^+}$	$\Delta\ N^-_{\phi\pi^+}$	$\Delta\ N^+_{\phi K^+}$	$\Delta\ N^-_{\phi K^+}$	$\Delta\ N^+_{f_0\pi^+}$	$\Delta\ N^-_{f_0\pi^+}$	$\Delta\ N^+_{f_0 K^+}$	$\Delta\ N^-_{f_0 K^+}$
Sig. l_2	0.360	0.350	0.550	1.177	0.506	0.508	1.153	1.323
Sig. $\lvert\cos\theta_H\rvert$	0.193	0.201	0.353	0.683	0.284	0.291	0.892	0.614
Sig. θ_c	0.389	0.413	1.011	0.958	0.570	0.580	1.434	1.426
$\mathsf{f_0(980)}$ modeling	0.479	0.263	2.958	2.422	0.894	0.509	3.961	1.452
Tot.	0.693	1.264	3.225	2.988	1.216	0.999	4.461	2.513

Table 8.18: Summary of $B^+ \to \phi h^+$ systematic uncertainties due to the PDF parameterization.

Fit Bias

Only in the central value of the branching fraction, we include a systematic uncertainty due to the fit bias. We decide to assign 1/2 of the deviation of the median from the expected value, as determined by the relation shown in Fig. 8.29 for $B^0 \to \phi\pi^0$ and in Fig. 8.32 for $B^+ \to \phi\pi^+$.

Summary of Systematic Uncertainties

In Table 8.19 we give the summary of the systematic uncertainties on the branching fraction for $B^+ \to \phi\pi^+$ and for $B^0 \to \phi\pi^0$.

Table 8.19: Summary of systematic uncertainties contributing to the total error for the upper limit on the branching fraction. They are given in units of 10^{-8}.

	$B^+ \to \phi\pi^+$	$B^0 \to \phi\pi^0$
PDF Uncertainty	$^{+1.9}_{-2.8}$	$^{+3.6}_{-4.2}$
PID Efficiency	0.1	0.1
Tracking Efficiency	0.1	0.2
π^0 Efficiency	-	0.1
L_2/L_0 Cut	0.1	0.3
$B\bar{B}$ Pair Counting	0.1	0.2
Interference Effects	0.3	0.6
$\mathcal{B}(\phi \to K^+K^-)$, $\mathcal{B}(\pi^0 \to \gamma\gamma)$	0.1	0.1
Total	$^{+2.8}_{-3.6}$	$^{+3.7}_{-4.3}$

Chapter 9

Interpretation of the Results and Constraints on New Physics Parameters

CP violation in the B_d decays has been well established through the measurements of time-dependent asymmetries in the $B^0 \to [c\bar{c}]K^0$ decays at the B-factories [89, 90]. The world average of the "sine term" in the CP asymmetry of Eq. 1.55 is $S_{[c\bar{c}]K^0} = \sin 2\beta = 0.674 \pm 0.026$, in good agreement with the Standard Model (SM) prediction.

In the limit of one dominant decay amplitude, the CP violating asymmetries measured in the time dependent decays of neutral B mesons to CP eigenstates depend only on the sum of the phase of the $B^0 - \bar{B}^0$ mixing amplitude and the phase of the decay amplitude. The only two large phases in the CKM matrix belong to the elements V_{ub} (γ) and V_{td} (β). In principle, one can determine β and γ from the available data on K and B decays. However, given the large theoretical uncertainties in the input parameters (e.g. B_K, f_B) the size of these phases remains uncertain [91, 92]. Based on these fact the Standard Model predicts that the CP asymmetries in all B_d decays that do not involve direct $b \to u$ (or $b \to d$) transitions have to be the same.

In Sec. 1.4.1 we have described the decay amplitudes of $B^0 \to \phi K^0$ and the one of B to three kaons, and we have shown that the expected deviation of the time-dependent CP asymmetry in the Standard Model, due to suppressed $b \to u$ tree amplitudes, are negligible for $B^0 \to \phi K^0$ and $B^0 \to K^0_S K^0_S K^0_S$, while can be larger in $B^0 \to K^+K^-K^0$ (excluding ϕK^0).

Then, a measurement of the time-dependent CP asymmetry in these decay modes $S_f \neq \sin 2\beta$ would be a signature of new physics.

New physics could in principle contribute to both the B^0-$\overline{B}^0$ mixing and to the decay amplitudes. It is plausible that the new contributions to the mixing could be of the same size as the Standard Model contribution since it is already a one-loop effect. This is why most of the existing studies on the effects of new physics on CP violating B meson decays have concentrated on effects in the B^0-$\overline{B}^0$ mixing, and assume the decay amplitudes are those in the Standard Model [93, 94, 95]. The distinguishing feature of new physics in mixing is that its effect is universal, i.e. although it changes the magnitude of the asymmetries it does not change the patterns predicted by the Standard Model. Thus, the best way to search for these effects would be to compare the observed CP asymmetry in a particular $b \to s$ decay mode with the asymmetry predicted in the Standard Model.

In contrast, the effects of new physics in decay amplitudes are manifestly non-universal, i.e. they depend on the specific process and decay channel under consideration. Experiments on different decay modes that would measure the same CP violating quantity in the absence of new contributions to decay amplitudes, in this scenario measure different CP violating quantities.

9.1 New Physics Signatures with Supersymmetry

Supersymmetry (SUSY) is an extension of the Standard Model that was introduced to cancel out the quantum corrections from virtual particles coupled with the Higgs field which make the Higgs mass running up to the Plank scale. This is achieved in SUSY introducing a bosonic partner of the standard fermions and vice versa, with the condition that these new particles have the same properties under the Standard Model gauge transformations.

In looking for new physics beyond the electroweak SM it is useful to regard the SM itself as an effective low energy theory valid up to some energy scale Λ at which the new physics sets in. One is then led to write all possible operators invariant under $SU(3)\otimes SU(2)\otimes U(1)$ using the fields of the SM. They can be organized according to their dependence on Λ. It is well known that as long as one writes operators not exceeding dimension four there are crucial conservations which automatically show up: baryon (B) and lepton (L) numbers and the absence of tree-level flavour changing neutral currents (FCNC). However, as soon as one proceeds beyond dimension four (i.e., one considers non-renormalizable operators which are suppressed by powers of Λ), these conservations are no longer automatically

guaranteed. Either one has to choose large values for Λ (for instance, the grand unification or the Planck scale), or, if Λ is assumed to be not so far from the Fermi scale, additional constraints have to be imposed to play on the safe side in relation to B, L and FCNC violating processes.

Low energy Supersymmetry (SUSY) [97] enters this latter class of models with new physics close enough to the Fermi scale. The problem of too violent B and L violations is more elegantly solved by the imposition of an additional discrete symmetry, the R-parity. We discuss experimental constraints on validity of this assumption based on some of the measurements presented in this work in Sec. 9.3.

As for the FCNC issue, given that now we are in the presence of new particles, the scalar partners of the fermions (sfermions) carrying flavour number, new constraints will have to be imposed to suppress operators of dimension greater than four, leading to potentially large FCNC rates. They amount to very severe limitations on the pattern of the sfermion mass matrices: they must be either very close to the unit matrix in flavour space (flavour universality) or almost proportional to the corresponding fermion mass matrices (alignment).

The Minimal Supersymmetric Standard Model is the extension of the Standard Model which only introduces the partners of the standard particles without additional interaction or field.

9.1.1 Mass Insertion Approximation

A way to parameterize the FCNC and *CP* quantities in SUSY which is model-independent is the so-called mass insertion approximation [98]. It concerns the most peculiar source of FCNC SUSY contributions that do not arise from the mere supersymmetrization of the FCNC in the SM. They originate from the FC couplings of gluinos and neutralinos to fermions and sfermions [99]. One chooses a basis for the fermion and sfermion states where all the couplings of these particles to neutral gauginos are flavour diagonal, while the FC is exhibited by the non-diagonality of the sfermion propagators. Denoting by Δ the off-diagonal terms in the sfermion mass matrices (i.e. the mass terms relating sfermion of the same electric charge, but different flavour), the sfermion propagators can be expanded as a series in terms of the dimensionless quantity $\delta = \Delta/\tilde{m}^2$ where $\tilde{m}$ is an average sfermion mass. As long as Δ is significantly smaller than $\tilde{m}^2$, we can just take the first term of this expansion and, then, the experimental information concerning FCNC

and CP violating phenomena translates into upper bounds on these δ's.

The above mass insertion method presents the major advantage that one does not need the full diagonalization of the sfermion mass matrices to perform a test of the SUSY model under consideration in the FCNC sector. It is enough to compute ratios of the off-diagonal over the diagonal entries of the sfermion mass matrices and compare the results with the general bounds on the δ's that we provide here from all available experimental information.

There exist four different Δ mass insertions connecting flavours i and j along a sfermion propagator: $(\Delta_{ij})_{LL}$, $(\Delta_{ij})_{RR}$, $(\Delta_{ij})_{LR}$ and $(\Delta_{ij})_{RL}$. The indices L and R refer to the helicity of the fermion partners. The size of these Δ's can be quite different. For instance, in the MSSM case, only the LL mass insertion can change flavour, while all the other three above mass insertions are flavour conserving, i.e. they have $i = j$. In this case to realize a LR or RL flavour change one needs a double mass insertion with the flavour changed only in a LL mass insertion and a subsequent flavour-conserving LR mass insertion. Even worse is the case of a FC RR transition: in the MSSM this can be accomplished only through a laborious set of three mass insertions, two flavour-conserving LR transitions and an LL FC insertion. Generally the Δ_{LR} quantity does not necessarily coincide with Δ_{RL}. For instance, in the MSSM and in several other cases, one flavour-conserving mass insertion is proportional to the mass of the corresponding right-handed fermion. Hence , $(\Delta_{ij})_{LR}$ and $(\Delta_{ij})_{RL}$ are proportional to the mass of the i-th and j-th fermion, respectively.

The measurements of $b \to s$ transitions determine the allowed regions in the SUSY parameter space providing constraints on the δ's. The Standard Model and SUSY contributions are evaluated making use of the method of effective Hamiltonian in $\Delta B = 1$ processes.

9.2 Effective Hamiltonian for $\Delta B = 1$ Transitions

To evaluate the Effective Hamiltonian for a given process one has to go through the following steps:

1. calculate the amplitude between quark and gluon states of definite momenta in the full theory;

2. choose a basis of local operators for the effective theory and calculate their matrix

elements between the same states used in point 1;

3. determine the coefficients of the operators in the Effective Hamiltonian by matching the full theory with the effective one.

The matching is given by the following relation:

$$\langle f|S|i\rangle = -i\sum_j C_j\langle f|O_j|i\rangle \ , \tag{9.1}$$

where C_i are the Wilson coefficients and O_i the operators of the Effective Hamiltonian:

$$\mathcal{H}_{eff} = \sum_i C_i O_i \tag{9.2}$$

In the case of $\Delta B = 1$ processes it can be written as:

$$\mathcal{H}_{\rm eff}^{\Delta B=1} = -\frac{G_F}{\sqrt{2}}V_{tb}V_{ts}^*\left[\sum_{i=3}^{6} C_i O_i + C_g O_g \sum_{i=3}^{6}\tilde{C}_i\tilde{O}_i + \tilde{C}_g\tilde{O}_g\right], \tag{9.3}$$

where

$$\begin{aligned}
O_3 &= \bar{s}_\alpha\gamma^\mu L b_\alpha \bar{s}_\beta\gamma^\mu L s_\beta, && (9.4)\\
O_4 &= \bar{s}_\alpha\gamma^\mu L b_\beta \bar{s}_\beta\gamma^\mu L s_\alpha, && (9.5)\\
O_5 &= \bar{s}_\alpha\gamma^\mu L b_\alpha \bar{s}_\beta\gamma^\mu L s_\beta, && (9.6)\\
O_6 &= \bar{s}_\alpha\gamma^\mu L b_\beta \bar{s}_\beta\gamma^\mu R s_\alpha, && (9.7)\\
O_g &= \frac{g_s}{8\pi^2} m_b \bar{s}_\alpha \sigma^{\mu\nu} R \frac{\lambda^A_{\alpha\beta}}{2} b_\beta G^A_{\mu\nu}. && (9.8)
\end{aligned}$$

where $L = 1-\gamma_5$ and $R = 1+\gamma_5$. The terms with tilde are obtained from $C_{i,g}$ and $O_{i,g}$ by exchanging $L \leftrightarrow R$. The Wilson coefficient $C_{i(g)}$ includes both SM and SUSY contributions. In this case, the effect of the operator $O_\gamma = \frac{e}{8\pi^2} m_b \bar{s}_\alpha \sigma^{\mu\nu} R b_\alpha F_{\mu\nu}$ and the electroweak penguin operators, which give very small contributions, has been neglected.

The amplitude in the full theory is given by the calculation in the diagrams in Fig. 9.1, for example in the QCD factorization approach [96]. The general form of the amplitude can be written as:

$$\overline{A}(\phi K) = \overline{A}^{\rm SM}(\phi K) + \overline{A}^{\tilde{g}}(\phi K) + \overline{A}^{\tilde{\chi}^\pm}(\phi K), \tag{9.9}$$

where $\overline{A}^{\rm SM}$, $\overline{A}^{\tilde{g}}$, and $\overline{A}^{\tilde{\chi}^\pm}$ refer to the SM, gluino, and chargino contributions, respectively. Performing the matching with the effective Hamiltonian one obtains the Wilson

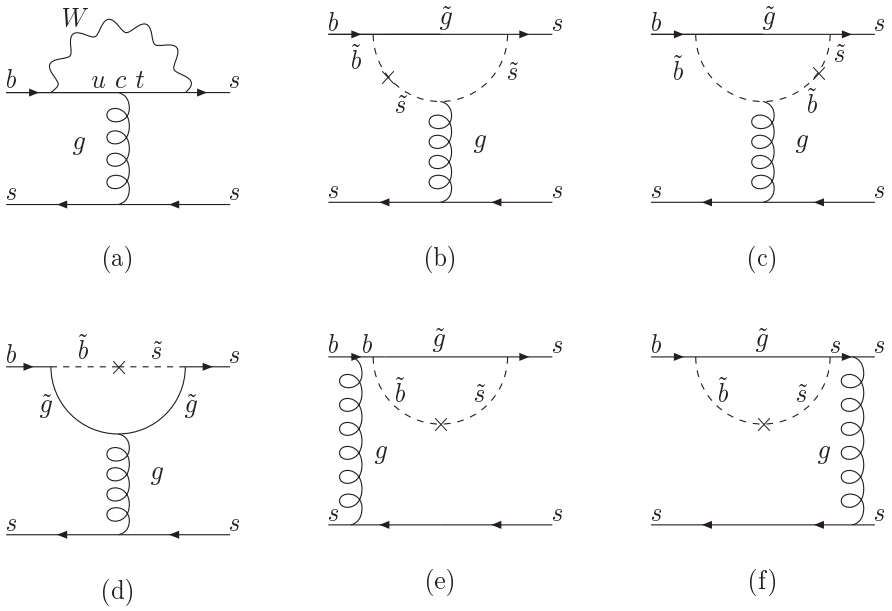

Figure 9.1: The Standard Model contribution (a) and the gluino–down squark contributions (b)–(f) to the $b \to s$ transitions.

coefficients, which contain the $(\delta_{ij})_{AB}$.

The calculation has been done for the golden mode $B^0 \to \phi K^0$ [100, 101]. In the following, we consider only the gluino exchanges through $\Delta B = 1$ penguin diagrams which give the dominant contribution to the amplitude $\overline{A}^{\rm SUSY}(\phi K^0)$.

9.2.1 Supersymmetric Contributions to $B^0 \to \phi K^0$ Decay

From the matching of the full theory with the effective Hamiltonian, at the first order in the mass insertion approximation, the gluino contributions to the Wilson coefficients $C_{i,g}$ at SUSY scale M_S can be evaluated (full expression is given in [102]) in terms of the parameters $(\delta^d_{23})_{AB}$.

The absolute value of the mass insertions $(\delta^d_{23})_{AB}$, is constrained by the experimental results for:

1. The BR($B \to X_s\gamma$)

2. The CP asymmetry $A_{CP}(B \to X_s\gamma)$

3. The BR($B \to X_s\ell^+\ell^-$)

4. The recent measurement of the $B_s - \bar{B}_s$ mass difference $\Delta M_{B_s} = 17.77 \pm 0.10 \pm 0.07\ ps^{-1}$ [103]

With a Monte Carlo analysis, weighted random configurations of input parameters are generated (see ref. [105] for details of this procedure) and computing for each configuration the processes listed above. The constraints induce a clustering on various observables and parameters, assuming that each unconstrained δ^d_{23} fills uniformly a square $(-1 \ldots 1, -1 \ldots 1)$ in the complex plane. The ranges of CKM parameters have been taken from the Unitarity Triangle fit [30], and hadronic parameter ranges are as given in refs. [104, 106, 107].

Concerning SUSY parameters, the masses are fixed to $m_{\tilde{q}} = m_{\tilde{g}} = 350$ GeV/c^2 and different possibilities for the mass insertions are considered.

In Fig. 9.2 the clustering of events in the $\mathrm{Re}(\delta^d_{23})_{AB}$–$\mathrm{Im}(\delta^d_{23})_{AB}$ plane in the single insertion case is shown [108].

In Figs. 9.3 and 9.4, we study the correlations between $S_{\phi K}$ and $C_{\phi K}$, $\mathrm{Im}(\delta^d_{23})_{AB}$ for the various SUSY insertions considered in the present analysis.

In the case of LR and RL mass insertions small positive values of $S_{\phi K}$, as the ones obtained in our measurement, can be more easily obtained than the other cases.

The LR mass insertion contributes to $b_R \to s_L\gamma$, much like the SM. The interference with the Standard Model amplitude produces the "semi-hole" in Fig. 9.2, lower left. On the contrary, the RL mass insertion contributes to $b_L \to s_R\gamma$ and thus it does not interfere. Consequently, the $B^0 \to \phi K^0$ CP asymmetry is as small as in the Standard Model and the RL mass insertion is less constrained than the LR one by $B \to X_s\gamma$, allowing for small values (and also negative values) of $S_{\phi K}$ to be produced more easily.

As a conclusion, these results shown for the golden mode $B^0 \to \phi K^0$, but representative in general of $b \to s$ decays, say that this sector of the flavour physics still offers opportunities to disentangle effects genuinely due to New Physics. In the MSSM discrepancy in the observed CP asymmetries in $b \to s$ transitions with the one measured in $B^0 \to [c\bar{c}]K^0$ can be accounted even respecting the existing constraints in B physics, first of all $\mathcal{B}(B \to X_s\gamma)$. With an increased statistical significance of the discrepancy between the $b \to s$ and $\sin 2\beta$, these processes would become decisive in discriminating among different Supersymmetric realizations.

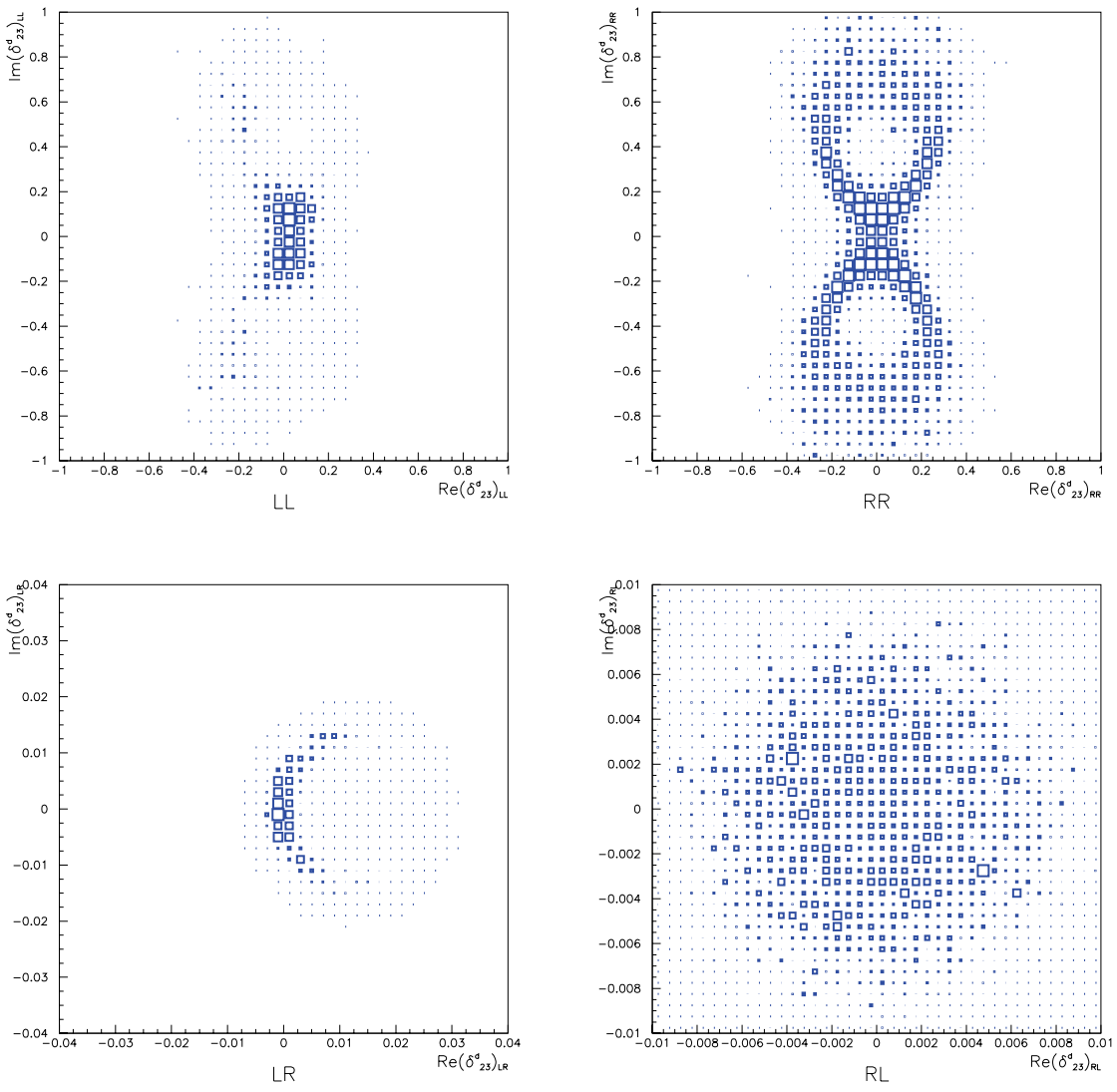

Figure 9.2: Allowed regions in the $\mathrm{Re}(\delta^d_{23})_{AB}$–$\mathrm{Im}(\delta^d_{23})_{AB}$ space for $m_{\tilde{q}} = m_{\tilde{g}} = 350$ GeV and $AB = (LL, RR, LR, RL)$. Constraints from $BR(B \to X_s\gamma)$, $A_{CP}(B \to X_s\gamma)$, $BR(B \to X_s l^+ l^-)$ and ΔM_s have been used.

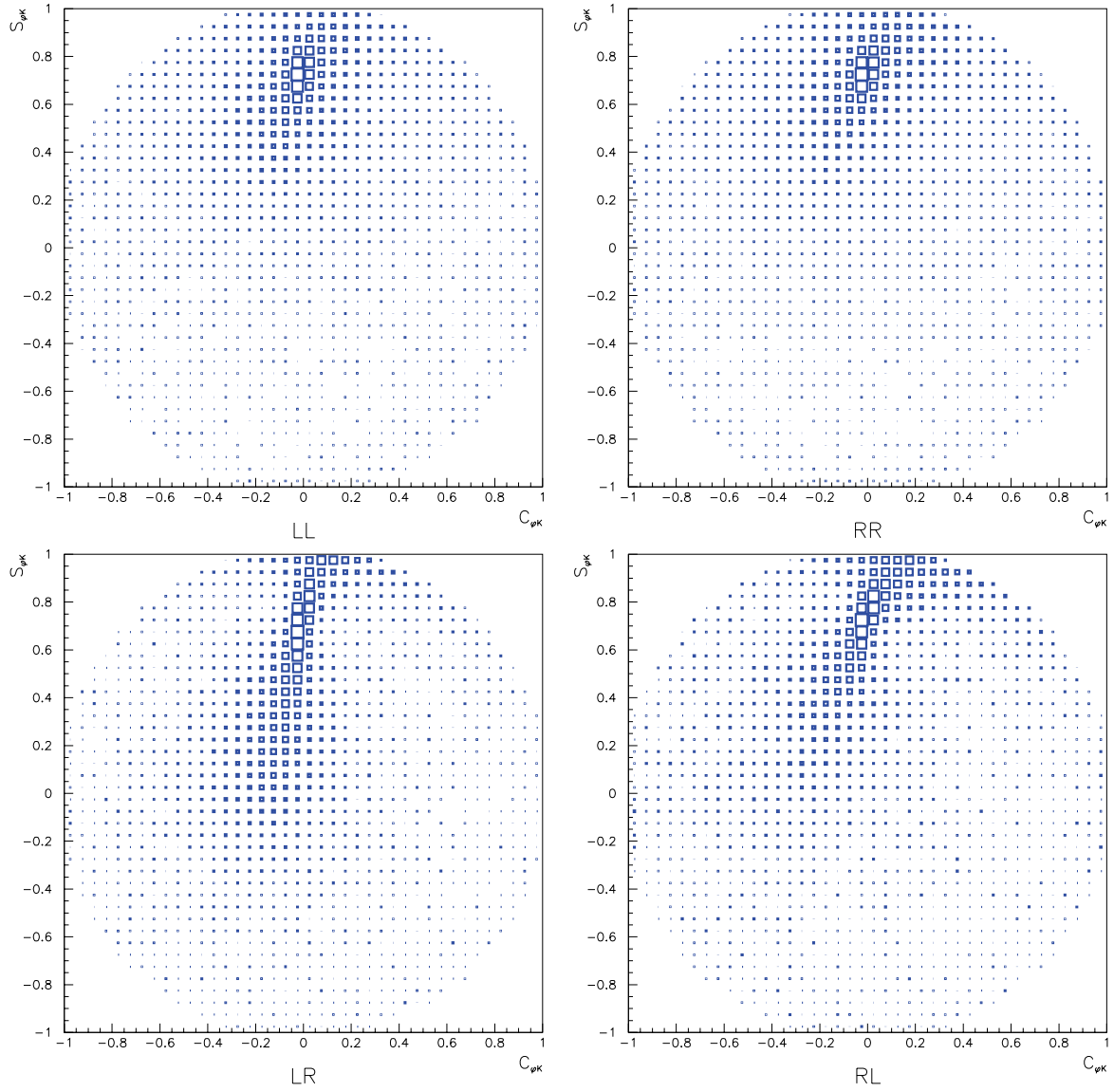

Figure 9.3: Correlations between the sine ($S_{\phi K}$) and cosine ($C_{\phi K}$) coefficients of the time-dependent CP asymmetry of $B \to \phi K_s$ for $m_{\tilde{q}} = m_{\tilde{g}} = 350$ GeV and various SUSY mass insertions $(\delta^d_{23})_{AB}$ with $AB = (LL, RR, LR, RL)$. Constraints from $BR(B \to X_s\gamma)$, $A_{CP}(B \to X_s\gamma)$, $BR(B \to X_s l^+ l^-)$ and the lower bound on ΔM_s have been used.

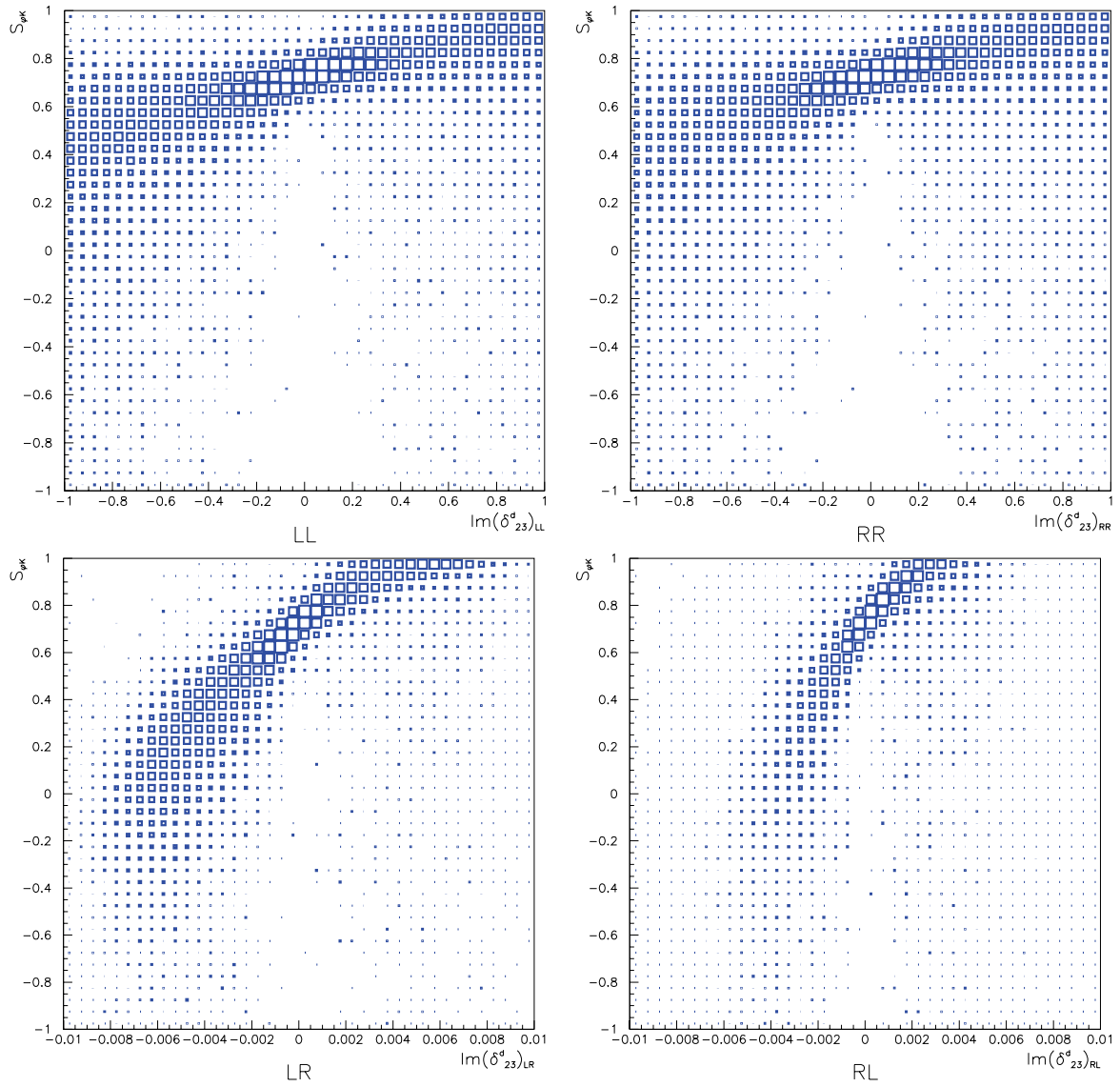

Figure 9.4: Correlations between $S_{\phi K}$ and $\mathrm{Im}(\delta^d_{23})_{AB}$ for $m_{\tilde{q}} = m_{\tilde{g}} = 350$ GeV and $AB = (LL, RR, LR, RL)$. Constraints from $BR(B \to X_s\gamma)$, $A_{CP}(B \to X_s\gamma)$, $BR(B \to X_s l^+ l^-)$ and the lower bound on ΔM_s have been used.

9.3 Bounds on R-Parity Violation with $B \to \phi\pi$ Decays

In principle one can include in the supersymmetric Lagrangian general terms which are gauge-invariant and renormalizable which violate the total lepton number (L) by one unit or the barion number (B) by one unit. The existence of such terms is allowed in general by the Supersymmetric theories, but it is disturbing, since it corresponds to $B-$ and $L-$violating processes that have not seen experimentally. The most stringent experimental constraint comes from the non-observation of proton decay, which would violate both B and L by one unit. Feynman diagrams like the ones in Fig. 9.5 would lead to $p^+ \to e^+\pi^0$ (shown) or e^+K^0 or $\mu^+\pi^0$ or μ^+K^0 or $\nu\pi^+$ or νK^+ etc. As a rough estimate based on

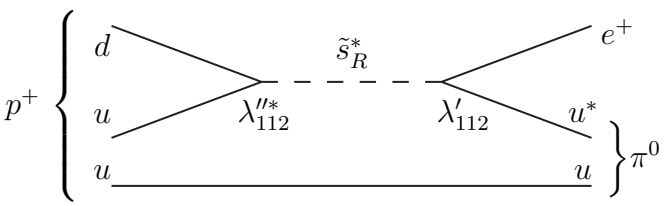

Figure 9.5: Squarks would mediate disastrously rapid proton decay if R-parity were violated by both ΔB = 1 and ΔL = 1 interactions. This example shows $p \to e^+\pi^0$ mediated by a strange (or bottom) squark.

dimensional analysis, for example, the lifetime would be a tiny fraction of a second if the couplings were of order unity and the squarks have masses of order 1 TeV. In contrast, the decay time of the proton into lepton+meson final states is known experimentally to be in excess of 10^{32} years. Many other processes also give strong constraints on the violation of lepton and baryon numbers [109, 110]. Instead of postulating the conservation of B and L numbers, in Supersymmetry usually a new symmetry is introduced, called *R-parity* or equivalently *matter parity* [111]. Matter parity is a multiplicatively conserved quantum number defined as

$$P_M = (-1)^{3(B-L)} \tag{9.10}$$

for each particle of the theory. The R-parity assignment is very useful for phenomenology because all of the Standard Model particles and the Higgs bosons have even R-parity ($P_R = +1$), while all of the squarks, sleptons, gauginos, and higgsinos have odd R-parity ($P_R = -1$). The conservation of R-parity has the consequence of reduce B and L violation to tiny amount.

The measured limits on the decay rate of $B \to \phi\pi$ decays (Chapt. 8) can be used to put constraints on R-parity violating couplings λ' and λ''.

In the Standard Model, the effective Hamiltonian for a $b \to ds\bar{s}$ transition is:

$$\mathcal{H}_{eff} = -\frac{4G_F}{\sqrt{2}} V_{tb}V_{td}^* \sum_{i=3}^{10} C_i O_i \ . \tag{9.11}$$

where the operators relevant here are given in [86]. The QCD factorization approach allows to calculate the amplitude for $B \to \phi\pi$ in Eq. 8.1 accounting also for possible non-factorizable contributions. In this framework, the non-factorizable contributions to $B^- \to \phi\pi^-$ can be obtained by calculating the diagrams in Fig. 9.6. The computation

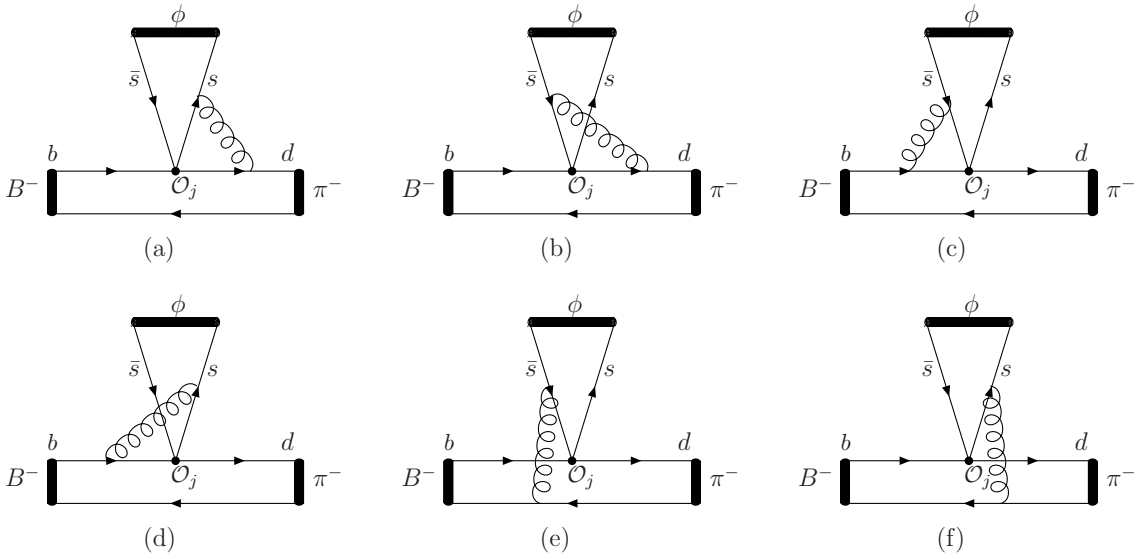

Figure 9.6: Non-factorizable diagrams for $B^- \to \phi\pi^-$.

of the amplitudes, including the non-factorizable terms, can be found in [87]. The expected branching fractions are $\mathcal{B}(B^\pm \to \phi\pi^\pm) = 2\mathcal{B}(B^0 \to \phi\pi^0) = 2.0^{+0.3}_{-0.1} \times 10^{-8}$. The non-factorizable contributions dominate these decays and there is no isospin symmetry breaking because annihilation contributions are absent.

The supersymmetric contributions which can violate R-parity are expressed by trilinear terms in the *superpotential* W. The superpotential is the analytic function of the superfields of the theory[1], which describe the model [97].

The amount of R-parity violation depends on the magnitude of the trilinear coupling constants λ'_{ijk} and λ''_{ijk}, where i, j, k are generation indices. Allowing these terms in the

[1]A superfield is a single object that contains as components all of the bosonic, fermionic and auxiliary fields within the corresponding super-multiplet.

effective Hamiltonian the amplitude of $B^- \to \phi\pi^-$ is

$$\begin{aligned} A^{\not R}(B^- \to \phi\pi^-) &= -\frac{1}{8m^2_{\tilde{\nu}_i}}\left(\lambda'_{i21}\lambda'^*_{i23} + \lambda'^*_{i12}\lambda'_{i32}\right)\eta^{-8/\beta_0} f_\phi F^{B\to\pi}(m^2_\phi) M_B^2 \left[\frac{1}{N_c} + \frac{\alpha_s}{4\pi}\frac{C_F}{N_c}\left(-F_\phi - 12\right)\right] \\ &\quad -\frac{1}{2m^2_{\tilde{u}_i}}\lambda''_{i23}\lambda''^*_{i12}\eta^{-4/\beta_0} f_\phi F^{B\to\pi}(m^2_\phi) M_B^2 \left(\frac{2}{3} - \frac{\alpha_s}{4\pi}\frac{C_F}{N_c}F_\phi\right), \end{aligned} \tag{9.12}$$

where $\eta = \frac{\alpha_s(m_{\tilde{f}_i})}{\alpha_s(m_b)}$ and $\beta_0 = 11 - \frac{2}{3}n_f$, f_B and f_ϕ are the B and ϕ decay constant, respectively, $N_c = 3$ (SU(3) colors) and $F^{B\to\pi}(m^2_\phi)$ is the B the form factor ($F^{B\to\pi}(0) = 0.28$). F_ϕ is the term describing the long-distance QCD dynamics of the matrix elements of quarks for the ϕ meson [87].

Assuming that only one sfermion contributes at a time and they have a mass of 100 GeV/c^2, the limits on the R-parity violating trilinear coupling constants (in terms of products of λ's) are shown in Fig. 9.7.

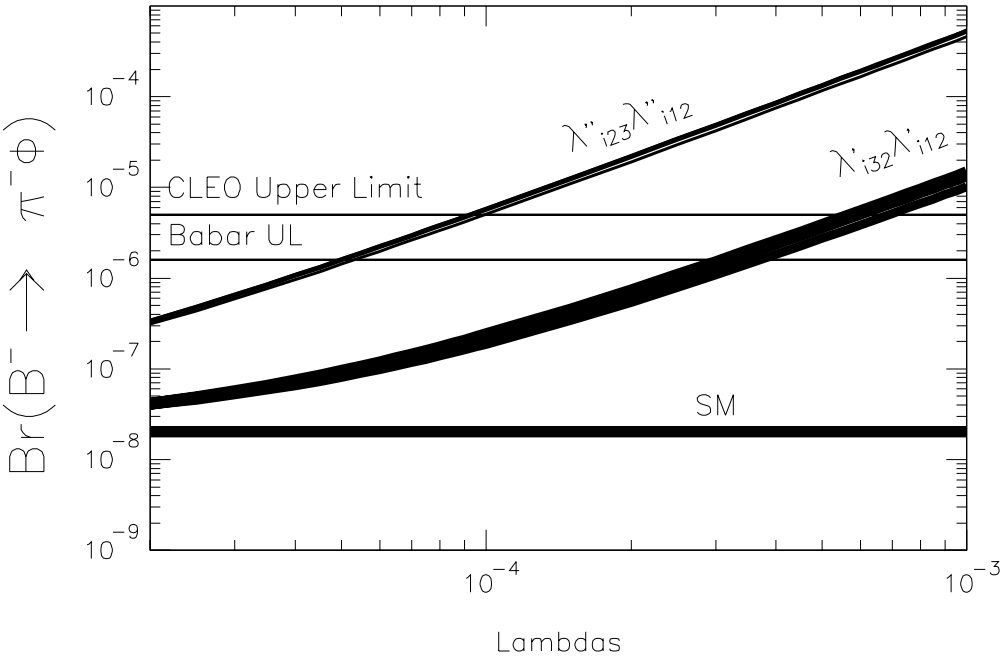

Figure 9.7: The branching ratio of $B^- \to \phi\pi^-$ as a function of the RPV couplings $|\lambda''_{i23}\lambda''^*_{i12}|$(upper curve), $|\lambda'_{i23}\lambda'_{i21}|$ and $|\lambda'_{i32}\lambda'_{i12}|$ (lower curve) respectively. The thickness of curves represent theoretical uncertainties. The horizontal lines are the upper limits and the SM prediction as labeled respectively. The $B^- \to \phi\pi^-$ upper limit we set on *BABAR*'s 210 fb^{-1} dataset is smaller than the one displayed: $\mathcal{B}(B^- \to \phi\pi^-) < 2.4 \times 10^{-7}$ (Table 8.16).

Conclusions

In this work we presented measurements of *CP* violation and decay rates of B decays in final states not involving a charm quark in the final state. In particular, the time-dependent *CP* asymmetries of decays which proceed through $b \to s$ elementary transition is a particularly sensitive probe of physics beyond the Standard Model. In fact, even if the precise measurements of *CP* conserving and *CP* violating processes show the success of the CKM picture of the flavour physics, the sector of $b \to s$ transitions is still not strongly constrained and leaves room for new physics contributions.

In particular, we considered the decays which have the cleanest theoretical prediction within the Standard Model: $B^0 \to \phi K^0$ and $B^0 \to K^0_S K^0_S K^0_S$ ($\beta^{SM}_{eff} = 0.379$). We examined the former with a completely new approach with respect to the past: the study of *CP* violation in the whole $K^+K^-K^0$ phase space through a time-dependent Dalitz plot analysis. With this approach, we simultaneously measured the *CP*-violating asymmetries of the ϕK^0, $\mathsf{f_0(980)K^0}$ resonant and $K^+K^-K^0$ non-resonant contributions, avoiding one of the largest uncertainties which affected the previous measurements of $B^0 \to \phi K^0$. We find $\beta_{eff}(B^0 \to \phi K^0) = 0.06 \pm 0.16 \pm 0.05$, which is lower than the Standard Model expectation, but it is consistent with it within two standard deviations.

Moreover, only a recently developed experimental technique, which allows the determination of the position of B decay vertex when no charged tracks are originating from it, has made possible the measurement of the time-dependent *CP* asymmetry in $B^0 \to K^0_S K^0_S K^0_S$ decays.

The mixing-induced *CP* parameter S in the Standard Model should be equal to $\sin 2\beta$ parameter, which is measured with high precision in $B \to [c\bar{c}]K^0$ decays by the B-factories. This statement is true, in the Standard Model, with excellent approximation for the decays studied in this work. The summary of the measurements in the $b \to s$ sector is shown in Fig. 9.8

A naive average of the $b \to s$ penguins, which does not account for the correlations

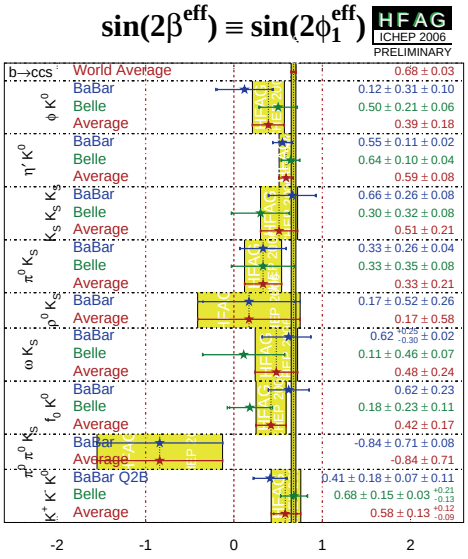

Figure 9.8: Summary of results, updated at the time of ICHEP 06 conference, of $-\eta_{CP} \times S \approx \sin 2\beta_{eff}$ from $b \to s$ penguin B decays.

existing among ϕK^0, $f_0(980)K^0$ and $K^+K^-K^0$, and that includes also modes with larger theoretical uncertainties, shows that $-\eta_{CP} \times S$ is lower than $\sin 2\beta$. This is not an evidence of physics beyond the Standard Model, but the systematic deviation from the expected value is an hint that there is room for it.

More compelling evidence for new physics could be obtained measuring significant deviation in each decay channel from Standard Model prediction. Currently all the measurement are statistically limited and therefore an increase in accumulated statistics will shed more light into this quest for New Physics.

Bibliography

[1] Wu, C.S.,Ambler, E., Haywood, R. W., Hoppes, D. D., and Hudson, R. P. (1957). Phys. Rev. **105**, 1413.

[2] Goldhaber, M., Grodzins, L., and Sunyar, A. W. (1958). Phys. Rev. **109**, 1015.

[3] J.H. Christenson, J.W. Cronin, V.L. Fitch, and R. Turlay, Phys. Rev. Lett. **13** (1964).

[4] Sakharov, A. D. (197). JETP Letters **5**, 24.

[5] N. Cabibbo, Phys. Rev. Lett. **10**, 531 (1963); M. Kobayashi and T. Maskawa, Prog. Th. Phys. **49**, 652 (1973).

[6] *BABAR* Collaboration, B. Aubert et al., Phys. Rev. Lett. **87**, 091801 (2001).

[7] BELLE Collaboration, K. Abe et al., Phys. Rev. Lett. **87**, 091802 (2001).

[8] S.L. Glashow, Nucl. Phys. **22**, 579 (1961);
S. Weinberg, Phys. Rev. Lett. **19**, 1264 (1967);
A. Salam, in *Procceedings of the 8th Nobel Symposium*, ed. N. Swartholm, Almquist and Wiksells, Stockholm (1968).

[9] C. Jarlskog, Phys. Rev. Lett. **55**, 1039 (1985);

[10] L. L. Chau and W. Y. Keung, Phys. Rev. Lett. **53**, 1802 (1984).

[11] A. J. Buras and R. Fleischer, (1997) hep-ph/9704376, to appear in *Heavy Flavours II*, World Scientific, eds. A. J. Buras and M. Linder.

[12] L. Wolfenstein, Phys. Rev. Lett. **51**, 1945 (1983).

[13] A. J. Buras, M. E. Lautenbacher and G. Ostermaier, Phys. Rev. D **50**, 3433 (1994).

[14] C. O. Dib *et al.*, Phys. Rev. D **41**, 1522 (1990).

[15] V. F. Weisskopf, E. P. Wigner, *Zeitschrift für Physik* **63**, 54. V. F. Weisskopf, E. P. Wigner, *Zeitschrift für Physik* **65**, 18.

[16] A. B. Carter and A. I. Sanda, Phys. Rev. D **45** (1980)

[17] Y. Grossman, G. Isidori and M.P. Worah, Phys. Rev. **D58**, (1998) 057504.

[18] B. Aubert et al., hep-ex/020770

[19] K. Abe et al., hep-ex/0207098

[20] R. Fleischer and T. Mannel, Phys. Lett. **B511**, (2001) 240; G. Hiller, Phys. Rev. **D66**, (2002) 071502; A. Datta, Phys. Rev. **D66**, (2002) 071702; M. Ciuchini and L. Silvestrini, Phys. Rev. Lett. **89**, (2002) 231802; M. Raidal, Phys. Rev. Lett. **89**, (2002) 231803;. Y. Grossman, Z. Ligeti, Y. Nir and H. Quinn, hep-ph/0303171; S. Khalil and E. Kou, hep-ph/0307024

[21] S. Eidelman *et al.* [Particle Data Group], Phys. Lett. B **592**, 1 (2004).

[22] [Heavy Flavor Averaging Group (HFAG)], arXiv:hep-ex/0603003.

[23] *BABAR* Collaboration, B. Aubert *et al.*, Phys. Rev. D **69**, 071101 (2004).

[24] M Neubert, arXiv:hep-ph/9801269

[25] M. Beneke, G. Buchalla, M. Neubert, and C.T. Sachrajda, Phys. Rev. Lett. **83**, 1914 (1999); Nucl. Phys. **B 591**, 313 (2000); *ibid.* B **606**, 245 (2001).

[26] H. Y. Cheng, C. K. Chua and A. Soni, Phys. Rev. D **72**, 094003 (2005) [arXiv:hep-ph/0506268].

[27] C. L. Y. Lee, M. Lu, and M. B. Wise, Phys. Rev. D **46**, 5040 (1992).

[28] H. Y. Cheng and K. C. Yang, Phys. Rev. D **66**, 054015 (2002).

[29] V. V. Anisovich, V. A. Nikonov and A. V. Sarantsev, Phys. Atom. Nucl. **65**, 1545 (2002) [Yad. Fiz. **65**, 1583 (2002)] [arXiv:hep-ph/0102338].

[30] UTfit Collaboration, M. Bona *et al.,* [hep-ph/0501199].
CKMfitter Group, J. Charles *et al.,* Eur. Phys. J. C **41**, 1 (2005)

[31] B. Aubert *et al.* [BABAR Collaboration], Phys. Rev. Lett. **93**, 131805 (2004) [arXiv:hep-ex/0403001].

[32] ARGUS Collaboration, *Z. Phys.* **C48**, 543 (1990)

[33] R. E. Kalman, "Transactions of the ASME-Journal of Basic Engineering", Vol. 82, Series D, 35-45, 1960.
P. Billoir, Nucl. Instr. and Meth. A **225** (1984) 225.
W. D. Hulsbergen, "Decay Chain Fitting with a Kalman Filter", Nucl. Instrum. Meth. A **552**, 566-575 (2005) [arXiv:physics/0503191].

[34] Dalitz R.H., Phil. Mag. **44**, 1068 (1953).

[35] A. E. Snyder and H. R. Quinn, Phys. Rev. D **48**, 2139 (1993).

[36] J. Charles, A. Le Yaouanc, L. Oliver, O. Pene and J. C. Raynal, Phys. Lett. B **425**, 375 (1998) [Erratum-ibid. B **433**, 441 (1998)] [arXiv:hep-ph/9801363].

[37] B. Aubert *et al.* [BABAR Collaboration], Phys. Rev. Lett. **94**, 161803 (2005) [arXiv:hep-ex/0408127].

[38] K. Abe *et al.* [Belle Collaboration], [arXiv:hep-ex/0507037].

[39] E.P. Wigner, Phys. Rew. **70** (1946) 15.

[40] E.P. Wigner and L.Eisenbud, Phys. Rew. **72** (1947) 29.

[41] R.H. Dalitz and S. Tuan, Ann. Phys. **10** 1960 307.

[42] W.Heisenberg, Z.Phy. **120** (1943) 513

[43] K.L. Au, D. Morgan, M.R. Penningtom, Phys. Rew. D**35** (1987) 1633

[44] JP Cummings, DP Weygand - Brookhaven Report BNL-64637, unpublished (1997) - phy.bnl.gov

[45] J. Blatt and V.E. Weisskopf, Theoretical Nuclear Physics, Willey (N.Y.) (1952),p.361

[46] C. Zemach, Phys. Rev. **133**, B1201 (1964).

[47] F.v. Hippel and C. Quigg, Phys. Rev **5** (1972) 624

[48] S. M. Flatté, Phys. Lett. B **63**, 228 (1976).

[49] I. J. R. Aitchison, Nucl. Phys. **A189**, 417 (1972).

[50] S. Fajfer, R. J. Oakes and T. N. Pham, Phys. Rev. D **60**, 054029 (1999) [arXiv:hep-ph/9812313].

[51] S. Fajfer, T. N. Pham and A. Prapotnik, Phys. Rev. D **70**, 034033 (2004) [arXiv:hep-ph/0405065].

[52] B. Aubert *et al.* [BABAR Collaboration], Nucl. Instrum. Meth. A **479**, 1 (2002) [arXiv:hep-ex/0105044].

[53] D.N. Brown, E.A. Charles, D.A. Roberts, The *BABAR* Track Fitting Algorithm, *Proceedings of ICHEP 2000*, Padova, Italy (2000).

[54] A. Dresher, *et al.* Nucl. Instr. Methods **A237**, 484 (1985)

[55] P. F. . Harrison and H. R. . Quinn [BABAR Collaboration], "The BaBar physics book: Physics at an asymmetric B factory," SLAC-R-0504 *Papers from Workshop on Physics at an Asymmetric B Factory (BaBar Collaboration Meeting), Rome, Italy, 11-14 Nov 1996, Princeton, NJ, 17-20 Mar 1997, Orsay, France, 16-19 Jun 1997 and Pasadena, CA, 22-24 Sep 1997*

[56] F. Zernike, Physica 1, 689-704, 1934

[57] J. Irion [Crystal Ball Collaboration], SLAC-PUB-3643 *Invited talk given at 1985 Int. Conf. on Hadron Spectroscopy, College Park ,MD, Apr 20-22, 1985*

[58] H. W. Bertini, ORNL-3383 http://www.slac.stanford.edu/spires/find/hep/www?r=ornl-3383 [SPIRES entry]

[59] H. J. Yang, B. P. Roe and J. Zhu, arXiv:physics/0508045.

[60] B. P. Roe, H. J. Yang, J. Zhu, Y. Liu, I. Stancu and G. McGregor, Nucl. Instrum. Meth. A **543**, 577 (2005) [arXiv:physics/0408124].

[61] D. E. Goldberg, "Genetic Algorithms in Search Optimization and Machine Learning", Addison Wesley (1989).

[62] G. Organtini, Int. Jour. Mod. Phys. **C6**, 605 (1995).

[63] G. Cavoto and F. Ferroni, *BABAR Note* # 377, (1997).

[64] C. M. Bishop, "Neural Networks for pattern recognition", Oxford University Press (1995).

[65] M. Artuso *et al.* [CLEO Collaboration], Phys. Rev. D **70** (2004) 112001 [arXiv:hep-ex/0402040].

[66] M. Beneke, Phys. Lett. B **620**, 143 (2005) [arXiv:hep-ph/0505075].

[67] G. Buchalla, G. Hiller, Y. Nir and G. Raz, JHEP **0509**, 074 (2005) [arXiv:hep-ph/0503151].

[68] G. Fox, S. Wolfram, Nucl. Phys. **B149**, 413 (1979).

[69] S. L. Wu, Phys. rep. **107**, 59 (1984)

[70] S. Brandt, *et al.*, Phys. Rev. Lett. **12**, 57 (1964). E. Farchi, Phys. Rev. Lett. **39**, 1587 (1977).

[71] R. A. Fisher, *Annals of Eugenics* **7**, 179 (1936). M. G. Kendall, A. Stuart, "The Advanced Theory of Statistics", Vol. III, 2nd Ed., *Hafner Publishing*, NY (1968).

[72] B. Aubert *et al.* [BABAR Collaboration], Phys. Rev. Lett. **93**, 231804 (2004) [arXiv:hep-ex/0408017].

[73] B. Aubert *et al.* [BABAR Collaboration], Phys. Rev. Lett. **87**, 151801 (2001) [arXiv:hep-ex/0105001].

[74] H. Albrecht *et al.* [ARGUS Collaboration], "Exclusive Hadronic Decays Of B Mesons", Z. Phys. C **48** 543 (1990)

[75] A. Garmash *et al.* [BELLE Collaboration], Phys. Rev. D **71**, 092003 (2005) [arXiv:hep-ex/0412066].

[76] B. Aubert *et al.* [BABAR Collaboration], [arXiv:hep-ex/0605003].

[77] B. Aubert *et al.* [BABAR Collaboration], Phys. Rev. D **71**, 091102 (2005) [arXiv:hep-ex/0502019].

[78] P. Minkowski and W. Ochs, Eur. Phys. J. C **39**, 71 (2005) [arXiv:hep-ph/0404194].

[79] M. Ablikim *et al.* [BES Collaboration], Phys. Lett. B **607**, 243 (2005) [arXiv:hep-ex/0411001].

[80] M. Pivk and F. R. Le Diberder, Nucl. Instrum. Meth. A **555**, 356 (2005) [arXiv:physics/0402083].

[81] M. Gronau and J. L. Rosner, Phys. Rev. D **72**, 094031 (2005) [arXiv:hep-ph/0509155].

[82] B. Aubert *et al.* [BABAR Collaboration], Phys. Rev. D **72**, 072003 (2005) [arXiv:hep-ex/0507004].

[83] O. Long *et al.*, Physical Review D **68**, 034010 (2003)

[84] T. Gershon and M. Hazumi, Phys. Lett. B **596**, 163 (2004).

[85] N. Brambilla *et al.*, "Heavy quarkonium physics", [arXiv:hep-ph/0412158]

[86] A. J. Buras and L. Silvestrini, Nucl. Phys. B **569** (2000) 3 [arXiv:hep-ph/9812392].

[87] S. Bar-Shalom, G. Eilam and Y. D. Yang, Phys. Rev. D **67**, 014007 (2003).

[88] Y. Grossman *et al.*, Phys. Rev. D **68**, 015004 (2003). [arXiv: hep-ph/0303171]

[89] B. Aubert [BABAR Collaboration], arXiv:hep-ex/0607107.

[90] K. Abe [Belle Collaboration], arXiv:hep-ex/0608039.

[91] A. Ali and D. London, Nucl. Phys. Proc. Suppl. **54A**, 297 (1997) [arXiv:hep-ph/9607392].

[92] A. J. Buras, arXiv:hep-ph/9610461.

[93] Y. Nir, Lectures presented in the 20th SLAC Summer Institute, SLAC-PUB-5874 (1992); Y. Nir and H.R. Quinn, Ann. Rev. Nucl. Part. Sci. **42** (1992) 211; I. Dunietz, Ann. Phys. **184** (1988) 350.

[94] C. Dib, D. London and Y. Nir, Int. J. Mod. Phys. **A6** (1991) 1253; T. Goto, N. Kitazawa, Y. Okada and M. Tanaka Phys. Rev. D **53** (1996) 6662; J.P. Silva and L. Wolfenstein, CFNUL-96-09, hep-ph/9610208.

[95] N.G. Deshpande, B. Dutta and S. Oh, Phys. Rev. Lett. **77** (1996) 4499.

[96] M. Beneke, G. Buchalla, M. Neubert and C. T. Sachrajda, Nucl. Phys. B **606**, 245 (2001) [arXiv:hep-ph/0104110].

[97] For a phenomenologically oriented review, see:
P. Fayet and S. Ferrara, Phys. Rep. **32C**77249;
H.P. Nilles, Phys. Rep. **110C**841.
For spontaneously broken N=1 supergravity, see:
E. Cremmer, S. Ferrara, L. Girardello and A. Van Proeyen, Nucl. Phys. B **212**83413 and references therein.
For a complete primer, see:
S. P. Martin, arXiv:hep-ph/9709356.

[98] L.J. Hall, V.A. Kostelecky and S. Raby, Nucl. Phys. B **267** (1986) 415.

[99] M.J. Duncan, Nucl. Phys. B **221** (1983) 285;
J.F. Donoghue, H.P. Nilles and D. Wyler, Phys. Lett. B **128** 1983 55.

[100] S. Khalil and E. Kou, Phys. Rev. Lett. **91**, 241602 (2003) [arXiv:hep-ph/0303214].

[101] M. Ciuchini, E. Franco, A. Masiero and L. Silvestrini, Phys. Rev. D **67**, 075016 (2003) [Erratum-ibid. D **68**, 079901 (2003)] [arXiv:hep-ph/0212397].

[102] F. Gabbiani, E. Gabrielli, A. Masiero and L. Silvestrini, Nucl. Phys. B **477**, 321 (1996) [arXiv:hep-ph/9604387].

[103] A. Abulencia *et al.* [CDF Collaboration], arXiv:hep-ex/0609040.

[104] P. Gambino and M. Misiak, Nucl. Phys. B **611** (2001) 338 [arXiv:hep-ph/0104034].

[105] M. Ciuchini *et al.*, JHEP **0107** (2001) 013 [arXiv:hep-ph/0012308].

[106] D. Becirevic, V. Gimenez, G. Martinelli, M. Papinutto and J. Reyes, JHEP **0204** (2002) 025 [arXiv:hep-lat/0110091]; see also Nucl. Phys. Proc. Suppl. **106** (2002) 385 [arXiv:hep-lat/0110117].

[107] M. Ciuchini, E. Franco, G. Martinelli, M. Pierini and L. Silvestrini, Phys. Lett. B **515** (2001) 33 [arXiv:hep-ph/0104126]; arXiv:hep-ph/0208048.

[108] V. Porretti, L. Silvestrini, by a private communication.

[109] F. Zwirner, Phys. Lett. B **132**, 103 (1983); S. Dawson, Nucl. Phys. B **261**, 297 (1985); R. Barbieri and A. Masiero, Nucl. Phys. B **267**, 679 (1986);

[110] For a review, see G. Bhattacharyya, Nucl. Phys. Proc. Suppl. **52A**, 83 (1997) [hep-ph/9608415];

[111] S. Dimopoulos and H. Georgi, Nucl. Phys. B **193**, 150 (1981); S. Weinberg, Phys. Rev. D **26**, 287 (1982);

Acknowledgements

The experience of my Ph.D. course has been a fortunate one, because of working on the right topics, with the right people, in the right moment. By sure the master artificer of this circumstance is Fernando Ferroni, which inspired to me the enthusiasm for this work, and for teaching the critical ability to look at physics that cannot be read on books.
But the succes of this four years-long work can be easily addressed to the "charmless group", Gianluca Cavoto and Maurizio Pierini, with their patience and wisdom which guided me day by day. I am particularly grateful to them for the respect of my ideas and for they having been not simply supervisors, but collegues.
I cannot also forget the year of strict collaboration with Marco Vignati, the 4 a.m. exciting bug solving and the Saturday perl sessions. Once I have considered Fabio Bellini the best friend of the undergrad, then it has been the best friend of the Ph.D., I begin to suspect he is the best friend in general. I have also been fortunate for having shared the *BABAR* experience with very good friends, like Giacinto and Viola, from which I learned more than what I tried to give in term of experience.
I also remember with pleasure the time spent at SLAC with Marco Bomben, Francesco and Alessia, for sharing the same worries during the Ph.D. course. Er Conte and Emmanuele also have been important characters for the life in the "baita", for the relaxing periods with me. Silvia in this years shared with me all the thoughts and feelings about people and situations, with incredible agreement. Marcella has been always an example of vitality and creativity in physics such as in life.
And I have also have been surrounded by my friends, David, Mauro, Simone, and my family (a particular thought goes to E.L.), which always gave me strenght and inspiration.